Proceedings

International Conference on Nuclear Science and Technology

Nuclear Society Of Iran | Atomic Energy Organization of Iran | Nuclear Sciences and Technologies Research Institute

Papers on:

Radiation Applications (Industry, Medical And Environment) 2

*In this booklet, you will find the selected papers presented at the **First International Conference on Nuclear Science and Technology**, held from May 6-8, 2024, in Isfahan, Iran.*
We hope you find it informative and enjoyable!

ICNST 2024

Contact and Accessibility
icnst2024.com
registration@icnst2024.com


بسم الله الرحمن الرحیم

The Conference President's Message
ICNST 2024

Attendees, guests, and colleagues

I would like to warmly welcome you to the first International Conference on Nuclear Science and Technology (ICNST 2024). It has been a real honor and privilege to serve as the president of this conference. The conference this year has brought together an incredible diversity of authors and speakers from universities, government, and industry to share ideas and new perspectives on a wide range of radiation applications, nuclear reactors, particle accelerators, radiation measurements, fusion and plasma, stable and radioactive isotopes, radiation safety and security, nuclear agriculture, fuel cycle, lasers, education and training and nuclear governance.

Climate change, a new topic which has been added to this year's agenda as an important worldwide issue. a matter that has been brought up as a critical concern at the majority of IAEA conferences and nuclear scientific assemblies in recent years.

Panel discussions and exhibitions are being introduced as side activities in an attempt to keep this scientific meeting from becoming one-dimensional and increase its effectiveness.

More than 520 complete papers have been approved for this conference; when combined with the additional panels, get-togethers, and side activities, it is anticipated that over 1000 people will attend in person in the historical and touristic city of Isfahan. We look forward to welcoming participants to share their practical ideas and to enjoy an academical and cultural three days in Isfahan.

I'll close by wishing you everyone an incredible, instructive, and transformative experience during ICNST2024 and I hope that this conference can pave the route for academic materials to be used in industry and everyday life.

Prof. Javad Karimi-Sabet
President of ICNST2024
Javad Karimi-Sabet

welcome statment of scientific secretary ICNST 2024

"In the name of God, the Merciful,

Prior to giving the stage to address this distinguished forum, let me take this opportunity to express our deep gratitude, on behalf of all attendees, for His Excellency Mr. Islami's scientific, educational, and motivational remarks, as well as for his excellent organization of this conference.

I would also like to express our appreciation to His Excellency Dr. Mortazavi, Governor-General of Isfahan Province, for his constructive and useful support in enabling this meeting to take place.

This is a great pleasure and honor to extend a warm greeting to each and every one of you for the International Conference on Nuclear Science and Technology, scheduled from May 6th to May 8th, 2024, in the historic city of Isfahan, Iran.

With the aim of advancing our knowledge of nuclear science and technology, this conference is a major global convergence of experts, researchers, and practitioners. It is a platform for the sharing of creative concepts, the presentation of state-of-the-art research, and the formation of cooperative alliances.

As the scientific secretary of this prestigious event, I am particularly excited about the diverse array of participants expected to grace us with their presence. From the esteemed scientists and engineers of Russian universities and research centers to representatives from Islamic countries, friendly nations, and beyond, this conference promises to be a melting pot of perspectives, experiences, and expertise.

The extensive coverage of this conference is another aspect of its uniqueness. We have nearly 900 participants representing 22 countries around the world. Of the 900 participants, 620 are authors covering 13 major topics. There are 421 papers for oral and poster presentations, with additional documents for publication in ISC journals. There will be 3 plenary sessions, 16 panel discussions, 20 parallel oral presentation sessions, and 3 poster sessions.

Prof. Hosein Afarideh
Scientific Secretariat of ICNST2024

Organizers

Nuclear Society Of Iran (NSI)

Atomic Energy Organization of Iran (AEOI)

Nuclear Science and Technology Research Institute (NSTRI)

Scientific Partnership

International Atomic Energy Agency (IAEA)

Isfahan University

Sharif University

Kurchatov Institute

Amirkabir University of Technology (Tehran Polytechnique)

Shahid Beheshti University

Isfahan University of Technology

Shiraz University

Islamic Azad University

K. N. Toosi University of Technology

Ferdowsi University of Mashhad

Kerman Graduate University of Technology

Sahand University of Technology

University of Tabriz

Islamic World Scieence Citation Center

Journal of Nuclear Science and Technology (JonSat)

Radiation Physics and Engineering journal

Nuclear Watch

Cooperative Organization

Isfahan Governorate

Isfahan Municipality

Abbasi Hotel

Iran Atomic Energy Production & Development Co.

Iran's Nuclear Raw Materials & Fuel Production Co.

Radiation Application Development Co.

Ofogh Consulting Engineers Co.

Nuclear Power Plant Safety Development & Promotion Co.

Nuclear Power Plant Engineering & Construction Co.

Engineering & Design of Industrial Simulator Co.

Energy Industry Development Engineering Co

Atomic Power Plant Pepair & support

Nuclear Reactors Fuel Co.

Iran Radioactive Waste Management Co.

Mesbah Energy Co.

Iran Gharb Industrial, Mining and Energy Co.

Pars Isotope Co.

Center for Laser Science & Technology of Iran

Centrifuge Production of Iran Co.

Plasma Technology Development Co.

Rasa Technology and Innovation Center

Behyaar Sanaat Sepahan Co.

Nuclear Data Base of Iran (NDB)

Parto think tank (strategic studies of nuclear industry development)

International Conference Alerts

Local Scientific Board

RAW	NAME	ROLE	AFFILIATION
1	**Prof. Hossein Afarideh**	**Chairman of Local Scientific Board**	**Amirkabir University of Technology (Tehran Polytechnique)(AUT)**
2	**Prof. Mohammad Ghanadi Maragheh**	**Member of The Local Scientific Board**	**Nuclear Science and Technology Research Institute of Iran (NSTRI)**
3	**Prof. Mohammad Lamei Rashti**	**Member of The Local Scientific Board**	**Nuclear Science and Technology Research Institute of Iran (NSTRI)**
4	**Prof. Mohammad Bagher Ghofrani**	**Member of The Local Scientific Board**	**Sharif University of Technology (SUT)**
5	**Prof. Hosein Faghihian**	**Member of The Local Scientific Board**	**University of Isfahan (UI)**
6	**Prof. Javad Rahighi**	**Member of The Local Scientific Board**	**Institute for Research in Fundamental Sciences (IPM)**
7	**Prof. Seyed Amirhossein Feghhi**	**Member of The Local Scientific Board**	**Shahid Beheshti University (SBU)**

Scientific Committee

RAW	NAME	ROLE	AFFILIATION
1	**Prof. Ali Akbar Salehi**	**Member of The Scientific Committe**	**Sharif University of Technology (SUT)**
2	**Prof. Seyyed Javad Ahmadi**	**Member of The Scientific Committe**	**Nuclear Science and Technology Research Institute of Iran (NSTRI)**
3	**Prof. Farhoud Ziaee**	**Member of The Scientific Committe**	**Nuclear Science and Technology Research Institute of Iran (NSTRI)**
4	**Prof. Saeed Hamidi**	**Member of The Scientific Committe**	**University of Arak**
5	**Prof. Seyedzafarollah Kalantari**	**Member of The Scientific Committe**	**Isfahan University of Technology (IUT)**
6	**Prof. Naser Bagheri Moghaddam**	**Member of The Scientific Committe**	**National Research Institute for Science Policy (NRISP)**
7	**Prof. Naser Vosoghi**	**Member of The Scientific Committe**	**Sharif University of Technology (SUT)**
8	**Prof. Seied Rabi Mahdavi**	**Member of The Scientific Committe**	**Iran University of Medical Sciences**
9	**Prof. Meisam Torab Mostaedi**	**Member of The Scientific Committe**	**Nuclear Science and Technology Research Institute of Iran (NSTRI)**
10	**Prof. Fereydoun Abbasi Davani**	**Member of The Scientific Committe**	**Shahid Beheshti University (SBU)**
11	**Prof. Seyed Farhad Masoudi**	**Member of The Scientific Committe**	**K.N.Toosi University of Technology**
12	**Prof. Rasool Ruknizadeh**	**Member of The Scientific Committe**	**University of Isfahan (UI)**
13	**Prof. Gholamreza Raeesali**	**Member of The Scientific Committe**	**Nuclear Science and Technology Research Institute of Iran (NSTRI)**
14	**Prof. Asghar Sedighzadeh**	**Member of The Scientific Committe**	
15	**Prof. Hossein Kazeminejad**	**Member of The Scientific Committe**	**Nuclear Science and Technology Research Institute of Iran (NSTRI)**

RAW	Name	role	Affiliation
16	**Prof. Seyyed Jaber Safdari**	**Member of The Scientific Committe**	**Nuclear Science and Technology Research Institute of Iran (NSTRI)**
17	**Prof. Omid Reza Kakuee**	**Member of The Scientific Committe**	**Nuclear Science and Technology Research Institute of Iran (NSTRI)**
18	**Prof. Alireza Keshtkar**	**Member of The Scientific Committe**	**Nuclear Science and Technology Research Institute of Iran (NSTRI)**
19	**Prof. Fereshte Haj esmail Beigi**	**Member of The Scientific Committe**	**Nuclear Science and Technology Research Institute of Iran (NSTRI)**
20	**Prof. Masoud Mahjour-shafiei**	**Member of The Scientific Committe**	**Nuclear Science and Technology Research Institute of Iran (NSTRI)**
21	**Prof. Mahmoud Payami Shabestar**	**Member of The Scientific Committe**	**Nuclear Science and Technology Research Institute of Iran (NSTRI)**
22	**Prof. Ali Bahrami Samani**	**Member of The Scientific Committe**	**Nuclear Science and Technology Research Institute of Iran (NSTRI)**
23	**Dr. Farhanaz Motamedi**	**Member of The Scientific Committe**	**Nuclear Science and Technology Research Institute of Iran (NSTRI)**
24	**Dr. Faezeh Rahmani**	**Member of The Scientific Committe**	**K.N.Toosi University of Technology**
25	**Dr. Ebrahim Moghiseh**	**Member of The Scientific Committe**	**Nuclear Science and Technology Research Institute of Iran (NSTRI)**
26	**Dr. Iraj Jabari**	**Member of The Scientific Committe**	**University of Isfahan (UI)**
27	**Dr. Nima Ghal-Eh**	**Member of The Scientific Committe**	**Ferdowsi University of Mashhad**
28	**Dr. Mitra Athari Alaf**	**Member of The Scientific Committe**	**Islamic Azad University Science and Research Branch**
29	**Dr. Gholamreza Etaati**	**Member of The Scientific Committe**	
30	**Dr. Amir Movafeghi**	**Member of The Scientific Committe**	**Nuclear Science and Technology Research Institute of Iran (NSTRI)**

Executive Committee

RAW	NAME	ROLE
1	Dr. Farshad Ghasemi	Chairman of the Executive Committee
2	Dr. Ehsan Molazadeh	Member of The Executive Committee
3	Dr. Seyyed Ghasem Biniaz	Member of The Executive Committee
4	Mr. Aliakbar Aminidoust	Member of The Executive Committee
5	Ms. Fatemeh Zamani	Member of The Executive Committee
6	Ms. Mahya Pazoki	Member of The Executive Committee
7	Mr. Hosein Maleki	Member of The Executive Committee
8	Mr. Maziar Dalili	Member of The Executive Committee
9	Mr. Shojaei	Member of The Executive Committee
10	Ms. Fatemeh Rezaei	Member of The Executive Committee
11	Mr. Reza Rafiei	Member of The Executive Committee
12	Ms. Seyyedeh Elham Ebrahimi	Member of The Executive Committee

Radiation Applications (Industry, Medical And Environment)

Radiation Applications (Industry, Medical And Environment)

ICNST 2024
International Conference on Nuclear Science and Technology
6- 8 MAY 2024 | Isfahan, Iran

Preoperational radiomonitoring program of near-surface disposal; A Case Study of Anarak Radioactive Waste Repository (Paper ID : 1010)

Zare Ganjaroodi S.[1,2*], Boroumandi A.[2], Pakooyan H.[2], Maleki Farsani A.[2]

[1]*Energy and Physics Department, Amirkabir University of Technology, 424 Hafez Ave., Tehran, Iran*

[2]*Iran Radioactive Waste Company, Atomic Energy Organization of Iran (AEOI), Postcode: 1439955931, Tehran - Iran*

Abstract

According to the IAEA criteria, about 97% of nuclear waste is categorized as Low or Intermediate Level Waste (LLW or ILW). Such waste has been disposed of in near-surface repositories for many years all over the world. The main aim of this study is to investigate the pre-operation radiomonitoring program for near-surface disposal in the Anarak radioactive waste repository in Iran to estimate and analyze parameters such as activity concentration of radionuclides in water and atmosphere. In such a manner, after the site selection process, a comprehensive plan is designed for the Anarak waste repository including, experimental sampling methods, sampling periods, and radionuclides. The results show, based on Iran's regulatory authority, in almost all cases, the environmental radiation was Minimum Detectable Activity (MDA). Finally, all measured values were compared and analyzed with national and international standards to determine the accuracy and precision of the Anarak repository radiomonitoring process.

Keywords: Radioactivity**,** Waste, Radiomonitoring, Pre-operation**,** Repository.

Introduction

The radioactive waste consists of any material that is either intrinsically radioactive or has been contaminated by radioactivity. Government policy dictates whether certain materials such as used nuclear fuel and plutonium are categorized as waste [1-2]. According to the radioactivity level of the elements, nuclear waste is typically classified as LLW, ILW, or High-Level Waste (HLW) [3].

According to International Atomic Energy Agency (IAEA), monitoring is continuous or periodic measurement process which helps to evaluate the waste repository behavior. For near-surface repository, monitoring must be performed in different stages of site evolution, Pre-operational, Operational, and Post-closure. The data pre-operational, which is the most important phase starts from the site selection process and ends with construction facilities. Pre-

operational monitoring is divided into two categories of Baseline and facility monitoring. As the IAEA recommended, important Features, Events, and Processes (FEP) identification, data collection for site selection, and repetition of safety assessment steps must be considered as the main goals of the pre-operational monitoring phase [4].

Most of the LLW is sent to land-based disposal immediately after packaging for long-term management. For about 90% of all types of nuclear waste produced in the world, satisfactory disposal has been developed and is in operation [5]. Several reports and essays on various technical aspects of radiomonitoring programs of radioactive waste repositories have been studied in recent years. In this paper, preoperational radiomonitoring plans of the first near-surface disposal of Iran's radioactive waste repository in Anarak are performed in different steps such as plant, meat, water, and atmosphere. Umar and Onimisi in 2004 studied on Jonah Baseline Measurement of Natural Radioactivity in Soil, vegetation and water in the industrial District of the Federal Capital Territory (FCT) Abuja. Termizi et al, in 2004 investigated on terrestrial gamma radiation dose to determine the baseline for environmental radiological health practices in Melaka state [7]. In 2015, Eke et al, worked on the paper titled 'Baseline Measurements of Natural Radioactivity inSoil Samples from the Federal University of Technology' that is published in applied sicence and technology journal [8]. Laura Guidotti worked on the Gamma-spectrometric measurement of radioactivity in agricultural soils of the Lombardia region in 2015 [9].

Radiomonitoring Program and sampling procedures should be approved by a regulatory body. Other documents entitled source and environment criteria for radiation protection and operators should prepare at least one year before operation. The radiomonitoring program should consider important data including, hydrology, seismicity, geochemistry, population density, land use, meteorological conditions, and geology. Also, the license should keep result records for ten years and annual reports of radiomonitoring for seventy years [10].

Material and method

Anarak Nuclear Repository, a near-surface trench-type repository, is the most suitable site which is selected according to the international atomic energy agency (IAEA) and Iran Nuclear Regulatory Authority (INRA) requirements during 8 years' site selection phase; for both LLW and ILW, which are produced in Bushehr Nuclear Power Plant (BNPP) and other medical and research industrial applications in a period of seventy years. These wastes contain a wide range

of radionuclides including Uranium, Plutonium, Iodine, Technetium, Americium, Strontium, Cobalt, and Cesium.

The Anarak site has located in a syncline structure that consists of lower red formation sediments. The Lower Red Formation is considered as Eocene-Oligocene age with a thickness of about 400 m. This structure with an elevation of approximately 1480 m above means sea level and its bowl shape can act as the best protection against radionuclides migration. The Anarak site is located in the center of Iran and has an area of about 1 Km^2. The nearest town to Anarak disposal site is Anarak with less than 1300 population.

According to geophysical studies, Anarak disposal site does not contain any confined aquifer and the water level reaches a depth of about 300 m. Furthermore, there is not an effective groundwater flow at this depth. The hydrogeological environment is characterized by extremely low hydraulic gradient and low groundwater

recharge. A static hydrodynamic system, low recharge, and ineffective groundwater flow increase alkaline elements and dissolved anions in solutes to produce saline or even saline water sources. Also, underground water will have an alkaline composition and redox conditions due to dry weather, low rainfall, and low permeability. Most drainages are created by ephemeral streams, which carry water only for a short period of the year. Due to Anarak topography, there is not a sufficiently large enough catchment area to cause flood situations. The main sources of fresh drinking water for the surrounding people are wells and aqueducts. Well water is also used for livestock farming and crop irrigation on a small scale. The Anarak city climate data from 2015 to 2020 are listed in **Table 1**.

Table 1. The Anarak city climate profile from 2015 to 2020.

Parameters	Maximum (year)	Minimum (year)	Annual average
Precipitation	96.3	21.2	66.2
Temperatures (C)	42.9	-8.1	19.6
Evaporation	2780	2489	2648.3
Relative Humidity	99.9	1.3	29.6 %
Surface Wind	-	-	2.89

The main goal of radiomonitoring program is to determine and trace the radionuclides in possible pathways. Hence, Radiomonitoring program focuses on the determination of transfer pathways, frequency, numbers, and, the times of sampling. The preoperational radiomonitoring program of the Anarak disposal site is listed in **Table 2**.

Table 2. Preoperational radiomonitoring program design.

Media/Pathway		No. of Samples	Sampling Frequency	Radionuclides
Air	Air	5	Seasonal	**Gamma spectrometry, total alpha and Beta, radon, ^{3}H, and ^{14}C**
	Radon	5		
Soil	On-Site=18 Off-Site= 18		2 times in a year	**Gamma spectrometry, total alpha and Beta, Sr-90**
Sediment	15		2 times in a year	**Gamma spectrometry, total alpha and Beta, Sr-90**
Water resources	Ground water	9	2 times in a year	**Gamma spectrometry total alpha and Beta radon ،^{3}H, and ^{14}C**
	Surface water	6	Seasonal (if there is a surface water)	

Anarak weather is warm and dry, and the average annual rainfall is estimated at 38.6 mm. Due to the lack of surface water flow in this area, it is not possible to take samples of surface water in all seasons. Hence, most of the water sources in this area are underground sources. According to the direction of underground water flow, the location of underground aquifers, population density around sources, proximity to the site and different uses of water sources, three wells, three aqueducts, and three springs among 66 wells, 20 springs, and 83 aqueducts in this area was selected for sampling.

In the present paper, to measure ^{137}Cs, ^{232}Th, ^{226}Ra and, ^{40}K, filtering was performed using concentrated nitric aside on 4.5 liters' sample of water from each point to reduce the pH to less than two. Also, Gamma spectroscopy was carried out using HPGe and ISO10703 [11] method with 60% efficiency. low level Counter apparatus and EPA-900-0 [12] method were used to measure total alpha and Beta. Liquid scintillation spectrometry and ISO 9698 [13] standard were used to measure ^{3}H. Finally, the RAD7 apparatus was used to measure ^{222}Rn.

The airborne radiological monitoring network design for the pre-operational stage is performed according to meteorological, land use, and population data. In this project, a high-volume air sampler pump for aerosols and a radon-specific radionuclide device for radon measurement are used. These pumps should be equipped with an airflow meter, humidity recorder, air pressure recorder, and sampling time recorder. In this research, a high-volume air sampler pump

constructed by the Thermo company was used. The RAD-7 device was used to measure radon and thoron in the air for 24 hours continuously. Compared to other devices, according to the unique energy of alpha particles, this device can distinguish isotopes from each other to minimize interference in their measurement. Also, the RAD-7 counts radon and thoron particles separately and simultaneously with minimal interference [14].

The method used to measure radon and its daughters is based on the high-energy alpha particles released from these radionuclide daughters. Due to the low concentration of radon in the open air, it is possible to increase the quality of recorded data even for lower values using combined methods and long-term radon concentration measurement.

The glass fiber filters have a high collection capability for the particles and do not cause a drop in the pump flow rate. The pore diameter of these filters is in the range of 0.2-4.0 μm. The GF/A filter is an ideal particle sampler for gamma emitter radionuclides and alpha and Beta measurement.

For sampling with a thermo air high-volume sampler, the pump was installed at the station, and its energy was supplied at any point by either a 220 V power supply or a suitable electric motor. The GF-9 filter was used for air sampling at a flow rate of 87 cubic meters per hour for 24 hours for each point. After completion of the air sampling, the filter was opened, folded, and stored in a sample packet. Gamma analysis with HPGe detector type p-coaxial and alpha and Beta analysis with Multi Low Level Counter (LLC) has been performed.

It should be noted that the air volume of flows throws the filter depends on the Maximum Concentration Level (MCL) of radionuclide in the inhalation area of people and the Minimum Detectable Limit (MDL) of the detector. According to the seasonal and annual wind direction data and the population density.

Results and discussion

Results show that, ^{40}K، ^{137}Cs ,and ^{232}Th concentration in nine samples are less than Minimum Detectable Activity (MDA) criteria. The Gamma spectrometry on water samples is listed in **Table 3**. The range Beta particle radioactivity concentration in nine samples is from 0.12 to 0.94. Moreover, this range is from 0.14 to 0.90 for Alfa particles in the same samples. The radioactivity concentration of total alpha and beta particles is presented in **Table 4**. The MDAs are 0.087 and 0.120 $Bq.l^{-1}$ for the Alpha and Beta radioactivity concentration on water samples, respectively. The Radon radioactivity concentration values on water samples are given in **Table 5.**

Table 3. The gamma spectrometry on water samples results.

Sample number	Activity (Bq/Lit)			MDA (Bq/Lit)		
	^{40}K	^{137}Cs	^{232}Th	^{40}K	^{137}Cs	^{232}Th
1	<MDA	<MDA	<MDA	1.16	0.04	0.16
2	<MDA	<MDA	<MDA	1.19	0.03	0.16
3	<MDA	<MDA	<MDA	1.42	0.04	0.16
4	<MDA	<MDA	<MDA	1.56	0.03	0.17
5	<MDA	<MDA	<MDA	1.18	0.03	0.17
6	<MDA	<MDA	<MDA	1.22	0.04	0.16
7	<MDA	<MDA	<MDA	1.52	0.03	0.16
8	<MDA	<MDA	<MDA	1.19	0.03	0.16
9	<MDA	<MDA	<MDA	0.89	0.03	0.11

Table 4. The Alpha and Beta radioactivity concentration on water samples results.

Sample number	Radioactivity concentration (Bq.l^{-1})	
	Beta ± Uncertainty	Alfa ± Uncertainty
1	0.94 ± 0.51	0.32 ± 0.22
2	< MDA	< MDA
3	0.68 ± 0.52	< MDA
4	0.21 ± 0.08	0.19 ± 0.04
5	0.12 ± 0.05	< MDA
6	0.27 ± 0.15	0.28 ± 0.21
7	0.46 ± 0.25	0.90 ± 0.30
8	0.27 ± 0.07	0.14 ± 0.02
9	< MDA	< MDA

Table 5. The Radon radioactivity concentration on water samples results.

Sample number	Avg. RH (%)	Avg. Air Temp (°C)	Avg. Radon (Bq/Lit) ± Uncertainty
1	5.5	27.1	0.57 ± 0.35
2	5.25	27.3	40.42 ± 2.88
3	5.5	27.7	19.65 ± 2.01
4	5.25	27.3	7.69 ± 1.29
5	5.25	27.1	7.57 ± 1.29
6	5.25	27.1	2.39 ± 0.7
7	6.5	27	0.89 ± 0.43
8	6	26.8	4.02 ± 0.91
9	5.75	26.8	16.64 ± 1.76

Five locations, including the center of the disposal site, a distance of about 1 km from the south, southwest, and northwest of the site, as well as the center of Anarak city (RADUS1, RADUS2, RADUS3, RADUS4, and RADUS5, respectively) have been selected for air radioactivity concentration sampling which are based on the prevailing wind in the area and the nearest population centers within the site. The mean radioactivity concentration of Be-7 was 9.99 E-3 Bq/m^3, and other gamma emitter radionuclides were often less than MDA. On the other hand, the highest measured value of gamma radioactivity was for Be-7 radionuclide which is related to RADUS3. The Alpha, Beta and Gamma radioactivity concentration in air samples are demonstrated in **Figs 1 and 2**.

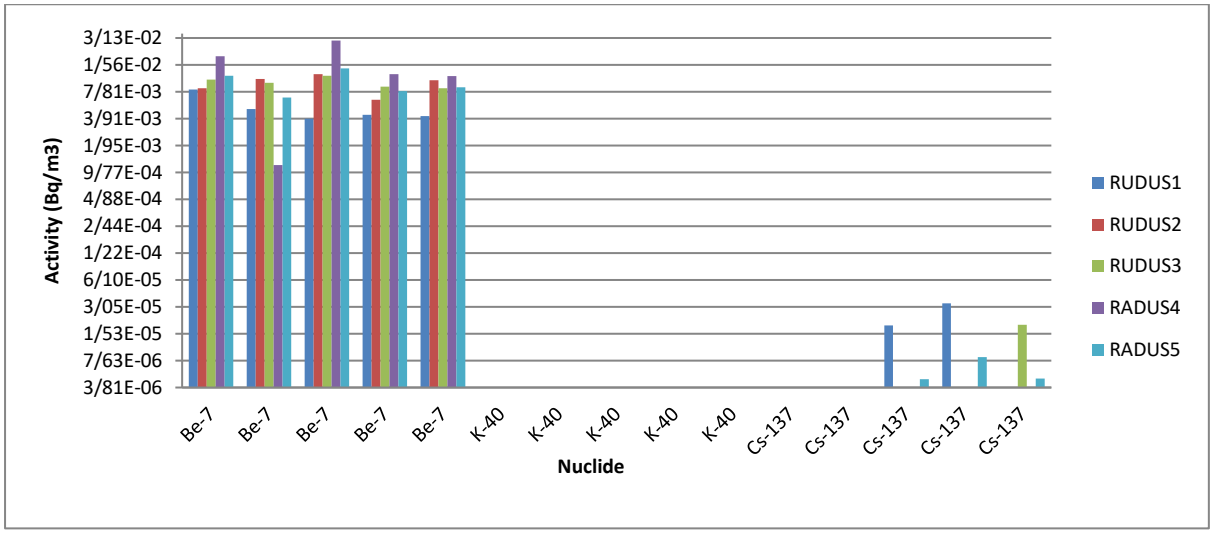

Fig 1. The Gamma radioactivity concentration in air samples.

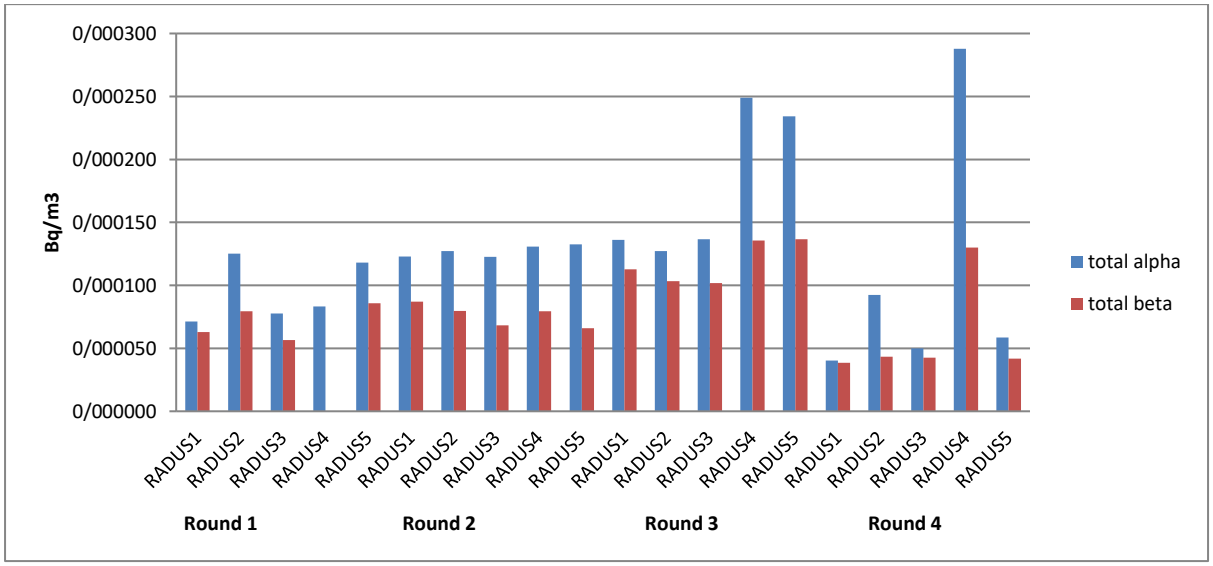

Fig 2. The Alpha and Beta radioactivity concentration in air samples.

The lowest value of Alpha radioactivity was measured at 1.75 E-4 Bq/m^3 at RADUS3. In contrast, the highest measured value was 12.64 E-4 Bq/m^3 at the RADUS4 point for Alpha particle. The lowest measured radioactivity value for total Beta was less than MDA at the RADUS4. Also, the highest measured value for this particle was 2.55 E-3 Bq/m^3 at RADUS1 point. The results illustrated that according to the distance of 22 km from the disposal site to the center of Anarak city (RADUS5), the radioactivity concentration of different radionuclides in the air is very small.

As the **Figs 3 and 4** picture**,** the background radiation in the Anarak is very low in all cases which cannot be determine by detectors. Hence, during the operation, the difference between any detectable amounts of detection limit can be recorded.

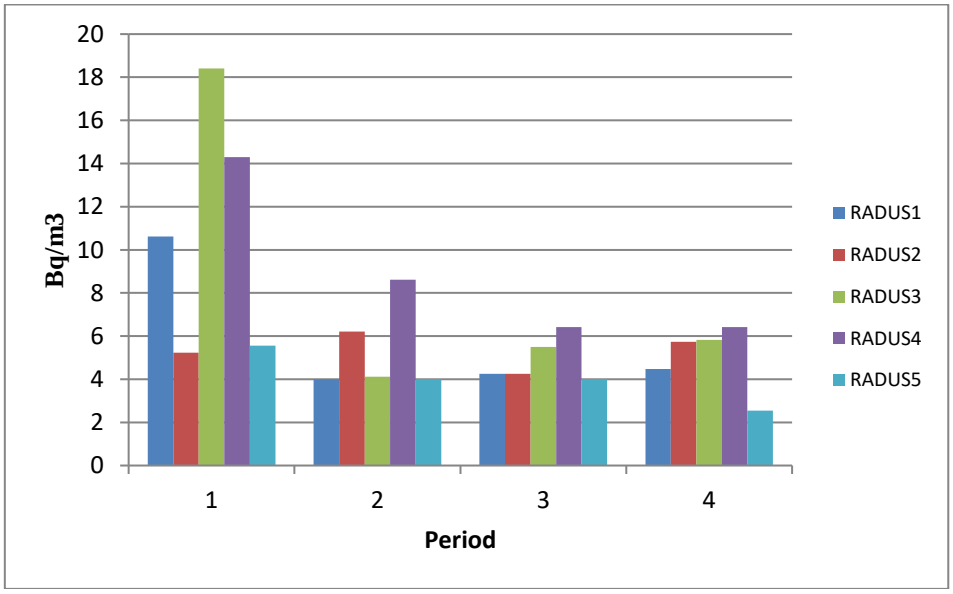

Fig 3. The Radon radioactivity concentration in air samples.

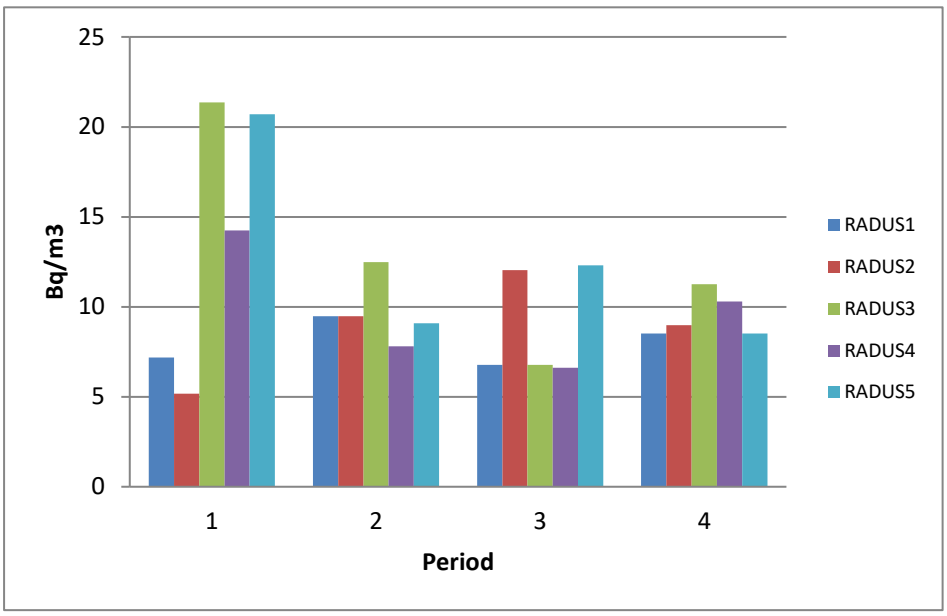

Fig 4. The Thoron radioactivity concentration in air samples.

Conclusions

The main goal of the pre-operational monitoring is to achieve the baseline values of natural radioactive material derived from atmospheric deposition in the environment of the repository of radioactive waste as well as their seasonal variations. In this experimental study, Anarak radioactive waste repository site pre-operational monitoring plan was investigated based on the policy and technical guidelines. The Gamma, Alfa, and Beta radiation dose rate, and the radioactivity concentrations of some radionuclides in air and water were carried out in different zones and time periods. Results presented that, the average concentrations of alpha and Beta radiation in water samples were 6.01 E-4 and 1.64 E-3 Bq/m^3, respectively. There is an inverse relationship between environmental temperature and Radon concentration. Moreover, the ^{40}K, ^{137}Cs and ^{232}Th concentrations in nine samples showed that all values are less than MDA. In case of any contamination throughout the time of closure, the effect of the site on contaminating the environment could be evaluated by comparing the measured values of concentration and background concentration limit.

References

[1]- IAEA, (2009), Classification of Radioactive Waste, IAEA Safety Standards Series No. SSG-1, IAEA, Vienna.

[2]- IAEA, (2021), Radioactive Waste Management Solutions for a Sustainable Future, Proceedings of an International Conference, Vienna, Austria.

[3]- S. Walker et al, Idaho, (1992), An Overview of in Situ Waste Treatment Technologies, presented at the Spectrum '92 Conference, Boise, Idaho.

[4]- IAEA, (2014), Near-surface Disposal Facilities for Radioactive Waste, Specific Safety Guide No. SSG-29.

[5]- NEA, (1989), The management of low- and intermediate-level radioactive waste, Nuclear Energy Agency, NEA Issue Brief: An analysis of principal nuclear issues, No. 6.

[6]- A.M. Umar, M.Y. Onimisi, S.A, (2012), Jonah Baseline Measurement of Natural Radioactivity in Soil, Vegetation and Water in the Industrial District of the Federal Capital Territory (FCT) Abuja, Nigeria, British Journal of Applied Science & Technology 2(3): 266-274.

[7]- Ahmad Termizi Ramli, Sallehudin Sahrone and Husin Wagiran, (2004), Terrestrial gamma radiation dose study to determine the baseline for environmental radiological health practices in Melaka state, Malaysia, Journal of Radiological Protection, Volume 25, Number 4.

[8]- B. C. Eke, N. N. Jibiri, B. C. Anusionwu, C. E. Orji and H. U. Emelue, (2015), Baseline Measurements of Natural Radioactivity inSoil Samples from the Federal University of Technology, Owerri, South-East, Nigeria British Journal of Applied Science & Technology 5(2): 142-149.

[9]- Laura Guidotti a, Franca Carini, Riccardo Rossi, Marina Gatti, Roberto M. Cenci, Gian Maria Beone, (2015), Gamma-spectrometric measurement of radioactivity in agricultural soils of the Lombardia region, northern Italy, Journal of Environmental Radioactivity 142 36-44.

[10]- IAEA-TECDOC-1092, (1999), Generic procedures for monitoring in a nuclear or radiological emergency, IAEA.

[11]- International standard ISO 10703, (2021), Water quality-Gamma-ray emitting radionuclides-Test method using high resolution gamma-ray spectrometry, ISO Third edition.

[12]- United states Enviromental Protection Agency (EPA), (2018), EPA Method 900.0, Rev 1.0: Gross Alpha and Gross Beta Radioactivity in Drinking Water, EPA.

[13]- International standard ISO 9698, (2019), Water quality-Tritium-Test method using liquid scintillation counting, ISO Third edition.

[14]- DURRIDGE Company Inc, (2015), RAD7 Radon detector User Manual, Boston.

International Conference on Nuclear Science and Technology
6- 8 MAY 2024 | Isfahan, Iran

Feasibility Study of the Computed Tomography of Oil and Gas Pipelines Using Dual-energy Technique (Paper ID : 1015)

Kabir M. First-Author[1*], Afarideh H. Correspondent[1], Ghergherechi M. Co-Author[2], Chai J. S. Co-Author[2]

[1] *Energy Engineering and Physics Department, Amirkabir University of Technology (Tehran Polytechnic), Tehran, Iran*

[2] *Department of Electrical and Computer Engineering, Sungkyunkwan University, Suwon, South Korea*

Abstract

Energy transmission pipelines are prone to corrosion and sediment buildup due to the nature of the materials they carry. Deposits on the pipeline walls can worsen corrosion, leading to micro-cracks and pitting. Neglecting to assess these factors can lead to pipeline failures with catastrophic consequences. Therefore, monitoring and measuring corrosion, erosion, and sedimentation levels within pipelines are crucial. Various methods have been developed for this purpose, with techniques using penetrating X-rays and gamma rays being the most accurate and non-destructive. In this study, computational gamma-ray dual-energy tomography was utilized as a precise and non-destructive method for detecting corrosion in pipeline walls. Data projections were obtained using the Limited-Number-Detector Computed Tomography (LNDCT) technique for defined pipeline phantoms with varying thicknesses. Dual-energy techniques were employed, emitting gamma rays from suitable radioactive isotopes such using two radioisotopes, Am-241 and Cs-137. Projections at different angles were recorded using 15 NaI(Tl) 2-inch detectors, and the corresponding photon peak pulses of each energy were separated and organized in the sinogram matrix. Subsequently, image reconstruction was performed using the Filtered-Back-Projection (FBP) algorithm, and the quality of the reconstructed image was assessed. The reconstructed images demonstrate the effectiveness of the dual-energy method in distinguishing between light and heavy materials, potentially leading to higher image quality compared to single-energy methods. Detailed analysis of the data obtained from dual-energy computational tomography enables precise identification of defects, failures, and sedimentation, thereby minimizing damage to pipeline structures. This research contributes to enhancing the evaluation and monitoring methods for pipelines,

improving the efficiency of these systems, and ultimately advancing safety and productivity in the oil and gas transportation industry.

Keywords: Computed Tomography, Dual-energy, Pipelines Corrosion, Scale Measurement, NaI(Tl) detector

1. INTRODUCTION

In the oil, gas, and petrochemical industries, deposits and corrosion pose serious problems for pipeline transportation systems[1], [2]. Significant volumes of chemicals leak from pipelines every year as a result of corrosion, endangering the environment or causing pipeline explosions. Deposit formation in pipeline veins lowers fluid flow volume and speeds up erosion and corrosion, which causes further damage. A good way to gauge and quantify corrosion is to take a measurement of the pipeline wall's thickness. For this goal, a number of non-destructive techniques have been developed; gamma ray attenuation, also known as X-ray penetrating radiography, is one of the most successful[3]–[8]. Gamma-ray tomography equipment has recently been available for cross-sectional imaging within pipelines. Kabir et al., introduced the limited-number-detector computed tomography (LNDCT) with a novel projection acquisition method [9]. With this method, silt thickness in pipelines may be measured without requiring shutdowns or discharge, giving pipeline system managers a proactive and accurate way to evaluate the condition of their pipes. These devices use 360-degree gamma-ray attenuation around the pipeline to produce projections, which are then followed by picture reconstruction [10]. Nevertheless, these systems have a limited number of detectors, which results in less-than-ideal image quality. As a result, a lot of study has been done on ways to either enhance image quality or make up for missing detectors [10], [11], [12], and [13]. Numerous studies have examined the use of Monte Carlo simulation for pipeline tomography parameter evaluation [15]– [17]. The primary area of feasibility study in this research is dual-energy approaches, which can improve the performance of single-energy scanning devices, especially when working with nearby light and heavy materials like scales or the insulation surrounding oil and gas pipelines. To produce an image, common systems now in use only use one gamma-ray emitting source and one photopeak [18]. Insufficient distinction is made between light and heavy elements in this kind of single energy tomographic image.

To enhance the most important image quality parameters like contrast and contrast-to-noise ratio and also having better analysis by discriminating materials lead us to propose and design dual-energy limited-number-detector feasibility study. In this way, this paper focused on the optimum design of and configuration to implement dual-energy LNDCT by a reliable approach of collecting low-energy (LE) and high-energy (HE) signals from detectors simultaneously. Monte-carlo simulation as a powerful tool was employed to study different aspects of dual-energy method for pipelines LNDCT.

2. MATERIALS AND METHODS

2.1 Monte Carlo Modelling

One of the most precise techniques for modeling of ionized radiation and transporting high-energy photons intracting with matter and predicting radiative parameters is Monte Carlo (MC) simulation[19], [20]. In a typical MC photon tracking code, gamma-ray photons at high and low energies are generated in source according to their different probabilities of emission. After traveling through the material, the photons reach the detector and are recorded and monte-carlo calculation terminates when a particle reaches to its energy or place cutt-off. The intensity (flux or fluence) of photons that enter the detector within the energy ranges given by the tally detectors is measured in order to calculate our interest radiation parameter such as flux, current, energy etc.[21].

It takes a lot of time to simulate the whole process of creating and running the 360-degree codes. As a result, a computer program was created to create the input files for the Monte Carlo code using a predefined template because of the huge number of inputs and high volume of outputs produced by the code. Following the execution of the programs for each angle, the results are kept apart in a folder. In the meantime, each detector's recorded data from the tally detectors is extracted of the outputs and saved as an angle-tagged matrix. The projections at

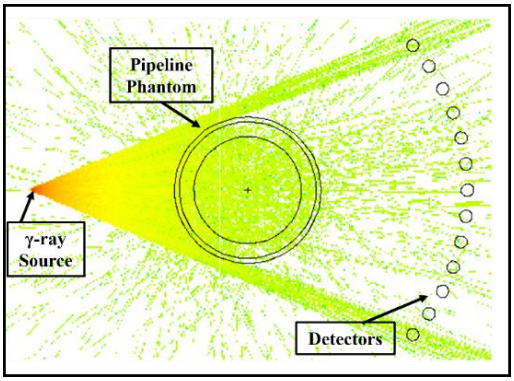

each angle are the outputs, and they are concatenated to create the sinogram matrix. At the end, the outputs are reconstructed into a cross-sectional image. Figure 1 shows a visual transport of

Fig. 1. Gamma-ray photon transport through pipeline phantom

Cs-137 gamma-ray photons which pass through pipeline and recorded on detectors. The main components implemented in the code is gamma-ray emitter source Cs-137, test phantom of a carbon steel pipe and anhydrite scale deposited in there as defined in section 2.3 and 15 NaI(Tl) detectors places on the curve line exactly in front of detector field-of-view (FOV) and there is nothing between two adjacent detectors. The beam shape is controlled by source bias card to prevent unwanted MC calculation as a variance reduction. The monte-carlo calculation continued to reaching >5% relative error.

2.2 Dual-Energy Method

Dual-energy (DE) gamma rays are released from the source and travel via a pipeline and any other medium in their course before reaching at detectors positioned on a curved trajectory and being recorded, as shown in Figure 2. Data from all 15 detectors, which are 2 inch-sized NaI(Tl)detector, are recorded at each primary angle θ. The projections are then extracted around the pipeline using the energy separation module for high (HE) and low energies (LE) (Figure 3). The sinogram matrix is then created by contrasting the projections that were acquired from the LE and HE signals. The filtered-back-projection analytical reconstruction algorithm is then used to reconstruct each matrix into a tomographic image, which is subsequently shown on the computer. Projection data acquisition is carried out by an automatic program. In the program using an input template of MC code in for example $\theta=0^{o}$, the other 359^{o} input files will generate. Then each prepared code executes automatically one by one. The output file then readout by another computer program and projection data (tallies on detectors) will be extracted.

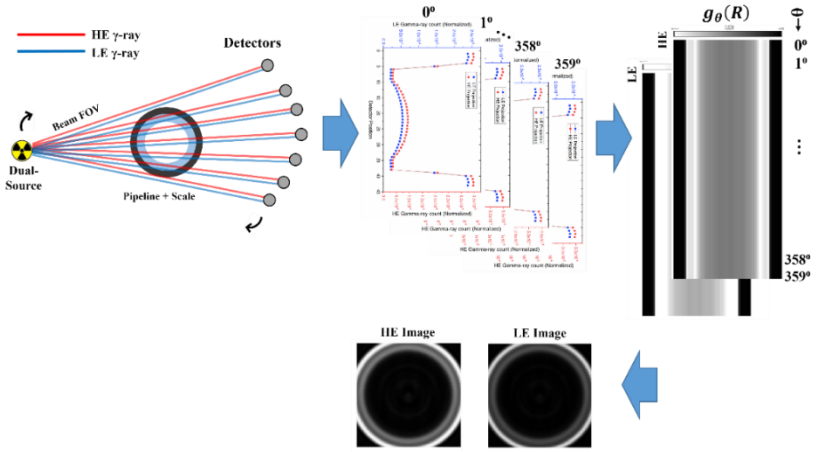

Fig. 2. Schematic process from signal acquisition to image reconstruction for dual-energy LNDCT.

2.3 Test Phantom

Since pipeline tomography and evaluation are the ultimate uses for this approach, the following definition of a phantom was established:

- Phantom A: pipeline constructed of carbon steel with an outside diameter of 15 cm and a wall thickness of 3 mm. The scale deposits are composed of 1.2 cm thick CaSO4 (anhydrite).

The material characteristics of the test and evaluation phantom used in the Monte Carlo code are shown in Table 1.

Table 1. Material used in MC study.

Material	Density (g/cm^3)
Anhydrite (Calcium Sulphate)	2.80
Carbon Steel	7.82

2.4 Sources

Due of the higher relative density of the materials traversed by the radiation, Phantom was irradiated using two gamma emitter sources: Americium-241 and Cesium-137. Table 2 displays the energy specifications of the sources that were used.

Table 2. gamma-ray emitter sources used in the feasibility study of the dual-energy method.

Radioisotope Source	Effective γ Energy (keV)	Probability (%)	Half-life (Years)
Cs-137	662	100%	**30.2**
Am-241	59.5	100%	**432**

*Two gamma-ray energies of 80.9keV and 356 keV is used in this study

2.5 Detectors and Signal Separation

NaI(Tl) detectors, which offer excellent energy discrimination capabilities and high efficiency, are used in this study. Following their interaction with the detector, the high-energy (HE) and low-energy (LE) gamma rays are separated using a multi-channel analyzer (MCA) and recorded one by one parallelly [27]. LE and HE signals are separated and recorded as distinct arrays for all detectors and at all angles. Fig. 3 shows the acquisition and separation of the signals corresponding to high-energy and low-energy gamma photons at each angle, from the first step to the projection data transfer to the computer.

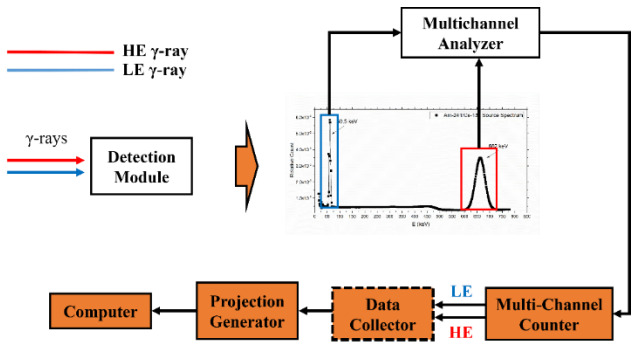

Fig. 3. Schematic of discrimination process of LE and HE signals to generate projections at each angle θ_i.

2.6 Filtered back-projection (FBP)

FBP image reconstruction method has been chosen for tomographic image formation due to the potentially large size of sinogram matrix. Iterative methods is proper when our projection

data is low and normal computational devices can handle it. The attenuation profile for each angle θ along each path R of the projections is represented by Equation 2[22].

$$g_\theta(R_i) = \frac{1}{d}\ln\left(\frac{I_\theta^0(R_i)}{I_\theta(R_i)}\right) \quad (1)$$

Where $g_\theta(R_i)$ represents the projection, d is the length passed, $I_\theta^0(R_i)$ is the intensity of the radiation recorded on the detector at angle θ in the absence of the pipeline, and $I_\theta(R_i)$ is the intensity of the gamma rays recorded on the detector at angle θ the phantom collecting will create sinogram matrix. A cross-sectional image of the item in spatial space can be obtained by backprojecting the sinogram matrix [23], [24]. We obtain the final image by backprojecting onto the rays' path, as per Equation 3.

$$g_\theta(R) = \int_{(\theta,R)line} \mu(x,y)dxdy \quad (2)$$

The spatially reconstructed image is a map of the attenuation coefficients μ(x,y). In addition to altering the space (from spatial frequency to space), backprojection also greatly amplifies noise. on order to lessen the noise effect on the image, filters should be applied (Equation 4). Without significantly increasing the computing load during the picture reconstruction process utilizing the FBP approach, the Hamming filter exhibits good performance in noise attenuation.

where ρm is the maximum spatial frequency that narrows or widens the frequency range and ρ is the spatial frequency. Equation 5 states that each row of the sinogram matrix receives a one-dimensional application of the Hamming filter [25]. Through backprojecting and a two-dimensional inverse Fourier transform applied to the projections' Fourier transform, the image is recreated in spatial space.

$$F^{-1}\left\{F\left\{g_\theta(R)|\rho|.\left[0.54+0.46\cos\left(\frac{\pi\rho}{\rho_m}\right)\right]\right\}\right\} = g_\theta(R) * F^{-1}\{|\rho|\} \quad (3)$$

As previously explained, the LE and HE signals are separated and recorded independently and simultaneously during the dual-energy process. Figure 4 illustrates the process of reconstructing the dual-energy image for each by going from the sinogram input to the spatial space image output.

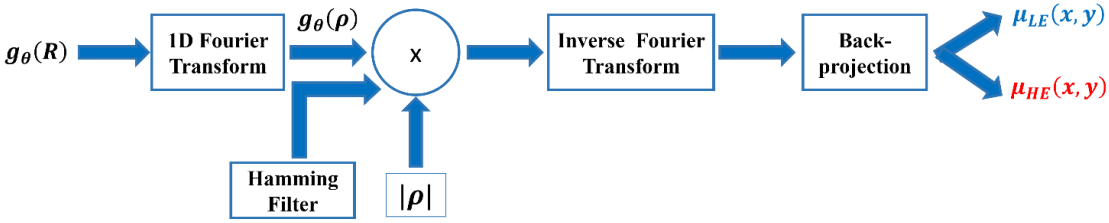

Fig. 4. Image Reconstruction of DE-LNDCT process using FBP algorithm

2.7 Evaluation of Reconstructed Image Quality

An appropriate quantitative indicator of the accuracy of the reconstructed image in comparison to the background is the Root Mean Square Error (RMSE). Formula 4[28] can be used to calculate this value.

$$RMSE = \sqrt{\frac{\sum_{j=1}^{N}\left(\mu_j^{reconstruction} - \mu_j^{true}\right)^2}{N}} \tag{4}$$

Where N is the number of pixels, reconstructed $\mu_j^{reconstructed}$ is the measured attenuation coefficient after reconstruction, and actual μ_j^{true} is the actual attenuation coefficient.

The contrast-to-noise ratio (CNR) is another crucial metric that may be used to assess the quality of any digital image. Equation 5[28] defines this parameter.

$$CNR = \frac{|S_{ROI} - S_B|}{\sigma_B} \tag{5}$$

Where ROI_S is the average of signal of pixels within the ROI corresponding to the pipeline wall or scale area, S_B is the average signal of the background area, and σ_B represents the standard deviation of pixels in the background.

3. RESULTS AND DISCUSSION

3.1 Image Reconstruction and Quantitative Evaluation

Reconstructed image by FBP is shown in the figure 5. The left image is high-energy image and the right one is the image reconstructed by low-energy signals.

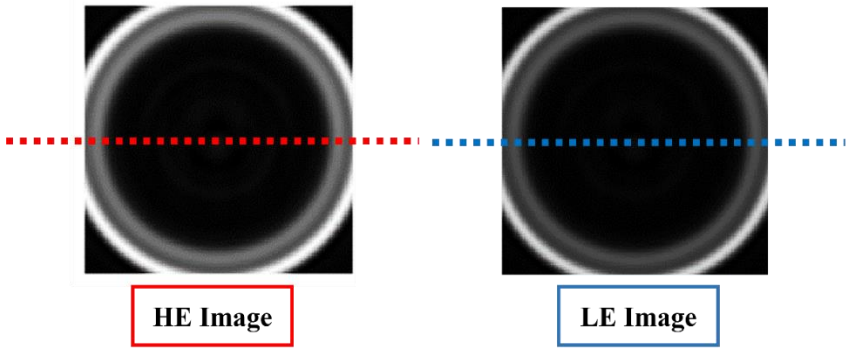

Fig. 5. Reconstructed HE and LE images

Linear profiles along an image center were used to assess the pipelines' reconstructed images. As can be seen in figure 5, the red dashed line is the linear profile for HE images gray value assessment and the blue dashed line represent the linear profile across the LE image. Gray levels represent the attenuation coefficient correspond to each voxel of final image. The reconstruction of the image corresponding to high- and low-energy photons for Phantom A yielded the following results, as seen in Figure 6, the gray level values for HE is more closely aligned with the actual value for the higher atomic number steel wall.

For materials with a lower atomic number (scale materials), the gray values are closer with the actual value for LE energy. This fact demonstrates that the cross-sectional interaction for low-energy photons is more prominent for light materials (low-Z), but for heavy materials the opposite is true.

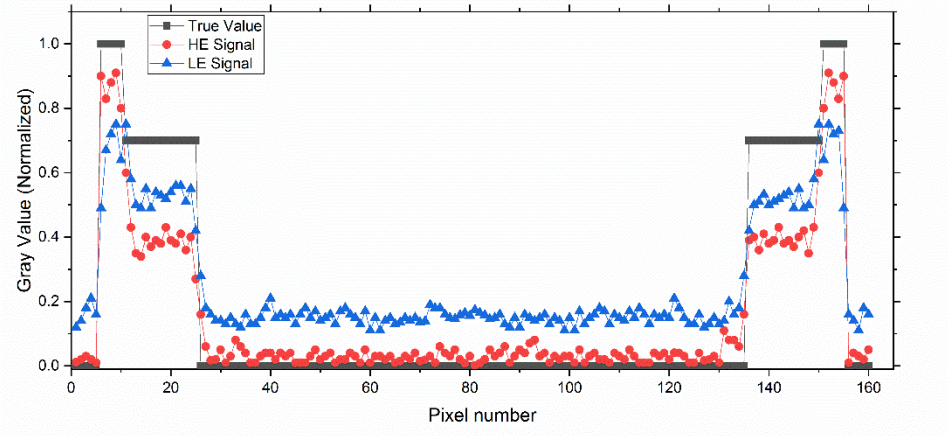

Fig. 6. linear profiles of gray values obtained from images resulting from LE and HE signals of phantom A: carbon steel pipeline and anhydrite deposits.

Due to the larger signal of the photon peak associated with high energy, the gray levels in the image for the pipeline wall region are closer to the normalized actual value for the steel wall with a high atomic number.

Table 3 presents quantitative measurements obtained from picture reconstruction.

Table 3. RMSE and CNR of test phantom A's reconstructed image

		RMS Error	CNR
Phantom A	LE	0.104	37.5
	HE	0.089	42.8

According to the measured data of reconstructed image of phantom A, LE image has a higher RMS Error than the HE but the contrast-to-noise ratio of HE is better than LE image.

4. Conclusion

This work used the Monte Carlo approach to conduct a feasible evaluation of the industrial design and construction of a portable pipeline tomography with limited dual-energy detectors. Originally, a computer program was used to carry out every step of the described approach, from defining the source to moving through the substance and registering in the detectors. The program receives a template file that contains the geometry definition and other pertinent information. Simultaneously, two tomographic images are reconstructed using FBP algorithm: one for high-energy (HE) and one for low-energy (LE). Gamma-ray sources of cesium-137 and americium-241 were employed for a carbon steel pipeline phantom with an anhydrite scale (phantom A) in order to implement the dual-energy approach. Following image reconstruction, the signal in the higher metal zone in HE was more desirable, whereas the signal in the lower density region in LE was closer to the genuine value. This demonstrates the dual-energy method's efficacy and correct operation in material differentiation. On the other hand, while employing more energy, the signal for the metal region is closer to the actual value. Better discriminating between heavy and light materials is demonstrated by the contrasts of the pictures and CNR in the regions of interest, particularly when the materials are adjacent. The results of this paper greatly enhance the pipeline tomography process and demonstrate that the experimental implementation and manufacturing of the DE-LNDCT equipment utilizing this

Monte Carlo study is totally feasible. Future research can concentrate on optimizing the choice of LE and HE energies according to the kind of material under evaluation for additional validation, which may result in even better reconstructed images.

References

[1] M. S. Kamal, I. Hussein, M. Mahmoud, A. S. Sultan, and M. A. S. Saad, "Oilfield scale formation and chemical removal: A review," J Pet Sci Eng, vol. 171, pp. 127–139, Dec. 2018, doi: 10.1016/j.petrol.2018.07.037.

[2] M. Zahedzadeh et al., "Comprehensive management of mineral scale deposition in carbonate oil fields - A case study," Chemical Engineering Research and Design, vol. 92, no. 11, pp. 2264–2272, Nov. 2014, doi: 10.1016/j.cherd.2014.03.014.

[3] W. Harara, "Evaluation of corrosion and deposit in pipes by radiography," Development of protocols for corrosion and deposits evaluation in pipes by radiography, p. 85, 2005.

[4] P. Rostron, "Critical Review of Pipeline Scale Measurement Technologies," Indian J Sci Technol, vol. 11, no. 17, pp. 1–18, May 2018, doi: 10.17485/ijst/2018/v11i17/121459.

[5] N. Azaman, K. A. M. Salleh, A. A. Abas, A. Yassin, and S. Ahmad, "Validation and Application of Computed Radiography (CR) Tangential Technique for Wall Thickness Measurement of 10 Inch Carbon Steel Pipe," in R&D Seminar 2016: Research and Development Seminar 2016, Malaysia, 2016. [Online]. Available: http://inis.iaea.org/search/search.aspx?orig_q=RN:48050427

[6] Eko Prasetyo, H. Pariaman, and Sulistijono, "Tangential X-Ray Radiography for Pitting Geometry Analysis of Outside Wall of Insulated Steel Pipes," Russian Journal of Nondestructive Testing, vol. 56, no. 3, pp. 249–258, Mar. 2020, doi: 10.1134/S1061830920030031.

[7] J. Zirnhelt, I. Einav, and S. Infanzón, "Radiographic evaluation of corrosion and deposits: An IAEA Co–ordinate Research Project," in 3rd PAN American Conference for NonDestructive Testing-PANNDT, 2003.

[8] D. F. Oliveira, J. R. Nascimento, C. A. Marinho, and R. T. Lopes, "Gamma transmission system for detection of scale in oil exploration pipelines," Nucl Instrum Methods Phys Res A, vol. 784, pp. 616–620, Jun. 2015, doi: 10.1016/j.nima.2014.11.030.

[9] H. A. M. G. J.-S. C. Mostafa Kabir, "Optimizing Portable LNDCT for Oil and Gas Pipeline Imaging with Innovative Projection Acquisition Algorithm (Under Review)," Nuclear Engineering and Technology, Feb. 2024.

[10] J. Kim, S. Jung, J. Moon, and G. Cho, "Industrial gamma-ray tomographic scan method for large scale industrial plants," Nucl Instrum Methods Phys Res A, vol. 640, no. 1, pp. 139–150, Jun. 2011, doi: 10.1016/j.nima.2011.02.082.

[11] J. Kim, S. Jung, J. Moon, and G. Cho, "A feasibility study on gamma-ray tomography by Monte Carlo simulation for development of portable tomographic system," Applied Radiation and Isotopes, vol. 70, no. 2, pp. 404–414, Feb. 2012, doi: 10.1016/j.apradiso.2011.09.019.

[12] J. Kim, S. Jung, J. Moon, J. Guen Park, J. Jin, and G. Cho, "Development of transportable gamma-ray tomographic system for industrial application," Nucl Instrum Methods Phys Res A, vol. 693, pp. 203–208, Nov. 2012, doi: 10.1016/j.nima.2012.07.046.

[13] M. Khorsandi and S. A. H. Feghhi, "Gamma-ray CT as a complementary technique for structural inspection of tray-type distillation columns," Measurement (Lond), vol. 78, pp. 1–8, Jan. 2016, doi: 10.1016/j.measurement.2015.09.040.

[14] M. Khorsandi and S. A. H. Feghhi, "Development of image reconstruction for Gamma-ray CT of large-dimension industrial plants using Monte Carlo simulation," Nucl Instrum Methods Phys Res B, vol. 356–357, pp. 176–185, May 2015, doi: 10.1016/j.nimb.2015.05.003.

[15] M. R. Ay and H. Zaidi, "Development and validation of MCNP4C-based Monte Carlo simulator for fan- and cone-beam x-ray CT," Phys Med Biol, vol. 50, no. 20, pp. 4863–4885, Oct. 2005, doi: 10.1088/0031-9155/50/20/009.

[16] A. F. Velo, M. M. Hamada, D. V. S. Carvalho, J. F. T. Martins, and C. H. Mesquita, "A portable tomography system with seventy detectors and five gamma-ray sources in fan beam geometry simulated by Monte Carlo method," Flow Measurement and Instrumentation, vol. 53, pp. 89–94, Mar. 2017, doi: 10.1016/j.flowmeasinst.2016.09.015.

[17] E. B. Smith, L. D. Patel, and D. Dreizin, "Postoperative Computed Tomography for Facial Fractures," Neuroimaging Clin N Am, vol. 32, no. 1, pp. 231–254, Feb. 2022, doi: 10.1016/j.nic.2021.08.004.

[18] R. Chung, B. Dane, B. M. Yeh, D. E. Morgan, D. V. Sahani, and A. Kambadakone, "Dual-Energy Computed Tomography: Technological Considerations," *Radiol Clin North Am*, vol. 61, no. 6, pp. 945–961, Nov. 2023, doi: 10.1016/j.rcl.2023.05.002.

[19] S. Srinivas-Rao, J. Cao, D. Marin, and A. Kambadakone, "Dual-Energy Computed Tomography to Photon Counting Computed Tomography: Emerging Technological Innovations," *Radiol Clin North Am*, vol. 61, no. 6, pp. 933–944, Nov. 2023, doi: 10.1016/j.rcl.2023.06.015.

[20] Z. J. Hartley-Blossom and S. R. Digumarthy, "Dual-Energy Computed Tomography Applications in Lung Cancer," Radiol Clin North Am, vol. 61, no. 6, pp. 987–994, Nov. 2023, doi: 10.1016/j.rcl.2023.06.001.

[21] B. Böttcher et al., "Dual-Energy Computed Tomography in Cardiac Imaging," Radiol Clin North Am, vol. 61, no. 6, pp. 995–1009, Nov. 2023, doi: 10.1016/j.rcl.2023.05.004.

[22] IAEA-TECDOC-1589, "Industrial Process Gamma Tomography," Vienna, 2008. Accessed: Nov. 03, 2023. [Online]. Available: https://www.iaea.org/publications/7921/industrial-process-gamma-tomography

[23] L. De Chiffre, S. Carmignato, J. P. Kruth, R. Schmitt, and A. Weckenmann, "Industrial applications of computed tomography," CIRP Ann Manuf Technol, vol. 63, no. 2, pp. 655–677, 2014, doi: 10.1016/j.cirp.2014.05.011.

[24] J. C. Yanch, A. B. Dobrzeniecki, C. Ramanathan, and R. Behrman, "Physically realistic Monte Carlo simulation of source, collimator and tomographic data acquisition for emission computed tomography," Phys Med Biol, vol. 37, no. 4, pp. 853–870, Apr. 1992, doi: 10.1088/0031-9155/37/4/003.

[25] A. Haghighat, *Monte Carlo Methods for Particle Transport*. Second edition. | Boca Raton : CRC Press, 2021.: CRC Press, 2020. doi: 10.1201/9780429198397.

[26] L. S. Waters et al., "The MCNPX Monte Carlo Radiation Transport Code," in AIP Conference Proceedings, AIP, 2007, pp. 81–90. doi: 10.1063/1.2720459.

[27] G. F. Knoll, Radiation detection and measurement. John Wiley & Sons, 2010.

[28] J. L. Prince and J. M. Links, Medical imaging signals and systems. 2023.

ICNST 2024
International Conference on Nuclear Science and Technology
6- 8 MAY 2024 | Isfahan, Iran

Efficiency Calculation of a milliwatt Radioisotope Thermoelectric Generator (RTG) using MCNP code and COMSOL software (Paper ID : 1020)

Abbaspour A. Correspondent[1*], Ezzati A. Co-Author[1,2], Jalilzadeh H. Co-Author[1]

[1]*Faculty of Physics, University of Tabriz, Tabriz, Iran*

[2]*Research institute for Applied Physics & Astronomy, University of Tabriz, Tabriz, Iran*

Abstract

Providing the ever-increasing human need for energy is one of the most important challenges. In this paper, we designed and simulated a Radioisotope Thermoelectric Generator (RTG) with milliwatt power. This RTG uses plutonium dioxide fuel as a heat source. The main radioisotope for decay and heat production is plutonium 238. The thermal power produced from the decay of alpha particles is converted into output electrical power through a thermoelectric generator (TEG) module. The MCNP code was used to calculate the thermal power produced from the decay of alpha particles. The thermoelectric generator module was designed and simulated in COMSOL software, and the output electrical power was obtained based on the corresponding load resistance. Based on the calculations and simulations, the thermal power of the heat source was calculated as 1.13 watts and the output electrical power was 0.0403 watts. Therefore, the total efficiency of the designed RTG obtained 3.56 percent (3.56 %).

Keywords: Thermoelectric generator, COMSOL software, MCNP code, Radioisotope

INTRODUCTION

For power source applications requiring small volumes and decades of operation where harvestable energy is unavailable, only devices that convert radioactive decay into electricity can provide high energy densities [1]. Radioisotope Power Supplies (RPSs) generate electrical power by converting the heat released from the nuclear decay of radioactive isotopes into electricity.

There are many competing types of nuclear batteries: thermoelectric, thermophotoelectric, direct charge collection, thermionic, scintillation intermediate,

and direction energy conversion alphavoltaics and betavoltaics [2]. One of the most practical and efficient types of nuclear batteries is the Radioisotope Thermoelectric Generators (RTGs) which convert heat produced from radiation into electricity by a thermoelectric generator (TEG) module. The power generated from the RPS can be used in a wide variety of applications such as providing surface electric power at remote locations, providing power for electric propulsion systems, and providing warmth in extremely cold conditions [3]. RTGs are in a variety of ranges. Their range of power is from milliwatts to kilowatts. These units differ enormously in size and power. for example, one of the 'Multi-Mission RTG(MMRTG) reported has thermal power upwards of 2000W by producing electric output of about 120W [4]. These RTGs are utilized in spacecraft machines. Space exploration applications of the RTGs are an important field of RTGs application. With the advancement of space exploration, the demand for spacecraft is increasing. At the same time, the space mission requires the battery of the spacecraft to be reliable, endurable, and environmentally adaptable. Solar cells cannot operate efficiently where the source of sunlight is not sustainable. The chemical cell, though it has high performance, cannot meet the requirement of long life. In contrast, the radioisotope thermoelectric generator (RTG) has been widely regarded as a promising battery for space missions [5]. In 1961, the first spacecraft equipped with RTG was launched by the United States for navigation purposes. In 1978, NASA designed a standard heat source which was called General-purpose Heat Source (GPHS) that uses Pu-238-based components as radioisotopes for heat sources. In the design, several different layers were used to ensure the radioactive elements would not leak from GPHS under any accidents. Also, according to different power requirements, this standard heat source could provide a wide range of thermal power by changing the number of Pu-238 pellets. RTGs with the power of milliwatts can be used in lighthouses and navigation towers without requiring maintenance [6], storage and data radio communications related to monitoring [7], navigational aids, hydrophone amplifiers, microwave repeater stations, and automated weather stations and for space applications [8]. Sensor nodes, which are used in wireless sensor network systems, approximately consume 100 μW of electric power for sensing, gathering, and processing data as well as for radiofrequency (RF) data transmission. Because of the large number of sensor nodes,

their small size, long-time operation, and inaccessibility in some cases, mini RTGs are very useful and compatible with this application [9]. In addition, RTGs can be used in microelectromechanical systems and microsystems. Hi-Z Technology, Inc. (Hi-Z) has been developing milliWatt Radioisotope Power Supplies (RPS) that provide 1 W of heat and can be expected to produce about 40 mW of electrical power using a thermoelectric generator. These electrical power systems, are generally called milliwatt power sources (MPS). Such MPS can be used in a small planetary rover, small communication transmitter, micro spacecraft, or an autonomous science package such as a remote weather station, that either uses continuous power at a level of a fraction of a watt or can operate intermittently by using energy from a battery that is continuously charged by a MPS for 20 years [10].

Generally, RTG consists of three basic parts: (1) a radioisotope heat source (RHS), or radioisotope heat unit (RHU) in literature (2) a surrounding heat insulator, and (3) a TEG for converting heat to electric power through the thermoelectric effect [11]. The radioisotope used in it can be alpha, beta, or gamma emitters. Almost Gamma emitters are not used in the construction of RTGs due to concerns about the leakage of harmful gamma rays. Sr-90 is a pure beta-emitter that has been used in some RTGs. The energy density of Sr-90 (0.916 W/g) suggests that it may be a viable option in the design of an RTG [12]. The strontium-90 isotope is still actively used in RTGs for terrestrial applications. The list of installations using this isotope is gathered in [13]. Until 2011 The efficiency of an RTG—the proportion of thermal energy converted to electrical energy—reached a limit of only around 7% [4]. However, some researchers in NASA further enhanced the performance of RTG by replacing the traditional TE materials with high-efficiency p-type and n-type skutterudites [5]. In this paper, we investigated and calculated the electrical power output from a milliwatt power RTG and its the total efficiency for selected materials. Plutonium dioxide was considered as the fuel (heat source). The MCNP code was used to calculate the thermal power produced from the source. We selected n-type and p-type semiconductor materials based on bismuth telluride as thermoelectric legs and simulated a thermoelectric generator in COMSOL software. After calculating the total thermal power produced by the heat source and the output electric power

produced by the thermoelectric generator, the total efficiency of the designed RTG was determined.

RESEARCH THEORIES

To calculate RTG's total efficiency, the total power input to it must be obtained. In this article, the MCNP code was used to calculate the displaced energy resulting from radioisotope decay in each cell. COMSOL software was used to design the thermoelectric generator and calculate its electric output power. For this purpose, the thermoelectric effect interface first was created in Comsol.
Readers can refer to the Comsol documentation for details on the design of the thermoelectric effect interface.

A thermoelectric generator is a power-generating device that directly converts thermal energy into electrical energy. A thermoelectric couple is shown in Fig1.

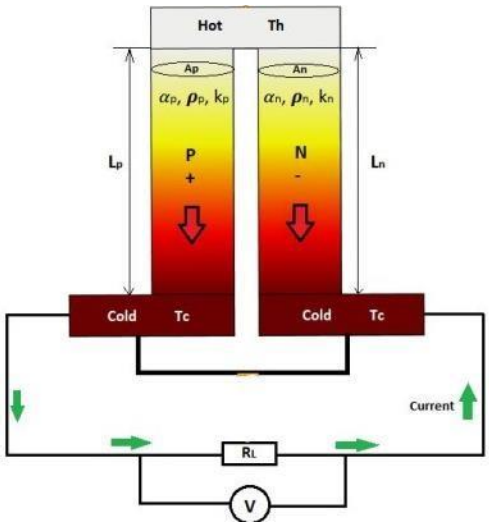

Fig 1. The TEG thermocouple Schematic Diagram

When the connected junctions of two dissimilar semiconductor materials (n-type and p-type) have a temperature difference, an electrical current is generated, the phenomenon is called as the Seebeck effect. At the atomic scale, an applied temperature gradient causes charge carriers in the material to diffuse from the hot side to the cold side. This effect can be used to generate electricity. The potential

difference created by applying the temperature difference between the two ends of the thermoelectric generator is given through the following equation [14]:

$$\boldsymbol{V = -S\Delta T} \qquad (\mathbf{1})$$

Where S is the Seebeck coefficient, a property of the local material, and ΔT is the temperature difference between the hot and cold sides. The Seebeck coefficients generally vary as a function of temperature and depend strongly on the composition of the material. According to equation 1, the greater the temperature difference applied to the two ends of the thermoelectric generator, the greater the voltage between its two ends. Thermoelectric materials must have high electrical conductivity (σ) and low thermal conductivity (K) to be good thermoelectric materials. Low thermal conductivity in these materials ensures that when one side becomes hot, the other side stays cool, which helps to generate high voltage while in a temperature difference. The efficiency of thermoelectric material is governed by its "figure of merit" which ordinarily is a constant between 0 and 2. Several materials have now been reported to display high ZT values over 2 [15]. However, only a few of them have been demonstrated in thermoelectric devices or modules. So the closer the figure of merit coefficient number is to one, that means the material has more merit to be used in thermoelectric generator. The electric output power of the thermoelectric generator is shown in fig1 can be obtained by $W = R_L I^2$ where R_L is load resistance. it also can be written as:

$$W = \alpha I\,(T_h - T_c) - RI^2 \qquad (2)$$

In aquation 2, α is the total Seebeck coefficient and equals $\boldsymbol{\alpha = \alpha_P - \alpha_n}$ where $\boldsymbol{\alpha_P}$ is P-leg and $\boldsymbol{\alpha_n}$ is N-leg Seebeck coefficient and R is thermoelectric couple electric resistance. Therefore, if we have n pairs of thermocouples in the thermoelectric generator, its internal resistance is obtained from the following equation3:

$$\boldsymbol{R = \frac{2n\rho h}{A_{leg}}} \qquad (\mathbf{3})$$

In addition, in equation 2, T_h is the temperature of the hot side, which is connected to the source, and T_c is the temperature of the cold side. As shown in equation 2, the greater the temperature difference between the hot and cold sides in the thermoelectric generator, the greater the output power of the converter.

Simulation

Table 1 shows the weight of plutonium isotopes in percent that makeup plutonium in plutonium dioxide cylindrical fuel as the heat source [16]. The density of plutonium dioxide fuel was considered equal to 9.6 grams per cubic centimeter, which is 84% of its density with theoretical calculations [17]. Pu-242 isotope was not included in the calculations due to its small amount and long half-life. The heat source was encapsulated in 1mm Pt-30Rh alloy surrounded by three layers of pyrolytic graphite as shown in Fig2, a and b, that cells recognized with 10-14 numbers.

Readers can refer to reference 15 to know the details of the designed source.

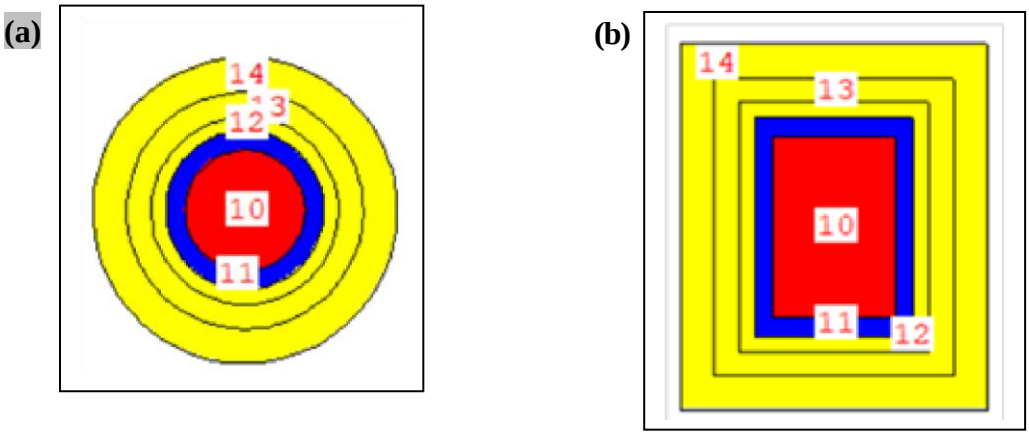

Fig.2. The heat source Schematic Diagram with (a) X-Y, (b) X-Z cross-sections.

The thermal power resulting from the decay of alpha particles of plutonium radioisotopes was obtained by using MCNP code. Table 2 shows the mass and the deposited energy of an alpha particle in the fuel (cell 10) and the surrounding Pt-30Rh alloy (cell 11), which was calculated using F6 tally in the MCNP code. The deposited energy of the alpha particle in the other cells was calculated as zero. The total thermal power (W_{th}) calculated according to Tabel 1 and Table 2 equal 1.13 W.

Table 1. Isotopic composition of Pu.

Isotope	Weight (%)
Pu-238	83.62
Pu-239	13.98
Pu-240	1.96
Pu-241	0.41
Pu-242	0.14

Table 2. Heat from Alpha decay in cells.

cell	Mass (gr)	Deposited Energy in cell$(Mev.\ gr^{-1})$	Density $(gr.\ cm^{-3})$
10	2.75969	2.01588	9.6
11	5.63778	8.85551E-04	17.6

To design the thermoelectric generator, Bi_2Te_3 MA+HP samples [18] and $Bi_{0.5}Sb_{1.5}Te_3$ [19] was chosen as n-type and p-type semiconductors thermoelectric material, respectively.

Semiconductor legs were placed inside Kapton MT [solid, type K275 with adhesive] as insulator. The semiconductor elements are $0.615mm \times 0.615mm \times 22.9mm$. These legs are connected electrically in series by copper strips with dimensions of $1.3mm \times 0.615mm \times 0.03mm$ and are thermally in parallel. On both sides of it, $13mm \times 12.5mm \times 1mm$ alumina blocks are placed. one block is in contact with the source (hot side) and the other block is in contact with the cold side. The temperature of the hot side and the temperature of the cold side are considered to be 250 degrees Celsius and 30 degrees Celsius, respectively. The designed thermoelectric generator contains 164 pairs of thermocouples in 18×18 array. To measure the electric current (I), internal resistance of the thermoelectric generator (R_{in}) and output electric power (W_e), we connected thermoelectric generator and load resistance (R_L) through External I vs. U feature in Electrical Circuit physics in COMSOL.

Results and discussion

Based on the value of R_L, different output electric power is obtained. The maximum electrical power output is obtained when the R_L equal to the R_{in} [11]. We considered $R_L = 1296.7\Omega$. Fig 3 shows the voltage obtained from the designed thermoelectric

generator for two states: (a) load resistance connected to the thermoelectric generator and (b) open-circuit voltage (load resistance is not connected). According to Fig 3, a and b, load voltage (V_L) and open-circuit voltage (V_{OP}) is equal 7.23V and 14.4V, respectively. According to the current obtained in the circuit, the internal resistance of the thermoelectric generator can be calculated.

(a)

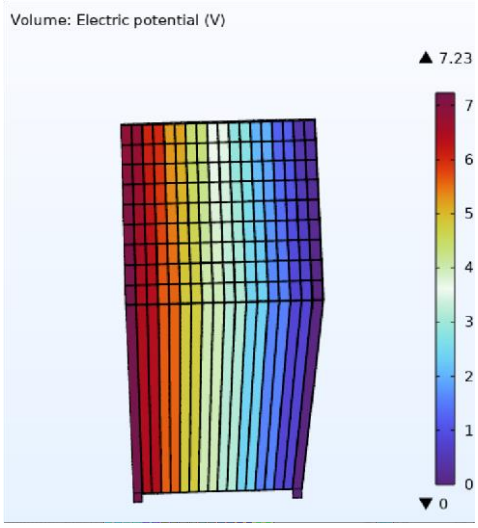

(b)

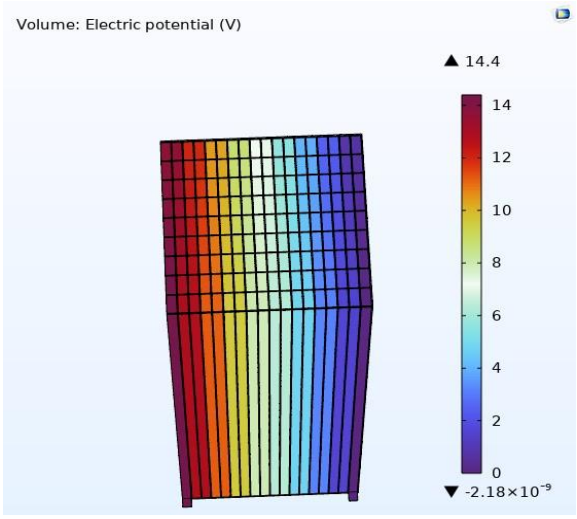

Fig. 3. The Generated voltage by TEG: (a) with $R_L = 1296.7\Omega$, (b) without R_L connected

Tabel 3 shows the relevant results. The ratio of load resistance to internal resistance is equal to

1.02 ($\frac{R_L}{R_{in}}$ = 1.02).

Table 3. Electric current and electric power relevant results.

$R_L(\Omega)$	$V_L(V)$	V_{OP}(V)	$R_{in}(\Omega)$	I(mA)	$W_e\,(mW)$
1296.7	7.23	14.4	1274.73	5.60	40.30

The total efficiency ($\boldsymbol{\eta_{tot}}$) of the RTG is equal to the ratio of the output electrical power to the thermal power produced by the heat source ($\boldsymbol{\eta_{tot} = W^{W_{th^e}}}$).

Considering that the total thermal power due to the decay of alpha particles in the source is calculated as 1.13 W and also the output electric power in Table 3, the total efficiency will be equal to:

$$\eta_{tot} = \frac{W}{W_{the}} = \frac{01.04}{03.13} = 0.0356$$

So, the total efficiency of designed RTG is equal to 3.56%.

Conclusions

In this paper, we designed a thermoelectric generator module that operate between 220K temperature difference that connected to a radioisotope heat source by using Pu-238 based component. The total efficiency of designed RTG calculated 3.56 % that is low. According to the results, it seems that thermoelectric material chosen has a low figure of merit for applying in thermoelectric generator and we must keep going on improve semiconducters used in our model. The use of skutterudites may increase the output electrical power and thus improve the overall efficiency of the designed RTG.

References

Whalen, S. A., Apblett, C. A., & Aselage, T. L. (2008). Improving power density and efficiency of miniature radioisotopic thermoelectric generators. Journal of Power Sources, 180(1), 657-663.

[1] Prelas, M. A., Weaver, C. L., Watermann, M. L., Lukosi, E. D., Schott, R. J., & Wisniewski, D. A. (2014). A review of nuclear batteries. Progress in Nuclear Energy, 75, 117-148 .

[2] Emrich Jr, W. J. (2008, June). General Purpose Heat Source Simulator. In International Congress on Advances in Nuclear Power Plants (ICAPP"08.

[3] Williams, H. R., Ambrosi, R. M., Bannister, N. P., Samara-Ratna, P., & Sykes, J. (2012). A conceptual spacecraft radioisotope thermoelectric and heating unit (RTHU). International Journal of Energy Research, 36(12), 1192-1200.

[4] Deng, W., Wang, X., Pan, X., Zhang, S., Ding, J., & Li, G. (2021). Geometry design and performance optimization of a terrestrial radioisotope thermoelectric generator based on finite element analysis. Annals of Nuclear Energy, 151, 107883.

[5] Elsheikh, M. H., Shnawah, D. A., Sabri, M. F. M., Said, S. B. M., Hassan, M. H., Bashir, M. B. A., & Mohamad, M. (2014). A review on thermoelectric renewable energy: Principle parameters that affect their performance. Renewable and sustainable energy reviews, 30, 337-355.

[6] Bennett, G., Lombardo, J., Hemler, R., Silverman, G., Whitmore, C., Amos, W., ... & Englehart, R. (2006, June). Mission of daring: the general-purpose heat source radioisotope thermoelectric generator. In 4th international energy conversion engineering conference and exhibit (IECEC) (p. 4096).

[7] O'Brien, R. C., Ambrosi, R. M., Bannister, N. P., Howe, S. D., & Atkinson, H. V. (2008). Safe radioisotope thermoelectric generators and heat sources for space applications. Journal of Nuclear Materials, 377(3), 506-521.

[8] Vullers, R. J. M., van Schaijk, R., Doms, I., Van Hoof, C., & Mertens, R. M. E. H.

(2009). Micropower energy harvesting. Solid-State Electronics, 53(7), 684-693.

[9] Allen, D. T., Hiller, N. D., Bass, J. C., & Elsner, N. B. (2004, February). Fabrication and testing of thermoelectric modules and milliwatt power supplies. In AIP Conference Proceedings (Vol. 699, No. 1, pp. 521-528). American Institute of Physics.

[10] Khajepour, A., & Rahmani, F. (2017). An approach to design a 90Sr radioisotope thermoelectric generator using analytical and Monte Carlo methods with ANSYS, COMSOL, and MCNP. Applied Radiation and Isotopes, 119, 51-59.

[11] Kingston, M. (2014). The Design of a Radioisotopic Thermoelectric Generator Powered by Strontium-90. Idaho State University.

[12] Mikhalev, A. V., Chernov, D. O., & Korobeinikov, V. V. (2020, November). Use of Am-241 in RTGs. In Journal of Physics: Conference Series (Vol. 1689, No. 1, p. 012063). IOP Publishing.

[13] Prasad, A., & Thiagarajan, R. C. (2018, August). Multiphysics modeling and multilevel optimization of thermoelectric generator for waste heat recovery. In Proceedings of the COMSOL Conference (pp. 1-7).

[14] Tan, G., Ohta, M., & Kanatzidis, M. G. (2019). Thermoelectric power generation: from new materials to devices. *Philosophical Transactions of the Royal Society A, 377*(2152), 20180450.

[15] Tate, R. E. (1982). Light weight radioisotope heater unit (LWRHU): a technical description of the reference design (No. LA-9078-MS). Los Alamos National Lab.(LANL), Los Alamos, NM (United States).

[16] Space, G. A. (1988). Final safety analysis report for the Galileo Mission. *Vol. IIAccident model*.

[17] Wang, S., Xie, W., Li, H., & Tang, X. (2010). High performance n-type (Bi, Sb) 2 (Te, Se) 3 for low temperature thermoelectric generator. Journal of Physics D: Applied Physics, 43(33), 335404.

[18] Zhu, B., Luo, Y., Wu, H., Sun, D., Liu, L., Shu, S., ... & Zheng, Y. (2023). Enhanced thermoelectric performance in Bi 0.5 Sb 1.5 Te 3/SiC composites prepared by lowtemperature liquid phase sintering. *Journal of Materials Chemistry A, 11*(16), 8912-8921

International Conference on Nuclear Science and Technology
6- 8 MAY 2024 | Isfahan, Iran

Design of the Mechanical Structure of a Portable Limited-Number-Detector Gamma-ray Computed Tomography (LNDCT) of Oil and Gas Pipelines (Paper ID : 1024)

Arami Rad M. First-Author[1], Kabir M. Co-Author[1] Afarideh H. Correspondent[1], Ghergherechi M. Co-Author[2], Chai J. S. Co-Author[2]

[1] *Energy Engineering and Physics Department, Amirkabir University of Technology (Tehran Polytechnic), Tehran, Iran*

[2] *Department of Electrical and Computer Engineering, Sungkyunkwan University, Suwon, South Korea*

Abstract

Nowadays, one of the non-destructive methods for measuring the thickness of sediment layers formed in fluid transmission pipelines and the wall thickness is the use of Gamma Ray Tomography (GCT). Computed Tomography (CT) with Limited-Number-Detector (LNDCT) is considered as an advanced method for evaluating oil and gas pipelines. This article investigates the design and construction of the mechanical structure of a portable tomography device for non-destructive evaluation of oil and gas pipelines. The mechanical structure of this device is one of the fundamental factors in improving the accuracy and efficiency of the evaluation process. The design of the mechanical structure of the portable tomography device is such that performing precise and accurate tomography measurements is possible in different environmental conditions. This structure should enable the device to be easily portable and operational in harsh situations and challenging environments. The use of lightweight and durable materials in the mechanical structure facilitates the portability of the equipment, allowing the user to study and evaluate remote and difficult-to-reach locations. Furthermore, the structure is resistant to various environmental conditions such as moisture, dust, and mechanical shocks. Different scenarios of being efficiently portable has been studied. The main components of the mechanical structure include a base connected to the pipeline wall, a fixed section, a movable (rotating) section, and the connection between them. The shielding of the gamma-ray source and the scintillator detector array are precisely placed on the movable (rotating) section. The shielding of the gamma ray source and the scintillator detector array against it are carefully placed on the movable part. In this article, initially, using pre-computed Monte Carlo calculations, optimal geometry and dimensions were selected. Subsequently, mechanical analysis of weight distribution was performed using Abaqus software, and finally,

engineering design was carried out using Solidworks software. After completing the designs, the components will be integrated. The present paper examines the mechanical dimensions of the portable tomography device with an emphasis on the design and construction of its structure. This research plays a fundamental role in improving the performance and accuracy of non-destructive evaluation processes for pipelines and can significantly contribute to enhancing the overall oil and gas transmission industry.

Keywords: Portable Computed Tomography, Pipelines Non-destructive Testing, Engineering Design, Limited-Number-Detector CT (LNDCT)

INTRODUCTION

Pipelines are currently among the best means of transporting gas and oil fluids. However, these pipelines are not immune to defects and damages. Due to the high impurities present in these fluids, deposits accumulate over time on the inner walls of the pipes, leading to a disruption in fluid flow due to pressure and flow rate reduction. Another concern is the internal or atmospheric corrosion of these pipelines, which can result in pipe rupture and fluid leakage into the environment. Apart from environmental damages, this can also halt service provision. Therefore, methods for evaluating and ensuring the integrity of pipelines and preventing damage to them need to be anticipated [1], [2], [3], [4], [5].

Since oil leaks can cause extensive environmental damage or pose life-threatening hazards, it is necessary to equip the predicted facilities to assess and test pipelines without any damage [6], [7]. Currently, one of the non-destructive methods for pipeline assessment is the use of gamma-ray tomography (CT scanning) [8], [9]. Computed Tomography is capable of non-destructively detecting and measuring both corrosion and deposits on the inner walls of pipes. Considering that pipeline routes may pass through obstacles and terrains with different weather conditions, the design of the mechanical structure of the device must be such that it is portable and usable in all these conditions or at least most of the time. In other words, the device must be firstly portable and transportable, secondly efficient and operational in various conditions, and thirdly, not compromise on the quality of imaging. As shown in figure 1, Efforts to construct and improve industrial tomography have led to four generations of these devices [10]:

- First generation: A single source and a single detector where the beam from the source is directed as a pencil beam and the pair of source and detector have translational and then rotational movements together.

- Second generation: It has multiple detectors, but still cannot fully cover an object. Hence, it requires translational movement again.

- Third generation: It utilizes a fan-shaped beam where, due to its fan angle, it can fully cover the object, and rotation alone is sufficient for detection.

- Fourth generation: The detector ring is fixed, and the source rotates alone around the object. However, its cost increases due to the increased number of detectors.

Unfortunately, first-generation CT scanners, despite their maneuverability and good resolution, have a measurement time of several hours. Recently, experiments with third-generation scanners are underway. [13,14]

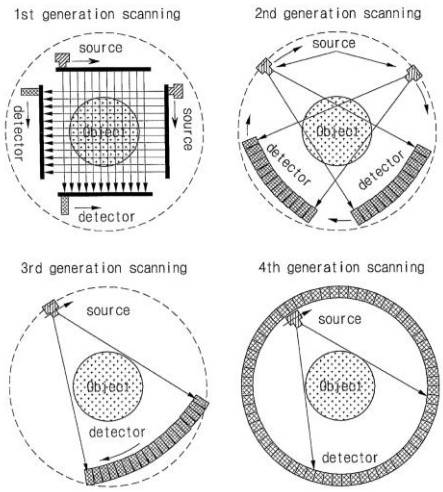

Fig.1. Four generations of industrial CT

Like other industrial devices, there are ongoing efforts to improve them. Improvements sought for CT scanners include: enhancing measurements, developing measurement methods, and comparing them with other measurement techniques [11], [12].

For the development of measurement methods, it should be noted that most Computed Tomography devices are not mobile. Therefore, the goal of such inventions and the

construction of such devices is to provide a scanning system that can be connected to the target and measure its cross-sectional area on-site. Since some of the components required for tomography are vulnerable to impacts that are inevitable during transportation, for easier transportation and preservation of these components, the device parts should be separable and installed on them during use. Hence, there is a need for minor yet significant changes in the structure of these types of devices. Two types of devices have been developed: The first type is not installed directly on the pipe itself. Instead, they are mounted on a separate base that holds the pipe in between. This type, like other CT devices, has the source on one side and the detectors on the other side. It rotates around the pipe by a motor and scans the entire cross-section of the pipe [13].

The second type, however, is installed directly on the pipe itself. The detectors are fixed on a C-shaped holder, and only the source rotates to around the circle. The point here is that to prevent problems arising from opening and closing, a “C” is used so that the pipe reaches the space between the detectors and the source from the “C”'s mouth. In this type, due to the structure of the “C”, incomplete scanning is performed, and the remaining projections will be reconstructed by computer simulation [14]. The second type, due to its installation on the pipe itself, will have more flexibility in operation, but its scan is not complete. This research aims to design and build a device with the flexibility of the second type but with complete scanning like the first type.

MATERIALS AND METHODS

In this article, the maximum diameter of the target pipe was measured to be 11 inches. Then, using Monte Carlo calculations with predefined weight and dimensional constraints, the distance between the source and detectors was determined to be 58 centimeters. The detectors are also arranged in an array of 11, with a spacing of 15 degrees directly opposite the source. Therefore, all components and movements were simulated using SolidWorks software shown in fig. 2.

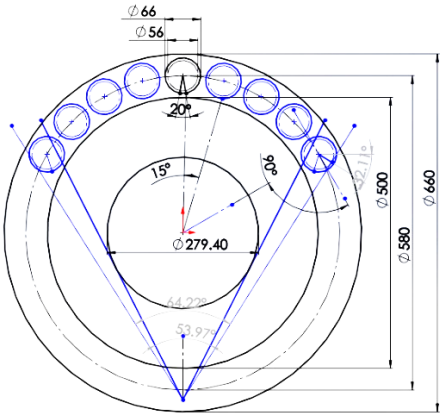

Fig. 2. Arrangement of pipe, source, and detector array relative to each other

1.2 General Structural Characteristics

For the sake of simplicity and ease of conceptualization, the device is divided into two main sections: fixed and movable. The General descriptions will be provided, and other subsidiary sections will be introduced thereafter. The details of each section will be presented in the third section:

1.1.2 Fixed Section

The fixed part or chassis, which is connected to the pipe, bears the weight of the movable part, transfers it to the pipe, and restricts the movable part to only one rotational degree of freedom. It cannot have vibrations or play in the remaining five translational and rotational directions. The fixed section includes the chassis and gear drive connections. The maximum pipe diameter for this device is 11 inches. The chassis attaches directly to the 11-inch pipe. But for smaller sizes, auxiliary jacks should be used.

2.1.2 Movable Section

The movable part, mounted on the chassis, has only one degree of freedom, consisting of the main gear onto which a ring is placed, along with the assembly of the source, collimator, and their detectors and bases fixed on it. The gear itself is connected to the chassis via a sliding polyethylene. The source is made of ^{137}Cs, and its collimator and shield are made of lead. The remaining parts are generally made of steel, unless otherwise specified. Different parts of the device do not require a specific surface finish and are completely disregarded.

2.1.3 Engine and Gearbox

The engine is installed at the top of the chassis and transmits the necessary torque for rotation to the main gear through an intermediary gear. Considering a safety factor of 1.25, the torque required for rotation is 25 N.m or 250 Kg.cm. Figure 8 illustrates the center of mass position of the rotating section. Due to the high precision required for rotation, a precise stepper motor must be used. Considering the low torque of stepper motors, a gearbox is required to increase the torque. However, the gearbox accuracy is approximately 1 to 8 minutes. Therefore, the gearbox must be tested, and if it does not provide satisfactory results with an accuracy of about 0.01 degrees, it is inevitable to use a stepper motor with higher torque that can provide the desired accuracy. Alternatively, a balance between cost and accuracy can be established, where for lower cost, less accuracy is accepted.

2.2 Load Tolerance and Stability Assessment

Before discussing the constructed section, the following points need to be mentioned. During operation, the device bears only the load caused by its own weight, Considering the strength of steel, from which most parts are made, and the weight they must bear, deformation seems unlikely. To illustrate this fact, it should be noted that the yield stress of ST37 steel is about 3700 Kg/cm^2. The schematic is shown in figure 3 and 4. Therefore, it is not necessary to measure the strength of the device itself.

The only potentially concerning aspect may be the possibility of pipe failure due to the weight of the device. With the equipment mounted, its weight reaches approximately 50 units. To create a sense of proportion, imagine a person sitting on an oil pipe. The maximum diameter of the tested pipe is 11 inches. The tube was also taken from the A333 type. It is evident that the greater the distance of the support from the device's workplace, the greater the displacement and stress on the pipe. Assuming a distance of 10 meters between two supports, the displacement would be 2 millimeters, and the maximum stress imposed on the pipe would be 6.7 megapascals.

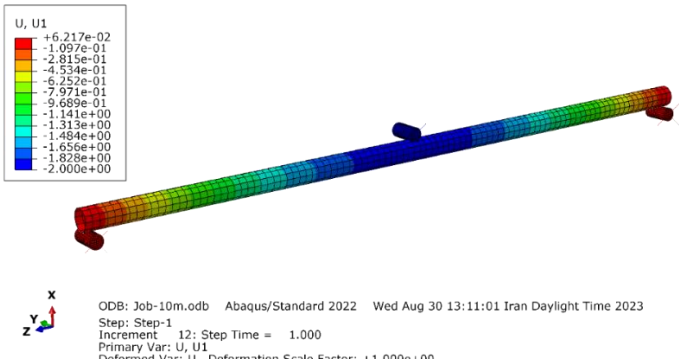

Fig. 3. Displacement in mm

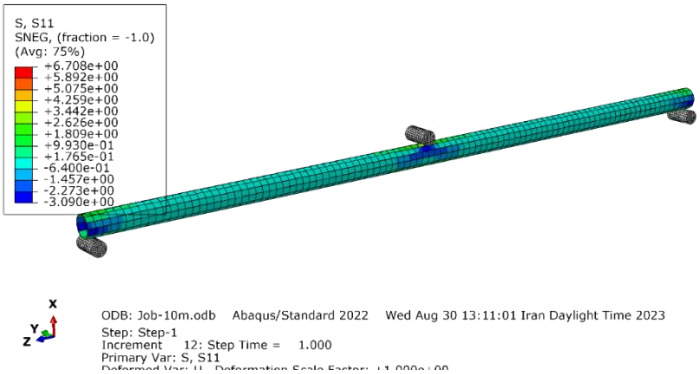

Fig. 4. Stress applied to the pipe in megapascals

3.2 Radiation Shielding

Common radioisotope sources for gamma ray tomography include 60Co, 137Cs, 241Am, and 133Ba. Considering the low energy of 241Am and 133Ba radiation and the short half-life of 60Co, the 137Cs isotope was chosen as the source. The shielding of the source, which also shapes the radiation into a beam, consists of a lead cube with the source placed within it.

1.3 Chassis

The chassis comprises two semi-cylindrical structures connected by screws while the pipe is sandwiched between them. The size of the chassis is matched to the outer diameter of the pipe, eliminating the need for jacks or other intermediaries for fastening. However, if the pipe diameter is smaller, a jack intermediary would be necessary. To attach the gear to the chassis, a portion of the chassis where the gear is mounted must be machined and completely rounded. Subsequently, the gear is mounted onto it using a smoothing intermediary.

2.3 Gear Clamping

The gear clamping mechanism serves to both constrain its movement and prevent friction between the gear and the clamping surface (figure 5). Due to space constraints and the inability to use various types of bearings, polyethylene and steel rings were utilized for smoothing and constraint, respectively. A polyethylene ring was also installed to provide spacing between the gear and the chassis. The advantage of polyethylene over bearings lies in its ease of opening and closing and its simplicity. Since the device operates in a dusty and sandy environment, the ring will easily shed any dirt and sand particles. In contrast, bearings do not easily open, and over time, sand particles will cause them to corrode.

Fig. 5. Two chassis parts after machining. the clamping of both sides of the gear is also visible in the image.

3.3 Gear

A gear with a module of 3 and 140 teeth (shown in Fig. 6), with a base circle diameter of 420 millimeters, was selected. For a pipe with a diameter of 300 millimeters, the entire radiation assembly must be placed on a diameter of 580 millimeters. Therefore, a ring of the same dimensions must be fabricated, and the detector and source should be mounted on it. It is noteworthy that the ring must be concentric with the gear to avoid eccentric rotation of the ring. In fact, what matters is the stationary center of rotation of the detectors and the source throughout the imaging process, whether the radiation assembly is fixed on a circular ring or on any other plane. To ensure accuracy in positioning the detector and source bases, the ring should be machined using a CNC machine and then cut into two pieces.

Fig. 6. Gear and polyethylene

4.3 Detector and Base

Two-inch CsI(Tl) detectors were used for this purpose. Steel bases are used to hold the detectors in place. The 3D shape is shown in figure 7. The bases serve two main functions: holding the detectors and preventing the entry of troublesome radiation. The base is a hollow cylinder with a groove to reduce noise. Although this significantly reduces incoming radiation to the detector, it also increases the signal-to-noise ratio, thereby improving image quality. The groove has a width of 10 millimeters and an aperture angle of 20 degrees.

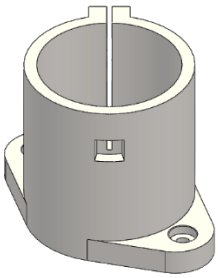

Fig. 7. Detector base

5.3 Source

The shield is a 10*10 lead block with a slotted aperture on its door, weighing approximately 11 kilograms, responsible for protecting the source and shaping and limiting its emitted rays.

6.3 Assembled Set

As shown in figures 8 and 9, In the assembled set, the total weight of the rotating part is 46 kilograms, and its center of mass is located at 42 millimeters from the axis of rotation.

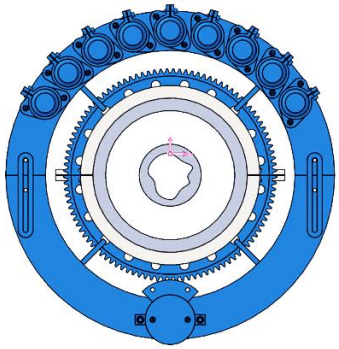

Fig. 8. The center of mass of the rotating part

Considering a safety factor of 1.25, the torque required for rotation is 25 N.m or 250 Kg.cm. The figure below illustrates the position of the center of mass of the rotating section.

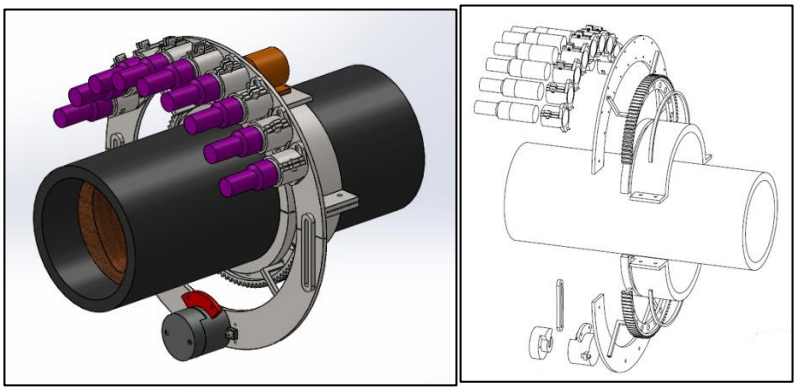

Fig. 9. Assembled view of the device and Exploded view of the device

Conclusions

In this research, we have presented a comprehensive design and assembly process for an industrial computed tomography (CT) scanner. The scanner consists of various components, including the chassis, moving parts, gears, detectors, and shielding materials, all meticulously engineered to ensure precise and reliable imaging of industrial objects. Through our design considerations, we addressed several critical factors influencing the scanner's performance, such as stability, weight distribution, and radiation protection. The integration of sturdy materials, such as steel and lead, along with careful attention to the arrangement of components, guarantees the scanner's robustness and safety during operation. Furthermore, our analysis of the mechanical and structural aspects of the scanner revealed insights into optimizing its performance while minimizing potential risks, such as tube breakage or

mechanical failure. By implementing innovative solutions, such as slotted lead shields and polyethylene spacers, we enhanced both the efficiency and safety of the scanner. The experimental validation of our design, including measurements of tube diameter, detector spacing, and torque requirements, confirmed the feasibility and effectiveness of our approach. The assembled scanner demonstrated reliable operation, achieving precise imaging results within acceptable tolerances. Overall, our study contributes to the advancement of industrial CT scanning technology by providing a systematic framework for designing, assembling, and evaluating CT scanners tailored for industrial applications. The insights gained from this research can inform future developments in industrial imaging systems, paving the way for enhanced quality control and non-destructive testing in various industrial sectors.

References

[1] J. -W. Wu, D. Bai, A. P. Baker, Z. -H. Li, and X. -B. Liu, "Electrochemical techniques correlation study of on-line corrosion monitoring probes," *Materials and Corrosion*, vol. 66, no. 2, pp. 143–151, Feb. 2015, doi: 10.1002/maco.201307175.

[2] , Alec Groysman, "Corrosion Monitoring," *Corrosion Reviews*, vol. 27, no. 4–5, pp. 205–343, Oct. 2009, doi: 10.1515/CORRREV.2009.27.4-5.205.

[3] P. Rostron, "Critical Review of Pipeline Scale Measurement Technologies," *Indian J Sci Technol*, vol. 11, no. 17, pp. 1–18, May 2018, doi: 10.17485/ijst/2018/v11i17/121459.

[4] M. S. Kamal, I. Hussein, M. Mahmoud, A. S. Sultan, and M. A. S. Saad, "Oilfield scale formation and chemical removal: A review," *J Pet Sci Eng*, vol. 171, pp. 127–139, Dec. 2018, doi: 10.1016/j.petrol.2018.07.037.

[5] I. A. Abdalsamed *et al.*, "Review Article: Scale Corrosion of Metallic Materials in Water Systems-A Review Citation I Scale Corrosion of Metallic Materials in Water Systems-A Review," *J. Chem. Rev*, vol. 4, no. 1, pp. 67–80, 2022, doi: 10.22034/JCR.2022.326770.1141.

[6] A. A. Carvalho, J. M. A. Rebello, M. P. V. Souza, L. V. S. Sagrilo, and S. D. Soares, "Reliability of non-destructive test techniques in the inspection of pipelines used in the oil industry," *International Journal of Pressure Vessels and Piping*, vol. 85, no. 11, pp. 745–751, Nov. 2008, doi: 10.1016/j.ijpvp.2008.05.001.

[7] C. H. de Mesquita, A. F. Velo, D. V. S. Carvalho, J. F. T. Martins, and M. M. Hamada, "Industrial tomography using three different gamma ray," *Flow Measurement and Instrumentation*, vol. 47, pp. 1–9, Mar. 2016, doi: 10.1016/j.flowmeasinst.2015.10.001.

[8] J. Kim, S. Jung, J. Moon, and G. Cho, "A feasibility study on gamma-ray tomography by Monte Carlo simulation for development of portable tomographic system," Applied Radiation and Isotopes, vol. 70, no. 2, pp. 404–414, Feb. 2012, doi: 10.1016/j.apradiso.2011.09.019.

[9] H. A. M. G. J.-S. C. Mostafa Kabir, "Optimizing Portable LNDCT for Oil and Gas Pipeline Imaging with Innovative Projection Acquisition Algorithm (Under Review)," Nuclear Engineering and Technology, Feb. 2024.

[10] J. L. Prince and J. M. Links, Medical imaging signals and systems. 2023.

[11] S. Carmignato, "Accuracy of industrial computed tomography measurements: Experimental results from an international comparison," CIRP Annals, vol. 61, no. 1, pp. 491–494, 2012, doi: 10.1016/j.cirp.2012.03.021.

[12] S. Carmignato, W. Dewulf, and R. Leach, Industrial X-ray computed tomography. Springer International Publishing, 2017. doi: 10.1007/978-3-319-59573-3.

[13] D. N. The Duy, N. Huu Quang, P. Van Dao, B. Trong Duy, and N. Van Chuan, "A THIRD GENERATION GAMMA-RAY INDUSTRIAL COMPUTED TOMOGRAPHY SYSTEMS FOR PIPELINE INSPECTION," J Teknol, vol. 77, no. 17, Nov. 2015, doi: 10.11113/jt.v77.6435.

[14] J. Kim, S. Jung, J. Moon, J. Guen Park, J. Jin, and G. Cho, "Development of transportable gamma-ray tomographic system for industrial application," Nucl Instrum Methods Phys Res A, vol. 693, pp. 203–208, Nov. 2012, doi: 10.1016/j.nima.2012.07.046.

ICNST 2024
International Conference on Nuclear Science and Technology
6- 8 MAY 2024 | Isfahan, Iran

Design and manufacture of 100 kV high voltage switched mode power supply with full bridge resonant topology for use in electromagnetic generators (Paper ID : 1032)

Jafari, H.[1,*], Abbasi, M.[2], Babaei, S.[3]

[1] *Faculty of Energy and Physics, Amirkabir University of Technology, Tehran, Iran*
[2] *Faculty of Electrical and Electronics Engineering, Shamsipour Technical and Vocational College, Tehran, Iran*
[3] *Faculty of Electrical Engineering, Tabriz University Tabriz, Iran*

Abstract

High power electromagnetic wave generator systems must be powered by high voltage DC power supplies with stable voltage level and low ripple to create a strong electric field and with the highest operating efficiency. In this work, we presented the technical considerations and design stages of different parts of a 100 kV switching high voltage power supply, as well as the results related to its construction and experimental tests. Considering that at the output of this power supply, a Marx generator has been used to increase the voltage to levels of more than 400 kV, the results showed that despite the presence of noises related to fast diodes and Marx generator gaps, there is no interference in performance of the switching circuit and control parts, and its accurate and correct operation can be seen in the waveforms related to the voltage across four legs IGBT switches and the current flowing through the resonant inductor.

Keywords: High voltage, Switched mode power supply, Resonant topology.

I. INTRODUCTION

In the last few decades, a lot of research has been done on increasing the efficiency and switching frequency of switching power supplies (and reducing their size and volume), as well as reducing their losses. Since the power switches pass through the linear region in some switching, at this moment the switch voltage and current have a magnitude that their overlap imposes major switching losses to the converter. Therefore, increasing the switching frequency increases the switching losses. In addition, the main cause of electromagnetic interference noise is the rapid changes in the voltage and current of the switches at the moment of switching, which also increases the frequency of switching, which causes this noise. But by providing different switching methods to solve the above problems, this converter has gained a special

place among other converters, which can be converted into three general categories of resonant, quasi-resonant and wide modulation converters. divided the pulse width [1-3].

On the other hand, due to the increasing development of high voltage pulse discharge systems (high pressure voltage) in large industries such as defense industries such as railguns, electromagnetic weapons and pulse

power lasers, crude oil processing improvement industries, Energy production industries such as nuclear fusion power plants using the laser-freeze method, etc., nowadays the focus of most research and development centers of applied sciences is to design and build high voltage switching power supplies (pulse and continuous) and then improve the characteristic Their electrical and physical parameters are flexible [2-4].

Electromagnetic generator systems, with the aim of achieving the highest operational efficiency, need high voltage DC power supplies with a stable voltage level and low ripple in order to create a strong electric field that leads to the flow of electrons on the electrodes and insulation. between them and finally ensure the occurrence of electric discharge between slow electrodes. In supplying very high voltages (several hundred kilovolts), some voltage boosters are often used in addition to switching power supplies. Despite the simplicity of the structure, the Marx generator can convert the input voltage to several times the initial value in order to produce electromagnetic waves in the form of pulses, high energy and frequency (repeatable) by feeding the appropriate load. These high power shock waves can be used to damage the electronic boards [5].

Considering the aforementioned, the purpose of this project is to design and build a high voltage switching power supply (varying from 10 kV to 100 kV/500 W) with a full-bridge resonant topology with the aim of running a 30 Hz/5 mA resonant Marx generator that works continuously. It should be able to supply its high voltage section by being powered by a battery and having only one portable operator unit. The advantage of this device is high reliability in operation, without being affected by electromagnetic noise and return voltage produced by Marx generator. This system has the following technical and general specifications:

1) adjustable output voltage of switching section from 10 kVDC to 100 kVDC, 2) average output current up to 5 mA, 3) 220 VAC input power supply voltage (if needed, it can be 12 VDC i.e. car battery), 4) with overload and overvoltage protection, 5) simple design of the control panel and command keys, 7) design circuit type: switching with full bridge resonance topology (suitable to load power), 8) dimensions of about 40x25x15 cubic centimeters.

II- TECHNICAL CONSIDERATIONS IN PERMANENT WORKING MODE

A- Electromagnetic protections

If high voltage power supplies are used in pulsed systems, the electronic and control subsystems will be severely exposed to strong electromagnetic noises. The process of harming through electromagnetic threats takes place in two forms, radiation and conduction. There are different methods, with different capabilities, to prevent radiation from entering the equipment, some of the most important of which are as follows:

- Shielding: Shielding means surrounding a circuit or covering its enclosure with metal and connecting it to the ground through a low resistance path. This method is considered one of the most effective methods and in most cases, the best method of preventing electromagnetic interference.
- Waveguides: Using Waveguides is an old method to prevent electromagnetic interference, but this method is not very useful for protecting equipment such as devices made of semiconductors.
- Filter: using filters made of passive elements such as capacitors and inductors to prevent low-power electromagnetic interference.
- Variable resistance with voltage: these parts, at high voltages, become conductive and are usually used to protect the circuit against overvoltage. The main disadvantage of these components is their relatively low response speed.
- Optical fiber: since electromagnetic pulses have no effect on light-sensitive equipment, optical fibers are resistant to all frequencies and voltages. But since it is still not possible to use optical fiber for all existing circuits, this method cannot be used as a comprehensive solution for whole sections of the power supply.

In the proposed plan, which aims to provide high voltage to the Marx generator, conventional methods of protection, filtering, optical fiber and the use of thermistor parts are used to protect the switching power supply against strong electromagnetic noises.

B- Protection against transient recovery voltage (return voltage) and its effect

One of the most common phenomena in the pulsed system that is not well introduced is called transient return voltage. This phenomenon occurs when there is an interruption in the supply of current. In other words, when the switch or gap in the Marx generator is short-circuited, the voltage at both ends of the Marx bridges increases. The magnitude of this voltage reaches twice

the value of the nominal voltage, which depends on the characteristics of the system, i.e. the type of load, the type of connection of cables and lines, and the type of earth system used. The most suitable method for protection against reverse voltage of Marx generator is to use diode circuits in the output part of the power supply. Therefore, this method is implemented according to the voltage level and the number of classes of the Marks generator in the proposed design.

C- Earthing system and safety earthing

The earthing system and safety earthing are two topics connected together, so that the leakage current inside the power supplies raises the potential of the safety ground and also causes a potential difference inside the power supplies and their peripheral control equipment. Since separating the above-mentioned two earthing systems can have disadvantages, after determining the type of use and the installation position of the pulsed equipment in the operating system, from effective earthing in order to prevent the creation of a higher short circuit current, preventing the passage of low current semiconductor devices will be used for power supply and covering the long distance created by separating the two earthing systems. It should be noted that the electronic boards and the printed circuit inside the operator panel will be completely isolated from the body so that the electronic noises related to the switching circuits will not harm the user through the body.

D- Placing the HV box inside the Marks generator chamber

Considering the operational importance of industrial systems, in the design and placement of high voltage equipment related to the power supply, it is possible to place the HV box inside the Marx generator compartment by interacting with the manufacturer of the Marks generator section to reduce lines power transmission, which itself increases the efficiency of pulsed power transmission, also led to a reduction in the dimensions of the defense system.

III- HIGH VOLTAGE SWITCHING POWER SUPPLY DESIGN CONSIDERATIONS IN PERMANENT WORK MODE

A- High voltage switching power supply

The optimal input power in the power supply is to use 220 VAC. However, due to the importance of operational industrial systems, it is possible to reduce the input voltage level to

12 VDC by using an inverter interface circuit at the beginning of the power supply, so that the 12 VDC battery can be used to supply energy to the system. The important point in this part is the special design of the inverter to produce full sinusoidal voltage by removing the effectiveness of electromagnetic noises and providing high direct current.

B- Supply of high voltages in isolation

In the past, in order to supply high output voltages, multiplier circuits or step-up transformers were used, but today, in order to supply high currents and voltages, resonance topology LLC or LCC with isolated multi-transformer circuits are used. In the proposed plan, in order to provide voltage of about 100 kVDC, five transformers are used in series with high current capability.

C- Control circuit of switches and feedback

Considering that the resonant converter in this work must be able to perform the switching operation in the condition of zero current, several important tasks are defined in its control part, which include the following:

1- high voltage detection,
2- detection of upper and lower limit current,
3- detection of zero current,
4- production of IGBT triggers according to the previous three tasks,
5- receiving the start command from the user and starting the circuit,
6- completely turning off the switching part by detecting high current or voltage.

In order to increase the response of the control circuit related to the detection of high and low limit current and zero current, three fast op amps have been used to detect the mentioned currents. There are two potentiometers to set the upper limit and the lower limit of the current, which can be used to control and limit the current desired by the user, and there is a potentiometer to control the zero current, by which the zero crossing current is controlled. The input of these comparators is the voltage on the shunt. Shunt resistance is used to accurately calculate the zero current. In order to get feedback from the output voltage, the output of the comparator related to the control of the output voltage is used to detect the high and low limit voltages. The input of all these comparators is a voltage that is applied to the circuit through a receiving diode.

In order to manage control inputs and outputs with reliability and high data transfer speed, an industrial CPLD controller with low noise effectiveness, which is from the family of FPGAs, is used. The CPLD controller circuit has nine inputs and one clock input, by which all operations are performed.

The switching circuit part of the proposed design, which is full-bridge resonant type using 4 IGBTs, is presented in Figure 1.

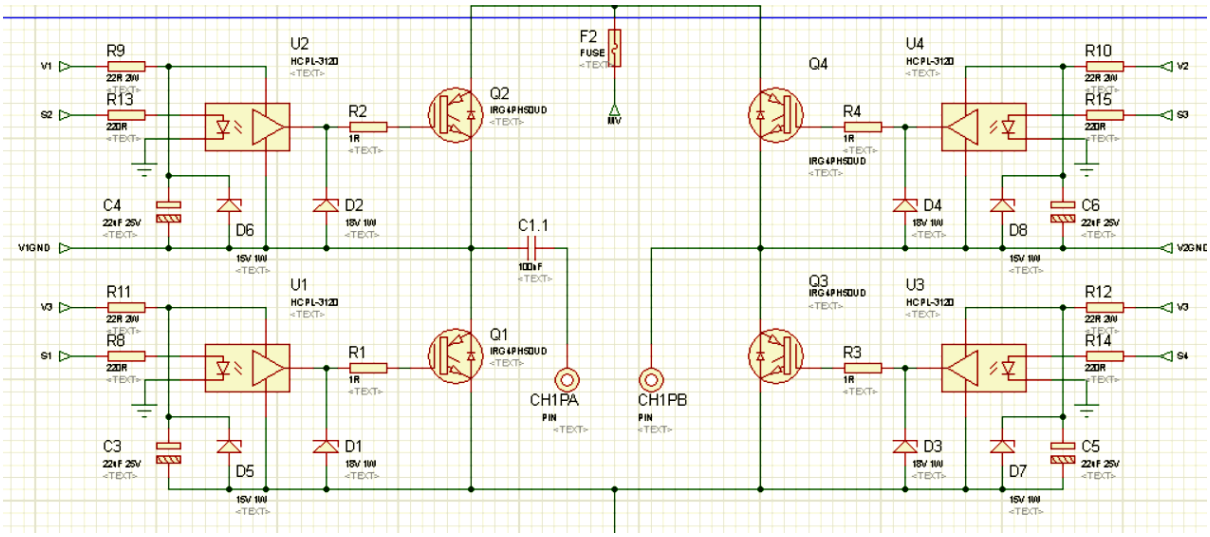

Fig. 1: Switching circuit part of the proposed design.

The design related to the voltage multipliers, which are related to the two parts of the switching power supply and Marx generator, is shown in Figure 2.

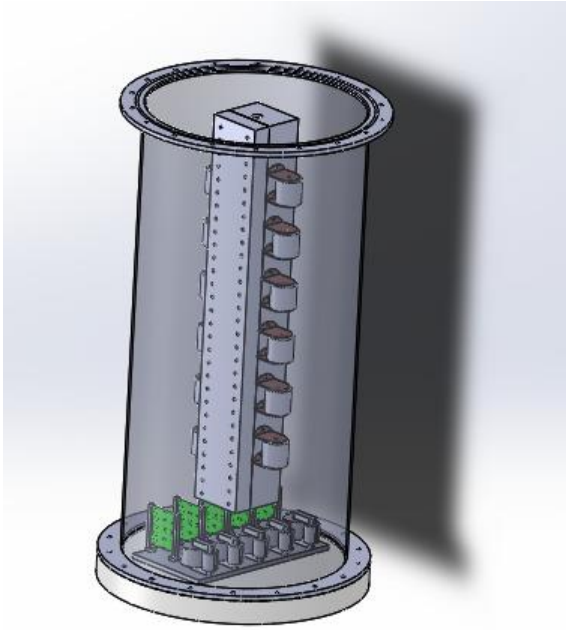

Fig. 2: The design of the voltage multipliers related to the two parts of the switching power supply (down board) and Marx generator (top section).

D. EXPERIMENTAL RESULTS AND DISCUSSION

After designing the various components of the desired power supply and taking into account technical considerations, an industrial example of a high voltage switching power supply (varying from 10 kV to 100 kV/500 W) with a full-bridge resonant topology with the aim of permanently setting up a 30 Hz/5 mA resonant Marx generator work was done. In Figures 3 and 4, you can see the control section and the switching circuit and the high voltage section of the power supply, respectively.

In Figure 3, it is clear that the control part of the device is designed in such a way that the output voltage can be adjusted from 10 to 100 kV, while the current passing through the Marks circuit can also be seen in the control panel of the device to that ensured the occurrence of repeated discharges and achieving high frequencies of high voltage discharges. Also, it is clear in Figure 4 that despite the use of equalizer circuits inside the oil box, the voltage isolation considerations are well respected in such a way that unwanted sparks can be prevented at voltage levels above a few tens of kilovolts.

Fig. 3: The control section and the switching circuit of the proposed high voltage power supply.

Fig. 4: The high voltage section of the proposed high voltage power supply.

In Figures 5 and 6, you can see the waveforms related to the voltage of the power switch legs, the resonance inductor current and the voltage of the resonance capacitor. It can be seen carefully in the voltage waveforms of the switches' legs and the inductor current waveform that a suitable homophase has been established between these two waveforms, which shows the accurate operation at the moment of switching. This achievement is very worthy in the presence of high frequency noises that are created and spread during the operation of the Marks generator, and it shows the accurate operation of the power supply protection circuits.

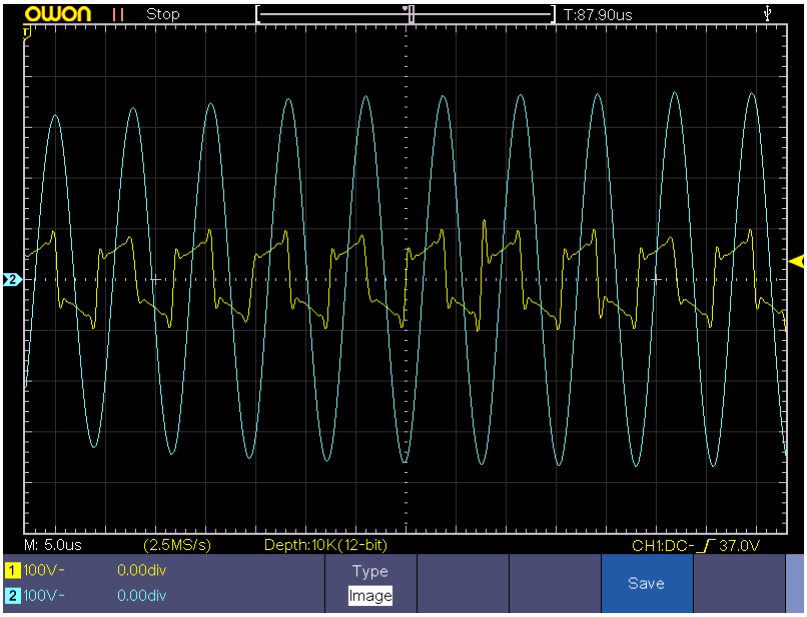

Fig. 4: The voltage of the power switch bases (squ.) and the resonance inductor current (sin.).

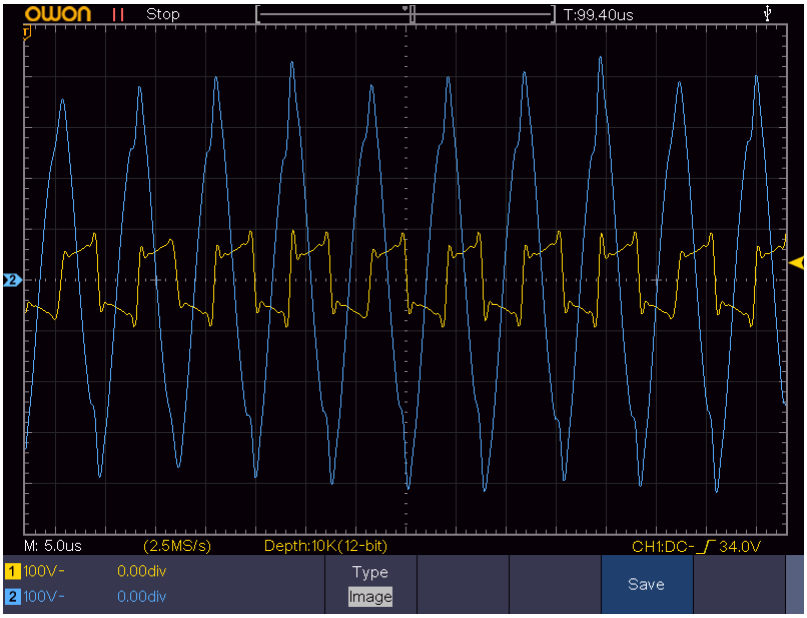

Fig. 5: power switch bases (squ.) and the voltage of the resonance capacitor (tri.).

IV- CONCLUSIONS

In this research, an attempt was made to present the design and construction steps of a high voltage switching power supply with application in powering a Marks generator to achieve an output pulse high voltage of above 400 kV. Also, all requirements and technical considerations needed in the construction of this device were also discussed. In the experimental results

section, it is shown that the waveforms of the switching circuit elements, including the resonant inductor and resonant capacitor, were obtained correctly, so that the smallest adverse effect on the switching circuit performance was not caused by Marx generator noises.

V- REFERENCES

[1] A. Chub, D. Vinnikov, F. Blaabjerg, and F. Z. Peng, "A Review of Galvanically Isolated Impedance-Source DC–DC Converters," IEEE Transactions on Power Electronics, vol. 31, pp. 2808-2828, 2016.

[2] M. Forouzesh, Y. P. Siwakoti, S. A. Gorji, F. Blaabjerg, and B. Lehman, "Step-up DC–DC converters: a comprehensive review of voltage-boosting techniques, topologies, and applications," IEEE Transactions on Power Electronics, vol. 32, pp. 9143-9178, 2017

[3] S.-H. Ahn, H.-J. Ryoo, J.-W. Gong, and S.-R. Jang, "Design and test of a 35-kJ/s high-voltage capacitor charger based on a delta-connected three-phase resonant converter," IEEE Transactions on Power Electronics, vol. 29, pp. 4039-4048, 2014.

[4] R. Nelms, B. Strickland, and M. Garbi, "High voltage capacitor charging power supplies for repetitive rate loads," in Industry Applications Society Annual Meeting, 1990., Conference Record of the 1990 IEEE, 1990, pp. 1281-1285.

[5] S. R. Jang, H. J. Ryoo, J. S. Kim, and Y. B. Kim, "Design and testing of the high voltage capacitor charger for 150kJ pulsed power application," in 2009 IEEE Pulsed Power Conference, 2009, pp. 1376-1379.

ICNST 2024
International Conference on Nuclear Science and Technology
6- 8 MAY 2024 | Isfahan, Iran

Image processing and X-ray image analysis techniques in vehicle inspection systems for material discrimination (Paper ID : 1034)

Jafari, H.[1,*], Arfaorafie S.[2]

[1] *Faculty of Energy and Physics, Amirkabir University of Technology, Tehran, Iran*
[2] *Faculty of Electrical Engineering, Shahrood University of Technology, Tehran, Iran*

Abstract

Inspection of cars in security places is very important and creating a quality image and proper visual vision helps the operator to make a more appropriate diagnosis. In this article, two methods are proposed for the separation of materials, which are based on the diagram of High and Low images and the ratio of the logarithm of High and Low images. In this research, by only having Low and High images of a car (without any information from the inspection device) material separation was done based on the above methods in such a way that first by having images of different materials (metal and non-metal) in different thicknesses, Aluminum was defined as the separation boundary between materials. Thresholds for separation were obtained by using the logarithm ratio method. To improve the gray images, first the images were normalized and the histogram matching was performed. Next, one image was made from two High and Low images. It was found that by applying the appropriate color map, an output with a suitable visual visibility was created. Finally, to improve the color image, we used the Median filter and sharpened the image to create a better visual visibility. The presented real-time algorithm is written in C++.

Keywords: Image processing, X-ray image, High and low images.

INTRODUCTION

The X-ray imaging system with two energy levels (high energy and low energy) has many applications in car and baggage inspection at airports and in medical science in tumor diagnosis and so on. In these systems, at high energies (more than 100 kW), the absorbed energy is primarily dependent on the density of the material, in such a way that the higher the density, the more energy is absorbed by the material, and as a result, the output image is darker. At lower energy levels (about 80 kV) the absorption depends primarily on the effective atomic number and also on the thickness of the material. Although regions with heavy metals are dark in both low-energy and high-energy images, regions with light elements are darker in the low-

energy image. Light elements such as carbon, nitrogen and oxygen can be distinguished by comparing these two types of images [1].

Some dual-energy X-ray detection systems are capable of dual-energy analysis to estimate the atomic number of the material inside the bag. The problem of separating a thin plate that is strongly absorbent from a thick plate that is weakly absorbent, faced by transmission X-ray imaging systems, is solved in dual-energy X-ray detection systems. However, dual-energy detection systems also have a major limitation, which is that the actual density of objects that may be in the bag is not fully known, and the system only provides an estimate of the atomic number (i.e., the effective atomic number). As a result of this limitation, the false alarm rate in these systems reaches about 30%.

Novikov et.al proposed a transformation for transmission values to obtain so-called alpha curves which have made it possible to discriminate between materials using 4 and 8 MeV sources [2]. Another space of curves is introduced by Ogorodnikov et.al which uses the ratio of logarithms of transmission coefficients to differentiate organic, inorganic and heavy metallic materials using 4 to 10 MeV energies [3]. Liu et.al have compared the technique used in [3] with systems using neutron sources. Dual energy systems are reported to have better penetrations while neutron sources having better sensitivities [4]. Zhang et.al have presented HL curves for 65 and 80 keV sources [5].

Due to the fact that the output of the X-ray system with two energy levels is high and low energy images, in order to separate materials into metal and non-metal, according to previous studies, we came to the conclusion that the pixel value in the High and Low images are related and in the method presented in the High-Low diagram, the value of the horizontal axis is the pixel value of the Low image and the value of the vertical axis is the pixel value of the High image. According to reference [1], we can conclude that these values should be on the function for a material with different thicknesses. In the following, according to the atomic number of aluminum, which has the lowest atomic number among common metals, this metal was considered as the boundary for separating metal from non-metal in the High-Low diagram. By using this border and separation of materials from two High and Low images, an image is obtained, which by applying color maps and image processing operators, a color image with a suitable visual vision is created. In this research, we used a dual energy system using a 160

keVand 1 mA source and sandwiched dual energy detectors with 2.5 mm/64 pixels (GOS:low energy scintilator and CsI(Tl): high energy scintilator).

HIGH-LOW DIAGRAM METHOD

In the presented method, first, using standard samples, the High-Low diagram is drawn for different materials with different thicknesses. Fig. (1) is a standard sample of aluminum that has been obtained in different thicknesses. The parts separated by the red frame are aluminum with different thicknesses. Due to the fact

that for drawing the diagram, the parts that are separated by the box are important by pre-processing the important parts that are separated and displayed in Fig. (2).

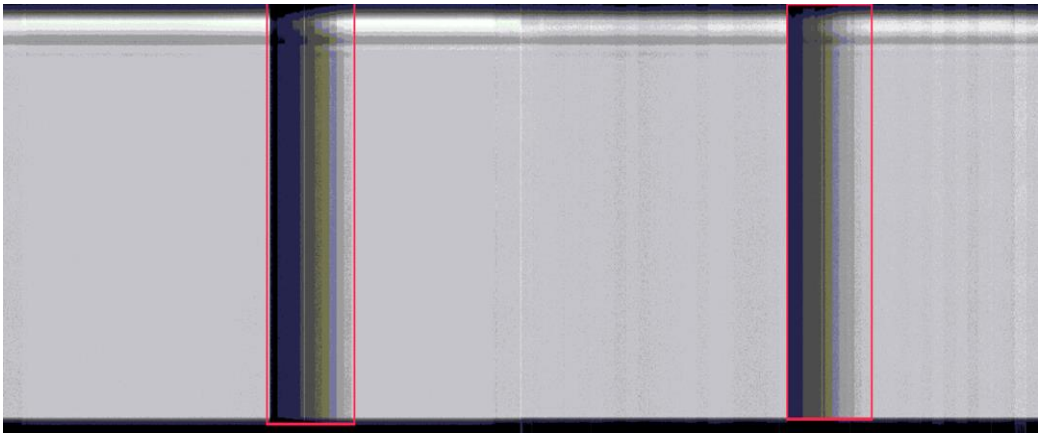

Fig. 1: High and Low image of standard aluminum sample. The right side of the Low image and the left side of the High image. The parts with red box contain information.

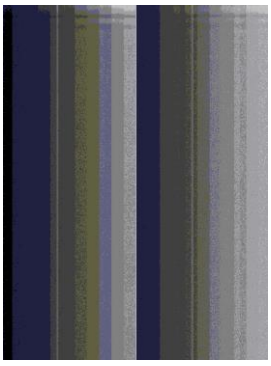

Fig. 2: Parts with information on the right side of the Low part and the right side of the High part image.

In the following, the High-Low diagram for different materials is drawn in a diagram and you can see it in Fig. (3). In the proposed method, according to the results of the standard material diagram and the fact that aluminum has the lowest atomic number among common metals, the resulting diagram of aluminum is used as a boundary to separate the materials. In the following, by comparing the Fig. (3) with the graph obtained from the extracted material function, it can be seen that the fitted function on the aluminum sample is very close to the extracted material function, for this reason, to reduce the calculations from the extracted function as the boundary of metals and other metals are used.

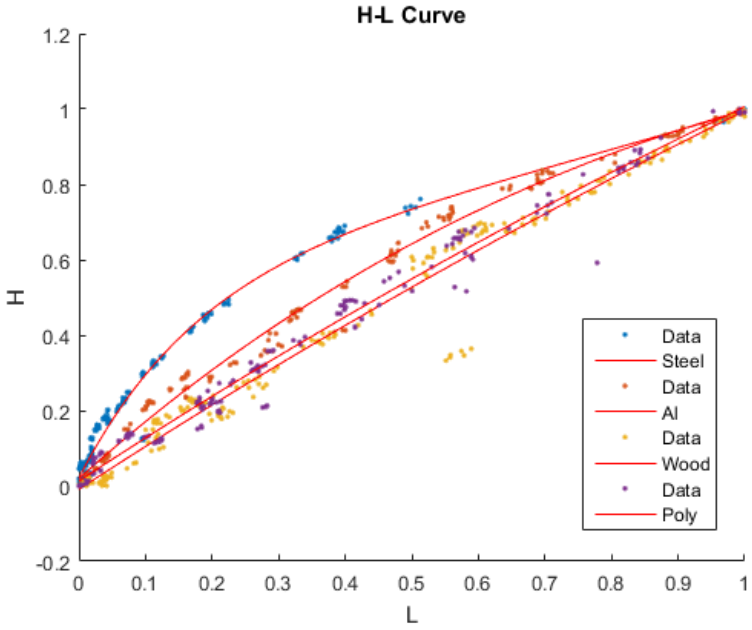

Fig. 3: High-Low diagram for standard examples of materials: steel, aluminum, wood and polymer.

In the next step, we apply our method on a complete image of a car whose High and Low images are given in Fig. (4). In this step, first the images are normalized and the histogram is equalized, and without pre-processing (getting the range with information), we obtain the High-Low diagram for the desired data. Then, using the proposed method, it is defined a mask for metals and a mask for non-metals, which can be seen in Fig. (5) of the results. In the following, according to the different thicknesses of the materials, a coefficient should be defined in the image so that we have a proper view of the thickness at the stage of applying the color map. For this purpose, according to the location of the pixel in the High-Low diagram, a coefficient

is assigned to it. In this way, according to the normalization of pixel values to the range of values close to zero, it indicates more thickness and values close to one indicate less thickness.

Fig. 4: High and Low images for a part of a car. The right side of the image is Low and the left side is High.

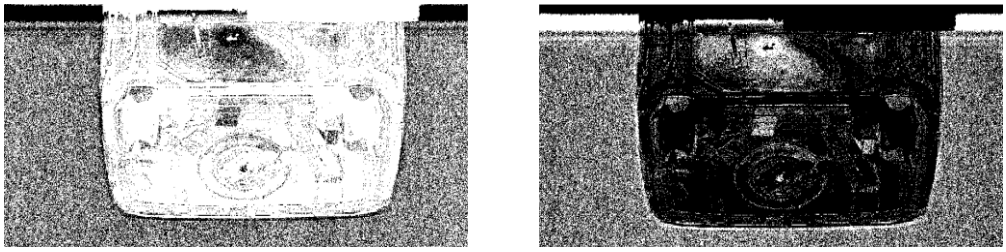

Fig. 5: The right side of the mask of non-metal materials and the left side of the metal mask. Black color indicates the presence of matter.

In the suggested color map that is used to create a color image, blue color is used for metals, which becomes black with increased thickness, and red color is used for non-metals for differentiation and prominence. In this color map, a white range is defined, which is used to remove the middle areas. The result of applying the color ramp on the image with the coefficient is as in Fig. (6) and it can be seen that the non-metal areas are discontinuous. To solve this problem, Median filter is used [5] and the image is sharpened, the output is shown in Fig. (7).

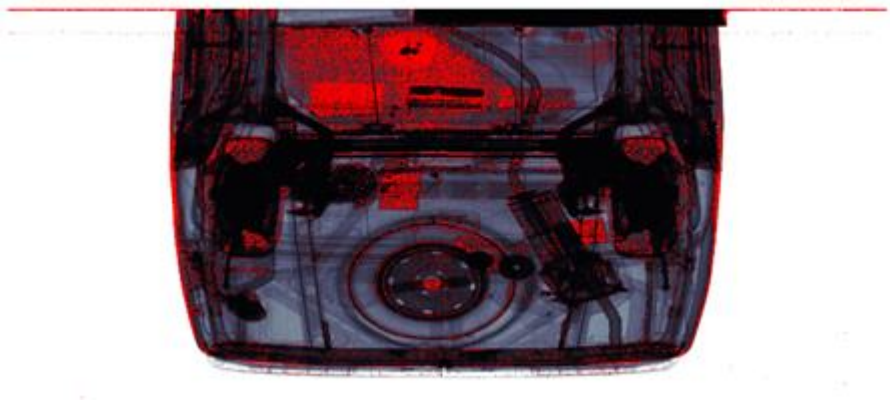

Fig. 6: Applying the color map.

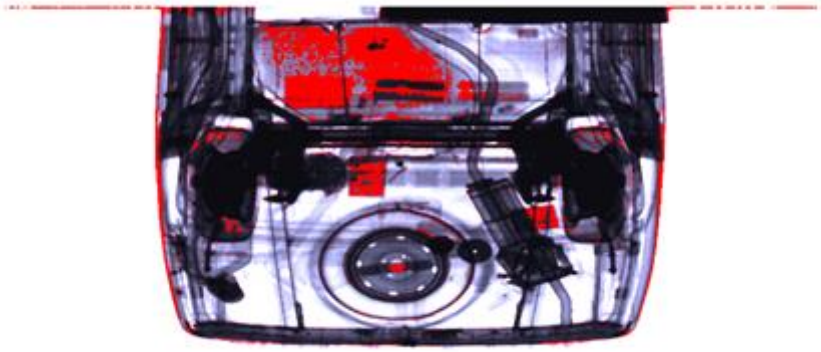

Fig. 7: Applying the Median filter and sharpening the image.

THE LOGARITHMIC RATIO METHOD

In this method, we used the logarithm of the values of High and Low images and by defining the variable $K = \frac{\log(T_L)}{\log(T_H)}$ that T_L and T_H are the values of High and Low images, we can separate the materials. In this method, we use thresholding to separate materials. In such a way that organic substances have a specific interval, and we separate organic substances by filtering this interval.

Next, to distinguish organic materials, we value each pixel according to its gray value in the Low image. In this method, R and G channels are quantified for organic materials. In the following, for the metal part, we used the pixel values in the Low image, which are displayed in gray. Next, to distinguish the parts with organic substances with higher density, the Median filter was used in such a way that this filter was applied only on the mask that was identified

as organic substances. Flowchart of Z-Image creation used in this reseach has been observed in Fig. 8.

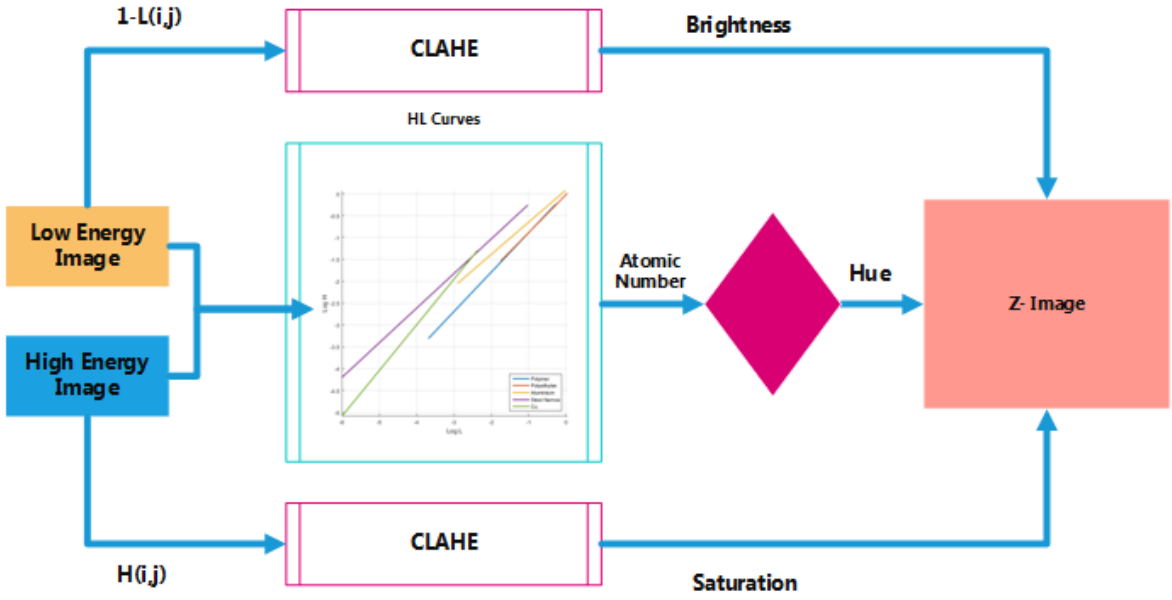

Fig. 8: Flowchart of Z-Image creation.

Table 1 shows the average error and standard deviation percentages of effective atomic number estimation. Fig.9 illustrates the output of the software which has successfully detected organic mateirals hidden in a gas tank of a car.

Table 1: Effective atomic number estimation accuracy.

Matter	Z_{eff}	Average Error %	Standard deviation %
Polymer	4	15.9	**1.6**
Polyethylene	5.5	4.8	**1.4**
Wood	6.3	22.6	**1.2**
Iron	26	4.8	**9.2**
Steel	20	7.4	**9.4**

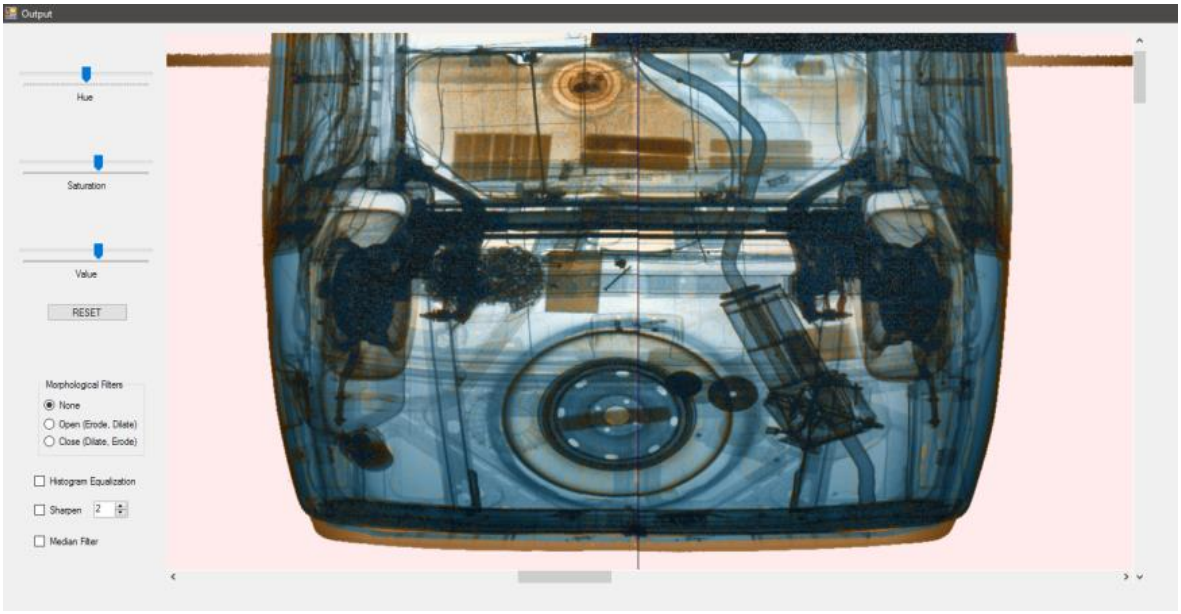

Fig. 9: Detection of hidden organic materials in a gas tank

Conclusions

In this research, after designing and making a number of standard step patterns of different materials (wood, polyethylene, aluminum, iron, copper and steel), we extracted high energy and low energy diagrams from their images. Then, by passing the car through the x-ray imaging machine, the high energy and low energy images created. Also, we reconstructed and processed the images in manner of dual-energy method using two techniques of high and low energy curves and logarithm ratio. The results showed that using both techniques at the same time can reduce the limitations of dual energy devices in material separation.

References

[1] Fu, Kenneth, Performance enhancement approaches for a dual energy X-ray, 2010.

[2] Novikov VL, Ogorodnikov SA, Petrunin VI. Dual energy method of material recognition in high energy introscopy systems, 1999.

[3] Ogorodnikov S, Petrunin V. Processing of interlaced images in 4–10 MeV dual energy customs system for material recognition. Physical Review Special Topics-Accelerators and Beams, 2002.

[4] Liu Y, Sowerby BD, Tickner JR. Comparison of neutron and high-energy X-ray dual-beam radiography for air cargo inspection. Applied Radiation and Isotopes, 2008.

[5] Zhang, Guowei, et al, "Exact reconstruction for dual energy computed tomography using an HL curve method," 2006 IEEE Nuclear Science Symposium Conference Record. Vol. 6. IEEE, 2006

[6] G. Bradski and A. Kaehler, Learning OpenCV: Computer vision with the OpenCV library: "O'Reilly Media, Inc.", 2008.

Removing Erythromycin from pharmaceutical wastewater using electron beam and detecting decomposition by-products by LC-MS (Paper ID : 1036)

Berenji Ardestani S., Akhavan A.*, Ahmadi-Roshan M.

Research School of Radiation Applications, Nuclear Science and Technology Research Institute, AEOI, P. O. Box: 14395-836, Tehran, Iran

Abstract

Erythromycin is the most important macrolide antibiotic, which is widely used in medicine and veterinary medicine. Erythromycin residue in the environment is not completely removed in the treatment process and causes resistance of microorganisms to these chemicals and diseases in humans and animals. Electron beam irradiation can destroy a wide range of pollutants in wastewater including antibiotics. High destruction efficiencies of ≥ 90% were gained at 25 kGy in samples at concentrations of 10-50 ppm. Innovatively, the radio-degradation of erythromycin was studied in real wastewater samples from a pharmaceutical Company in Iran. The degradation efficiency of the real effluent sample irradiated sample at 25 kGy was 100%. The obtained results from Liquid chromatography-mass spectrometry (LC-MS) analysis showed that degradation, inactivation of β-lactam structure, and other byproducts resulting from irradiated erythromycin samples had acceptable toxicity. Therefore, electron beam irradiation would be suggested to remove erythromycin from wastewater and return it to the industrial cycle.

Keywords: Erythromycin; electron beam; wastewater treatment; radio-degradation. LC-MS

INTRODUCTION

Antibiotics are one of the greatest classes of pharmaceuticals and are utilized to treat diseases in human beings. Also, they are applied to animals to inhibit disease and raise growth [1]. The presence of antibiotics in water sources, even in low concentrations, leads to the production and development of antibiotic-resistant genes and pathogens, which potentially threaten the functioning of the ecosystem and human health [2]. Therefore, various advanced oxidation processes (AOPs), such as irradiation, have been currently applied to treat non-degradable pharmaceuticals by conventional water treatment processes. Radiolysis is a new treatment

technology in the field of radiation-induced degradation of environmental pollutants. The ionizing radiation

process is an alternative method to eliminate a variety of non-degradable compounds and shows higher removal efficiency and non-specific degradative action. Radiolysis has advantages in minimizing the required energy cost for treatment, and is a fast and clean process, without chemical addition for oxidation. It is known that the radiolytic decomposition of aqueous pollutants is dominated by reactive species produced by water radiolysis, such as hydroxyl radical (°OH), and hydrated electron (e-aq) [3]. The application of electron beam has gained attention in the field of radiation-induced decomposition of environmental contaminants. When aqueous solutions are irradiated with an electron beam, water absorbs most of the radiation energy and produces some reactive species, of which hydroxyl radicals and hydrated electrons are principal. These activated species affect the decomposing aqueous contaminants. However, research considering the degradation of antibiotic substances by electron beam has expanded, and studies on the decomposition products are rare. In addition, there is inadequate data on the intermediates and products generated by electron beam irradiation. Some aqueous contaminants were not completely disintegrated by these powerful AOPs but yielded several intermediates or products. These can be more stable than the parent compound when released into the environment. When electron beam technology is applied for organic materials decomposition, it is very important to understand the structure and toxicity of the by-products likely to be formed by the electron beam [3]. Therefore, the present study aimed to identify the radiolytic degradation products of erythromycin in synthetic standard and real pharmaceutical wastewater samples that were subjected to the electron beam. The radiolytic products during the irradiation process were identified using LC-MS.

EXPERMENTAL

Chemicals

Formate-methanol buffer (70-30) and ammonium acetate (Analytical grade, Merck, Darmstadt Germany), methanol, ethanol (HPLC grade, Merck, Darmstadt Germany), working standard of erythromycin (Rooyan Darou Co., Iran) and real pharmaceutical effluent (Erfan Darou Co., Iran) were prepared.

Preparation of laboratory antibiotic samples

According to the literature standard solutions of erythromycin, 10, 50, and 100 ppm were prepared. The solutions were made in a volume of 10 ml, and according to solubility, it was solved in a relevant solvent consisting of 0.7 ml ethanol + 9.3 ml water deionized. All samples were stored at 4°C until irradiation [4].

Irradiation of real and synthetic pharmaceutical wastewater

Real and synthetic samples were irradiated by electron beam at doses of 10, 25, and 50 kGy using a Rhodotron TT200 (IBA, Belgium); continuous-wave (CW) electron accelerator, with an output of 10 MeV electron beam lines and a maximum power of 100 kW at the Radiation Application Development Company - Central Iran Research Complex, Yazd. All samples were stored at 4°C.

Determination of the concentration of erythromycin in irradiated synthetic and real pharmaceutical wastewater

The initial concentration of erythromycin in synthetic and real pharmaceutical wastewater samples was measured according to the method of Jiao et al. (2008) using HPLC analysis by C18- xbridge column and UV-VIS detector (2487, Waters, USA) at the wavelength of 220 nm [5].

The changes in the structure of compounds in irradiated samples using LC-MS

The structural study of erythromycin degradation products was based on total ion chromatogram (TIC) analysis and corresponding mass spectrum. The mass of different products from the peaks related to the protonated molecule, and $[M + H]^+$ were determined for positive ionization (Santoke et al., 2009). Additives in the positive mode were formic acid. LC-MS system was applied for analysis as follows: LC device Kenauer platin blue uhplc (Germany) and MS device LCT primier micro mass (Waters, USA). Analysis in real and synthetic pharmaceutical wastewater samples was done using HPLC device (Waters 1525 binary pump, USA) with a C18-xbridge reversed-phase column (250 mm × 4.5 mm, filler particle diameter 5 µm, Waters, USA) at 25±2 °C. The mobile phase was composed of two components: (A): ammonium acetate 20 mM with pH = 8, and (B): methanol with gradient program, at a flow rate of 1 $ml.min^{-1}$. Detection was performed by UV-VIS detector (2487, Waters, USA), at wavelengths of 220 nm [5,1].

Results and discussion

The effect of electron beam irradiation on the degradation of erythromycin

In this study, erythromycin showed a destruction efficiency of about 48% at 10 kGy, and by increasing the radiation dose to 25 and 50 kGy, a destruction efficiency of 100% was observed (Table 1). In a similar study, the degradation efficiency of erythromycin in antibiotic fermentation residues using ionizing radiation at 10 kGy was reported up to 86% [6]. More than 90% of β-lactam antibiotics in the concentration of 1 $mmoll^{-1}$ after gamma irradiation at 12 kGy using ^{137}Cs were removed. According to the results, $^{\circ}OH$ and eaq^{-} degrade the β-lactam ring with 55% and ~88% efficiency, respectively. The antibacterial ability decreased and eventually missed after ionizing irradiation [2]. For the treatment of water sources, it has been reported that the presence of dissolved organic carbon and some inorganic anions compete with the reactive species produced by water radiolysis and reduce the degradation efficiency of the target pollutants. The degradation rate of penicillin G from β-lactams and erythromycin family decreased with increasing initial concentration. When the initial concentration of penicillin G increased from 0.27 mmol to 1.34 and then to 2.68 mM, the degradation rate constant decreased from 2.10 to 0.49 and then to 0.31 kGy^{-1}, respectively. This issue would be due to the competition between degradation products and primary pollutant molecules for reactive radicals produced from water during gamma irradiation [2]. These findings are consistent with the results of the present study, in which at the same irradiation dose, at a higher concentration of erythromycin, the destruction percentage decreased, and in real pharmaceutical wastewater samples at the same concentration (1.94 ppm) the degradation efficiency percentage increased by increasing irradiation dose (Table 1).

Table 1. Effect of irradiation doses and initial concentrations on removal efficiency percentage of erythromycin samples

Irradiation dose	Standard solution concentrations (ppm)			Real sample (ppm)
(kGy)	10	50	100	1.94
0	(0.0±0) ^{f}	(0.0±0) ^{f}	(0.0±0) ^{f}	(0.0 ± 0) ^{a}
10	(100 ± 0.0) ^{a}	(82.3 ± 0.04) ^{d}	(64.0 ± 0.02) ^{e}	(47.8 ± 0.05) ^{a}
25	(100 ± 0.0) ^{a}	(100 ± 0.0) ^{a}	(92.4 ± 0.02) ^{c}	(0.07 ± 0.100) ^{a}
50	(100 ± 0.0) ^{a}	(100 ± 0.0) ^{a}	(99.0 ± 0.01) ^{b}	(0.0±0.100) ^{a}

The different letters indicate significant differences ($P \leq 0.05$).

Identification of radiolytic degradation products of erythromycin by LC-MS

Chromatograms in figs. 1,2 were obtained after injecting 100 ppm sample irradiated at 25 kGy.

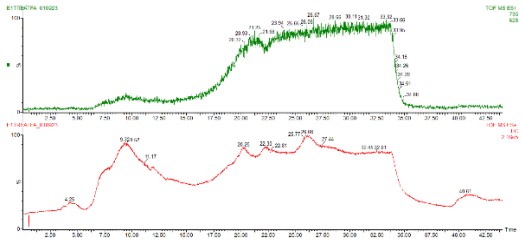

Fig. 1. LC-MS mass spectrum (up graph) and TIC chromatogram (down graph) of erythromycin sample 100 ppm irradiated at 25 kGy

According to Fig. 2 (A) the extracted peaks can be assigned to different compounds as follows inconsistent with previous researches [7]: 159.0105 m/z (158) cladinose sugar compound, m/z 732.7279, erythromycin epoxide A. Also, m/z 558.5619 resulted from the separation of a cladinose sugar unit and a water molecule from erythromycin A (EA), m/z 576.5499 resulted from the separation of a cladinose sugar unit from EA, m/z 592/5736 resulted from Decomposition compounds of erythromycin C-N oxide (ECNO) after separating one molecule of Mycarose sugar, two molecules of water, two molecules of propionaldehyde and two molecules of oxygenated ring units with m/z 56, m/z 279.2213, benzoylated and oxidized desosamine sugar, m/z 606.6010 resulted from the degradation compounds of erythromycin F-N oxide (EFNO) after the separation of one cladinose sugar unit and m/z 462.4323 from the separation of the cladinose sugar unit, 3 water molecules and one propionaldehyde unit from EA.

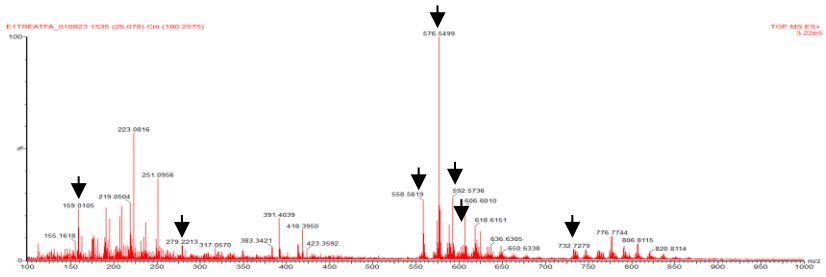

(A)

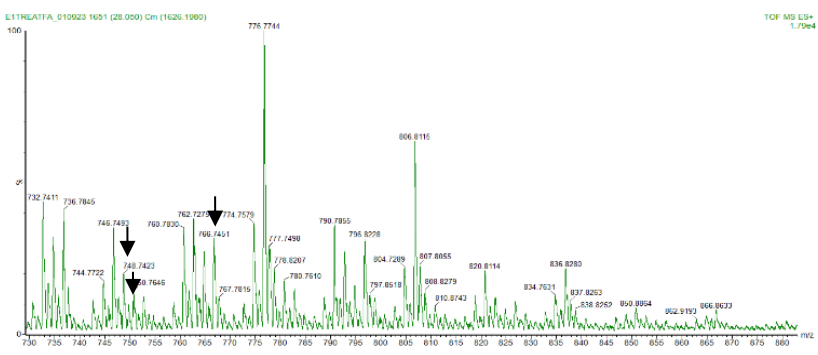

(B)

Fig. 2. LC-MS mass spectrum of erythromycin sample 100 ppm irradiated at 25 kGy; (A) Time 190-2575 s, (B) Time 1626-1980 s

In the present study, according to Fig. 2 (B) and according to similar papers [7], the extracted peaks with m/z 766.7451 can be assigned to the compound of erythromycin F-N oxide (EFNO), m/z 748.7423 assigned to erythromycin E (EE), m/z 750.7646 to erythromycin F (EF). It has been reported that the β-lactam ring is chemically unstable and sensitive to heat, acids, base and UV light, nucleophilic and enzymatic reactions, which as a result hydrolytic ring opens and the antibiotic loses its activity. This indicates that gamma irradiation can degrade and inactivate β-lactam antibiotics in water matrices [2].

Conclusions

Nowadays, irradiation has been introduced as one of the possible and effective methods to remove antibiotic pollutants. The main purpose of irradiation is to degradable non-biodegradable pollutants into inorganic and organic compounds, as well as remove microbial contamination caused by viruses and bacteria. According to the results of this study, in the standard solutions and real pharmaceutical wastewater samples, the removal efficiency of erythromycin at the same concentration increased significantly with increasing irradiation dose. Removal efficiency showed a decrease at the same radiation dose with increasing sample concentration. Most of the samples, at 25 kGy showed a destruction efficiency of ≥ 90%. Based on LC-MS results the toxicity of radio-degraded byproducts is acceptable. Finally, electron beam irradiation of antibiotics wastewater, at 25 kGy is proposed to purify and return wastewater to the industrial cycle.

Acknowledgments

The authors acknowledge the financial support provided by the Nuclear Science and Technology Research Institute.

References

[1] Jeong, J., Song, W., Cooper, WJ., Jung, J. and Greaves, J. (2010). Degradation of tetracycline antibiotics: Mechanisms and kinetic studies for advanced oxidation/reduction processes. Chemosphere, 78(5): 533–540.

[2] Chu, L., Zhuang, Sh. and Wang, J. (2018). Degradation kinetics and mechanism of penicillin G in aqueous matrices by ionizing radiation. Radiation Physics and Chemistry, 145: 34-38.

[3] Kim, HY., Kim, TH., Cha, SM. and Yu, S. (2017). Degradation of sulfamethoxazole by ionizing radiation: Identification and characterization of radiolytic products. Chemical Engineering Journal, 313: 556–566.

[4] Griessmann, K., Kaunzinger, A., Schubert-Zsilavecz, M. and Abdel-Tawab, M. (2007). A rapid HPLC-UV method for the quantification of erythromycin in dermatological preparations. Pharmazie, 62(9): 668-671.

[5] Jiao, Sh., Zheng, Sh., Yin, D., Wang, L. and Chen, L. (2008). Aqueous oxytetracycline degradation and the toxicity change of degradation compounds in photoirradiation process. Journal of Environmental Sciences, 20: 806–813.

[6] Zhuan, R. and Wang, J. (2019). Degradation of sulfamethoxazole by ionizing radiation: Kinetics and implications of additives. Science of the Total Environment, 668: 67–73.

[7] Haghedooren, E., Bhupathi, Raju KKRVS., Dehouck, P., Govaerts, C., Schepdael, AV., Hoogmartens, J. and Adams, E. (2006). Investigation of degradation products in a topical gel containing erythromycin and benzoyl peroxide by liquid chromatography–mass spectrometry. Journal of Pharmaceutical and Biomedical Analysis, 41: 165–175.

ICNST 2024
International Conference on Nuclear Science and Technology
6- 8 MAY 2024 | Isfahan, Iran

Enhancement of xylanase enzyme production by induced gamma radiation mutation of Trichoderma afroharzianum and wheat bran wastes as a substrate (Paper ID : 1040)

Hamed Askari[1, 2], Samira Shahbazi*[1], Sabihe Soleimanian-Zad[2, 3], Mahdi Kadivar [2]

[1] *Nuclear Agriculture School, Nuclear Science and Technology Research Institute (NSTRI), Atomic Energy Organization of Iran (AEOI), Karaj, Iran*
[2] *Department of Food Science and Technology, College of Agriculture, Isfahan University of Technology, Isfahan, 84156-83111, Iran*
[3] *Research Institute for Biotechnology and Bioengineering, Isfahan University of Technology, Isfahan, 84156-83111, Iran*
** Email address: sshahbazi@aeoi.org.ir, orcid.org/ 0000-0002-9923-7571*

Abstract

Xylanases are hydrolytic enzymes that randomly cleave the β-1, 4 backbones of the arabinoxylans of wheat flour and are widely used in the bakery industry as a dough texture improver in the formulations of flour products. Creating novel sources of a microbial strain using induced gamma irradiation mutants can increase enzyme production for bakery industrial use. According to this, Co^{60} gamma irradiation has been used to develop a mutant strain of Trichoderma afroharzianum. Trichoderma mutants were isolated, and qualitative and quantitative screening were performed to evaluate the production of extracellular enzymes on wheat bran waste as a substrate. The best *Trichoderma* mutant isolate was identified by DNA barcoding method. The highest xylanase activities were observed in the superior mutant isolate of *Trichoderma afroharzianum* NAS107-M82, which is approximately 3.3 times higher than its parent strain. The electrophoretic pattern of proteins showed that the exo-glucanase I, endo-glucanase III, and the xylanase I enzymes hydrolyzed the wheat bran, synergistically. Overall, gamma irradiation-induced mutation could be an expedient technique to access such superior mutants for the bioconversion of wheat bran wastes to xylanase enzyme.

Keywords: *Trichoderma*, Wheat bran, Cellulase, Xylanase, Gamma radiation, Mutation, SDS-PAGE.

1. INTRODUCTION

Wheat bran is primarily made up of cellulose and xylan, which is an abundant organic carbon source in the wheat flour industry. Worldwide production of wheat in 2023 was about 785.1 million tone, according to Food and Drug Administration (FAO)[1]. Bran's contribution to total

wheat grain weight is between 13 and 19%, depending on the milling process (wet or dry) utilized for its extraction [2], it currently has low commercial value, but can be used as the best carbon source for xylanase and cellulase production. Filamentous fungi such as *Trichoderma sp*. produce extracellular hydrolytic enzymes, which cleave the β-1, 4-glycosidic bonds present in cellulose and its derivatives [3]. *Trichoderma* is widely used in industrial fermentation because of their ability to produce large amounts of endo-glucanases (EGI/Cel7B, GII/Cel5A, EGIII/Cel12A, EGIV/Cel61A, and EGV/Cel45A) and exo-glucanases (the cellobiohydrolases, CBHI/Cel7A, and CBHII/Cel6A) that synergistically break down cellulose into cellobiose (glycosyl β-1,4-glucose) then subsequent hydrolysis to glucose by β-glucosidase [4]. The cost of enzyme production can be significantly decreased by strain improvement using irradiation, and the use of agricultural waste as a substrate for fermentation. Considering that the cost of the culture medium is about 25-50% of the production cost, the use of more effective microorganisms can reduce the reaction costs[5]. Also, microorganisms that produce both cellulases and xylanases under the same culture conditions hold great significance due to their synergistic action. Induction of random mutations by physical mutagens such as UV, X, and gamma radiation and chemical mutagens such as ethyl methane sulfonate have been used as useful tools to manipulate *Trichoderma* genetically [6]. Several studies have shown that gamma irradiation can cause genetic diversity of filamentous fungi and induce positive [4] or negative mutants [7] of specific genes. Due to enzymatic diversity of *Trichoderma* and its ability in biodegradation of hemicellulosic waste and production of extracellular enzymes, in this study, we will approach to simultaneously produce xylanase and cellulase enzymes on wheat bran as a substrate using superior gamma irradiated mutants of *Trichoderma.* Therefore, the best *Trichoderma* isolate was screened, identified and treated with different doses of gamma ray to investe the possible enhancement of xylanase, and cellulase production by gamma radiation-induced mutation.

2. MATERIALS AND METHODS

2.1. Isolation and purification of *Trichoderma*

In this study, 24 *Trichoderma* isolates were obtained from the fungal collection of the plant protection department of the nuclear agriculture research school, Alborz, Iran.

2.2.Qualitative screening of best xylanase-producing isolates

All wild-type *Trichoderma* isolates were screened for their xylanase activity using the plate screening method [8]. The best xylanase-producing isolate was screened by calculating

hydrolysis capacity that is the ratio between the clearing zone diameter of hydrolysis surrounding the colonies and colony zone diameter.

2.3. Gamma radiation-induced mutation of *Trichoderma*

The washed spore suspension of the best enzyme-producing isolate was irradiated using a gamma cobalt^{60} source in Gammacell 220 irradiator (MDS Nordion, Ottawa, Canada), located at the Radiation Application Research School, Nuclear Science and Technology Research Institute (NSTRI) of the Atomic Energy Organization, Tehran, Iran in July 2019. The average dose rate was 4.5 kGy per hour, as determined with a Fricke dosimeter. The applied dose levels were 0, 100, 250, 500, 750, and 1000 Gy (in triplicate). The selected colonies from an optimum dose of gamma irradiation [4] were used for qualitative screening of xylanase-producer mutant isolates similar to the method described above was performed.

2.4. Quantitative screening of *Trichoderma* mutant isolates

The best mutant isolates of *Trichoderma* were cultured in *Trichoderma* fermentation medium (TFM) which contained *Trichoderma* complete medium (TCM) supplemented with 0.5% w/v wheat bran powder as a substrate at pH 5.3. Growth conditions were carried out according to method of Askari and other[4]. Estimating extracellular protein and enzyme activity were assayed in TFM after centrifugation at 4500 ×g for seven min at 4°C.

2.5. Assay of extracellular protein production and enzyme activity

The extracellular protein content in the TFM supernatants was estimated in different mutant isolates of *Trichoderma* by the Bradford dye-binding method [9]. Exo-glucanase, endo-glucanase and β-glucosidase, total cellulase (Filter paperase or FPase), and xylanase activity were determined by measuring the amount of glucose or xylose released from substrates by the dinitrosalicylic acid (DNS) method with glucose or xylose as the standard [4].

2.6. Electrophoresis and molecular size determination of proteins

Protein samples (~ 200 µg) were precipitated from TFM supernatants with two volumes of cold acetone and kept at–20°C overnight. The molecular weight (kDa) of the proteins was determined by sodium dodecyl sulfate–polyacrylamide gel electrophoresis (SDS-PAGE) based on Laemmli method [4,10].

2.7. Genotypic identification of best *Trichoderma* isolates and their mutant

The total genomic DNA extraction and polymerase chain reaction (PCR) amplification for identification of *Trichoderma* isolates using the DNA barcoding method (ITS-rDNA region

and TEF1-α gene) were done according to the protocol previously described by Askari and other [4].

2.8. Statistical analysis

All experiments had three independent replications for each species. Differences in the mycelium growth rate, size of conidia for each *Trichoderma* isolate in PDA media, extracellular protein production and qualitative, and quantitative xylanase activities were analyzed using a completely randomized design and results were submitted to analysis of variance (ANOVA) with means compared by the Duncan test and HSD Tuky test ($p<0.05$), using the SPSS (ver. 16) statistical software.

3.RESULTS AND DISCUSSION

The purified wheat bran contains high amounts of xylan [11], which is typically present in higher concentrations on the outer surface of cellulose fibers but is also diffused into the interfibrillar space through fiber pores [12], and act as a physical barrier that limits the accessibility of the cellulase enzymes to the cellulose [13]. Thus, the initial screening of the *Trichoderma* wild-type strains was done first based on the

high xylanase enzyme activity, because the xylan forms a sheath on each cellulose microfibril and it might be affected the depolymerization of cellulose by cellulases within the fiber.

3.1. Qualitative screening of the best xylanase-producer strain

Figure 1 shows the qualitative evaluation of xylanase enzyme production in our 24 different isolates of *Trichoderma* by the plate screening method.

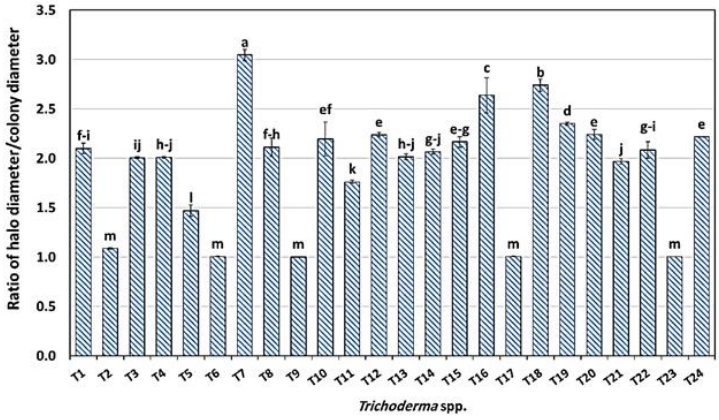

Fig 1. Qualitative evaluation of different *Trichoderma* isolates for their xylanase activity using the plate screening methods.

All the results of hydrolysis capacity in different isolates had a statistically significant difference ($p<0.05$). The highest hydrolysis capacity was observed in the T7 isolate, which

was selected for gamma radiation-induced mutation.

3.2. Gamma radiation-induced mutation

According to the qualitative screening results, the isolate code of T7 was selected and was exposed to different doses of gamma radiation (0-1000 Gy). With an increased radiation dose, the fungal viability significantly decreased and the results are shown in Figure 2.

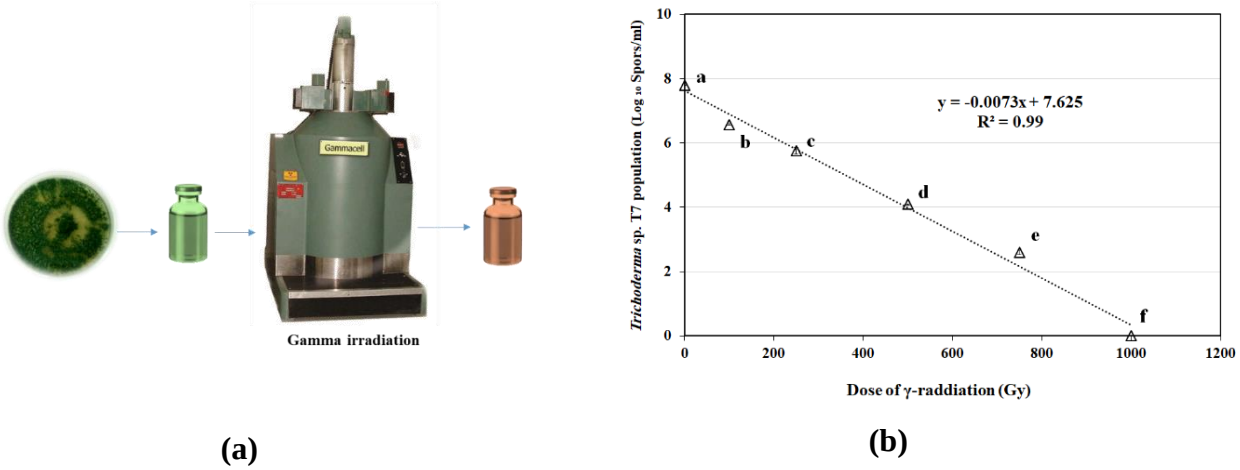

(a) **(b)**

Fig 2. Effect of gamma radiation doses of Gammacell 220 irradiator (a) on the viable count of *Trichoderma* sp. T7 (b).

High doses of gamma radiation cause more DNA damage and then lead to fungal death. Fungal viability was used to estimate the gamma radiation D_{10} value. D_{10} value of gamma radiation represented the dose of gamma radiation that reduced the fungal viability of one log cycle or 90%. According to the previous study, gamma rays are inclined to create multiple mutations in one gene at a dose higher than the D_{10} value [14]. The dose of 250 Gy was designated as an optimum dose of gamma irradiation-induced mutation that resulted in approximately 90-99 % (or 1-2 log cycle) reduction of spore sprouting on the PDA medium [4].

3.3. Screening of the best xylanase-cellulase producing mutant isolates

3.3.1.Qualitative screening of mutant isolates

Of the 118 mutant isolates (M1-M118) obtained from optimum dose of gamma radiation (250 Gy), 17 mutant isolates were selected based on the ratio between the hydrolysis capacity of the mutant isolate (HCM) and the hydrolysis capacity of the wild-type strain (HCW) of more than 1.25 (Table 1).

Table 1. Maximum hydrolytic capacity (HC) value of *Trichoderma* mutant isolates on plate screening media.

Strains	HC	Ratio $HC_{Mutant}/HC_{Wild\ type}$

Wild-type	3.34 ^{h} ± 0.02	1.00 ^{l} ± 0.00
M 10	4.37 ^{e} ± 0.00	1.31^{gh} ± 0.01
M 11	4.24 ^{f} ± 0.00	1.27 ^{i} ± 0.01
M 17	4.88 ^{bc} ± 0.05	1.46 ^{c} ± 0.02
M 44	4.79 ^{cd} ± 0.03	1.44 ^{d} ± 0.02
M49	4.46 ^{e} ± 0.01	1.34 ^{f} ± 0.01
M 51	4.45 ^{e} ± 0.00	1.33 ^{fg} ± 0.01
M 56	5.25 ^{a} ± 0.04	1.57 ^{a} ± 0.02
M 62	4.85 ^{c} ± 0.00	1.45 ^{cd} ± 0.01
M 69	3.60 ^{g} ± 0.02	1.08 ^{k} ± 0.00
M 72	4.37 ^{e} ± 0.05	1.31^{gh} ± 0.01
M 73	4.42 ^{e} ± 0.02	1.32 $^{f-h}$ ± 0.00
M 76	4.12 ^{f} ± 0.01	1.23 ^{j} ± 0.01
M 79	4.70 ^{d} ± 0.01	1.41 ^{e} ± 0.01
M 80	4.35 ^{e} ± 0.01	1.30 ^{h} ± 0.01
M 82	4.45 ^{e} ± 0.02	1.33 ^{fg} ± 0.01
M 86	4.16 ^{f} ± 0.03	1.25 ^{j} ± 0.02
M 87	2.86 ^{i} ± 0.01	0.86 ^{m} ± 0.01
M 89	4.91 ^{bc} ± 0.04	1.47 ^{c} ± 0.02
M 114	5.00 ^{b} ±0.05	1.50 ^{b} ± 0.02

* Different letters in each column indicate a statistically significant difference between different isolates.

Also, M17 and M79 isolates were selected as mutants with hydrolysis capacity similar to the wild-type strain (control) and weaker than the control, respectively. Table 1 displays the results of comparing the mean hydrolysis capacity of mutant isolates (19 mutants) with the wild-type strain. All results had a statistically significant difference at the level $p<0.05$. The highest hydrolysis capacity in qualitative screening tests was observed in mutant isolates of M56, M114, M89, M17, M62, and M44, respectively. These results suggested that xylanases or cellulase enzymes affecting the structure of arabinoxylan may be secreted into the culture medium by the mutant isolates. Therefore, xylanase and cellulase enzyme activity measured in the supernatant of TFM can show a better comparison of the ability of mutant isolates to hydrolyze wheat bran.

3.4. Quantitative screening of mutant isolates

The results of extracellular protein concentration and enzyme activity are shown in Table 2. All mutant isolates had significant differences ($p<0.05$). The changes in extracellular protein concentration varied from 56.97 to 185 µg/mL. The most extracellular protein concentration was observed in the TFM supernatant of M82 and other mutant isolates showed lower concentrations than this isolate. The highest xylanase activity was observed in the M82 mutant isolate (5.61 ± 0.48 U/mL), which was approximately 3.3 times higher than the wild-type, and

other mutant strains.

Table 2. Extracellular protein concentration (µg/ml) and enzyme activity (U/ml) of different mutant isolates of *Trichoderma* in the supernatant of the TFM containing wheat bran as a substrate.

Strains	Protein (µg/ml)	Enzyme activity (U/ml)				
		Xylanase	Exo-glucanase	Endo-glucanase	β-glucosidase	Total cellulase
W. T.*	87.89 ± 3.77 d-f	1.70 ± 0.06 ij	1.04 ± 0.01 b-d	0.79 ± 0.04 b-d	0.45 ± 0.00 l	2.24 ± 0.40 b-d
M 10	78.95 ± 6.65 gh	2.00 ± 0.04 hi	0.82 ± 0.02 de	0.60 ± 0.08 gh	3.00 ± 0.60 e	1.98 ± 0.36 c-e
M 11	116.84 ± 6.64 b	5.18 ± 0.14 b	0.82 ± 0.05 de	0.79 ± 0.11 b-d	1.89 ± 0.22 gh	1.97 ± 0.05 c-e
M 17	56.97 ± 1.94 j	1.63 ± 0.16 j	0.73 ± 0.07 de	0.68 ± 0.00 d-g	1.59 ± 0.15 hi	1.60 ± 0.05 d-g
M 44	81.58 ± 0.00 f-h	3.04 ± 0.06 ef	1.27 ± 0.06 b	0.66 ± 0.02 e-h	2.25 ± 0.18 fg	2.69 ± 0.05 b
M49	115.00 ± 0.71 b	2.60 ± 0.17 g	1.17 ± 0.70 bc	0.83 ± 0.01 bc	0.78 ± 0.03 kl	2.70 ± 0.18 b
M 51	93.42 ± 4.77 c-e	2.06 ± 0.25 h	0.89 ± 0.05 c-e	0.72 ± 0.08 c-f	2.07 ± 0.15 fg	1.84 ± 0.03 c-f
M 56	93.16 ± 4.71 c-e	3.87 ± 0.43 d	0.75 ± 0.05 de	0.73 ± 0.05 c-e	2.44 ± 0.01 f	1.92 ± 0.00 c-f
M 62	84.21 ± 0.53 fg	4.63 ± 0.24 c	0.69 ± 0.09 c-e	0.49 ± 0.04 i	6.04 ± 0.59 a	1.29 ± 0.17 fg
M 69	88.16 ± 1.32 d-f	5.21 ± 0.51 b	0.80 ± 0.02 de	0.87 ± 0.07 b	3.21 ± 0.05 e	2.13 ± 0.75 b-e
M 72	93.29 ± 7.49 c-e	2.94 ± 0.23 e-g	0.90 ± 0.08 de	0.56 ± 0.01 hi	4.88 ± 0.32 c	1.53 ± 0.04 e-g
M 73	94.47 ± 9.38 cd	1.72 ± 0.05 ij	0.74 ± 0.01 de	0.61 ± 0.00 f-h	5.42 ± 0.13 b	1.96 ± 0.04 c-e
M 76	75.13 ± 7.05 h	2.70 ± 0.18 fg	0.81 ± 0.01 de	0.66 ± 0.05 e-h	1.37 ± 0.05 ij	1.65 ± 0.19 d-g
M 79	86.45 ± 9.70 ef	2.87 ± 0.31 fg	0.75 ± 0.07 de	0.73 ± 0.12 c-e	4.89 ± 0.31 c	1.52 ± 0.19 e-g
M 80	78.95 ± 3.33 gh	2.23 ± 0.07 h	0.75 ± 0.03 de	0.60 ± 0.04 gh	1.85 ± 0.07 gh	1.92 ± 0.06 c-f
M 82	185.00 ± 0.26 a	5.61 ± 0.48 a	1.81 ± 0.12 a	1.17 ± 0.10 a	3.28 ± 0.19 e	4.68 ± 1.12 a
M 86	87.89 ± 9.20 d-f	2.68 ± 0.14 g	0.63 ± 0.02 e	0.57 ± 0.02 g-i	4.28 ± 0.44 d	1.63 ± 0.08 d-g
M 87	97.89 ± 1.41 c	3.24 ± 0.41 e	1.22 ± 0.11 b	0.80 ± 0.05 bc	0.95 ± 0.06 jk	2.33 ± 0.12 bc
M 89	67.11 ± 6.13 i	3.70 ± 0.05 d	0.74 ± 0.01 de	0.60 ± 0.06 gh	1.06 ± 0.08 jk	1.11 ± 0.07 g
M 114	81.58 ± 1.41 f-h	4.78 ± 0.49 c	0.81 ± 0.10 de	0.73 ± 0.09 c-e	0.81 ± 0.08 kl	1.59 ± 0.26 d-g

* Wild type

** Different letters in each column indicate a statistically significant difference between different mutant isolates.

Also, the results of cellulase activity are shown as international units (U), in which one unit of cellulase (Exo-, endo-glucanase, β-glucosidase, and total cellulase) activity is definite as the amount of enzyme required to liberate 1 μmol of glucose per hour. The highest exo-glucanase activity (U/mL) was observed in mutant isolates of M82, and M44, respectively. These results showed that these mutant isolates, probably have a high ability to decompose crystalline regions of lignocellulosic materials. Exo-glucanase activity in the mutant isolate of M82 was approximately 1.78 times higher than the wild-type strain. Exo-glucanases or cellobiohydrolase (I and II) cleave the accessible reducing and non-reducing wheat bran cellulose chain ends to liberate cellobiose and some glucose molecules [15]. Also, the highest endo-glucanase (EG) activity was observed in mutant isolates of M82, and M69, respectively. EG can randomly hydrolyze internal glycosidic bonds in cellulosic cell walls of wheat bran, especially in the amorphous regions of the cellulose chain. EG activity in the mutant isolate of M82 was approximately 1.48 times higher than the wild-type strain. Also, the mutant isolates of M62, M73, M72, M86, and M82 showed high β-glucosidase activity in comparison to other isolates, respectively. Overall, the total cellulase system contains exo-glucanases, endo-glucanases, and β-D-

glucosidases, all of which hydrolyze the crystalline cellulosic cell wall of wheat bran synergistically. Synergism between EGs and exo-glucanases is the foremost broadly examined sort of synergy and is among the foremost quantitatively imperative for the hydrolysis of crystalline cellulose. The highest FPase or total cellulase activity (U/ mL) was illustrated in mutant isolates of M82, M49, and M44, respectively. However, the mutant isolate of M44 could be the best superior mutant of cellulase producer due to that can produce a cellulase enzyme with higher activity in lower extracellular protein amounts, and a high level of total cellulase activity in this mutant isolate could be due to higher exo-glucanase activity and EG activity compared to other mutant isolates and the synergistic action of these enzymes on the cellulose chain.

3.5.The electrophoretic pattern of proteins

The variation and molecular weight distribution of enzyme-rich proteins in different superior mutants are shown in Figure 4 (a, b). The presence of diverse protein groups within the Mw extend of 11 to 135 kilodaltons (kDa), indicates the diversity of enzymes with various Mw, which can hydrolyze wheat bran cell wall compounds with different mechanisms. The proteins

that weigh 17, 21, 32, and 43 kDa belong to a group of enzymes called xylanase (Xyl I, II, III, and IV, respectively) [16–20].

According to the densitometry results, the most Xyl I concentration (18 kDa) was secreted in the TFM supernatant of M76, and M11 mutant isolates, respectively.

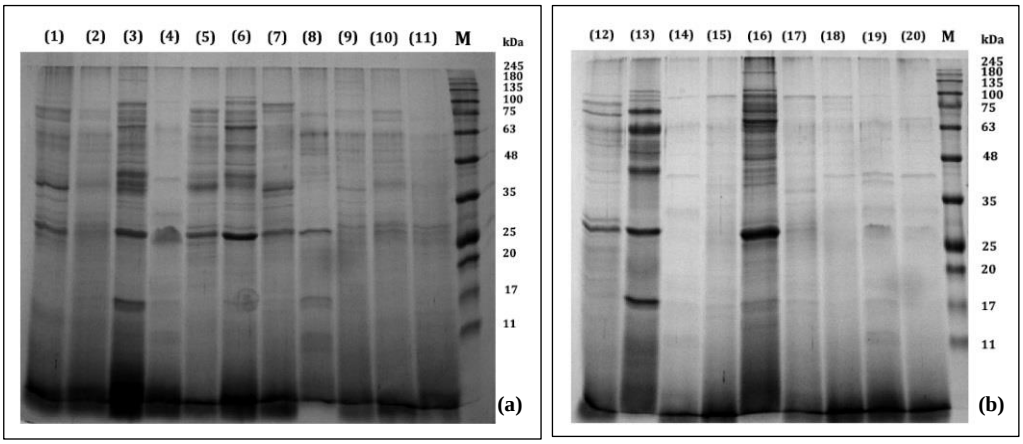

Fig 3. Protein profile analysis of extracellular protein secreted in the supernatant of the TFM: (a:1 & b: 12) wild-type strain T7, (a: 2-11 and b: 13-20) mutant isolates M10, M11, M17, M44, M49, M51, M56, M62, M72, M73, M76, M79, M80, M82, M86, M87, M89 and M114, respectively during fermentation time 72 h and pH of fermentation medium 5.5. (M) Protein molecular weight marker in the range of KDa 11-245.

However, the higher xylanase activity in M82 (Table 2) may be due to the presence of the Cel12A enzyme, which, besides acting in the cellulose chain, has acted against beta-1,3-glucan and beta-1,4-xylan hydrocolloids [21]. The results showed that the Cel12A protein band with a weight of 26 kDa was highest in the M82 lane when looking at the optical density analysis, and this was confirmed by testing the xylanase enzyme activity. Also, the highest concentration of xylanase IV (43 kDa) was observed in M17, M73, M44, M11, M49, M51, M89, M51, M82, M69, and M86 mutant isolates, respectively. *Trichoderma* species can be produced at least two cellobiohydrolases, Cel6A (CBH II, Mw 56-62 kDa), and Cel7A (CBH I, Mw 66 kDa; EC 3.2.1.91), and five endo-glucanases, Cel5A (EG II, Mw 48 kDa), Cel7B (EG I, Mw 50-55 kDa), Cel12A (EG III, Mw 25 kDa), Cel45A (EG V, Mw 23 kDa), and Cel61A (EG IV, Mw 34 kDa; EC 3.2.1.4)[4]. *Trichoderma* mutant isolate of M82 (lane 16), M76 (lane 13), M49 (lane 6), M44 (lane 5), and M17 (lane 3) had two enzyme bands called CBH I and CBH II. The highest optical density of CBH protein bands (CBH I and II) was observed in mutant isolates

M82. Also, the highest secreted proteins of CBH II (62 kDa) and Cel5A (EG II, 48 kDa) were observed in the mutant isolate M82, as confirmed by the results obtained from exo-glucanase and endo-glucanase enzyme activity, respectively. The Cel 3A protein band (which weighs 73 kilodaltons and is also called BGL I) was present in the profiles of M82 mutant isolate of *Trichoderma*. But Cel 1A (BGL II) weighed 110 kDa and was observed in the protein profile of M11, M49, M51, M14, M79, M80, M82, M86, and M87 mutant isolates.

3.6. Identification of the best *Trichoderma* strain and its mutant isolates

DNA extraction was performed from wild-type strain T7 and its superior mutants of M82 and M44. The quantity and quality of extracted DNA were examined by spectrophotometry and agarose gel electrophoresis (Figure 5-a).

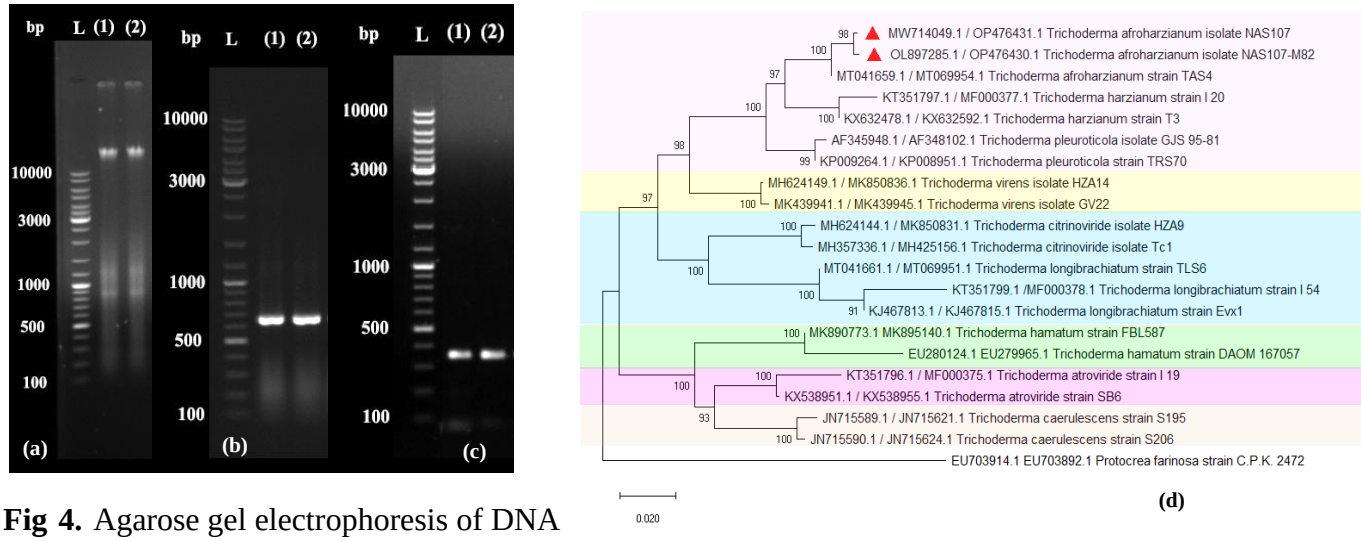

Fig 4. Agarose gel electrophoresis of DNA fungal isolates: The internal transcribed spacer (ITS) regions of the ribosomal DNA (b), and the translation elongation factor 1-α encoding gene (TEF1-α) (c); L: Molecular weight marker (100 bp-10 kb); (1, and 2): DNA or PCR product of the *Trichoderma* sp. T7 and its mutant isolate NAS107-M82, respectively. Phylogenetic relationship of *Trichoderma afroharzianum* NAS107 and its mutant of *T. afroharzianum* NAS107-M82 using ITS-rDNA regions and TEF1-α regions gene nucleotide sequence (d).

After the extraction operation, PCR amplification was performed for the amplification of the internal transcribed spacer (ITS) and the translation elongation factor 1-α encoding gene (TEF1-α) regions gene, which was successfully amplified in two isolates and sequenced for *Trichoderma* identification with approximately 650 and 350 bp, respectively (Figure 5-b, 5-c). Sequence analysis of the ITS-rDNA region and TEF-1α is widely used for the precise

reorganization of *Trichoderma* species [22]. The forward and reverse sequences of PCR products (ITS-rDNA and TEF-1α) were registered in the GenBank database at the National Center for Biotechnology Information (NCBI) and the accession numbers are presented in their phylogenetic tree. The superior isolate of *Trichoderma* T7 isolate and its mutant isolate of M82 were registered in the microbial collection of Iran Biological Resources Center (IBRC) with accession numbers IBRC-M 30594 (*T. afroharzianum* NAS107), and IBRC-M 30594 (*T. afroharzianum* NAS107-M82), respectively.

4.CONCLUSIONS

A complex of extracellular enzymes is present in *Trichoderma*, which is one of the most well-known cellular filamentous fungi for the degradation of wheat bran waste and other hemicellulose materials. Various organisms with different characteristics produce xylanase-cellulase complexes that are utilized in industrial

applications, such as in the food and baking industry. We evaluated different isolates of *Trichoderma* for their hydrolysis potential of arabinoxylan compounds and wheat bran through quantitative and qualitative screening and among them, *Trichoderma* isolate of T7 was selected as the best wild-type strain and was identified using ITS-rDNA and TEF1-α regions gene nucleotide sequence and its sequencing results were submitted in the GenBank database at the NCBI. Using genotypic identification, the T7 wild-type strain and its mutant isolates were identified as *T. afroharzianum* NAS107. Our results showed that, statistically significant changes in xylanase-cellulase production of *T. afroharzianum* NAS107 (or T7 isolate) after irradiated treatment were influenced by doses of the ray.

The highest extracellular enzyme activity was observed in mutant isolates of *T. afroharzianum* NAS107-M82, in which their xylanase and cellulase activities were approximately 3.3 times higher than wild-type strain. In this mutant isolate, exo-glucanase (CBH I, cell 7A), endo-glucanase (EG III, Cel 12A), and xylanase (Xyl I) hydrolyzed the wheat bran, synergistically.

According to our study, mutant isolate of *T. afroharzianum* NAS 107-M82 can be a successful extracellular enzyme producer candidate for the bioconversion of wheat bran wastes into xylanase-cellulase enzymes. Therefore, there could be improved strains by gamma radiation-induced mutation as a biological agent for xylanase-cellulase enzyme production. In other fungi, this technique can be utilized to create new mutants with various uses.

Acknowledgments

This study was supported by Project No. TGP-A-00-001 from the Nuclear Science and Technology Research Institute (NSTRI), Atomic Energy Organization of IRAN (AEOI).

References

[1] F.A.O. Faostat, Food and Agriculture Organization of the United Nations-Statistic Division https://www. fao. org/faost at/en/# data, (2019).

[2] O.O. Onipe, A.I.O. Jideani, D. Beswa, Composition and functionality of wheat bran and its application in some cereal food products, Int. J. Food Sci. Technol. 50 (2015) 2509–2518. https://doi.org/10.1111/ijfs.12935.

[3] R. Mach, S. Zeilinger, Regulation of gene expression in industrial fungi: Trichoderma, Appl. Microbiol. Biotechnol. 60 (2003) 515–522.

[4] H. Askari, S. Soleimanian-Zad, M. Kadivar, S. Shahbazi, Creating a novel genetic diversity of Trichoderma afroharzianum by γ-radiation for xylanase-cellulase production, Heliyon. 10 (2024). https://doi.org/10.1016/j.heliyon.2024.e28349.

[5] M.S. Shafei, T.A. Mohamed, I.S.A. Elsalam, Optimization of extracellular lipase production by Penicillium chrysogenum using factorial design, Malays. J. Microbiol. 7 (2011) 71–77.

[6] V. Gohel, C. Megha, P. Vyas, H.S. Chhatpar, Strain improvement of chitinolytic enzyme producing isolate Pantoea dispersa for enhancing its biocontrol potential against fungal plant pathogens, Ann. Microbiol. 54 (2004) 503–515.

[7] M.E. Zolan, C.J. Tremel, P.J. Pukkila, Production and characterization of radiation-sensitive meiotic mutants of Coprinus cinereus., Genetics. 120 (1988) 379–387. https://doi.org/10.1093/genetics/120.2.379.

[8] Yopi, W. Tasia, R. Melliawati, Cellulase and Xylanase Production from Three Isolates of Indigenous Endophytic Fungi, in: IOP Conf. Ser. Earth Environ. Sci., IOP Publishing, 2017: p. 12035. https://doi.org/10.1088/1755-1315/101/1/012035.

[9] M.M. Bradford, A rapid and sensitive method for the quantitation of microgram quantities of protein utilizing the principle of protein-dye binding, Anal. Biochem. 72 (1976) 248–254. https://doi.org/10.1016/0003-2697(76)90527-3.

[10] U.K. Laemmli, Cleavage of structural proteins during the assembly of the head of bacteriophage T4, Nature. 227 (1970) 680–685. https://doi.org/10.1038/227680a0.

[11] L.W. Doner, K.B. Hicks, Isolation of hemicellulose from corn fiber by alkaline

hydrogen peroxide extraction, Cereal Chem. 74 (1997) 176–181. https://doi.org/10.1094/CCHEM.1997.74.2.176.

[12] T. Köhnke, K. Lund, H. Brelid, G. Westman, Kraft pulp hornification: A closer look at the preventive effect gained by glucuronoxylan adsorption, Carbohydr. Polym. 81 (2010) 226–233. https://doi.org/10.1016/j.carbpol.2010.02.023.

[13] M. Pauly, P. Albersheim, A. Darvill, W.S. York, Molecular domains of the cellulose/xyloglucan network in the cell walls of higher plants, Plant J. 20 (1999) 629–639. https://doi.org/10.1046/j.1365-313X.1999.00630.x.

[14] F.L.N. Hidayati, Sardjono, Giyatmi, M.N. Cahyanto, Enhancement of Indigenous Fungal Cellulase Production by Gamma Rays, in: IOP Conf. Ser. Mater. Sci. Eng., IOP Publishing, 2021: p. 012004. https://doi.org/10.1088/1757-899x/1192/1/012004.

[15] Y.H.P. Zhang, L.R. Lynd, Toward an aggregated understanding of enzymatic hydrolysis of cellulose: Noncomplexed cellulase systems, Biotechnol. Bioeng. 88 (2004) 797–824. https://doi.org/10.1002/bit.20282.

[16] M. Tenkanen, J. Puls, K. Poutanen, Two major xylanases of Trichoderma reesei, Enzyme Microb. Technol. 14 (1992) 566–574. https://doi.org/10.1016/0141-0229(92)90128-B.

[17] A. Lappalainen, M. Siika-Aho, N. Kalkkinen, R. Fagerstrm, M. Tenkanen, Endoxylanase II from Trichoderma reesei has several isoforms with different isoelectric points, Biotechnol. Appl. Biochem. 31 (2000) 61. https://doi.org/10.1042/ba19990066.

[18] A.K. Torronen, The two major endo-1, 4-beta-xylanases from Trichoderma reesei: Characterization of both enzymes and genes, (1997).

[19] J. Xu, N. Takakuwa, M. Nogawa, H. Okada, Y. Morikawa, A third xylanase from Trichoderma reesei PC-3-7, Appl. Microbiol. Biotechnol. 49 (1998) 718–724. https://doi.org/10.1007/s002530051237.

[20] T. Parkkinen, N. Hakulinen, M. Tenkanen, M. Siika-aho, J. Rouvinen, Crystallization and preliminary X-ray analysis of a novel Trichoderma reesei xylanase IV belonging to glycoside hydrolase family 5, Acta Crystallogr. Sect. D Biol. Crystallogr. 60 (2004) 542–544. https://doi.org/10.1107/S0907444903029123.

[21] J. Karlsson, M. Siika-Aho, M. Tenkanen, F. Tjerneld, Enzymatic properties of the low molecular mass endoglucanases Cel12A (EG III) and Cel45A (EG V) of Trichoderma reesei, J. Biotechnol. 99 (2002) 63–78. https://doi.org/10.1016/S0168-1656(02)00156-

6.

[22] I.S. Druzhinina, A.G. Kopchinskiy, M. Komoń, J. Bissett, G. Szakacs, C.P. Kubicek, An oligonucleotide barcode for species identification in Trichoderma and Hypocrea, Fungal Genet. Biol. 42 (2005) 813–828. https://doi.org/10.1016/j.fgb.2005.06.007.

ICNST 2024
International Conference on Nuclear Science and Technology
6- 8 MAY 2024 | Isfahan, Iran

PET Imaging of Glioma using [18F] Fluoro-2,2-Dimethylpropionic Acid: Preparation and Labeling (Paper ID : 1043)

Bahareh Bahrami Khoundabi [1], Elham Sattarzadeh Khameneh[2], Seyed Mahmood Reza Aghamiri [1], Saeed Kakaei[*2], Fariba Johari Deha[2], Leila koopaei[2]

[1]Medical Radiation, Nuclear Engineering, Shahid Beheshti, P. O. Box 4716-19839, Tehran- Iran
[2]Radiation Application Research School, Nuclear Science and Technology Research Institute, P. O. Box 11365-3486, Tehran - Iran

Abstract

In this study, we will perform the synthesis of a fluoro pivalic acid compound for PET imaging of brain glioma tumors using the fatty acid metabolic pathway and radiolabeling with an ^{18}F radioisotope. Gliomas are the most common primary brain malice and are a miscellaneous group of central nervous system (CNS) tumors that can arise from normal glial cells, particularly astrocytes, oligodendrocytes, and ependymal cells. Gliomas are broadly divided into four categories based on their histological characteristics. (Class I-IV). Glioma cells mainly use fatty acid metabolism for energy production and reproduction. Radiopharmaceuticals such as ^{11}C-acetate, ^{18}F-FAC (2-^{18}F-fluoroacetate), [^{11}C] choline ([^{11}C]Cho) or [^{18}F] fluoroethyl-choline ([^{18}F]FCho) and [^{18}F]FDG have been used previously to study short-chain fatty acid (SCFA) metabolism.

Methyl 2, 2- dimethyl-3-hydroxypropionate, DMAP and tosyl chloride in pyridine were employed for synthesis as a precursor. Under nitrogen atmosphere reaction is carried out and the hydroxyl group is converted to a tosylate as the leaving group the final product is used for labeling with ^{18}F. The ^{18}F isotope, most commonly used in positron emission tomography (PET), is obtained by bombarding enriched water ($H_2{}^{18}O$) with hydrogen ions in a cyclotron accelerator, and fluorine-18 is extracted as an ^{18}F anion for labeling pivalic acid. After the synthesis of [^{18}F] FPIA, quality control tests are performed, chemical products are characterized using Fourier Transform Infrared Spectroscopy (FTIR) and Nuclear Magnetic Resonance (NMR), and the radiochemical purity is evaluated by RTLC techniques. Subsequently, in vitro studies to assess the stability of the final product (at room temperature and in the presence of human serum at 37 degrees) will be performed.

Keywords: [^{18}F] flouro pivalic acid, Glioma, Fatty acid metabolism, ^{18}F, PET.

Introduction

Glioma is the most common primary malignant brain tumor in adults and is known as grade IV astrocytoma, glioblastoma multiforme or glioblastoma [1-3]. Unfortunately, the prognosis and quality of life of these patients is dismal, with median survival of about a year, despite treatment, which may include surgical resection, radiotherapy, and chemotherapy or acombination of these [2,1]. Positron emission tomography (PET) is used for diagnose cancers such as glioma, where small amount of radioactive drugs or radiotracers are used to show differentiation between tumor and normal tissue. Several studies have shown that fatty acid oxidation is highly active in number of cancers, including glioma And therefore, similar to glucose metabolism, which was previously mentioned for the radiopharmaceutical [^{18}F]FDG, imaging of fatty acid metabolism may be possible to detect cancer cells. Since glioma cells primarily use fatty acid metabolism for energy production and proliferation [4-6]. In this study, we intend to synthesize a fatty acid-based radiopharmaceutical called [^{18}F] fluoropivalic acid to image the metabolic pathway of fatty acids and then by labeling with fluorine-18 obtained from the cyclotron accelerator, the radiochemical purity of the compound [^{18}F] FPIA will include RTLC and HPLC tests and biodistribution studies.

Results and Discussion

I. Synthesis protocol

In the first step and to start the synthesis, a suitable precursor called methyl 2,2-dimethyl-3-hydroxypropionate will be used. The precursor in pyridine will be dissolved in DMAP in pyiridine. Under nitrogen atmosphere reaction mixture will be stirred then Tosyl chloride in pyridine added to the reaction vessel. We will dilute reaction with dichloromethane and water. Phases will be separated and aqueous layer will be extracted with dichloromethane. Combined organic layers will be washed with HCl and brine and dried over Na_2SO_4. The salt will be then filtered off, the reaction mixture concentrated in vacuo and the residue purified by chromatography (15% EtOAc/PE). The compound will be isolated as a white solid and taken forward for radiochemistry (Fig.1).

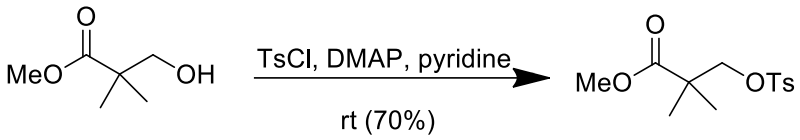

Figure 1

II. Labaling protocol

[^{18}F] fluoride will be carried out using with K_2CO_3 and kryptofix .The fluoride will be dried with MeCN at 120 °C. Compound in DMF will be added and reaction mixture will be heated for 10 min and cooled down. The reaction mixture will be quenched with water. The material [^{18}F] will isolate by HPLC column, NaOH will be added and the mixture heated for 5min, cooled down to room temperature and neutralized with HCl .

Ethanol will be removed under vacuum and PBS will be added, and the desired final [^{18}F] FPIA product will be ready for injection (Fig.2).

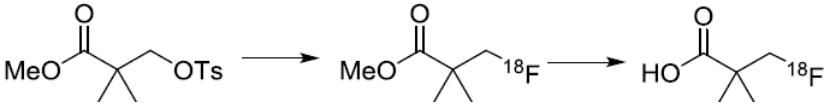

Figure 2

Conclusions

This method allows efficient, reliable production of [^{18}F] Fluoro-2,2-Dimethylpropionic Acid. In conclusion, the improved preparation of the precursor has a group of tosylate in combination with the labeling procedure provide the tools necessary for the investigation of the efficacy of [^{18}F]FPIA for tumor detection using the fatty acid metabolic pathway by PET imaging in large numbers of patients have brain glioma tumors .

Acknowledgements

The authors are grateful to Radiation Application Research School, Foundation of Nuclear Science and Technology Research Institute (P.O. Box 11365-3486) for supporting this research work.

References

[1] Dolecek, T.A.; Propp, J.M.; Stroup, N.E.; Kruchko, C. CBTRUS statistical report: Primary brain and central nervous system tumors diagnosed in the United States in 2005-2009. Neuro-Oncology 2012, 14 (Suppl. 5), v1–v49.

[2] Omuro, A.; De Angelis, L.M. Glioblastoma and Other Malignant Gliomas: A Clinical ReviewGlioblastoma and Other Malignant GliomasGlioblastoma and Other Malignant Gliomas. JAMA **2013**, 310, 1842–1850.

[3] Ostrom, Q.T.; Gittleman, H.; Barnholtz-Sloan, J.S.; Wolinsky, Y.; Kruchko, C.; Xu, J.; Kromer, C. CBTRUS Statistical Report: Primary Brain and Other Central Nervous System Tumors Diagnosed in the United States in 2009–2013. Neuro. Oncol. **2016**, 18 v1–v75.

[4] Clark, P.M.; Mai, W.X.; Cloughesy, T.F.; Nathanson, D.A. Emerging Approaches for Targeting Metabolic Vulnerabilities in Malignant Glioma. Curr. Neurol. Neurosci. Rep. **2016**, 16, 17.

[5] Lin, H.; Patel, S.; Affleck, V.S.; Wilson, I.; Turnbull, D.M.; Joshi, A.R.; Maxwell, R.; Stoll, E.A. Fatty acid oxidation is required for the respiration and proliferation of malignant glioma cells. Neuro. Oncol. **2017**, 19, 43–54.

[6] Pike, L.S.; Smift, A.L.; Croteau, N.J.; Ferrick, D.A.; Wu, M. Inhibition of fatty acid oxidation by etomoxir impairs NADPH production and increases reactive oxygen species resulting in ATP depletion and cell death in human glioblastoma cells. Biochim.Biophys. Acta (BBA) Bioenerg. **2011**, 1807, 726–734.

International Conference on Nuclear Science and Technology
6- 8 MAY 2024 | Isfahan, Iran

Impact of Irradiation for Improving Quality of food preservation (Paper ID : 1047)

Javidmehr A.[1], Mohamadian M. [1*], Hajivand P.[1]

[1]*Physics and Energy Engineering Department, Amirkabir University of Technology, Tehran, Iran*
[*]mohamadian@aut.ac.ir

Abstract

Food preservation is a critical aspect of ensuring food safety and security, particularly in the context of increasing global food demand and the need to minimize food waste. One of the methods that has been explored for improving the bacteriological quality of food preservation is irradiation. This paper provides an overview of the current understanding of the impact of irradiation on improving the bacteriological quality of food preservation, exploring its potential benefits, challenges, and future directions. Key topics addressed include the mechanisms of action of irradiation on microorganisms, the impact of irradiation on the nutritional and sensory properties of food, the regulatory framework governing the use of irradiation in food preservation, and the potential role of irradiation in addressing food safety and security challenges.

Keywords: Ionizing radiation, Bacteriological Quality of food, Gamma ray, X-ray, Electron Beam

INTRODUCTION

Food preservation is a critical aspect of ensuring food safety and security, particularly in the context of increasing global food demand and the need to minimize food waste. One of the methods that has been explored for improving the bacteriological quality of food preservation is irradiation. Irradiation involves the use of ionizing radiation to eliminate harmful microorganisms in food, thereby extending its shelf life and reducing the risk of foodborne illnesses.

The impact of irradiation on food preservation has been a subject of extensive research and debate, with studies focusing on its effectiveness in reducing bacterial contamination, maintaining food quality, and addressing consumer perceptions and regulatory considerations. This paper aims to provide an overview of the current understanding of the impact of irradiation

on improving the bacteriological quality of food preservation, exploring its potential benefits, challenges, and future directions.

Key topics to be addressed include the mechanisms of irradiation on microorganisms, the impacts of irradiation on the nutritional and sensory properties of food, the regulatory framework governing the use of irradiation in food preservation, and the potential role of irradiation in addressing food safety and security challenges. This paper seeks to contribute to a comprehensive understanding of the role of irradiation in enhancing the bacteriological quality of preserved foods.

Current methods for food preservation and their limitations

There are several methods for food preservation, each with their own advantages and limitations. Some of the most common methods consist of; 1. Refrigeration and freezing: This method involves storing food at low temperatures to slow down the growth of bacteria and other microorganisms. However, this method is limited by the shelf life of the food, as well as the need for constant temperature control. 2. Canning: Canning involves heating food to high temperatures to kill bacteria and other microorganisms, and then sealing it in airtight containers. However, this method can alter the taste and texture of the food, and is not suitable for all types of food. 3. Drying: Drying involves removing the moisture from food, which inhibits the growth of bacteria and other microorganisms. However, this method can also alter the taste and texture of the food, and is not suitable for all types of food. 4. Chemical preservation: Chemical preservatives, such as salt, vinegar, and citric acid, can be added to food to inhibit the growth of bacteria and other microorganisms. However, some people are sensitive to these preservatives, and it may not be suitable for all types of food. 5. Irradiation: Irradiation involves exposing food to ionizing radiation to kill bacteria and other microorganisms. This method does not alter the taste or texture of the food, and is suitable for a wide range of food products in proper irradiation dose. 6. Packaging.

— Irradiation benefits

Irradiation is a method of food preservation that involves exposing food to ionizing radiation, such as gamma rays, X-rays, or electron beams. This radiation penetrates the food and kills bacteria and other microorganisms that can cause spoilage and foodborne illness. Irradiation

has been shown to be effective in reducing bacterial contamination in a wide range of food products, including meat, poultry, seafood, fruits, and vegetables [1].

Irradiation has several advantages over other methods of food preservation. It does not alter the taste or texture of the food for proper dose, and it can be used to extend the shelf life of food without the need for refrigeration or chemical preservatives. Irradiation can also be used to control insect infestations in stored grains and other food products [2].

Despite its benefits, irradiation is not widely used in the food industry. Some consumers are concerned about the safety of irradiated food, and there are regulatory hurdles to overcome, and regulations in place to ensure that the process is carried out safely. However, the use of irradiation for food preservation is gaining acceptance, and it has been approved for use in many countries around the world [3]. As research continues to demonstrate the safety and effectiveness of irradiation, it is likely that more food products will be treated with this method in the future.

The use of gamma ray irradiation to increase the shelf life of sodium-reduced hot dog wieners, has discussed in [4]. Some studies evaluated the effects of different doses of irradiation on the microbiological safety and quality parameters of the wieners. The results showed that irradiation effectively reduced microbial load without compromising the product's quality (7-9 kGy). Higher doses of irradiation led to increased lipid oxidation but did not impair sensory acceptance. [4-6].

An overview of effects of gamma radiation on the biological, physicochemical and nutritional parameters of oilseeds and oils has considered in [7]. The purpose of this study was to explore the potential use of gamma irradiation as a method for prolonging the shelf-life of oilseeds and oils by inhibiting pests and microorganisms, as well as the reactions caused by enzymes. They found that while gamma radiation can improve the quality, stability, and safety characteristics of oilseeds and oils, it can also change their physicochemical and nutritive characteristics. The authors suggest that further research into other radiation techniques, such as x-rays and electron beams, may also have potential for use in this area [7-8].

The application of high energy electromagnetic radiations (HEERs) in reducing anti-nutritional factors (ANFs) from oilseeds discussed in [9]. They outline the major ANFs present in oilseeds

and highlights the use of HEERs such as gamma, ultraviolet, microwave, and infrared radiation to minimize these ANFs. The review also discusses the effects of HEERs on sensory and physiochemical attributes, as well as the functional properties of protein extracted from oilseeds. The article compares HEERs with other emerging technologies and addresses regulatory and safety issues related to food irradiation. Overall, the review emphasizes the potential of HEERs in improving the nutritional and economic value of oilseeds [9].

The effectiveness of gamma irradiation on fish quality and its impact on food-borne pathogens evaluated in [10]. The study aimed to address the health threats associated with fish consumption by assessing gamma radiation as a fish preservation method. The researchers found that gamma irradiation reduced aerobic plate count and pathogenic bacterial counts in a dose-dependent manner, with a complete eradication of aerobic plate count at a dose of 5 KGy. The study also showed that gamma irradiation had no significant effect on the proximate composition of fish, making it an effective and safe method for reducing microbial contamination of fish [10-11].

The process of food irradiation, its effectiveness in killing harmful bacteria and microorganisms, and its approval by food control authorities discussed in [12]. The study explores the principles of food irradiation, the sources and dosage of irradiation, and its effects on food-borne microbial pathogens. It also highlights the mechanisms of irradiation, its advantages over traditional preservation methods, and the limitations of its use in Nigeria. The study emphasizes the need for more irradiation facilities, cost considerations, and the importance of sensitization and training for farmers [12-13].

MATERIALS AND METHODS

The experimental design for studying the impact of irradiation on the bacteriological quality of food preservation involves several key components such as; 1. Types of food products used 2. Irradiation parameters (Fig. 1) [14-15]. 3. Bacterial contamination. In addition to these components, the experimental design also involve a control group of non-irradiated food samples to provide a baseline for comparison [16].

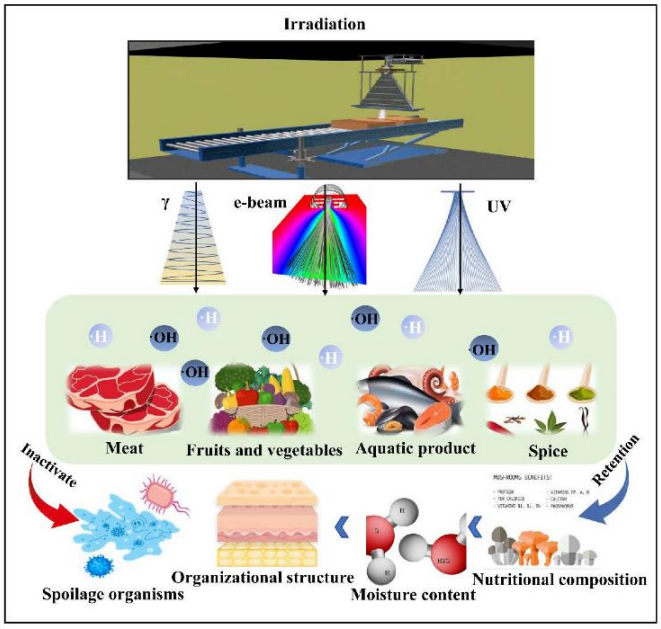

Fig. 1. The food system under irradiation technology [14]

Also factors such as sample size, replication, and statistical analysis to ensure the reliability and validity of the results, should be considered. The bacteriological analysis methods used to assess the impact of irradiation on food samples typically involve a series of microbiological and biochemical assays to evaluate the presence and viability of bacteria before and after irradiation [16-18]. Some of the common bacteriological analysis methods consist of:

1. Total Bacterial Count 2. Specific Pathogen Detection, 3. Microbiological Assays 4. Biochemical Analysis 5. Molecular Techniques.

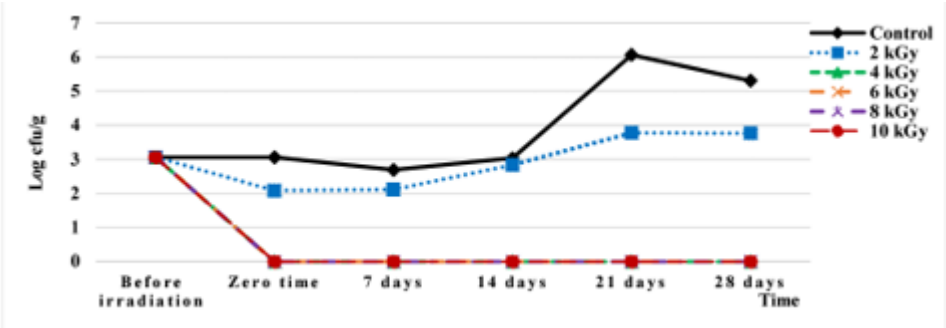

Fig. 2. The effect of gamma irradiation on minced meat on total fungal counts of minced beef meat stored at 4-5°C [19]

These bacteriological analysis methods are crucial for evaluating the effectiveness of irradiation in reducing bacterial contamination in food samples and for assessing the overall bacteriological quality of irradiated food products (Fig. 2).

DISCUSSION

The presentation of data obtained from the bacteriological analysis of irradiated and non-irradiated food samples involves the organization and visualization of the results (Fig. 3).

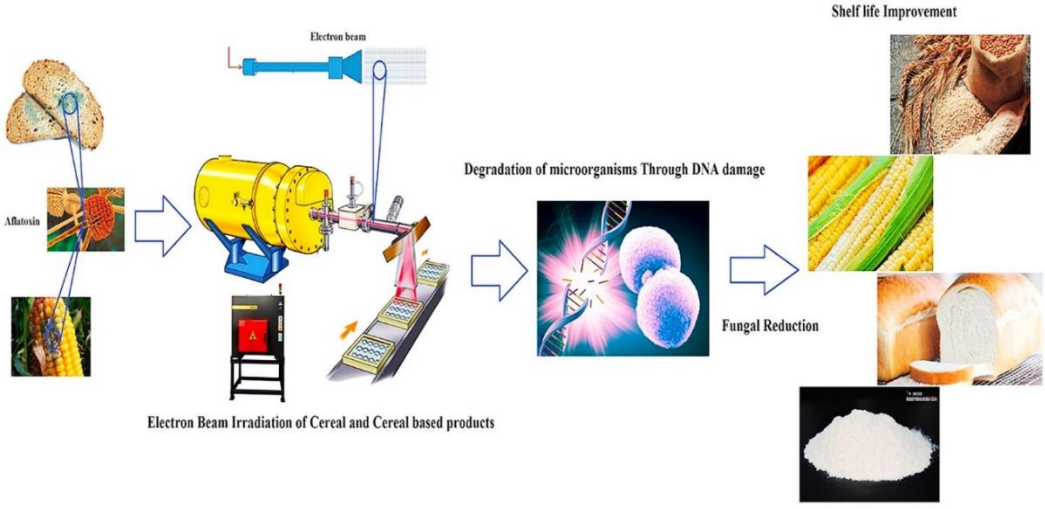

Fig. 3. The process of food decontamination through Irradiation [42].

Statistical analysis

Statistical analysis plays a crucial role in determining the significance of the impact of irradiation on the bacteriological quality of food samples. When conducting statistical analysis, several approaches can be used to assess the significance of the differences observed between irradiated and non-irradiated samples. Some common statistical methods can be used are [20]; 1. T-tests [21-22] 2. Analysis of Variance (ANOVA) [23-24] 3. Non-parametric Tests 4. Chi-Square [25] Test 5. Regression Analysis.

Interpreting the results of bacteriological analysis is crucial for understanding the implications of using irradiation in food preservation. Some key points to consider include: 1. Reduction in Bacterial Contamination: Significant reduction in bacterial counts or specific pathogens in irradiated food samples indicates the effectiveness of irradiation in reducing contamination [26-27]. 2. Preservation of Microbiological Quality: Assessing how irradiation preserves

microbiological quality by inhibiting bacterial growth supports its use as a preservation technique [28]. 3. Safety and Shelf-Life Extension: Reduction in foodborne pathogens and extension of shelf life due to irradiation enhance food safety and preservation [29-30]. 4. Regulatory Compliance: Meeting regulatory safety requirements with irradiated food supports its compliance as a preservation method [31]. 5. Consumer Acceptance: Effective reduction in contamination without compromising sensory or nutritional quality can boost consumer confidence in irradiated foods [32]. 6. Consideration of Other Factors: Understanding limitations like changes in food composition or the development of resistant bacteria is essential when evaluating the use of irradiation [33] (**Table** 1).

Table 1. Radiation resistance of selected micro-organisms.[33]

Organism	D10 value (kGy)	Substrate	Irradiation conditions
Campylobacter jejuni	0.13-0.19	Raw chicken	3-4°C; air
Clostridium botulinum (spores)	3.45-3.60	Cooked beef	25°C; Type A spores
Escherichia coli O157:H7	0.28	Beef	5°C; vacuum packed
Escherichia coli O157:H7	0.44	Beef	-5°C; vacuum packed
Listeria monocytogenes	0.49	Chicken	12°C; Packaged in air
Salmonella Enteritidis	0.70	Low (3.3-5.6%) fat beef	Packaged in air
Vibrio parahaemolyticus	0.04-0.06	Shrimp homogenate	Frozen
Candida zeylanoides	0.68	Chicken skin	10°C; in air; D10 value
Penicillum expansum	0.32	grain	10°C; in air;D10 value
Fusarium culmorum	8	grain	10°C; calculated as dose required to reduce count from log 5.5 to < than log 1/ g.
Coxsackie virus	6.8	Cooked beef	-30
Rotavirus	2.4	Clams and oysters	Not given

By carefully interpreting the results and considering their broader implications, researchers and food industry professionals can make informed decisions regarding the use of irradiation in food preservation.

With comparing the findings of studies on the impact of irradiation on bacteriological quality and considering potential reasons for any discrepancies, it is crucial to focus on the following items; 1. Experimental Design [34], 2. Methodological Variations [35-36], 3. Sample Size and Statistical Power, 4. Heterogeneity of Food Products [37], 5. Microbial Strain Variability [38], 6. Environmental Factors [37-39], 7. Evolution of Technology and Practices [40-42].

Table 2. Applications of food irradiation [43-51]

	Application	**Dose (kGy)**
Low dose (up to 1 kGy)	Inhibit sprouting (potatoes, onions, yams, garlic)	0.06 – 0.2
	Delay in ripening (strawberries, potatoes)	0.5 – 1.0
	Prevent insect infestation (grains, cereals, coffee beans, spices, dried nuts, dried fruits, dried fish, mangoes, papayas)	0.15 – 1.0
	Parasite control and inactivation (tape worm, trichina)	0.3 – 1.0
Medium dose (1 kGy to 10 kGy)	Extend shelf-life of raw and fresh fish, seafood, fresh produce	1.0 – 5.5
	Extend shelf-life of refrigerated and frozen meat products	4.5 – 7.0
	Reduce risk of pathogenic and spoilage microbes (meat, seafood, spices, and poultry)	1.0 – 7.0
	Increased juice yield, reduction in cooking time of dried vegetables	3.0 – 7.0
High dose (above 10 kGy)	Enzymes (dehydrated)	10.0
	Sterilization of spices, dry vegetable seasonings	30.0 max
	Sterilization of packaging material	10.0 – 25.0
	Sterilization of foods (NASA and hospitals)	44.0

By engaging in a comprehensive discussion of these potential benefits and drawbacks, stakeholders in the food industry, regulatory agencies, and research communities can gain a nuanced understanding of the implications of using irradiation for improving bacteriological quality in food preservation (**Table** 2).

CONCLUSION

In general, the impact of irradiation on bacteriological quality in food preservation has significant implications for informing best practices, guiding regulatory decisions, and ensuring food safety and quality. Future research should focus on strain-specific responses, combined preservation methods, consumer perception studies, environmental impact assessments, and long-term effects of irradiation. Potential applications of irradiation include pathogen reduction, shelf-life extension, quarantine treatment, food safety interventions, and emergency preparedness. By exploring these areas and considering the applications of

irradiation, the food industry, regulatory agencies, and research communities can advance the adoption of this preservation method to enhance food safety, security, and sustainability.

References

[1] Bhawna Bisht et al. (2021). Effect of ionizing and non-ionizing radiations on preservation of fruits and vegetables. Trends in Food Science & Technology, 114: 372–85.

[2] Maherani B, Hossain F, Criado P, Ben-Fadhel Y, Salmieri S, Lacroix M. (2016). World Market Development and Consumer Acceptance of Irradiation Technology. Foods, 5(4):79

[3] Rodrigues I., Baldini A., et al. (2021). Gamma ray irradiation: A new strategy to increase the shelf life of salt-reduced hot dog wieners, LWT, 135 (110265)

[4] Naebi M, Torbati M, Azadmard-Damirchi S, Siabi S, Savage GP. (2023) An overview of effects of gamma radiation on the biological, physicochemical and nutritional parameters of oilseeds and oils. Int J Radiat Biol.;99(10):1495-1502.

[5] Dattatreya M. Kadam, Manoj Kumar, Akansha Kasara, (2021) Application of high energy electromagnetic radiations in elimination of anti-nutritional factors from oilseeds, LWT, 151 (112085).

[6] Farkas, J. (1989). Microbiological safety of irradiated foods. International Journal of Food Microbiology, 9(1): 1–15.

[7] Mohamed EFE, Hafez AEE, et. Al. (2023). Irradiation as a Promising Technology to Improve Bacteriological and Physicochemical Quality of Fish. Microorganisms. 23;11(5):1105.

[8] Shahhosseini, G., Karimi, A., Amanpour, S., Mansouri, M.A. (2019). Effect of Gamma Irradiation on Microbial Decontamination, Crude Nutrient Content, and Mineral Nutrient Composition of Laboratory Animal Diets. Archives of Razi Institute, 74(2): 175–182.

[9] Joshua Ajibola, O. (2020). An overview of irradiation as a food preservation technique. Novel Research in Microbiology Journal, 4(3), 779-789.

[10] Fellows, P.J. (2018). Food Processing Technology: Principles and Practices. Consultant Food Technologist.

[11] Zhong, Y., Dong, S., Cui, Y., Dong, X., Xu, H., Li, M. (2023). Recent Advances in Postharvest Irradiation Preservation Technology of Edible Fungi: A Review. Foods 103.

[12] Barkaoui, S., Madureira, J., M P Santos, P. (2020). Effect of Ionizing Radiation and Refrigeration on the Antioxidants of Strawberries. Food and Bioprocess Technology,13(10).

[13] Canciu, A., Tertis, M., Hosu, O., Cernat, A., Cristea, C., Graur, F. (2021). Modern Analytical Techniques for Detection of Bacteria in Surface and Wastewaters. Sustainability, 13:7229.

[14] W. Kaspar, C. and Tartera, C. (1990). 16 Methods for Detecting Microbial Pathogens in Food and Water. In Methods in Microbiology, 22: 497–531.

[15] Rodriguez, P. and Fernando, et al. (2013). Predictive microbiology in foods. Springer New York.

[16] Bektashi, Limani, N., Mladenoska, Irina, Popovska, Olga, Dimitrovski, Darko, Spasevska, Hristina, Reka, Arianit A. and Mašić, Slobodan. (2023). Assessment of the impact of γ-irradiation on the piperine content and microbial quality of black pepper. Open Chemistry, 21(20220356).

[17] Indiarto, R. Irawan, A.N., Subroto, E. (2023) Meat Irradiation: A Comprehensive Review of Its Impact on Food Quality and Safety. Foods, 12, 1845.

[18] Bliznyuk, U., Avdyukhina, V., Borshchegovskaya, P. et al. (2022). Effect of electron and X-ray irradiation on microbiological and chemical parameters of chilled turkey. Sci Rep 12, 750

[19] Khalafalla, M. Nasr, F., Nasr, A. and Rahma, Abo-Zaid, M. (2018). Effect of gamma irradiation on microbial load, physicochemical characteristics and shelf-life of raw minced beef meat Galal. Middle East Journal of Applied Sciences ISSN 2077-4613, 8(2): 625–634.

[20] Goeman, J. and Solari, A. (2022). Comparing three groups. The American Statistician 76(2):168–176.

[21] Richardson, S.S.W. (1994). The first t-test. Statistics in medicine 13(8):785-803.

[22] de Oliveira, Silva, E. et al. (2023). A t-test ranking-based discriminant analysis for classification of free-range and barn-raised broiler chickens by 1H NMR spectroscopy. Food Chemistry 399:134004.

[23] St, Lars, and Svante Wold. (1989). Analysis of variance (ANOVA). Chemometrics and intelligent laboratory systems 6.4:259–272.

[24] Chen, Wei-Hsin, et al. (2022). A comprehensive review of thermoelectric generation optimization by statistical approach: Taguchi method, analysis of variance (ANOVA), and response surface methodology (RSM). Renewable and Sustainable Energy Reviews 169:112917

[25] Rana, Rakesh, and Richa Singhal. (2015). Chi-square test and its application in hypothesis testing. Journal of Primary Care Specialties 1(1):69-71

[26] Radomyski, Tomasz, et al. (1994). Elimination of pathogens of significance in food by low-dose irradiation: a review. Journal of food protection 57(1):73-86.

[27] Mshelia, R.Dz., Dibal, N.I. and Chiroma, S.M. (2023). Food irradiation: an effective but under-utilized technique for food preservations. J Food Sci Technol 60: 2517–2525.

[28] Munir, M.T. and Federighi, M. (2020). Control of Foodborne Biological Hazards by Ionizing Radiations. Foods, 9, 878.

[29] Khattak, Badshah, A. et al. (2005). Shelf life extension of minimally processed cabbage and cucumber through gamma irradiation. Journal of food protection 68(1):105-110.

[30] Singh, A.D.R. (2016). Shelf Life Extension of Tomatoes by Gamma Radiation, Radiation Science and Technology, 2(2):17-24.

[31] Mohácsi-Farkas, F.J.C. (2011). History and future of food irradiation. Trends in Food Science & Technology 22(3):121-12667.

[32]D'Souza, Clare, et al. (2021). Consumer acceptance of irradiated food and information disclosure–A retail imperative. Journal of retailing and consumer services 63:102699.

[33] Patterson, M. (2005). New Frontier of Irradiated food and Non-Food Products, International Symposium Food Irradiation: Microbiological Safety and Disinfestation 22-23, KMUTT, Bangkok, Thailand.

[34] Savvaidis, and Ioannis, N., et al. (2002). Control of natural microbial flora and Listeria monocytogenes in vacuum-packaged trout at 4 and 10 C using irradiation. Journal of food protection 65(3):515-522.

[35] Corry, Janet EL, G. D. W. Curtis, and Rosamund M. Baird, eds. (2003). Handbook of culture media for food microbiology. 37.

[36] Vasilev, S.R.N and Stefan L. Spassov. (2010). Irradiation of food, current legislation framework, and detection of irradiated foods. Food Analytical Methods 3:225-252.

[37] Madihi-Bidgoli, Soheila, et al. (2021). Azurobine degradation using Fe2O3@ multi-walled carbon nanotube activated peroxymonosulfate (PMS) under UVA-LED irradiation: performance, mechanism and environmental application. Journal of Environmental Chemical Engineering 9(6):106660

[38] Lianou, Alexandra, and Konstantinos P. Koutsoumanis. (2013). Strain variability of the behavior of foodborne bacterial pathogens: a review. International Journal of Food Microbiology 167(3):310-321

[39] El-Gameel, Essam A., and Suzan R. Amin. (2021). Environmental Impact Assessment of Food Irradiation Technology as A Comparative Study with Some Other Food Preservation Methods. Egyptian Journal of Radiation Sciences and Applications 34(1):79–85

[40] Obileke, KeChrist, et al. (2022). Recent advances in radio frequency, pulsed light, and cold plasma technologies for food safety. Journal of Food Process Engineering 45(10):14138.

[41] Sahoo, M., Aradwad, P., Panigrahi, C., Kumar, V. and Naik, S.N. (2023). Irradiation of Food. In Novel Technologies in Food Science (eds N. Chhikara, A. Panghal and G. Chaudhary).

[42] Khaneghah, A.M. Moosavi, M.H. Carlos A. F. Oliveira, Vanin, F. and Anderson S. (2020). Electron beam irradiation to reduce the mycotoxin and microbial contaminations of cereal-based products: An overview. Food and Chemical Toxicology, 143: 111557.

[43] Indiarto, Rossi, et al. (2020). Food irradiation technology: A review of the uses and their capabilities. Int. J. Eng. Trends Technol 68(12):91–98.

[44] Khade, H. D., et al. (2023). Gamma radiation processing for extending shelf-life and ensuring quality of minimally processed ready-to-eat onions. Journal of Food Science and Technology, 1–10.

[45] Fernandes, Ângela, et al. (2011). Assessing the effects of gamma irradiation and storage time in energetic value and in major individual nutrients of chestnuts. Food and Chemical Toxicology 49(9):2429-2432.

[46] Ardestani, S.B. and Ahmadi-Roshan, M. (2021). Effects of Gamma Irradiation on Microbial and Sensory Properties of Fresh Dill and Savory. (in en), Innovative Food Technologies, 9(1): 13–26.

[47] Ozkan, Gulay, et al. (2019). A review of microencapsulation methods for food antioxidants: Principles, advantages, drawbacks and applications. Food chemistry 272:494–506

[48] Hammad, A., A. Gabarty, and R. A. Zinhoum. (2020). Assessment irradiation effects on different development stages of Callosobruchus maculatus and on chemical, physical and microbiological quality of cowpea seeds. Bulletin of Entomological Research 110(4):97-505

[49] Xuetong, F. (2018). Food Irradiation Research and Technology. Wiley-Blackwell.

[50] Fillet Oraei, M., Motalebi, A. A. Hoseini, E. Javan, S. (2011). Effect of Gamma irradiation and frozen storage on microbial quality of Rainbow trout (Oncorhynchus mykiss), Iranian Journal of Fisheries Sciences, 10(1):75.

[51] Oyeyemi, S. M., et al. (2023). Effect of 300Gy Gamma (ϒ) radiation dose on Nigerian onion: A proximate composition.

Development of 99mTc-Chelat-conjugated HEDP as a novel bone scintigraphy agent (Paper ID : 1048)

Sarah Shouhani[۱], Elham Sattarzadeh Khameneh[۲], Fariba Johari Deha[۲], Saeed Kakaei[*۲], Leila koopaei[۲], Seyed Javad Farahani Barzabadi[۲]

School of Physics, Damghan University, P.O.BOX ۳۶۷۱۶-۴۱۱۶۷, Damghan, Iran . ۱
.Radiation Application Research School, Nuclear Science and Technology Research Institute, P. O . ۲
Box ۱۱۳۶۵-۳۴۸۶, Tehran - Iran

Abstract

Bone-related diseases, including bone metastases, osteoporosis, and pathologic fractures, can have significant impact on a patient' s quality of life. The use of bone-targeted radiopharmaceuticals such a bisphosphonates is an effective approach to aid in the diagnosis and treatment of these diseases. This study focuses on the development of a novel radiopharmaceutical for the diagnosis and detection of bone-related diseases and aims to address this need by developing new synthesis method for HEDP compound as a bone seeking agent and improving its properties using the innovative MAX chelator. The resulting ^{۹۹m}Tc-labeled MAX-HEDP compound offers the advantages of reproducibility and compatibility .with other therapeutic modalities

The HEDP is synthesized using cost-effective and accessible methods, and a novel chelating agent called MAX is conjugated, using the DCC-NHS and is labeled with ^{۹۹m}Tc. The yield of the synthesis reaction is calculated to be ۸۹٪, and the radiolabeling of MAX- HEDP with ^{۹۹m}Tc .achieves a purity of ۹۸٪ using thin layer chromatography

The stability of the final product was evaluated in albumin serum. After ۱ hour at room ,temperature, the compound shows a stability of ۹۶٪. Even after ۶ hours at ۳۷ degrees Celsius .the compound remains stable with a decrease of less than ۱۰٪

The findings of this study contribute to the advancement of bone disease diagnosis and pave .the way for future research in this field

Key word: HEDP, ^{۹۹m}Tc, Chelate agent, Bone diseases, MAX

Introduction

Patients with bone metastases often experience severe and persistent pain, which may be accompanied by pathological fractures, spinal cord compression, hypercalcemia, and other complications that significantly impact their quality of life. Therefore, timely and effective diagnosis and treatment are essential to reduce symptoms, pain, and improve quality of life [1-

3]. The use of bone-targeting radiopharmaceuticals is an effective method for tracking and assisting in the design of bone-related interventions, offering advantages such as repeatability and combination with other treatments [4].

The aim of this research is preparation of Tc-MAX-HEDP as a novel bone seeking agent to diagnose various bone-related diseases, such as bone metastases caused by cancer, osteoporosis, pathological fractures, and other bone disorders, using a novel synthesis method of HEDP by ultrasonic as an energy source, coupling to the innovative chelator MAX, and labeling of the compound with the radionuclide ^{99m}Tc.

Methods and Materials

Synthesis

The synthesis of HEDP was performed using efficient and novel methods. In brief phosphorous trichloride was added dropwise to acetic acid and reaction was continued under ultra-sonic. Then the reaction was diluted with water and stirred. Finally, pH was adjusted to 1.8 with NaOH and recrystallization was performed with ethyl acetate. For the synthesis of the MAX chelator, we utilized Xanthate and chloroacetamide [5, 6]. Finally, the HEDP compound was combined with the MAX chelator using the DCC-NHS method and prepared for labeling.

Radiolabeling

MAX-HEDP were dissolved in water, $SnCl_2$ and ascorbic acid were added to enhance stability, prevent side reactions during labeling, and increase the labeling efficiency. Then, a phosphate buffer was added to adjust the solution's pH to 7. Technetium-99m pertechnetate was added and the reaction mixture was incubated for 60 minutes. Subsequently, it was passed through a 0.22-micrometer filter.

The radionuclide and radiochemical purity and radiolabeling efficiency were performed using thin-layer chromatography. Normal saline 0.9%, methanol: acetone 50:50, and H_3PO_4 (15%). The obtained results indicate a radiochemical purity and efficiency of over 98%.

The RTLC chromatogram obtained after 30 minutes of incubation in the H_3PO_4 (15%) mobile phase at room temperature is shown in figure 1.

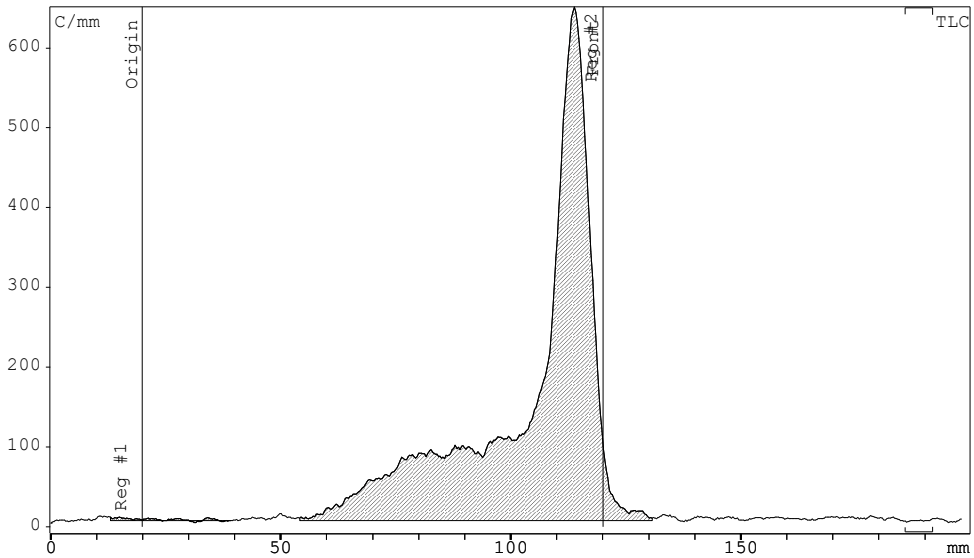

Figure ۱:Chromatogram ^{۹۹m}Tc-MAX-HEDP in the mobile phase of $H_۳PO_۴$ ۱۵٪ after ۳۰ minutes at room temperature.

Results and discussion

The direct labeling of the MAX-HEDP compound with ^{99m}Tc was performed. The radiolabeling purity of ^{99m}Tc was assessed using thin-layer chromatography (TLC) using H_3PO_4 15%, methanol: acetone (50:50), and normal saline 0.9% as mobile phases. The evaluation of the labeling efficiency of the ^{99m}Tc-MAX-HEDP compound was conducted using TLC technique with ITLC-SG paper (2×13 cm) and three different solvent systems: H_3PO_4 15%, methanol: acetone (50:50), and normal saline 0.9%.

The results obtained from spectral analysis indicate the percentage of radiolabeling, which achieved an acceptable yield of 98%.

In the quality control and stability assessment of the synthesized ^{99m}Tc-MAX-HEDP compound in albumin and saline serums, after one hour at room temperature, it remained stable at 96%. After 6 hours at 37 degrees Celsius, it showed a stability with less than 10% decrease.

In conclusion, this research presents a new radiopharmaceutical approach for the diagnosis bone-related diseases. The synthesis and radiolabeling of the ^{99m}Tc-MAX-HEDP compound were successfully achieved with high efficiency and purity. The stability of the compound in saline and albumin serums demonstrates indicates potential for further development as a diagnostic agent.

Acknowledgements

The authors are grateful to Radiation Application Research School, Foundation of Nuclear Science and Technology Research Institute (P.O. Box 11365-3486) for supporting this research work.

References

١. Pandit-Taskar, N., M. Batraki, and C.R. Divgi (2004) Radiopharmaceutical therapy for palliation of bone pain from osseous metastases. Journal of Nuclear Medicine, **45**(8): p. 1358-1365.

٢. Harrison, M.R., et al. (2013). Radium-223 chloride: a potential new treatment for castration-resistant prostate cancer patients with metastatic bone disease. Cancer management and research, p. 1-14.

٣. Di Lorenzo, G., et al. (2003) Bone metastases are a severe problem in oncology, since they usually are associated with pain .Oncol Rep. 10: p. 399-404.

٤. Ayati, N., et al. (2013) Treatment efficacy of ^{153}Sm-EDTMP for painful bone metastasis. Asia Oceania Journal of Nuclear Medicine and Biology. 1(1): p. 27.

٥. Arab Halvaei Bagheri, Z., et al. (2022) Estimation of the absorbed dose of ^{99m}Tc-MAX in human based on the biological distribution of balb/c mice by MIRD method. Radiation Safety and Measurement. 11(1): p. 1-10.

٦. Mohareri, M.M., et al. (2021) Preparation and application of Fe_3O_4@ Acetamidoxanthate as a unique nanosorbent in heavy metal removing. Main Group Chemistry. 20: p. 633-643.

International Conference on Nuclear Science and Technology
6- 8 MAY 2024 | Isfahan, Iran

Investigating the possibility of Well logging in Iran's copper mines using the PGNAA method activated by Am-Be neutron source (Paper ID : 1053)

valizadeh B [1*], Esmaeili Ranjbar L [2], Rezaie M [2]

[1] *Nuclear Science and Technology Research Institute, Atomic Energy Organization, Tehran, Iran*
[2] *Department of Nuclear Engineering, Faculty of Sciences and Modern Technologies, Graduate University of Advanced Technology, Kerman, Iran*

Abstract

Prompt gamma neutron activation analysis (PGNAA) is one of the methods of measuring the percentage of elements in various metallic and semi-metallic compounds, which is done using thermal neutrons.

The main purpose of this article is to investigate the possibility of detecting elements and well-logging in copper mines using fast neutrons.This article has tried using 5 Ci Am-Be neutron source and CsI(Tl) detector, the possibility of well logging in the copper mines of the Sanandaj-Sirjan region in Iran using the PGNAA and Monte Carlo simulation methods checked and investigated the possibility measuring of the percentage of elements in it with the above method. The interpretation of the simulation results of the characteristic gamma yield for the copper mine material and element in the copper mine, which was done by the MCNPX code, shows that it is possible to do logging and element well with the Am-Be neutron source in mines of Sanandaj-Sirjan area in Iran. The conducted investigations show that the characteristic gammas for measuring copper and titanium in copper mines in the above area are 1.24 and 0.34 MeV, respectively.

Keywords: Element Detection, Neutron, Monte Carlo, Neutron Activation, Characteristic Gamma, Copper Mines

INTRODUCTION

Nuclear well logging is one of the efficient methods for measuring underground mines [1]. In addition to this method, many methods have been used to identify underground mines [2]. For example, various nuclear and atomic methods for determining the percentage of elements in a sample can be mentioned, which include XRF, XRD, Pige, Pixe, PGNAA, etc [3]. Each of these methods has its advantages and disadvantages [4]. In XRF and XRD device, an X-ray tube is usually used to produce X-rays, that need a high voltage generator for operation [5]. The element detection devices also made using radioactive source that can measure specific

elements [6]. In this research, we have tried to investigate the possibility of using the PGNAA method using an Am-Be neutron source to measure all the elements in a compound, such as compounds of copper mines. The above method has been used a lot for well-logging and detecting elements [7]. However, in determining the gamma spectrum of the elements in a sample, there are not many reports that try to check this process using MCNPX. The MCNPX code is a nuclear atomic code based on Carlo's principles, which can be used to track 32 nuclear particles [8]. In the PGNAA method, the materials in target are activated by absorbing irradiated neutrons and an excited nucleus is created. The excited nucleus deexcited to the ground state with gamma radiation, which is considered as characteristic gamma ray of each element. The methods of measuring the characteristic gammas as well as the borehole survey are described below.

EXPERIMENTAL

For well logging, a borehole with a diameter of 1 meter is considered in a copper mine, and then an Am- Be neutron source is irradiating into the body of the well. By activating the elements in the sample, the characteristic gamma spectrum is measured using a CsI (Tl) detector. A schematic of the geometry used to perform this process is shown in Figure 1. In Figure 1, D represents the diameter of the well in the copper mine, 1 represents the CsI(Tl) detector, 2 represents the source shield and the detector, 3 represents the amercium beryllium source, 4 represents the copper mine body, and 5 represents the air inside the well give.

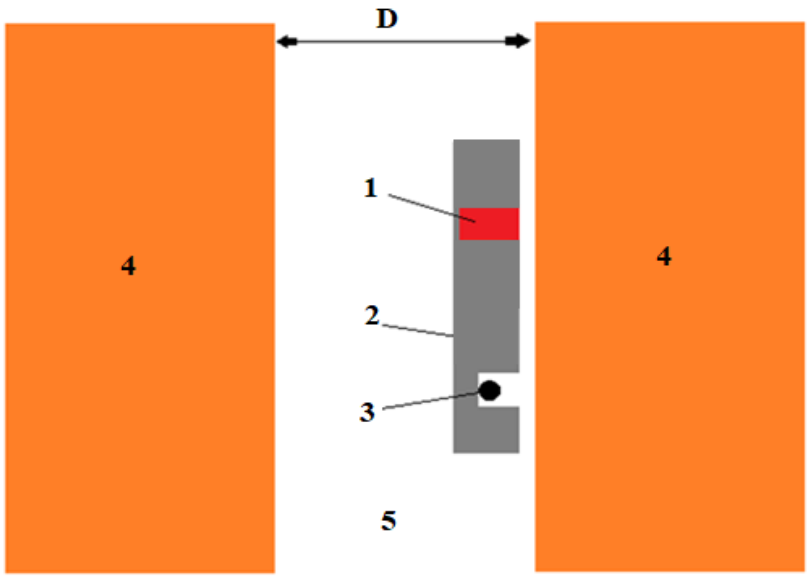

Fig. 1. Schematic of the geometry used for well logging Iranian in copper mines with Am-Be neutron source

The percentage of elements of the copper mines of Iran and the Sanandaj- Sirjan zone have been extracted from reliable sources. The percentage of elements in Iran's copper mines was measured by the XRF method[9], but for the analysis of the copper sample of Sanandaj- Sirjan zone, the percentage of compounds was given, and the percentage of elements in the sample was calculated using that data[10,11]. The results of the percentage of elements present of copper mines in Iran and the Sanandaj - Sirjan zone are given in Table1.

Table 1. The percentage of elements in the Iran and Sanandaj - Sirjan zone copper mines

Elements	Iran	Sirjan	Elements	Iran	Sirjan
K	0.0168	0	O	0.4972	0.383373
Ca	0.0057	0.199613	Mg	0.0149	0.014474
Ti	0.009	0.007911	Al	0.131	0.040834
Mn	0	0.00635	Si	0.215	0.13762
Fe	0.0809	0.160023	S	0	0.001001
Cu	0.0092	0.0488		0.4972	0.383373

The neutron spectrum of the Am-Be source (Figure 2) [12] is used as a neutron source in the MCNPx code. The neutron beam is perpendicular to the borehole body in Figure 1.

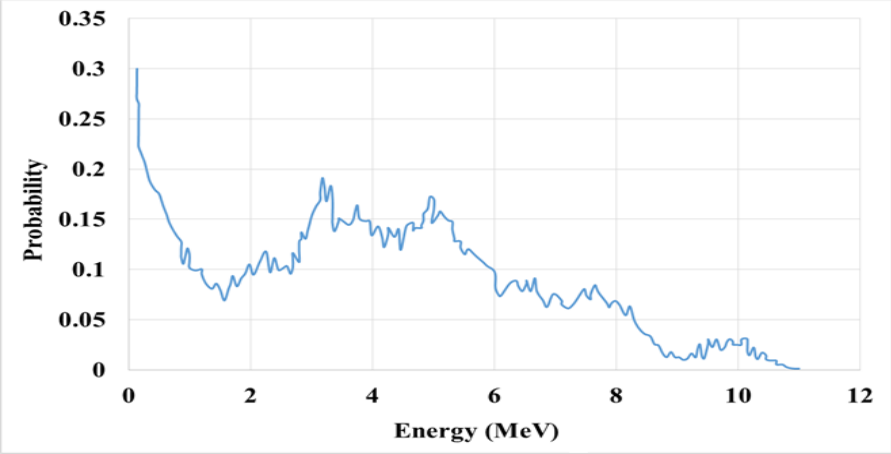

Fig. 2. Neutron spectrum of Am_Be Based on energy and probability [13]

The elements in Table 1 are activated and excited by the X(n,γ)Y interaction, and some of the excited levels created by characteristic gamma radiation return to the base state. It is also possible to perform two and multiple neutron absorption processes, and also perform the neutron spallation process13, in which the created compound nucleus turns into a variety of secondary nuclei with a mass number smaller than the primary nucleus, and the secondary particles produced are also due to being in an excited state. It emits a rich spectrum of prompt and delay gammas. The characteristic neutron activation gamma spectrum of the elements in copper of Iran and the Sirjan – Sanandaj zone along with their benefits have been extracted from reliable sources, the results of which are shown in Figure 3. [14,15]

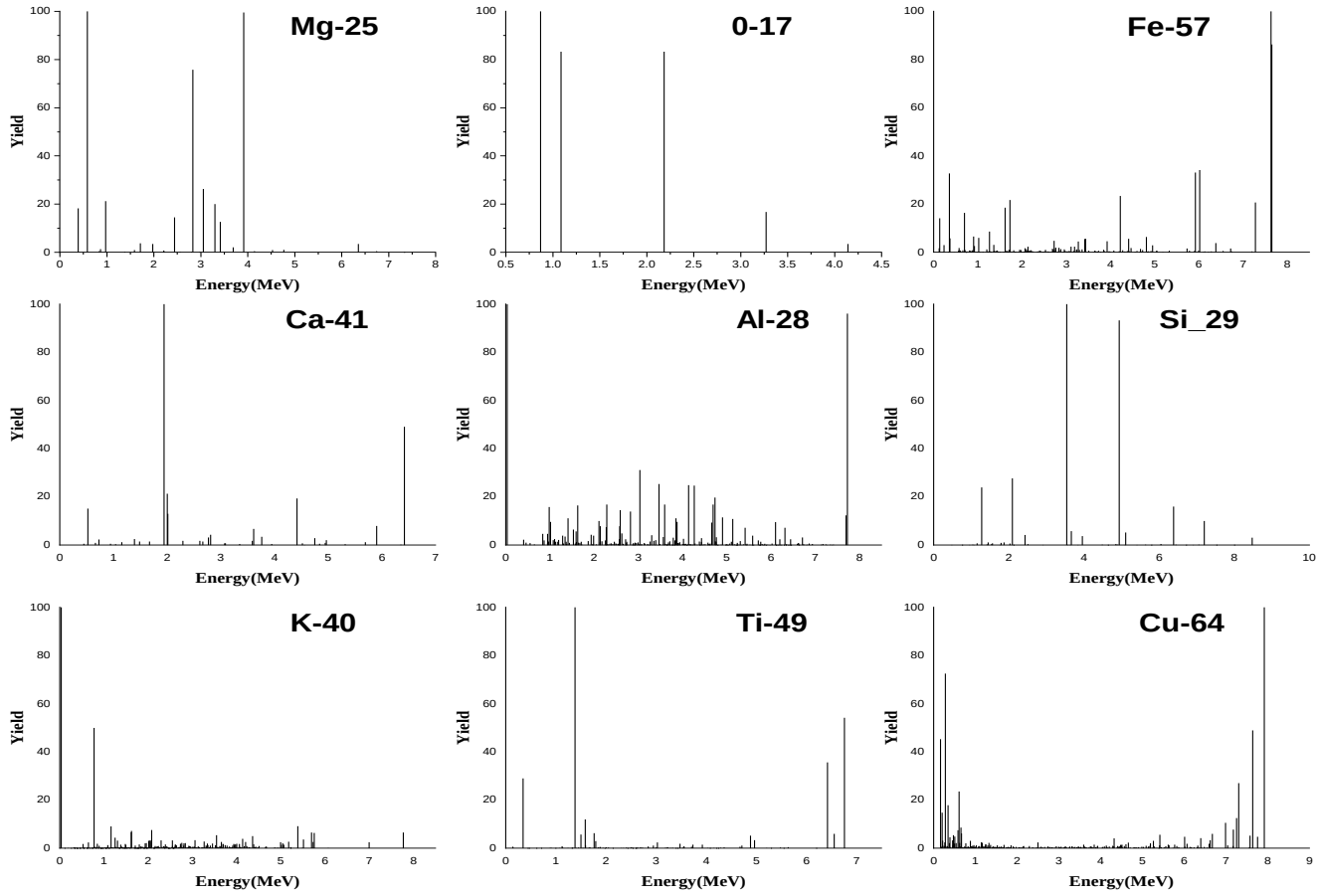

Fig. 3. The characteristic gamma spectrum of the elements in the compounds of copper mines

The gamma detector is also a CsI (Tl) detector. For the simulation, 10^8 neutrons were tracked to reach an error below one percent. The data of the gamma spectrum emitted from the samples for the PGNAA method has been calculated using F2 and F8 tally, in which F8 tally calculates

the gamma spectrum measured in the CsI (Tl) crystal. There is also the possibility of the effect of secondary particles produced in the sample as a result of the spallation process with ft8 res command.

Results and discussion

First, the characteristic gamma spectrum was obtained by the PGNAA method for copper mines in Iran, the results of which are shown in (Figure 4).

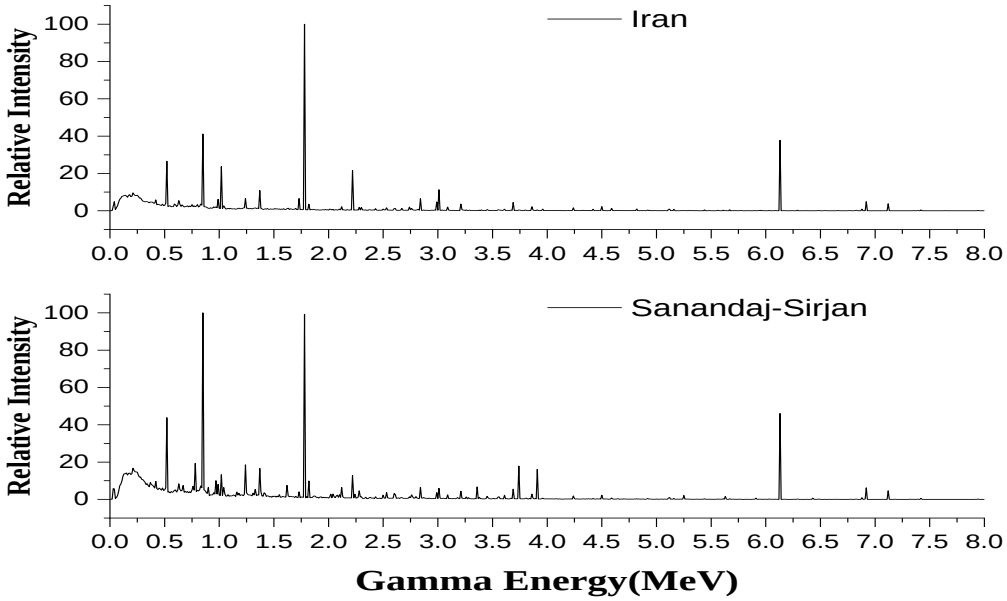

Fig. 4. Measured gamma spectrum of Iran and Sirjan – Sanandaj zone copper mines

The characteristic gamma of each of the elements in copper compounds by comparing the gamma spectrum calculated in Figure 4 with the characteristic gamma spectrum of the elements in each of the samples in Figures 3, are extracted that energies with a higher probability are mentioned in Table 2.

Table 2. The yield (%) for useful characteristic gamma ray emission of elements in the Iran and Sirjan – Sanandaj zone copper mines

Energy (MeV)	Yield (%)				Energy (MeV)	Yield (%)			
	Iran	Sirjan	Iran	Sirjan		Iran	Sirjan	Iran	Sirjan
	MCNPX	MCNPX	XRF	XRF		MCNPX	MCNPX	XRF	XRF

		O					Si		
0.87	2.07	4.72	0.50	0.38	1.27	1.06	2.38	0.22	0.14
1.09	1.01	1.71	0.50	0.38	1.45	0.84	1.80	0.22	0.14
2.19	0.36	0.85	0.50	0.38	2.1	0.93	1.50	0.22	0.14
3.27	0.12	0.31	0.50	0.38	2.43	1.1	1.42	0.22	0.14
4.14	0.13	0.18	0.50	0.38	3.96	0.91	0.73	0.22	0.14
		Mg					S		
0.98	1.63	2.90	0.015	0.02	0.85	41.183	100	0	0.001
0.99	6.13	8.08	0.015	0.02	0.91	1.287	1.95	0	0.001
1.38	1.32	4.28	0.015	0.02	0.94	1.43	2.44	0	0.001
1.59	1.09	1.37	0.015	0.02	1.7	1.26	1.61	0	0.001
1.68	0.85	1.40	0.015	0.02	2.23	2.22	0.77	0	0.001
		Al					Ca		
0.98	1.63	2.90	0.131	0.04	1.15	0.81	1.59	0.01	0.20
1.17	1.25	2.30	0.131	0.04	1.39	1.05	1.86	0.01	0.20
1.7	1.26	1.60	0.131	0.04	1.67	0.72	1.39	0.01	0.20
3.21	3.65	4.41	0.131	0.04	2.01	0.88	1.23	0.01	0.20
4.24	1.57	1.87	0.131	0.04	2.61	1.26	2.69	0.01	0.20
		Ti					Cu		
0.34	4.84	8.41	0.009	0.01	1.24	6.55	18.49	0.01	0.05
0.91	1.28	1.94	0.009	0.01	1.32	1.38	2.35	0.01	0.05
1.33	1.53	3.37	0.009	0.01	2.84	6.48	6.49	0.01	0.05
1.36	1.16	2.31	0.009	0.01	2.99	4.7	3.64	0.01	0.05
2.84	6.48	6.49	0.009	0.01	4.5	2.22	2.33	0.01	0.05
		Mn					Fe		
0.03	2.45	5.78	0	0.01	1	1.38	2.32	0.01	0.16
2.28	1.91	4.57	0	0.01	1.05	1.7	2.99	0.01	0.16
2.74	2.04	1.40	0	0.01	1.23	1.62	7.50	0.01	0.16
2.99	4.7	3.64	0	0.01	2.53	1.57	3.70	0.01	0.16
3.86	2.13	2.86	0	0.01	6.12	37.7	0.03	0.01	0.16
		K							
0.25	0	14.5	0	0.02					
0.77	0	4.92	0	0.02					
1.16	0	3.96	0	0.02					
1.61	0	7.2	0	0.02					

3.74	0	17.8	0	0.02

This data is obtained with the comparison of the radiation lines of the sample and the characteristic gamma lines of that element. By removing the common characteristic gamma line between the different elements in Table 1, the useful characteristic gamma line of each element is obtained. From these useful characteristic gammas, the characteristic gammas that are more sensitive to the change in the percentage of elements in the two copper samples of Iran and the Sanandaj –Sirjan zone have been selected the results are given in Table 3.

Table 3. The yield (%) for important characteristic gammas of elements in the Iran and Sirjan – Sanandaj zone copper mines

Energy (MeV)	Yield (%) Iran MCNPX	Sirjan MCNPX	Iran XRF	Sirjan XRF	Energy (MeV)	Yield (%) Iran MCNPX	Sirjan MCNPX	Iran XRF	Sirjan XRF
		O					Si		
0.87	2.07	4.72	0.50	0.38	1.27	1.06	2.38	0.22	0.14
					3.96	0.91	0.73	0.22	0.14
		Mg					S		
0.99	6.13	8.08	0.02	0.014	0.85	41.183	100	0	0.001
		Al					Ca		
3.21	3.65	4.41	0.13	0.041	1.15	0.81	1.59	0.01	0.20
					2.61	1.26	2.69	0.01	0.20
		Ti					Cu		
0.34	4.84	8.41	0.01	0.01	1.24	6.55	18.49	0.01	0.05
		Mn					Fe		
3.86	2.13	2.86	0	0.01	1.23	1.62	7.50	0.08	0.16
					6.12	37.7	0.03	0.08	0.16
		K							
0.25	0	14.5	0	0.02					
3.74	0	17.8	0	0.02					

As a result, the characteristic gamma data listed in Table 3 can be used to measure the percentage of elements in each copper mine sample.

Conclusions

In this article, using the PGNAA method, the well-logging of Iran's copper mines has been carried out using the Am-Be neutron source. Its results show that it is possible to use this method for well logging and copper mine detection. By comparing the radiation gamma spectrum of the elements present in Iran's copper mine and the mines of the Sanandaj-Sirjan zone copper mine with the specific gamma values of the elements present in the composition, the useful characteristic gamma line for measuring each element in the composition of copper mines was extracted. Its results show that 0.87, 0.99, 3.21, 0.34, 3.86, 3.74, 1.27, 0.85, 2.61, 1.24, 1.23 MeV gammas line is proper for measuring the O, Mg, Al, Ti, Mn, K, Si, S, Ca, Cu and Fe elements respectively in copper mines. The sensitive characteristic Gamma line for each element was obtained by comparing the simulated data related to the gamma spectrum with the values of the percentage of elements in copper compounds, which was obtained from the specific gamma lines of each element. So far, the PGNAA method has been used to determine the percentage of copper in different mines. J.Charbucinsiki et al have used the PGNAA method to determine the grade of copper in the Chuquicamata mine. They have used ^{252}Cf source as neutron source, and Bismuth Germanate Scintillator (BGO) detector as characteristic gamma ray detector. The difference between the result of this research and J.Charbucinsiki et al is the Am-Be source and the CsI (TI) detector were used as the neutron source and characteristic gamma ray detector respectively.

J.Charbucinsiki et al show that characteristic gamma ray is 7.91 MeV for copper detection and is 6.02 MeV for Fe detection. But the results of this research show that the characteristic gamma can be 1– 6.12 MeV for Fe detection and 1.24 – 4.5 MeV for copper detection, that result for Fe is near in two researches but for copper is different[16]. The results show that the percentage of sensitivity in the PGNAA method with Am-Be neutron source depends on the composition of the elements in the sample, also the 1.24 MeV gamma line is proper for detecting the copper element present in the copper mine sample.

References

[1] Matinkia, M., Hashami, R., Mehrad, M., Hajsaeedi, M.R. and Velayati, A., 2023. Prediction of permeability from well logs using a new hybrid machine learning algorithm. *Petroleum*, *9*(1), pp.108-123.

[2] Adajar, M.A.Q. and Cutora, M.D., 2018. The effect of void ratio, moisture content and vertical pressure on the hydrocompression settlement of copper mine tailing. *GEOMATE Journal*, *14*(44), pp.82-89.

[3] Mirea, D.A., Ciulavu, F., Ilie, M.V. and Iancu, D.A., 2021. PIXE, ED-XRF and optical analysis to authenticate the Garvăn gold monetary treasury. *Archaeometry*, *63*(3), pp.641-650.

[4] Breiter, K., Frýda, J., Seltmann, R. and Thomas, R., 1997. Mineralogical evidence for two magmatic stages in the evolution of an extremely fractionated P-rich rare-metal granite: the Podlesí stock, Krušné hory, Czech Republic. *Journal of Petrology*, *38*(12), pp.1723-1739.

[5] Nheta, W. and Ola-Omole, O.O., 2023. Exploring the characterization, liberation and flotation response of a Nigerian low-grade copper ore. *Journal of Sustainable Mining*, *22*(1), pp.20-32.

[6] Heydartaemeh, M., Karamoozian, M. and Potgieter, H., 2019. Application of nano high-entropy alloys to reduce energy consumption and wear of copper oxide and high-grade iron ores in heavy mining industries—A case study. *Minerals*, *10*(1), p.16.

[7] Lark, R.M., Hamilton, E.M., Kaninga, B., Maseka, K.K., Mutondo, M., Sakala, G.M. and Watts, M.J., 2017. Nested sampling and spatial analysis for reconnaissance investigations of soil: an example from agricultural land near mine tailings in Zambia. *European Journal of Soil Science*, *68*(5), pp.605-620.

[8] Hassanpour, M., Hassanpour, M., Faghihi, S., Khezripour, S., Rezaie, M., Dehghanipour, P., Faruque, M.R.I. and Khandaker, M.U., 2022. Introduction of graphene/h-BN metamaterial as neutron radiation shielding by implementing Monte Carlo simulation. *Materials*, *15*(19), p.6667.

[9] Heydartaemeh, M., Karamoozian, M. and Potgieter, H., 2019. Application of nano high-entropy alloys to reduce energy consumption and wear of copper oxide and high-grade iron ores in heavy mining industries—A case study. *Minerals*, *10*(1), p.16.

[10]Konari, M.B., Rastad, E., Kojima, S. and Omran, N.R., 2013. Volcanic redbed-type copper mineralization in the Lower Cretaceous volcano-sedimentary sequence of the Keshtmahaki deposit, southern Sanandaj-Sirjan Zone, Iran. *Neues Jahrbuch für Mineralogie-Abhandlungen*, *190*, pp.107-121.

[11]Sheikhrahimi, A., Pour, A.B., Pradhan, B. and Zoheir, B., 2019. Mapping hydrothermal alteration zones and lineaments associated with orogenic gold mineralization using ASTER

data: A case study from the Sanandaj-Sirjan Zone, Iran. *Advances in Space Research*, *63*(10), pp.3315-3332.

[12] Galahom, A.A., Mohsen, M.Y. and Amrani, N., 2022. Explore the possible advantages of using thorium-based fuel in a pressurized water reactor (PWR) Part 1: Neutronic analysis. *Nuclear Engineering and Technology*, *54*(1), pp.1-10.

[13] Sogbadji, R.B.M., Abrefah, R.G., Nyarko, B.J.B., Akaho, E.H.K., Odoi, H.C. and Attakorah-Birinkorang, S., 2014. The design of a multisource americium–beryllium (Am–Be) neutron irradiation facility using MCNP for the neutronic performance calculation. Applied Radiation and Isotopes, 90, pp.192-196.

[14] Konari, M.B., Rastad, E., Kojima, S. and Omran, N.R., 2013. Volcanic redbed-type copper mineralization in the Lower Cretaceous volcano-sedimentary sequence of the Keshtmahaki deposit, southern Sanandaj-Sirjan Zone, Iran. Neues Jahrbuch für Mineralogie-Abhandlungen, 190, pp.107-121.

[15] Adajar, M.A.Q. and Cutora, M.D., 2018. The effect of void ratio, moisture content and vertical pressure on the hydrocompression settlement of copper mine tailing. GEOMATE Journal, 14(44), pp.82-89.

[16] Charbucinski, J., Duran, O., Freraut, R., Heresi, N. and Pineyro, I., 2004. The application of PGNAA borehole logging for copper grade estimation at Chuquicamata mine. Applied radiation and isotopes, 60(5), pp.771-777.

ICNST 2024
International Conference on Nuclear Science and Technology
6- 8 MAY 2024 | Isfahan, Iran

Gamma-ray shielding properties of phosphate glasses containing different rates of Bi2O3, PbO, and BaO metal oxides (Paper ID : 1065)

Reza Bagheri[1,*], Hassan Ranjbar[2]

[1]*Radiation Applications Research School, Nuclear Science and Technology Research Institute, Tehran, Iran*
[2]*Nuclear Fuel Cycle Research School, Nuclear Science and Technology Research Institute, Tehran, Iran*

Abstract

Glass-based materials are one of the most common shielding materials. Phosphate glasses have unique properties that make them useful for some technical and industrial applications. The mass attenuation coefficients (μ_m) and effective atomic cross sections (σ_a) of phosphate glasses containing different concentrations of Bi_2O_3, PbO, and BaO (30–70% by weight) have been determined in the energy range of 10 keV–10 MeV. To calculate these parameters, XCOM and XMuDat computer programs have been used. The results of XCOM and XMuDat programs were in good agreement. It was found that the μ_m and σ_a parameters decrease as the photon energy increase. Also, the σ_a values improve by increasing the Bi_2O_3, PbO and BaO contents, while increasing these contents to the same fraction has no significant effect on μ_m in the energy range of 0.4–4 MeV, where the Compton Effect takes over as dominant process. The results presented in this study indicates that the chosen computer programs may be useful to calculate the gamma-ray shielding characteristics of different glass systems.

Keywords: Mass attenuation coefficient, Effective atomic cross section, Phosphate glass, XCOM, XMuDat.

INTRODUCTION

Nowadays with the extensive application of radiation sources and radioactive materials in various fields, utilization of gamma-ray sources with care and safety is essential [1]. Concrete, a common construction material, is widely used as radiation-shielding material; however, concrete has many disadvantages such as no transparency, bacterial corrosion, leaching, immobility, and so on, [2, 3].

Glass containing the functions of being transparency to visible light, simplicity to manufacture, 100% recyclability, and easy property modification through composition and preparation techniques provides an appropriate radiation shielding material against gamma rays and neutrons [4].

Various types of glasses have been used in different nuclear applications. The mass attenuation coefficients and effective atomic numbers of silicate glasses containing Bi_2O_3, PbO, and BaO metal oxides, were experimentally investigated by Kirdsiri et al. [4], at 662-keV gamma-ray energy. Bagheri et al. [5] studied gamma-ray shielding properties of silicate glasses containing Bi_2O_3, PbO, and BaO metal oxides using MCNP-4C code, XCOM and XMuDat programs. Also they theoretically determined gamma ray shielding properties of barium bismuth borosilicate glasses for 662, 1.173 and 1.332 keV gamma ray energies [6].

During the last decades, silicate, borate and phosphate glasses have been investigated extensively; however, the reports of phosphate glass in radiation shielding glass are very limited. Arbuzov et al. [7] investigated the spectral, optical, physicochemical, radiative, and radiation-shielding properties of glasses in the $PbO:P_2O_5:R_mO_n$ system (where R_mO_n stands for Group I–V element oxides). In addition, the spectral, radiation-optical and shielding properties of phosphate glasses with high lead content (up to 40% by mol.) were studied by Arbuzov et al. [8] in other work. Mass attenuation coefficients and effective atomic numbers of phosphate glass containing Bi_2O_3, PbO and BaO metal oxides were calculated by Kaewkhao and Limsuwan [9], using WinXCom program at 662 keV photon energy. Salem et al. [10], experimentally investigated the electrical transport properties and gamma-ray attenuation coefficient of phosphate glasses containing by-pass cement dust. Radiation shielding parameters of $BaO\text{-}Nb_2O_5\text{-}P_2O_5$ glass system was evaluated by Sayyed et al. [11], using MCNP5 code and XCOM software.

Phosphate glasses have unique attributes such as low melting temperature, excellent transmission of visible light, high refractive index and high thermal expansion coefficient that make them useful for industrial applications [12]. Adding metal oxides to glass systems improves the physical and chemical as well as radiation shielding properties of the glass systems. Lead (Pb) is a pollutant with environmental toxicity properties; hence, bismuth (Bi) and barium (Ba) are the two alternatives that are most extensively used in the radiation shielding field [4].

In this work, three phosphate glass systems, namely $xBi_2O_3:(100\text{-}x)P_2O_5$, $xPbO:(100\text{-}x)P_2O_5$, and $xBaO:(100\text{-}x)P_2O_5$ glasses, where x is expressed in terms of weight% (x is 30, 40, 50, 60, and 70) were considered. The mass attenuation coefficients (μ_m) and effective atomic cross sections (σ_a) of these phosphate glass systems are calculated in the energy range of 10 keV–10 MeV. To calculate these parameters XCOM, and XMuDat computer programs are used.

EXPERIMENTAL

Programs

The theoretical values of mass attenuation coefficients over wide photon energy range were tabulated by Hubbell and Seltzer [13] and Boone and Chavez [14], for different elements, compounds, and mixtures. From these tables and computerized programs such as WinXCom (or its predecessor, XCOM) and XMuDat programs, mass attenuation coefficients are calculated at energies 1 keV to 100 GeV [15, 16]. XCOM program applies Hubbell and Seltzer database while XMuDat program is able to produce a mass attenuation coefficient values on the base of both Hubbell and Seltzer and Boone and Chavez data. In this research, we applied Boone and Chaves database for XMuDat program. The percentages by weight of the elements in the glass samples are presented in Table 1.

Table 1. Percentage composition of glass samples

Element	Atomic number	BaO-glass					Bi_2O_3-glass					PbO-glass				
		30	40	50	60	70	30	40	50	60	70	30	40	50	60	70
Oxygen	8	40.41	36.13	31.85	27.56	23.28	40.37	36.07	31.78	27.48	23.19	39.43	34.82	30.21	25.60	20.99
Silicon	14	32.72	28.05	23.37	18.70	14.02	32.72	28.05	23.37	18.70	14.02	32.72	28.05	23.37	18.70	14.02
Barium	56	26.87	35.83	44.78	53.74	62.70	---	---	---	---	---	---	---	---	---	---
Lead	82	---	---	---	---	---	---	---	---	---	---	27.85	37.13	46.42	55.70	64.98
Bismuth	83	---	---	---	---	---	26.91	35.88	44.85	53.82	62.79	---	---	---	---	---

Theory

The mass attenuation coefficients of glass samples were calculated using XCOM and XMuDat programs data with equation (1), in which w_i and $\mu_{m,I}$ are the percentage by weight and mass attenuation coefficient of the *i*th element in the sample, respectively [17]:

$$\mu_m = \sum_{i=1}^{n} w_i \times \mu_{m,i} \qquad (1)$$

The effective atomic cross sections (σ_a) of materials are calculated from the following relationship [17]:

$$\sigma_a = \frac{1}{N_A}\sum f_i A_i \, \mu_{m,i} \qquad (2)$$

where A_i is the atomic mass of the ith element and N_A is the Avogadro's number. Also f_i holds out the fractional abundance of the ith element with respect to the number of atoms such that $f_1+f_2+f_3+\ldots+f_i = 1$.

RESULTS AND DISCUSSION

Mass attenuation coefficients of glasses

Calculated values of mass attenuation coefficients are given in Figures 1-3 for the studied gamma-ray energies of glass samples. A good agreement was observed between XCOM and XMuDat results. It is obvious from Figures 1-3 that the μ_m values decrease as the photon energy increases which beyond 1 MeV photon energy, these variations reduce and an extended smooth region appears. Multiple discontinuous peaks are observed in the low photon energy region (0.01 to 0.1 MeV) of Figures 1-3. These peaks are K–, L– and M–photoelectric absorption edges of Ba, Bi and Pb elements, respectively. The energies of absorption edges are given in Table 2. As seen in Table 2 and Figures 2-4, Ba, Pb and Bi elements have 1 (K edge), 4 (K, L1, L2 and L3 edges) and 4 (K, L1, L2 and L3 edges) absorption edges in this energy region respectively. These sudden increases in the mass attenuation coefficients of glasses are due to photoelectric absorptions which occur at energies just above the binding energy of the K and L shell electrons of the Ba, Bi and Pb elements.

Table 2. Energies (in keV) of absorption edges for Pb, Bi and Ba elements above 1 keV

Element	Z	M5	M4	M3	M2	M1	L3	L2	L1	K
Pb	82	2.484	2.586	3.066	3.554	3.851	13.035	15.200	15.861	88.005
Bi	83	2.580	2.688	3.177	3.696	3.999	13.419	15.711	16.388	90.526
Ba	56	---	---	1.062	1.137	1.293	5.247	5.624	5.989	37.441

Also, dependency of μ_m values of xR_mO_n:$(100\text{-}x)P_2O_5$ glasses on percentage by weight of BaO, Bi_2O_3, and PbO metal oxides were shown in Figures 1-3. The μ_m values of the glasses improve with increasing Bi_2O_3, PbO and BaO concentrations, excluding the energy range of 0.4–4 MeV, where the Compton Effect is revealed as dominant process.

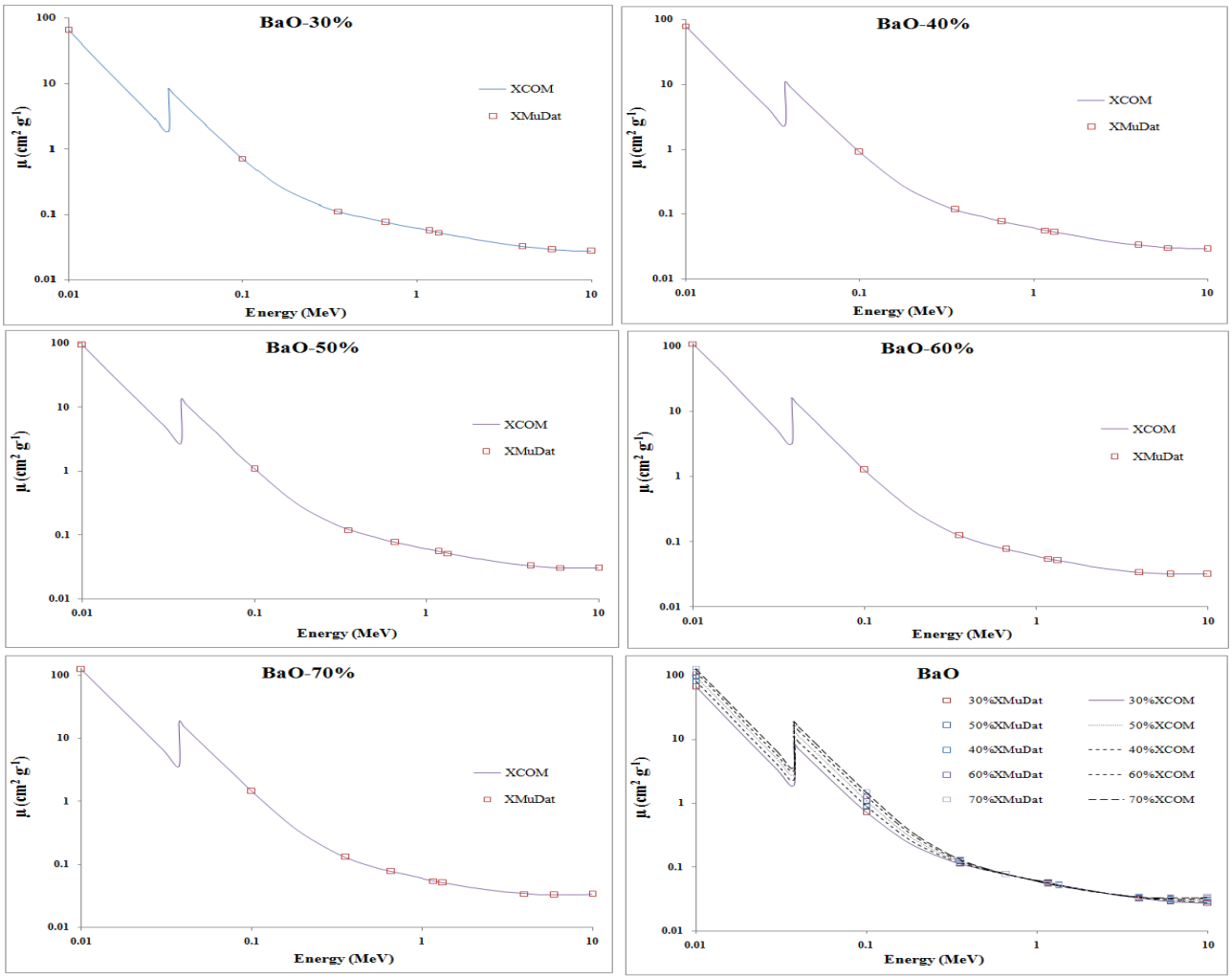

Fig. 1. Mass attenuation coefficients of $xBaO:(100-x)P_2O_5$ glass system, where x is the composition by weight (30, 40, 50, 60, and 70)

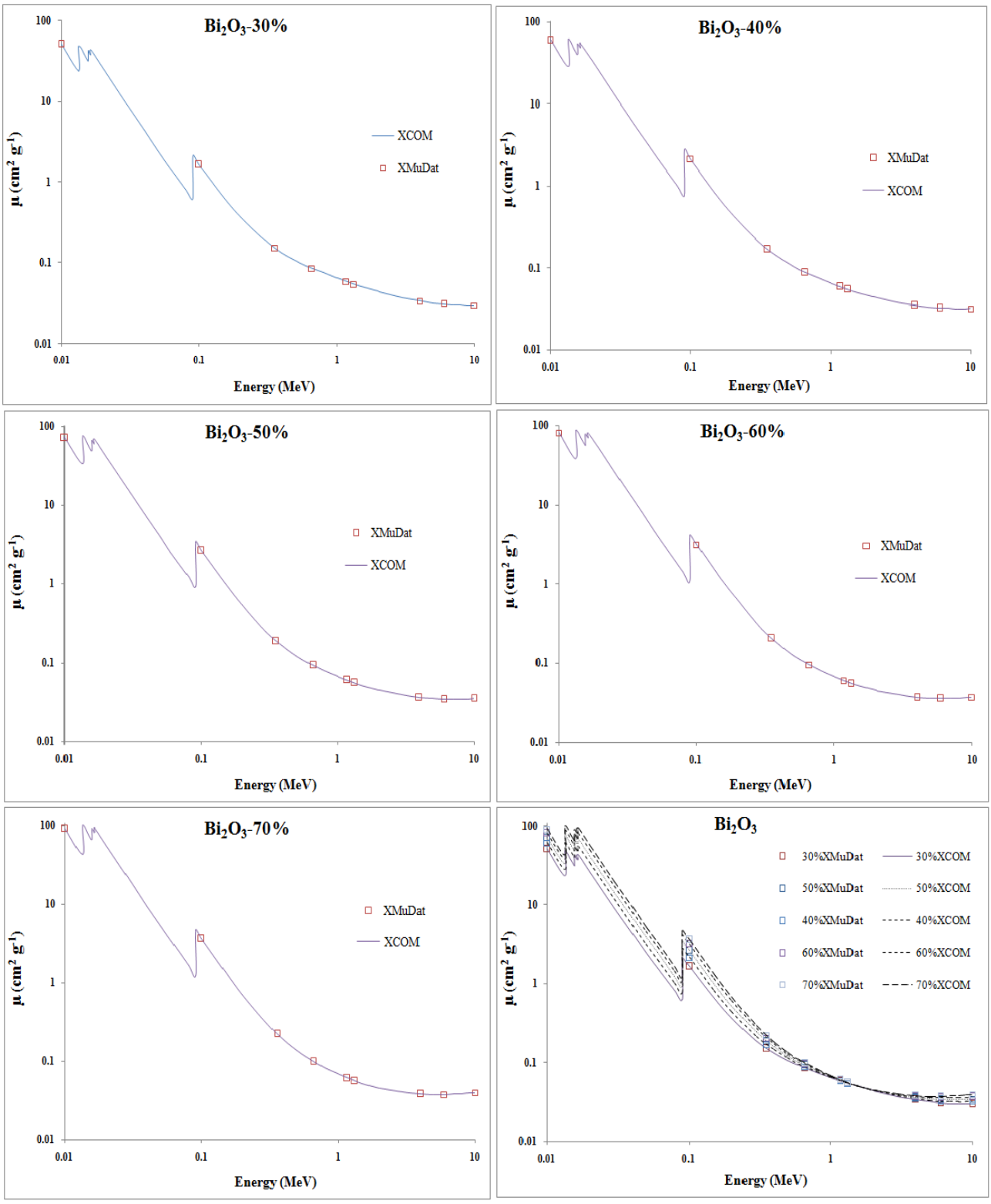

Fig. 2. Mass attenuation coefficients of xBi_2O_3:$(100-x)P_2O_5$ glass system, where x is the composition by weight (30, 40, 50, 60, and 70)

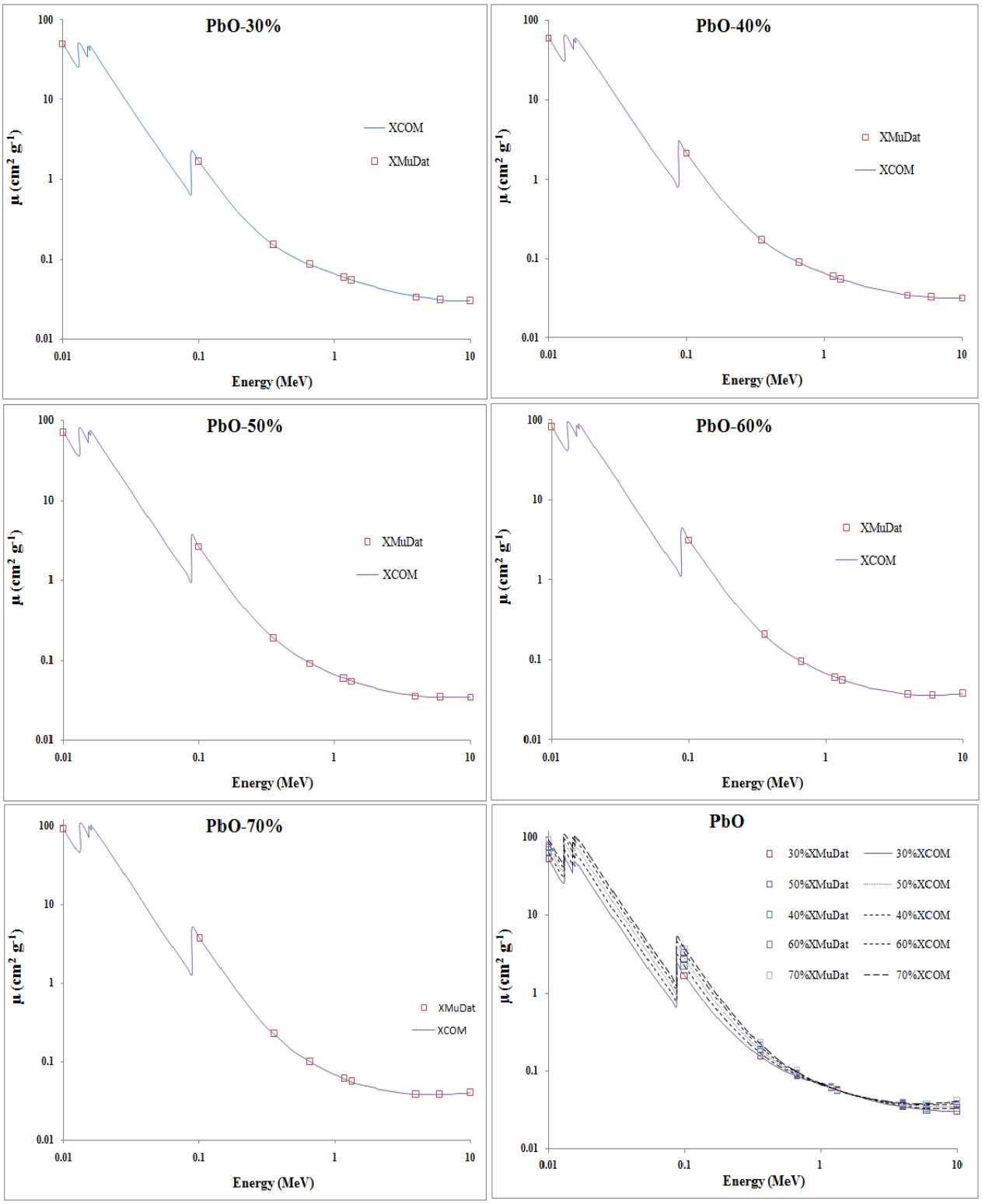

Fig. 3. Mass attenuation coefficients of xPbO:(100-x)P_2O_5 glass system, where x is the composition by weight (30, 40, 50, 60, and 70)

Effective atomic cross section of glasses

Using equation (2), the effective atomic cross sections (σ_a) of glasses are shown in Figure 4. It was found for all glass samples, that the σ_a decreases as the photon energy increases. Figure 4 depicts that in the energy region of interest, the σ_a values of glasses improve by increasing their Bi_2O_3, PbO and BaO concentrations.

For photon energies above 0.1 MeV, of all the glass samples, the σ_a values of BaO glass is the lowest ones, while those of the Bi_2O_3 and PbO glasses are approximately in the same order of magnitude (see Figure 5). This could be due to the presence of high atomic numbers of bismuth and lead elements (83 and 82, respectively) compared with barium element (56) in related glasses. It should be noted that, the weight fractions of high atomic number elements (Bi, Pb, and Ba) are approximately identical at all concentrations (see Table 1).

At low and high energy regions, the probabilities of photoelectric and pair production interactions are great for high atomic number absorbers. It is seen that at energies which Compton Effect gradually appears as the main interaction process (approximately 0.4 to 4 MeV), the σ_a values are almost independent of the atomic number of the constituent elements. The σ_a curve of barium phosphate glass shows a disorder at 37.44 keV photon energy and temporarily stands above lead and bismuth phosphate glasses curves. This is due to photoelectric absorption at K edge of barium in this energy.

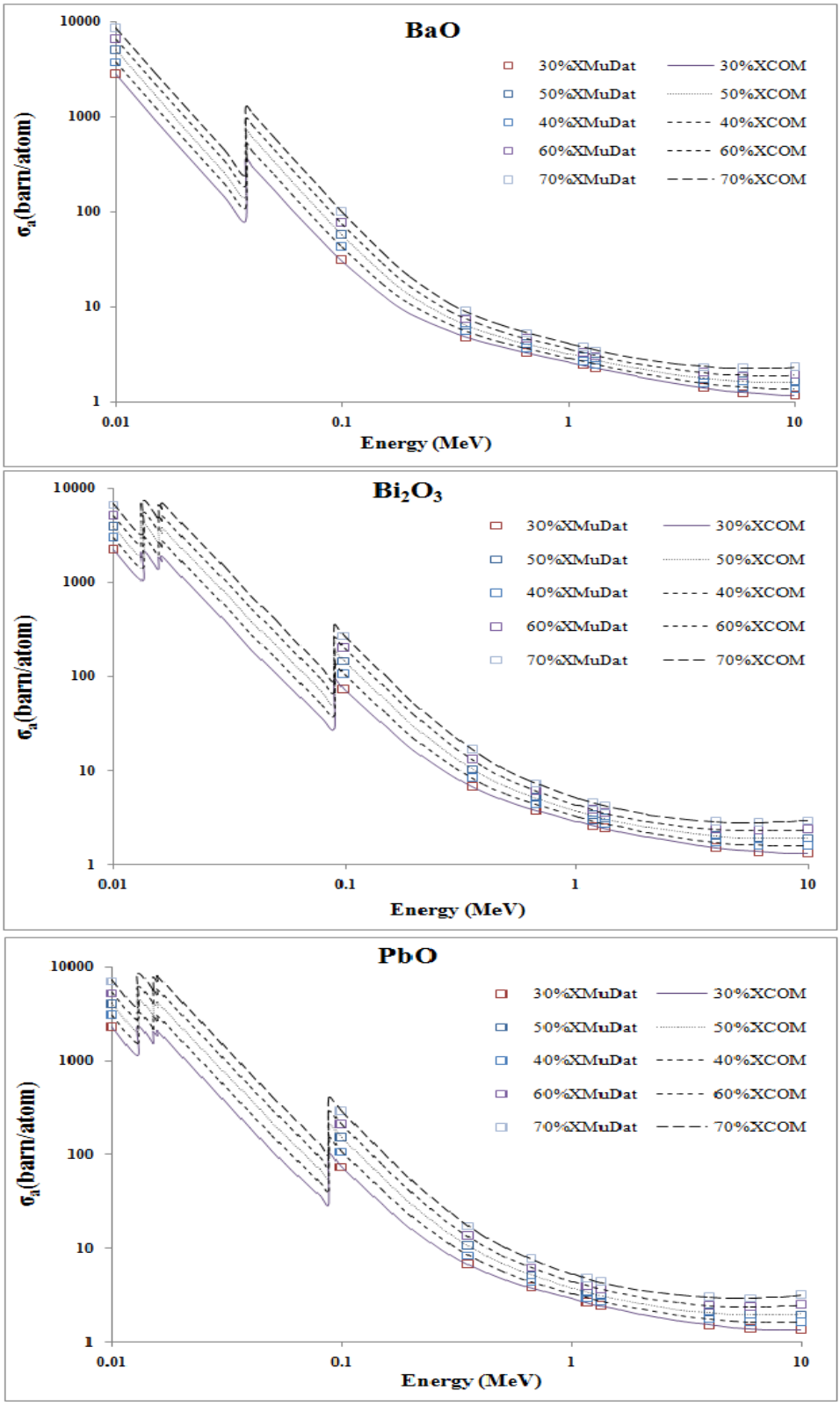

Fig. 4. Effective atomic cross sections (σ_a) of glasses

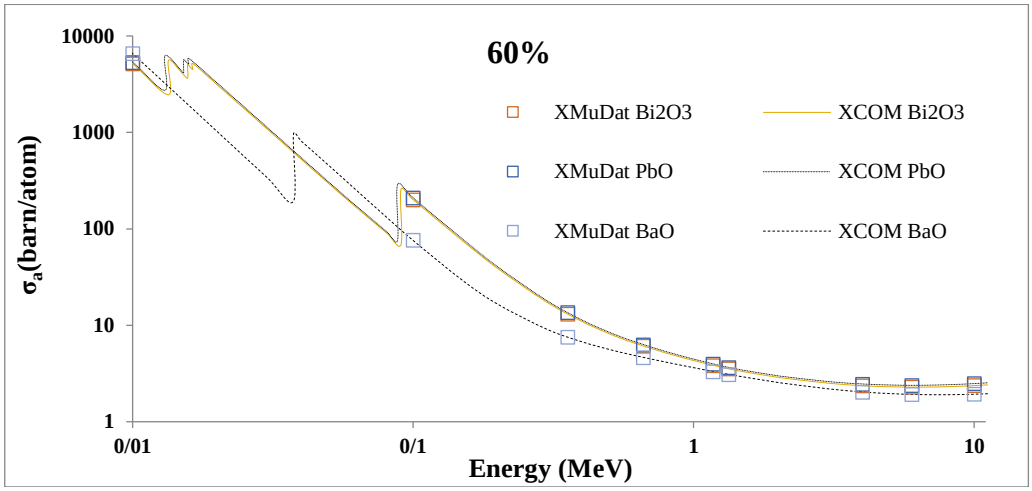

Fig. 5. Effective atomic cross sections of $40R_mO_n{:}60P_2O_5$ glass systems at 60% concentration of metal oxides

It is noteworthy that some observed differences in the results of XCOM and XMuDat programs could be because of the some differences in the physical and mathematical models, uncertainties in the nuclear/atomic data, differences in the techniques and databases used in each program, etc.

CONCLUSIONS

In the present work, the gamma-ray shielding properties of phosphate glasses containing BaO, Bi_2O_3, and PbO metal oxides in different rates were calculated using the XCOM and XMuDat computer programs at the 10 keV–10 MeV gamma-ray energies. This study shows that after mentioned programs provide reliable values of the photon interactions properties for various compositions of phosphate glasses. It was found that the μ_m and σ_a parameters decrease as the photon energy increase. The σ_a values of the glasses increased with increasing the Bi_2O_3, PbO and BaO concentrations. Most probably the results presented in this study indicates that the chosen computer programs may be useful to calculate the gamma-ray shielding characteristics of different glass systems, particularly in cases without available experimental data.

REFERENCES

[1] Singh, V.P. and Badiger N.M. (2012). Comprehensive study of energy absorption and exposure buildup factor for concrete shielding in photon energy range 0.015–15 MeV up to 40 mfp penetration depth: dependency of density, chemical element, photon energy. International Journal of Nuclear Energy Science and Technology, 7:75–99.

[2] Bagheri, R., Moghaddam, A.K. and Yousefi, A. (2017). Gamma-ray shielding study of light to heavyweight concretes using MCNP-4C code. Nuclear Science and Techniques, 28(15):1–8.

[3] Singh, V.P., Ali, A.M., Badiger, N.M. and El-Khayatt, A.M. (2013). Monte Carlo simulation of gamma ray shielding parameters of concretes. Nuclear Engineering and Design, 265:1071–1077.

[4] Kirdsiri, K., Kaewkhao, J., Chanthima, N. and Limsuwan, P. (2011). Comparative study of silicate glasses containing Bi_2O_3, PbO and BaO: Radiation shielding and optical properties. Annuals of Nuclear Energy, 38:1438-1441.

[5] Bagheri, R., Moghaddam, A.K., Shirmardi, S.P., Azadbakht, B. and Salehi, M. (2018). Determination of gamma-ray shielding properties for silicate glasses containing Bi_2O_3, PbO, and BaO. Journal of Non-Crystalline Solids, 479:62–71.

[6] Bagheri, R., Moghaddam, A.K. and Yousefnia, H. (2017). Gamma Ray shielding study of barium-bismuth-borosilicate glasses as transparent shielding materials using MCNP-4C code, XCOM program, and available experimental data. Nuclear Engineering and Technology, 49(1):216–223.

[7] Arbuzov, V.I., Andreeva, N.Z., Leko, N.A., Nikitina, S.I., Orlov, N.F. and Fedorov, Y.K. (2005). Optical, spectral, and radiation-shielding properties of high-lead phosphate glasses. Glass Physics and Chemistry, 31:583–590.

[8] Arbuzov, V.I. and Fyodorov, Y.K. (2008). Spectral, radiation-optical and shielding properties of phosphate glasses with high lead content. Advanced Materials Research, 39:213–218.

[9] Kaewkhao, J. and Limsuwan, P. (2010). Mass attenuation coefficients and effective atomic numbers in phosphate glass containing Bi_2O_3, PbO and BaO at 662 keV. Nuclear Instruments and Methods A, 619:295–297.

[10] Salem, S.M., Mostafa, A.G., Ahmed, M.A., Yassin, O.M. and Abu Gasser, R.A. (2017). Electrical transport properties and gamma-ray attenuation coefficient of some phosphate glasses containing by-pass cement dust. Bioceramics Development and Applications, 7:1-7.

[11] Sayyed, M.I., Khattari, Z.Y., Kumar, A., Al-Jundi, J., Dong, M.G. and AlZaatreh, M.Y. (2018). Radiation shielding parameters of $BaO\text{-}Nb_2O_5\text{-}P_2O_5$ glass system using MCNP5 and XCOM software. Materials Research Express, 5:1-17.

[12] Agar, O., Khattari, Z.Y., Sayyed, M.I., Tekin, H.O., Al-Omari, S., Maghrabi, M., Zaid, M.H.M. and Kityk I.V. (2019). Evaluation of the shielding parameters of alkaline earth based phosphate glasses using MCNPX code. Results in Physics, 12:101–106.

[13] Hubbell J.H. and Seltzer, S.M. (1995). Tables of X-ray mass attenuation coefficients and mass energy-absorption coefficients 1 keV–20 MeV for elements 1<Z<92 and 48 additional substances of dosimetric interest, NISTIR 5632 (Gaithersburg, MD: National Institute of Standards and Physics Laboratory, 1995), 13–111.

[14] Boone J.M. and Chavez, A.E. (1996). Comparison of X-ray cross sections for diagnostic and therapeutic medical physics. Medical Physics, 23(12):1997–2005.

[15] Gerward, L., Guilbert, N., Jensen, K.B. and Levring H. (2004). WinXCom–A program for calculating X-ray attenuation coefficients. Radiation Physics and Chemistry, 71(3):653–654.

[16] Nowotny, R. (1998). XMuDat: Photon attenuation sata on PC, Tech. Rep. IAEA-NDS-195 (Vienna: International Atomic Energy Agency, 1998).

[17] Azadbakht, B. and Bagheri, R. (2020). Photon interaction properties of different bones from human body using MCNPX, WinXCom, XMuDat, and Auto-Zeff programs. Journal of Testing and Evaluation, 48(6):20180730.

ICNST 2024
International Conference on Nuclear Science and Technology
6- 8 MAY 2024 | Isfahan, Iran

Production of new hybrid superabsorbent polymer for controlled release of fertilizer/water based on grafted biopolymers using electron irradiation method and investigating its performance in the plant growth (Paper ID : 1085)

Hafezi Moghaddam R.[1*], Shirmardi SP[1]., Masoudi H[1]

[1] *Central Iran Research Complex, Iran Radiation Application Development Company, Atomic Energy Organization of Iran, Tehran, Iran.*

Abstract

Water and soil fertility are the two main factors in developing agriculture and food production. The construction of biocompatible and biodegradable systems for the controlled release of water and fertilizer can play an important role in improving the agricultural industry. Herein, a humic acid-gelatin (HA-Gel) hydrogel, a gallic acid-xanthan gum (GA-XG) hydrogel, a hybrid hydrogel, and HA-Gel/GA- XG/polyacrylamide (PAM) as the superabsorbent polymer (SAP) were synthesized using the electron beam irradiation method. The capability of the synthesized hydrogels as the sorbents in the loading and controlled release of fulvic acid (FA) was studied. The chemical and physical structure of the sorbents was confirmed by FTIR and XRD. The effect of irradiation dose on mechanical properties, gel content, swelling, and absorbency under load (AUL) of the sorbents was investigated. By changing the hydrogel structures into the SAP form, its swelling capacity was increased from 37 to 320 g/g. In comparison to the hydrogels, the SAP showed a slower-release performance. The significant improvement in the growth of fodder corn treated with FA-loaded SAP in the greenhouse media in comparison to the control groups showed the effective performance of the designed SAP, favoring its practical applications.

Keywords: Electron beam irradiation, Water/fertilizer slow-release, Superabsorbent polymer, Plant growth

INTRODUCTION

In the last few decades, new irrigation methods based on smart materials have been developed to solve the global problem of water shortage. Creating a new material or method that can reduce the loss of water and fertilizer in the soil as well as increase the yield and durability of these two vital elements in plant roots can revolutionize the agricultural industry [1]. Superabsorbent polymers (SAPs) are among the smart materials that can increase the quantity and quality of agricultural products by improving water retention

capacity and release of fertilizers [2]. SAPs are hydrogels with polymer networks formed through the cross-linking of superhydrophilic polymer chains and can absorb large amounts of water and chemicals (such as fertilizer). Recently, the design and green synthesis of hydrogels or superabsorbents based on biodegradable and biocompatible natural materials with the ability to slow-release fertilizer has attracted a lot of attention [3].

Biopolymers are good candidates for hydrogel and SAP production due to their abundance, availability, non-toxicity, and low price. In this regard, in this project, two biopolymers of gelatin (Gel) and xanthan gum (XG), commonly used in the food, pharmaceutical, and cosmetic industries [4], are selected for the synthesis of hydrogels. Among the chemical methods, irradiation with high-energy rays of gamma, electron beam, or X-ray is more attractive in the production of clean and sterile polymers with biomedicine or environmental applications because they need no organic solvents or chemical reagents. [5]. It should be noted that within the irradiation methods, electron beam irradiation (EBI) is more popular due to the high speed of production at room temperature and the clarity of the direction of the beam path. However, as the molecular weight of biopolymers is lower than synthetic polymers, irradiation of biopolymers with a high-energy beam resulted in chain breaking rather than crosslinking reactions. To solve these limitations, we take a new approach that involves the grafting of natural polyphenols on biopolymers before the irradiation [6]. Irradiation of biopolymers grafted with polyphenols in the aqueous media causes the formation of polyphenoxy macroradicals, that act as a quasi-crosslinker, resulting in the crosslinking reactions through the recombination of polyphenoxy macroradicals. Thus, for the synthesis of suitable hydrogels for loading and controlled release of fertilizer, in this project, humic acid (HA) and epicatechin gallate (ECG) that are useful for soil were selected as the polyphenolic reagents and grafted on Gel and XG, respectively. Also, fulvic acid (FA), the light derivative of HA [7] was selected as the model fertilizer. In addition, the effect of hybrid SAP containing FA on the qualitative and quantitative performance of the growth of fodder corn as the most important and widely consumed source of animal feed production was studied in the greenhouse environment.

EXPERIMENTAL

Reagents and instrumentation

All reagents and chemicals with analytical grade were prepared from Merck (Darmstadt, Germany). The amount of FA and other species in the solution was determined by a dual-

beam spectrophotometer (model PC 2501, Shimadzu Company, Japan) with a wavelength range of 200 to 800 nm. For the preparation of the sorbents, a high-energy Rhodotron industrial electron accelerator device, model TT200, with energies of 10 MeV (located in Yazd, Iran), was used. Irradiation dosimetry was done by cellulose triacetate film. The irradiation dose rate was 7.5 kGy s^{-1} and the electron beam current was 5.0 mA

Grafting humic acid with gelatin (HA-Gel) and gallic acid with xanthan gum (GA-XG)

1.0 g of Gel and 0.2 g of potassium humate were added to 50 mL of distilled water. To improve the solubility of humate salt, the pH of the mixture was adjusted to 8.0 using NaOH solution and with high-intensity stirring; the mixture was refluxed for 24 hours at 60 ºC. After the completion of the homogenous aminolysis reaction of the aldehyde groups of HA and grafting on the Gel, 100 mL of ethanol was added to the above solution. The mixture was stirred by a mechanical stirrer at room temperature to remove unreacted HA, and the brownish cream HA-Gel particle sediments. The suspension was placed in an ice water bath and gently stirred for 1 hour until the HA-Gel deposition process was completed. The resulting sediments were separated by centrifuging the suspension for 5 minutes at a speed of 5000 rpm. Then, the HA-Gel deposits were washed three times with ethanol and dried at room temperature. 1.0 g of XG and 0.2 g of ECG were added to 50 mL of distilled water. The pH of the mixture was adjusted higher than the pKa of XG (~pH 7) using NaOH solution, and the mixture was refluxed for 10 hours at 70 ºC with continuous stirring. 100 mL of dimethylformamide (DMF) was added to the above solution and stirred by a mechanical stirrer at room temperature to remove unreacted ECGs. In this stage, the GA-XG particles appear as white deposits. The suspension was then placed in an ice water bath and gently stirred for 2 hours to complete the deposition process of GA-XG. The resulting sediments were separated by centrifuging the suspension for 5 minutes at 5000 rpm. Then XG-GA sediments were washed three times with methanol and dried at room temperature.

Preparation of HA-Gel, GA-XG and hybrid hydrogels/superabsorbent polymer

0.3 g of the grafted HA-Gel or GA-XG was added to 100 mL of distilled water and the mixtures were stirred at room temperature with a mechanical stirrer for 2 hours until a homogeneous gel was obtained. Then, to prevent water evaporation, each gel solution was transferred into a plastic package and, exposed to EBI in the range of 10-40 kGy. In this stage, the gels were converted into an elastic hydrogel. The unreacted biopolymers or

biopolymers formed with low molecular weight were then, removed by washing the resulting mixture several times with distilled water, and the hydrogels were dried in a vacuum oven at 60 °C for two days. Finally, the dried hydrogels were converted into fine granules (200-350 microns) by a hammer mill and kept in a desiccator before use. For the preparation of hybrid hydrogel, 1.5 g of HA-Gel along with 1.5 g of GA-XG was added to 100 mL of distilled water and the mixture was stirred by a mechanical stirrer for 2 hours until a homogeneous pasty gel was obtained at room temperature. The resulting gels were transferred into the plastic package and treated according to the above procedure for the preparation of hydrogels. The fine granules of the prepared HA-Gel/GA-XG hybrid hydrogel were saved in a desiccator for further use. The superabsorbent polymer of HA-Gel/GA-XG/PAM hybrid was synthesized by adding 1.0 g of PAM along with 1.5 g of HA-Gel and, 1.5 g of GA-XG into 100 mL of distilled water and the mixture was stirred at room temperature by a mechanical stirrer for 4 hours to obtain a homogeneous composite paste gel. Then, the obtained gel was transferred into the plastic package, and SAP of HA-Gel/GA-XG/PAM was prepared according to the mentioned method for the preparation of HA-Gel or GA-XG biopolymer hydrogels.

Plant growth treated with FA-loaded SAP

To provide a preliminary comparison and to see the effect of FA-loaded SAP performance on plant growth traits, plant growth studies were done on fodder corn seed as the model plant in a greenhouse (located in Yazd) from the time of planting to yield. The greenhouse area was divided into the sections of negative control (A), positive control (B), and study area (C). The study area of C (soil and FA-loaded SAP) was prepared by uniformly distributing 200 g m^{-2} of the FA-loaded SAP on the surface of the greenhouse soil (30 m^2), plowed, and buried at a depth of approximately 20 cm. After one flood irrigation, fodder corn seeds were planted in four rows at equal intervals at a depth of 15 cm. In the positive control area of B having soil and fertilizer, 0.8 g m^{-2} of pure FA equivalent to the amount of fertilizer used in section C was poured on the surface of the greenhouse soil (10 m^2), irrigated and, buried like area C. The fodder corn seeds were then, planted in two rows. For the negative control area of A (20 m^2) containing only soil, after plowing and one flood irrigation, fodder corn seeds were planted at the same intervals at a depth of 15 cm in three rows. All three areas were irrigated with the same flow rate once every four days (30 minutes for C area and 30 minutes

for areas A and B). To see the effect of water deficit conditions, after the first 3 periods of irrigation, the irrigation of all areas was reduced to every eight-day cycle. Plant growth indices including plant height, stem and leaves width, number of leaves, germination speed, and number of fruit flowers in each row were accurately recorded in different periods.

Results and discussion

Mechanism of production

In early experiments, it was observed that when an aqueous solution of HA and Gel in a neutral pH (above the pKa of gelatin, 4.6) is refluxed, the HA grafted with Gel through the Schiff-base reaction of amine groups of Gel with the aldehyde groups of HA (Fig. 1a). In the preliminary experiments, it was observed that when EGC is refluxed with XG in an alkaline medium (with a pH of ~10, higher than the pKa of the primary alcohol group of XG) the GA part of the EGC molecule grafted with XG through the nucleophilic attack of the anionic groups of primary alcohol of XG with the ester groups of EGC as demonstrated in Fig.

1b. About 9.5% and 11.1% (w/w) of HA and GA were grafted with Gel and XG, respectively. Then, the aqueous solutions of HA-Gel, GA-XG, and their mixture were separately subjected to EBI, leading to the formation of poly phenoxy-free macroradicals on the molecular chains of Gel or XG. Subsequently, the hydrogels with a variety of homogeneous and heterogeneous IPNs (Fig. 2) were formed through random recombination of macroradicals by covalent cross-linking of C-C and C-O bonds of biopolymer chains. To improve the mechanical properties and AUL of the hybrid hydrogel, the linear synthetic polymer of PAM with a large number of hydrophilic amide functional groups, commonly used in the manufacture of commercial agricultural SAP, was added to the mixture of HA-Gel and GA-XG. The aqueous solution containing PAM, HA-Gel, and GA-XG was then subjected to EBI, and a hydrogel with superabsorbent properties called SAP was formed. By changing the HA-Gel hydrogel structures into the HA-Gel/GA-XG/PAM SAP form, its swelling capacity was increased from 37 to 320 g/g.

Characterizations of synthesized hydrogels, hybrid hydrogel, and SAP

The successful synthesis of hybrid hydrogel and SAP (synthesized in a EBI dose of 30 kGy) were confirmed by considering their FTIR spectra along with the spectra of their components (Fig. 3). The reduction of the primary N-H bending band of the Gel at 1586 cm^{-1}, the appearance of C=C aromatic stretching band of HA at 1520 cm^{-1} and also the increase

in the intensity and width of the band at 1647 cm^{-1} that is due to the overlap of the new C=N band and C=O amide groups of the Gel in the HA-Gel hydrogel spectrum compared to the Gel spectra indicate the successful grafting of HA on the Gel. Similarly, the presence of the specific C=C aromatic band of phenolic rings of GA at 1517 cm^{-1} in the spectrum of GA-XG hydrogel compared to the spectrum of raw XG indicates the successful grafting of the GA part of ECG on XG. The appearance of the C-N stretching band at 1150 cm^{-1} and N- H bending at 1158 cm^{-1} in the hybrid hydrogel spectrum compared to the GA-XG hydrogel spectrum indicates the presence of HA-Gel chains in the hybrid hydrogel network structure. Comparing the SAP and hybrid hydrogel spectra, the increase in the intensity of the amide of the C=O stretching band at 1664 cm^{-1} and the increase in the intensity and broadening of the N-H stretching peak at 3394 cm^{-1} resulted from its overlap with the O-H stretching peaks of biopolymers indicates the presence of PAM in the SAP structure

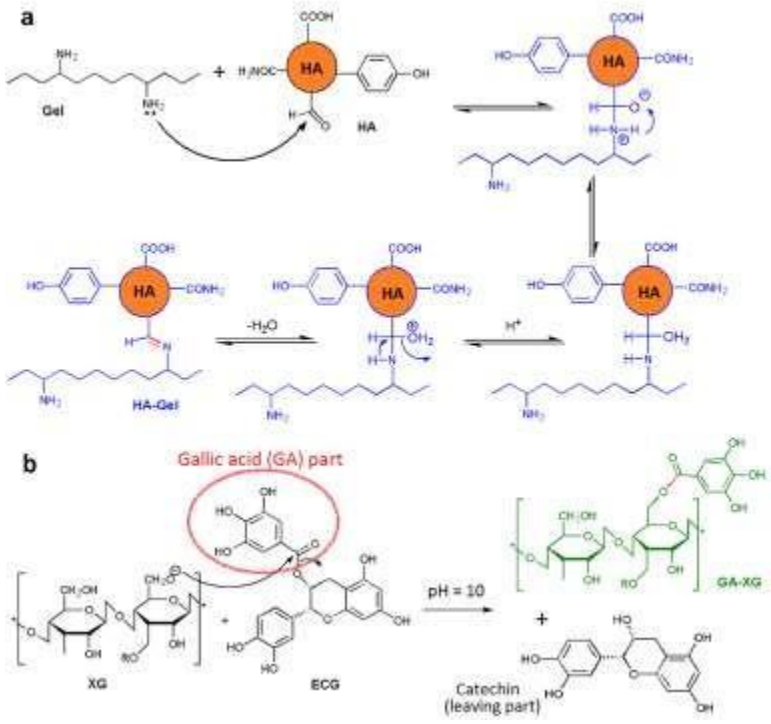

Fig. 1. Scheme of the reaction of HA grafting on Gel (a) and GA grafting on XG (b).

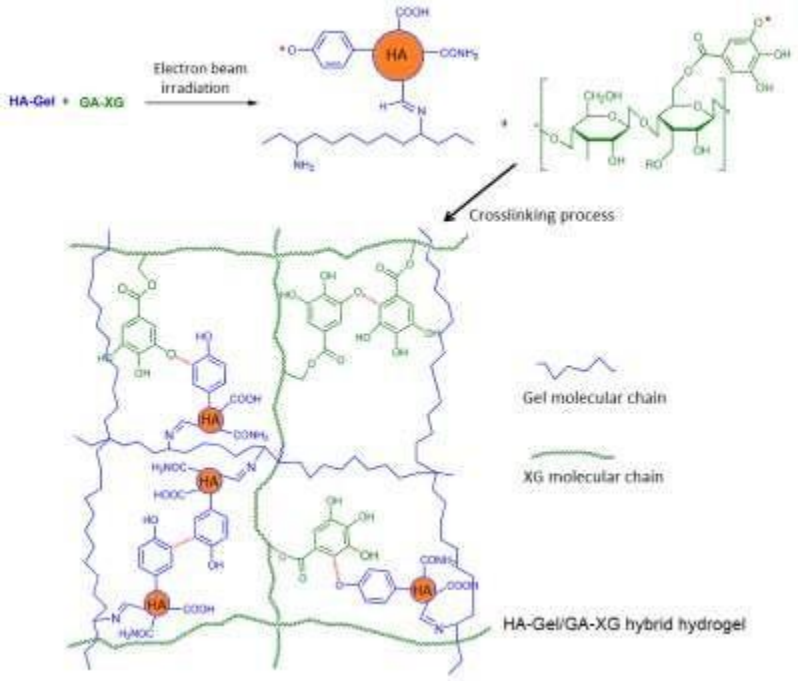

Fig. 2. Formation mechanism of the biopolymeric hybrid hydrogel.

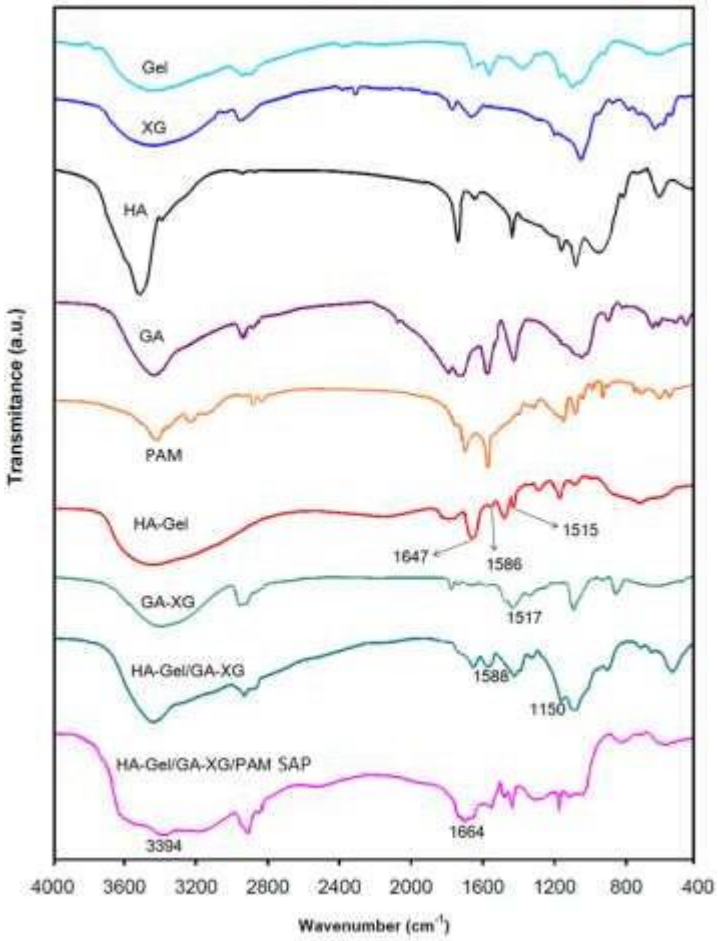

Fig. 3. FTIR spectra of hybrid hydrogel, SAP and their components.

The XRD pattern of Gel, XG, hydrogels, as well as SAP synthesized in a EBI dose of 30 kGy in the 2θ range of 10-80° was recorded (Fig. 4). The presence of a common sharp diffraction peak around 2θ of 20° in the XRD pattern of Gel and XG biopolymers, due to the quasi-crystalline nature of most biopolymers [8]. This can be attributed to the formation of inter/intramolecular hydrogen bonds between the chains of Gel or XG. In the XRD patterns of hydrogels and SAP, this crystalline peak is shifted to 2θ of 23° and its appearance is changed to a broad peak that confirms the formation of the irregular amorphous network structure. This is because EBI causes the intermolecular hydrogen bonds to break, whereas, the random cross-linking between chains of HA-Gel, GA-XG, and PAM to predominate. In the XRD pattern of the SAP compared to the XRD patterns of the HA-Gel and GA-XG hydrogels, the sharp decrease in peak at the 2θ of 23° is due to the intensification of the random cross-linking process by the PAM chains. Thus, SAP has higher disorder and more amorphous structure than other prepared hydrogels.

The mechanical properties and gel content of the sorbents prepared with different doses of EBI were investigated and the results are presented in Fig. 5a-d. Based on the results the tensile strength and gel content of all hydrogels increased with increasing EBI doses up to 30 kGy. While from HA-Gel hydrogel

structure to the SAP structure these trends continued to increase up to 40 kGy. This behavior is due to the formation of a higher amount of free polyphenoxy radicals on biopolymeric chains at higher EBI doses, increasing the crosslinking density. Swelling and AUL of sorbent prepared with different doses of EBI were studied. The results (Fig. 5e) show that the swelling of both sorbents decreases with increasing the EBI dose. This is because of the formation of more free polyphenoxy radicals on the polymer chains in higher doses of EBI, increasing the crosslinking density. While AUL changes is opposite to the trend of changes in swelling. Thus, increasing the crosslinking density by the increased EBI dose, increased the AUL of the sorbents.

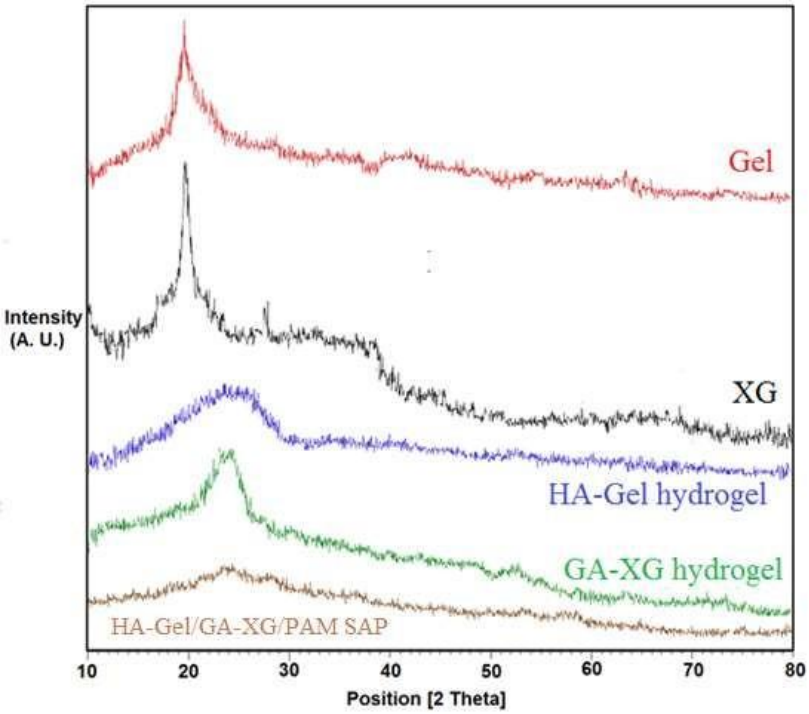

Fig. 4. XRD patterns for raw Gel, raw XG, HA-Gel hydrogel, GA-XG hydrogel, and SAP.

Investigating the release of fertilizer from SAP and hybrid hydrogel in soil

The release profile of FA from the hybrid samples loaded with FA in the sandy soils is provided in Fig. 6. In general, FA release from the soil containing FA in pure formulation, or FA loaded hybrid hydrogel or SAP significantly is slower than its release in aqueous media. This behavior is because of the less mobility of FA molecules in the soil as well as insufficient water molecules in the soil for its complete dissolution. Furthermore, the rate of the release of FA from the soil treated with FA loaded on either hybrid hydrogel or SAP is slower than its rate from the soil treated with pure FA. Thus, on the first day, 97% of the FA was released from the soil treated with pure FA, whereas, from the soil containing FA loaded hybrid hydrogel or SAP, 86% and 81% of FA were released within 15, and 30 days, respectively. The slower release of the FA from the SAP compared to the hybrid hydrogel is due to the higher density of crosslinking between the biopolymer and PAM chains, which leads to the harder penetration and transfer of FA molecules from the depth of the polymer to the soil. The higher FA loading capacity and swelling, as well as the slower release of the FA from the SAP compared to the hybrid hydrogel, make it more suitable for practical applications.

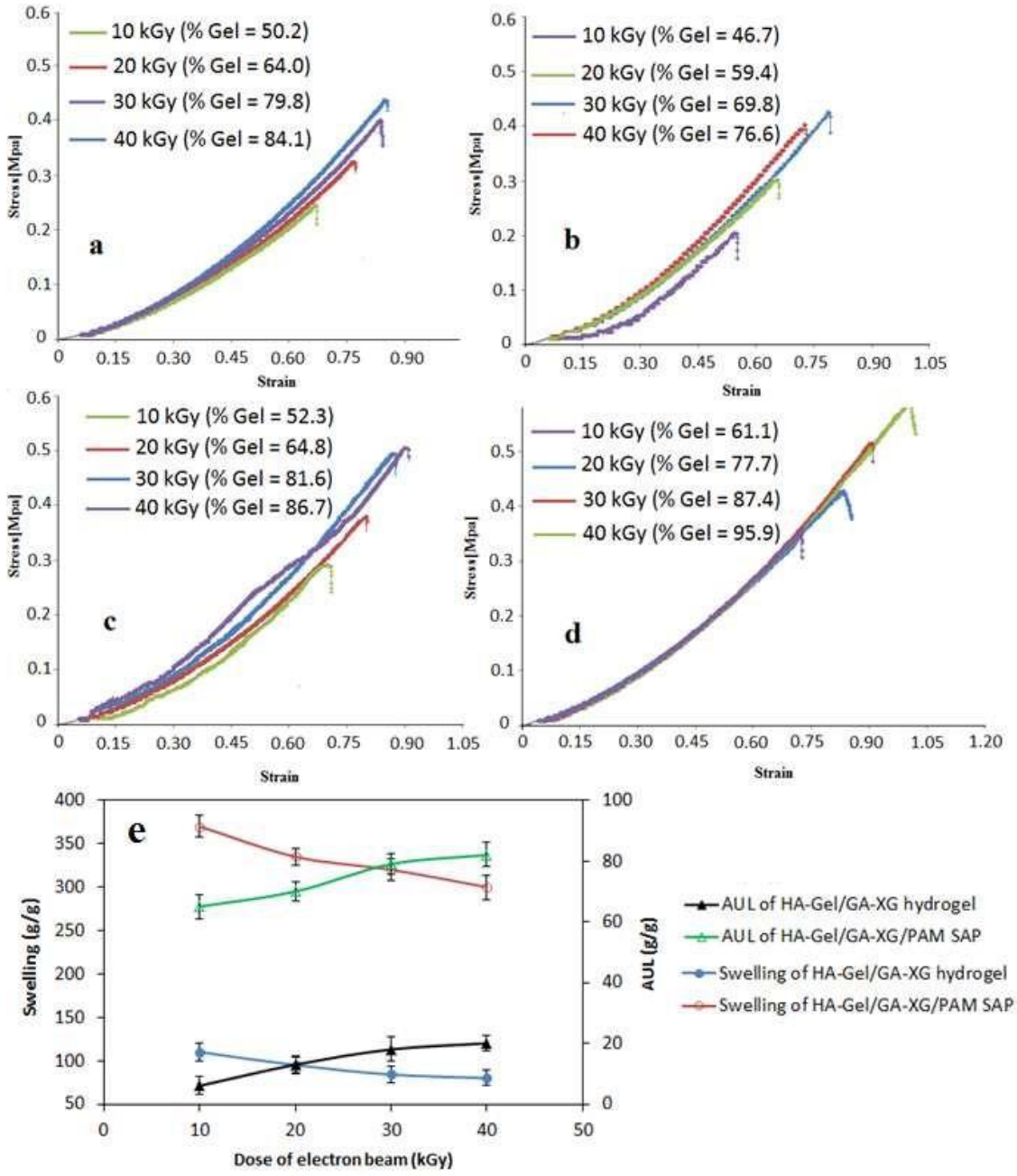

Fig. 6. The mechanical properties and gel percentage of HA-Gel hydrogel (a), GA-XG hydrogel (b), hybrid hydrogel (c), and SAP (d) in different doses of EBI. The effect of EBI dose on the swelling and AUL (by applying a pressure of 0.7 psi) of hybrid hydrogel and SAP in distilled water (e).

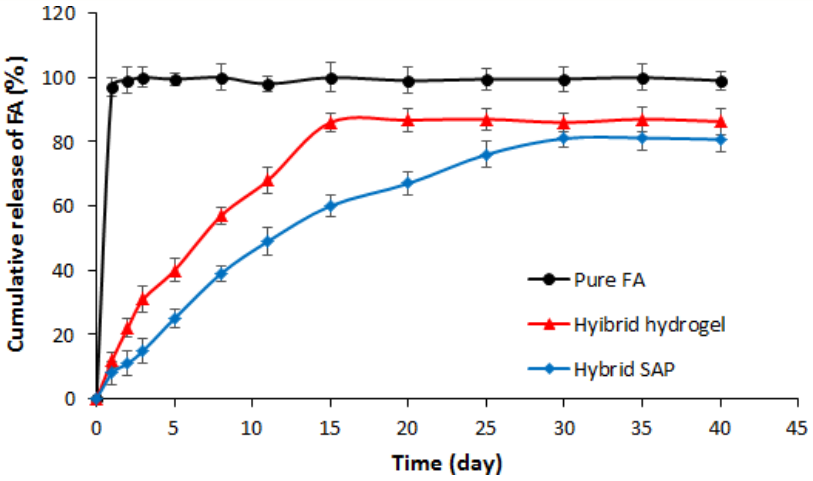

Fig. 6. Release profile of FA as pure formulation and loaded in hybrid hydrogel and SAP in soil.

Evaluation of the effect of FA-loaded SAP on the growth of fodder corn

The results of the investigation of the effectiveness of FA-loaded HA-Gel/GA-XG/PAM (SAP synthesized in a EBI dose of 30 kGy) on the growth of fodder corn in different periods are provided in Fig. 7. As the results show, the germination speed of the plant in the soil treated with FA-loaded SAP in the study area of C is higher area of A and B. Thus, after 3 days, the average height of fodder corn sprouts in the study area of C was equal to 6.4 cm while in the areas of A and B were 3.7 and 4.4 cm, respectively. In all periods, the freshness and the considered growth indicators of the plants in the area of C were significantly higher compared to plant growth in areas A and B. The first flowers of group C were ripened after 57 days whereas for group A it happens after 75 days. Furthermore, over time the number of flowers produced in group C increased compared to groups A and B, resulting in a quantitative increase in the yield of corn planting in soil treated with FA-loaded SAP. The increase in considered growth indicators for group B compared to group A is due to the presence of pure FA in the soil. It was also observed that a reduction of the amount of water consumption to half, after the first 3 periods of irrigation has no disturbance effect on the growth of fodder corn in region C, while it caused the growth of plants in areas A and B to be slower and weaker (especially from the 25th day onwards). These performances can greatly alleviate the problem of the limitation of water resources in dry areas and ultimately increase the economic benefit of greenhouse production.

Conclusions

In this study, two hydrogels, a hybrid hydrogel, and SAP were prepared based on Gel, XG, HA, GA

biopolymers, and PAM by the EBI method. Preparation with the clean and sterile method of electron irradiation, rather than toxic and allergenic chemicals, commonly used in polymerization processes, improves the biocompatibility of the synthesized hydrogel/SAP for soil and plants. Compared to the hybrid hydrogel, SAP showed a higher capacity for fertilizer loading, slower FA release, and a higher ability in water absorption. The addition of FA-loaded SAP, as the miniature storage source of water and fertilizer, to the soil, significantly improved plant growth performance because of the increased soil moisture, as well as longer water and fertilizer availability to the roots because of the gradual and slow release

Fig. 6. Digital photographs of the growth process of fodder corn

References

[1] Dong, G. Mu, Z. Liu, D. Shang, L. Zhang, W. Gao, Y. Zhao, M. Zhang, X. Chen, S. Wei, M. (2021). Starch phosphate carbamate hydrogel based slow-release urea formulation with good water retentivity. Int. J. Biol. Macromol., 190: 189-197.

[2] Li, J. Zhu, Y. Liu, M. Liu, Z. Zhou, T. Liu, Y. Cheng, D. (2023). Network interpenetrating slow-release nitrogen fertilizer based on carrageenan and urea: A new low-cost water and fertilizer regulation carrier. Int. J. Biol. Macromol., 242:124858.

[3] Hu, Z.Y. Chen, G. Yi, S.H. Wang, Y. Liu, Q. Wang, R. (2021). Multifunctional porous hydrogel with nutrient controlled- release and excellent biodegradation. J. Environ. Chem. Eng., 9:106146.

[4] Das, S. Dalei, G. (2023). In situ forming dialdehyde xanthan gum-gelatin Schiff-base hydrogels as potent controlled release fertilizers. Sci. Total Environ., 875:162660.

[5] Sayed, A. Mohamed, M.M. Abdel-raouf, M.E.S. Mahmoud, G.A. (2022). Radiation synthesis of green nanoarchitectonics of guar gum-pectin/polyacrylamide/zinc oxide superabsorbent hydrogel for sustainable agriculture. J. Inorg. Organomet. Polym. Mater., 32:4589-4600.

[6] Moghaddam, R.H. Dadfarnia, S. Shabani, A.M.H. Shirmardi, S.P. Moghaddam, Z.H. (2022). Fabrication of two hydrogels composites through the coupling of gelatin with ethyl vanillin/polyvinyl alcohol using electron beam irradiation for ciprofloxacin delivery. Polym. Bull., 80:8407–8429.

[7] Wang, Y. Zhu, Y. Liu, Y. Mu, B. Wang, A. (2022). Slow release and water retention performance of poly (acrylic acid- co-acrylamide)/fulvic acid/oil shale semicoke superabsorbent composites. Polymers, 14:1719.

[8] Wang, L. Xiang, D. Li, C. Zhang, W. Bai, X. (2021). Effects of lyophilization and low-temperature treatment on the properties and conformation of xanthan gum. Food Hydrocoll., 112:106352.

ICNST 2024
International Conference on Nuclear Science and Technology
6- 8 MAY 2024 | Isfahan, Iran

Fabrication of hemostatic powder based on modified starch by electron beam irradiation method (Paper ID : 1086)

Hafezi Moghaddam R.[1*], Shirmardi SP[1]., Masoudi H[1]

[1] *Central Iran Research Complex, Iran Radiation Application Development Company, Atomic Energy Organization of Iran, Tehran, Iran.*

Abstract

In the present work, hemostatic powder based on starch (St) biopolymer was synthesized using a new and innovative production method with the help of electron beam irradiation (EBI). Compared to common chemical methods, the Irradiation methods have advantages such as high production speed (suitable for industrial scale production), no use of common chemicals in polymerization processes (such as initiators or crosslinkers), sterilization and production at the same time, no waste generation and performing the reaction at room temperature. In the first stage, by using and introducing a new method (chlorination and amination of starch and subsequent grafting of plant polyphenols on starch), crosslinking reactions prevailed over chain breaking reactions (under high-energy electron beam irradiation). The chemical and physical structure of the product was studied by FTIR, SEM, EDX, XRD, TGA. The effect of electron beam irradiation dose on swelling, gel percentage and mechanical properties of hemostat product was studied. Considering the higher swelling and appropriate mechanical properties of hemostatic samples synthesized at 15 kGy irradiation dose, this dose was selected for product synthesis. Fortunately, the absorption rate and capacity of hemostatic powder synthesized by irradiation method was higher than commercial samples.

Keywords: Electron beam irradiation, Hemostatic powder, Modified biopolymers, Starch

INTRODUCTION

One of the main concerns of surgeons during surgery is maintaining blood flow in the body and minimizing blood loss, because in many cases the bleeding is a threat to the patient's life. Therefore, it is very necessary to prepare a suitable hemostatic agent with high blood coagulation efficiency in order to achieve the desired surgical results. Often, surgeons' first choice to control bleeding is to apply direct pressure or compact the bleeding site, however compression or other mechanical methods may

not be appropriate in all surgical procedures. For example, if the place of bleeding is unidentifiable (or scattered) or the patient has an inherent coagulation disorder, these methods cannot be used to control bleeding. Recently, thermal methods such as lasers have become suitable surgical options to reduce bleeding. However, since the frequent use of burning and other thermal methods can cause problems, the use of this method is limited [1, 2].

Hemostatic powders (can be used in all types of bleeding) are among the most common, fastest, easiest, and most accessible methods for surgeons to stop bleeding. These hydrophilic polymer powders with a network structure, by absorbing blood plasma, cause concentration and accumulation of platelets and blood coagulation factors at the bleeding site. In addition, after these substances come into contact with blood, they quickly create a gel matrix and create a mechanical barrier by connecting to the blood tissue. Hemostatic powders are usually used as an absorbable (degradable) powder in heart, vascular, orthopedic, spinal, nerve surgeries to prevent bleeding from capillary, venous or vessels under pressure. These powders are also used in wars for soldiers and war casualties, accidents and general injuries that lead to bleeding [3].

Hemostatic powder products are mainly made on natural biopolymers or synthetic polymers (polycyanoacrylate, polyacrylate, polyalkyne oxides). The use of biopolymers compared to all kinds of synthetic polymers in the manufacture of the mentioned product has advantages such as not causing sensitivity or toxicity to the body, more similar to the molecular structure of body tissues, biocompatibility and degradability (faster absorption in the body) [1-4]. In addition, their production resources are cheap and available. Since hemostatic powders will remain in the body for a considerable period of time, they must show very good biocompatibility so as not to lead to immune or chronic inflammatory responses, tissue adhesion or infection. Therefore, the best choice of raw materials to make them are biopolymers such as starch. However, so far no study has been done for the synthesis of homeostatic compounds based on biopolymers, especially starch modified (chlorinated and aminated) with polyphenols using EBI method, and the present design is based on a new formulation and an innovative production method with suitable innovation for production of hemostatic powder.

EXPERIMENTAL

Reagents and instrumentation

All reagents and chemicals with analytical grade were prepared from Sigma-Aldrich (St. Louis, MO, USA). For the preparation of the sorbents, a high-energy Rhodotron industrial electron accelerator device, model TT200, with energies of 10 MeV (located in Yazd, Iran), was used. Irradiation dosimetry was done by cellulose triacetate film. The irradiation dose rate was 7.5 kGy s^{-1} and the electron beam current was 5.0 mA.

Chlorination and amination of raw starch

For starch chlorination (St-Cl), 0.2 g of raw starch was added to 100 mL of alkaline ethanol mixture and it was made into a suspension. Then 10 mL of epichlorohydrin (ECH) was added to the suspension mixture and refluxed for 6 hours. At this stage, ECH was attached to the surface of St. Then the starch deposits were separated with filter paper and washed with ethanol 3 times to remove unreacted reagents and finally dried at room temperature. To amination starch, 0.2 g of St-Cl was added to 50.0 mL of water/ethylene diamine (EDA) mixture (1:1 v/v) and then it was stirred at 55°C for 4 hours by a magnetic stirrer. After the completion of the St-Cl aminolysis reaction, 200 mL of ethanol was added to the solution and stirred by a mechanical stirrer at room temperature to remove unreacted EDAs. The resulting St-N deposits appeared in the form of a white suspension, which was gently stirred in an ice water bath for 2 hours to complete the St-N deposition process. Then the resulting mixture was centrifuged at 5000 rpm for 5 minutes. Finally, the St-N precipitates were separated, washed three times with ethanol and air-dried at room temperature.

Grafting of caffeic acid (CA) on St-N

0.2 g of St-N and 0.6 g of chlorogenic acid (CGA) were added to 100 mL of distilled water. The pH of the mixture was adjusted to 7 using NaOH solution, and the mixture was refluxed at 60 ºC for 6 hours while vigorously stirring. After the completion of the aminolysis reaction of CGA ester groups and the capture of the CA part of CGA on St-N, 200 mL of ethanol was added to the above solution and stirred by a mechanical stirrer at room temperature to remove unreacted CGAs with St-N and St-N- CA particles appear as yellow deposits. The resulting suspension was placed in

an ice water bath and gently stirred for 2 hours to complete the deposition process of St-N-CA. The resulting sediments were separated by centrifuging the suspension for 5 minutes at 5000 rpm. Then the St-N-CA deposits were washed three times with ethanol and dried at room temperature.

Preparation of hemostatic powder based on St-N-CA by crosslinking process through EBI

0.2 g of St-N-CA was added to 50 mL of distilled water and the mixture was stirred for 2 hours at room temperature by a mechanical stirrer until it was completely dissolved. Then 20 mL of the gel solution was transferred to a Petri dish and covered with plastic film to prevent water evaporation and subjected to EBI in the range of 5-20 kGy. The resulting crosslinked biopolymers were washed several times with distilled water to remove unreacted biopolymers or biopolymers formed with low molecular mass, and then dried in a vacuum oven at 50 °C for 2 days. Finally, the dried film was converted into fine granules (below 100 microns) by hammer mill and stored in a desiccator before use.

Results and discussion

Mechanism of production

In this project, by using and introducing a new method (chlorination and amination of St and subsequent grafting of plant polyphenols on St such as CGA, cross-linking reactions prevailed over chain breakage reactions (under high-energy EBI) [5, 6]. It is not possible to graft polyphenolic reagents on starch to create suitable sites for radiation crosslinking reactions by raw starch biopolymer chains. Therefore, before carrying out polyphenol grafting and radiation crosslinking, modification reactions such as chlorination and amination of raw starch must be done. In the first step, to chlorinate raw starch, St was chlorinated by ECH during a heterogeneous chemical reaction (Fig. 1a). Here, ECH can react as a cross-linker with the hydroxyl groups of St, and it can also be attached and stabilized on the surface of St. The use of ethanol solvent mixture reduces more cross-linking ractions and causes more ECH binding on the St surface. First, ECH is attached to the St surface through the attack of St hydroxyl groups on the epoxy ring of ECH and its opening. A summary of the mentioned chlorination reaction for St is shown schematically in Figure 1a. In the

second step, in order to amination the St-Cl, EDA is added to the St-Cl aqueous solution and refluxed. EDA, through the anionic attack of its amine groups on the residual chloride end of ECH immobilized on St, removes chlorine and binds to the St surface. A summary of the starch amination mechanism and St-N preparation is shown in Figure 1b. The grafting of the phenolic part of CGA (CA) on St-N takes place through the nucleophilic attack of the amino groups of St-N on the ester groups of CGA (Figure 1c) and thus the CA part of the CGA molecule is grafted on the St-N. The color change of St to yellow indicates the successful grafting of CA on St. In the last step (Fig. 2), St-N-CA in the aqueous media and exposed to EBI leads to the production of stable and non-destructive polyphenoxy macroradicals, which as soon as the biopolymeric chains come close to each other, the macroradicals are connected together and thus cause the crosslinking of the biopolymeric chains (made of covalent bonds, C-C or C-O).

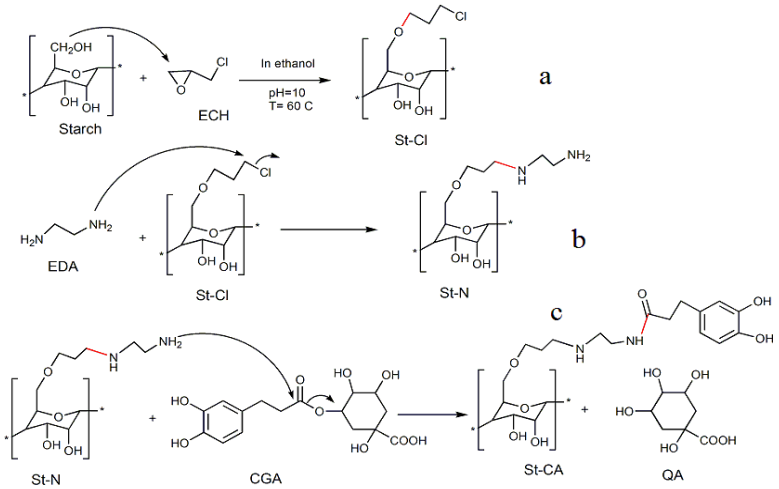

Fig .1. View of St chlorination reaction (a), St-Cl amination (b) and CA grafting on St-N (c).

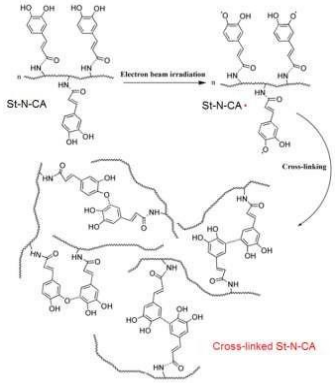

Fig. 2. Schematic of crosslinking mechanism of St-N-CA biopolymeric chains due to electron irradiation and synthesis of the final product of hemostatic.

Characterizations of synthesized hemostatic powder

FTIR analysis was performed to confirm the amination of St and also grafting of CA on St-N (Fig. 3). The appearance of amine bands in spectrum St-N and the appearance of amide bands in spectrum St-N-CA (C=O stretching peaks at 1652 cm^{-1}, C-N stretching at 1150 cm^{-1}, N-H stretching at 3095 cm^{-1} and N-H bending at 1534 cm^{-1}) respectively, confirming the St amination reaction and the successful grafting of the CA part of CGA on St-N. The presence of C=C aromatic stretching peaks of the benzene ring of the CA part of CGA at 1601 cm^{-1} and also the increase in the

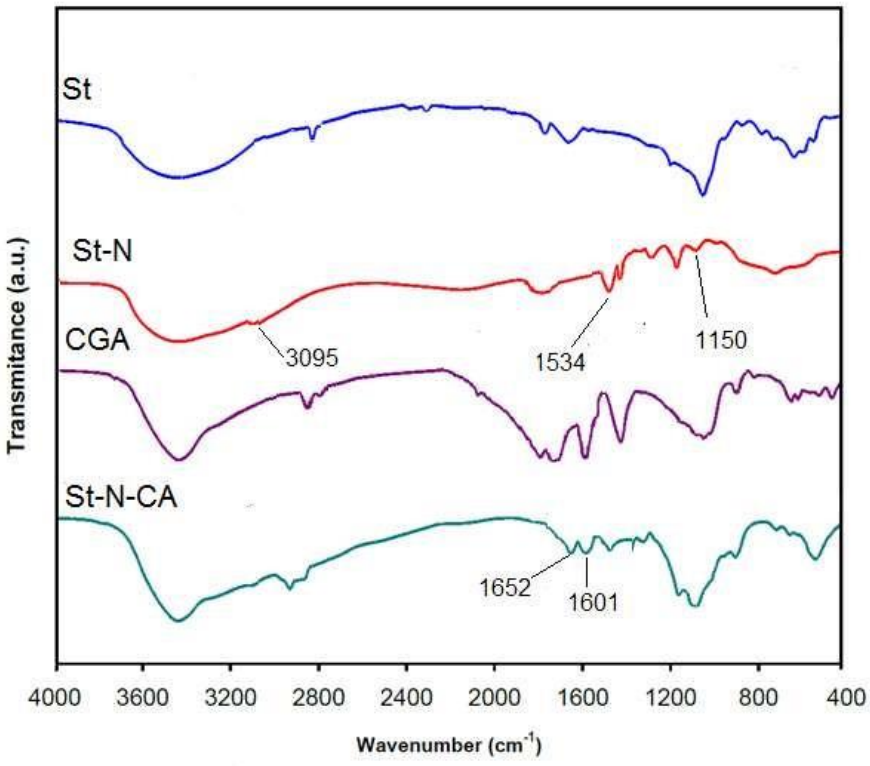

intensity of the peak at 1652 cm^{-1} due to the overlapping of the CA vinyl group and

the newly formed amide C=O groups in the spectrum of St- N-CA compared to the pure St spectrum also indicates the successful grafting of the CA part of CGA on St-N.

Fig. 3. FTIR spectra of components of hemostatic powder.

The surface morphology of freeze-drying sample of St-N-CA before and after EBI (15 kGy) was examined by SEM images (Fig. 4a, b). The different appearance of morphology, porosity and uneven surface created in the material before (Fig. 4a) and after (Fig. 4b) EBI indicates the formation of a 3-D network polymer structure (which is distributed heterogeneously) in hemostatic powder. The open and porous structure

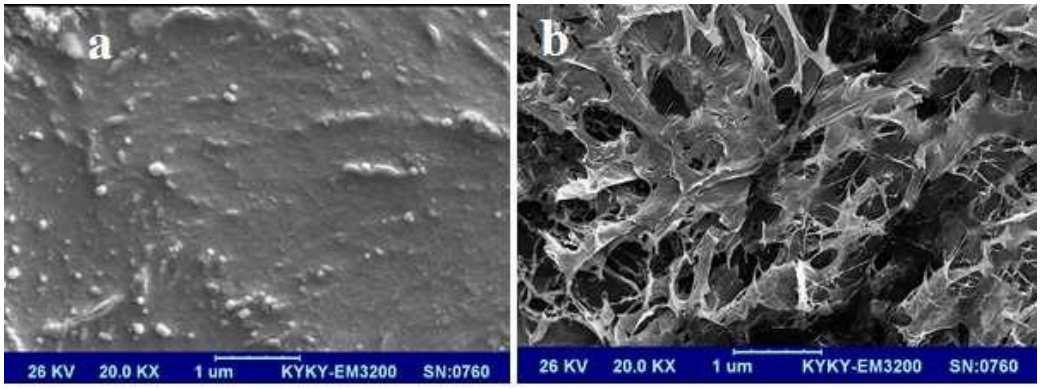

Fig. 4. SEM images of St-N-CA samples before (a) and after (b) EBI.

related to the created networks polymer increases the permeability and easier transfer of the molecules of the aqueous media of the blood (during the swelling phenomenon) to the depth of the network structure of hemostatic powder and thus increases its absorption capacity and rate.

EDA immobilized to the structure of hemostatic was also investigated by EDX analyzes (Fig. 5). The presence of the nitrogen signal and the disappearance of the chlorine peak in the St-N and St-N- CA spectra indicate the successful stabilization of EDA with St-Cl through the removal of chlorine.

The thermal stability of raw St, St-N-CA before and after EBI (15 kGy) was investigated by TGA analysis (Fig. 6). As can be seen, the thermal stability of St-N-CA is reduced compared to raw St. This behavior can be due to breakage of starch caused by the successive process of chlorination, aminolysis and grafting. The thermal stability of hemostatic powder based on cross-linked St-N-CA compared to raw St is clearly

improved. For example, the residual weight of raw St at 350 ºC is equal to 32%, which is less than the residual weight of hemostatic powder (42.5%) at the same temperature. In general, the thermogram of hemostatic powder shows a gradual decrease in weight with less intense weight loss at different temperatures compared to the thermograms of raw St and St-N-CA. This improvement in thermal stability is due to the random crosslinking between St-N-CA chains through EBI, which can act as a thermal barrier (Because of the hydrophilic network structure of the samples).

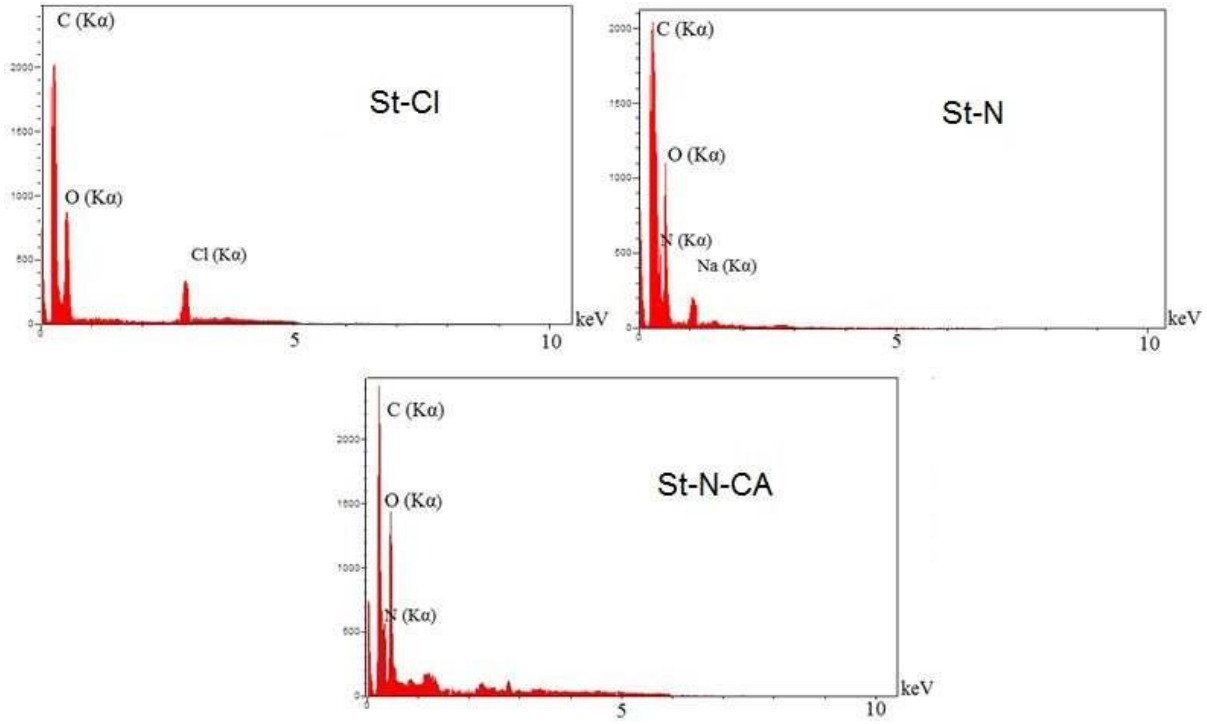

Fig. 5. EDX spectra of St-Cl, St-N and St-N-CA

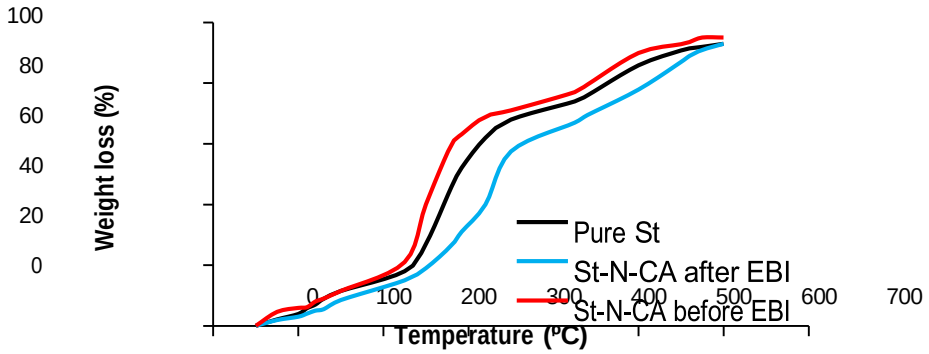

Fig. 6. TGA graphs of St and St-N-CA before and after EBI.

Raw St usually has a granular structure with 15 to 45% crystallinity, which belongs to its type A structure, which can be recognized by the sharp peaks at the positions of 15.5º, 17.1º, 18.3º and 23.4º (Fig. 7). The XRD patterns of raw St, St-N-CA before and after the cross-linking process using EBI (15 kGy) are shown in Fig. 7. However, when St is subjected to the successive reactions of chlorination, aminolysis and polyphenolic grafting, the crystal structure changes. The created amine or polyphenolic groups play an important role in the order and stabilization of linear starch amylose molecules and minimizing retrogression. The reduction and disappearance of some crystal peaks for St-N-CA before EBI and only the observation of 2 peaks at the positions of 17.0º and 20.1º indicate the change in the nature of part of the St crystallinity due to the mentioned reactions. However, the intensity of these crystal peaks in the XRD pattern of St-N-CA hemostatic powder has been greatly reduced or disappeared due to the random crosslinking process with EBI and the formation of an amorphous structure.

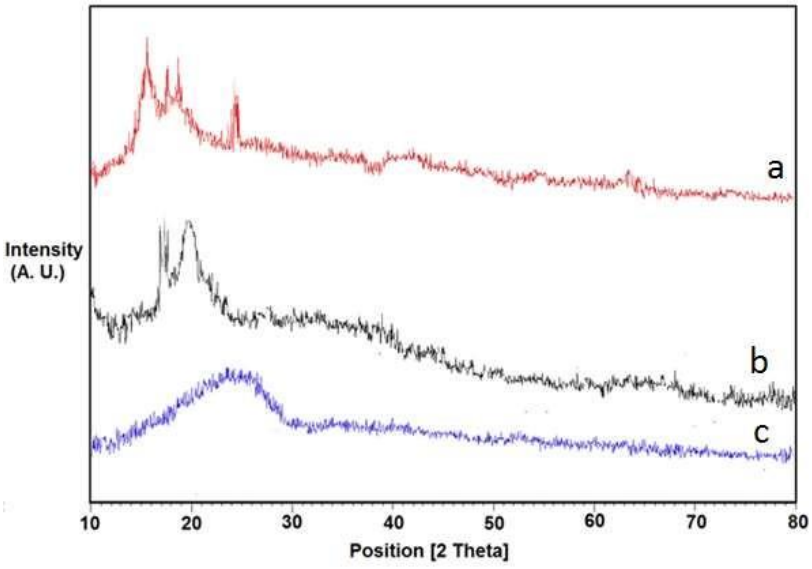

Fig. 7. XRD patterns of raw St (a), St-N-CA before (b) and after (c) the cross-linking process using EBI.

Effect of EBI dose on swelling, gel percentage and mechanical properties of synthesized hemostatic powder

As can be seen from the results of Fig. 8, swelling of hemostatic powder has decreased with increasing EBI dose. These observations can be related to the production of more free macroradicals of polyphenoxy grafted on St followed by the increase of cross-linking density at higher EBI doses. Because as a result of this

process, the mobility of biopolymer chains is reduced and water molecules hardly penetrate into the hemostatic networks. Also, the effect of EBI on the mechanical properties of hemostat hydrogel films (before the drying and grinding processes) was investigated. With increasing EBI dose, gel percentage and mechanical properties (compressive and tensile strength, Fig. 8b) of hemostatic samples increased due to the formation of polyphenoxy free macroradicals and as a result of increasing the density of crosslinking between St biopolymer chains. The compressive strength of more than 60% for samples of synthesized at EBI dose values higher than 10 kGy indicates the appropriate hardness of the prepared hemostatic powder for practical applications. Considering more economical in production with lower irradiation doses, the higher swelling and also appropriate mechanical properties of hemostatic samples

synthesized at 15 kGy irradiation dose, this dose was used for product synthesis and further studies.

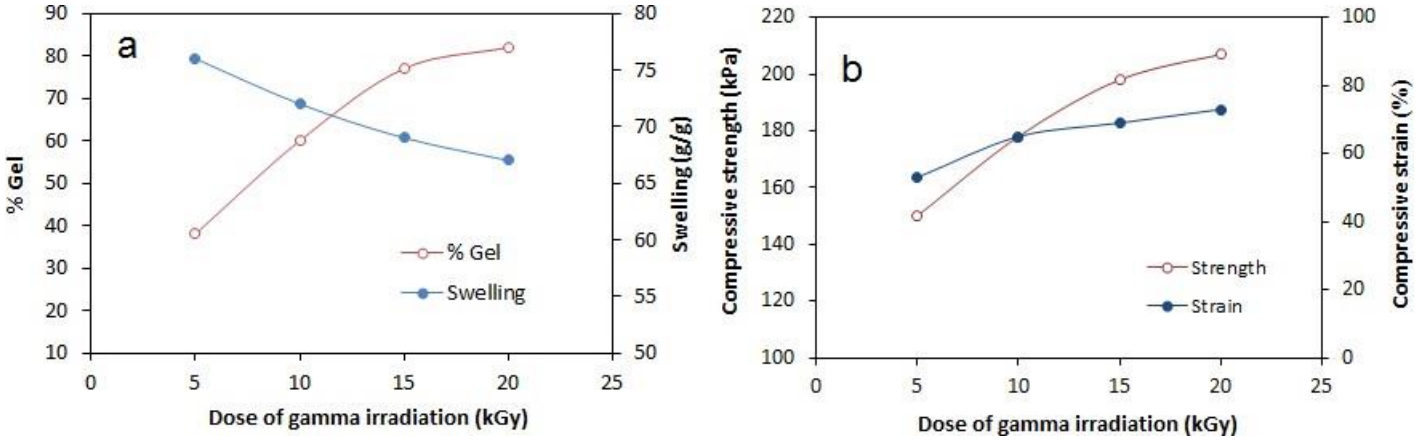

Fig. 8. Effect of EBI dose on swelling, gel percentage and mechanical properties of hemostatic powder.

Study and comparison of absorption rate of synthesized hemostatic powder with other commercial products

In general, the mechanism of action of hemostatic products in stopping bleeding is through the absorption of the aqueous media of blood plasma and as a result the concentration of blood coagulation factors, which accelerates the process of stopping bleeding. To check and compare the effectiveness of the synthesized product (at 15 kGy) as a hemostatic agent, the results of the time profile of blood absorption capacity by commercial hemostatic powders (Perclot, Celox, Arista and Chitohem) and the synthesized hemostatic product are shown in Fig. 9. As it is known, the synthesized product has a better absorption capacity and rate (less time) than the introduced commercial products, which is caused by the synergistic effect of EBI in creating porosity (to carry out the crosslinking reaction in the aqueous media and the confinement of water molecules in polymer networks and finally the exit of water in the drying stage) in nano and micro dimensions during the crosslinking reaction of the biopolymer chains. For example, the synthesized product reaches the maximum swelling capacity of 33 g/g in 35 seconds, while the Perclot and Chitohem products (in this time) reach swelling values of 18 and 7 g/g, respectively. Also, the Celox product reaches the maximum swelling capacity of 15 g/g in 55 seconds, and the Arista product reaches the swelling value of 16 g/g in 60 seconds.

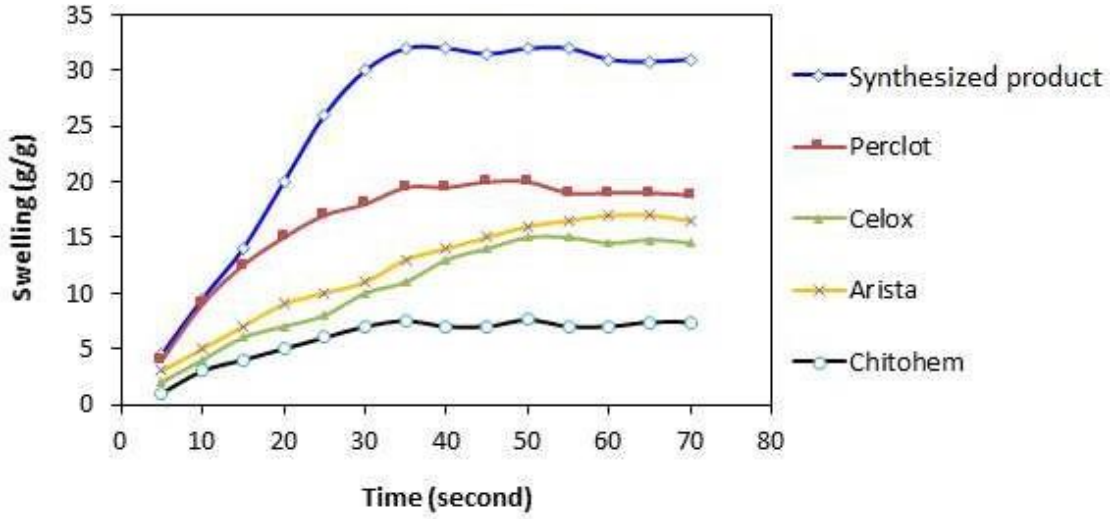

Fig. 9. A comparison of the time profile of absorption capacity of commercial hemostat powders and synthesized product in the blood media.

Conclusions

In this work, hemostatic powder was prepared by introducing a new production method based on modified starch biopolymers using the EBI method.

Production with the clean and sterile method of EBI, rather than toxic and allergenic chemicals, commonly used in polymerization processes, improves the biocompatibility of the synthesized hemostatic powder for human body. The chemical and physical structure of the product was confirmed by FTIR, SEM, EDX, XRD, TGA. With increasing EBI dose, gel percentage and mechanical properties of hemostatic samples increased. Considering the higher swelling and appropriate mechanical properties of hemostatic samples synthesized at 15 kGy irradiation dose, this dose was selected for product synthesis. The absorption rate and capacity of hemostatic powder synthesized by irradiation method was higher than commercial samples. Full compatibility with green chemistry production processes, no waste generation, high production speed, reaction at room temperature and pressure are among the advantages of this synthesis method for hemostatic products.

References

[1] Mao, Y. Li, P. Yin, J. Bai, Y. Zhou, H. Lin, X. Zhao, M. Yang, H. Yang, L. (2021). Starch-based adhesive hydrogel with gel-point viscoelastic behavior and its application in wound sealing and hemostasis. Journal of Materials Science & Technology, 63:228-235.

[2] Wang, C. Lu, W. Li, P. Li, S. Yang, Z. Hu, Z. Liu, Y. (2017). Preparation and evaluation of chitosan/alginate porous microspheres/Bletilla striata polysaccharide composite hemostatic sponges. Carbohydrate Polymers, 174: 432-442.

[3] Chen, J. Lv, L. Li, Y. Ren, X. Lou, H. Gao, Y. (2019). Preparation and evaluation of Bletilla striata polysaccharide/graphene oxide composite hemostatic sponge. International Journal of Biological Macromolecules, 130: 827-835.

[4] Shi, X. Fang, Q. Ding, M. Wu, J. Ye, F. (2016). Microspheres of carboxymethyl chitosan, sodium alginate and collagen for a novel hemostatic in vitro study. Journal of Biomaterials Applications, 30(7):1092-102.

[5] Sayed, A. Mohamed, M.M. Abdel-raouf, M.E.S. Mahmoud, G.A. (2022). Radiation synthesis of green nanoarchitectonics of guar gum-pectin/polyacrylamide/zinc oxide superabsorbent hydrogel for sustainable agriculture. J. Inorg. Organomet. Polym. Mater., 32:4589-4600.

[6] Moghaddam, R.H. Dadfarnia, S. Shabani, A.M.H. Shirmardi, S.P. Moghaddam, Z.H. (2022). Fabrication of two hydrogels composites through the coupling of gelatin

with ethyl vanillin/polyvinyl alcohol using electron beam irradiation for ciprofloxacin delivery. Polym. Bull., 80:8407–8429.

ICNST 2024
International Conference on Nuclear Science and Technology
6- 8 MAY 2024 | Isfahan, Iran

Feasibility study of fuel cladding sample performance at TRR under simulated KHRR condition (Paper ID : 1089)

Golshanian M. [1*], Hosseinipanah MSh. [1]

[1]*Reactor and Nuclear Safety Research School, Nuclear Science and Technology Research Institute (NSTRI),Tehran,Iran*

Abstract

In order to ascertain the lifespans of fuel elements in reactors, determine the safety thresholds for reactor operation, or simulate fuel performance, it is imperative to acquire a more comprehensive understanding of the mechanical interactions between metallic fuels and cladding. In this investigation, the feasibility of mechanical testing fuel clad samples under KHRR conditions was evaluated at the Tehran Research Reactor. In order to determine the high flux position, the TRR core's irradiation positions have been studied. Through the implementation of a novel fuel assembly arrangement referred to as compact-core, the placement of high-flux radiation, C6, was successfully achieved by using MCNPX v2.7 code. The fuel clad sample was simulated with two mechanical tests of rings and rectangular tension due to the presence of IPS in C6 and the space constraint of approximately 14 mm. The neutronic parameters of the core were calculated both in the presence and absence of the mechanical test cladding sample. The sample's radiation dose rate was also computed. The results indicate that the Tehran Research Reactor offers a good chance of being used for fuel clad mechanical testing. Additionally, the estimated dose rate computed from the fuel clad sample may be helpful in determining the permissible dose for sample transportation following irradiation.

Keywords: Fuel clad sample, fast flux, mechanical prototype testing, dose, MCNPX v2.7

1 INTRODUCTION

In a nuclear reactor, investigation of the radiation effect on the structure material performance has a crucial role in the fuel loading process at the new research

reactor design [1, 2]. As metallic fuels are exposed to radiation, they undergo a swelling process until reaching a burnup of 1-2 at. %, at which point they come into contact with the cladding [3]. In regions of the fuel-

cladding interface where there is sufficient contact, there is a possibility of interdiffusion occurring between the fuel, fission products, and cladding constituents. This chemical interaction between the fuel and cladding can give rise to the formation of interaction zones along the inner surface of the cladding. These interaction zones can have an impact on the performance of a fuel element. They can be brittle, leading to the initiation of cracks that can compromise the mechanical integrity of the cladding [4, 5]. Therefore, To find the fuel element lifetimes in reactors, calculate the safety limits for reactor operation, or model fuel performance, a deeper comprehension of the mechanical interactions between metallic fuels and different kinds of cladding is necessary [4]. Tehran Research Reactor (TRR) as Material Testing Reactor (MTR) can be used to evaluate the performance of structural materials in the new reactor design. This article investigates the use of the TRR for the fuel clad mechanical test samples and their dose during 1-cycle operation of the Khondab Research Reactor (KHRR) under radiation conditions (the required fluence is 6.2×10^{20} (n/cm^2)).

2. Material and method

2.1 Simulation of at TRR's compact core

TRR is a pool type and light water moderated research reactor with a 5 MW nominal power. The water is used for reflecting, cooling and biological shielding. Its solid fuel assemblies include low enriched uranium fuel plates in the form of U_3O_8Al alloy [6]. To make a high flux radiation position in the core of TRR the new fuel assemblies' arrangement, compact-core, has been considered. The compact-core contains 19 Standard Fuel Element (SFE), 5 Control Fuel Element (CFE) and 6 irradiation positions. In order to estimate high neutron flux, the position of the fuel assemblies of the compact-core has been modeled using MCNPX v2.7 code [7] (illustrated in fig. 1). It is notable that, the MCNPX code

which was applied in this study has been verified by ref [8]. Furthermore, the first core of TRR has been simulated using MCNPX v2.7 and compared with FSAR in order to verify the results of these computations.

2.2 Mechanical testing of fuel clad sample

The ASTM E 453 standard lists several mechanical test methods for fuel clad samples, such as rings, rectangular, tensile tests and etc. [9]. Due to the insufficient space (~14mm) available for irradiating test samples, the radiation testing of fuel clad sample will focus on the rectangular and ring tension tests [9]. The fuel clad of the KHRR reactor is composed of 99 % Zr and 1% Nb. Since zirconium alloys have a very low thermal neutron absorption cross-section, they are frequently used as fuel rod cladding [10]. Due to the high flux of neutron in C6 and presence of an In-pile section in the center of the C6 irradiation position, the KHRR fuel clad sample is simulated in the corners of it using MCNPX v2.7 code. This samples are visualized in fig2. Calculations were also made for some fundamental parameters of the TRR such as multiplication factor (K_{eff}) and power with and without fuel clad sample. In order to make operation condition of the KHRR, the fluence is considered 6.2×10^{20} (n/cm^2). The fast neutron flux ($En\geq$ 1MeV) along the C6 at points A and B has been calculated using the MCNPX Tmesh card (see fig 2), to estimate the appropriate irradiation time for the sample of fuel cladding. To identify another suitable palace for the mechanical test of the fuel cladding sample, the vertical fast neutron flux in the channels F9, F6, F4, A9, and A3 has also been calculated.

2.3 Calculation of fuel clad sample dose

The ORIGEN code [11], which was used as a gamma source in the MCNPX v2.7 code input for the gamma dose rate calculations, was utilized to calculate the uranium oxide fuel assembly gamma-emission rates. In the computational simulation the detector dimension (2.25*18 cm^2) was applied. The source's gamma particle transport distribution in the axial and radial directions in the clad is depicted in Figures 3a. The detector simulation at a distance of 50 cm from the clad surface is depicted in Fig3b.

The gamma dose rates were determined by applying the DE/DF flux to dose conversion factors and using the F4 tally of the MCNPX v2.7 code. At a distance of 0, 50 and 100 cm from the clad surface, the gamma dose rates in water and air were computed.

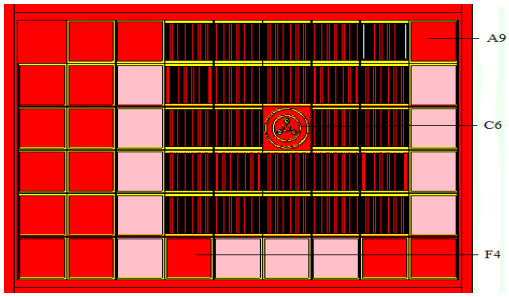

Fig. 1. Top view of TRR core simulation input of MCNPX v2.7 code taken by Visual Editor ver.x-22s.

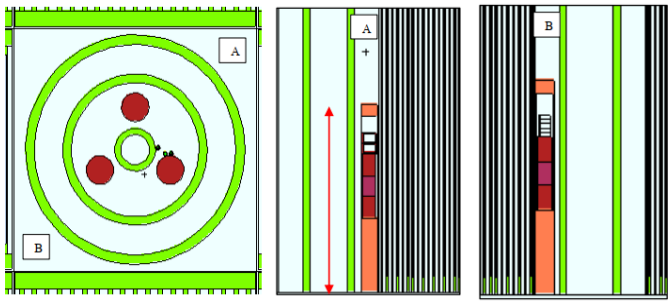

Fig. 2. Top and side view of the fuel clad sample taken by the Visual Editor ver.x-22s.

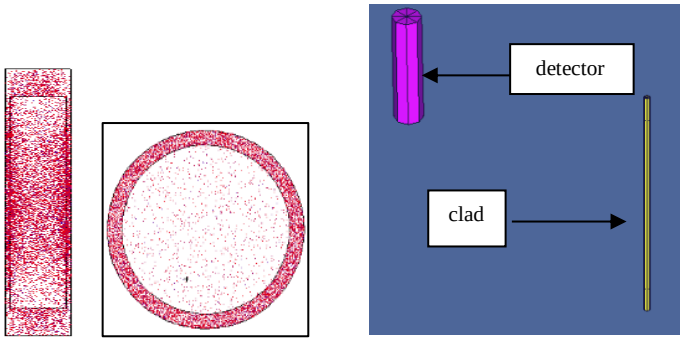

Fig. 3a. the axial and radial view of gamma source,
3b. detector simulation at a distance of 50 cm from the clad

3. Result and discussion

Table 1 presents the calculated values of average fast neutron flux for the situation (A) and (B) of C6 and other irradiation positions of the TRR core. The radiation required time to overtake the considered fluence 6.2×10^{20} (n/cm^2) of KHRR, are indicated in table1. Since position C6 has a higher average fast neutron flux than the other irradiation positions, it takes less time for irradiation to reach the KHRR's fluence conditions. So, for the purpose of continuing to examine the mechanical test samples of the clad, irradiation position C6 was selected. The calculated multiplication factor (K_{eff}) and power during the presence or absence of the ring and rectangular fuel clad sample are reported in table 2. The results in Table 2 demonstrate that the TRR core's safe operation is unaffected by the presence of clad mechanical test samples on the sample surface at 0, 50, and 100 cm away, fuel clad sample test dose rate in (mSv/h) units at different cooling times is shown in Tables 3 and 4 respectively. Figures 4, 5, and 6 present a comparison of the dose rate computed in the air and water at various cooling times and at 0, 50, and 100 cm from the clad surface.

Conclusion

Using the MCNPX v2.7 code, the average of fast neutron flux and radiation time required have been calculated for two points in C6 and the other irradiation positions of the TRR core. Multiplication factor and power during the presence or absence of KHRR fuel clad sample in the TRR core have been reported in table 1. The obtained results show that, the C6 irradiation position of the TRR core is useful for mechanical test of fuel clad sample and structural materials under KHRR conditions. Furthermore, the other irradiation positions of TRR core can be useful in long-term TRR core operation. The dose of fuel clad sample was also computed at various cooling times in order to produce information that was helpful from the perspective of transportation following irradiation.

Table1. Average Fast neutron flux and required irradiation time in the corner of C6 irradiation position and other irradiation positions

point (A) in C6	point (B) in C6	A3	A9	F4	F6	F9	A3

Fast Neutron Flux $\times 10^{13}$(n/cm2.s)	5.83	2.96	0.51	0.48	0.69	0.86	0.29	0.51
time for irradiation (Days)	120	235	1400	1505	1047	834	2459	1400

Table2. safety parameters of TRR core

Safety parameters				
	Keff (pcm)	Δk	Power(kW)	%Δp(kW)
With the sample in TRR core	1.00257 ±0.0006	127	25.1	3.3
Without the sample in TRR core	1.00384 ±0.0006		25.9	

Table3. dose in water from the surface of the clad

	Dose in the air (mSv/h)		
Time of cooling (day)	from the clad surface		
	0cm	50cm	100m
0	1.47E+05	1.39E+03	3.55E+02
10	1.07E+05	1.01E+03	2.59E+02
20	9.21E+04	8.70E+02	2.23E+02
30	7.94E+04	7.50E+02	1.92E+02
40	6.85E+04	6.47E+02	1.66E+02
50	5.92E+04	5.59E+02	1.43E+02
60	5.10E+04	4.82E+02	1.23E+02

Table4. dose in the air from the surface of the clad

	Dose in the water (mSv/h)
Time of cooling (day)	from the clad surface

	0cm	50cm	100m
0	1.70E+05	2.40E+02	2.34E+00
10	1.24E+05	1.70E+02	1.55E+00
20	1.07E+05	1.47E+02	1.33E+00
30	9.21E+04	1.27E+02	1.14E+00
40	7.94E+04	1.10E+02	1.03E+00
50	6.86E+04	9.58E+01	8.91E-01
60	5.90E+04	8.31E+01	7.85E-01

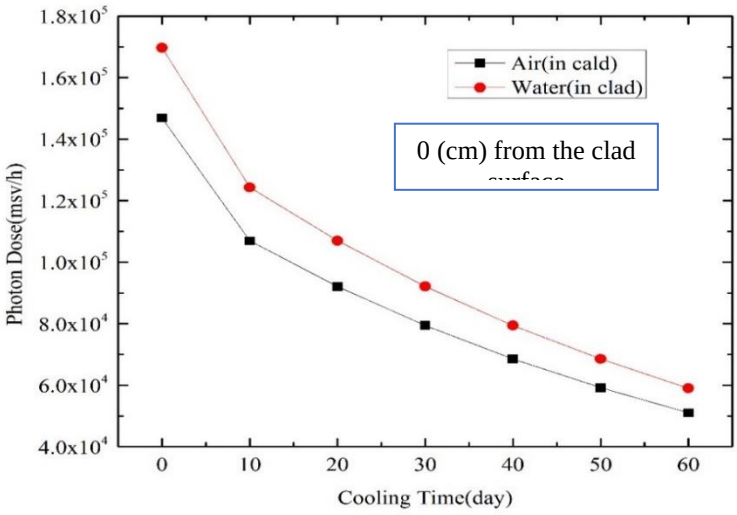

Fig. 4. comparison of the sample clad dose rate in the air and water from 0 cm of the surface clad

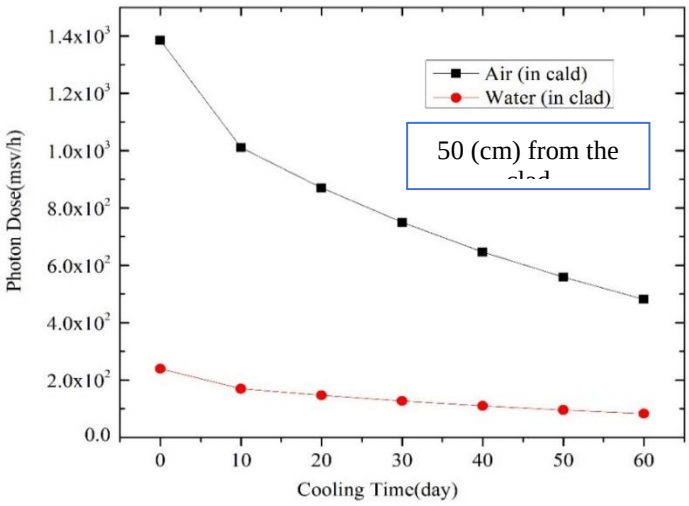

Fig. 5. comparison of the sample clad dose rate in the air and water from 50 cm of the surface clad

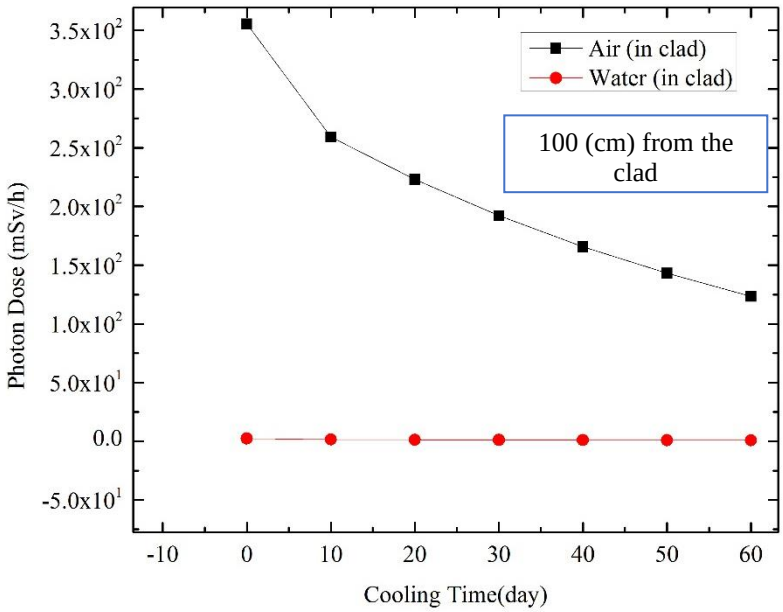

Fig. 6. comparison of the sample clad dose rate in the air and water from 100 cm of the surface clad

References

[1] Koutský, J. and J. Kočík, Radiation damage of structural materials. 2013: Elsevier.

[2] Was, G.S. and T.R. Allen, Radiation damage from different particle types, in Radiation Effects in Solids. 2007, Springer. p. 65-98.

[3] Hofman, G.L., L.C. Walters, and T. Bauer, Metallic fast reactor fuels. Progress in nuclear energy, 1997. **31**(1-2): p. 83-110.

[4] Konings, R. and R.E. Stoller, Comprehensive nuclear materials. 2020: Elsevier.

[5] McGeary, R., Mechanical packing of spherical particles. Journal of the American ceramic Society, 1961. **44**(10): p. 513-522.

[6] TRR, S.f., Safety analysis report for Tehran research reactor. Nuclear Research Center of the Atomic Energy Organization of Iran, Tehran.. october 2002.

[7] Pelowitz, D.B., MCNPX™ User's Manual, Version 2.7. 0. LA-CP-11-00438. Los Alamos National Laboratory, 2011.

[8] Kasesaz, Y., et al., Design and construction of a thermal neutron beam for BNCT at Tehran Research Reactor. Applied Radiation and Isotopes, 2014. **94**: p. 149-151.

[9] Standard Practice for Examination of Fuel Element Cladding Including theDetermination of the Mechanical Properties. 2001.

[10] Motta, A.T., Effects of Reactor Exposure on Nuclear Fuel Cladding. Transactions, 2014. **110**(1): p. 809.

[11] Croff, A.G., User's manual for the ORIGEN2 computer code. 1980, Oak Ridge National Lab.

ICNST 2024
International Conference on Nuclear Science and Technology
6- 8 MAY 2024 | Isfahan, Iran

Design and manufacture of new porous superabsorbent polymer by electron beam irradiation method for sanitary purposes (Paper ID : 1095)

Hafezi Moghaddam R[1*]., Shirmardi SP[1]., Masoudi H[1]., Dehshiri S[1]

[1] *Central Iran Research Complex, Iran Radiation Application Development Company, Atomic Energy Organization of Iran, Tehran, Iran.*

Abstract

Almost more than 80% of superabsorbent polymers are used in the production of baby diapers. In the present project, hygienic superabsorbent polymers (SAP) based on neutral polyacrylamide polymer were created and synthesized in aqueous medium using a new production method with the help of sodium dodecyl sulfate micelles and clean and sterile electron beam irradiation method. The use of high-energy irradiation processing methods is a suitable alternative for making sanitary polymer products (especially in biomedical applications) compared to traditional and common chemical methods. By creating a porous structure in the SAP, the swelling increased from 46 to 58 g/g. Also, according to the increase of irradiation dose from 10 to 40 kGy, the swelling of the porous SAP decreased from 68 to 54 g/g and its absorbency under load (AUL) increased from 14 to 28 g/g. The porous SAP designed in order to improve the AUL properties and non-blocking of the gel was surface modified with the help of the new reagent 1, 6-hexanediol in the next step. By performing this surface modification process, AUL of the porous SAP was improved from 22 to 28 g/g. The chemical and physical structure of the product was studied and confirmed by SEM, BET, EDX, XRD and gel percentage. The effect of electron beam irradiation dose on swelling properties and AUL of the product was studied. Fortunately, by using the HPLC method, the amount of residual monomer in the final product was obtained with the present method much less than the permissible limit declared in scientific references.

Keywords: Electron beam irradiation, Superabsorbent polymers, Hygienic purposes, Polyacrylamide, Porous polymer

INTRODUCTION

Super absorbent polymers (SAP) were first produced in the late 1960s in USA, and their commercial types were introduced to the USA market in the early 1970s. The main use of this product was initially in agriculture and horticulture, where it was used as a hydrogel to maintain soil moisture during the growth stages of plants [1]. With the passage of time, the range of SAPs used in the production of other polymer products also increased, and in this way, hygienic industries benefited more than other sectors from the characteristics and properties of SAPs. So that in 1982, Japan was able to revolutionize the baby diaper production industry and introduce superabsorbent diapers to the market [2]. Hygienic SAP can be formed in pure or composite form of highly hydrophilic polymeric materials that have high water absorption speed and capacity. These polymers are able to quickly absorb the aqueous media up to 100 of times their weight, which are usually made of neutralized acrylic acid and are converted into polymer networks by crosslinking linear polymer chains. In hygienic products, these polymers quickly absorb and store biological fluids and prevent further leakage and penetration of these fluids into different areas of the skin. As a result, skin inflammations and infections are greatly reduced [3].

The common chemical method for the production of SAPs in several phases of petrochemical centers starts from the extraction of sea gas and in the later stages it is converted into propylene, propylene oxide, acrylic acid and sodium polyacrylate [1-3]. Due to the lack of petrochemical facilities required for the production of acrylic acid raw material and its expensive supply through imports to the country, in the current proposed method, the neutral polyacrylamide (PAM) is used instead of acrylic acid and also the electron beam irradiation (EBI) system is used instead of petrochemical facilities. Considering the polymerization reactions in the aqueous solvent media and at room temperature and pressure for the EBI method as well as the removal of toxic and expensive chemical reagents (such as catalysts, initiators and crosslinkers) common in petrochemical processes, the proposed method can be a suitable method for producing hygienic SAP products [4, 5].

Increasing the rate of absorption is one of the most important quality parameters of sanitary superabsorbent products. One of the ways to increase the speed of water absorption in superabsorbent SAPs is to create interconnected pores in the polymer tissue, which accelerates the water absorption process. Since in this project we use viscous polymer solution to make sanitary SAP, therefore applying porosity by foaming chemical reagents in them is not as easy as monomeric polymerization processes. Surfactants (in addition to having antimicrobial properties) by forming a self-assembled structure in the aqueous media, create a suitable template for the formation of holes in the polymer tissue in the polymerization process [6]. Therefore, in this project, the ability to form a micellar self- assembly structure of an anionic surfactant (sodium dodecyl sulfate) can be used to improve the porosity of the SAP structure. In order to prevent the phenomenon of gel blocking and also to improve AUL in this project, by the method of partial surface modification of hydrophobicity (in order to partially increase the surface hydrophobicity) of SAP granules with the help of a new diol reagent (1,6- hexanediol) in an anti-solvent media with the help of thermal reactions

EXPERIMENTAL

Reagents and instrumentation

All reagents and chemicals with analytical grade were prepared from Merck (Darmstadt, Germany). For the preparation of the sorbents, a high-energy Rhodotron industrial electron accelerator device, model TT200, with energies of 10 MeV (located in Yazd, Iran), was used. Irradiation dosimetry was done by cellulose triacetate film. The irradiation dose rate was 7.5 kGy s^{-1} and the electron beam current was 5.0 mA.

Preparation of porous and non-porous SAP by EBI method

To prepare porous SAP, 3.0 g of PAM with 0.1 g of sodium dodecyl sulfate (SDS) was added to 50 mL of 4.0% w/v sodium chloride solution and then stirred for 2 hours at room temperature with a magnetic stirrer. 20 mL of

the resulting gel solution was transferred to a Petri dish and covered with a thin plastic sheet to prevent water evaporation, and then subjected to electron irradiation in the range of 10 to 40 kGy. The resulting SAPs were washed several times with distilled water to remove unreacted polymers or polymers with lower molecular mass. Finally, to remove the SDS micelles trapped in the polymer networks, the SAPs were washed several times with ethanol-water mixture (8:2 v/v) and the prepared porous SAPs were dried for 2 days at 45 ºC. The dried porous SAPs were converted into granules in the range of 250-700 microns using a hammer mill and stored in a sealed polyethylene bag for further use. Non-porous SAP was prepared as above but without adding SDS and NaCl salt.

Surface modification of porous SAP particles with 1,6-hexanediol

5.0 g of the porous SAPs milled in the previous step were added to a flask containing 200 cc of ethanol/1,6-hexanediol two-part solution (1:3 ratio) and the resulting suspension was refluxed for 4 hours at 65 °C. After performing partial stabilization reaction of diol reagent on the surface of PAM hydrophilic amide functional groups and coating some of them (increasing surface hydrophobicity), the resulting porous SAP sediments were separated with filter paper and three times with ethanol and then once with distilled water (to remove unreacted diols) was washed using a magnetic stirrer. After completing the washing process, SAP granules were dried again in the oven.

Results and discussion

Mechanism of production

The use of EBI method to perform polymerization and cross-linking of polymers is a suitable and environmentally friendly method that eliminates all the disadvantages of traditional chemical methods and does not require the use of toxic and dangerous chemical solvents or reagents, as well as time-consuming processes common in chemical polymerization methods. In addition, EBI methods have advantages such as high speed of production (suitable for production in industrial dimensions), sterilization and product

production at the same time, no waste generation, and reaction at room temperature (less energy and fuel consumption). In this work, the aqueous PAM solution was subjected to electron beam irradiation, which

results in the formation of free radicals on the PAM polymer chain and the subsequent recombination of these macroradicals, the process of inter-chain crosslinking occurs. Also, in this study, the ability to form the self-assembly structure of SDS micelles in aqueous media was used to improve the porosity of the SAP structure (Fig. 1). As can be seen, in the process of network formation, SDS micelles enclosed in the polymer network act as a template to create holes. In addition, the hydrophobic interactions between the R-alkyl SDS chains can reduce the hydrogen bonds between the chains of PAM molecules, resulting in the expansion and stability of the cavity. Also, adding NaCl salt to the mixture of polymer and surfactant before the irradiation stage due to the reduction of the repulsive force between the charged heads of SDS causes the formation of larger and more stable micelles and finally the formation of larger pores in the SAP structure. Finally, the micelles trapped in the polymer network can be removed by washing with water and ethanol, and a SAP with a porous structure can be obtained.

Conducting the surface modification reaction by 1,6-hexanediol in anti-solvent media is due to the non-penetration of the surface modification reaction in the depth of the SAP networks and limiting the reaction on the surface of the SAP particles. This covering effect (partial hydrophobicity) of the diol surrounding the 6-carbon chain on the hydrophilic functional groups of the SAP is possible through the hydrogen bonds of the alcohol groups at the two ends of the 1,6-hexanediol with the hydrophilic amide functional groups of PAM. A view of the proposed reaction is shown schematically in Fig. 2. 1,6-Hexanediol has less toxicity than other surface modifying chemical reagents (such as dihalides, silane derivatives, aldehyde derivatives, vinyl reagents, etc.) and is generally considered safe. So far, there have been no reports of skin irritation for this diol reagent.

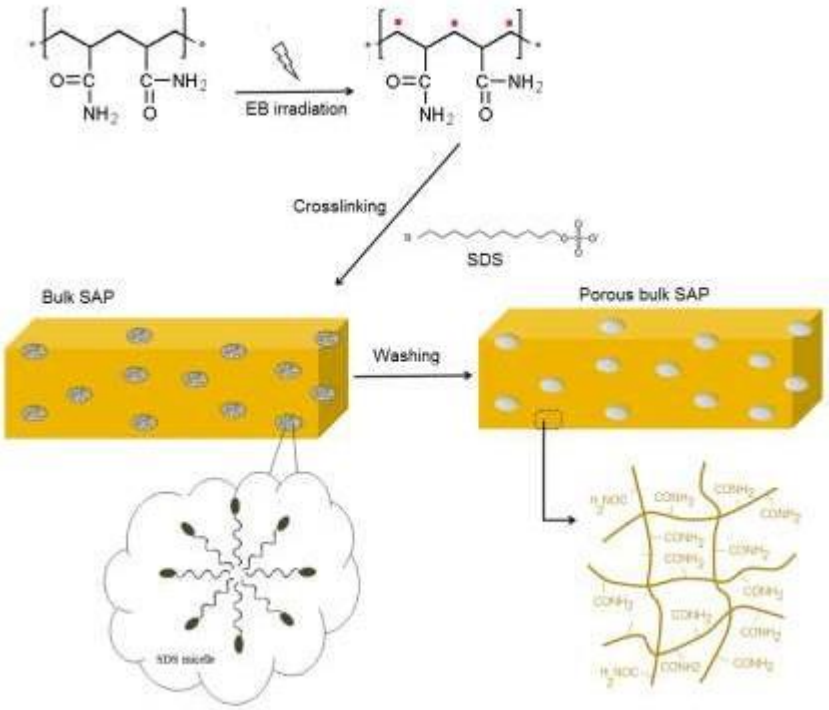

Fig. 1. View of the formation of SAP structure by EBI method and creation of porosity in SAP tissue by SDS micelles.

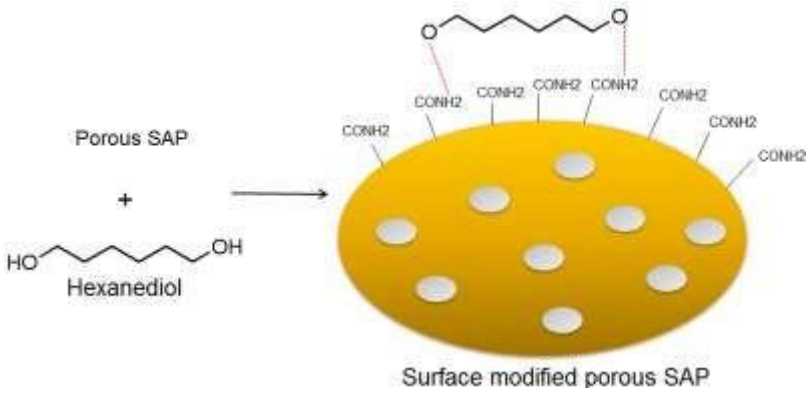

Fig. 2. View of the surface modification process of porous SAP with 1-6 hexanediol reagent

Characterizations of porous and non-porous SAP

For SEM studies, porous and non-porous SAP were prepared by freeze drying method. SEM images of the surface of samples (Fig. 3) clearly show that the preparation of SAP in the presence of SDS (as micellar template) has significantly increased the porosity of the SAP and the pores are distributed

heterogeneously in the three-dimensional network structure of the polymer. The porous structure with open and interconnected holes is suitable for increasing the permeability of water molecules and makes it easier to transfer the aqueous solution to the depth of the SAP network structure, which increases the absorption capacity of the porous SAP compared to the non-porous SAP.

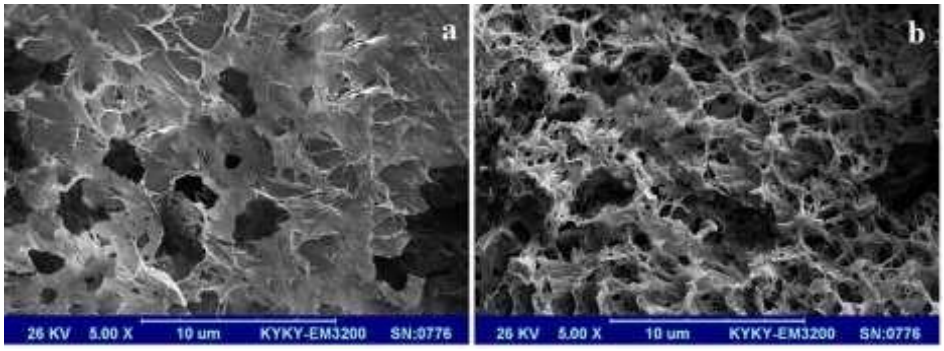

Fig. 3. SEM images of non-porous SAP surface (a) and porous SAP (b)

The effect of the presence and absence of SDS micelles in the porous SAP structure was investigated by EDX analysis (Fig. 4). The disappearance of the S peak and the strong reduction of Na and Cl signals in the porous SAP after the washing step confirm the correct removal of micelles and NaCl from the porous polymer structure.

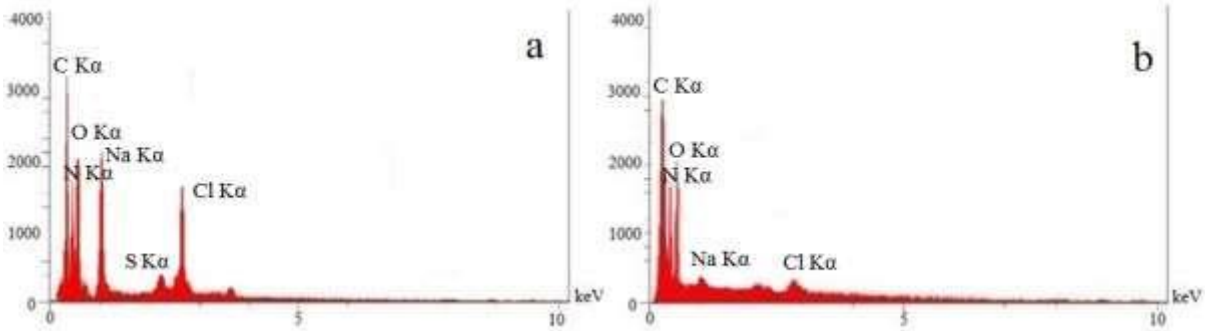

Fig. 4. EDX spectrum of porous SAP before (a) and after (b) micellar and NaCl washing.

Based on the analysis of the BET results of freeze-dried samples of porous and non-porous SAP (Fig. 5), the specific surface area, cumulative volume, and size distribution of the pores in the non- porous SAP are 0.608 m^2/g, 295.10 mm^3/g and 215-609 nm, respectively, and in the porous SAP are 0.931 m^2/g, 899.23 mm^3/g and 298-810 nm, respectively. An increase in the values

of the mentioned parameters indicates an increase in the porosity in the structure of the porous SAP compared to the non-porous SAP, which can lead to an increase in the capacity and rate of absorption of the SAP.

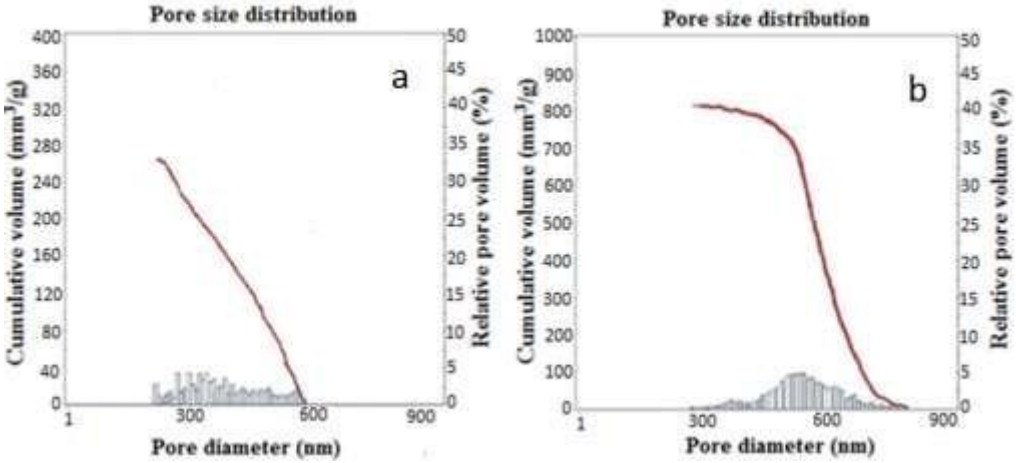

Fig. 5. Results of the BET analysis of non-porous SAP surface (a) and porous SAP (b)

The XRD patterns of pure PAM, porous and non-porous SAP (prepared in EBI dose 30 kGy) show that the pure polymer has special peaks of quasi-crystalline structure (19.5º) due to the formation of inter/intra molecular hydrogen bonds between the chain of PAM molecules and is similar to XRD pattern of crystal structure (Fig. 6). The elimination of these crystalline peaks and the appearance of a broad peak at 23º in the XRD pattern of porous (with lower intensity) and non-porous (with higher intensity) SAP is due to the process of random cross-linking with EBI and the formation of SAP with an amorphous structure. In other words, the breaking of intermolecular hydrogen bonds in PAM, followed by the formation of a networked and porous structure of the polymer, has reduced the interactions between PAM chains and, as a result, reduced its quasi-crystalline nature. The greater decrease in the intensity of the 23º peak in the porous SAP is due to the additional process of porosification by the micelles (compared to the non-porous SAP).

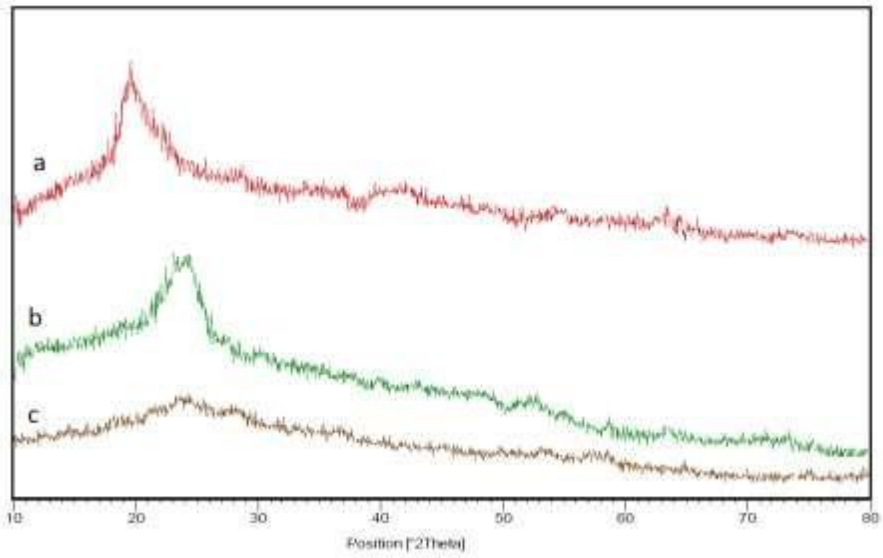

Fig. 6. XRD patterns of pure PAM (a), non-porous SAP (b) and porous SAP (c).

Effect of EBI dose on SAP swelling and AUL

The rapid swelling in the initial times can be attributed to the presence of many hydrophilic amide functional groups of PAM polymer in the SAP networks, as well as hydrogen bonding between these chains and water molecules (Fig. 7a). The increase in the capacity and swelling rate of the porous SAP sample (58 g/g) compared to the non-porous SAP (46 g/g) is also caused by the additional porosities and subsequently the easier mass transfer of water molecules to the depth of the polymer network. EBI dose is one of the important parameters affecting the properties of equilibrium swelling and AUL of SAP samples. Swelling capacity and AUL of porous and non-porous SAP prepared in the irradiation dose range of 10-40 kGy were studied. The results of this study (Fig. 7b) show that with increasing irradiation dose, the amount of swelling of both porous and non-porous samples decreases. The reason for observing this phenomenon can be related to the formation of more free macroradicals on the polymer chains and as a result of increasing the crosslinking density in higher doses of irradiation, which causes the networks of the polymer sample to become tighter and the penetration of water into the depth of the polymer network more difficult. As can be seen, the trend of changes in AUL (by applying a pressure of 0.7 psi) is completely opposite to

the trend of changes in the swelling, and with the increase in the crosslinking density caused by the increase in irradiation dose, the AUL has also increased. This behavior can be related to the increase in the mechanical strength of the samples due to the increase in the surface and depth crosslinking density in higher irradiation doses. To continue the studies, the irradiation dose of 30 kGy was chosen in order to achieve the most suitable amount of swelling and AUL for SAP in saline solution media.

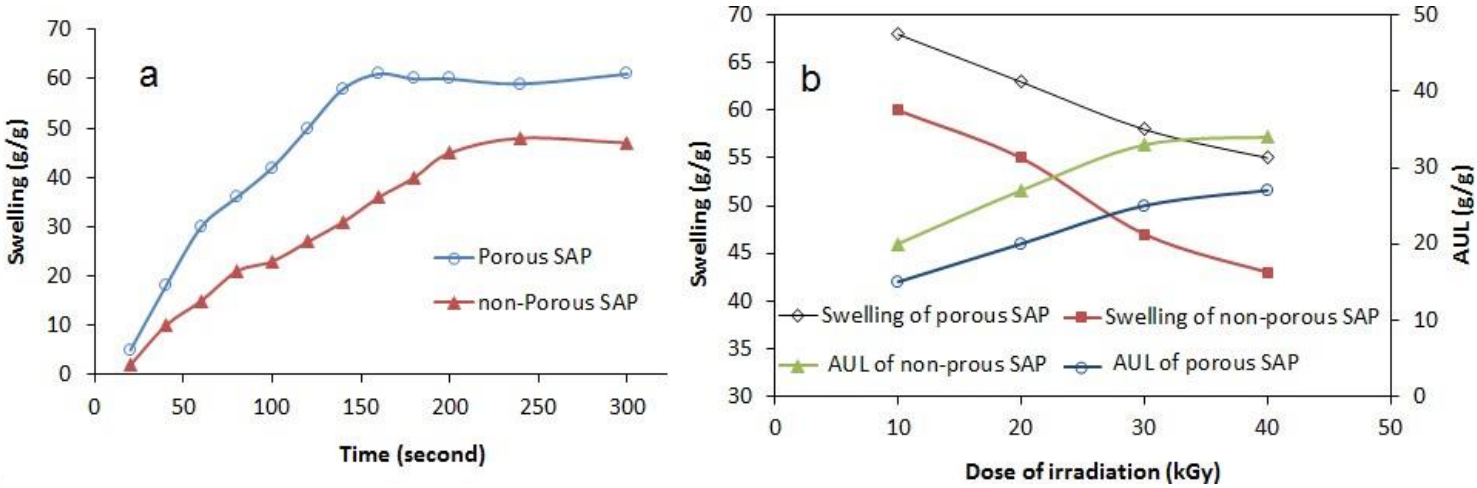

Fig. 6. Time profile of swelling of porous and non-porous SAP in 0.9 wt% salt solution (a). The effect of EBI dose on the swelling and AUL (0.7 psi) of porous and non-porous SAP in 0.9 wt% salt solution (b).

Investigating the surface modification of SAP particles with hexanediol on its properties

The role of this modification process in improving the AUL and gel percentage of different SAP samples prepared at an irradiation dose of 30 kGy is clearly defined in Table 1. The slight reduction of swelling in surface-modified SAPs compared to surface-unmodified SAPs is due to the additional process of connections or surface crosslinking on the surface of SAP particles, which is due to the intensification of crosslinking on the polymer surface (compared to the depth of the polymer). Therefore, the penetration of water molecules into the depth of the internal networks of the polymer becomes more difficult. According to the observation of this behavior, it is quite reasonable to increase the gel percentage and AUL of surface-modified SAPs compared to surface-unmodified SAPs. The goal of introducing the new

process of porosity was to increase the capacity and rate of swelling. As shown in Fig. 6a, the non-porous SAP reaches the maximum equilibrium swelling capacity (46 g/g) after 250 seconds, while the porous SAP reaches the maximum equilibrium swelling capacity (58 g/g) after 150 seconds. However, the amount of AUL of the porous SAP was reduced due to the loss of mechanical properties (22 g/g). Therefore, to compensate for this decrease in AUL value, the introduced surface-modification process was used and its value was improved to 28 g/g. But at the same time, the surface-modified porous SAP has better swelling properties than surface- modified/unmodified non-porous SAP.

Table 1. Investigating the process of surface modification of SAPs on its properties.

Sample	Gel%	AUL (0.7 psi) in saline solution (g/g)	Swelling in saline solution (g/g)
Surface non-modified non-porous SAP	92	31	46
Surface modified non-porous SAP	96	35	44
Surface non-modified porous SAP	90	22	58
Surface modified porous SAP	95	28	56

Measurement of the remaining monomer in the SAP by HPLC method

Acrylamide monomer was measured in sanitary porous SAP samples synthesized by EBI method with HPLC method with UV-Vis detector [7]. Briefly, 5 g of porous superabsorbent was added to 100 mL of methanol-water

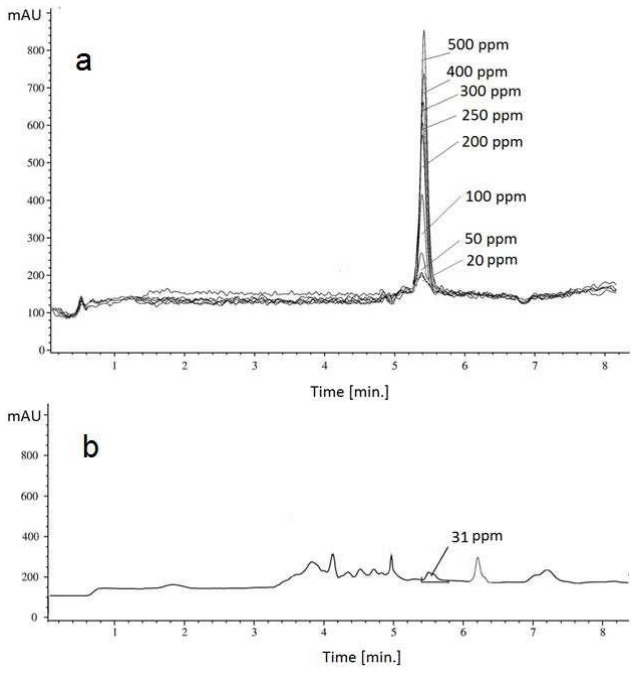

Fig. 7. HPLC spectra of a standard sample of acrylamide in the concentration range of 20 to 500 ppm (a). HPLC spectrum of acrylamide in porous SAP (b).

mixed solvent (at a ratio of 2:8) and it was stirred for 4 hours by a magnetic stirrer. Then 20 µL of its supernatant solution was introduced into the chromatography column with an injection rate of 0.2 in/min. Distilled water was used as a washing solvent. The HPLC spectra of the standard samples of acrylamide to achieve the calibration curve (in the concentration range of 20 to 500 ppm) as well as the HPLC spectrum of the acrylamide present in the porous SAP sample are shown in Fig. 7a and 7b, respectively. According to the scientific reference [8] announcing the permissible limit of acrylamide in cosmetic products and the results obtained, it is clear that the amount of residual monomer is much less than the permissible limit of acrylamide (0.01% or 100 ppm) in hygenic products.

Conclusions

In this study, a hygienic SAP based on a neutral polymer was synthesized in an aqueous solvent environment without the presence of chemical initiators, crosslinkers and organic solvents using a clean and sterile method of EBI. Therefore, the product of this work, due to the absence of the mentioned chemicals and its neutrality, can lead to less skin sensitivity and inflammation for the use of sanitary diapers for babies. The introduced production method is compatible with green chemistry production methods due to the use of electron irradiation method and the creation of minimal waste. The introduced production method is compatible with green chemistry production methods due to the use of electron irradiation method, performing reactions at room temperature and pressure, simultaneous production and sterilization, and also creating minimal waste. The chemical and physical structure of the product was confirmed by SEM, BET, EDX, XRD analysis. By creating a porous structure in the SAP, the swelling increased from 46 to 58 g/g. Also, according to the increase of irradiation dose from 10 to 40 kGy, the swelling of the porous SAP decreased 54 g/g and its absorbency under load (AUL) increased from 28 g/g. By performing this surface-modification process, AUL of the porous SAP was improved from 22 to 28 g/g. By using the HPLC method, the amount of residual monomer in the final product

was obtained with the present method much less than the permissible limit declared in scientific references.

References

[1] Ma, X. Wen, G. (2020). Development history and synthesis of super-absorbent polymers: a review. Int. Journal of Polymer Research, 27: 45-59.

[2] Bachra, Y. Damiri, F. Berrada, M. Tuteja, J. Sand, A. (2023). Introduction of Superabsorbent Polymers. Properties and Applications of Superabsorbent Polymers, 242:1-18.

[3] Venkatachalam, D. Kaliappa, S. (2023). Superabsorbent polymers: a state-of-art review on their classification, synthesis, physicochemical properties, and applications. Reviews in Chemical Engineering, 39: 127-171.

[4] Moghaddam, R.H. Dadfarnia, S. Shabani, A.M.H. Shirmardi, S.P. Moghaddam, Z.H. (2022). Fabrication of two hydrogels composites through the coupling of gelatin with ethyl vanillin/polyvinyl alcohol using electron beam irradiation for ciprofloxacin delivery. Polym. Bull., 80:8407–8429.

[5] Moghaddam, R.H. Dadfarnia, S. Shabani, A.M.H. Moghaddam, Z.H. Tavakol, M. (2019). Electron beam irradiation synthesis of porous and non-porous pectin based hydrogels for a tetracycline drug delivery system. Materials Science and Engineering: C, 102: 391-404.

[6] Benhalima, T. Ferfera-Harrar, H. Lerari, D. Optimization of carboxymethyl cellulose hydrogels beads generated by an anionic surfactant micelle templating for cationic dye uptake: Swelling, sorption and reusability studies. International Journal of Biological Macromolecules, 105: 1025-1042.

[7] Skelly, N.E. Husser, E.R. (1978). Determination of Acrylamide Monomer in Polyacrylamide and in Environmental Samples by High Performance Liquid Chromatography. Analytical Chemistry, 50:1959-1962.

[8] Andersen, F.A. (2005). Amended final report on the safety assessment of polyacrylamide and acrylamide residues in cosmetics. International Journal of Toxicolgy, 24:21-50.

International Conference on Nuclear Science and Technology
6- 8 MAY 2024 | Isfahan, Iran

Preparation and quality control of 177Lu-doped calcium phosphate-based ceramic material (Paper ID : 1098)

M. R. Aboudzadeh*, S. Attar Nosrati, M. Salahinejad, M. Amiri

Radiation Application Research School, Nuclear Science and Technology Research Institute, Tehran, Iran.

Corresponding author: **E-mail**: mraboudzadeh@aeoi,org,ir, **Fax/Tel**: +982188221119

Abstrat

The doping technique can used for direct radiolabeling of several radiopharmaceuticals with high efficiency and reliability. Calcium phosphate-based ceramic materials such as hydroxyapatite (HA) are promising molecules as a drug-delivery system for bone therapy applications since they possess a chemical composition similar to that of bones. In this research, ^{177}Lu-doped calcium phosphate-based ceramic material has been investigated as a theranostic agent for bone and joint disorders due to its excellent properties including biocompatibility, bioactivity, and affinity for bone tissues. The ceramic-based carrier molecule was successfully synthesized and characterized using different techniques to elucidate its chemical structure and physiochemical properties. The prepared carrier molecule was then radiolabeled via doping technique and quality control tests, i.e., radiochemical purity, stability, and biodistribution studies were performed on the resultant radiopharmaceutical. In the work reported herein, HA could be radiolabeled with ^{177}Lu through the dopping technique in high radiochemical purity (>99%). In vitro studies showed <5% loss of ^{177}Lu activity in normal saline and <10% in human serum for 7 days. The biodistribution studies in rats revealed complete retention of activity within the knee cavity with no measurable radioactivity leaching out of the joints over 96 hours, indicating excellent in vivo stability of the final product. These results demonstrated that the prepared radiopharmaceutical can be potentially used as diagnostic imaging, therapeutic agents or even theranostic combinations.

Keywords: Radiopharmaceutical, Radiosynovectomy, Calcium phosphate, ^{177}Lu

INTRODUCTION

Rheumatic disorders are conditions that affect the joints, tendons, muscles, ligaments, and bones. Bone tissue engineering has attracted great interest in the last few years, as the frequency

of tissue-damaging or degenerative diseases has increased exponentially [1]. The need for bioactive and non-toxic biomaterials is on high demand in tissue engineering applications nowadays. To obtain an ideal treatment solution, researchers have focused on the development of optimum biomaterials to be applied for the enhancement of bioactivity and the regeneration process, which are necessary to support the proper healing process of osseous tissues. Having unique physical and chemical properties, calcium phosphate-based ceramic materials such as hydroxyapatite become the center of interest for their potential uses in bone tissue engineering [2]. Hydroxyapatite which has a chemical formula of (HA, Ca10(PO4)6(OH)2) has similar physical and chemical characteristics to bone. This ceramic material displays favorable properties such as biodegradability, bioactivity, biocompatibility, slow-degradation, osteoconduction, osteointegration, and osteoinduction [3]. Its porous structure resembles native bone. The mentioned properties make it extensively useful in biomedical applications. One of the major challenges with using HA in engineering applications is its brittleness [4]. To overcome this problem, it's important to react to it with a material that can enhance its fragility. Several studies have reported that doping of hydroxyapatite with suitable cations can ultimately enhance its mechanical properties [5]. One of the applications of hydroxyapatite is in the radiosynovectomy procedure [6]. Radiosynovectomy is a therapy that relieves pain and inflammation from rheumatoid arthritis and related diseases. The biochemical aspects of ideal radiopharmaceutical used in this process include in-vivo stability, toxicity, target uptake, spatial and temporal distribution, retention, metabolism, clearance, and excretion within the body [7]. A radiosynovectomy agent contains a beta emitter radionuclide with sufficient penetrating power and appropriate half-life such as 90Y, 153Sm, 186,188Re, 165Dy, 166Ho, and 177Lu [8-11]. Several colloid materials were used as radionuclide carriers in the radiosynovectomy agents [12]. Among the biomaterials used as radionuclide carriers during the preparation of, radiosynovectomy agents hydroxyapatite has several advantages because of its excellent biocompatibility, bioactivity, and biodegradability. Several methods have been used for the radiolabeling of hydroxyapatite with radionuclides including the substitution of radionuclides with Ca2+ in HA structure and the incorporation of radionuclides into the structure of HA at the synthesis process and the doping [13, 14]. During the doping technique, the radionuclide is replaced with specific functional groups in the carrier molecule which leads to the production of radiopharmaceuticals with high efficiency, purity, and stability. In the

present research, we used the doping method for radiolabeling hydroxyapatite with ^{177}Lu as a novel radiopharmaceutical for use in the radiosynovectomy process.

EXPERIMENTAL

Materials and methods

$Ca(NO_3)_2.4H_2O$ and $(NH_4)_2HPO_4$ were of analytic grade and were purchased from Sigma-Aldrich. Acetic acid (HAc, 99.8%) was obtained from Merck. All other chemical reagents were purchased from Merck (Darmstadt, Germany). $^{153}LuCl_3$ solution was obtained from Pars Isotope Co., Iran. Chromatography paper, Whatman No. 2 was obtained from Whatman (Maidstone, UK). Radio-chromatography was performed by using a Bioscan AR-2000 radio TLC scanner instrument (Bioscan, Paris, France). A high-purity germanium (HPGe) detector coupled with a Canberra™ (model GC1020-7500SL) multichannel analyzer and a dose calibrator ISOMED 1010 (Dresden, Germany) were used for counting distributed activity in mice organs. All rats purchased from NSTRI weighing 180-220 g (n=5) were kept at routine day/night light program and were kept under common rodent diet pellets. Quantitative gamma counting was performed on an ORTEC Model 4001M γ-system well counter. The mean size distribution of the samples was analyzed using Zeta Sizer 3000HS (Malvern, UK).

Radiolabeling process of HA particles with ^{177}Lu

Lutetium-177-labeled HA particles were prepared using an HA cold kit. For the preparation of the HA Cold kit of HA, firstly HA particles were prepared by the co-precipitation method. For this purpose, 0.3 M calcium nitrate tetrahydrate [$Ca(NO_3)_2 \cdot 4H_2O$] solution (**A**) and diammonium hydrogen phosphate [$(NH_4)_2HPO_4$] solution (**B**) were prepared separately in such an amount to keep the molar ratio of Ca/P at 1.67 (Table 1).

Table 1. Molarity and molar ratio of elements present in HA synthesis.

Molarity ($g.mol^{-1}$)		Molar ratio
Ca^{2+}	PO_4^{3-}	Ca/P
0.5	0.3	1.67

After that, B was added gradually to A, which was followed by the formation of a white precipitate. Subsequently, the pH was set by NH_4OH (25%) solution to 10 and the mixture was stirred for 1 h at room temperature. Finally, the precipitate was collected by centrifugation at

2000 rpm for 5 min. After the supernatant was removed, the precipitate was washed 3–4 times with distilled water through vortexing and centrifuging. The HA Cold kit was obtained after freeze-drying. The particle size distribution of the as-synthesized sample was determined by Zetasizer. For this purpose, 0.01mg of sample was added to 20 ml of water and sonicated 2 ml of solution. The sample was transferred to a disposable cuvette for size measurement at room temperature. The result of the particle size distribution analysis of the sample is shown in Fig. 1. As it can be seen the sample has a particle size distribution between 5 and 10 μm with an average particle size of 7 μm which is desirable for radiosynovectomy applications [6].

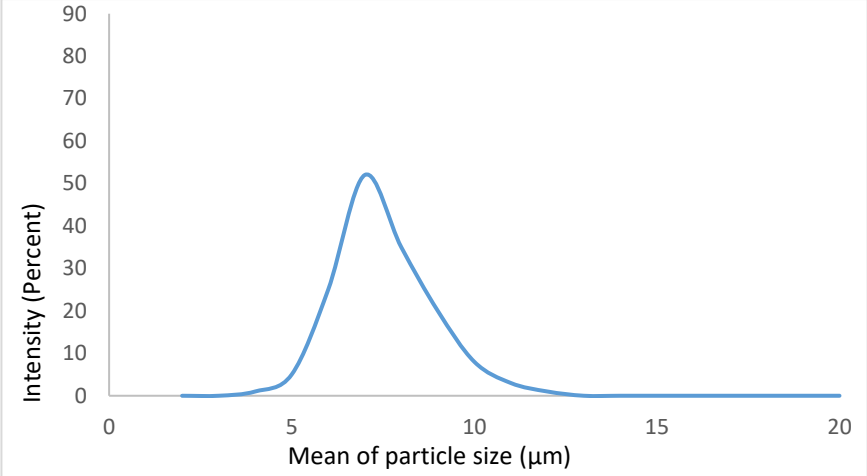

Fig. 1. Particle size distribution of as-synthesized hydroxyapatite.

For radiolabeling with ^{177}Lu, 1 mL of sterile normal saline solution was added to the prepared kit vial containing 5.0 ± 0.2 mg of HA particles resulting in a suspension of HA particles in a buffer solution of pH ~ 7.5, and vortex mixing was performed for 30 min at room temperature.

The radiolabeling with ^{177}Lu was conducted by the addition of ~ 0.37 GBq (10 mCi) of ^{177}Lu activity as a $^{177}LuCl_3$ solution to the reaction vial. The vial was sealed and then shaking was continued for 30 min. The pH of the reaction mixture was found to be ~ 7–8 which resulted in the formulation of the ^{177}Lu-HA with high radiochemical purity. The resulting suspension was centrifuged at 3000 rpm for 5 min. Subsequently, the supernatant was carefully separated from the precipitated ^{177}Lu-labeled HA particulates. The radiolabeled HA particles obtained as precipitate were subjected to further washing using 1 mL of sterile, pyrogen-free normal saline to ensure the removal of free ^{177}Lu activity. The washing step was repeated twice with 1 ml of saline and the washings were collected and counted for any leakage of radioactivity. The

radiolabeling efficiency was calculated as the fraction of radioactivity associated with the precipitate to the total radioactivity. Finally, the radiolabeled particulates with a specific activity of 2 mCi/mg were resuspended in sterile normal saline, autoclaved, and used for animal studies. The radiochemical purity of the ^{177}Lu-labeled HA particles was determined by following the procedure already reported [10].

Assessment of radiochemical purity

For measuring radiochemical purity, 1 µl of the prepared ^{177}Lu-HA was spotted on a chromatography paper (Whatman No. 2) and developed in 5 mM DTPA solution as a mobile phase. A similar test was carried out with $^{177}LuCl_3$ as blank. It was observed that ^{177}Lu-HA remained at its origin (Rf = 0.1), whereas unreacted $^{177}LuCl_3$ moved towards the solvent front (Rf = 0.8), due to the formation of ^{177}Lu-DTPA complex.

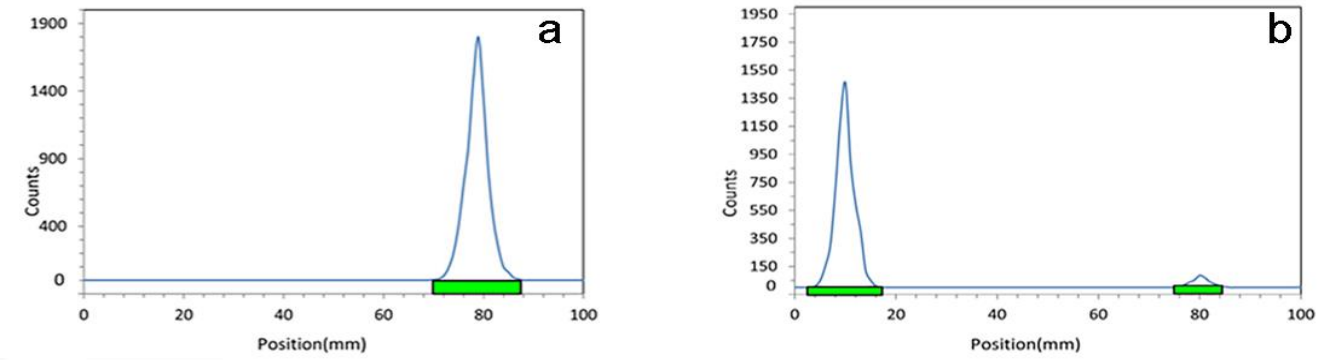

Figure 1. ITLC chromatograms of $^{177}LuCl_3$ solution (a) 177Lu-HA (b) on Whatman no. 2 paper using 5 mM DTPA solution.

Assessment of in-vitro stability

In-vitro stability of ^{177}Lu-labeled HA particles was studied in normal saline as well as in human serum. For this, an amount of 5 mg of the radiolabeled particles was suspended in 1 mL of normal saline and freshly isolated human serum. The suspensions were stored at 37°C for 21 days (>3 half-lives of ^{177}Lu). At the end of different time intervals, the radiochemical purities of the suspended ^{177}Lu-HA particles were determined by following the reported procedure [13].

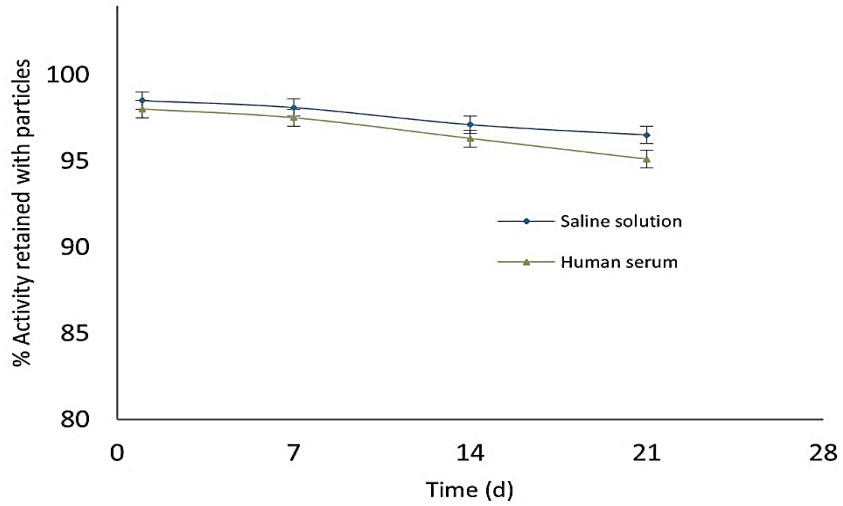

Figure 2. In vitro stability of ^{177}Lu-HA in saline and human serum.

Assessment of biodistribution

The biological behavior of ^{177}Lu-HA particles was ascertained by carrying out biodistribution and imaging studies in rats. All animal studies were performed in compliance with approved protocols by the Animal Care and Use Committee at the Nuclear Science and Technology Research Institute (NSTRI). To determine the accumulation of prepared radiopharmaceutical in the intraarticular cavity, Doses of 100 ± 2 μCi /0.1 mL of final ^{177}Lu-HA suspension were injected intra-articularly in one joint knee was injected intraarticularly into one knee joint of wild-type rats, each weighing 200–300 g (n = 4).

The animals were sacrificed 4-, 24-, 48-, and 96 hours post-injection. Different organs and the injected knee were excised and counted. The uptake by different organs/tissues was calculated from these data and expressed as a percentage injected dose per gram (%ID/g) to determine the retention and leakage of the activity from the knee (synovium). (Fig. 3).

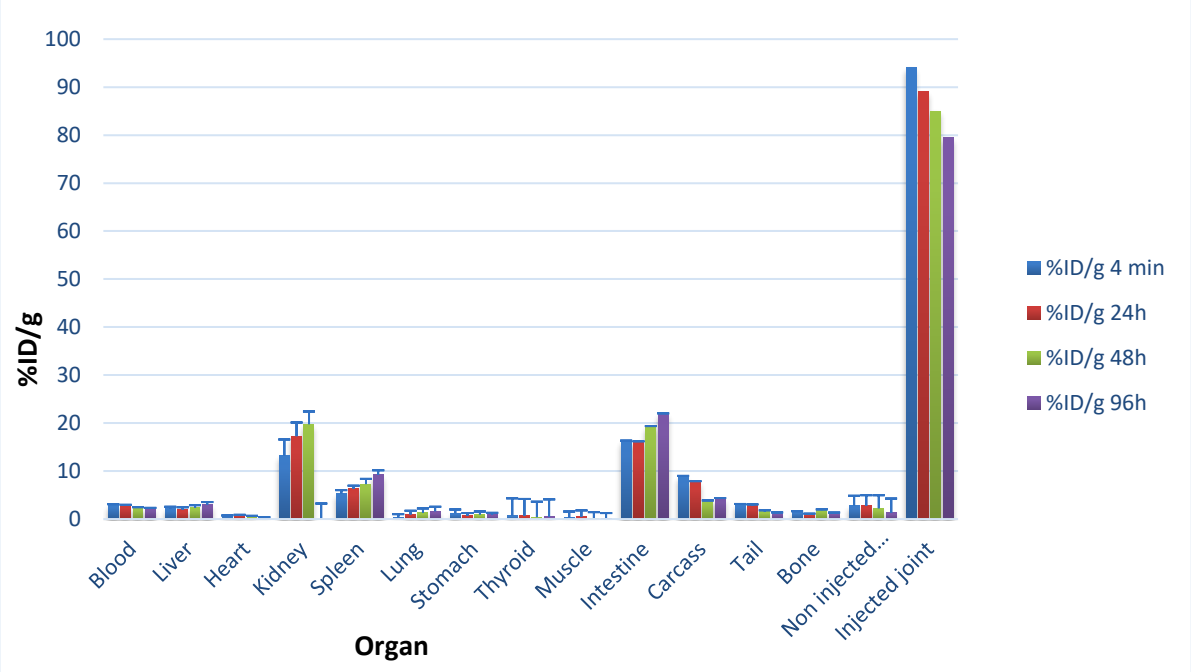

Fig.3. Percentage of injected dose per gram of tissues (ID/g %) at 4, 24, 48, and 96 hours after injection of ^{177}Lu-HA in wild-type rats (n=4 animals per time point). All values were expressed as mean±standard deviation (mean±SD).

Results and discussion

In the present study hydroxyapatite as a calcium phosphate-based ceramic material was successfully radiolabeled with ^{177}Lu through a simple and efficient method with a labeling yield of 98%. The radiochemical purity of ^{177}Lu-HA colloid was further ascertained by employing the ITLC technique on Whatman No. 2 paper using 5 mM DTPA solution as a mobile phase. As expected, the R_f values of ^{177}Lu-HA and free $^{177}LuCl_3$ in the solvent system were 0.0–0.2 and 0.7–0.9, respectively [15]. The paper chromatography patterns of $^{177}LuCl_3$ (blank) and ^{177}Lu-HA are shown in Fig. 1(a) and Fig. 1(b), respectively. The calculated radiochemical purity was over 98%.

The in-vitro stability of radiolabeled HA was studied over 21 days. It was found that 97% and 95% of activity remained bound to particles incubated in normal saline and human serum, respectively (Fig. 2). This finding confirmed excellent in vitro stability of the prepared radiopharmaceutical in saline and human serum up to 21 days (>3 half-lives of ^{177}Lu), at 37°C. Fig. 3 shows selected organ or tissue activity distribution, after 4, 24, 48, and 96 hours of ^{177}Lu-HA intraarticular administration to wild-type rats. The results of the biodistribution studies

showed retention of 80% of the injected activity within the joint cavity even after 96 hours and negligible activity was detected in blood and other organs/tissues indicating the adequate intra-articular distribution of the radiopharmaceutical (Fig. 3). The blood activity content at all time intervals confirms removal of activity in the circulation. while the activity of the lung, heart, stomach, thyroid, muscle, bond, and tail is low at all time intervals. In the case of the kidney, a gradual increase in activity was observed which suggests the urinary elimination of the radiopharmaceutical. Gradual increases in activity content over time were also observed in the intestine which indicates the elimination of the compound from the digestive tract. It can be seen from the results that almost all the injected activity remained at the site of injection even after 96 h post-injection and minimal leakage from the synovial membrane which confirms the excellent in-vivo stability of the radiopharmaceutical. These results demonstrated the superior efficacy of this compound compared to other similar radiosynovectomy agents. The advantages of this agent are firstly related to the ^{177}Lu radioisotope that emits gamma rays with moderate energy and sufficient abundance to enable direct imaging while avoiding radiation exposure of personnel. Another advantage of ^{177}Lu over the other beta emitters includes decreased damage to non-target tissues owing to the shorter beta particle range and the potential for reduced marrow toxicity coupled with increased energy deposition to target because of the better match between physical half-life and biological half-life of the radiolabeled particles. On the other hand, in the present study, ^{177}Lu-HA radiopharmaceutical was prepared through the doping method, in which ^{177}Lu can be stably and effectively incorporated into the HA particles leading to the preparation of a compound with high efficiency, purity, and stability. [6-10].

Conclusions

In this study, ^{177}Lu-HA as a new possible agent for radiosynovectomy has been designed and prepared through an efficient and reliable method with high radiolabeling yield (98%) and characterized using different methods for evaluation of its physicochemical characteristics. The prepared radiopharmaceutical demonstrates high radiochemical purity (99.6%) and high in vitro stability in either saline or human serum up to three half-lives of the radionuclide. The Biodistribution experiments showed good localization in the synovium revealing no leaching of the activity from the synovial joints over three days and consequently high in-vivo stability of the prepared radiopharmaceutical. These studies demonstrated that the prepared ^{177}Lu-HA offers potential as a therapeutic radiopharmaceutical for use in radiosynovectomy procedures.

References

[1] Valesan, L. F., Da-Cas, C. D., Réus, J. C., Denardin, A. C. S., Garanhani, R. R., Bonotto, D., de Souza, B. D. M. (2021). Prevalence of temporomandibular joint disorders: a systematic review and meta-analysis. Clinical Oral Investigations, 25(2), 441-453.

[2] Mondal, S., Park, S., Choi, J., Vu, T. T. H., Doan, V. H. M., Vo, T. T., Oh, J. (2023). Hydroxyapatite: A journey from biomaterials to advanced functional materials. Advances in Colloid and Interface Science, 321, 103013.

[3] Attar Nosrati, S., Alizadeh, R., Ahmadi, S. J., & Erfani, M. (2020). Optimized precipitation process for efficient and size-controlled synthesis of hydroxyapatite–chitosan nanocomposite. Journal of the Korean Ceramic Society, 57(6), 632-644.

[4] Ofudje, E. A., Akande, J. A., Sodiya, E. F., Ajayi, G. O., Ademoyegun, A. J., Al-Sehemi, A. G., Bakheet, A. M. (2023). Bioactivity properties of hydroxyapatite/clay nanocomposites. Scientific Reports, 13(1), 19896.

[5] Ratha, I., Datta, P., Balla, V. K., Nandi, S. K., & Kundu, B. (2021). Effect of doping in hydroxyapatite as coating material on biomedical implants by plasma spraying method: A review. Ceramics International, 47(4), 4426-4445.

[6] Davarpanah, M. R., Khoshhosn, H. A., Harati, M., Attar Nosrati, S., Zoghi, M., Mazidi, M. R., & Ghannadi Maragheh, M. (2014). Optimization of fundamental parameters in routine production of 90Y-hydroxyapatite for radiosynovectomy. Journal of Radioanalytical and Nuclear Chemistry, 302, 69-77.

[7] Chojnowski, M. M., Owczarczak, D., Płazińska, M. T., Dedecjus, M., & Królicki, L. (2023). Radiosynovectomy of the hip joint - preliminary experience. Reumatologia, 61(3), 186-190.

[8] Markou, P., & Chatzopoulos, D. (2009). Yttrium-90 silicate radiosynovectomy treatment of painful synovitis in knee osteoarthritis. Results after 6 months. Hellenic journal of nuclear medicine, 12, 33-36.

[9] Shamim, S., Kumar, R., Halanaik, D., Kumar, A., Shandal, V., Shukla, J., Malhotra, A. (2010). Role of rhenium-188 tin colloid radiosynovectomy in patients with inflammatory knee joint conditions refractory to conventional therapy. Nuclear medicine communications, 31, 814-820.

[10] Attar Nosrati, S., Alizadeh, R., Ahmadi, S. J., & Erfani, M. (2020). Design, synthesis and characterization of hydroxyapatite-chitosan nanocomposite radiolabelled with ^{153}Sm as radiopharmaceutical for use in radiosynovectomy. Radiochimica acta, 108(1), 57-65.

[11] Vimalnath, K. V., Chakraborty, S., Rajeswari, A., Sharma, K. S., Sarma, H. D., Ningthoujam, R. S., Dash, A. (2017). Formulation, Characterization and Bio-evaluation of Holmium-166 labeled Agglomerated Iron Oxide Nanoparticles for Treatment of Arthritis of Knee Joints. Materials Today: Proceedings, 4(2, Part C), 4329-4338.

[12] Liepe, K. (2015). Radiosynovectomy in the Therapeutic Management of Arthritis. World Journal of Nuclear Medicine, 14, 10.

[13] Baskaran, T., Mohammad, N. F., Shuhadah, S., Mohd Nasir, N., & Diana, F. (2021). Synthesis Methods of Doped Hydroxyapatite: A Brief Review. Journal of Physics: Conference Series, 2071, 012008.

[14] Piecuch, A., Targońska, S., Rewak-Sorczyńska, J., Ogórek, R., & Wiglusz, R. J. (2023). New silicate-substituted hydroxyapatite materials doped with silver ions as potential antifungal agents. BMC Microbiology, 23(1), 193.

[15] Li, J., Zhang, L., Li, W., Lei, C., Cao, Y., Wang, Y., . . . Pang, H. (2020). Preparation and SPECT/CT Imaging of 177Lu-Labeled Peptide Nucleic Acid (PNA) Targeting CITED1: Therapeutic Evaluation in Tumor-Bearing Nude Mice. OncoTargets and Therapy, 13(null), 487-496.

ICNST 2024
International Conference on Nuclear Science and Technology
6- 8 MAY 2024 | Isfahan, Iran

The Response Surface Modeling (RSM) Optimization of the Radiolabeling Process of 177Lu-hydroxyapatite as a Potential Radiosynovectomy Agent (Paper ID : 1099)

M.R. Aboudzadeh*, M. Salahinejad, S. Attar Nosrati, A. Roozbahani

Nuclear Science and Technology Research Institue, Tehran, Iran
Corresponding author: **E-mail**: mraboudzadeh@aeoi,org,ir, **Fax/Tel**: +982188221119

Abstract

^{177}Lu labeled hydroxyapatite is a potential substance for use in radiosynovectomy of tiny joints. The radiochemical yield (RCY) and, consequently, the quality of the final product is directly impacted by the parameters of the radiolabeling process during the design and production of radiopharmaceuticals, necessitating exact optimization. In this study, response surface methodology (RSM)-based Box-Behnken design (BBD) is utilized to develop prediction models and examine the impact of critical factors in the radiolabeling of hydroxyapatite (HA) using ^{177}Lu radionuclide. The initial ^{177}Lu radionuclide concentration (0.12-0.32), pH (3-9), radiolabeling reaction time (10-25), and temperature (20-40) were the factors that directly impacted the labeling reaction. At the starting concentration of ^{177}Lu radionuclide = 0.132 (GBq), pH = 6.4, and temperature = 39.5 (^{o}C), the greatest radiochemical yield (>98%) is determined by carrying out the RSM.

Keywords: Radiolabeling, Radiochemical yield, ^{177}Lu-hydroxyapatite, Response surface methodology (RSM)

INTRODUCTION

Radiosynovectomy, a new method of treating various acute and chronic inflammatory joint diseases, is one of the therapeutic uses of radiopharmaceuticals by injecting beta-emitting particles into the joint. Radiosynovectomy has provided a safe, rapid, and patient-friendly reconstructive option for the treatment of various types of joint diseases [1-3]. Among the various particles used in radiosynovectomy, hydroxyapatite biomaterial has several advantages, such as biocompatibility, biodegradability, bioactivity, relatively simple synthesis protocol, and easy functionality [4-6]. Hydroxyapatite (HA) can be appropriately radiolabeled with lanthanide radionuclides by an ion exchange mechanism [7].

The radionuclide ^{177}Lu can be used as a suitable beta-emitting radionuclide for the development of radiosynovectomy agents due to its favorable degradation and easy radiolabeling properties [8]. In arrange to plan a high-quality radiopharmaceutical, careful control and validation of the radiolabeling process is required, which is the foremost basic step in radiopharmaceutical manufacturing [9]. The development and production of radiopharmaceuticals always requires a high radiochemical yield (RCY), which directly reflects radiochemical purity.

Response surface methodology (RSM) is a multivariate method that estimates the relationship between independent variables and responses through empirical modeling using a variety of appropriate mathematical and statistical procedures [10]. RSM methods have attracted great interest in both research and industry due to its advantages of requiring fewer tests, less time and overhead to generate experimental information, to identify ideal conditions for important preparation variables, and to to accurately predict the observed responses [11, 12]. A widely used RSM method for the optimization of many phenomena is the Box-Behnken design (BBD) method, a class of rotation or near-rotation quadratic designs based on three-level incomplete factorial designs [13, 14].

In this study, several experiments were performed based on the Box-Behnken design-response surface methodology (BBD-RSM) to collect the output variables such as radioactive concentration of radionuclide, pH, reaction time, and reaction temperature as a function of radiochemical yield (RCY) during radiolabeling process of ^{177}Lu-hydroxyapatite radiopharmaceutical preparation.

RESEARCH THEORIES

EXPERIMENTAL DESIGN OPTIMIZATION

The aim of this study was to utilize the BBD-RSM method as a statistical tool to determine the optimal values for radiolabeling parameters in order to achieve an effective and optimized process of radiolabeling hydroxyapatite with ^{177}Lu-radionuclide. The Box-Behnken designs are rotatable or nearly rotatable and require 3 levels for each factor. However, they have limited capability for orthogonal blocking compared to central composite designs [15].

A four-factor three-level BBD with four center points was adopted to conduct 29 experiments taking into consideration given parameters. The response obtained from the BBD is used to construct the best second-order polynomial quadratic regression equation given in Equation 1:

$$Y = \beta_0 + \sum_{i=1}^{n} \beta_i X_i + \sum_{i=1}^{n} \beta_{ii} X_i^2 + \sum_{i=1}^{n} \sum_{j>1}^{n} \beta_{ij} X_i X_j + \varepsilon \quad (1)$$

No	Radionuclide concentration	pH	Temperature	Time	RCY-Exp	RCY--Pred
1	0.287	3	20	10	72.81	75.85
2	0.287	9	20	10	78.13	79.01
3	0.204	9	40	15	82.37	79.58
4*	0.204	6	30	25	98.03	98.11
5	0.12	9	20	20	94.22	94.51
6	0.287	3	40	20	67.35	68.92
7	0.204	6	40	15	98.1	98.11
8	0.12	9	40	20	93.07	94.08
9	0.204	3	40	15	81.87	76.11
10*	0.204	6	30	25	98.7	98.11
11	0.12	9	40	10	89.17	89.59
12*	0.204	6	40	15	97.7	98.11
13	0.287	3	20	20	76.37	80.29
14	0.12	9	20	10	92.55	95.02
15	0.12	3	20	20	93.9	94.5
16	0.204	6	20	15	92.29	91.39
17	0.12	3	40	20	90.21	93.78
18*	0.204	6	30	25	98.6	98.11
19	0.204	6	40	5	90.83	86.18
20	0.204	6	40	15	97.23	98.11
21*	0.204	6	30	25	98.2	98.11
22	0.204	6	40	25	99.01	95.11
23	0.12	3	20	10	91.88	90.96
24	0.287	9	40	20	62.95	68.33
25	0.287	9	20	20	79.4	79.4
26	0.287	3	40	10	55.35	59.48
27	0.12	3	40	10	81.15	85.23
28	0.204	6	40	15	82.28	74.59
29	0.287	9	40	10	59.44	62.93

*center point

Here, Y is the dependent variable (RCY,%), β_0 is a constant coefficient, β_{ij} is the coefficient of the linear terms indicating the interaction of the variables, and β_{ii} represents the quadratic coefficients. The X terms are coded values that represent independent variables, namely radionuclide concentration (GBq), pH, time (min), and temperature (°C).

The influence of the parameters and their interaction on the answer was examined using significance tests and analysis of variance (ANOVA) on each response to ensure the model's goodness of fit. The regression analysis of the experimental data, response surfaces, and contour plot at the ideal condition were all plotted with Minitab (Minitab Inc., State College, USA). Table 1 shows the anticipated values for each independent variable, as well as the experimental value for the only response variable, radiochemical yield.

Table 1. Experimental design matrix for the four-factor three-level BBD.

MODEL VALIDATION

The accuracy of fitted linear and nonlinear models is evaluated using coefficients of determination (R^2), coefficients of determination for prediction (R^2_{pred}), relative standard error of prediction (REP), root mean square error of prediction (RMSEP), and mean square error (MSE). The F-test was employed to confirm the statistical significance [16, 17]. The 95% confidence interval's probability value (P-value) was used to assess the significant model terms.

EXPERIMENTAL

Acetic acid (HAc, 99.8%) obtained from Merck. All the chemicals used were of analytical grade and obtained from Merck (Darmstadt, Germany). $^{177}LuCl_3$ solution obtained from Pars Isotope Co. Hydroxyapatite particles used in this research were synthesized in our laboratory according to the procedure reported earlier [5]. Radio-chromatography was performed by using a Bioscan AR-2000 radio TLC scanner instrument (Bioscan, Paris, France). Quantitative gamma counting was performed on an ORTEC Model 4001M γ-system well counter.

The radiolabeling of hydroxyapatite with ^{177}Lu was carried out based on previous work [18]. A reaction vial was prepared by transferring 40 mg of hydroxyapatite precursor and dissolving it in 1 ml of normal saline solution. The mixture was stirred vigorously for 5 minutes at room temperature to ensure complete dispersion of hydroxyapatite particles. The desired volume of ^{177}LuCl3 solution, containing the required activity of ^{177}Lu radionuclide, was then added to the reaction vial to determine the optimal quantity for the labeling procedure. The pH of the mixture was adjusted using 0.1 M HCl and 0.1 M NaOH solutions. The vial was sealed and continuously stirred for different time intervals to determine the optimum time for the radiolabeling procedure. The effect of reaction temperature on radiolabeling yield was also investigated by applying different temperatures during stirring. The ^{177}Lu-labeled hydroxyapatite particles were separated by centrifuging the suspension at 3000 rpm for 5 minutes. The radiochemical yield was calculated as a percentage of the radioactivity (GBq) associated with the precipitate to the initial radioactivity (GBq) used in the process.

RESULTS AND DISCUSSION

The first and most essential output data of the radiolabeling process is the yield, which measures the operation's quality and efficacy [19]. The "radiochemical yield" is the ability of

a radiopharmaceutical vector to form a radionuclide complex and according to nomenclature guidelines, the RCY [%] was calculated by dividing the product activity (AP) by the initial beginning activity (A_i). Thus, the following equation was used to compute the radiochemical yield:

$$RCY = A_p/A_i \times 100 \qquad (2)$$

A_p is the amount of activity in the product, A_i starting activity used in the synthesis process.
It has been found that during radiolabeling process, different reaction parameters directly affect the final RCY [18, 20]. The parameters which can notably affect the radiolabeling efficiency are the initial radioactivity of the radionuclide, pH, time and temperature of radiolabeling reaction [21].

BBD Optimization, ANOVA AND COEFFICIENT ESTIMATION

The experimental conditions for optimization of ^{177}Lu-hydroxyapatite radiolabeling was carried out according to the four-factor three-level BBD in which radionuclide concentration, pH, temperature and reaction time were used as variable parameters. The experimental runs are mentioned in Table 1.
To determine the importance of the model coefficients, 29 BBD experiments were conducted to analyze the coefficients of each model using linear and quadratic regression analysis with ANOVA. The P-values demonstrate the significance of each coefficient, as well as the intensity of the interaction between the independent variables. Table 1 presents the analysis of variance (ANOVA) for the suggested second-order model and coefficients for significant terms for the %RCY of ^{177}Lu-hydroxyapatite process. The coefficient of determination (R^2) for the model was 0.944, indicating that 94% of the response variability could be explained by the model. Agreeing to the model, C_{rad}, pH, and temperature all had a noteworthy affect on RCY (p=0.00), but response time had a negligible affect (p=0.29>p=0.05). Each of these components impacts RCY favorably and appear a positive impact on RCY. Quadratic terms for temperature, pH, and Crad too had a noteworthy affect (p= 0.00) on RCY and illustrated a negative relationship with RCY. Time's square term had no recognizable affect (p=0.05). In any case, as it were the Crad×Temp term appeared a noteworthy impact (p=0.03< p=0.05) among the interaction terms (Crad×pH, Crad ×Time, pH×Temp, and Temp×Time) and uncovered a negative affect on RCY.

The response surface plots shown in Figure 1 provide a clear visual representation of the impact of key factors and their interactions with each other on RCY. Visual inspection of the surfaces shows how the following performance factors interact with each other: Crad×pH, Crad×Temp, and pH×Temp. It is clear that increasing the radionuclide concentration, pH and temperature leads to an increase in the RCY ratio. pH is an important factor that greatly influences the ionic strength, solubility, and participation of radiometals in radiolabeling reactions [7]. The results show that the initial radioactivity of the radionuclide is an important factor influencing the radiolabeling process of ^{177}Lu-hydroxyapatite [22].

This emerges from explanations that support the overall findings that pH plays a critical role in the radiolabeling of hydroxyapatite with ^{177}Lu [23]. It can be assumed that increasing the temperature leads to a higher effective collision rate between HA molecules and the ^{177}Lu isotope, thus increasing the efficiency of the reaction [20]. The maximum radiochemical yield is found at the initial concentration of radionuclide= 0.128 (GB_q), pH=6.4 and temperature=38.9 (^oC).

RESPONSE SURFACE PLOTS

The response surface plots shown in Figure 1 provide a clear visual representation of the impact of key factors and their interactions with each other on RCY. Visual inspection of the surfaces shows how the following performance factors interact with each other: Crad×pH, Crad×Temp, and pH×Temp. It is clear that increasing the radionuclide concentration, pH and temperature leads to an increase in the RCY ratio. pH is an important factor that greatly influences the ionic strength, solubility, and participation of radiometals in radiolabeling reactions [7]. The results show that the initial radioactivity of the radionuclide is an important factor influencing the radiolabeling process of ^{177}Lu-hydroxyapatite [22].

This emerges from explanations that support the overall findings that pH plays a critical role in the radiolabeling of hydroxyapatite with ^{177}Lu [23]. It can be assumed that increasing the temperature leads to a higher effective collision rate between HA molecules and the ^{177}Lu isotope, thus increasing the efficiency of the reaction [20].

Table 1. Analysis of variance (ANOVA) for the suggested second-order model and coefficients for significant terms for the %RCY of ^{177}Lu-hydroxyapatite process.

Source	Df	Seq SS	MS	F	P	Coefficient ±SE	T
Regression	14	4878.05	4878.05	17.43	0.002		
Linear	4	3066.22	612.14	7.66	0.003		
Crad	1	2505.13	222.53	11.13	0.002	368.00±110.28	3.34
pH	1	18.03	398.34	19.93	0.001	29.73±6.66	4.47
Temp	1	423.36	249.95	12.51	0.002	5.15±1.46	3.54
Time	1	119.71	23.72	1.19	0.29		
Square	4	1655.29	1655.29	20.71	0.005		
C_{rad}×*Crad*	1	586.66	835.60	41.81	0.008	-779.97±120.62	-6.47
pH×*pH*	1	597.74	734.52	36.75	0.011	-2.25±0.37	-6.06
Temp×*Temp*	1	371.09	408.73	20.45	0.008	-0.07±0.02	-4.52
Time×*Time*	1	99.80	99.80	4.99	0.058		
Interaction	6	156.53	156.53	1.31	0.31		
Crad×*pH*	1	0.81	0.81	0.04	0.84		
Crad×*Temp*	1	113.42	113.42	5.68	0.03		
Crad×*Time*	1	0.81	0.81	0.04	0.84		
pH×*Temp*	1	0.09	0.09	0.00	0.95		
pH×*Time*	1	16.40	16.40	0.82	0.38		
Temp×*Time*	1	25.00	25.00	1.25	0.28		
Residual Error	16	319.76	319.76				
Lack-of-Fit	10	318.13	318.13	117.21	0.32		
Pure Error	6	1.63	1.63				
Total	30	5197.81	4878.05	17.43	0.00		

R^2=0.944, $R^2_{pred=}$ 0.674, REP= 4.470, RMSEP= 13.45, MSE= 12.36

To ensure model adequacy, the difference between experimental and predicted responses was calculated using a residual analysis. Model adequacy requires that the relationship between the residual and observation order do not follow a regular pattern. Figure 2 shows a very strong convergence between anticipated and experimental results. It is worth noting that the plot displays both the consistency of the variance analysis and the regression model's validity. The scatter plot of experimental versus calculated values, which are predicted by RSM model, of radiochemical yield (RCY) displays in Figure 2C.

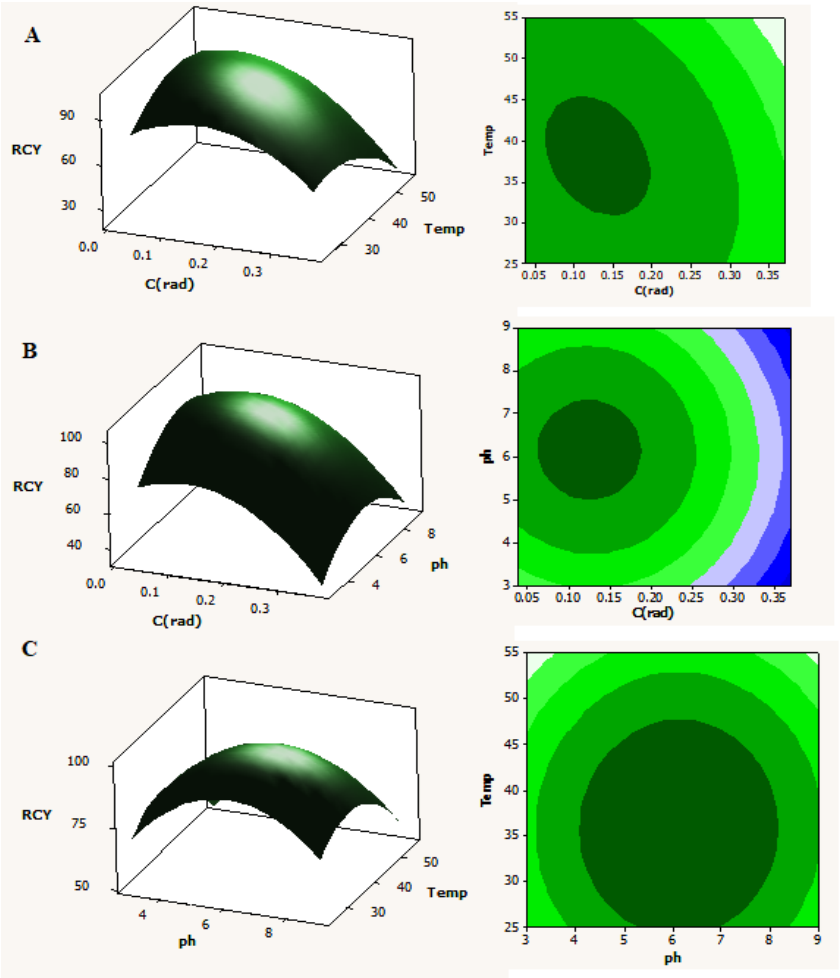

Figure 1. Response surface plot and a contour-lines map displaying: (A) the effects of C_{rad}, pH, and their mutual effect on the radiochemical yield while the Temp and Time are at center level; (B) the effect of C_{rad}, Temp, and their mutual effect on the RCY while pH and Time are at center level; (C) the effect of pH and Temp, and their mutual effect on the RCY while C_{rad} and Time are at center level.

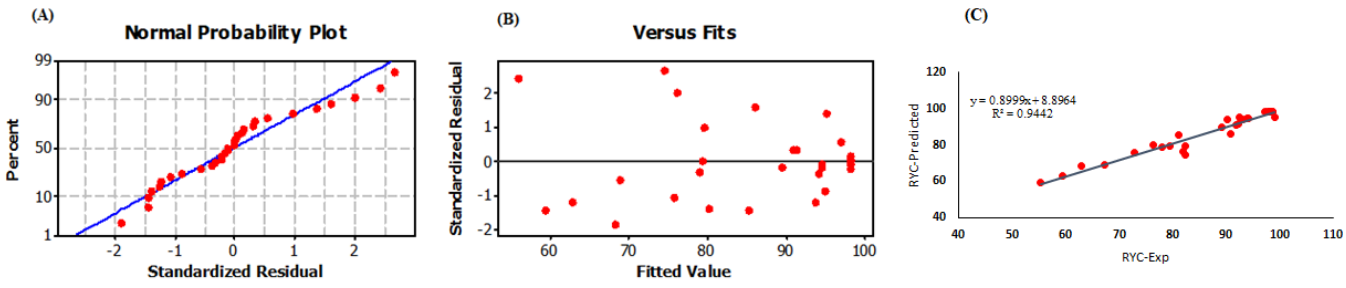

Figure 2. The normal probability plot of (A) residuals, (B) residuals vs predicted response, and (C) predicted versus experimental values for radiochemical yield (RCY).

CONCLUSIONS

The study utilized a Box-Behnken design (BBD) based on response surface methodology (RSM) to create prediction models and examine the impact of critical variables in the radiolabeling of hydroxyapatite (HA) with the ^{177}Lu radionuclide. One of the key advantages

of using multivariate optimization methods over traditional methods in radiation-related activities, such as the production of radiopharmaceuticals, is the ability to generate more data with fewer experiments, leading to improved optimization and production. This is particularly important for ensuring worker safety and health.

REFERENCES

[1] W.U. Kampen, B. Boddenberg-Pätzold, M. Fischer, M. Gabriel, R. Klett, M. Konijnenberg, E. Kresnik, H. Lellouche, F. Paycha, L. Terslev, C. Turkmen, F. van der Zant, L. Antunovic, E. Panagiotidis, G. Gnanasegaran, T. Kuwert, T. Van den Wyngaert, E. Bone (2022), The EANM guideline for radiosynoviorthesis, European Journal of Nuclear Medicine and Molecular Imaging, 49, 681-708.

[2] N. Lepareur, B. Ramée, M. Mougin-Degraef, M. Bourgeois (2023), Clinical Advances and Perspectives in Targeted Radionuclide Therapy, Pharmaceutics 15, 1733.

[3] E.C. Rodriguez-Merchan, H. De la Corte-Rodriguez, M.T. Alvarez-Roman, P. Gomez-Cardero, V. Jimenez-Yuste (2022), Radiosynovectomy for the Treatment of Chronic Hemophilic Synovitis: An Old Technique, but Still Very Effective, Journal of Clinical Medicine, 11, 7475.

[4] B. Ghiasi, Y. Sefidbakht, S. Mozaffari-Jovin, B. Gharehcheloo, M. Mehrarya, A. Khodadadi, M. Rezaei, S.O. Ranaei Siadat, V. Uskoković (2020), Hydroxyapatite as a biomaterial - a gift that keeps on giving, Drug development and industrial pharmacy, 46, 1035-1062.

[5] S. Attar Nosrati, R. Alizadeh, S.J. Ahmadi, M. Erfani (2020), Optimized precipitation process for efficient and size-controlled synthesis of hydroxyapatite–chitosan nanocomposite, Journal of the Korean Ceramic Society, 57, 632-644.

[6] J.F. Cawthray, A.L. Creagh, C.A. Haynes, C. Orvig (2015), Ion exchange in hydroxyapatite with lanthanides, Inorganic Chemistry, 54, 1440-1445.

[7] M. C. De Lama-Odría, L. J. del Valle, J. Puiggalí (2023), Lanthanides-Substituted Hydroxyapatite for Biomedical Applications, International Journal of Molecular Sciences, 24 3446.

[8] T. Das, S. Banerjee (2016), Theranostic Applications of Lutetium-177 in Radionuclide Therapy, Current Radiopharmaceuticals, 9, 94-101.

[9] F. Bartoli, P. Elsinga, L.R. Nazario, A. Zana, A. Galbiati, J. Millul, F. Migliorini, S. Cazzamalli, D. Neri, R. Slart, P.A. Erba (2022)., Automated Radiosynthesis, Preliminary In Vitro/In Vivo Characterization of OncoFAP-Based Radiopharmaceuticals for Cancer Imaging and Therapy, Pharmaceuticals (Basel, Switzerland), 15, 958.

[10] A.I. Khuri, S. Mukhopadhyay (2010), Response surface methodology, Wiley Interdisciplinary Reviews: Computational Statistics, 2, 128-149.

[11] M. Salahinejad, F. Aflaki (2011, Optimization and determination of Cd (II) in different environmental water samples with dispersive liquid–liquid microextraction preconcentration combined with inductively coupled plasma optical emission spectrometry, Environmental Monitoring and Assessment, 177, 115-125.

[12] Z. Tamiji, M. Salahinejad, A.J.C.P.A. Niazi (2020, Optimized Vortex-Assisted Dispersive Liquid–Liquid Microextraction Coupled with Spectrofluorimetry for Determination of Aspirin in Human Urine: Response Surface Methodology, Current Pharmaceutical Analysis, 16, 201-209.

[13] J. Jaynes, X. Ding, H. Xu, W.K. Wong, C.M. Ho (2013), Application of fractional factorial designs to study drug combinations, Statistics in Medicine, 32, 307-318.

[14] N. Szpisják-Gulyás, A.N. Al-Tayawi, Z.H. Horváth, Z. László, S. Kertész, C. Hodúr (2023), Methods for experimental design, central composite design and the Box–Behnken design, to optimise operational parameters: A review, Acta Alimentaria, 52, 521-537.

[15] D. R. Pinheiro, R. F. Neves, S. P.A. Paz (2021), A sequential Box-Behnken Design (BBD) and Response Surface Methodology (RSM) to optimize SAPO-34 synthesis from kaolin waste, Microporous and Mesoporous Materials, 323, 111250.

[16] E. Breck, N. Polyzotis, S. Roy, S. Whang, M. Zinkevich (2019), Machine Learning Systems.

[17] D. Maulud, A.M. Abdulazeez (2020), A review on linear regression comprehensive in machine learning, Journal of Applied Science and Technology Trends,1, 140-147.

[18] M.R. Davarpanah, H.A. Khoshhosn, M. Harati, S. Attar Nosrati, M. Zoghi, M.R. Mazidi, M. Ghannadi Maragheh (2014), Optimization of fundamental parameters in routine production of 90Y-hydroxyapatite for radiosynovectomy, Journal of Radioanalytical and Nuclear Chemistry, 302, 69-77.

[19] B. Erik de, Z. Rory de, B. Wouter (2017), Radiochemical and analytical aspects of inter-institutional quality control measurements on radiopharmaceutical, Journal of Nuclear Medicine, 58, 259.

[20] M. Chochevska, M. Velichkovska, M. Atanasova Lazareva, K. Kolevska, F. Jolevski, J. Razmoska, Z. Filipovski, S. Nikolovski, M. Zdraveska Kocovska (2023), Ugrinska, Evaluation of factors with potential influence on [18F]FDG radiochemical synthesis yield, Applied Radiation and Isotopes, 199, 110900.

[21] Z. Talip, C. Favaretto, S. Geistlich, M. Nicholas (2020), A step-by-step guide for the novel radiometal production for medical applications: case studies with 68Ga, 44Sc, 177Lu and 161Tb, Molecules, 25, 966.

[22] A. Larenkov, I. Mitrofanov, E. Pavlenko, M. Rakhimov (2023), Radiolysis-Associated Decrease in Radiochemical Purity of 177Lu-Radiopharmaceuticals and Comparison of the Effectiveness of Selected Quenchers against This Process, Molecules, 28, 1884.

[23] S. Attar Nosrati, R. Alizadeh, S.J. Ahmadi, M. Erfani (2020), Design, synthesis and characterization of hydroxyapatite-chitosan nanocomposite radiolabelled with 153Sm as radiopharmaceutical for use in radiosynovectomy, Radiochimica Acta, 108, 57-65.

ICNST 2024
International Conference on Nuclear Science and Technology
6- 8 MAY 2024 | Isfahan, Iran

A simulation study on the presence of GNPs in healthy tissues during photon radiotherapy (Paper ID : 1105)

Fatemeh S. Rasouli *, S. Farhad Masoudi

Department of Physics, K.N. Toosi University of Technology, P.O. Box 15875-4416, Tehran, Iran

Abstract

Due to their unique properties, gold nanoparticles (GNPs) are used for a wide range of applications such as improvement of radiotherapeutic performance. Our previous reports emphasize the importance of accurate modeling of the distribution of GNPs in the tissue on the results since the experimental documents show that the injected nanoparticles tend to heterogenetically disperse in the medium and accumulate around the cell nucleus. The present study is devoted to investigating the importance of considering GNPs around the cells (including the nucleus and cytoplasm) of the tissues surrounding the tumor in radiotherapy performance, which has been neglected so far. To this aim, the MCNPX code was used to simulate a three-layer phantom containing sets of various concentrations with ratios of 1:0.5:0.25 of 50/100 nm GNPs irradiated by 10-100 keV photons. The results show that the presence of GNPs in the non-target layers considerably changes the criterion parameter by about 14% to 330%.

Keywords: Gold Nanoparticles, Radiotherapy, DEF, Monte Carlo simulation, cytoplasm

INTRODUCTION

Gold nanoparticles (GNPs) have been proposed for use for a wide range of medical applications, including providing better penetration ability for substances used for therapy and diagnosis with lower risk compared to conventional drugs. As another case, in photon radiation therapy, due to the dominance of the photoelectric interaction between kilovoltage photons and high-Z constituent atoms of GNPs, the produced secondary electrons cause the increment in the energy deposited to the target and improve the radiotherapeutic performance. This issue has been investigated by in-vivo and in-vitro experiments, as well as simulation studies [1-4]. These results have brought targeted GNP therapy a step closer to clinical use [5-6], though there are yet challenges to fulfilling accurate dosimetry in the presence of GNPs, especially in simulation-based works.

Regarding the images reported in experimental documents, it can be found that the injected nanoparticles tend to accumulate around the cell nucleus [7-8]. In previous studies, we have shown that in simulation-based works, considering nanoparticles as a gold-water (or gold-tissue) mixture or as the homogeneously distributed GNP spheres in the medium leads to different results from those of considering the fact of tendency of GNPs to heterogenetically disperse in the medium, mostly in the cytoplasm around the nucleus [9-11]. The results obtained emphasize the significance of accurate modeling of the distribution of GNPs in cells on the estimation of the dose to the medium. Nonetheless, in these works, the effect of the presence of heterogenetically distributed GNPs in healthy tissues that surround the tumor has been neglected. However, since the injection of the drugs containing GNPs is intravenous, the neighboring tissues also receive the drug in a lower concentration, reported in the experimental works, have the potential to absorb the radiation. Considering that paying attention to minimal damage to healthy tissue is one of the important factors in determining the quality of the treatment, these concentrations may influence the treatment procedure by forcing in reduction of the treatment time. Therefore, considering the effect of the presence of the neighboring tissue on the dose delivered to the area under irradiation and the performance of the treatment is vital. While being a worthy of attention subject, to our knowledge there is not research devoted to study differences in dose enhancement arisen from using GNPs in both the tumor and healthy organs. The present study aims to examine this issue using Monte Carlo simulations. The dose enhancement factor (DEF), defined as the ratio of the absorbed dose to the desired volume in the presence of GNPs to the absorbed dose in the same volume in the absence of nanoparticles, has been considered the criterion to assess the dose enhancement.

The paper has been organized as follows: The cell model, including the nucleus and cytoplasm, is been introduced. A typical phantom, containing the tumor volume and the surrounding healthy tissue, filled with these cells is designed. The physical DEF in the nuclei due to the irradiation of 10 to 100 keV photons to the GNPs that have localized in the cytoplasm in various sets of concentrations is estimated. The effect of the presence of GNPs in the neighboring tissue, their concentration, and size on the dose enhancement is inquired.

METHODS

Simulations and particle tracking have been carried out using the Monte Carlo N-Particle eXtended code (MCNPX), version 2.6. In order to examine the dose enhancement in the

presence of GNPs in the designed geometries, we used dose enhancement factor (DEF) notation, defined as the ratio of the dose to the target of interest in the presence of GNPs to that in the absence of these particles. Because the biological outcomes cannot be directly simulated, the dose enhancement values reported in this work are actually physical DEFs. To reach the acceptable relative errors, ~1×10^9 histories have been considered.

A cubic water phantom of 4×4×4 cm^3 was designed. This phantom contains three layers: The first one is a hemisphere of 0.5 cm radius, centered on the surface of the phantom, which has been considered as the tumor and contains the highest concentration of GNPs. The second and third layers are concentric hemispheres of 0.7 and 0.9 cm radius respectively and have been designed so that cover the tumor layer. The rest of the phantom is considered as water. The mentioned layers, depending on the concentration of GNPs, are filled with several cells, each modeled as described in our previous work [9]: an ellipsoid with a semi-major axis of 18 μm and two equal semi-minor axes of 10 μm with a centrally located sphere of 7 μm radius as the nucleus. The volume delimited between this ellipsoid and the nucleus is named the cytoplasm. Monoenergetic photons of 10 to 100 keV have been emitted from a point source located at a 1 cm distance from the surface of the phantom. A control phantom, i.e. without GNPs, has been used to test the dose enhancement due to the presence of GNPs in three layers. The physical doses due to the irradiation of the photons in either the presence or absence of GNPs were scored in the nucleus of each cell. The data were averaged over all the nuclei of the cells located in the layers, without dealing with the calculation of either the dose or damage delivered to the DNA and subcellular structures of a single nucleus. Figure 1 shows a schematic view of the designed phantom, containing three layers. The figure also presents the simulated cells in the boundary of two layers with various concentrations of GNPs in the cytoplasm. It is worthy to mention that given that MCNP is a general-purpose Monte Carlo code, using MCNP tallies for scoring quantities in a nano-scale cell may be of concern. Nevertheless, in the present work, we have evaluated the dose deposited in the cell nucleus, which is considerably larger than nanometer dimensions, making the simulations carried out reliable

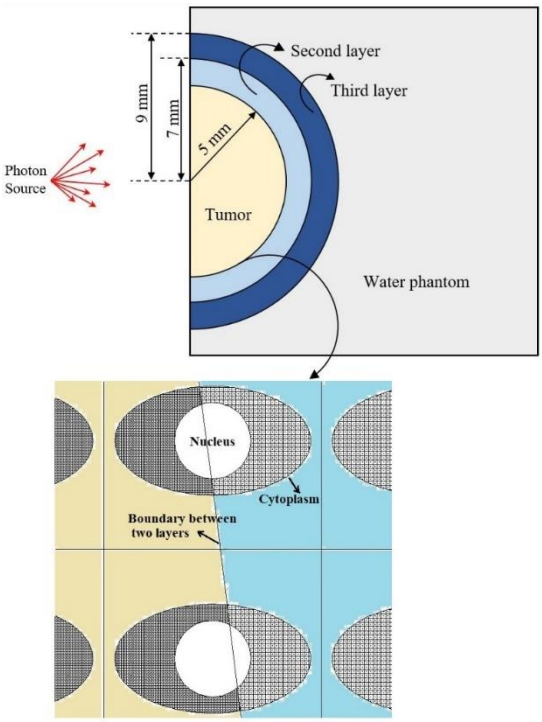

Fig. 1. A schematic cross-sectional view of the designed phantom containing three layers, the dimensions, and the source position. Each layer is filled with cells with different GNP concentrations. The cells in the boundary of two layers with GNPs localized in the cytoplasm are also shown. The medium, the nucleus, and the free space between the GNPs are filled with water.

To show the concentration of gold nanoparticles per gram of water, the notation of mg_{Au}/g_{water} has been used. Three various concentrations of 7, 15, and 30 mg_{Au}/g_{water} have been considered for GNPs in the tumor, and the ratio of the concentration in the tumor:second layer:third layer is 1:0.5:0.25. To investigate the effect of the presence of GNPs in the healthy tissues, the sets of 7:0:0, 15:0:0, and 30:0:0 have also been simulated. Based on the given concentration, the number of GNPs and cells is determined. Each GNP has been simulated as a sphere of pure gold of either 50 or 100 nm in diameter. To fill the volumes with cells, the repeated-structures by using the FILL, UNIVERSE, and LAT cards in the MCNPX code have been simulated.

RESULTS AND DISCUSSION

Figure 2 reports the DEFs calculated in the nuclei of the cells in each layer for a typical concentration of 30 mg_{Au}/g_{water} of 100 nm GNPs in the tumor irradiated by 10 to 100 keV photons. This concentration has been considered to be 15 and 7.5 mg_{Au}/g_{water} in other layers taking into account the ratio of 1:0.5:0.25 mentioned before. This figure also presents the results of 30:0:0 concentrations for the layers, i.e. in the absence of GNPs in the healthy tissue. As can be seen, the dose in the tumor is not affected by the presence of the tumor in healthy tissue. Strictly speaking, the DEFs for the concentration set of 30:15:7.5 deviate from those of 30:0:0 concentration set between about 0.01% to 0.6%. However, there is distinct differences between the DEFs calculated for these sets in the surrounding healthy layers so that this

deviation ranges between about 14.8% and 436.7%, and about 5.4% and 338.7% for the second and third layers, respectively. For both layers, the minimum and maximum deviations correspond to 10 keV and 30 keV photons, respectively.

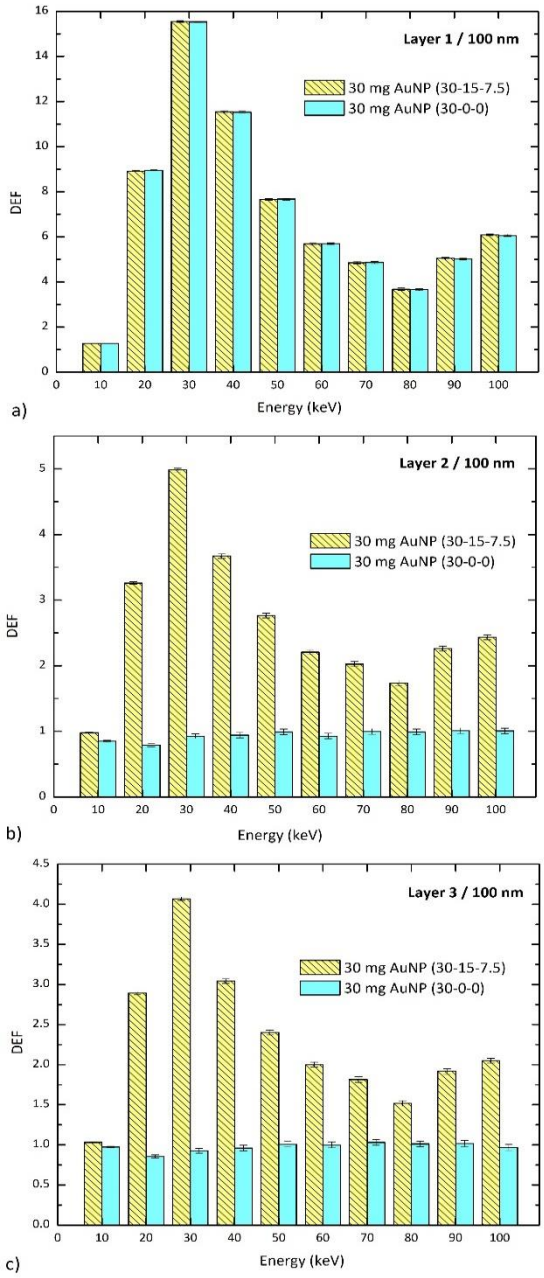

Fig. 2. The values of DEF calculated in the nuclei of a) tumor, b) the second layer, and c) the third layer, exposed to irradiation of monoenergetic photons of 10 to 100 keV. The curves correspond to the typical concentration of 30 mg_{Au}/g_{water} (diameter: 100 nm) in the tumor, and 15 and 7.5 mg_{Au}/g_{water} in the second and third layers, respectively (30:15:7.5). The data have been compared with those in

the absence of GNPs in the second and third layers (30:0:0). Error bars indicate the relative uncertainties.

A similar investigation has been made for 100 nm GNPs of 15 and 7 mg_{Au}/g_{water} concentration in the tumor, with the ratio of 1:0.5:0.25 for the concentration in the tumor:second layer:third layer. For the purpose of this study, the calculated DEFs have been compared with those of the absence of GNPs in healthy tissues. Figure 3 shows the deviations in detail for three layers for the tested energies. As can be seen, the deviations are negligible in the tumor. For other two layers, in a given concentration, approximately follow the same behavior for various primary energies though their corresponding values significantly differ. Furthermore, it can be found that the deviations get the largest value in the second layer which is caused by being closer to the tumor and thus receiving a larger amount of the injected nanoparticles. The figure also shows that these deviations in both the healthy layers are highly dependent on the energies of the irradiated photons and peak around 30 keV. The results highlight the importance of paying attention to the penetration of GNPs in surrounding healthy tissues.

In order to assess the effect of GNP size on the results, the other typical diameter of 50 nm has been investigated. Figure 4 shows the DEFs for the concentration set of 30:15:7.5 mg_{Au}/g_{water} of 50 nm GNPs versus both the layer number and the irradiated energy. To reach a more precise on the effect of the size on the DEFs (Figs. 2 and 4), the deviation between the results of the typical concentration of 30:15:7.5 mg_{Au}/g_{water} for 50 nm GNPs and the same set of concentration in the same layer for 100 nm GNPs has been caclulated. The results can be found in Table 1. By keeping the concentration of GNPs constant, it was found that dose enhancement do not change significantly by size variation for the incident energies tested and while dose enhancements are energy-dependent, they show a small change, on the order of a few percent, by changing the GNPs' size. For the constant concentration mentioned, these variations range between about 0.01% and 3.5% for the tumor, about 0.12% to 7.6% for the second layer, and about 0.31% to 6.6% for the third layer. It is worth noting that the sizes investigated in this work are not necessarily advantageous in clinical works and other parameters such as performance of the GNPs in delivery to the target and intracellular uptake play influential roles.

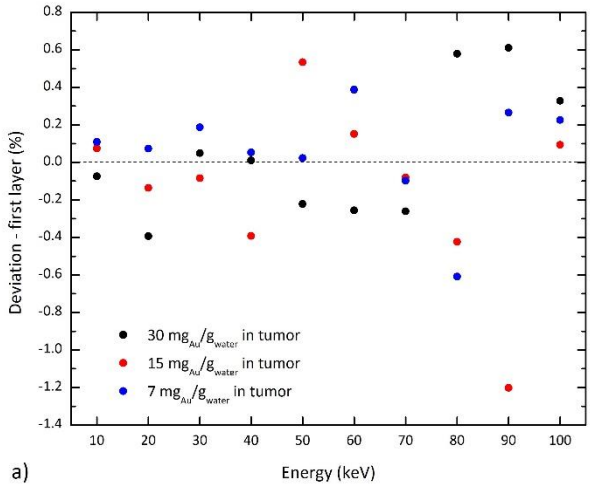

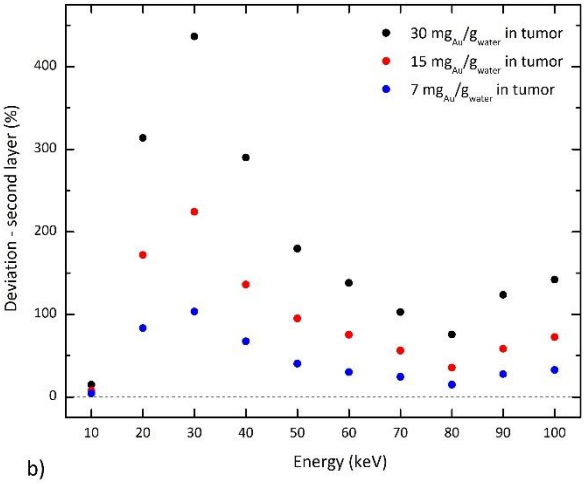

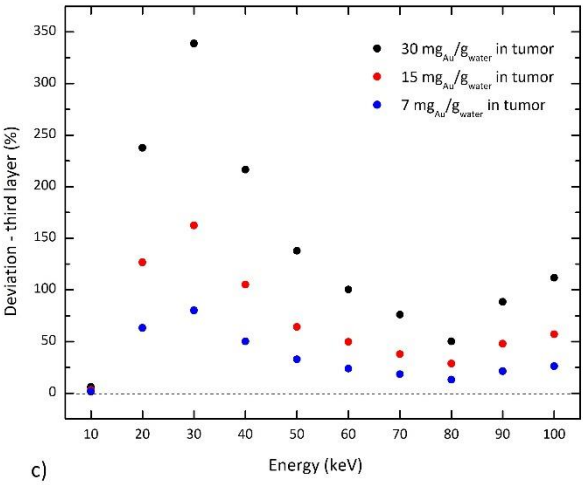

Fig. 3. Deviations (in percent) between the DEFs calculated in the nuclei of a) tumor, b) the second layer, c) the third layer, for three sets of 30:15:7.5, 15:7.5:3.75, and 7:3.5:1.75 mg_{Au}/g_{water} as tumor:second layer:third layer and those of 30:0:0, 15:0:0, and 7:0:0 mg_{Au}/g_{water}, respectively.

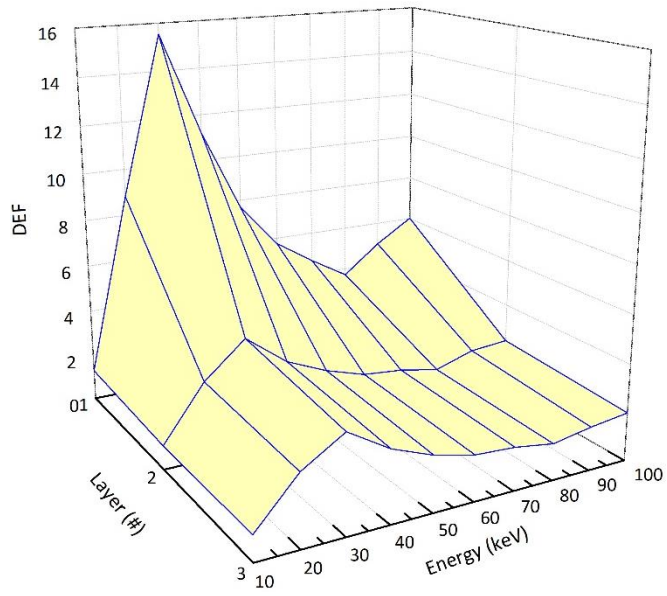

Fig. 4. 3-D presentation of the DEFs calculated in the nuclei of three layers of the phantom exposed to irradiation of monoenergetic photons of 10 to 100 keV. The curves correspond to the concentration set of 30:7.5:3.75 mg_{Au}/g_{water} of 50 nm GNPs.

Table 1. Deviation from the values of DEF in the nuclei of three layers for 50 nm GNPs of 30:15:7.5 mg_{Au}/g_{water} of those corresponding to the same set of concentration of 100 nm GNPs for various primary photon energies.

Energy (keV)	Deviation from $DEF_{50\ nm}$ of $DEF_{100\ nm}$ (%)		
	Layer 1	Layer 2	Layer 3
10	-0.79	-1.50	-0.31
20	1.16	-0.12	-0.40
30	0.01	5.83	2.91
40	2.92	7.57	4.09
50	-0.25	2.64	5.27
60	-1.08	1.20	6.61
70	3.51	0.13	2.03
80	-0.90	1.65	0.10
90	1.34	1.22	6.34
100	1.20	2.83	2.57

Conclusions

This work presents a simulation study to make clear the importance of detailed modeling for the distribution of GNPs in non-target tissues in the computation of dose enhancement in radiation therapy. To this aim, a model considering the widely documented observation of GNPs' trend to heterogenetically distribute around the nucleus (in the cytoplasm) was investigated. The simulated cells were employed to fill the tumor, and its surrounding healthy tissue as well. The concentration was decreased by getting more distance from the tumor with a ratio of 1:0.5:0.25. The results show that for 100 nm GNPs, the DEFs for the concentration set of 30:15:7.5 deviate from those of 30:0:0 concentration set by about 0.6%, 436.7%, and 338.7% for the tumor, the second layer, and the third layer, respectively. Similar results were obtained for 15:7.5:3.75, and 7:3.5:1.75 concentration sets. Performing the same calculations for different GNP size show that the dose enhancement is not significantly sensitive to the size of GNPs, leading to a small change, on the order of a few percent.

The results show that not only the subcellular location of GNPs strongly governs the dose enhancement and the prediction of its behavior depends highly on the modeling of nanoparticles, but also the penetration of the GNPs toward the non-target healthy tissues increases the dose delivered to these volumes and, therefore, influences the treatment procedure. This claim can be supported by the fact that the allowable dose to the healthy tissue is the most common criterion for determining the duration time of the treatment in radiation therapies. As an example, for eye plaque brachytherapy purposes, a dose ranging between 30 and 60 Gy is suggested to avoid damage to critical structures such as the optic nerve. By the presence of the GNPs in healthy neighboring tissues and absorbing the radiation accordingly, this allowed dose value can be achieved in a shorter time and, therefore, the duration of time that the patient will need to wear the plaque decreases. Hence, a longer treatment period may be required to deliver the same dose to the tumor. Taking into account that precise simulations are required so that can be used for pre-clinical tests, our work emphasizes the significance of accurate modeling of the distribution of GNPs in the medium, both the tumor and healthy tissues, to demonstrate the more precise potential of GNPs in improving radiotherapy treatments. It is worthy to mention that changing in geometry of the models used would clearly affect the values calculated for DEF. Our values reported hence are not absolute. However,

owing that these simulations leads to better understand the effects of distribution of GNPs in the non-target organs on dose enhancements, these calculations are worthwhile.

References

[1] Butterworth, K. T., McMahon, S. J., Currell, F. J., & Prise, K. M. (2012). Physical basis and biological mechanisms of gold nanoparticle radiosensitization. Nanoscale, 4(16), 4830-4838.

[2] Kuncic, Z., & Lacombe, S. (2018). Nanoparticle radio-enhancement: principles, progress and application to cancer treatment. Physics in Medicine & Biology, 63(2), 02TR01.

[3] Perrault, S. D., Walkey, C., Jennings, T., Fischer, H. C., & Chan, W. C. (2009). Mediating tumor targeting efficiency of nanoparticles through design. Nano letters, 9(5), 1909-1915.

[4] Chithrani, D. B., Jelveh, S., Jalali, F., Van Prooijen, M., Allen, C., Bristow, R. G., ... & Jaffray, D. A. (2010). Gold nanoparticles as radiation sensitizers in cancer therapy. Radiation research, 173(6), 719-728.

[5] Cho, S. H. (2005). Estimation of tumour dose enhancement due to gold nanoparticles during typical radiation treatments: a preliminary Monte Carlo study. Physics in Medicine & Biology, 50(15), N163.

[6] Lechtman, E., Chattopadhyay, N., Cai, Z., Mashouf, S., Reilly, R., & Pignol, J. P. (2011). Implications on clinical scenario of gold nanoparticle radiosensitization in regards to photon energy, nanoparticle size, concentration and location. Physics in Medicine & Biology, 56(15), 4631.

[7] Štefančíková, L., Porcel, E., Eustache, P., Li, S., Salado, D., Marco, S., ... & Lacombe, S. (2014). Cell localisation of gadolinium-based nanoparticles and related radiosensitising efficacy in glioblastoma cells. Cancer nanotechnology, 5(1), 1-15.

[8] Lechtman, E., Mashouf, S., Chattopadhyay, N., Keller, B. M., Lai, P., Cai, Z., ... & Pignol, J. P. (2013). A Monte Carlo-based model of gold nanoparticle radiosensitization accounting for increased radiobiological effectiveness. Physics in Medicine & Biology, 58(10), 3075.

[9] Rasouli, F. S., & Masoudi, S. F. (2019). Monte Carlo investigation of the effect of gold nanoparticles' distribution on cellular dose enhancement. Radiation Physics and Chemistry, 158, 6-12.

[10] Rasouli, F. S., Masoudi, S. F., & Asadi, S. (2019). On the importance of modeling gold nanoparticles distribution in dose-enhanced radiotherapy. International Journal of Nanomedicine, 5865-5874.

[11] Masoudi, S. F., Daryabari, F. S., & Rasouli, F. S. (2020). Distribution modeling of nanoparticles for brachytherapy of human eye tumor. EJNMMI physics, 7(1), 1-13.

International Conference on Nuclear Science and Technology
6- 8 MAY 2024 | Isfahan, Iran

Investigation of secondary radiation in laser-accelerated proton beamline (LAP) based on pulsed power solenoid (Paper ID : 1108)

S. A. Mahdipour*[1], M. Shafeei Servestani[1], H. Abdi Roknabadi[2]

[1]*Hakim Sabzevari University, P.O. Box 397, Sabzevar, Iran*
[2]*Yazd University, Yazd, Iran*

Abstract

Radiation pressure acceleration (RPA) and target normal sheath acceleration (TNSA) are the most important methods of Laser-accelerated proton beams (LAP) planning systems. LAP has inspired novel applications that can benefit from proton bunch properties different from conventionally accelerated proton beams.

The secondary neutron and photon produced in the collision of protons with beamline components are of the important concern in proton therapy. Various published Monte Carlo researches evaluated the beamline and shielding considerations for TNSA method but there is no studies directly address secondary neutron and photon production from RPA method in LAP. The purpose of this study is to calculate the flux distribution of neutron and photon secondary radiations on the first area of LAP and to determine the optimize thickness and radius of the energy selector in a LAP planning system based on RPA method. Also, we present the Monte Carlo calculations to determine the appropriate beam pipe for shielding a LAP planning system. The *GEANT4* Monte Carlo toolkit has been used to simulate a secondary radiation production in LAP. A section of new multifunctional LAP beamline has been proposed, based on the pulsed power solenoid scheme as a *GEANT4* toolkit.

The results show that the energy selector is the most important source of neutron and photon secondary particles in LAP beamline. According to the calculations, the pure Tungsten energy selector not be proper case and using of Tungsten+Polyethylene or Tungsten+Graphite composite selectors will reduce the production of neutron and photon intensities by approximately ~10% and ~25% respectively. Also the optimal radiuses of energy selectors were found to be ~4 *cm* and ~6 *cm* for a 3 degree and 5 degree proton deviation angles respectively.

KEYWORDS: Neutron, photon, flux distribution, energy selector, *GEANT4* toolkit.

1.Introduction

Conventional proton cyclotrons have a diameter of about 4 m and a weight of 200 t. Due to the size and cost of beam therapy systems, more compact facilities are desired and different technologies are under investigation. An attractive approach is the use of laser plasma acceleration for proton therapy [1–3]. The use of this technology has different mechanisms.

Nowadays, the target normal sheath acceleration method (TNSA) dominates the laser-plasma interaction at laser intensities above 10^{20} W/cm^2 and is thus accessible with existing laser systems [4]. The TNSA regime produces non thermal equilibrium plasma in the rear side of the laser irradiated target [5]. Future generation laser systems based on the radiation pressure acceleration method (RPA) promise a narrower energy spread and a more efficient conversion of laser energy to proton energy [4]. In comparison to the TNSA, the conversion efficiency with the RPA scheme is estimated to be more than 40 times higher [6, 7].

Commonly in LAP, two different Particle-in-cell (PIC) and envelope tracking groups of computer codes are used for beam transport simulations. Some of them are: TRACE2D, GPT, TRACK, TRACEWIN [8] and etc. The transport beamline has to ensure the beam parameters such as intensity, energy spectrum and field size. In a LAP facility only a very small part of the laser accelerated protons is used and transported to the irradiation site. The codes mentioned above, cannot evaluate the real effects of transportation such as secondary radiation production resulting from dumping the large portion of unused protons. In order to design a transport beamline which considers all experimental conditions, the use of Monte Carlo codes (such as GEANT4, Fluka and etc.) is crucial.

Although proton therapy is regarded as one of the most effective forms of radiotherapy in terms of secondary radiation dose, but small amounts of radiation will inevitably be deposited outside the path of the primary beam. Secondary photons, neutrons, protons, and heavier recoils may deposit their energy outside beamline [9-12]. Neutrons are the major contribution to the dose equivalent outside the treatment volume because of their high-relative biological effectiveness [13]. The production of secondary particles increases inside the beam modifier material such as collimator, energy selector and etc. Also range modulator wheel (RMW) and beam pipes employed in high-energy proton beams can also be a significant source of secondary radiation [14].

Some GEANT4 and Fluka simulations and preliminary experimental tests have been already performed for LAP based on TNSA method [15-19]. Furthermore, GEANT4 simulation of the

energy selector system has been developed and reported in Ref [20]. But in RPA method, Monte Carlo simulation with accurate details of proton transport beamline consisting of pulsed magnet, energy selector and etc. before the design and construction of the device has never been developed. Secondary radiation calculations have not been carried out in RPA method up to now. Our GEANT4 calculations make it possible to study the production of secondary particles inside the LAP beamline. In this work, our purpose is developed a compact particle selection and beam collimating system using the GEANT4 package. As an important step, the GEANT4 proposed design is capable of investigating the production of secondary particles. The shape of magnetic field and energy selection process applied here is based on theoretical model of the work of Refs [21-23] which are used DYNAMION [24] and TRACEWIN [25] ready codes.

2.Material and methods

2.1 Simulation of geometry and proton source

We have used the GEANT4 Monte Carlo toolkit [26], which is one of the most powerful and widespread codes for beam transport and focusing of particles. GEANT4 is a C++ object-oriented and open source code authorizing the simulation of particle interactions with matter. It initially developed for high energy physics experiments simulation and it is now used also for low energy medical physics applications, such as ion therapy. Schematic demonstration of the compact particle selection and beam collimating components are drawn in Fig 1. Our GEANT4 simulations setup is based on configuration of Ref [27]. The first part of the beamline consists of proton beam source, first pulsed solenoid, energy selector and beam pipe as main components.

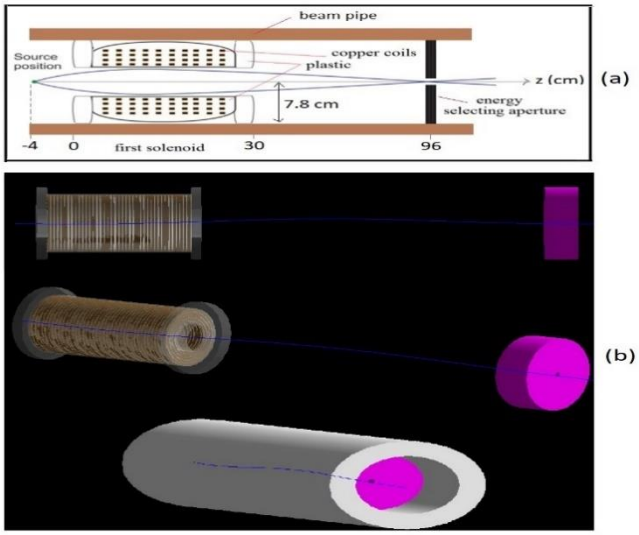

Fig. 1. (a) The schematic layout of design based on pulsed power solenoids and (b) *GEANT4* simulation of pulsed power solenoid system, beam pipe and energy selection target.

In The RPA method, transport properties of the proton beam can be evaluated by definition of the spectral yield of protons as function of energy E and production cone angle Ω [21-23, 28,29]:

$$\frac{dN(E,\Omega)}{dE}(MeV^{-1}) \quad (1)$$

which determined the number of protons in an energy interval dE and within a cone angle $\pm \Omega$. The proton energy spectrum is quasi-monoenergetic with a peak at about 220 *MeV*. To introduce the RPA proton source into our *GEANT4* simulations, we take a bi-Gaussian approximation [22]:

$$N(E) = 1.1\ \exp[-(\frac{E-220}{30})^2] + 0.4\ \exp[-(\frac{E-150}{100})^2] \quad (2)$$

Ignoring the relatively weak dependence on Ω according to Ref [21] this continues energy spectrum is evaluated at about 120 points and plotted in Fig 2 (a).

In the *GEANT4* toolkit, the *General Particle Source* (*GPS*) class allows to specify the spectral, spatial and angular distribution of the primary source particles. The users can use the *GPS* class to define their arbitrary sources. We apply the *GPS* class in our program to define the proton source in the simulation process. The radius of the circle proton beam is considered to be 10 μm [22] and the beam direction is along *z* axis. The distance proton source (with Gaussian phase space distributions of standard deviation Ω = ±87.26 *mrad* (± 5°)) to the initial of the solenoid is 4 *cm*. The function of the solenoid filed maps based on the conditions for coordinates *x*, *y* and *z*, is defined in a separate file. The shape of solenoid filed map versus distance in the *z* direction is shown in Fig 2 (b). It should be noted that the shape of the magnetic field of the solenoid are similar with approach presented in Ref [21].

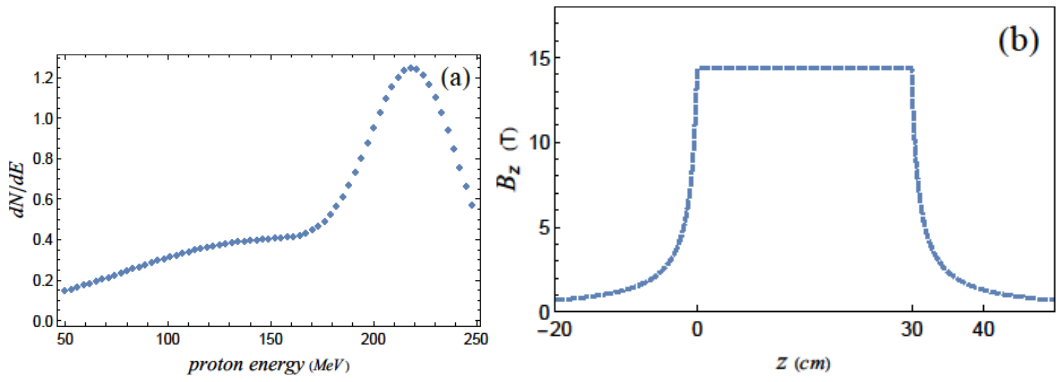

Fig. 2. (a) Spectral energy distribution of protons (RPA spectrum) implemented in the *GEANT4* and (b) demonstration of solenoid filed map versus distance in *z* direction.

2.2 *Beamline components and physics processes in the simulation*

The first part of beamline components and *GEANT4* design of the pulsed power solenoid consist of the elements shown in Fig. 1 (b). The elements were positioned in an air tube volume (*mother volume*). The proton beam, coming from the source, enters the solenoid with 3 *cm* inner radius. The aperture with 0.5 *cm* radius, placed after the solenoid. The aperture is inside the cylindrical energy selector. By means of this aperture, protons with particular energy are selected and transported [23]. The material, thickness and radius of the selector and beam pipe are variable and they are explained in the results section. The main body of the solenoids is composed of five centered cylinders (with a different inner and outer radius). Copper and plastic (Polyurethane) rings are made of thin layers positioned at the correct depth inside the solenoids (See Fig 1). In different conditions, the cylindrical selector is made of different materials: Tungsten (W), Tungsten+Polyethylene (WP), Tungsten+Graphite (WC) and Iron+Polyethylene (FeP) in which the two cylinders stick together successively. In cases where the composite selector is made of two kinds of material, the first (that is closer to the solenoid) and the second parts have a thickness of 4 *cm* and 2 *cm* respectively. Also the beam pipe is a cylinder with 120 *cm* length along *z* direction. The inner and outer radiuses of the beam pipe are 7.8 *cm* and 11.8 *cm* respectively. Beam pipe made of Iron+Polyethylene and polyethylene materials in two cases.

The densities of air, plastic, copper, iron, polyethylene, graphite and tungsten are 0.0012 g/cm^3, 1.03 g/cm^3, 8.96 g/cm^3, 7.87 g/cm^3, 0.96 g/cm^3, 2.23 g/cm^3 and 19.3 g/cm^3 respectively. These materials are used in simulation processes. During GEANT4 simulation, many physics packages such as: G4EmStandardPhysics, G4HadronElasticPhysics, G4RadioactiveDecayPhysics, G4HadronInelasticQBBC, G4ComptonScattering and etc. were activated [26]. In the simulation process all particles were subjected to be tracked if their ranges are longer than the defined “Setcut” threshold of 0.01 mm in the simulation process.

3. Results and discussion

3.1 Focusing the RPA proton beam

At the first step, we have characterized the proprieties of magnetic field, simulating a uniform reference proton beam as an input source. We choose the E = 220±0.01*MeV* as a reference energy for adjusting the field strengths, because it is approximately the energy of the peak of

the RPA spectrum (see Fig. 2 (a)). The strength of the magnetic field adjusted to create a focal spot at 100 *cm* from the proton source (*z* = 96 *cm)* (see Fig 1 (a)). To create this focal point, we adjust the amplitude of the magnetic field of the solenoid. The maximum magnetic field needed to create a focal distance for 220±0.01*MeV* protons was found ~15 *T* from *z* = 0 to *z*=30 *cm* in the center of the solenoid. The blue curve in the Fig 1 (b) is a number of proton trajectories for 220 ± 0.01*MeV* protons. This part of simulation was realized with 3×10^6 events and detected by a transverse detector, positioned at the focal spot position. The protons typical cone angle is $\Omega = \pm 5$ degree. The resulting distribution is shown in Fig. 3 (a) taken at the focal spot. According to Fig 3 (a), approximately 1.5 *mm* diameter waist at the aperture region is founded. As previously mentioned we want to filter a maximum value of about ΔE/E of RPA full spectrum [23]. In all subsequent calculations the simulation is performed with RPA proton source. We have simulated a vertical detector after the aperture for storing the energy distribution outputs. The results show that for a quasi monoenergitic RPA source of Fig. 2 (a), the energy spread of the selected beam is ~ ±10 *MeV*. This result shown in Fig 3 (b) and is obtained by using 5 *mm* diameter aperture with 6 *cm* thickness of W selector. The energy distributions are normalized to theirs maximum values. In Fig 3 (b), logarithmic scale of initial and selected (output) proton energy spectra have been compared. As expected, the aperture provided a suitable energy filtering which prevented low energy protons to pass through.

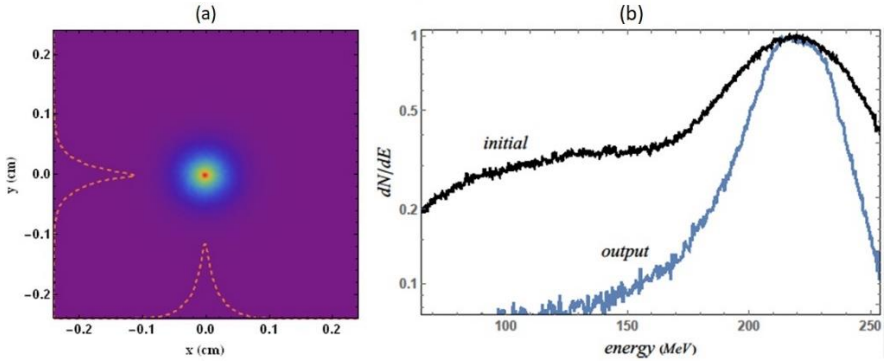

Fig. 3. (a) *x-y* 2D density plot of proton flux and corresponding profiles inside the aperture region. The proton energy is 220±0.01*MeV* and (b) Initial and selected (output) proton energy spectra with the *GEANT4* simulation, performed with a RPA proton source. The distributions are normalized to theirs maximum values.

Fig. 4 shows the proton (a) neutron (b) and (c) photon 3D and 2D flux maps per unit source particle. The fluxes is scored with the box detector geometry consists of a grid containing 100 × 100 × 200 voxels, each with dimension 0.24 × 0.24 × 0.6 cm^3. In this area of the beamline, the maximum flux of neutron and photon both cases are located around the W energy selector.

As seen in Fig 4 the production of secondary neutrons and photons increases around the selector and the most important source of secondary radiations is energy selector. So finding the optimal thickness and radius for the energy selector is a fundamental investigation. The solenoid structures can also be a significant source of secondary radiation (see the solenoid region in Fig 4 (b) and (c)).

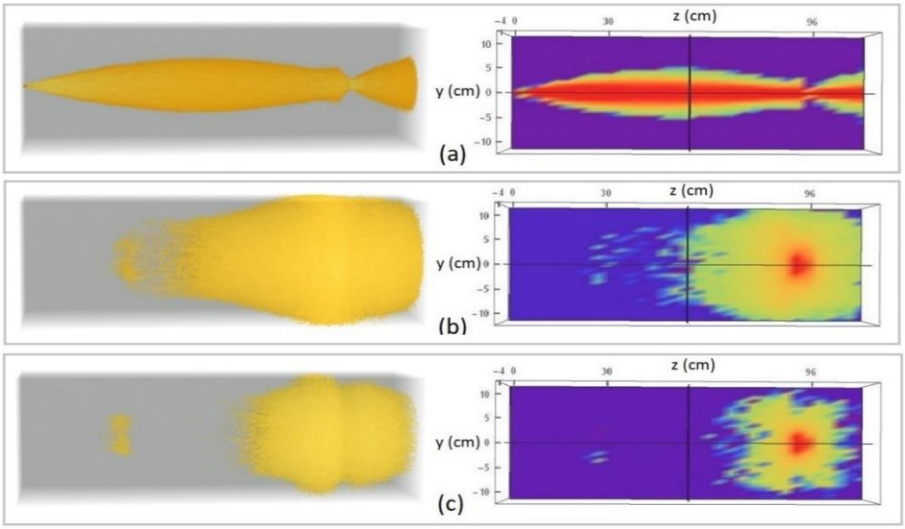

Fig. 4. 3D view of primary and secondary flux of RPA protons from the source position (z = -4 *cm*) to after the focal length (aperture position). Primary proton (a), neutron (b) and photon (c) flux distributions. Material, thickness and radius of the selector are W, 6 *cm* and 7.8 *cm* respectively. It should be noted that outputs with very small amounts are not plotted in the figure.

3.2 Selector and beam pipe calculations

The comparison of secondary neutron flux with respect to the different W selector depths is shown in Fig. 5. The radiuses of three W selectors are 7.8 cm that is equal to the outer radius of the solenoid plastic edges. For these calculations the detector is a cylinder of radius 3 cm and three different thicknesses (4 cm, 5 cm and 6 cm). The detector is sliced to 300 cells along z axis. It is in the vicinity of the aperture and does not include it. According to Fig. 5, using of three different W selectors causes stopping of useless protons but the secondary photons and neutrons passes through this selectors. As can be seen, using of thicker W selector will increase the intensity of neutrons and photon fluxes. Therefore, increasing the thickness of the tungsten selector is not an appropriate method to reduce the secondary radiations. It is very important to use a suitable shielding around this area of LAP beamline. It is obvious that the contributions of primary protons were decreased when the position moved deeper into the selector. It should

be noted that there is considerable leakage for the secondary particles in this area of LAP beamline. According to Fig. 5, the simulated primary selector has a length of ~ 4 cm which can fully stop all the useless RPA protons. This choice prevents the production of further neutron and photon secondary particles. The percentage ratios of the neutron intensity to photon intensity are ~74%, ~75% and ~77% for 4 cm, 5 cm, and 6 cm thicknesses respectively. Also the results show the percentage ratio of the neutron intensity of two 4 cm and 5 cm thicknesses is ~23%. This ratio between 5cm and 4 cm thicknesses is equal to ~19%.

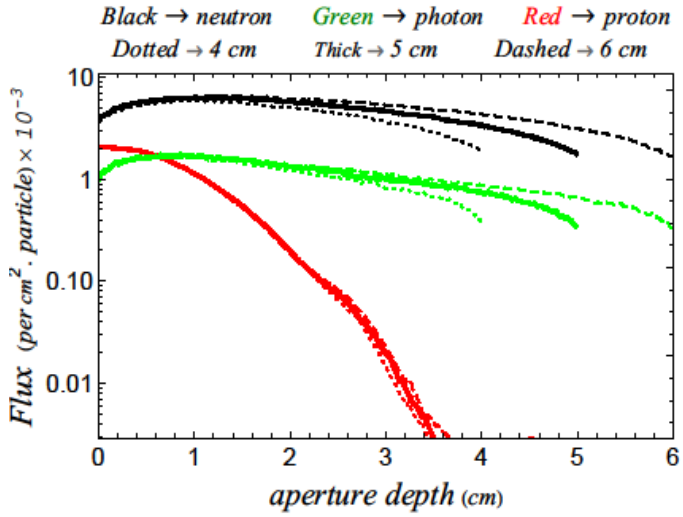

Fig. 5. The comparison of proton, neutron and photon fluxes with respect to different tungsten depths (4 *cm*, 5 *cm and* 6 *cm*). Primary beam is proton RPA spectrum. The flux distributions were produced inside a cylinder detector positioned at the absorber and did not cover the aperture. The thickness of the detector and absorber is the same and the vertical axis is plotted in log scale.

Mostly the neutrons are the major concern of shielding calculations. Polyethylene and Graphite are considered the proper neutron shielding materials available [18]. To study the effect of potential selector materials on neutron production and elimination, calculations of neutron flux distributions were made for WP and WC energy selectors. For calculation of figures 6 to 9, the detector is a cylinder of length 6 *cm* with radius 7.8 *cm* and sliced to 300 cells along *z* axis. It includes both aperture and selector. As observed in Fig 6 (a), W is indeed the material with the highest neutron and photon production cross sections among the W and WP selectors. The results show, compared to W, the use of WP selector reduces the intensity of photons and neutrons by ~10% and ~25% respectively. Because Polyethylene has a large neutron capture cross-section and performs better. According to Fig 6 (b) there is no significant difference between the result of WP and WC selectors and can be concluded using of composite selector design (WP and WC) reduce the intensity of secondary neutrons and photons.

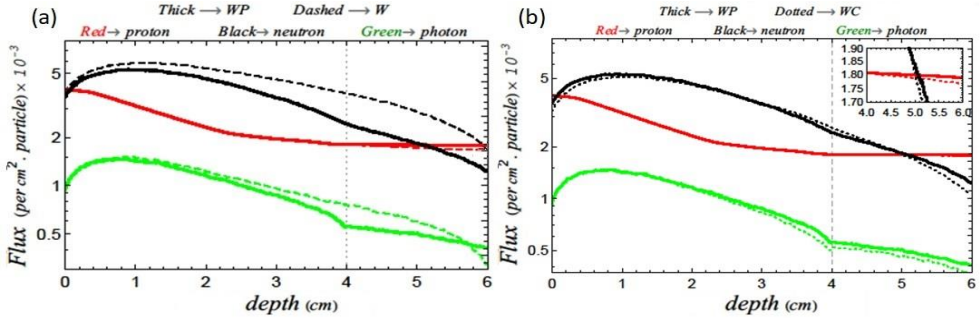

Fig. 6. Calculated primary and secondary particle flux from RPA protons, inside the W, WP and WC selectors. Each thick of selector here is 6 *cm*. The vertical axis is plotted in log scale and the vertical (in x=4 *cm*) dashed line represents the boundary between two materials.

The secondary radiation that was recorded in the cylinder detector (after the selector) during the irradiation of the energy selector with RPA beam is visualized in Fig. 7. This figure shown logarithmically (of course the internal figures are non-logarithmic). As seen in Fig 7 (a), most of the neutrons produced have energies less than ~10 *MeV* and the distribution does not change significantly for larger energies with W, WP and WC selectors. According to neutron distribution, WP selector has a lowest intensity of low-energy neutrons. For this reason, an appropriate moderator like Polyethylene (or Graphite) must be mixed with tungsten to stop low-energy neutrons. In the photon flux distribution produced from proton interaction with selectors, some of the peaks correspond to exited nucleus.

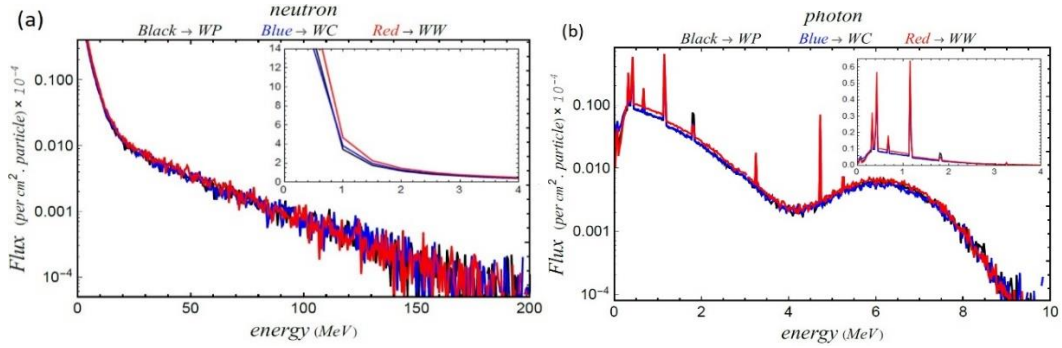

Fig. 7. Flux-energy distribution of secondary neutrons and photons scored after the energy selector, (a) The flux distribution of the neutrons, (b) distribution of the flux of the photons. The comparison is done for three W, WP and WC different selectors. The thickness of selectors is 6 *cm*.

The proton, neutron and photon flux per selector depth are shown in Fig 8 (a) for the WP and FeP selectors both 6 *cm* thicknesses. As it can be seen, in comparison with FeP, WP has stopped a greater amount of protons because the stopping range is linearly dependent on material density and materials of low density will have large stopping ranges [30]. A difference of ~19% in proton intensities was found for WP and FeP selectors. It indicates that WP is good selector for stopping the primary protons while FeP does not perform well at the RPA energy range.

Also the secondary radiation differences (In Fig 8 (a)) are ~14% and ~70% for photons and neutrons respectively. As seen in Fig 8 (b), The FeP selector has less neutron distribution than the WP selector at energies up to ~20 *MeV*. This process is reversed for larger energies (of course much less). It indicates that WP is appropriate selector for slowing down the neutrons with higher energies (>20 *MeV*) while FeP perform well at the lower energy ranges.

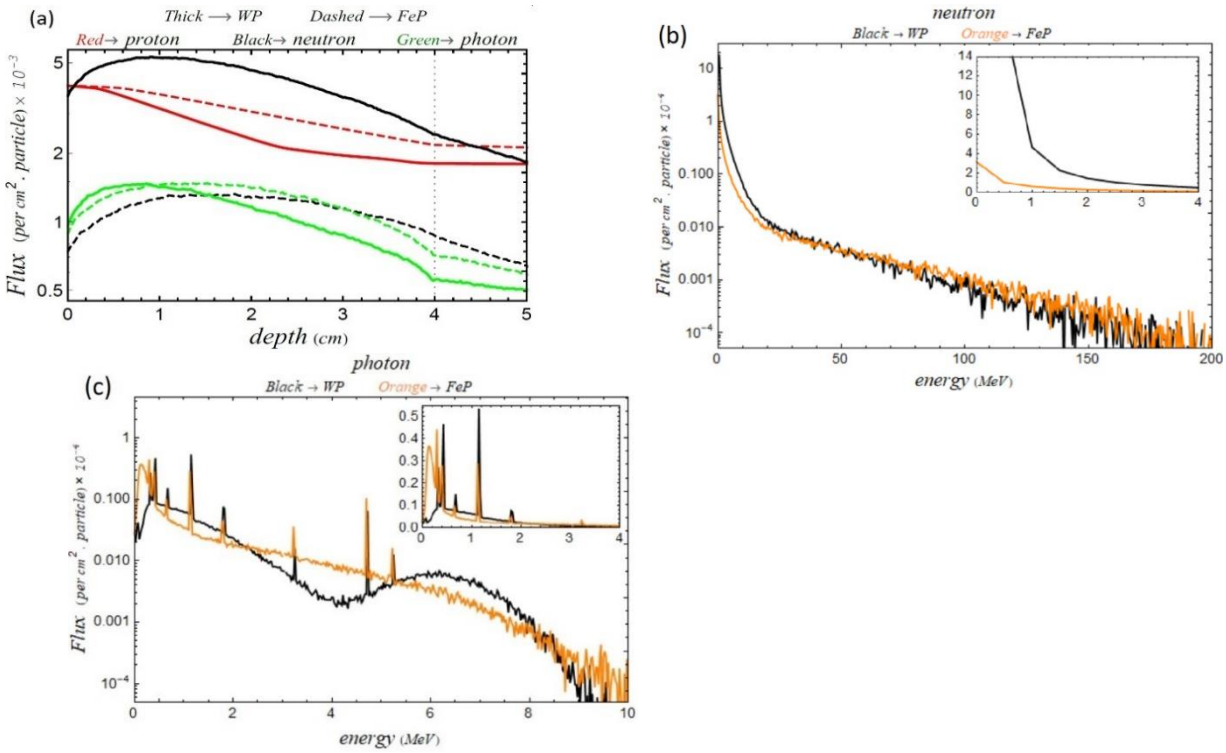

Fig. 8. (a) Simulation of particle flux as a function depth for WP and FeP selectors. (b) The flux distribution against energy of the neutrons, (c) flux-energy distribution of the photons. The comparison is done for three WP and FeP two selectors. The thickness of selectors is 6 *cm*.

In the next step, a W selector (with thickness of 6 *cm*) was located against the primary protons with different radiuses as used in the calculation. The proton and neutron fluxes for 3 degree and 5 degree beam deviation angles from the different radiuses of selector are shown in Fig 9 where the flux is plotted against the depth of the selector. In the neutron flux distributions only cases relative to three selected radiuses are shown. This is evident in Fig 9 (a) and Fig 9 (b) where the radius of the selector is increases the proton flux intensity is degreased because the simulated selector has a bigger cross-section in front of the RPA source. Moreover according to Fig 9 (a) and Fig 9 (b), if the selector radius is bigger than a certain radius, the difference between the intensity of the proton spectra is significantly reduced (smaller than ~0.2%). Indeed, this radius can be selected as optimal radius because after this value by increasing the

radius, the intensity of the production of secondary radiation only increases (see the neutron distributions in Fig 9 (a) and Fig 9 (b)). For example the difference of neutron intensity in Fig 9 (a) is ~4% between the curves corresponded to 6 *cm* and 7 *cm* radiuses. The optimal radiuses were found to be ~4 *cm* and ~6 *cm* for a 3 degree and 5 degree proton deviation angles respectively.

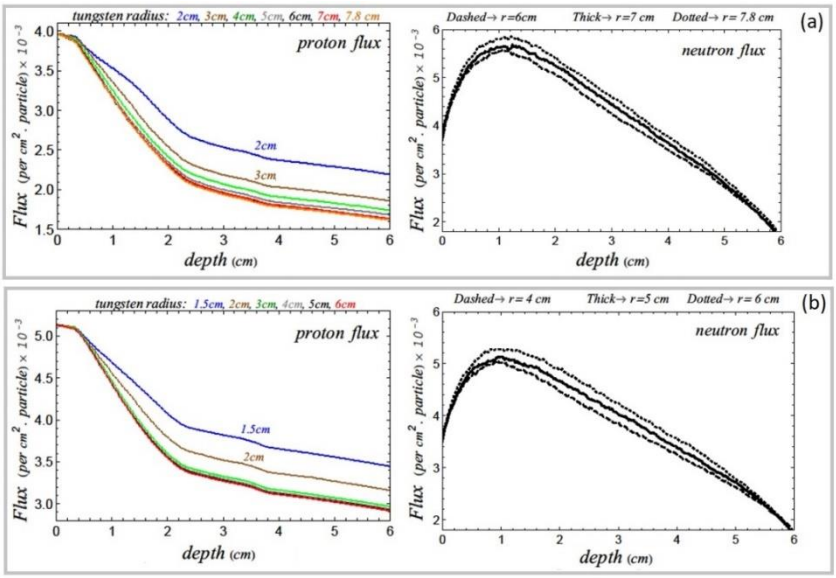

Fig. 9. Flux distribution against selector depth for a WP selector of *6 cm*, for protons and neutrons at (a) 5 degree and (b) 3 degree beam deviation angles.

When the RPA protons entering the solenoid field in the beamline will be deflected and have a spatial distribution due to their energy spread. So some of them are able to escape from the beamline path and it is essential to shield the beamline with beam pipes. As we know, neutron shielding requires materials rich in hydrogen, while photon shielding needs materials of high atomic number and density. One can use separate materials for the two purposes or materials that are good shields for both neutrons and photons [18]. The shielding ability of Polyethylene and Iron+Polyethylene beam pipes is investigated. The reason for choosing Polyethylene is that it has a large neutron capture cross-section and performance in the energy range up to 300 MeV. Also, iron is an effective shielding material for secondary neutrons, which can significantly reduce the neutron intensity (see Fig 8 (a)). The flux profiles of primary and secondary particles and for two different beam pipe configurations are shown in Fig 10. For the primary protons, the 3D view of flux map is also plotted (see the left panel of Fig 10 (a)). According to Fig 10 (a), Iron+Polyethylene beam pipe represent a good choice for primary proton stopping. Moreover as seen in Fig 10 (c) it reduces the intensity of secondary photons

especially around the selector area. This is another reason for choosing the Iron+Polyethylene beam pipe design. Also the Polyethylene beam pipe somewhat can reduce the neutron intensity (Fig 10 (b)). As a solution, the second layer materials (Polyethylene) could have larger thickness.

It can be concluded to reduce the proton, photon and neutron intensity as much as possible; FeP was selected as a proper shielding material in the beam pipe design. It is also not a good choice to add a layer of tungsten (instead of iron) to the constructing beam pipe due to the high cost, heavy weight and high production of secondary neutrons.

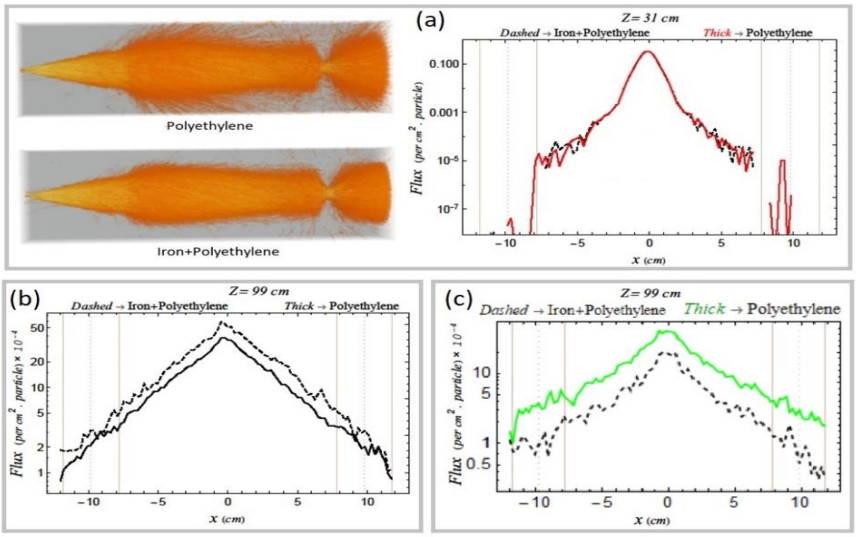

Fig.10. (a) Variation of proton flux along the beamline and its profile (in *y*=0) at the position after the solenoid against the x position. Lateral flux profile (in *y*=0) at the position after the solenoid against the x position for (a) neutron and (b) photon particles.

Conclusion

Our general purpose is to simulate the designed compact particle selection and beam collimating system of LAP using the *GEANT4* MC toolkit. This purpose requires a step-by-step study and simulation. We have presented pulsed power solenoid system in *GEANT4* toolkit. This pulse power solenoid is a first-generation design based on Monte Carlo results and later designs will be optimized. This is an ongoing work to study and develop radiation protection for ongoing experiments and future therapy applications. We studied the performance of a pulsed power solenoid designed for RPA method with respect to generation of secondary radiation in a compact LAP design. In order to reduce the neutron and photon secondary radiation different materials, thickness and radiuses for the energy selector construction will be studied. We found that the consideration of accurate structure of the

solenoid should not be ignored and it is also one of important source of secondary radiation production.

From the simulations, it can be concluded the composite WP and WC energy selectors induced the lowest intensity of secondary radiation because the pure tungsten induced a neutron and photon fluxes of approximately ~25% and ~%10 higher than the W selector. For these composite selectors, a length of ~ 4 *cm* of W can fully stop all the useless RPA protons. Moreover WP selector has a lowest intensity of low-energy neutrons. For this reason, an appropriate moderator like Polyethylene (or Graphite) must be mixed with tungsten to stop low-energy neutrons (< ~10 *MeV*) that they have largest contribution of the flux-energy distribution. We also calculated the optimal selector radius for two 3 degree and 5 degree proton deviation angles .These optimal radiuses are ~4 *cm* and ~6 *cm* respectively. It can be concluded to reduce the proton, photon and neutron intensity as much as possible; FeP was selected as a proper shielding material for the beam pipe design. In the next steps we will also simulate more components of the designed beamline such as beam accurate structure of quadrupole and etc. The presented simulation of the accurate solenoid components in this article can be used by interested *GEANT4* users in different physics fields.

References

[1] V. Malka, et al., Nat. Phys (4) (2008) 447–453.

[2] K. Ledingham, W. Galster, New J. Phys (12) (2010) 045005.

[3] H. Daido, M. Nishiuchi, A.S. Pirozhkov, Rep. Prog. Phys (75) (2012) 056401.

[4] F.H. Lindner, et al., Nuclear Instruments and Methods in Physics Research B (402) (2017) 354-357.

[5] L. Torrisi, et al., Nuclear Instruments and Methods in Physics Research B (355) (2015) 221–226.

[6] T. P. Yu, et al., Phys. Plasmas (18), (2011) 043110.

[7] M. Chen, et al., Phys. Plasmas (18), (2011) 073106.

[8] S. Yaramishev, et al., Nucl. Instrum. Methods Phys. Res., Sect. A (558) (2006) 90.

[9] A. Carnicer, et al., Med. Phys. 39 (12), (2012), 7303.

[10] X.Wang, et al., Int. J. Radiat. Oncol. Biol. Phys. 76 (5), (2010), 1563–1570.

[11] A. Pérez-Andujar, W. D. Newhauser, and P. M. DeLuca, Phys. Med. Biol. (54) (2009), 993–1008.

[12] J. C. Polf and W. D. Newhauser," Phys. Med. Biol. 50, (2005) 3859–3873.

[13] W. Sauerwein, et al., Strahlenther. Onkol. 185 (S1), 140 (2009).

[14] A. Pérez-Andujar, W. D. Newhauser, and P. M. DeLuca, Phys. Med. Biol. 54, (2009), 993–1008.

[15] V. Scuderi, et al., Nuclear Instruments and Methods in Physics Research A (740) (2014) 87–93.

[16] A. Tramontana, et al., Journal of Instrumentation, (9) (2014).

[17] F. Romano, et al, AIP Conf. Proc (63) (2013) 1546.

[18] J Fan, et al., Phys. Med. Biol. (52), (2007) 3913–3930.

[19] S. Faby, J.Wilkens, Zeitschrift für Medizinische Physik, 25 (2), (2015), 112-122.

[20] G.Milluzzo, et al., Nuclear Instruments and Methods in Physics Research A (909) (2018) 298-302.

[21] I. Hofmann, et al., PHYSICAL REVIEW SPECIAL TOPICS - ACCELERATORS AND BEAMS (14) (2011) 031304.

[22] I. Hofmann, et al., Nuclear Instruments and Methods in Physics Research A (681) (2012) 44–54.

[23] I. Hofmann, PHYSICAL REVIEW SPECIAL TOPICS - ACCELERATORS AND BEAMS (16) (2013) 041302.

[24] /http://irfu.cea.fr/Sacm/logiciels/index3.phpS.

[25] S. Yaramishev, et al., Nucl. Instrum. Methods Phys. Res., Sect. A (558) (2006) 90.

[26] GEANT4 collaboration, S. Agostinelli et al., Nucl. Instrum. Meth. A (506) (2003) 250.

[27] U. Masood, et al., Phys Med Biol (13) (2017).

[28] A. Henig, et al., Phys. Rev. Lett (103) (2009) 045002.

[29] A. Henig, et al., Phys. Rev. Lett (103) (2009) 245003.

[30] J. F. Ziegler et al. SRIM-2008.03, The Stopping of Range and Ions in Matter calculation code, http://www.srim.org/.

International Conference on Nuclear Science and Technology
6- 8 MAY 2024 | Isfahan, Iran

Investigating Cobalt Mobility in Agricultural Soil and its Uptake by Saffron Through Neutron Activation Analysis Method (Paper ID : 1112)

Taghizadeh Tousi E.

Department of Mechanical Engineering, University of Torbat Heydarieh, Torbat Heydarieh, Iran

Abstract

This research employs Neutron Activation Analysis (NAA) to assess cobalt concentrations in saffron plants and the soil of saffron farms. Given that the greater Khorasan region is responsible for over 90% of Iran's saffron production, and Iran itself contributes to over 90% of global saffron output, the study focuses on Torbat Heydarieh county, a key saffron-producing area. The NAA results demonstrate that cobalt concentrations in both saffron corm and aerial parts are within ranges conducive to plant growth and remain below toxicity thresholds. The findings suggest that saffron does not significantly accumulate cobalt, as the calculated Bioaccumulation Factors (BAFs) for aerial parts consistently register below 0.5, indicating limited direct soil-to-organ cobalt accumulation. Furthermore, the Translocation Factor (TF) for cobalt from the corm to all aerial tissues is below one, implying a diminished uptake and accumulation of cobalt in aerial tissues compared to the saffron corm. This research sheds light on the nuanced dynamics of cobalt distribution within saffron plants in a crucial saffron-producing region.

Keywords: Bioaccumulation Factors, Neutron Activation Analysis (NAA), Saffron (*Crocus sativus* L.)

INTROUCTION

The nutrient elements play a crucial role in shaping biochemical processes, ultimately influencing the comprehensive growth of different crops and their production efficiency. While these elements are not universally essential for all plants, they can have an impact on both plant growth and yield. The nutrient under consideration in this research is Cobalt (Co). Cobalt serves as a vital component of cobalamin, necessary for the functioning of numerous enzymes and coenzymes. It plays a crucial role in the formation of leghemoglobin, participating in the process of nitrogen fixation within the nodules of leguminous plants [1].

By enhancing the number of nodules per plant, it also regulates both the quantity and size of root nodules. Cobalt has been demonstrated to be indispensable for the process of symbiotic nitrogen fixation in legumes. It plays a crucial role as a cofactor of cobalamin (Vitamin B12), functioning as a coenzyme that actively participates in both nitrogen fixation and the growth of nodules [2].

Cobalt exhibits both positive and negative effects on plants. At relatively lower concentrations, cobalt has been observed to enhance nodulation, leading to improved overall growth and yield. Conversely, higher concentrations of cobalt have been found to reduce the bacterial population in the rhizosphere, adversely affecting nodulation and resulting in decreased crop growth and yield. Detrimental effects on plant growth, including chlorosis and necrosis, were reported at elevated cobalt concentrations. Additionally, high cobalt levels were found to inhibit root growth by retarding cell division, impeding the uptake and translocation of nutrients and water [3].

Minerals undergo constant circulation between living organisms and their environment. The uptake and assimilation of minerals by plants constitute a pivotal step in the mineral cycle within the biosphere. Therefore, the expansion of the root system, particularly its capacity to absorb varied concentrations of soil mineral nutrients, significantly influences the nutrient uptake process. The movement of ions within plant tissues, involving the transfer of water from one cell's vacuole to another, occurs along a specific route termed the cytoplasmic pathway. This trajectory serves as the primary path for ion movement. It is essential to acknowledge the movement of ions from the cytoplasm and their entry into the cytoplasm of neighboring cells. Additionally, there exists an alternative route known as the extra-cytoplasmic pathway, which traverses the structural walls of cells and intercellular spaces.

Saffron (*Crocus sativus* L.) is a perennial herbaceous plant classified as a monocot flowering and stemless herb within the *Iridaceae* family of the *Asparagales* order. Typically reaching a height of up to 35 cm, saffron is cultivated on more than 100,000 hectares of Iranian farms, yielding an annual saffron production of approximately 340 tons. Remarkably, Iran is responsible for over 90% of global saffron output [4]. Despite saffron cultivation being distributed across 20 provinces in Iran, the vast Khorasan region, encompassing North, South and Khorasan Razavi provinces, contributes to over 90% of the national saffron production. Within the great Khorasan region, Torbat Heydarieh County emerges as a pivotal contributor to the overall production of Iranian saffron [5].Selection is the cellular property through which

a cell selectively absorbs and stores certain elements from its environment, or conversely, absorbs minimal amounts of others. The penetration rate of materials into lethal fibers' cells is inversely proportional to the coarseness of the adsorbed particles. Cell permeability demonstrates variability based on mineral concentrations within the cells, even in non-root cells isolated from a plant tissue. Maintaining a balance between cations and anions is crucial within cells. The observed connections between intracellular factors and substance permeability in the cell establish links between metabolism and substance absorption [6].

The primary objective of this investigation is to assess cobalt concentrations in saffron and a farm, utilizing neutron activation analysis as a nuclear spectrometry method. Additionally, the study explores the translocation potential of cobalt in saffron through translocation indexes.

RESEARCH THEORIES AND EXPERIMENTAL

This study involves the collection of two distinct types of samples: (I) soil samples and (II) plant samples. The saffron plant's organs can be categorized into three main groups. The corm, situated beneath the soil surface, constitutes the initial part of the plant. Herbaceous organs encompass leaves, petals, and stems. The stigmas, represented by the red threads, serve as the final organ and are the sole edible part of the saffron plant. Consequently, saffron plant samples for this study comprise three primary categories: (a) corm: C sample, (b) herbaceous specimens: H sample, and (c) stigmas: S sample. Saffron corms are positioned at a soil depth of 15–30 cm. Therefore, in cultivated farms, the soil is plowed to a depth of 30 cm. However, beyond a depth of 30 cm, the soil becomes considerably dense, hindering easy water absorption [7]. As a result, soil samples were collected from two specific types: (a) topsoil (up to a depth of 15 cm): TS sample and (b) soil surrounding the saffron corm: CS sample (at a depth of 15–30 cm).

Torbat Heydarieh is situated in the Khorasan Razavi province, approximately 150 km south of Mashhad. The geographic coordinates for Torbat Heydarieh are a longitude of 35°:16' and a latitude of 59°:13'. The area of Torbat Heydarieh spans 3681 km^2 [8]. Figure 1 displays maps of IRAN (left), Khorasan Razavi province (middle), and Torbat Heydarieh (right).

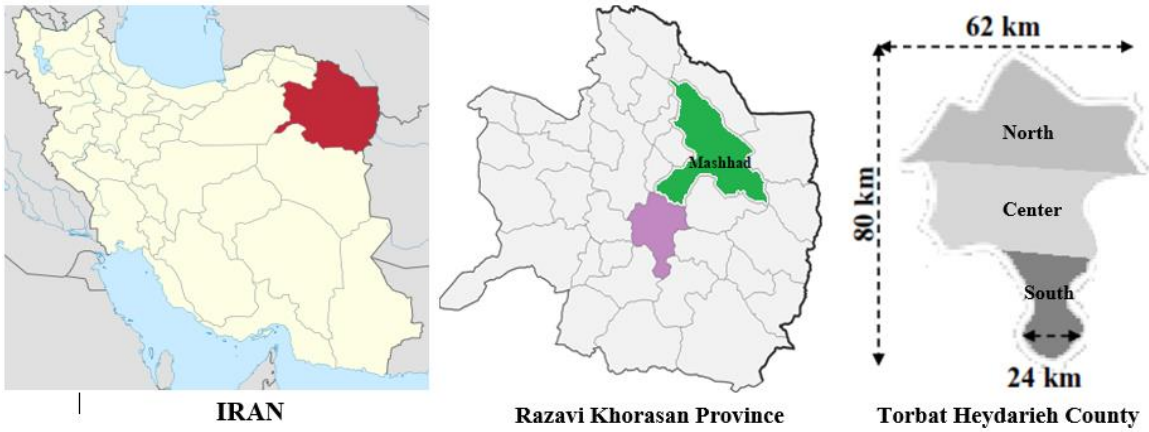

Fig. 1. Maps of IRAN (left), Khorasan Razavi province (middle), and Torbat Heydarieh (right).

In this study, the stratified random sampling method was implemented. The study area was divided into three zones (North (N), Center (C), and South (S)), as depicted in Figure 1 (left), based on administrative divisions. Subsequently, four roughly equal parts were designated for sampling within each zone, resulting in sampled areas of approximately 300 km^2 each. The focus was on saffron farms with the highest cultivation and production levels in each sampled area, and a composite sample for each type was then prepared for every farm.

For the collection of plant and soil samples, a combination of a garden shovel, scissors, and a manual earth auger was employed. The plant samples underwent a washing process with distilled water, followed by a reduction in humidity using dry air over approximately one week. Following this, both soil and plant samples were initially crushed using an electric grinder and then finely powdered using a ceramic mortar and pestle. The final step involved sifting the samples through a lab sieve shaker, and the resulting material was packaged in specialized plastic cylinders.

In this investigation, neutron activation analysis (NAA) was employed to ascertain the concentrations of cobalt in the samples. NAA is recognized as one of the most precise analytical methods, involving a comparison of the sample's activity with that of a standard

sample to overcome certain practical limitations. The primary equations of relative NAA are outlined in Eq. 1 [6]:

$$R = \frac{M}{T}\frac{A_{sam}}{A_{st}} \quad (1)$$

where R is the weight concentration of cobalt in the sample, A_{sam} and A_{st} are the activities of cobalt in the sample and standard, respectively, T and M are the sample total mass and cobalt mass of standard, respectively.

The selection of a particle or photon source is a critical aspect of spectrometry systems. Neutron sources can be categorized into three main groups, each with distinct applications: (I) radioisotope, (II) neutron generator, and (III) nuclear reactor. Among these, the nuclear reactor stands out as the most reliable and effective source of neutrons [9]. In the present study, the Tehran Research Reactor (TRR) was employed as the neutron source.

The evaluation of phytoremediation capacity for absorbing an element from the soil often relies on two widely used factors. The first is the Biological Concentration Factor (BCF), which quantifies the translocation ability of an element from the soil to the plant root. BCF is calculated using Eq. 2. The second index used to assess the translocation ability of an element from soil to a plant is the Biological Accumulation Factor (BAF), calculated using Eq. 3 [10]:

$$BCF = \frac{Element\ in\ root}{Element\ in\ soil} \quad (2)$$

$$BAF = \frac{Element\ in\ aerial\ parts}{Element\ in\ soil} \quad (3)$$

While the BAF of a plant reflects the uptake of a specific element from all exposure paths (such as soil, water, and air), the plant BCF specifically denotes the element uptake from the soil. A plant is deemed a proficient accumulator of a trace element when BCF > 1 (or BAF for all exposure paths).

Conversely, a BCF less than 1 implies a plant is a poor accumulator of a specific element from the soil. Additionally, the estimation of an element's translocation ability within a plant, from

roots to aerial parts, is represented by the translocation factor (TF) value. A higher TF signifies increased translocation ability, and Eq. 4 is employed to calculate TF [11]:

$$TF = \frac{Element\ in\ aerial\ parts}{Element\ in\ root} \quad (4)$$

Results and discussion

In this investigation, three standard samples sourced from the TRR reactor underwent repeated measurements, exceeding 10 iterations, utilizing neutron activation analysis (NAA) to evaluate precision and accuracy. The study involved the calculation of relative standard deviation (RSD) and average RSD (ARSD) specifically for cobalt, yielding an ARSD of less than 5%, signifying a notable level of precision. Precision is deemed satisfactory when RSD is under 20%, aligning with the International Atomic Energy Agency's recommendation of RSD values below 10% in the realms of biomedical and biophysics [6]. The accuracy of NAA results was substantiated through the comparison of measured and confirmed concentrations, revealing minimal standard deviations and relative errors, thereby establishing its suitability for discerning cobalt concentrations in bio-samples from saffron plants and soil. Prior research further corroborated NAA's elevated accuracy in determining trace elements within biological samples [12].

The samples and established standards underwent simultaneous exposure to the TRR reactor core, following which cobalt concentrations were computed using Equation 1. This process was iterated a minimum of three times for each sample. Figure 2 depicts the average cobalt concentrations and their comparison across different sites.

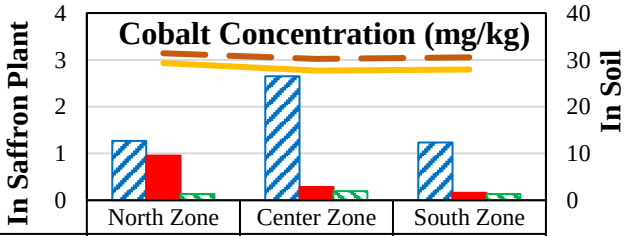

	North Zone	Center Zone	South Zone
Corm	1/27	2/65	1/23
Herbaceous	0/95	0/28	0/16
Stigmas	0/14	0/20	0/14
Soil at 0-15 cm	31/40	30/20	30/50
Soil at 15–30 cm	29/30	27/70	27/90

Fig. 2. Average cobalt concentrations and their comparison across different sites.

To assess the mobility of each mineral at different soil depths, a paired t-test was employed for cobalt. This involved forming statistical pairs for two distinct soil depths. The computed p-values from the paired t-test indicated that cobalt concentrations were statistically consistent between the topsoil and the adjacent soil surrounding the saffron corm in all studied zones of

Torbat Heydarieh. This finding suggests a significant translocation ability of cobalt throughout the soil.

In this investigation, three parameters were employed to evaluate the pathways of cobalt absorption from the environment to the saffron plant, as depicted in Figure 3.

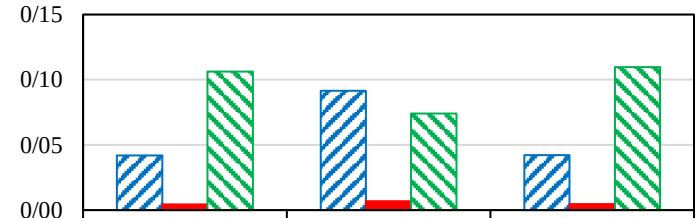

	North Zone	Center Zone	South Zone
BCF	0/042	0/092	0/042
BAF	0/004	0/007	0/005
TA	0/106	0/074	0/110

Fig. 3. Bioconcentration Factor (BCF), Bioaccumulation Factor (BAF), and Translocation Ability (TA) of cobalt in three study zones of Torbat Heydarieh.

Firstly, the Bioconcentration Factor (BCF) assessed metal absorption by the saffron root (corm). Secondly, the Bioaccumulation Factor (BAF) estimated metal intake by the aerial parts of the saffron plant from the soil. Lastly, the Translocation Ability (TA) of cobalt from the corm to the aerial parts of the saffron plant was calculated. BCF values for cobalt were

consistently below 0.10 across all study zones, indicating that saffron cannot be categorized as an effective absorber of cobalt. Additionally, calculated BAFs for the aerial parts of saffron were all below 0.01, suggesting that these parts are poor accumulators of cobalt directly from the soil. The Translocation Factor (TF) index, reflecting the movement of minerals from the root to other plant parts, was greater than 0.05 for cobalt in all study zones, indicating a robust translocation ability of cobalt throughout the saffron plant.

Conclusions

This research utilizes Neutron Activation Analysis (NAA) to ascertain cobalt concentrations in saffron plants and a farm. With the greater Khorasan region contributing over 90% of Iran's saffron production, and Iran itself accounting for over 90% of global saffron output, Torbat Heydarieh county, a key saffron-producing area, was selected for sampling. NAA results reveal cobalt concentrations in saffron corm and aerial parts within adequate ranges for plant growth, with levels below toxicity thresholds. Saffron is not identified as a significant cobalt

accumulator; calculated Bioaccumulation Factors (BAFs) for aerial parts are consistently below 0.5, indicating limited direct soil-to-organ cobalt accumulation. The Translocation Factor (TF) for cobalt from petals and threads to all aerial tissues is less than one, suggesting lower uptake and accumulation of cobalt in aerial tissues compared to the corm of the saffron plant.

Acknowledgements

This research has been financially supported by the University of Torbat Heydarieh..

References

[1] Mathur N., Singh J., Bohra S., Bohra A., and Vyas A. (2006). Effect of Soil Compaction, Potassium and Cobalt on Growth. International Journal of Soil Science, 1(3): 269-271.

[2] Minz A., Sinha A.K., Kumar R., Kumar B., Deep K.P., and Kumar S.B. (2018). A review on importance of cobalt in crop growth and production. International Journal of Current Microbiology and Applied Sciences, 7: 2978-2984.

[3] Jayakumar K., Jaleel C.A., and Azooz M. (2008). Impact of cobalt on germination and seedling growth of Eleusine coracana L. and Oryza sativa L. under hydroponic culture. Global Journal of Molecular Sciences, 3(1): 18-20.

[4] Koocheki A., Moghaddam P.R., and Seyyedi S.M. (2019). Saffron-pumpkin/watermelon: A clean and sustainable strategy for increasing economic land equivalent ratio under limited irrigation. Journal of Cleaner Production, 208: 1327-1338.

[5] Koocheki A. and Seyyedi S.M. (2015). Phonological stages and formation of replacement corms of saffron (Crocus sativus L.) during growing period. Journal of Saffron Research, 3: 134-154.

[6] Tousi E.T. (2022). Determining the mobility of some essential elements in saffron (*Crocus sativus L.*) by the neutron activation analysis. Baghdad Science Journal, 19(2): 0283-0283.

[7] Koocheki A. and Seyyedi S.M. (2019). Mother corm origin and planting depth affect physiological responses in saffron (Crocus sativus L.) under controlled freezing conditions. Industrial Crops and Products, 138: 111468.

[8] Mirzabeygi M., Yousefi N., Abbasnia A., Youzi H., Alikhani M., and Mahvi A.H. (2017). Evaluation of groundwater quality and assessment of scaling potential and corrosiveness of water supply networks, Iran. Journal of Water Supply: Research and Technology—AQUA, 66(6): 416-425.

[9] Klix A., Arbeiter F., Majerle M., Qiu Y., and Štefánik M. (2019). Measurement of neutron fluence in the High-Flux Test Module of the Early Neutron Source by neutron activation. Fusion Engineering and Design, 146: 1258-1261.

[10] Rai P.K., Lee S.S., Zhang M., Tsang Y.F., and Kim K.H. (2019). Heavy metals in food crops: Health risks, fate, mechanisms, and management. Environment International, 125: 365-385.

[11] Coakley S., Cahill G., Enright A.M., O'Rourke B., and Petti C. (2019). Cadmium hyperaccumulation and translocation in *impatiens glandulifera*: From foe to friend? Sustainability, 11(18): 5018-5035.

[12] Dybczyński R.S. (2019). The role of NAA in securing the accuracy of analytical results in the inorganic trace analysis. Journal of Radioanalytical and Nuclear Chemistry, 322(3): 1505-1515.

ICNST 2024
International Conference on Nuclear Science and Technology
6- 8 MAY 2024 | Isfahan, Iran

Simulation of SARS-CoV-2 virus inactivation by electron irradiation using Geant4 toolkit (Paper ID : 1120)

Jalili Torkamani M.[1*], Sayyah-Koohi P.[1], Zolfagharpour F.[1], Sabouri H. [1], Karami Ch.[2]

[1] *Department of Physics, Faculty of Science, University of Mohaghegh Ardabili, Ardabil, Iran*

[2] *Department of Microbiology, Parasitology and Immunology, Ardabil University of Medical Sciences, Ardabil, Iran*

Abstract

One of the effective strategies for inactivating the SARS CoV-2 virus is using of radioactive radiation. In this research, after designing and simulating the Omicron variant of SARS-CoV-2 virus, it was exposed to electron radiation up to 20 keV. The absorbed energy and absorbed dose in spike protein, nucleocapsid protein and envelope lipid was measured by the Geant4-DNA toolkit in the water environment. Since the viral RNA is located inside the nucleocapsid protein, damaging to this area can lead to damage to the viral RNA and thus its inactivation. The findings in this research show that the most appropriate energy region for causing maximum damage occurs in the nucleocapsid region for electrons with energy of 2-3 keV, which has a peak at 2.5 keV. Our findings show that electron beams with an energy of 2.5 keV could cause a maximum absorption dose and consequently maximum damage to the nucleocapsid and effectively be used for inactivation virus purposes.

Keywords: Geant4, electron radiation, SARS-CoV-2, Omicron Variant

INTRODUCTION

Covid-19 infections were observed from early October to mid-November 2019 in China [1]. The SARS-CoV-2 virus is known as the main source of the Covid-19 infections. Although there is no certainty about the place and time of the first SARS-CoV-2 infection cases. SARS-CoV-2 virus consists of single-stranded RNA [2, 3]. The virus is made of enveloped, positive-sense, and single-stranded RNA. SARS-CoV-2 has 29 proteins; 16 of them are non-structural and 4 are main structural proteins [4,5]. These four structural proteins play a major role in virus transmission and RNA packaging [6]. Four structural proteins were nucleocapsid protein (N), spike protein (S), envelope protein (E), and membrane protein (M). The N protein was bound to RNA to build up the nucleocapsid. S protein was responsible for virus binding to host cells

and RNA transmission. The E protein interacts with M to form a viral envelope. And M protein has two essential functions: central organizer of virus assembly and shape determinant of viral envelope [7, 8]. Spike is an essential protein for interacting with host cell receptors and then fusing with the host cell membrane to initiate infection [9]. Spikes of viruses are located on the outer surface of the membrane through which entry the host cell is carried out.

The most recent and widespread one based on recent reports is omicron (B.1.1.529). This variant was detected in November 2021 in South Africa and detected in many countries in a short time [10]. There are several ways to inactivate viruses, including thermal methods, irradiation with UV, and chemical approaches. Thermal methods at 56°C for SARS-CoV and 80°C for SARS-CoV-2 could effectively inactivate the virus [11]. UV light with energies higher than 0.04 J/cm2 [12] or femtosecond lasers might also inactivate SARS-CoV2 [13]. One of the novel methods for SARS-CoV-2 inactivation, ionization irradiation, is promising. This method has already been used for decades to inactivate viruses [14]. Charged particles such as proton and alpha radiation would also inactivate the virus completely. Monte Carlo simulations showed accelerated heavy ions could be an option for virus inactivation. The choice of an effective method is usually determined by its characteristics and response time. Radiations with high linear energy transfer (high-LET) were more effective in virus inactivation than low-LET radiations [15].

In this study, due to the presence of water, indirect effects play a major role. Fortunately, Geant4-DNA provides features to analyze water radiolysis [16]. Features of this toolkit also let us study excitations and charge exchange in water. This software was able to track lengths in the order of a few nanometers.

RESEARCH THEORIES

Geant4.11 version has been used in this study. This version was updated in December 2021 by the collaboration of CERN. Geant4-DNA provides an environment to analyze molecular damages caused by ionizing radiation [17]. In this toolkit, all molecules and DNA strands were defined by default in the water environment [18, 19].

G4EmDNAPhysics.hh class was used in this simulation to investigate indirect collisions and study the effects of secondary ionization of particles when they collide with water molecules. This class is used as a standard class to investigate the collision of ionizing particles with the

intended target in molecular dimensions, so it is a suitable class for collecting secondary particles and thus the energy transferred to the target.

EXPERIMENTAL

To design the Omicron variant, its four coat proteins were defined as follows in the software. To design nucleocapsid protein a sphere with a radius of 80 nm simulated by using G4Orb class. Following elements with respective percentages were placed in. Nitrogen 9.52%, Oxygen 9.86%, Carbon 31.05%, Sulfur 0.11% and hydrogen 49.46%. Total density of the designed sphere was 0.968 g/cm^3 at the end.

Next step, was designing of envelope. A 3D ring drew using the G4Sphere class. Inner radius was set to 80 nm and outer radius set to 100 nm. Constituents were following elements with respective percentages: Nitrogen 7.47%, Oxygen 8.38%, Carbon 32.18%, Sulfur 0.33% and Hydrogen 51.64%. Total density of designed envelope was 0.726 g/cm^3.

Using the G4Cons class the spike structure was designed. We chose a conical shape for spikes with an upper diameter of 8 nm, lower diameter 4 nm and height of 10 nm. 426 spikes were designed with a total density of 1.054 g/cm^3. Fig 1 shows the simulated virus with each spikes. According to obtained sequence spikes designed to consist of 8.38% Nitrogen, 32.18% Oxygen, 0.28% Carbon, 9.51% Sulfur and 49.65% hydrogen. Spikes were placed symmetrically and isotropically over envelope. To rotated spikes over envelope G4RotationMatrix class was used and entire surface of the virus was covered uniformly by spikes.

Virus was placed in a cubic box with dimensions of 170 nm. The box surrounded by water and density of water was density of 1 g/cm^3 with temperature of 293.15 K and pressure is 101.325 kPa.

According to the LEA Target Theory, which is one of the first interpretation methods to express the effect of radiation leading to cell killing, the survival fraction for a target called the Single Hit Single Target (SHST) model is expressed as follows [20].

$$(1) S = e^{-VD}$$

Where D represents the radiation dose and V denotes the target volume.

In the next part of this study, the effect of the electron beam on the molecular structure of the Omicron spike has been studied using its PDB structure implementation.

Results and discussion

After running the spike of Omicron PDB file, these molecules were exposed to electron irradiation. Figure1 shows spike inside a box filled with water. The elements Carbon, Oxygen, Nitrogen, Phosphorus, and Hydrogen are denoted by gray, red, blue, yellow, and white colors, respectively. Figure1 displays the spike before and after collision with single-energy electron particles, with the left side depicting the spike before collision and the right side showing the spike after collision.

To clearly convey the shape of the molecule after collision, the figure includes 20 electron particles. The background color of the box is blue to better illustrate the water inside. As mentioned in the Materials and Methods section, the radiation electrons hit the target from the edges.

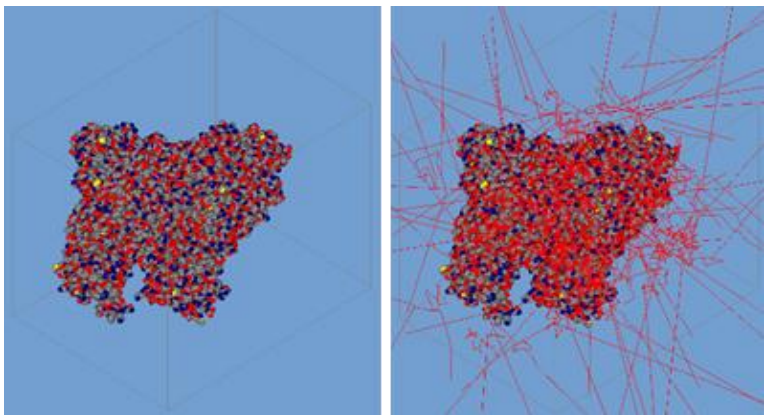

Figure. 1. Displays the spike structure of the Omicron viruses in a water environment within a box measuring 1000 Å in dimensions. The left side of Figure 1a shows the Omicron virus spike, while the right side shows the same spike after being impacted by 20 electrons with an energy of 400 eV [21].

Figure.2a, shows the energy absorbed by the Omicron spike in terms of the energy of emitted electrons, in each step the number of electrons emitted from the source of electron production was considered 1000. Figure.2b, shows the number of electrons that have been able to interact with the Omicron spike and leave energy in it at each stage.

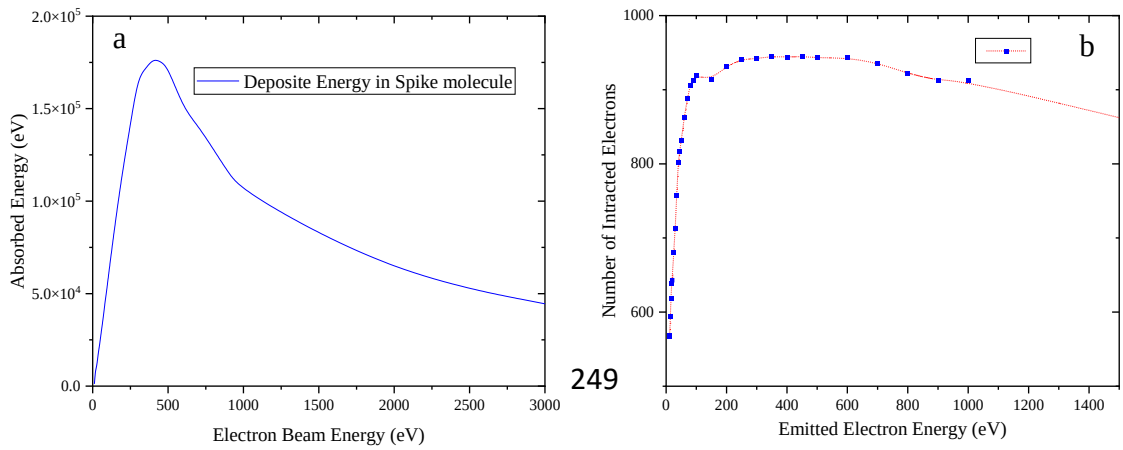

Figure. 2a shows absorbed energy in spike molecule versus emitted electrons energy**. b** shows interacted number of electrons with spike protein in each energy step. All number of emitted electrons is 1000 in each step.

In next assumption in this study, after designing the virus, electrons were randomly emitted towards the box in a parallel planar beam to the z axis. Fig. 3 shows the simulation stage scheme. A large enough number of electrons would cover the entire cross-section of the simulation box and hit water and viruses. This energy was transferred from the water environment to the virus by secondary electrons.

When these electrons interact with the target, the process ends by transferring the energy of the electrons to the virus. In this study, the minimum energy of electrons to transfer to the virus was considered to be 7.4 eV, which is compatible with the elastic interaction model.

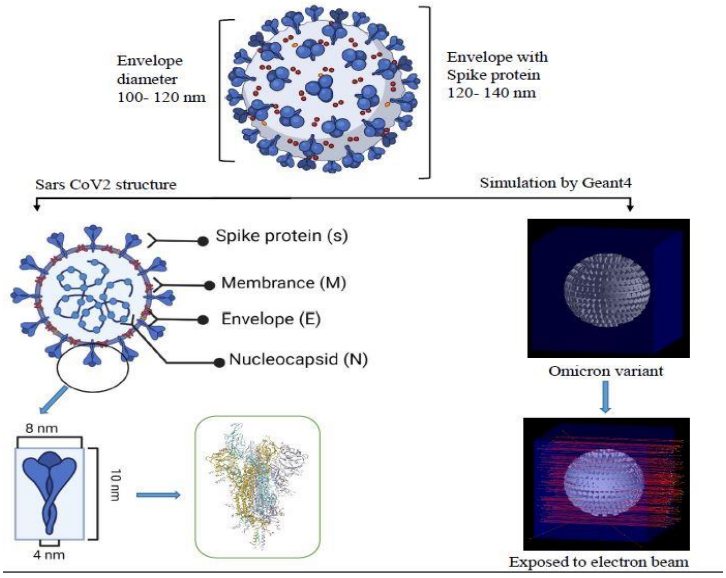

Figure. 3. Simulation stage scheme.

Due to the high importance of the three areas of nucleocapsid, spike and envelope, in this study, the effect of energy on these three areas was studied. The spike is the virus's first line of defense against radiation and environmental hazards, so absorbing energy in this area can greatly affect the survival or non-survival of the virus.

The nucleocapsid region includes the virus genome and its RNA, therefore energy absorption and dose in this region can be involved as an important parameter in the survival of the virus. For this reason, the amount of energy absorption in the above three areas is of particular importance.

Figure 4 shows the amount of energy absorbed by the above-mentioned three areas in the virus in terms of electron beam energy, and in part B, the absorbed dose is drawn in these areas.

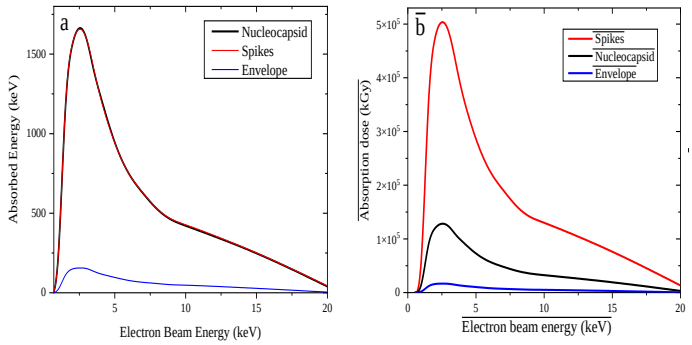

Figure. 4 a Absorbed energy in terms of incident electron energy for the spike, nucleocapsid and envelope. **b** Absorbed energy in terms of incident electron energy for the spike, nucleocapsid and envelope.

Figure 4 shows that the amount of energy absorption in the spike and nucleocapsid regions is higher than the environment of the envelope, this can be due to the structures of these two regions. Because we know that the spike and nucleocapsid regions have protein properties, but the envelope has a lipid environment. But the absorbed dose in the spike area is higher than the other two areas. As expected, the spike area, as a defensive area against environmental hazards, was able to absorb a large fraction of the absorbed dose by the virus.

Figure 4 also shows that most of the dose and energy absorption in the virus is in the area where the incident electron energy is around 2-3 keV. Therefore, this region of energy for incident electrons can be considered as the best energy region for the inactivation of this virus by electron beam.

Using equation 1 and having the data of chart 4 in hand, the virus survival table can be drawn. In Table 1, the survival rate and probability of virus inactivation are calculated according to the intensity of incident electron radiation. It should be noted that considering that damage to the nucleocapsid region can lead to the rupture of this region and the leakage of viral RNA from it, the effective dose in the nucleocapsid region has been used in the calculations of the table.

Table 1. The electron numbers with various energies (E_e), survival fraction (S), and inactivation probabilities (P) were calculated for the Omicron variant [22].

E_e (keV)	Electron Number	S	P
2	10^3	94%	6%
	10^4	54.8%	45.2%

2.5	10^3	88%	12%
	10^4	28%	72%
3	10^3	94.7%	5.3%
	10^4	58%	42%

According to Table 1, it can be seen that the most appropriate energy for electron beams to inactivate the Omicron variant of SARS-CoV-2 is 2.5 keV. According to the information in Table 1, for intensity10^4, this value is around 72%

Conclusions

In conclusion, the most suitable energy for the inactivation of the Omicron variant of the SARS-CoV-2 virus is through the impact of electron beams with an energy of 2.5 keV. In this energy, according to the intensity of the electron beam, it can be expected that the variant will be inactivated by at least 72% to more than 90%.

Acknowledgements

The authors would like to acknowledge staff of nuclear lab of University of Mohaghegh Ardabili to giving allow access to their computer.

Supplementary information

Supplementary data to this article can be found online at https://doi.org/10.1016/j.net.2024.01.056.

References

[1] D.L. Roberts, J.S. Rossman, and I. Jaric,Dating first cases of COVID-19, Plos Pathogens.17(6), e1009620 (2021).

[2] L. Min, and Q. Sun, Antibodies and Vaccines Target RBD of SARS-CoV-2, Frontiers in Molecular Biosciences. (8), 671633 (2021).

[3] R. Lu et al. February 2020. Genomic characterization and epidemiology of 2019 novel coronavirus: implications for virus origins and receptor binding, The Lancet. 395(10224), 565-574 (2020).

[4] Aboubakr, H., et al., Stability of SARS-CoV-2 and other coronaviruses in the environment and on common touch surfaces and the influence of climatic conditions: A review. Transboundary and Emerging Diseases, 2021. 68(2): p. 296-312.

[5] Alsobaie S. Understanding the Molecular Biology of SARS-CoV-2 and the COVID-19 Pandemic: A Review. Infect Drug Resist. 2019. 14:2259-2268.

[6] Yang, Q., et al., Structural Analysis of the SARS-CoV-2 Omicron Variant Proteins. Research. 2021. p. 9769586.

[7] Seah, I., X. Su, and G. Lingam, Revisiting the dangers of the coronavirus in the ophthalmology practice. Eye (Lond), 2020. **34**(7): p. 1155-1157.

[8] M. J. Torkamani, et al. Investigation of electron beam irradiation effect on spikes of SARS-COV2, MERS-COV, UK variant, SARS-COV by Geant4-DNA toolkit. J. Science and Technology, 2023. Vol. 87, No. 2.

[9] X. Dong Wu et al. The spike protein of severe acute respiratory syndrome (SARS) is cleaved in virus infected Vero-E6 cells. Cell Research, 14, 400-406 (2004).

[10] Pascarella, S., et al., The electrostatic potential of the Omicron variant spike is higher than in Delta and Delta-plus variants: A hint to higher transmissibility? J Med Virol, 2022. 94(4): p. 1277-1280.

[11] Patterson, E.I., et al., Methods of Inactivation of SARS-CoV-2 for Downstream Biological Assays. J Infect Dis, 2020. 222(9): p. 1462-1467.

[12] Xiling, G., et al., In vitro inactivation of SARS-CoV-2 by commonly used disinfection products and methods. Sci Rep, 2021. 11(1): p. 2418.

[13] Pereira, P.F.S., et al., Inactivation of SARS-CoV-2 by a chitosan/alpha-Ag2WO4 composite generated by femtosecond laser irradiation. Sci Rep, 2022. 12(1): p. 8118.

[14] Durante, M., et al., Virus Irradiation and COVID-19 Disease. Frontiers in Physics, 2020.

[15] Francis, Z., et al., Monte Carlo Simulation of SARS-CoV-2 Radiation-Induced Inactivation for Vaccine Development. Radiat Res, 2021. 195(3): p. 221-229.

[16] Bernal, M.A., et al., Track structure modeling in liquid water: A review of the Geant4-DNA very low energy extension of the Geant4 Monte Carlo simulation toolkit. Phys Med, 2015. 31(8): p. 861-874.

[17] Incerti, S., et al., Energy deposition in small-scale targets of liquid water using the very low energy electromagnetic physics processes of the Geant4 toolkit. Nuclear Instruments and Methods in Physics Research Section B: Beam Interactions with Materials and Atoms, 2013. 306: p. 158-164.

[18] Incerti, S., et al., The Geant4-DNA Project. Int. J. Model. Simul. Sci. Comput., 2010. 1.

[19] Incerti, S., et al., Review of Geant4-DNA applications for micro and nanoscale simulations. Phys Med, 2016. 32(10): p. 1187-1200.

[20] Zhao, L., et al., A generalized target theory and its applications. Scientific Reports, 2015. 05: p. 14568.

[21] M. J. Torkamani, et al., Simulation of energy absorption and dose of ionizing radiation on spike of SARS-CoV-2 and comparing it with human mortality statistics, using Geant4-DNA toolkit. Eur. Phys. J. Plus, 2024. 139- 103.

[22] M. J. Torkamani, et al., Dose absorption of Omicron variant SARS-CoV-2 by electron radiation: Using Geant4-DNA toolkit. Nuclear Engineering and Technology, 2024. 1738-5733.

ICNST 2024
International Conference on Nuclear Science and Technology
6- 8 MAY 2024 | Isfahan, Iran

X-Ray Absorption Spectroscopy as a tool to study Lanthanide-based complexes and MOFs to nuclear energy appplications (Paper ID : 1130)

Danilo Oliveira de Souza[1*], João Victor Viana da Silva[1], Juliana Fonseca de Lilma[1], Seyedeh Zahra Karrari[2], Marcos Vinícius Colaço Gonçalves[1],

[1]*Physics Institute, State University of Rio de Janeiro, Rio de Janeiro, Brazil*

[2] *Department of Energy Engineering and Physics, Amirkabir University of Technology, Tehran, Iran*

Abstract

The search for cleaner nuclear energy has attract an extra attention nowadays. Lanthanide-based materials, such as complexes and metal-organic frameworks (MOFs) are versatile materials that can be used, for instance, as fluorescent probes for very diluted UO_2^{2+} in water, can act as scintillators when stimulated by ionizing radiation or as a trap to radioactive nuclides or their byproducts. Our group have been synthesizing new Ln-based materials presenting properties to be potentially used in the nuclear energy production chain. We have been concerned mainly on the description of the structure and properties of such materials aiming targeted applications. Here we present the XAS (X-ray absorption spectroscopy) study of some samples recently carried by our group in harsh conditions, e.g., high temperature. Specifically, we have observed the dynamics of the oxidation state of Lanthanide-complexes of luminescent materials with increasing the temperature up to 500 °C.

Keywords: Lanthanides, Luminescence, Metal-organic frameworks, nuclear energy, X-ray absorption spectroscopy

Introduction

The current global efforts to gradual depletion of nonrenewable fossil-based energy production have turned attention to further developments of efficient and cleaner nuclear energy. Although the advances in the low-carbon and sustainable energy sources developed, the nuclear power still plays an important role in electricity generation in an increasing global demand [1]. Further, radionuclide for practical applications, such as in medicine or agriculture, have been more widespread. In this picture, an extra attention has been devoted to the harmful environment and biological byproducts resulted from radioactive management, such as radioactive wastewater or radioactive nuclides. As an example, one can number certain species

that either difficult to capture in the environment, such as I, Cs and Tc, or that are like common elements in biological environment, such as Cs^+ and Sr^{2+}, which can replace K^+/Na^+ and Ca^{2+}, respectively [2]. On another aspect, uranium is a central character in the nuclear industry, not only because it represents the main mineral source of radiation that feeds the power plants, but also by the high toxicity for human body. Particularly, in wastewater from energy production, it presents under form of UO_2^{2+} ion. Due to its high half-life, it can enter in the human body by many ways [3]. Thus, monitoring uranium (also deal with the detection, separation, and recovery), and particularly, uranyl (UO_2^{2+}, where U has formal oxidation state equals to 6+), the most common and stable form of uranium in solution, is a crucial factor when dealing with nuclear energy production.

Among the methods presented to handle uranium in solution, metal-organic frameworks (MOFs) have been widely explored nowadays. MOFs are a class of porous-crystalline compounds with high specific surface area that have been developed to a huge number of applications due to their versatility in be tailored by changing the metal cluster, the ligands, and the coordination modes in the metal-ligand bridge [4]. They present one-, two-, or three-dimensional structures in which the pores are usually used to interact with guess molecules or surfaces. Therefore, MOFs are of a major interest in the field of gas storage and separation, catalysis, or sensing small molecules, especially in the field of nuclear management [1], [5], [6]. In this picture, a key feature presented by MOFs is that of the design to make them tunable for sequestration and separation of gas-phase radionuclides as well as cationic and anionic radionuclide sequestration [6], [7]. Since nuclear processes, as mentioned before, occurs in harsh conditions, such as high-temperature or high-acidity, it is important to develop structures with high thermal stability, and so, keeping the ordered pores to allow the diffusion of sorbates toward binding sites. One of such structures is the so called UiO-66 series of metal-organic framework (UiO stands for Universitetet i Oslo), which is made up of $[Zr_6O_4(OH)_4]$ clusters with 1,4-benzodicarboxylic acid struts [8]. Modifications (functionalization) on the basic structure have been performed to tailor such structures for I_2 and radioactive organic iodides sequestration by selecting ligands with more affinity for I_2, Xe/Kr adsorption with high selectivity, or uranyl sequestration [6].

As mentioned above, MOFs functionalization is done to make them more efficient for the target application. Concerning U(VI) adsorption by MOF-based materials, the functionalization

allows enhanced performance depending on the factors that influence the adsorption properties, named, pH value of the solution, adsorption time and temperature, ionic strength, and coexisting ions [9]. Particularly, concerning the UiO-66 series, the addition of a -NH_2 group has proven to have increased selectivity for UO_2^{2+} and I_2, which was attributed to the increasing of the ionic strength, and the addition of carboxyl groups (COOH) plays with the pH in the solution increasing the adsorption capacity [6], [9], [10]. It is also reported that functionalization with metals other than Zr (particularly, lanthanide substitution) can promote the target properties, such as the resistance to ionizing radiation, to MOFs for applications in nuclear processes [11], [12]. Accordingly, it seems clear that the most of the properties important to a good efficiency of MOFs are ruled by molecular features of the MOF itself, the functionalization group, and the interaction (the chemistry) of the target and the MOF.

In this context, X-ray Absorption Spectroscopy (XAS) has been no consolidated as a strong tool to study the interplay between structure and material properties at molecular/atomic level, taking advantage to allow implementation of harsh conditions, such as temperature and pressure, as well as time-resolved, in situ or operando conditions. XAS has been applied to investigate MOFs and Ln-based materials with nuclear interest applications ([13], [14], [15], [16]). Thus, to get newer insights on the role played by the functionalization of Ln-based materials to nuclear applications, we present XAS as a tool to unravel features of such systems. Herein, we describe some solids we have been synthesizing with potential application to nuclear interest and we show results of temperature-dependent XAS studies.

Research Theories: X-Ray Absorption Spectroscopy

X-ray absorption Spectroscopy (XAS) spectroscopy is one of the most powerful tools we have for mapping local structure. In this technique, one probes a sample with x-rays that are tuned to the energy of a core electron shell in the element we wish to study. One may monitor how many x-rays are absorbed as a function of their energy. If taken with sufficient accuracy, the spectrum exhibits small oscillations that are the result of the local environment's influence on the target element's basic absorption probability. This turns out to be a unique signature of a given material; it also depends on the detailed atomic structure and electronic and vibrational properties of the material. From the spectrum, one can extract the distances between the absorber and its near-neighbor atoms, the number and type of those atoms, and the oxidation state of the absorbing element—all parameters that determine local structure. By selecting a

different x-ray energy, one can obtain this information for any element in the sample, called atomic selectivity. Element-specific data can be obtained over a wide range of temperatures (room temperature to > 1000 K), and pressures (from sub ambient to well more than 100 bar). Because the specimen can be investigated under such a wide range of conditions, XAS has become one of the most frequently applied techniques for structural characterization of materials. Often there is no other way to obtain the structural information provided by this technique that allows one to develop specific structure-activity relationships. XAS is applicable to a broad range of elemental concentrations (from tens of ppm to wt. % levels), and therefore is used to characterize both high-surface-area supported systems and bulk materials (e.g., oxides). Although XAS has been used for almost 40 years as a tool of material characterization in the working state, methodology, equipment, and applications are still being advanced.

For this reason, XAS is a very important probe of materials, since knowledge of local atomic structure, i.e., the species of atoms present and their locations, is essential to progress in many scientific fields, whether for biology, chemistry, electronics, geophysics, metallurgy, or materials science. However, extracting this information with precision in the often complicated, aperiodic materials of importance in modern science and technology is not easy, even with the subtle and refined experimental techniques currently available.

XAS (or XAFS, X-Ray Absorption Fine Structure, when refereed to the specific structure on the XAS spectrum) began to emerge as a practical experimental tool in the early 1970s, after Dale Sayer, Edward Stern, and Farrel Lytle demonstrated that a Fourier transform could be used to analyze the absorption spectra ([17], [18]). Their work coincided with the development of synchrotron x-ray sources that emit enough x-ray photons in the right spectral range to enable rapid, highly accurate absorption measurements. With the subsequent availability of inexpensive computing power to analyze the data and implement the increasingly accurate theoretical models, XAS flourished.

When the X-ray energy is scanned through the binding energy of a core shell, there is an abrupt increase in absorption cross-section. This gives rise to a so-called absorption edge, with each edge representing a different core-electron binding energy (Figure 1). The absorption edge is not simply a discontinuous increase in absorption, but in fact shows significant structure both

in the immediate vicinity of the edge jump and well above the edge. The structure in the vicinity of the edge is referred to as X-ray absorption near-edge structure (XANES). The oscillations above the edge, which can extend for 1000 eV or more, are referred to as extended X-ray absorption fine structure (EXAFS). The XANES region is sensitive to oxidation state and geometry, but is not, in most cases, analyzed quantitatively. The EXAFS region is sensitive to the radial distribution of electron density around the absorbing atom and is used for quantitative determination of bond length and coordination number.

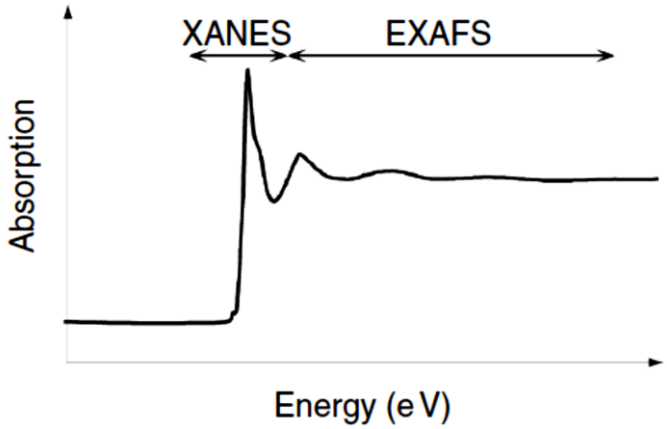

Figure 5. Schematic illustration of an X-ray absorption spectrum with the XANES and EXAFS

The main point in dealing with XAFS measurements is to get atomic structural information. A beautiful theory was developed to treat the EXAFS part of a XAS spectrum and it has shown work very well with a great sort of systems (e.g., [19]). The way it is used nowadays for this task is the so-called EXAFS equation. Since it is a quantum complex system, the derivation of the equation carries some approximations, which pass from the dipole-electron approximation, the scattering potential (the Muffin-tin approximation is the most known), relativistic effects, many-body effects, and so on [20]. Thus, the EXAFS equation is written as:

$$\chi(E) = \sum_R S_0^2 N_R \frac{|f(k)|}{kR^2} \sin(2kR + 2\delta_c + \Phi)\, e^{-2R/\lambda(k)} e^{-2\sigma^2 k^2}$$

(Eq. 1)

Here the structural parameters are the interatomic distances R, the coordination number (or number of equivalent scatters) N_R, and the temperature dependent *rms* fluctuation in bond length σ, which should also include effects due to structural disorder. In addition, $f(k)$ =

$|f(k)|e^{i\phi(k)}$ is the backscattering amplitude, δc is central-atom partial-wave phase shift of the final state, and $\lambda(k)$ is the energy-dependent XAFS mean free path. Although the overall amplitude factor S_0^2 did not appear in the original formula, one has added it here for completeness, since it considers many-body theory, provided the terms are appropriately renormalized. Moreover, although the original EXAFS formula referred only to single-scattering contributions from neighboring shells of atoms, the same formula can be generalized to represent the contribution from N_R equivalent multiple-scattering contributions of path length $R/2$. This formalism led to the interpretation of the short-range scattering around an absorber atom, and allowed the construction of the now-consolidated interpretation of EXAFS (Figure 2).

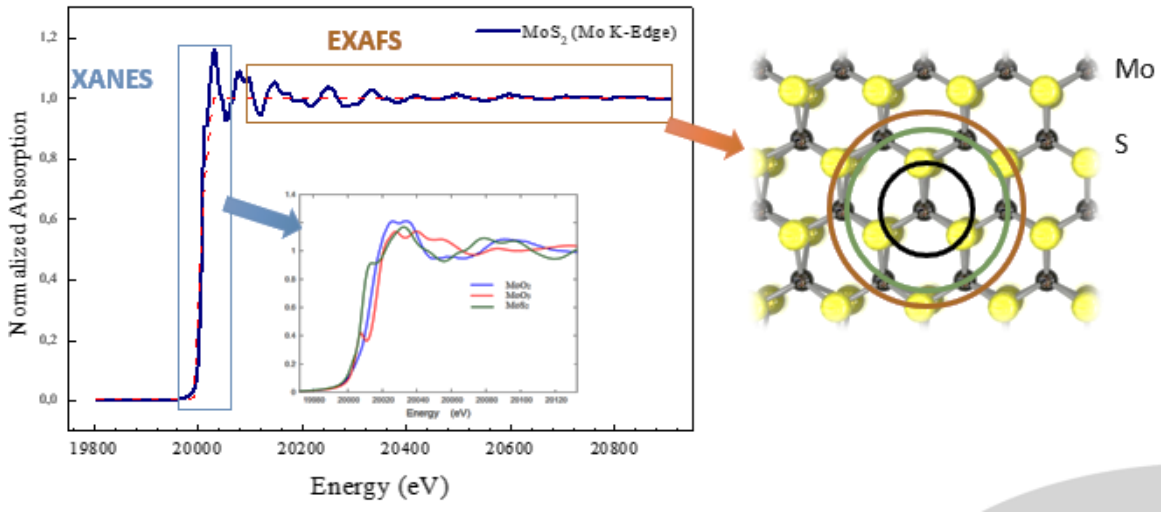

Figure 6. Standard depiction of XANES and EXAFS region and the construction of a molecular model obtained from EXAFS analysis.

Experimental

We have synthesized some Ln-based materials with potential applications to nuclear energy interest. Among them, we highlight the Ln-MOFS Ce-UiO-66 and MIL-53(Fe). The former was synthesized by solvothermal method, mixing the precursors (a solution of Terephthalic acid into Dimethylformamide and a solution of Ammonium cerium(IV) nitrate into water) at 100 °C. Then, the material is dried at 80 °C for h. The latter is prepared considering a solution of Fe(III) chlorite in Dimethylformamide and another of Terephthalic acid using the same solvent. After stabilization under stirring, the solution is dropped under heating (100 °C) for around 12h. The synthesis of other Ln-based materials, namely, Eu- and Gd-based complexes, is described elsewhere ([21], [22]).

The experiment was performed at XAFS beamline at Elettra ([23]) operating at 2.0 GeV. The beamline was set up for Eu L_3- and Gd L_3-edges at energy, respectively, of 6.977 and 7.243 keV. The Ionization chambers were filled with gas mixture to be optimized at 7 keV. The monochromatized beam, by Si(111) pair of crystals, was calibrated using a Fe-metal foil. A detuning of 30% on the second crystal was set to harmonic rejections. A set of samples (5 containing Eu and 5 containing Gd) and two oxide references (Eu oxide and Gd oxide) were collected ex-situ, and measurements at high temperature, namely, 100 ºC up to ~400 ºC, using the Aquila-Camerino furnace [23].

Results and discussion

Gd-based samples changed slightly upon temperature, as seen by the decreasing of the white-line intensity and the first few bumps after the edge (Figure 3a). Also, we see a slightly change on the oxidation state (Figure 3c) and EXAFS pattern (Figure 3b), indicating structural changes.

Surprisingly, the Eu-based equivalent samples were found to be much more temperature sensitive. Huge reduction from Eu^{3+} to Eu^{2+} was observed (Figure 3d). The peak at left of the white line (~ 6975 eV) represents the rising of the reduced Eu contribution increasing.

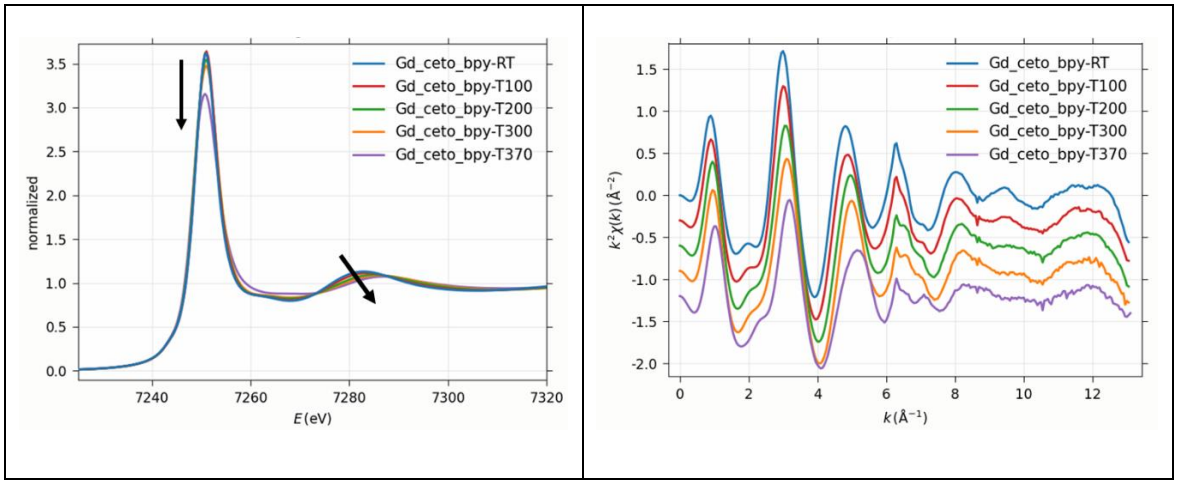

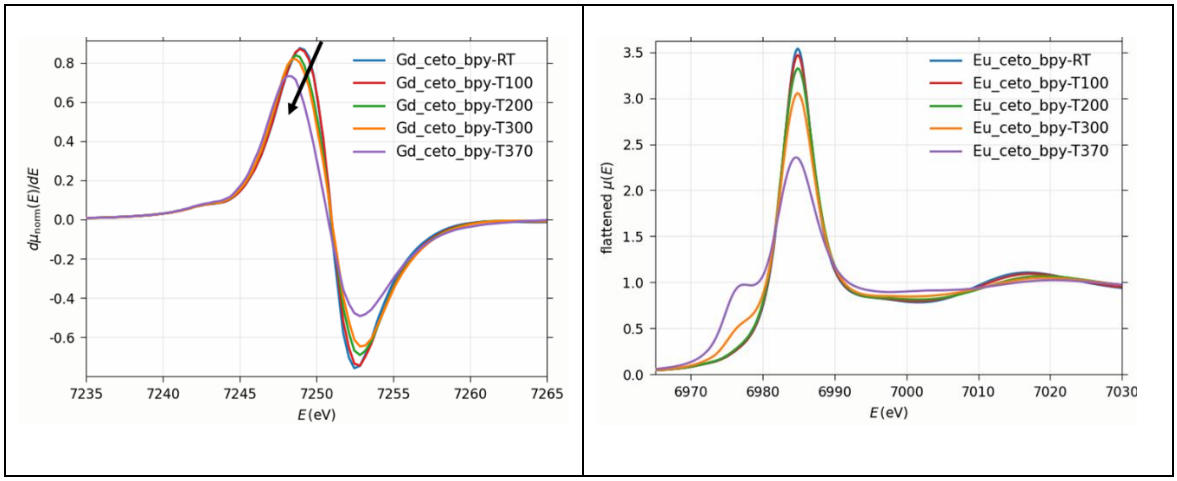

Figure 3. Temperature-dependent XAS study of Ln-based complexes at Gd and Eu L3-edges: (a) Gd XANES, (b) Gd EXAFS, (c) first derivative XANES, and (d) Eu XANES at temperatures from RT to 370 °C as indicated in the Figure.

Conclusions

In Conclusion, here we presented a preliminary result from temperature-dependent XAS study in Ln-based materials with potential interest to nuclear energy applications. XAS has proved to be a suitable tool to depict fine details in oxidation state and crystalline structure even considering harsh conditions.

Similar materials as ours, especially, Ce-UiO-66 and MIL-53(Fe) have been already described in literature with specific nuclear energy applications and we are at characterization stage, but we have plan to perform real tests and synchrotron-based experiments very soon (in this year, at Petra III synchrotron at Hamburg, Germany and at Elettra-Sincrotrone Trieste, Italy).

Acknowledgements

This project is founded by the FAPERJ agency (Fundação de Amparo à Pesquisa do Rio de Janeiro) at Rio de Janeiro, Brazil (fund code E-26/203.423/2023). The authors are thankful to Elettra Sincrotrone-Trieste (Italy) to the beamtime at XAFS beamline (proposal n. 20205451).

References

[1] N. Kaltsoyannis and S. T. Liddle, “Catalyst: Nuclear Power in the 21st Century,” *Chem*, vol. 1, no. 5, pp. 659–662, Nov. 2016, doi: 10.1016/J.CHEMPR.2016.10.003.

[2] Y. H. Koo, Y. S. Yang, and K. W. Song, “Radioactivity release from the Fukushima accident and its consequences: A review,” *Progress in Nuclear Energy*, vol. 74, pp. 61–70, Jul. 2014, doi: 10.1016/J.PNUCENE.2014.02.013.

[3] J. Dai, S. Li, J. Bi, and Z. Ma, "The health risk-benefit feasibility of nuclear power development," *J Clean Prod*, vol. 224, pp. 198–206, Jul. 2019, doi: 10.1016/J.JCLEPRO.2019.03.206.

[4] H. Furukawa, K. E. Cordova, M. O'Keeffe, and O. M. Yaghi, "The Chemistry and Applications of Metal-Organic Frameworks," *Science (1979)*, vol. 341, no. 6149, Aug. 2013, doi: 10.1126/science.1230444.

[5] C. Altintas, O. F. Altundal, S. Keskin, and R. Yildirim, "Machine Learning Meets with Metal Organic Frameworks for Gas Storage and Separation," *J Chem Inf Model*, vol. 61, no. 5, pp. 2131–2146, May 2021, doi: 10.1021/ACS.JCIM.1C00191/ASSET/IMAGES/LARGE/CI1C00191_0005.JPEG.

[6] K. Jin, B. Lee, and J. Park, "Metal-organic frameworks as a versatile platform for radionuclide management," *Coord Chem Rev*, vol. 427, p. 213473, Jan. 2021, doi: 10.1016/j.ccr.2020.213473.

[7] M. Hao *et al.*, "Advanced porous adsorbents for radionuclides elimination," *EnergyChem*, vol. 5, no. 4, p. 100101, Jul. 2023, doi: 10.1016/J.ENCHEM.2023.100101.

[8] J. Winarta *et al.*, "A Decade of UiO-66 Research: A Historic Review of Dynamic Structure, Synthesis Mechanisms, and Characterization Techniques of an Archetypal Metal-Organic Framework," *Cryst Growth Des*, vol. 20, no. 2, pp. 1347–1362, Feb. 2020, doi: 10.1021/ACS.CGD.9B00955/ASSET/IMAGES/MEDIUM/CG9B00955_0010.GIF.

[9] H. Liu, T. Fu, and Y. Mao, "Metal-Organic Framework-Based Materials for Adsorption and Detection of Uranium(VI) from Aqueous Solution," *ACS Omega*, vol. 7, no. 17, pp. 14430–14456, May 2022, doi: 10.1021/ACSOMEGA.2C00597/ASSET/IMAGES/LARGE/AO2C00597_0017.JPEG.

[10] F. Huang and Z. Li, "The amino-functionalized Ce doped UiO-66 presents high potential in nuclear energy wastewater treatment," *Energy Reports*, vol. 8, pp. 341–346, Oct. 2022, doi: 10.1016/J.EGYR.2022.05.057.

[11] Z. Hu, Y. Wang, and D. Zhao, "The chemistry and applications of hafnium and cerium(IV) metal–organic frameworks," *Chem Soc Rev*, vol. 50, no. 7, pp. 4629–4683, Apr. 2021, doi: 10.1039/D0CS00920B.

[12] A. M. Hastings *et al.*, "Role of Metal Selection in the Radiation Stability of Isostructural M-UiO-66 Metal-Organic Frameworks," *Chemistry of Materials*, vol. 34, no. 18, pp. 84038417, Sep. 2022, doi: 10.1021/ACS.CHEMMATER.2C02170/SUPPL_FILE/CM2C02170_SI_003.ZIP.

[13] S. Smolders *et al.*, "Unravelling the Redox-catalytic Behavior of Ce4+ Metal–Organic Frameworks by X-ray Absorption Spectroscopy," *ChemPhysChem*, vol. 19, no. 4, pp. 373–378, Feb. 2018, doi: 10.1002/CPHC.201700967.

[14] J. Bitzer, S. L. Heck, and W. Kleist, "Tailoring the breathing behavior of functionalized MIL-53(Al,M)-NH2 materials by using the mixed-metal concept," *Microporous and Mesoporous Materials*, vol. 308, p. 110329, Dec. 2020, doi: 10.1016/J.MICROMESO.2020.110329.

[15] L. Chen *et al.*, "Ultrafast and Efficient Extraction of Uranium from Seawater Using an Amidoxime Appended Metal-Organic Framework," *ACS Appl Mater Interfaces*, vol. 9, no. 38, pp. 32446–32451, Sep. 2017, doi: 10.1021/ACSAMI.7B12396/SUPPL_FILE/AM7B12396_SI_001.PDF.

[16] W. Liu *et al.*, "Highly Sensitive and Selective Uranium Detection in Natural Water Systems Using a Luminescent Mesoporous Metal-Organic Framework Equipped with Abundant Lewis Basic Sites: A Combined Batch, X-ray Absorption Spectroscopy, and First Principles Simulation Investigation," *Environ Sci Technol*, vol. 51, no. 7, pp. 3911–3921, Apr. 2017, doi: 10.1021/ACS.EST.6B06305/SUPPL_FILE/ES6B06305_SI_001.PDF.

[17] E. A. Stern, "Theory of the extended x-ray-absorption fine structure," *Phys Rev B*, vol. 10, no. 8, p. 3027, Oct. 1974, doi: 10.1103/PhysRevB.10.3027.

[18] F. W. Lytle, D. E. Sayers, and E. A. Stern, "Extended x-ray-absorption fine-structure technique. II. Experimental practice and selected results," *Phys Rev B*, vol. 11, no. 12, p. 4825, Jun. 1975, doi: 10.1103/PhysRevB.11.4825.

[19] P. A. Lee, P. H. Citrin, P. Eisenberger, and B. M. Kincaid, "Extended x-ray absorption fine structure—its strengths and limitations as a structural tool," *Rev Mod Phys*, vol. 53, no. 4, p. 769, Oct. 1981, doi: 10.1103/RevModPhys.53.769.

[20] J. J. Rehr and R. C. Albers, "Theoretical approaches to x-ray absorption fine structure," *Rev Mod Phys*, vol. 72, no. 3, p. 621, Jul. 2000, doi: 10.1103/RevModPhys.72.621.

[21] T. C. de Oliveira *et al.*, "Elucidating the energy transfer process in mononuclear and binuclear lanthanide complexes of the anti-inflammatory drug ibuprofen: From synthesis to high luminescence emission," *J Lumin*, vol. 181, pp. 196–210, Jan. 2017, doi: 10.1016/J.JLUMIN.2016.09.024.

[22] T. C. de Oliveira, J. F. de Lima, M. V. Colaço, L. T. Jesus, R. O. Freire, and L. F. Marques, "Synthesis, characterization and spectroscopic studies of binuclear lanthanide complexes containing the anti-inflammatory drug Ibuprofen and CH3-disubstituted bipyridine ligands:

Influence of methyl group position in the photoluminescence," *J Lumin*, vol. 194, pp. 747–759, Feb. 2018, doi: 10.1016/J.JLUMIN.2017.09.046.

[23] A. Di Cicco *et al.*, "Novel XAFS capabilities at ELETTRA synchrotron light source," *J Phys Conf Ser*, vol. 190, no. 1, p. 012043, Nov. 2009, doi: 10.1088/1742-6596/190/1/012043.

International Conference on Nuclear Science and Technology
6- 8 MAY 2024 | Isfahan, Iran

Investigating the effect of the presence of plasma in the reduction of radar cross section in cylindrical and conical surfaces (Paper ID : 1146)

Hashemi Z. Co-Author [1], Tatari M. Correspondent[1*], Razavi Nejad R. Co-Author[2]

[1]*Department of Physics, Yazd University, Yazd, Iran*

[2]*Department of Physics, Imam Hosein University, Tehran, Iran*

Abstract

Various techniques, including shaping, engineered materials, etc., have attempted to reduce an object's radar cross section (RCS). Likewise, plasma-based stealth is a radar cross section reduction technique associated with the reflection and absorption of incident EM waves by the plasma layer surrounding the structure. This article discusses the effect of the geometric shape of the target in the form of a cylinder and a cone. First, the electron density of air due to alpha isotope with activity 1 Ci/cm^2 in standard temperature and pressure (STP) conditions has been calculated using the GEANT4 code. Then, the CST software calculates the radar cross section of a cylindrical surface and a conical surface in the presence and absence of plasma. The obtained results show a reduction of 6 dB for cylindrical surfaces and a reduction of 5 dB for conical surfaces in the radar cross-section in the frequency range of 2 to 20 GHz.

Keywords: RCS, Plasma, CST software, radar stealth.

INTRODUCTION

Stealth or low observability does not imply complete disappearance from the radar sources. Rather, it means low radar signature, i.e., the target is detected and tracked at a shorter distance from the radar. Generally, stealth technology includes everything that minimizes the signatures and prevents the detection and identification of the target [1]. Plasma is considered as the fourth state of matter. It has been reported that 99 % of matter in the universe is in a plasma state. Examples of plasma include lightning bolt flash, the conducting gas within the fluorescent tube, the glow of the aurora borealis, ionization in the rocket exhaust, etc. Plasma is known to be a gas of charged particles. More specifically, it is an electrically neutral, highly ionized gas consisting of positively charged ions, negatively charged electrons, and neutral particles co-existing together. Energy is required to extract electrons from a stable atom for generating plasma. Any ionized gas cannot be called plasma. There should be some degree of ionization.

Thus plasma is defined as a quasi-neutral gas consisting of both charged and neutral particles [2]. Plasma-based shielding is based on the fact that plasma being dispersive media absorbs the incident EM radiation before it is scattered by the target. Furthermore, the plasma–air interface, being continuous in terms of electrical dimensions, results in reduced radar signatures as compared to the target surface, which poses a sharp discontinuity for the incident wave. In short, the importance of the Radar Cross Section (RCS) relies on the fact that it directly affects the detection range of the radar. This is apparent from the radar range equation, expressed as [3]:

$$R_{max} = \sqrt[4]{\frac{P_t G A_e \sigma}{(4\pi)^2 S_{min}}} \quad (1)$$

where R_{max} is the maximum detection range, P_t is the transmitted power, G and A_e are the gain and effective area of the transmitting and receiving antenna (which coincides with the monostatic case), σ is RCS of the target, and S_{min} is the minimum detectable signal [3]. Vidmar [4] analyzed the plasma generated by an ionization source in helium or air at atmospheric pressure and ascertained that it could be used to absorb EM waves over a wide band frequency. After that, the research on plasma-based stealth increased. Xuyang et al showed that plasma with a thickness greater than 10 cm has a high absorption of electromagnetic waves [5]. Ramezani et al investigated plasma coating on cylindrical and spherical surfaces and showed that the presence of plasma can reduce the RCS [6,7]. There are three mechanisms to ionize the gas for plasma generation. These are (i) thermal ionization, (ii) electrical ionization, and (iii) radiant ionization. In the case of thermal ionization, the electron–ion pair generated due to the thermal excitation is unstable. When the temperature and electron density are high enough, each recombination is followed by ionization and the plasma can maintain itself. However, the required temperature for this process is at least 10,000 °C, which is more than any metal's endurance [8]. The electrical ionization is done by applying a high-intensity electric field to the gas. The electrons get excited and move out of the atoms. These accelerated electrons collide with neutral atoms resulting in further ionization. Storm lightning comes under this type of ionization. The radiant ionization is done through electromagnetic radiation. The incident photons should have energy higher than that of the ionization threshold. For example, in the ionosphere, ionization takes place due to the UV radiation from the Sun [8]. Ionization due to particle radiation is also included in this category. In this research, the effect of plasma

produced by an alpha-emitting nucleus with the activity of 1 Ci/cm^2 on reducing the RCS of cylindrical and conical surfaces has been investigated. The cylindrical surface was considered as a simple model of the aircraft body and the conical surface as the nose of the aircraft.

RESEARCH THEORIES

The main mechanism of energy loss of alpha particles is their collision with the electrons of the absorbing medium. These interactions cause the excitation and ionization of absorbing atoms. An alpha particle loses an average of 36.08 eV of energy per ion pair produced by passing through air or soft tissue. Considering that alpha particles leave their relatively high energy in a short distance, they can ionize the surrounding air and produce a high density of electrons in a layer of the surface, and they are a good choice to study their effect on RCS. Therefore, in this study, we chose the ^{241}Am radioisotope, the alpha particles emitted from it have an energy of 5.45 MeV.

At first, a cylindrical shell with a height of 20 cm, external radius of 5 cm, and thickness of 1 mm made of PEC[1] was simulated, whose external surface was deposition with the ^{241}Am and using the GEANT4 Monte Carlo toolkit, the discharged energy was obtained at intervals of 1 mm, 4 mm, 10 mm, 20 mm, 30 mm, and 45 mm. All these steps were done for a conical shell with a height of 20 cm a large radius of 5 cm and a small radius of 0.5 cm with a thickness of 1 mm made of PEC, and finally, using the CST[2] software version 2023, the RCS of these shells were calculated for a source with the activity of 1 Ci/cm^2. **Fig.1** shows the simulation of two cylindrical and conical surfaces in CST software.

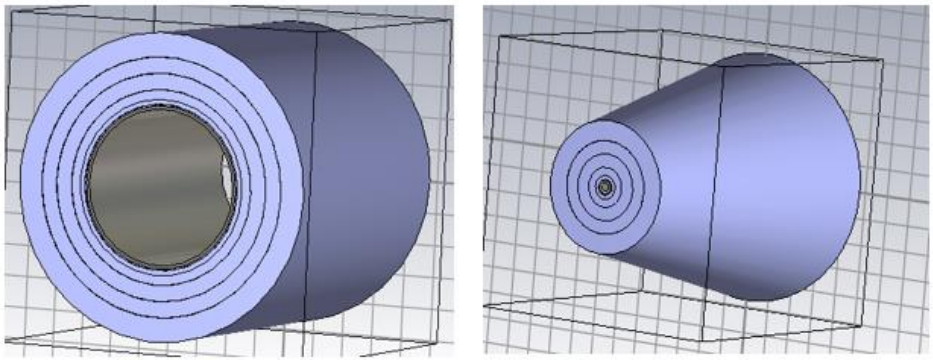

Fig.1. Simulated cylindrical and conical surfaces.

[1] Perfect Electrical Conductor
[2] Computer Simulation Technology

Results and discussion

Using the GEANT4 Monte Carlo toolkit, the amount of energy discharged in each layer was obtained. **Fig.2** shows the Bragg peak caused by the energy discharge of 5.45 MeV alpha particles. By dividing the amount of discharged energy by the value of 36.08 eV for the production of each ion pair, the number of electron-ion pairs produced per passage of an alpha particle in the air is calculated. The number of electrons produced by alpha particles n(R) (#/mm) are lost in the processes of recombination and addition to the neutral atom. Therefore, the value of the obtained electron density should be corrected. In STP[3] conditions and with the assumption that the density of electrons and ions are equal, the modified electron density is obtained from equation (2) [9]:

$$n_e = \sqrt{\frac{q}{r}} \tag{2}$$

where n_e is modified electron density, r is the recombination coefficient which is equal to $r_{STP} = 5.75 \times 10^{-9}\, {cm^3}/{sec.e}$ in the STP conditions, and q is the electron production rate from the alpha emitting radioisotope and it can be obtained using equation (3) [9]:

$$q = \frac{N_a}{2\pi} \int \frac{n(R)}{R^2} dA \tag{3}$$

Where R is distance from the conductor surface and N_a is the number of decays in $\frac{Bq}{cm^2}$. The change of electron density with distance from the surface is shown in the **Fig.3** for cylindrical and conical surfaces.

The plasma frequency is calculated in terms of $\frac{\text{rad}}{\text{sec}}$ using equation (4), the results are shown in **Fig.4** [10].

[3] Standard Conditions for Temperature and Pressure

$$\omega_p = \sqrt{\frac{n_e e^2}{m_e \varepsilon_0}} \quad (4)$$

Using equation (5), the plasma collision frequency was calculated, the results are shown in **Fig.5.**

$$\nu_c = 8.3 \times 10^{15} \times \pi a_{air}^2 \sqrt{T} n_e \quad (5)$$

Where a_{air} is the radius of the air molecule[4] and T is the air temperature [11].

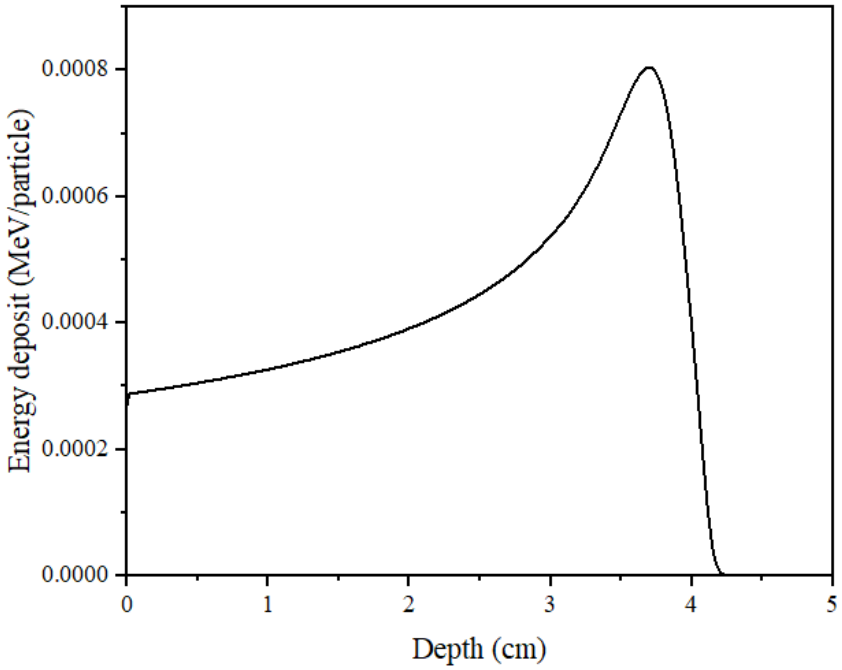

Fig.2. Bragg peak for alpha particle with the energy of 5.45 MeV in air.

[4] $a_{air} = 4.845 \times 10^{-8} cm$

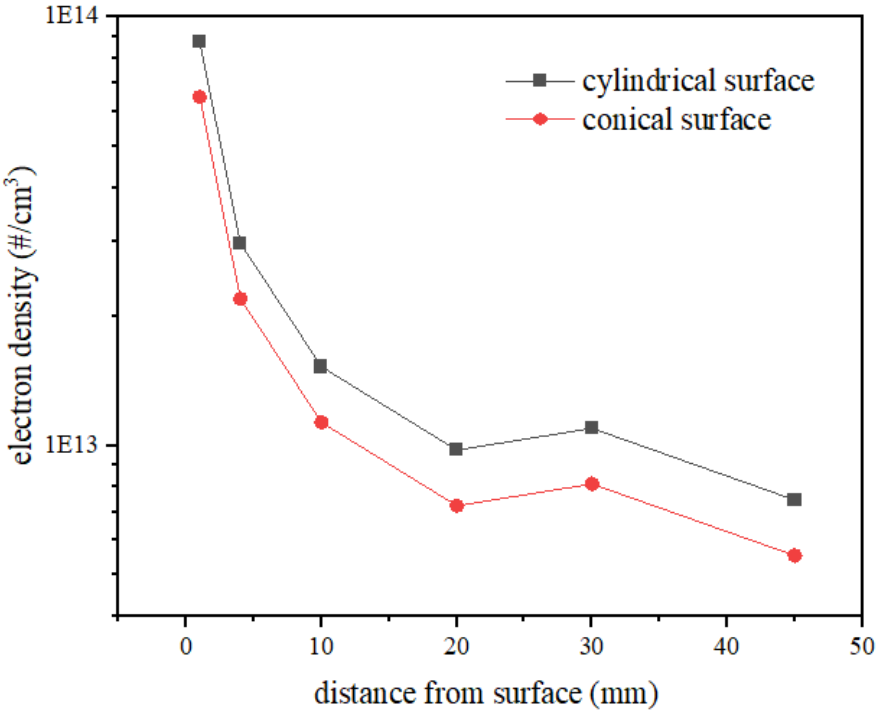

Fig.3. Electron density in terms of the distance from the conductor surface for cylindrical and conical surfaces in the STP conditions.

Finally, using the CST software, the value of RCS was calculated for two cylindrical and conical surfaces. The collision frequency and plasma frequency values were used to describe the material's dielectric behavior by the Drude model [12]. The problem has been analyzed in the time domain using the Finite Element Method in monostatic mode. The RCS was calculated for source with the activity of $1\frac{Ci}{cm^2}$, in the frequency range of 2 GHz to 20 GHz, and the results for cylindrical and conical surfaces are shown in **Figs. 6** and **7**, respectively. The parameters used in the CST software to calculate the radar range are listed in Table 1.

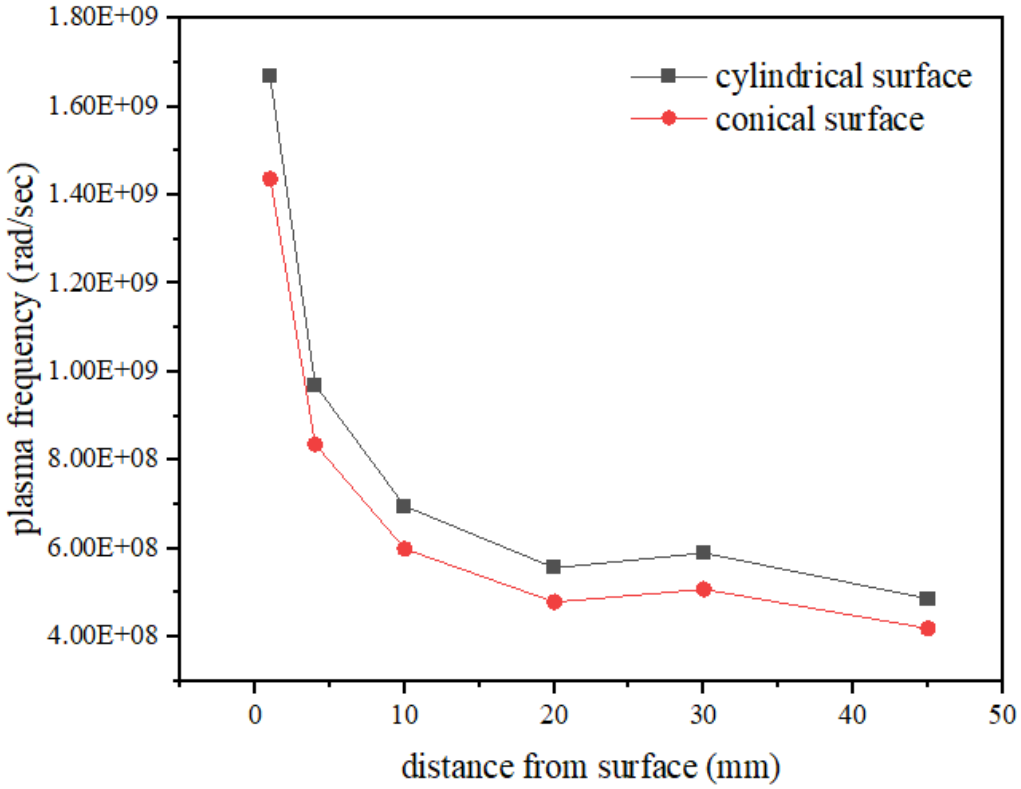

Fig.4. Plasma frequency in terms of the distance from the conductor surface for two cylindrical and conical surfaces in the STP conditions.

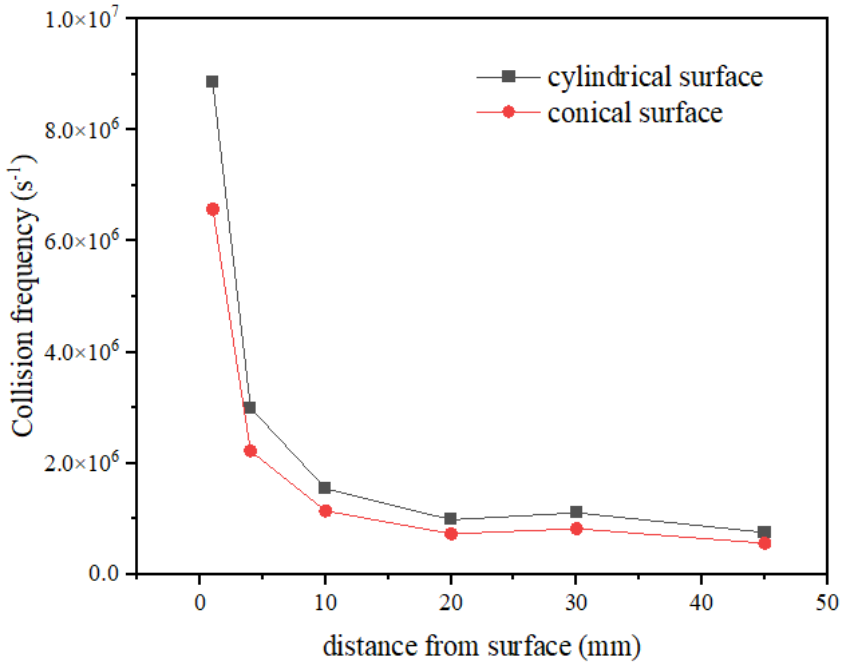

Fig.5. Collision frequency in terms of the distance from the conductor surface for two cylindrical and conical surfaces in the STP conditions.

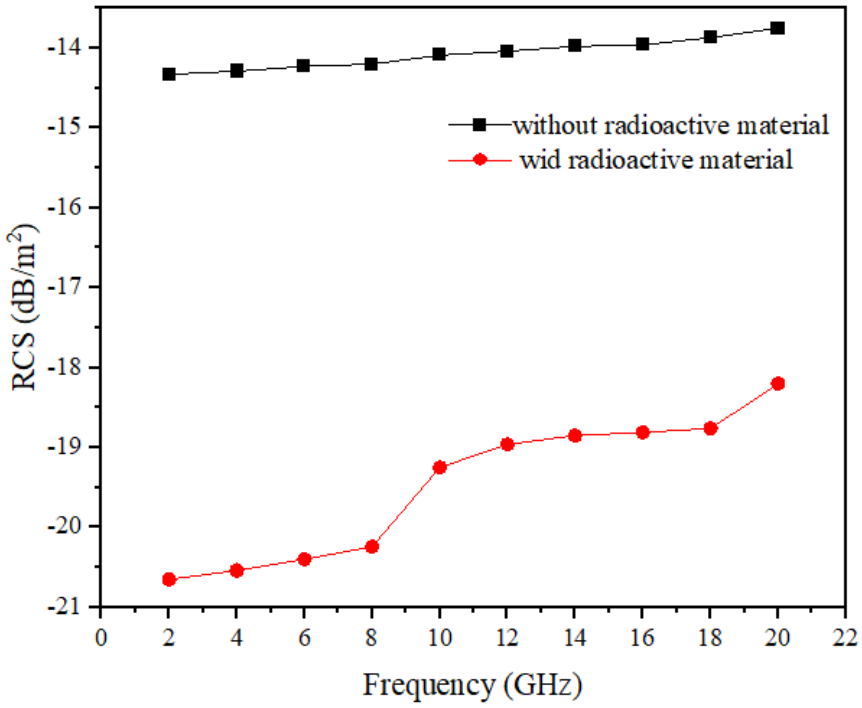

Fig.6. Simulation of monostatic RCS of cylindrical surface in the frequency range of 2 GHz to 20 GHz.

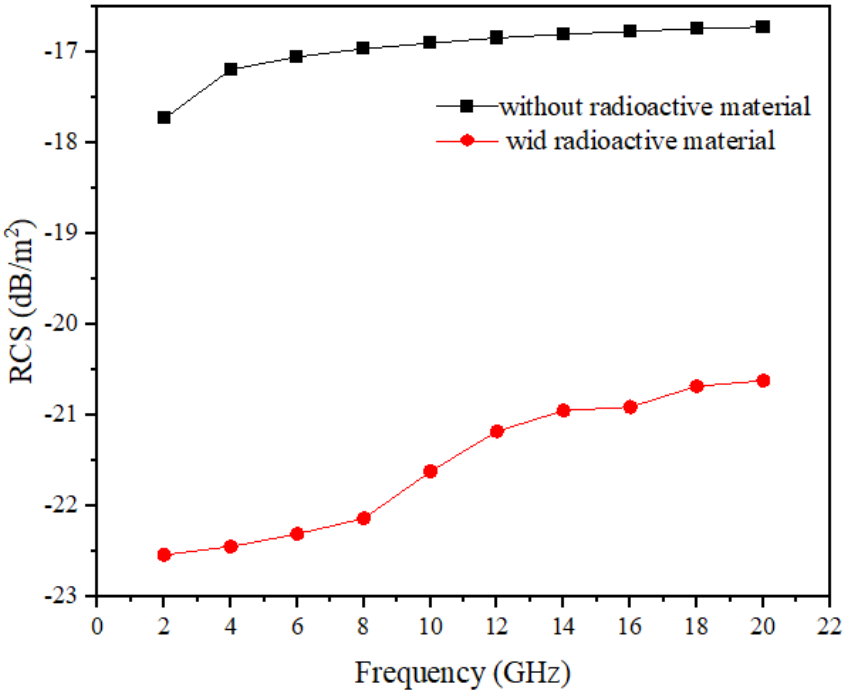

Fig.7. Simulation of monostatic RCS of conical surface in the frequency range of 2 GHz to 20 GHz.

Table 3: The parameters used in CST software to calculate the radar range.

parameter	explanation
$\omega_p\ (\frac{rad}{sec})$	Plasma frequency
$\upsilon_c\ (\frac{1}{sec})$	Plasma collision frequency
T (K)	Air temperature
F (GHz)	Wave frequency

Conclusion

In this study, the effect of the presence of plasma caused by the alpha source with the activity of $1\frac{Ci}{cm^2}$ on the reduction of RCS in both cylindrical and conical surfaces is simulated. For this purpose, using the GEANT4 Monte Carlo toolkit, the energy discharged at different distances from cylindrical and conical surfaces was obtained. Then, using CST software, the reduction of RCS in the frequency range of 2 GHz to 20 GHz was calculated. According to the results, it

can be concluded that the presence of plasma around a cylindrical and conical surface reduces RCS by 6 dB and 5 dB, respectively.

References

[1] Vass, S. (2003). Stealth technology deployed on the battlefield. Informatics Robotics, 2(2): 257– 269.

[2] Chen, F.F. (1974). Introduction to plasma physics. New York: Plenum press, ISBN: 0-306-30755-3,329 pp.

[3] Skolnik, M.I. (2003). Introduction to Radar Systems, 3rd edn. New York: Tata McGraw-Hill Education, ISBN: 0070445338, 772 pp.

[4] Stalder K. R, Vidmar R. J, Eckstrom D. J. (1992). Observations of strong microwave absorption in collisional plasmas with gradual density gradients. Journal of Applied Physics 72.

[5] C Xuyang, S Fangfang, LIU Yanming, AI Wei, L Xiaoping. (2018) Study of plasma-based stable and ultra-wideband electromagnetic wave absorption for stealth application. Plasma Science and Technology.

[6] M. Ramezani and R. Razavi. (2022). Wideband RCS reduction due to plasma generated by radioactive nuclei for cylindrical object. Scientific reports.

[7] M. Ramezani and R. Razavi. (2023) Taylor & Francis Online.

[8] Singh, H. Antony, S and Mohan Jha, R. (2016). Plasma-based radar cross section reduction. Springer, ISSN 2191-8112.

[9] IAEA (1966). August, H. Plasma Properties Induced in Air by Alpha Radiation Proc. of a Symposiumon Magneto International Atomic Energy Agency Hydrodynamic Electrical Power Generation Jointly Organized, IAEA, Vienna.

[10] J. Bittencourt. (2004) Fundamentals of Plasma Physics, 3rd edn, New York: Springer Science and Business Media.

[11] R. P. S. Shul. (2000) Handbook of Advanced Plasma Processing Techniques, New York: Springer Science.

[12] H. Kuzmany. (1998) Solid-State Spectroscopy: An Introduction, New York: Springer Science.

ICNST 2024
International Conference on Nuclear Science and Technology
6- 8 MAY 2024 | Isfahan, Iran

Influence of Particle Size of GGBS Slag from Khorasan Steel Complex on the Radiation Shielding Properties of Fabricated Concrete (Paper ID : 1161)

Taghizadeh Tousi E.

Department of Mechanical Engineering, University of Torbat Heydarieh, Torbat Heydarieh, Iran

Abstract

This study delves into the radiation protection properties of concrete samples incorporating a by-product from Neyshabour Steel Plant, utilized as radiation shielding concrete (RSC). Four distinct sample types were created for analysis. A typical sample does not contain slag, while the second and third types saw complete substitution of coarse aggregate (gravel) and fine aggregate (sand) with slag. In the fourth sample, 20% of the cement was replaced with slag. Each sample type yielded four concrete variations with different thicknesses. Employing Cobalt-60 as a gamma ray source and a Geiger-Muller (GM) counter, the attenuation coefficients and Half-Value Layer (HVL) were determined. The findings revealed a reduction in concrete HVL by 35%, 37.5%, and 39% when slag replaced cement, sand, and gravel, respectively. Consequently, the substitution of slag enhances the radiation shielding capability of concrete in the range of 35-40%. Furthermore, it is evident that an increase in the size of slag particles positively influences the radiation shielding properties of concrete.

Keywords: Ground Granulated Blast-Furnace Slag (GGBFS), Half-Value Layer (HVL), Radiation Shielding Concrete (RSC).

INTRODUCTION

In contemporary times, there is a pressing demand for the development and implementation of radiation barriers to mitigate the adverse impact of radiation on both human health and the environment. While lead alloys have conventionally served as the primary shielding material against gamma rays, considerable research efforts have been directed toward exploring alternative materials as a means to alleviate concerns related to lead toxicity [1].

In radiation centers, building materials can significantly contribute to radiation protection strategies. Concrete, a fundamental component of modern construction, plays a crucial role in

our daily lives. The predominant advantages of concrete, including adaptability, stability, and strength, have positioned it as one of the most widely used construction materials in the industry [2]. As evidenced by global reports, the widespread use of concrete averages at 1 m3 per person, underscoring its ubiquitous presence in construction practices [1].

Radiation Shielding Concrete (RSC) assumes a crucial role in radiation protection efforts. While ordinary concrete typically consists of components such as sand, gravel, cement, water, and additives, researchers have demonstrated that the shielding characteristics of ordinary concrete can exhibit variations. These differences arise from the diverse properties of concrete components, including variations in water hardness, the manufacturing process of cement, and the characteristics of sand, which are influenced by geographical and regional distinctions [3].

Conventional concrete raises environmental apprehensions as it heavily relies on natural resources and emits significant amounts of greenhouse gases. Additionally, to achieve effective radiation protection, standard concrete requires substantial thickness, leading to escalated volume, weight, and expenses. As a result, there is a discernible shift towards investigating alternative materials that offer greater environmental sustainability and can improve the attributes of radiation shielding concrete (RSC). Studies suggest that substituting heavy materials into regular concrete can significantly improve the shielding properties against both ionizing and non-ionizing radiation [4].

The construction of radiation shielding concrete (RSC) has extensively utilized natural rocks, plastic bases, slags, and industrial waste materials. In recent decades, there has been a significant focus on integrating recycled materials into various industries, including the concrete manufacturing process, to preserve natural resources and address environmental pollution. Among these industries, the iron-steel sector emerges as one of the largest and most widely employed. The iron-steel industry produces substantial amounts of wastes and byproducts [1].

There is a growing body of research dedicated to exploring the application of steel slag in the production of radiation shielding concrete (RSC). Studies indicate that the utilization of steel slag in RSC comes with both advantages and disadvantages [5]. Researchers conducted an assessment of the attenuation coefficients for various lead and silver alloys within the photon energy range of 81 keV to 1333 keV. Their findings revealed that the alloy consisting of 3 parts

Pd and one part Ag displayed the highest level of radiation protection [6]. In a distinct investigation, some researchers employed different combinations of ground granulated blast-furnace slag (GGBFS) and copper slag (CS) as replacements for cement in the formulation of radiation shielding concrete (RSC). The outcomes underscored the efficacy of these mixtures in satisfying both the radiation shielding requirements and structural strength criteria for RSC [1].

While numerous studies have explored the impact of employing various metal slags in radiation shielding concrete, there is a gap in the existing literature as no research has been identified that specifically investigates the influence of slag particle size on the radiation shielding characteristics of concrete.

Each concrete composition typically comprises four primary ingredients: water, cement (binder), fine aggregate (sand), and coarse aggregate (gravel). Previous research indicates that, considering the function of cement in concrete, it is feasible to substitute up to 20% of the cement with an alternative material. Nevertheless, there are no restrictions on replacing sand and gravel, permitting a complete substitution (100%) of these components with appropriate alternatives [1, 6].

In this study, iron slag obtained as a byproduct from Khorasan Steel Complex (KSC) in Neishabour, Razavi Khorasan, was employed. The collected slag from KSC underwent sieving through an electric sieve, resulting in three distinct sizes. The 12 mm-sized particles were utilized as gravel, the aggregate with a size of about 4 mm functioned as sand, and the very fine slag powder served as a substitute for cement. Four samples were fabricated for experimentation. Sample A did not incorporate any slag. In sample B, all gravel was replaced with slag. For sample C, all sand was substituted with slag. Lastly, in sample D, 20% of the cement in concrete was replaced with slag. Subsequently, the half-value layers (HVL) of the samples were calculated and compared using a gamma cobalt source and a Geiger-Mueller counter.

RESEARCH THEORIES AND EXPERIMENTAL

Throughout this study, type 5 cement sourced from Zaveh Cement Co. (ZTCC) in Torbat Heydarieh, slag acquired from Khorasan Steel Complex (KSC) in Neyshabour, and natural sand and gravel obtained from the construction materials market in Mashhad were utilized.

Considerable research has indicated that an appropriate mixing formulation involves ratios of 1:3:3 for cement, sand, and gravel, respectively, along with 0.5 parts water. In the current study,

concrete samples were manufactured in accordance with the ASTM C192 standard within the laboratory setting [7]. The mixing plans for radiation shielding concrete employed in this research are detailed in Table 1. Particle sizes utilized in the mixing process were selected based on the specifications outlined in ASTM C637 [8].

Table 1. Mixing plans of radiation shielding concrete.

Components of concrete	Sample			
	A	B	C	D
Water	0.5	0.5	0.5	0.5
Cement	1.0	1.0	1.0	0.8
Ordinary Sand	3.0	3.0	0.0	3.0
Ordinary Gravel	3.0	0.0	3.0	3.0
Slag (Soft powder)	0.0	0.0	0.0	0.2
Slag (<4 mm)	0.0	0.0	3.0	0.0
Slag (<12 mm)	0.0	3.0	0.0	0.0

Initially, the stone materials underwent a meticulous sieving process using an electric sieve device, ensuring strict adherence to established standards. Subsequently, the sieved stone materials were introduced into the mixer and underwent thorough mixing for a duration of 30 seconds. Following this, precise proportions of water and cement materials were added to the concrete mixer, and the mixing process continued for 10 minutes. In the subsequent phase, the resulting mixture was shaped into a specialized mold. To ascertain the half layer, samples of varying thicknesses were created using custom molds with a square base measuring 15 × 15 cm^2 and thicknesses of 3, 5, 7, and 12 cm. After the molding process, the samples underwent a 24-hour curing period. Following this duration, they were meticulously de-molded and then placed in a container filled with water to initiate the concrete processing phase.

After the molding process, the samples underwent a 24-hour curing period. Following this duration, they were meticulously de-molded and placed in a container filled with water to commence the concrete processing phase. The passing beam attenuation, considered the most crucial property of a pure radiation shielding material, is defined by the Beer-Lambert law in Eq. 1, where I_0 and I represent initial and transferred photon intensities, respectively. The thickness of the material (cm) is denoted by x. The linear attenuation coefficient (cm^{-1}) of the shielding instrument, represented by the line slope in the graph $\ln(I_0/I)$ against X axes, is denoted as μ [9].

$$I = I_0 e^{-\frac{\mu}{x}} \Rightarrow \mu = \frac{1}{x}\ln(\frac{I_0}{I}) \quad (1)$$

The assessment of the shielding characteristics of Radiation Shielding Concrete (RSC) samples utilized a ^{60}Co gamma source and a Geiger-Muller (GM) counter. The Geiger-Muller counter is characterized by its straightforward operation, producing signals independent of the type and energy of incoming particles. The intensity of the passing radiation through each type of RSC was measured for at least four different sample thicknesses (I) and in the absence of samples (I_0).

The experimental setup for the Geiger-Muller (GM) counter, employed to determine the attenuation properties of RSC samples, is illustrated in Figure 1. To ensure accuracy during the attenuation test for each RSC type, the Source-Detector Distance (SDD) and Source-Sample Distance (SSD) remained constant.

Fig. 1. Experimental setup.

The necessary thickness of shielding material to diminish radiation intensity is a critical aspect of radiation protection. The Half-Value Layer (HVL) is a key parameter in Eq. 2, representing the thickness of a shielding substance that reduces the incoming radiation intensity by half [10].

$$HVL = \frac{\ln 2}{\mu} = \frac{0.693}{\mu} \quad (2)$$

Results and discussion

Based on the first equation, the linear damping coefficient (μ) for the concrete samples is determined as the slope of the Ln(I0/I)-X graph. Figure 2 illustrates the values of this coefficient for the four concrete samples analyzed in this study.

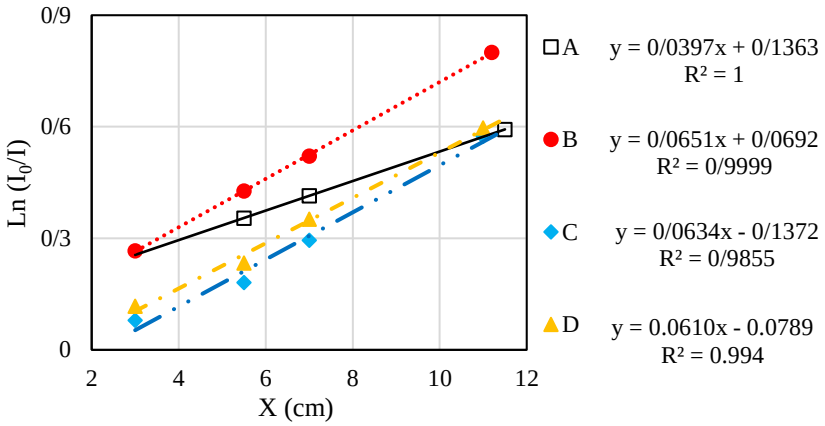

Fig. 2. The graphs to measure the Samples' linear attenuation coefficients (μ).

Following this, equation 2 is employed to present the semi-layer value index of the samples, as depicted in Table 2. The research findings reveal that the Half-Value Layer (HVL) of regular concrete is 17.42 cm. However, the incorporation of slag in various forms and sizes significantly reduces HVL. In essence, the utilization of slag, irrespective of its form or particle size, leads to a decrease in HVL, thereby enhancing the radiation protection characteristics of the concrete samples.

Table 2. Linear attenuation coefficients and Half-Value Layers (HVL) of Samples.

Name	μ (cm)	HVL (cm)
A	0.0397	17.46
B	0.0651	10.65
C	0.0634	10.93
D	0.0610	11.36

Sample A constitutes standard concrete, possessing an HVL of 17.46 (cm). In Sample B, gravel is entirely substituted with slag having a particle size of approximately 12 mm. The resulting HVL for Sample B was determined to be 10.65 (cm), showcasing a significant 39.5% reduction compared to conventional concrete. Within Sample C, slag with a particle size of about 4 mm completely replaces gravel, leading to a measured HVL of 10.93 (cm). This signifies a notable

37% reduction when contrasted with ordinary concrete. Sample D incorporates a 20% replacement of cement with finely ground slag powder, resulting in a calculated HVL of 11.36 (cm). This denotes a substantial 35% reduction in comparison to standard concrete.

According to the current study's findings, substituting slag in conventional concrete leads to a decrease in the Half-Value Layer (HVL) of concrete, thereby enhancing its radiation shielding characteristics. Furthermore, a reduction in the size of slag particles is observed to increase the HVL. Consequently, employing slag as a replacement for gravel yields the most favorable outcome, specifically the lowest HVL.

Conclusions

This research investigates the radiation protection characteristics of concrete samples incorporating a by-product from Neyshabour Steel Plant, serving as radiation shielding concrete (RSC). Four distinct sample categories were formulated for examination. The first category comprises a standard sample without slag, while the second and third categories involve the complete replacement of coarse aggregate (gravel) and fine aggregate (sand) with slag. In the fourth category, 20% of the cement was substituted with slag. Each sample category resulted in four variations of concrete with varying thicknesses. Using Cobalt-60 as a gamma ray source and a Geiger-Muller (GM) counter, we determined the attenuation coefficients and Half-Value Layer (HVL). The results indicate a reduction in concrete HVL by 35%, 37.5%, and 39% when slag replaced cement, sand, and gravel, respectively. Consequently, the incorporation of slag enhances the radiation shielding capability of concrete within the range of 35-40%. Additionally, it is evident that an increase in the size of slag particles positively influences the radiation shielding properties of concrete.

Acknowledgements

This research has been financially supported by the University of Torbat Heydarieh..

References

[1] Esfahani S.M.R.A., Zareei S.A., Madhkhan M., Ameri F., Rashidiani J., and Taheri R.A. (2021). Mechanical and gamma-ray shielding properties and environmental benefits of concrete incorporating GGBFS and copper slag. Journal of Building Engineering, 33: 101615.

[2] Jain A., Agrawal V., and Gupta R. (2023). Using serpentine in concrete: A literature review. Materials Today: Proceedings.

[3] Maglad A.M., Amin M., Zeyad A.M., Tayeh B.A., and Agwa I.S. (2023). Engineering properties of ultra-high strength concrete containing sugarcane bagasse and corn stalk ashes. Journal of Materials Research and Technology, 23: 3196-3218.

[4] Ardiansyah A., Tahir D., Heryanto H., Armynah B., Salah H., Sulieman A., and Bradley D.A. (2023). Science mapping for concrete composites as radiation shielding: A review. Radiation Physics and Chemistry: 110835.

[5] Aliyah F., Kambali I., Setiawan A.F., Radzi Y.M., and Rahman A.A. (2023). Utilization of steel slag from industrial waste for ionizing radiation shielding concrete: A systematic review. Construction and Building Materials, 382: 131360.

[6] Agar O., Sayyed M., Akman F., Tekin H., and Kaçal M. (2019). An extensive investigation on gamma ray shielding features of Pd/Ag-based alloys. Nuclear Engineering and Technology, 51(3): 853-859.

[7] ASTM-C192/C192M (2019) Standard practice for making and curing concrete test specimens in the laboratory, in *ASTM Standard Book*. ASTM International: West Conshohocken, PA, USA.

[8] ASTM-C637 (2020) Standard Specification for Aggregates for Radiation-Shielding Concrete, in *ASTM Standard Book*. ASTM International: West Conshohocken, PA, USA.

[9] Tousi E.T. (2023). Evaluation of Some Toxic Trace Elements in Crocus Sativus L. and Soil Using Neutron Activation Analysis Technique. The Philippine Agricultural Scientist, 106(1): 26-38.

[10] Tousi E.T., Aboarrah A., Bauk S., Hashim R., and Jaafar M.S. (2018). Measurement of percentage depth dose and half value layer of the *Rhizophora* spp. particleboard bonded by *Eremurus* spp. to 60, 80 and 100 kVp diagnostic x-rays. Mapan, 33(3): 321-328.

ICNST 2024
International Conference on Nuclear Science and Technology
6- 8 MAY 2024 | Isfahan, Iran

Comparison of rod and plate plastic scintillators for use in position sensitive detectors (Paper ID : 1162)

Kochakpour J. [1, 2*], Hosseini S.A.[1], Taheri A.[2], Askari M.[2]

[1]*Department of Energy Engineering, Sharif University of Technology, Tehran, Iran*

[2]*Radiation Applications Research School, Nuclear Science and Technology Research Institute, Tehran, Iran*

Abstract

Position-sensitive detectors are crucial in industrial applications, typically utilizing array or pixel detectors. Challenges such as needing multiple detectors and photomultiplier tubes, complex calibration, and data analysis issues can impede their effectiveness. A proposed solution involves employing large-volume scintillator detectors with fewer photomultiplier tubes. Plastic scintillators, known for their manufacturing simplicity, versatility, affordability, quick response times, radiation sensitivity, and resistance to optical self-absorption effects, emerge as a promising choice for position-sensitive detectors in industrial environments. In this study, we have conducted a comparison between rod and plate plastic scintillators to evaluate their optical and spatial characteristics, considering the importance of position sensitive detectors and their applications in various scientific fields. We selected a 50 × 5 cm (L × D) rod scintillator and a 50 × 5 × 50 cm (L × W × H) plate scintillator. Through Geant4 Monte Carlo toolkit simulation using a 1D setup, we examined the spectral responses, light scintillation processes, and spatial resolution of both detectors. The maximum error in the rod detector is 1 cm, while in the plate detector, it is 1.9 cm. The study findings indicate that the spatial resolution accuracy of the rod detector surpasses that of the plate detector. The smaller dimensions of the rod scintillator contribute to its ability to provide more precise source position assessment. The plate scintillator exhibits higher spatial resolution due to its larger dimensions, making it suitable for 2D position analysis and detection of larger objects. Therefore, it may be a more preferable choice in certain applications.

Keywords: Position sensitive detector, large plastic scintillator (rod and plate), Geant4 Monte Carlo toolkit, scintillation and light emission processes.

1. INTRODUCTION

Position-sensitive detectors (PSDs) are crucial components in a wide range of industrial applications, serving as key tools for precise spatial detection and analysis. One prevalent

method for achieving such detectors involves the utilization of array or pixel detectors, which offer the capability to pinpoint the position of radiation events with high accuracy. However, the current systems designed for industrial applications encounter several inherent challenges that impede their efficiency and practicality. These challenges include the necessity for multiple detectors and photomultiplier tubes, which can lead to increased complexity, higher costs, and potential points of failure within the system. Additionally, the calibration process for these systems is often time-consuming and labor-intensive, requiring meticulous adjustments to ensure accurate and reliable performance. The intricate electronics involved in these detectors further add to the complexity, making maintenance and troubleshooting a cumbersome task for operators. Moreover, the lack of modularity in existing systems limits their flexibility and adaptability to different experimental setups and applications. This lack of modularity can hinder the scalability and versatility of the detectors, preventing seamless integration into diverse industrial environments. Furthermore, the complexities involved in data analysis, interpretation, and visualization pose significant challenges for researchers and engineers working with these systems, often requiring specialized expertise and resources to extract meaningful insights from the collected data.

To address these prevailing issues and enhance the efficiency and usability of position-sensitive detectors in industrial applications, a novel approach involving the use of large-volume scintillator detectors with a minimal number of photomultiplier tubes has been proposed. Plastic scintillator detectors [1], known for their simplicity in manufacturing, availability in various forms, cost-effectiveness, rapid response times, sensitivity to different radiation types, and mitigation of optical self-absorption effects caused by impurities [2], present a promising solution for improving the performance and usability of position-sensitive detection systems.

Two special types of high-dimensional scintillators are rod and plate plastic scintillators. Choosing a position-sensitive detector between rod and plate scintillators depends on the specific application needs in terms of spatial resolution, detection area, and dimensional considerations. In this study, the optical and spatial characteristics of these two scintillators have been investigated for potential use in one-dimensional position-sensitive detectors through the utilization of the Geant4 Monte Carlo toolkit.

2. Research Theories

A mathematical model exists to predict the 1D position of a gamma ray source using a large plastic scintillator [3]. The structure of the large plastic scintillator is shown in Fig. 1. This schematic illustrates the strategic placement of two PMTs at the center of each side of the plastic scintillator along an axis, efficiently collecting the scintillator light generated. When a gamma-ray interacts with the plastic scintillator, it generates scintillation light. The distribution of this scintillation light across the surface of the scintillator depends on the specific location where the gamma-ray interacts. By collecting the scintillation light independently, the two PMTs positioned around the scintillator offer valuable insights into the 1D position of the gamma source. The recorded scintillation light in each PMT will vary based on the location of the beam interaction with the plastic scintillator. Through analysis of the signals from these PMTs, the mathematical model can accurately determine the 1D position of the gamma source.

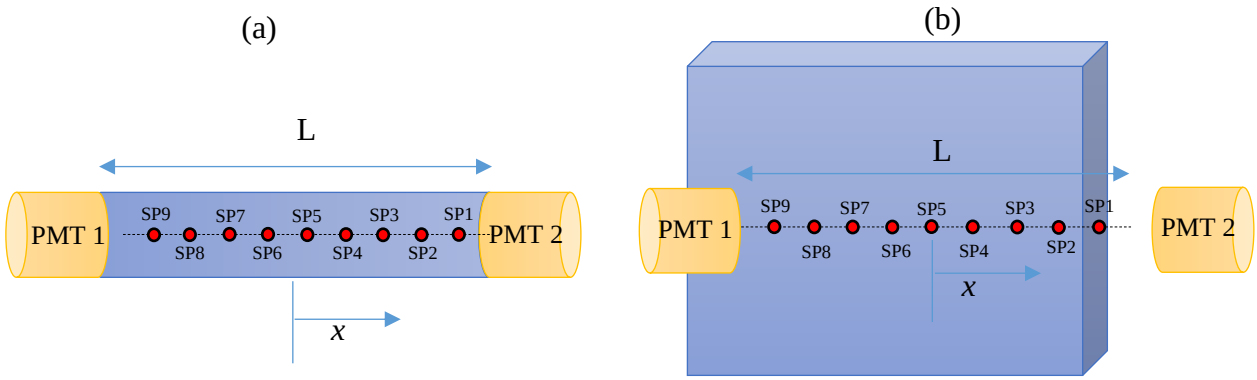

Fig. 1. Schematic of the large plastic scintillator: a) Rod shaped, b) Plate shaped

As a result, the output signals of the PMTs, S1, and S2, could be obtained using Eq (1) as follows [3]:

$$S_1 = \frac{E_\gamma P}{E_0} exp\left[-\alpha\left(\frac{L}{2} + x\right)\right] \quad (1\text{-a})$$

$$S_2 = \frac{E_\gamma P}{E_0} exp\left[-\alpha\left(\frac{L}{2} - x\right)\right] \quad (1\text{-b})$$

Where P is the probability that the generated light in one side makes a signal on the opposite PMT, E_0 is the required energy for generating a single scintillation photon and α is the optical attenuation coefficient. Furthermore, E_γ is the energy of the incident gamma-rays and can be obtained independently from the interaction position of the gamma-rays using Eq (2):

$$E_\gamma = \sqrt{S_1 S_2}\frac{E_0}{P}\exp\left(\alpha\frac{L}{2}\right) \quad (2)$$

Finally, the interaction position of the pencil beam can be obtained using Eq (3) derived by dividing Eq (1-a) by Eq (1-b) as follows:

$$x = \frac{1}{2\alpha} \ln\left(\frac{S_2}{S_1}\right) \quad (3)$$

Using the stated relationship, by measuring the light scintillation recorded in each PMT (S_1, S_2), the position of the beam interaction with the rod and plate detectors will be estimated. To verify the accuracy and reliability of the derived equations as well as to compare the optical and spatial parameters of the two proposed detectors, a simulation test was performed with the Geant4 Monte Carlo toolkit, as discussed in the next section.

3. Monte Carlo Simulation (Geant4 toolkit)

Nowadays, the use of simulation has become a reliable method for analyzing the nuclear detectors. Such simulations allow us to have a deeper understanding about what is happening and better analyzing the detector performance. For this reason, we decided to employ the Geant4 Monte Carlo toolkit to simulate the scintillation/optical behavior and the performance of the rod and plate detectors [4]. Geant4 has the ability to simulate the optical processes such as scintillation processes, Chernokov radiation, as well as the transmission of light in different environments and boundaries [5]. This one was the most important feature that led to employing this code to perform the simulations in this study. The simulations were conducted using Geant4 version 10.4.

3.1. Geant4 Setting

The detectors presented in Fig. 1 are individually simulated in the Geant4 code with 2 PMTs. To increase efficiency, Al-Mylar was used as a reflector for scintillating light. As a result of the interaction of the radiation with the detector, a flickering light is produced inside it. This light is either absorbed or reaches the PMTs after multiple reflections in the detector. As light photons move through the length and depth of the detector, their intensity decreases exponentially due to self-absorption.

Photoelectric effect, pair production, Compton scattering, and Rayleigh scattering for gamma rays, ionization, multiple scattering, and bremsstrahlung for produced electrons, bulk absorption, Mie or Rayleigh scattering, and interactions at the optical interfaces (scattering, reflection, transmission, and absorption) for an optical process that is applied in the physic class of the simulation code. Also, the "G4OpBoundaryProcess" class simulates the possible

events at the optical interfaces [6]. The surface of the rod and plate plastic scintillators were considered a polished dielectric-metal interface. To transport the optical photons, G4EMLOW 7.3 low-energy electromagnetic data library was used. The characteristics of the plastic scintillator, reflector, PMT, and source used in the simulation are provided in Table 1.

Table 1. Specifications of the simulation components [7]

Parameter		Value
Scintillator	Shape	- Rod - plate
	Material	Polystyrene (PS)
	Dimension	50 × 5 cm (L × W) – Rod 50 × 5 × 50 cm (L × W × H) - Plate
	Density	1.04 gr/cm^3
	Light yield	10000 Photon/MeV
	Decay time	2.4 ns
	Refractive index	1.58
Reflector	Type	Al-Mylar
	Reflectivity	98 %
PMT	Size	2 inch
	Structure	Glass + photocathode
	Reflectivity of the window	25 %
Source	Radiation	Gamma-
	Direction	Pencil beam
	Type	^{137}Cs
	Energy	662 keV
	Distance to detector	50 cm
	beamOn	30000

In the simulation setup, the X axis of the plastic scintillators under examination was divided into nine equally spaced segments, each segment spanning a distance of 5cm. Adjacently, a gamma-ray source was positioned at a fixed distance of 50cm from each of these segmented locations. During the course of the simulation, at every source position (SP) for each beamOn event, the scintillation light intensities detected by both PMTs were recorded and subsequently saved in ASCII files. These ASCII files meticulously encapsulated detailed information pertaining to the scintillation light characteristics for every individual beamOn event, thereby providing a comprehensive dataset for analysis. Leveraging the capabilities of MATLAB R2018b programming, an in-depth analysis was conducted to thoroughly scrutinize and interpret the intricate patterns of scintillation light at each specific source position, enabling a nuanced understanding of the outcomes.

In Fig. 2, the setup is illustrated with the pencil beam incident position denoted as SP5 in two proposed detectors. The blue line in the figure symbolizes the gamma-ray pencil beam, while the green lines represent the emitted scintillation light. Additionally, the figure visually portrays the process of collecting the scintillation light by the PMTs.

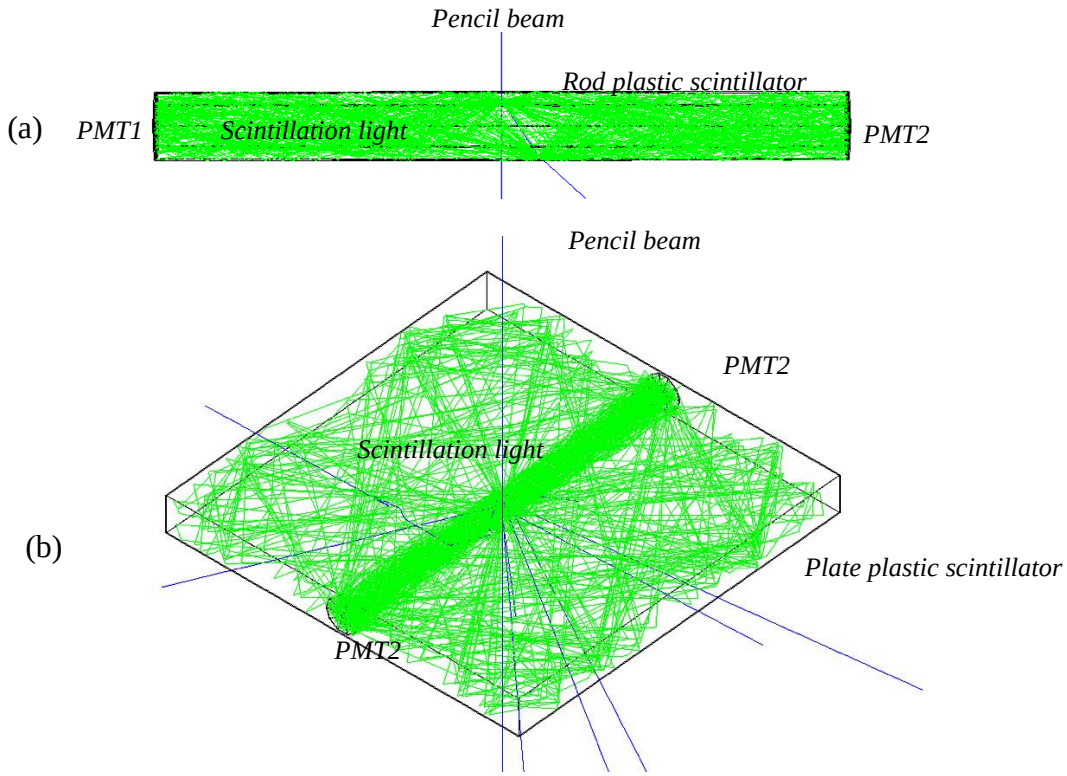

Fig. 2. Geant4 simulated detection setup in SP5: a) rod detector, b) plate detector

In the simulation phase, optical behavior and spectral characteristics of rod and plate plastic scintillators were modeled and compared with each other. The next step of the simulation involves discussing the spatial behavior of the two detectors, focusing on their performance as position-sensitive detectors.

4. Results and discussion

In Fig. 3, the simulated gamma energy spectrum for PMT2 is depicted for rod and plate detectors. The simulation consisted of 30,000 beamOn events where a ^{137}Cs pencil beam hits SP1 and SP5. The figure visually represents the energy spectrum by PMT2 in response to these simulated gamma-ray interactions across the various parts of the detector. In both detectors,

when scintillator with a PMT on one side, the farther away the beam hits the PMT, e.g. SP5 (25 cm), the energy spectrum will appear in the lower channels due to the attenuation of the optical photons inside the scintillator itself. As shown in Fig. 3, when the beam incident is close to the PMT2, e.g. SP1 (5 cm), the Compton maximum appears in the highest channel and as the beam incident is farther from the PMT2, the related energy spectrum moves to the lower channels, accordingly. This is the basis of the proposed detector function, which inherently turns it into a position-sensitive detector.

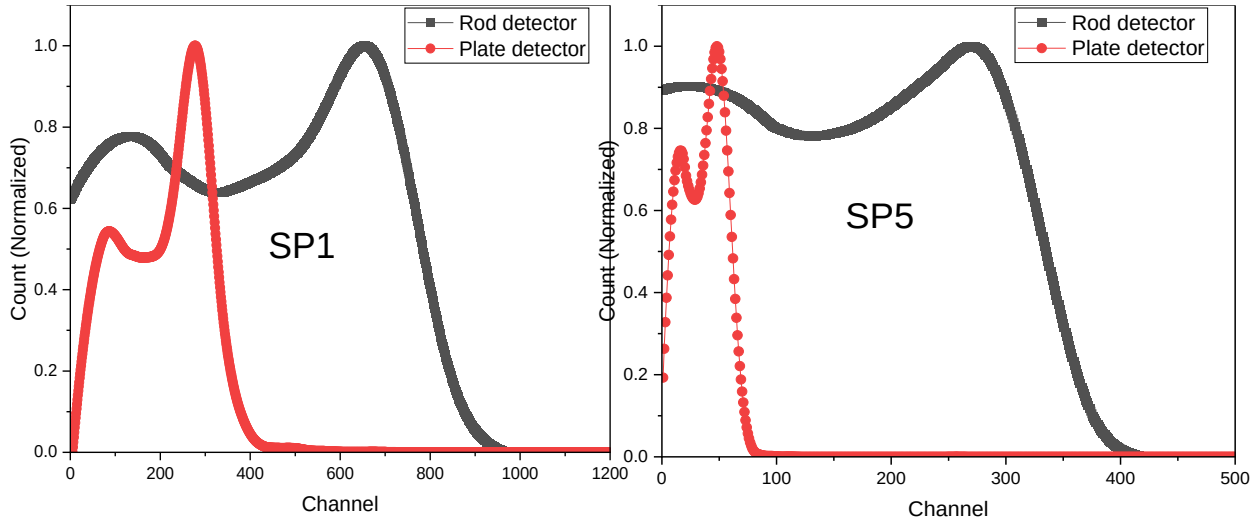

Fig. 3. Simulated gamma-ray spectra for PMT2.

After simulating the energy spectrum responses of the proposed detectors, the spatial responses of the detectors were explored. To investigate this, the detector's response was simulated with a pencil beam positioned at the specified locations as illustrated in Fig. 1. Eq (3) was utilized to estimate the incident positions of gamma rays. The outcomes for both detectors were depicted in Fig. 4, showcasing the insights gained from this spatial analysis. In this figure, the calibration equation for determining the incident source position for both detectors is presented. Fig. 5 shows the source position using the calibration equation obtained in rod and plate detectors.

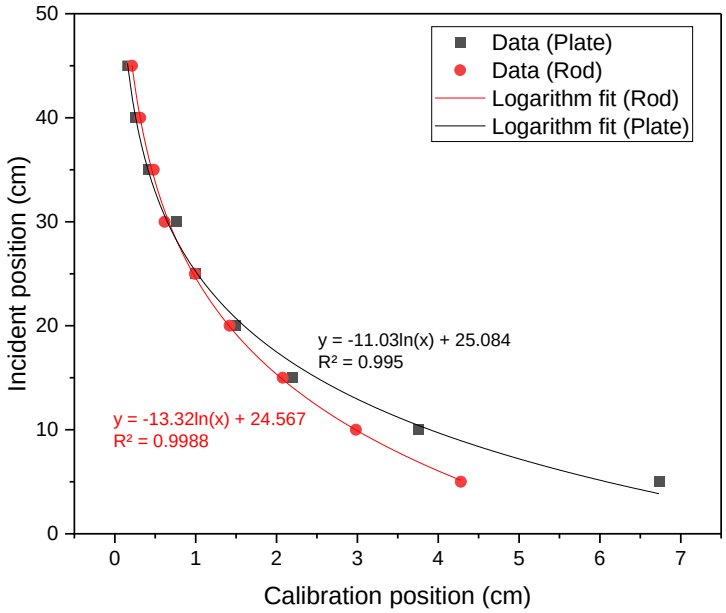

Fig. 4. Calibration diagram of incident source position in rod and plate detectors.

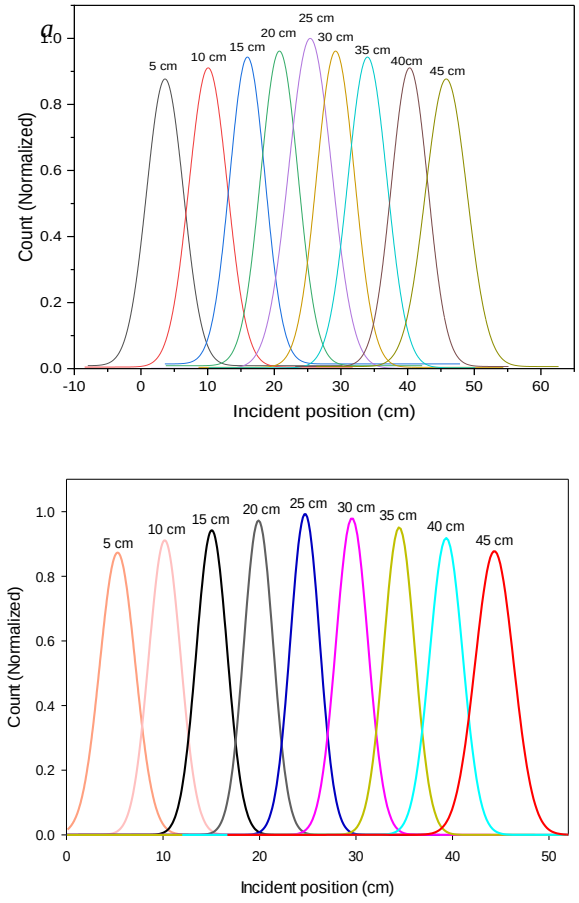

Fig. 5. Spatial response of the detector for a pencil beam at different positions, numbers on each plot show the source distances from the PMT2.

In Table 2, the precision of the source position assessment in rod and plate detectors is outlined. The maximum error in the rod detector is 1 cm, while in the plate detector, it is 1.9 cm. The findings indicate that the rod detector exhibits less error in determining the source position, attributed to its smaller dimensions compared to the plate detector.

Table 2. The precision of the source position assessment in rod and plate detectors

Incident position (cm)	Calculated source position (cm)	
	Rod (error)	Plate (error)
5	5.2 (0.2)	4.1 (0.9)
10	10.1 (0.1)	10.5 (0.5)
15	14.8 (0.2)	16.4 (1.4)
20	19.8 (0.2)	20.7 (0.7)
25	24.7 (0.3)	25.1 (0.1)
30	31 (1)	28.1 (1.9)
35	34.4 (0.6)	34.7 (0.3)
40	39.9 (0.1)	39.9 (0.1)
45	45.1 (0.1)	45.5 (0.5)

5. Conclusions

The comparison between rod and plate plastic scintillators in this study has provided valuable insights into their optical and spatial characteristics, particularly in the context of position-sensitive detectors widely used across scientific fields. The selected 50 × 5 cm rod scintillator and 50 × 5 × 50 cm plate scintillator underwent detailed analysis through Geant4 Monte Carlo simulations in a 1D setup, focusing on spectral responses, light scintillation processes, and spatial resolution. The results of the study revealed significant disparities between the rod and plate detectors, notably in terms of spatial resolution. The maximum error in source position assessment was 1 cm for the rod detector and 1.9 cm for the plate detector. This discrepancy underscores the advantage of the rod detector in expressing source position accurately, attributed to its smaller dimensions compared to the plate detector. The plate scintillator, with its larger dimensions, exhibited enhanced spatial resolution, making it well-suited for 2D position analysis and the detection of larger objects. In conclusion, this study underscores the nuanced trade-offs between rod and plate plastic scintillators, offering valuable insights for optimizing detector selection based on specific application requirements.

References

[1] Christophe Dujardin, Matthieu Hamel, Introduction—Overview on Plastic and Inorganic Scintillators, vol. 140, 2020.

[2] S.W. Moser, W.F. Harder, C.R.Hurlbut, M.R.Kusner, "Principles and practice of plastic scintillator design," *Radiation Physics and Chemistry,* vol. 41, pp. 31-36, 1993.

[3] M. Askari, A. Taheri, M. Mojtahedzadeh larijani, A. Movafeghi, "Industrial gamma computed tomography using high aspect ratio scintillator detectors (A Geant4 simulation)," *Nuclear Inst. and Methods in Physics Research,* vol. 923, pp. 109-117, 2019.

[4] S. Agostinelli, J. Allison, K. Amako, J. Apostolakis, H. Araujo, P. Arce, M. Asai, D. Axen, S. Banerjee, G. Barrand, F. Behner, L. Bellagamba, J. Boudreau, L. Broglia, A. Brunengo, H. Burkhardt, S. Chauvie, J. Chuma, R. Chytracek, G. Cooperman and G. Cosm, "Geant4—a simulation toolkit," *Nuclear Instruments and Methods in Physics Research Section A: Accelerators, Spectrometers, Detectors and Associated Equipment,* vol. 506, pp. 250-303, 2003.

[5] "GEANT4 collaboration, Physics Reference Manual, available online at," http://geant4-userdoc.web.cern.ch/geant4-userdoc/UsersGuides/PhysicsReferenceManual/html/index.html," [Online].. [Online].

[6] A. Taheri and M. Askari, "Monte Carlo study of plastic rod scintillators for use in industrial computed tomography," *Journal of Instrumentation,* vol. 17, 2022.

[7] Ali Taheri, Mojtaba Askari, Ali Biganeh, Javad Kochakpour, "Industrial gamma-ray computed tomography utilizing rod plastic scintillators," *Journal of Instrumentation,* vol. 18, no. 09, 2023.

ICNST 2024
International Conference on Nuclear Science and Technology
6- 8 MAY 2024 | Isfahan, Iran

Investigating the impact of thulium impurity on the thermoluminescence characteristics of lithium tetraborate nanoparticles (Paper ID : 1165)

Soheila Hasanloo[1*], Mehran Gholiour[1, 3], Peyman Rezaeian[2], Gholamreza Nabiyouni[1,3]

[1]*Department of Physics, Faculty of Science, Arak University, Arak, Iran*
[2]*Radiation Applications Research School, Nuclear Science and Technology Research Institute, Tehran, Iran*
[3] *Institute of Nanoscience & Nanotechnology, Arak University, Arak, Iran*

Abstract

This research investigates the influence of thulium (Tm) impurity on the thermoluminescence properties of lithium tetraborate (Li2B4O7 or LTB) nanoparticles synthesized by the combustion method. First, X-ray diffraction pattern (XRD) was used to check the structure and size of nanoparticles made without and with thulium impurity. This analysis confirms the formation of the LTB nanoparticles. Then, the scanning electron microscope (SEM) equipped with EDAX was used to investigate the shape and morphology of the samples and also the existence of Tm (thulium impurity) in the sample. The samples were exposed to ^{60}Co gamma rays ranging from 100Gy to 1000Gy, and their thermoluminescence curves were investigated. The analysis focused on samples that were contaminated with thulium as well as those without impurities. Dose-response curve was drawn and analyzed for both types of samples (with and without impurity). The results show that adding thulium impurity increases thermoluminescence intensity and creates a linear response curve.

Keywords: Lithium tetraborate, Combustion, Nanofibers, Thermoluminescence, Thulium impurity

INTRODUCTION

Thermoluminescence dosimetry (TLD) has been utilized for almost a century to measure the amount of ionizing radiation exposure. It is widely used in various fields such as archaeology, medicine, health physics, biology, solid-state physics, and organic chemistry. TL is considered a vital laboratory method [1] introduced by Daniels et al as a dosimetry technique for the first time. According to their research, the matter that was exposed to radiation has the potential to release stored energy due to heat. Li2B4O7:Mn phosphor was the initial material used in radiation dosimetry, but it displayed various flaws, such as weak TL intensity, limited dose linearity, and energy dependency. Only a few tissue-equivalent TL materials are available for

radiation dosimetry, particularly in clinical and radiation therapy applications. Lithium tetraborate is one of the most widely used materials for testing the personal dosimeters. [2] The effective atomic number of body tissue is 7.4 and TL dosimeters based on lithium borate with an effective atomic number of 7.3 are the most interesting and practical devices [3] for clinical dosimetry.

Researchers used the combustion method to synthesize lithium tetraborate nanorods with copper impurity and studied their thermoluminescence properties for the first time [4]. Various methods have been used to synthesize lithium tetraborate nanoparticles, including Pechini, sol-gel, solution, microwave, and solid-state, with varying impurities in recent years [5-7]. In 2016, Soheilian et al. conducted research on lithium-tetraborate with copper impurity using three methods: solid state at high temperature, wet reaction, and combustion. They investigated its thermoluminescence property and compared the nanoparticle in powder form to the same nanoparticle converted into pellets [8]. Mehrabi et al. synthesized lithium tetraborate nanopowders with copper and copper-manganese nanoparticles through the combustion process and studied their optical properties [9].

In this study, lithium tetraborate nanoparticles were synthesized using a combustion method. The nanoparticles were synthesized with and without thulium impurities, and their thermoluminescence properties were investigated.

EXPERIMENTAL

The synthesis of lithium tetraborate nanoparticles was achieved through the combustion method, using high-purity lithium nitrate, boric acid, urea, and ammonium nitrate as the raw materials. To produce lithium tetraborate nanofibers with thulium impurity, thulium nitrate was added to the materials. First, all the ingredients are combined and mixed thoroughly for 5 minutes until they are completely uniform. Then, the resulting mixture is poured into a ceramic container and placed in a preheated oven at 580°C for one hour. During this time, the materials react and any excess materials evaporate. The material is ground again in the mortar and annealed at 450°C for 10 minutes, resulting in lithium tetraborate nanoparticles in the form of a white powder.

Results and discussion

The X-ray diffraction pattern from the PHILIPS Xpert-PW3040/60 device with a nickel filter and copper Kα radiation was used to investigate the structure of nanoparticles. Figure .1 shows that the obtained patterns are compatible with the (01-079-0963) reference code number and confirms the structure of lithium tetraborate. Figure. 1(a) represents the pattern for sensitized lithium tetraborate nanoparticles with 0.3% thulium impurity (LBO: Tm 3.0%). The XRD pattern in Figure. 1(b) shows that the impurity has no significant effect on the crystal structure of the LBO sample, and no difference is observed in the XRD patterns of these samples.

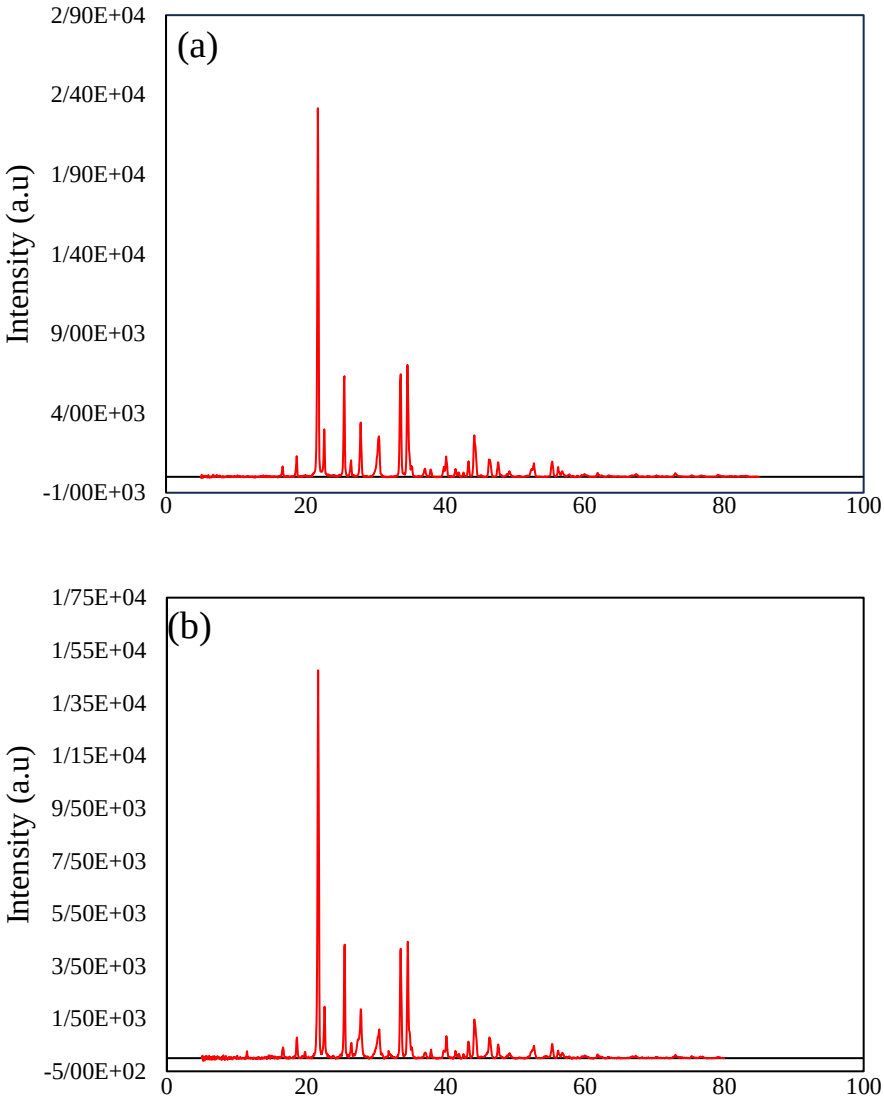

Fig. 1. X-ray diffraction diagram of lithium tetraborate nanoparticles, (a) without impurity, (b) lithium tetraborate nanofiber with thulium impurity (LBO: Tm 3.0%).

Scherer's formula was used to estimate the average particle size of the samples. The average size of nanoparticles in this research is estimated to be 42 nm for nanoparticles without impurity and 48 nm for nanoparticles with thulium impurity. The morphology and SEM images of lithium tetraborate nanoparticles with and without impurity are presented in Figure. 2 (a) and (b), respectively. The results in Figure. 2 show that the sample's morphology is changed to nanofibers in princes of thulium impurity. Thulium's presence in the LBO: Tm 3.0% sample was confirmed by EDAX analysis, as presented in Figure. 3.

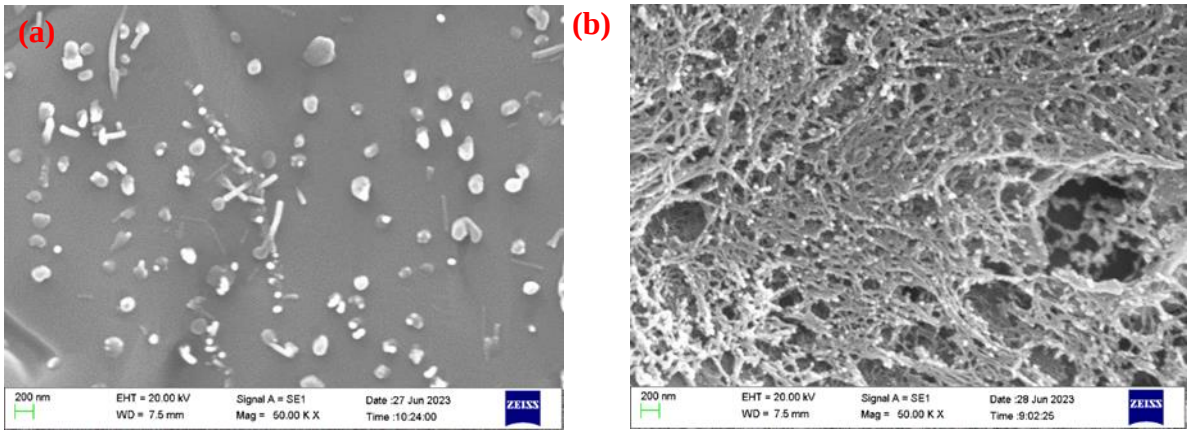

Fig. 2. SEM images of the sensitized Lithium tetraborate nanoparticles, (a) without impurities, (b) with 0.3% thulium impurity

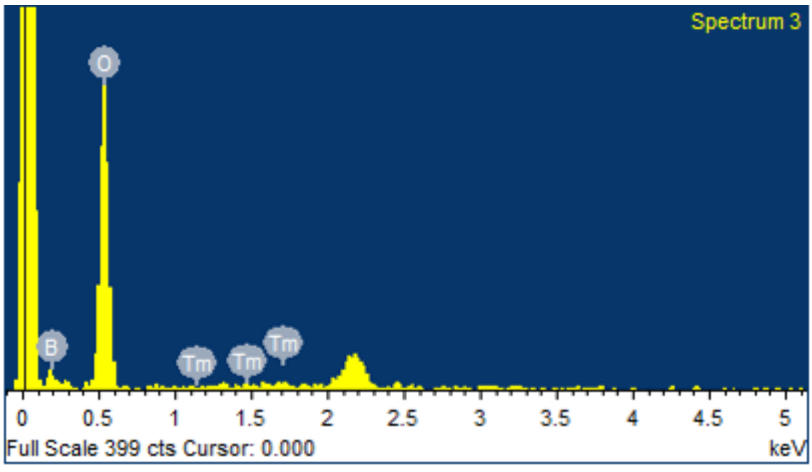

Fig. 3. EDAX analysis of lithium tetraborate nanoparticles with thulium impurity.

After obtaining certainty about the formation of the lithium tetraborate nanoparticles and the presence of thulium impurity in the LBO: Tm 0.3% sample, the influence of thulium impurity on Thermoluminescence properties of the samples have been investigated. The synthesized

samples were irradiated by gamma rays from 60Co source. Figure. 4 shows the thermoluminescence curve of the samples.

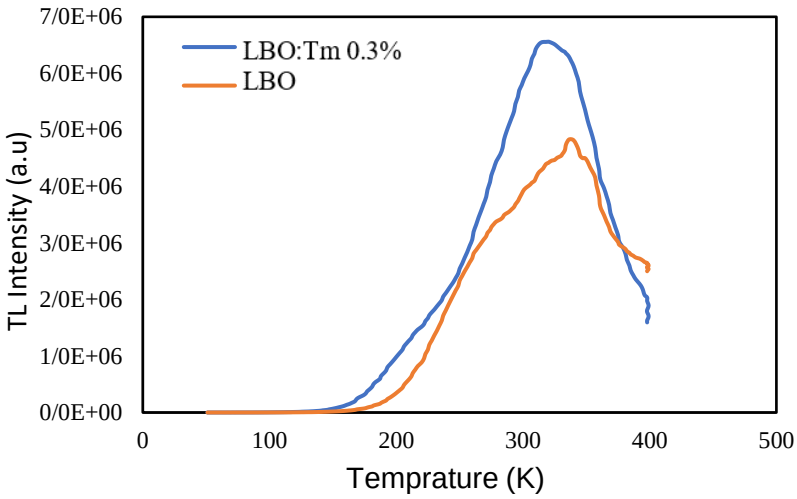

Fig. 4. Glow curve of lithium tetraborate nanoparticles without impurity and contaminated with 0.3% thulium impurity

As evident from the recent graph, the thermoluminescence has an enhancement of about 150% by adding thulium impurity. In this research, to investigate the sensitivity of nanoparticles they were irradiated by a ^{60}Co gamma-ray source with different doses ranging from 100 Gy to 10^3 Gy. Figure. 5 represents the dose-response diagram of lithium tetraborate nanoparticles without impurity and nanofibers with 0.3% thulium impurity. The graph indicates that the nanoparticles exhibit an almost linear behavior within the range of 100 Gy to 900 Gy and in all doses the TL of the samples with thulium impurity are higher than the pristine samples.

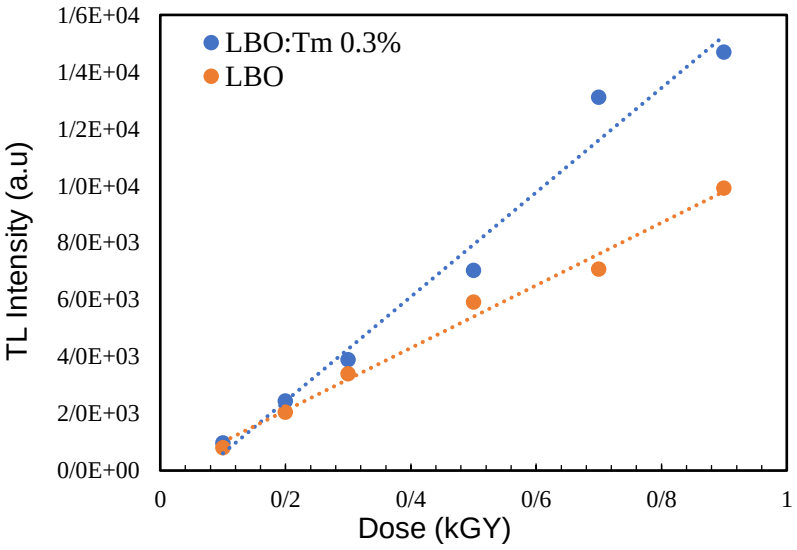

Fig. 5. The response curve of lithium tetraborate nanoparticles without impurity and with 0.3% thulium impurity.

Conclusions

Based on the X-ray diffraction spectrum and electron microscope photo analysis, it has been determined that the structure formed is related to lithium tetraborate nanoparticles. These nanoparticles have demonstrated a high sensitivity to gamma rays, and their linear response makes them an ideal option for dosimetry up to a dose of 1000 Gy. By adding thulium impurity TL curves have significantly improved.

References

[1] Garcia, P. R. D. A. F., Loza, K., Daumann, S., Grasmik, V., Pappert, K., Rostek, A., ... & Oliveira, C. L. P. D. (2019). Combining small-angle x-ray scattering and x-ray powder diffraction to investigate size, shape and crystallinity of silver, gold and alloyed silver-gold nanoparticles. Brazilian Journal of Physics, 49, 183-190.

[2] Khalilzadeh, N., Saion, E. B., Mirabolghasemi, H., Soltani, N., Shaari, A. H. B., Hashim, M. B., ... & Dehzangi, A. (2016). Formation and characterization of ultrafine nanophosphors of lithium tetraborate (Li2B4O7) for personnel and medical dosimetry. Journal of Materials Research and Technology, 5(3), 206-212.

[3] Proki, M. (2002). Dosimetric characteristics of Li2B4O7: Cu, Ag, P solid TL detectors. Radiation protection dosimetry, 100(1-4), 265-268.

[4] Singh, L., Chopra, V., & Lochab, S. P. (2011). Synthesis and characterization of thermoluminescent Li2B4O7 nanophosphor. Journal of Luminescence, 131(6), 1177-1183.

[5] Celik, M. G., Yilmaz, A., & Yazici, A. N. (2017). Synthesis and thermoluminescence characterization of lithium tetraborate (Li2B4O7) doped with copper and silver metals. Radiation Measurements, 102, 16-26.

[6] Ozdemir, A., Altunal, V. O. L. K. A. N., Kurt, K., Depci, T. O. L. G. A., Yu, Y., Lawrence, Y., ... & Yegingil, Z. (2017). Thermoluminescence properties of Li2B4O7: Cu, B phosphor synthesized using solution combustion technique. Radiation Physics and Chemistry, 141, 352-362.

[7] Hemam, R., Singh, L. R., Prasad, A. I., Gogoi, P., Kumar, M., Chougaonkar, M. P., ... & Sharan, R. N. (2016). Critical view on TL/OSL properties of Li2B4O7 nanoparticles doped with Cu, Ag and co-doping Cu, Ag: dose response study. Radiation Measurements, 95, 44-54.

[8] Soheilian, S., Movahedi, B., Nasrabadi, M. N., & Jabbari, I. (2016). A different approach to fabricate nanocrystalline LTB: Cu pellets with thermoluminescence response. Radiation Measurements, 89, 14-22.

[9] Mehrabi, M., Zahedifar, M., Hasanloo, S., Kohzadi, K., Nikmanesh, H., & Li, Y. (2023). Improving thermoluminescence properties of Li2B4O7: Cu nanoparticles by co-doping Mn impurities for gamma dosimetry application. The European Physical Journal Plus, 138(7), 584.

ICNST 2024
International Conference on Nuclear Science and Technology
6- 8 MAY 2024 | Isfahan, Iran

Effect of Gamma Irradiation on Biofilm Formation and virulence of Paenibacillus larvae, the etiologic agent of Foulbrood disease in honeybee larvae (Paper ID : 1166)

Ramsina Betesho Babroud[5]*, Mojtaba Moharrami[2], Rouha Kasrai Kermanshahi [3], Farahnaz Motamedi Sedeh [4], Seyedeh Zahra Mousavinejad [3]

[1]Radiation Applications Research School, Nuclear Science and Technology Research Institute, Tehran, Iran;[2]Department of Honey Bee, Silk Worm and Wildlife Research Diseases, Razi Vaccine and Serum Research Institute, Karaj, Iran.[3]Biological science, Alzahra University, Tehran, Iran;[4]Agricultural, Medical and Industrial Research School, Nuclear Science and Technology Research Institute, Karaj, Iran;

Abstract

American Foul Brood is a fatal disease in honey-bee larvae. It is known as a contagious and fatal disease in bee larvae causing massive death in the hives, reduces the role of bees in terms of pollination, production of honey, wax, and propolis in the area where beehives are established. The causative agent, *Paenibacillus larvae*, a gram-positive spore-forming rod, transferred from the infected parts of the hive and worker bees to the food of the babies. The role of sublethal doses of gamma rays on the biofilm, as a virulence factor, and the mortality has been investigated in this article.

The Iranian strain of *Paenibacillus larvae* was isolated from bee wax and deposited in Genbank with accession number MH000685. The bacterial isolate was irradiated with sublethal doses of 30, 60 and 100 Gy in a 60Co GC-220. The mutant showed a significant decrease of 68% in biofilm formation in microtiter-plate method ($p \leq 0.05$), more elongated cells and less extracellular polymeric substances in scanning electron microscope. Exposure bioassay in “wildtype” group showed 52.08%, “mutant” 16.67% ($p \leq 0.05$) and "wildtype+mutant" 29.17% ($p \leq 0.05$) virulence.

In conclusion, the mutant strain obtained from gamma irradiation has a significant decrease of biofilm formation *in vitro* and lower mortality rate *in vivo*. The mutant strain had a good performance to be a suitable strain in the biocontrol of the disease.

Keywords: *Paenibacillus larvae*, gamma irradiation, biofilm, microtiter-plate, SEM, virulence

[5] Corresponding author, *rbetesho@aeoi.org.ir

INTRODUCTION

American Foul Brood (AFB) disease, as the deadliest disease of *Apis mellifera* bee larvae, decreases the role of bees in pollination, production of honey, wax, and propolis. The causative agent of the disease, *Paenibacillus larvae*, is a spore-forming Gram-positive bacillus. The disease is caused by swallowing spores by first instar larvae. Spores can be isolated from dead larvae, wax, honey and adult bees. *P. larvae* has been shown to have several identified virulence factors like proteases, chitinases, S-layer, biofilm [1]. Bacterial biofilms are clusters of bacteria that are attached to a surface and/or to each other and embedded in a self-produced matrix. The biofilm matrix consists of substances like proteins, polysaccharide , as well as eDNA [2]. Biofilms protect bacterial community against environmental stresses like antibiotics, acidity, oxidative stress, and irradiations. *P. larvae* in both genotypes, ERICI and ERIC II, are able to form free floating biofilm which aggregate loosely and attach to the walls of the culture wells *invitro* but with structural differences between the biofilms formed [3].

Antibiotics are not sufficient to combat the disease due to increasing resistance among *P. larvae* strains. Residual antibiotics in honeybee products is also of concern, and this has resulted in many countries banning their use. Therefore, alternative therapeutic methods like the use of bacteriophages [4], growth inhibitory Lactic Acid Bacteria [5] [6] and herbal extracts [7], and biocontrol by other bacteria [8] against *P. larvae* are of a great interest.

The use of a gamma-irradiated mutants of pathogens with reduced pathogenicity for the biological control in crop disease are reported earlier [9]. Irradiation directly makes damages in DNA of living cells which originate mutagenesis perhaps mutate to be of higher or lower virulence. Studies on transcriptional changes of *Salmonella typhimurium* using gamma irradiation showed that the expression of the virulence genes in irradiated mutants was reduced in comparison with non-irradiated controls [10]. Considering the random mutation effect of irradiation, mutants with reduced pathogenicity are used for biocontrol of diseases, especially in plants. This issue has been discussed in numerous articles. For example, the mutants of *Fusarium solani* obtained at 60 to 180 Gy of gamma rays were investigated in terms of reduced pathogenicity in competition with wild type. The root rot disease was reduced by 55% compared to the wild type [11]. Gamma irradiation by 100 - 3000 Gy induced mutagenesis in

Bacillus subtilis UTB1, which induced enhanced biosurfactants and biofilm production and was proposed as a biocontrol agent of Aspergillus flavus [12].

The extent of the morphological and physiological changes of bacteria in radiation and oxidative stress and the effect on their pathogenicity is unknown. Not much information is available about the adaptive mechanisms in these stress and thus the bacteria-host relationship for individual bacteria [13]. In this paper, ^{60}Co Gamma irradiation was used to create random mutations in a native Iranian P. larvae isolate, and mutants with less invitro pathogenic properties were screened. The property of biofilm production was investigated by microtiter plate method and SEM observation. Finally, the death rate of the mutants compared to the wild type in first instar larvae of A. mellifera was investigated invivo. Its potential of use as a biocontrol mutant was investigated by mortality rate of honey bee larvae.

EXPERIMENTALS

1- Irradiation

Exponentially growing culture of *P. larvae* KB10 (isolated from bee wax, accession number MH000685- GenBank), in Muller Hinton yeast pyruvate glucose phosphate broth (MYPGP-broth) at 37°C was harvested by centrifugation, washed with PBS buffer (0.067 M, pH 7.0) and resuspended in the same buffer to achieve an approximate concentration of 1.5×10^8 CFU ml^{-1} (OD_{595}=0.08-0.1). The cell suspensions (2 ml aliquots) were irradiated at 30, 60, 100 Gy at room temperature in a ^{60}Co GC-220 Gamma cell (activity of 7198 Curies, dose rate 1.71 Gy Sec^{-1}).

2- Survival of bacteria after exposure to gamma irradiation

After exposure to gamma rays cell suspensions were serially diluted and 100 ml from each suspension was spread in duplicate on MYPGP-agar. The viable bacteria were determined after 5 days of incubation at 37°C, subcultured on the same medium and stored at 4°C.

3- Biofilm formation ability

Microplate technique was used to assay biofilm forming according to Cai et al. [14]. Optical density (OD) was read at 595 nm by a microplate reader (Epoch BioTek). The cut-off (ODC) was defined as the mean OD value of the negative control (sterile MYPGP-broth) [15].

4- Microscopic observation technique

Microscopic observation of biofilms on glass slides was evaluated according to Shahandashti et al [16] using MYPGP-broth culture of wild type and mutant strains after 48 h incubation at 37°C and studied using scanning electron microscopy (SEM) (Zeiss).

5- Exposure bioassay

First instar larvae of *Apis mellifera* were collected and transferred to plastic microtiter trays (96 wells) in three groups of 8 larvae for rearing, as described by Crailsheim at al [17]. Larvae were fed ad libitum with an excess of a liquid diet consisting of 66% (vol/vol) royal jelly, 6% (wt/vol) glucose, 6% (wt/vol) fructose and 1% (wt/vol) yeast extract in sterile double distilled water. Three groups of larval food was supplemented with 5×10^3 ml^{-1} spores of wild type *P.larvae* KB10, 5×10^3 ml^{-1} spores of mutant, and "wild type + mutant" (each of 2.5×10^3 spore ml^{-1})[5].

Larvae were fed with contaminated diet for first day after grafting and thereafter, normal diet was used for feeding. Control larvae were fed with normal diet throughout the experiment. Microtiter trays were incubated at 34.5 °C with high humidity for 6 days. Each day, plates were taken out from the incubator and examined. Larvae were classified as dead when they lost their body elasticity or displayed a color change to brownish. The number of dead larvae was recorded, and surviving larvae were transferred to new wells filled with fresh food [17][18].

Uniform suspensions of dead larvae were cultured on MYPGP-agar then incubated in CO_2 for 6-7 days at 37°C. Larvae from which *P. larvae* were not isolated were excluded from the number of AFB dead larvae. Total mortality was calculated by considering 100% for the total number of infected larvae. Time course of infection (LT_{100}) was obtained using a curve of cumulative mortality versus time. In drawing this curve, 100% was equivalent to all dead larvae that died due to AFB [17].

6- Statistical analysis

Statistical analyses were conducted using SPSS 27. One-way analysis of variance (ANOVA) and independent samples T-tests were performed after assumptions of normality and variances of homogeneity were checked. Significance levels were set at $p<0.05$

RESULTS

1- Irradiation and sublethal dose

Surviving mutants of m-22, m-27, and m-21 obtained from 30, 60, and 100 Gy respectively were investigated for biofilm formation.

2- The effect of irradiation on biofilm formation

The results of biofilm formation in 48 h at 37°C in microtiter plate technique in three mutants showed that there was a 68% reduction in the m-27 mutant biofilm (obtained from 60 Gy irradiation) compared to the wild type ($p<0.05$) (Fig. 1).

Microscopic observations confirmed biofilm formation of m-27 mutant compared to wild type had more elongated cells with lower extracellular polymeric substances (Fig.2).

3- Exposure bioassay

The plates containing the larvae were incubated at 34.5 ± 0.5°C and RH of 90%. Larval growth and mortality were checked every day. Total mortality and LT_{100} were plotted as previously

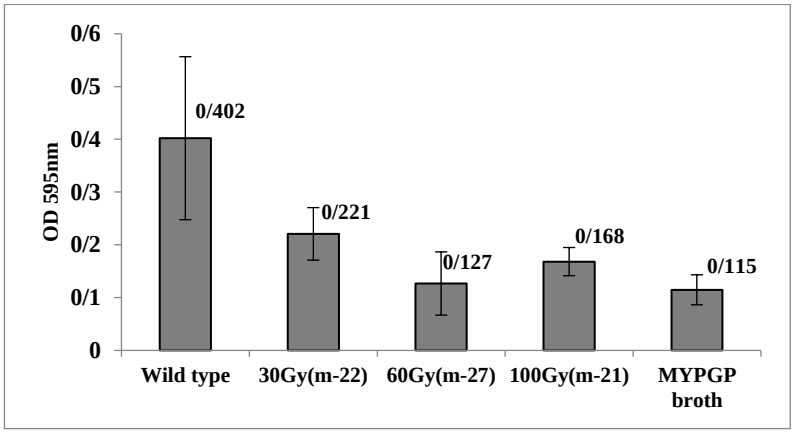

Fig. 1. The mean of biofilm formation of gamma irradiated *P. larvae* KB10 by microtiter plate method ± standard deviation (SD)

Described. The total mortality in wildtype group of larvae was 81.25%, 45.83%in the "mutant" group ($p<0.05$), and 58.33% in the "wild type + mutant" group, which compared to the wild type group had a decrease of 28% ($p<0.05$) (Fig.3).

The time course of infection (LT_{100}) was obtained using the mortality curve of the studied groups. As can be seen, LT_{100} for the "wild type" group was 7 ± 1.58 days, for "mutant " group 7.5 ± 1.2 days, and for the "wild type + mutant" group was 7 ± 1.58 days. The difference between the groups was not significant.

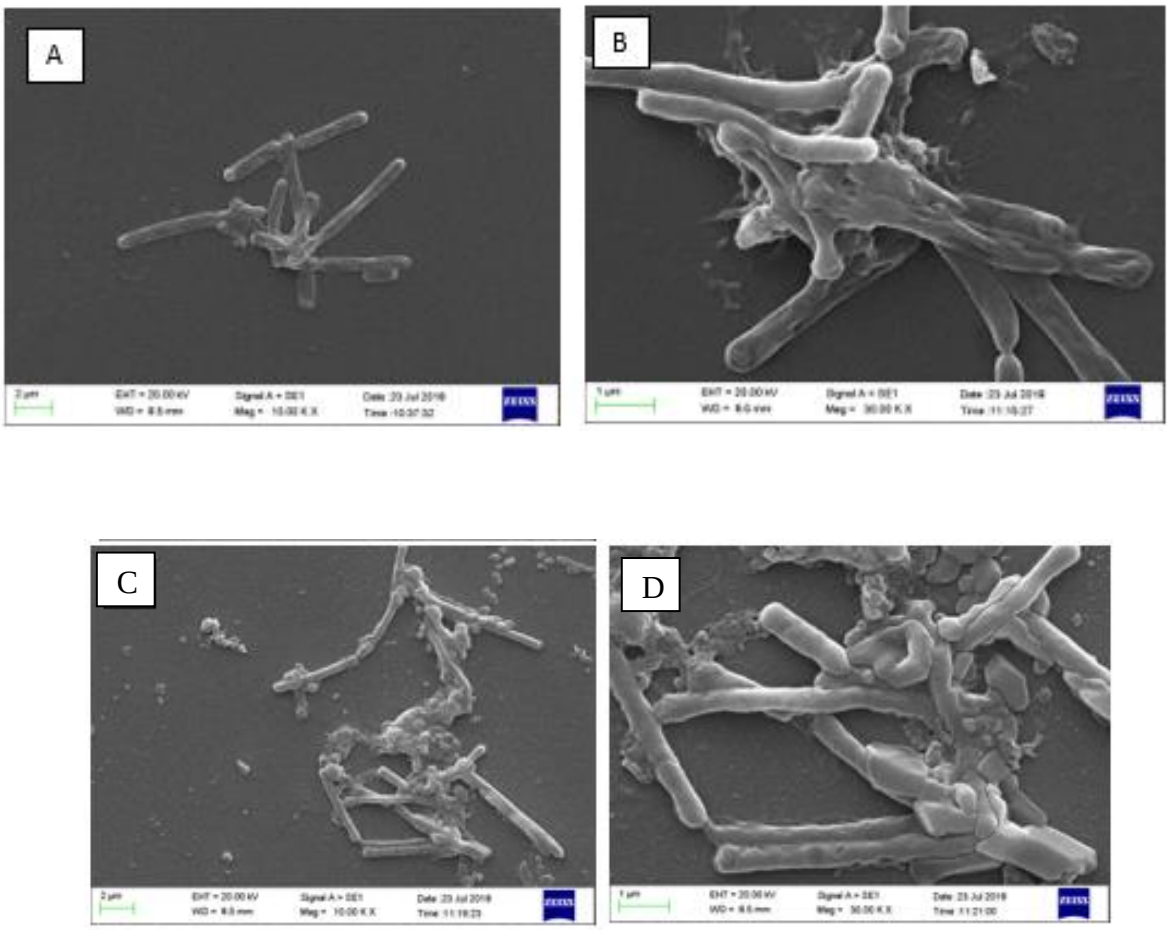

Fig.2 Scanning electron microscopy images from biofilms of *P. larvae* KB10 wild type (A, B) and irradiated m-27 mutant (at 60 Gy gamma radiation) (C, D) on glass slides in MYPGP-broth after 48h at 37°C. A, C)1000×, B, D)30000×

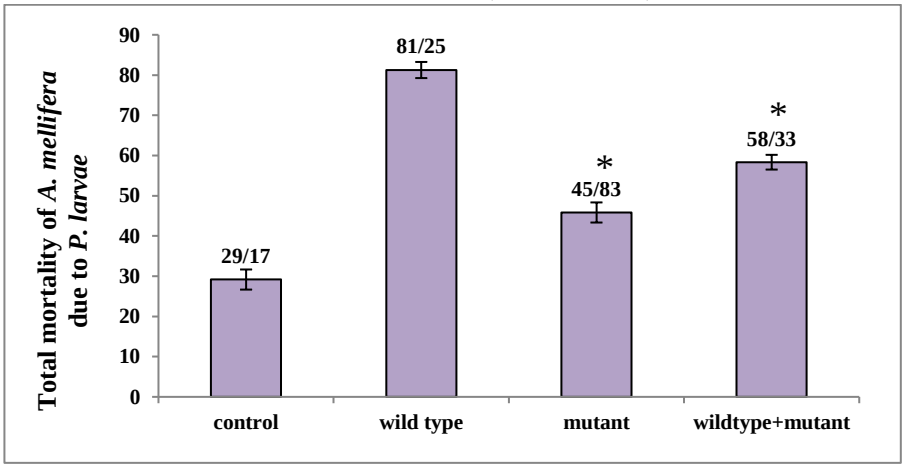

Fig.3 Total mortality of *A. mellifera* larvae fed with *P. larvae* KB10 in diet in three groups: wild type, mutant and wildtype + mutant. Control larvae fed with sterile diet. Mean values obtained from two independent replicates± SD. 100% is equivalent to all larvae that were fed with bacteria. Unpaired T-Test ($P<0.05$), *: significant difference.

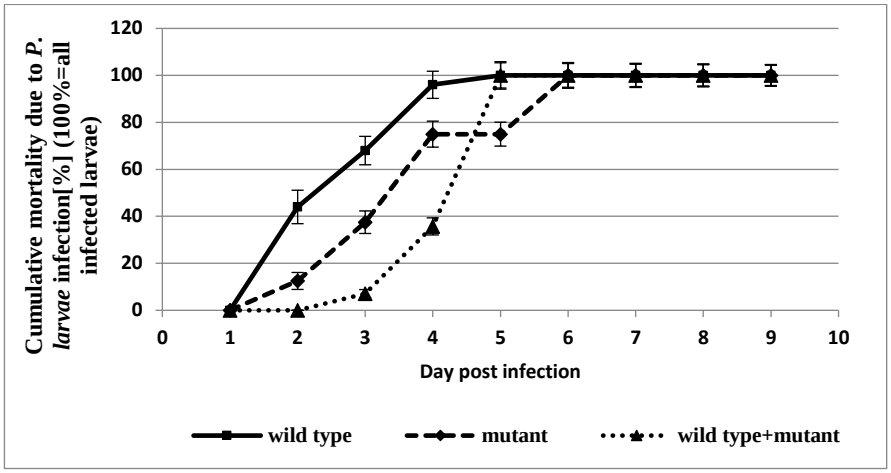

Fig.4 Time course of infection: Cumulative mortality in three groups of wild type, mutant and wildtype + mutant. Mean values obtained from two independent replicates± SD. 100% is equivalent to all larvae that were died of AFB.

Discussion

In sub-lethal doses, bacteria undergo various mutations that do not have predictable manifestations. For example, increase and decrease of xylanase in Thrichoderma [19], increase of protease in Bacillus [20] with sub-lethal doses have been reported.

A significant decrease invitro biofilm production and invivo mortality was observed in mutant m-27 (obtained from 60 Gy). Marjani et al. also reported a decrease of biofilm formation in hospital irradiated isolates with gamma rays and attributed it to the decrease in hydrophobicity and the swimming movement of bacteria [21], but Atsumi et al. reported no effects of gamma on E. coli swimming [22]. It is recommended to investigate the reason for the reduction of m-27 mutant biofilm by examining the swimming, hydrophobicity, quorum sensing and genes involved in biofilm formation.

This bacterium has many other virulence factors like toxins, siderophores, chitinases, non-ribosomal proteins, surface layer etc. that were not investigated in this study. Gamma irradiation may increase or decrease the expression of encoding genes due to some sets of mutations. The interaction of expressed genes caused a significant reduction in the mortality of larvae fed with the mutant compared to the wild type.

In order to investigate the possibility of using the m-27 mutant in AFB biocontrol, this strain was mixed with the wild type and added to the diet of the larvae. The mortality reduced significantly compared to the wild type group. The first step after spore germination in the

larval gut is bacterial attachment to epithelial cells. It seems that m-27 mutant has competed with the wild type for receptors of epithelial cells. This may be the reason of reduced mortality.

Regarding the results obtained from this paper, it can be said that the reduction of pathogenicity in “mutant + wild type” may have happened by competing available food in larva midgut.

CONCLUSION

Gamma irradiated P. larvae KB10 -the native strain- at a sub lethal dose showed a significant decrease invitro biofilm formation and a reduced total mortality in first instar larvae. Larvae fed with a mixture of this mutant and the wild type in diet had lower total mortality than larvae fed with the wild type in diet. It can be concluded that this mutant can be a suitable strain in the biological control of AFB.

REFERENCES

[1] Poppinga, L. et al., (2012). Identification and functional analysis of the S-layer protein SplA of Paenibacillus larvae, the causative agent of American Foulbrood of honey bees. Plos pathogens. 8(5):10.1371/journal.ppat.1002716.

[2] Vestby, L. K., Grønseth, T., Simm, R., and Nesse, L. L. (2020). Bacterial biofilm and its role in the pathogenesis of disease. Antibiotics. 9(2):10.3390/antibiotics9020059.

[3] Fünfhaus, A., Göbel, J., Ebeling, J., Knispel, H., Garcia-Gonzalez, E., and Genersch, H. (2018). Swarming motility and biofilm formation of Paenibacillus larvae, the etiological agent of American Foulbrood of honey bees (Apis mellifera), Scientific Reports., 8:8840:doi: 10.1038/s41598-018-27193-8.

[4] Ghorbani-Nezami, S., LeBlanc, L., Yost, D. G., Amy, P. S., and Jeanne, R. (2015). Phage therapy is effective in protecting honeybee larvae from American foulbrood disease. Journal of Insect Science. 15(1):1–5, doi: 10.1093/jisesa/iev051.

[5] Forsgren, E., Olofsson, T. C., Vásquez, A., and Fries, I. (2009) Novel lactic acid bacteria inhibiting Paenibacillus larvae in honey bee larvae. Apidologie, 41(1):99–108, doi:10.1051/apido/2009065.

[6] Yoshiyama, M. , Wu, M., Sugimura, Y., Takaya, N., Kimoto-Nira, H., and Suzuki, C.

(2012) Inhibition of Paenibacillus larvae by lactic acid bacteria isolated from fermented materials. Journal of Invertebrate Pathology. 112(1):62–67. doi: 10.1016/j.jip.2012.09.002.

[7] Piana M. et al., (2015) In vitro growth-inhibitory effect of brazilian plants extracts against Paenibacillus larvae and toxicity in bees. Anais da Academia Brasileira de Ciências. 87(2):1041–1047, doi: 10.1590/0001-3765201520140282.

[8] Minnaard, J. and Alippi, A. M. (2016) Partial characterization of bacteriocin-like compounds from two strains of Bacillus cereus with biological activity against Paenibacillus larvae, the causal agent of American Foulbrood disease. Letters in Applied Microbiology. 63(6): 10.1111/lam.12665.

[9] Abbasi, S., Safaie, N., Shams-bakhsh, M., and Shahbazi, S. (2016) Biocontrol Activities of Gamma Induced Mutants of Trichoderma harzianum against some Soilborne Fungal Pathogens and their DNA Fingerprinting. Iranian Journal of Biotechnology.14(4):260–269, doi: 10.15171/ijb.1224.

[10] Liang, K., Liu, Q., Li, P., Luo, H., Wang, H., and Kong, Q. (2019) Genetically engineered Salmonella Typhimurium: Recent advances in cancer therapy. Cancer Letters. 448:168–181, doi: 10.1016/j.canlet.2019.01.037.

[11] Ahari Mostafavi, H. et al. (2012) The use of a gamma-irradiated mutants of F. solani .sp. phaseoli with reduced pathogenicity for the biological control of fusarium root rot of bean (Phaseolus vulgaris) in field conditions. Journal of Agricultural Science and Technology.14(6):1415–1423

[12] Afsharmanesh, H., Ahmadzadeh, M., Majdabadi, A., Motamedi, F., Behboudi, K., and Javan-Nikkhah, M. (2013) Enhancement of biosurfactants and biofilm production after gamma irradiation-induced mutagenesis of Bacillus subtilis UTB1, a biocontrol agent of Aspergillus flavus. Archives of Phytopathology and Plant Protection. 46(15):1874–1884, doi: 10.1080/03235408.2013.780374.

[13] Santos S. G., et al., (2007) Effects of oxidative stress on the virulence profile of Prevotella intermedia during experimental infection in gnotobiotic mice. Journal of Medical Microbiology.56(3):289–297, doi: 10.1099/jmm.0.46748-0.

[14] Cai, W., De La Fuente, L., and Arias, C. R. (2013) Biofilm formation by the fish pathogen flavobacterium columnare: Development and parameters affecting surface attachment. Applied and Environmental Microbiology.79(18);5633–5642, doi: 10.1128/AEM.01192-13.

[15] Gómez, N. C., Ramiro, J. M. P., Quecan, B. X. V., and de Melo Franco, B. D. G. (2016) Use of Potential Probiotic Lactic Acid Bacteria (LAB) Biofilms for the Control of Listeria monocytogenes, Salmonella Typhimurium, and Escherichia coli O157:H7 Biofilms Formation. Frontiers in Microbiology. 7: 1–15, doi: 10.3389/fmicb.2016.00863.

[16] Vahedi Shahandashti, R., Kasra Kermanshahi, R., and Ghadam, P. (2016) The inhibitory effect of bacteriocin produced by Lactobacillus acidophilus ATCC 4356 and Lactobacillus plantarum ATCC 8014 on planktonic cells and biofilms of Serratia marcescens. Turkish Journal of Medical Sciences.46(4):1188–1196, doi: 10.3906/sag-1505-51.

[17] Crailsheim, K. et al., (2009) Standard methods for artificial rearing of Apis mellifera larvae. Journal of Apicultural Research. 52(1):1–16, doi: 10.3896/IBRA.1.52.1.05.

[18] Antúnez, K., Anido, M., Schlapp, G., Evans, J. D., and Zunino, P. (2009) Characterization of secreted proteases of Paenibacillus larvae, potential virulence factors involved in honeybee larval infection. Journal of Invertebrate Pathology.102(2): 129–132, doi: 10.1016/j.jip.2009.07.010.

[19] Shahbazi, S., Behgar, M., and Askari, H. (2015) The effect of gamma radiation on xylanase activity in theTrichoderma harzianum and Trichoderma reesei. The 4th National Congress on Nuclear Technology Application in Agricultural and Natural Resource Sciences, Nuclear Agriculture Research School), 360–365.

[20] Mohsin, I., Muhammad, A., and Fareeha, B. (2017) Development of Bacillus subtilis Mutants for Overproduction of Protease. Journal of Microbial and Biochemical Technology.9(4):174–180, doi: 10.4172/1948-5948.1000363.

[21] Al Marjani, M. F. (2017) Effect of Gamma Irradiation on Biofilm Formation of Some

Gram-Negative Bacteria Isolated From Burn and Wound. International Journal of PharmTech Research. 9(12): 607–613,

[22] Atsumi, T., Fujimoto, E., Furuta, M., and Kato, M. (2014) Effect of gamma-ray irradiation on Escherichia coli motility. Central European Journal of Biology. 9(10): 28–31, doi: 10.2478/s11535-014-0332-z.

ICNST 2024
International Conference on Nuclear Science and Technology
6- 8 MAY 2024 | Isfahan, Iran

Performance Accuracy of motion tracking models in external beam radiotherapy :A comparative study (Paper ID : 1168)

Mohadeseh Torabi,MSc[1]* ,Ahmad Esmaili Torshabi,phD[1,]

[1] *Department of Nuclear Engineering, Faculty of Sciences and Modern Technologies, Graduate University of Advanced Technology, Kerman, Iran*

Abstract

Real-time tracking of moving tumors requires a predictive model using patients' breathing patterns. The challenge in such tracking is due to differences in breathing patterns of different patients and tumor movement due to various factors including breathing. Therefore, to solve this challenge and achieve successful and accurate tracking, it can be useful to use a predictive model with high-performance accuracy. In this study, three models of fuzzy logic, adaptive neuro-fuzzy inference system and LSTM have been compared for tumor tracking in motion tumors radiotherapy; as there is no available comparative study assessing the performance accuracy of these models in tumor tracking and comparing them with each other. For this comparison, the motion database of 10 real patients, divided into two groups, control and worst, has been used. The conducted evaluations indicate a reduction in tracking error after implementing these models compared to the model used in the CyberKnife system. Among the considered models, the fuzzy logic-based model performed best for control group patients, while the LSTM model showed optimal performance for worst group patients. Overall, LSTM model has better performance accuracy while its error reduction is 1.4 mm regarding with fuzzy and 2.2 regarding with Adaptive neuro fuzzy based models.

Keywords: Radiotherapy, Tumor motion, External markers, Predictive models

Introduction

Cancer is a complication in which abnormal cells proliferate in an uncontrolled manner and can involve nearby tissues. There are more than 200 different types of cancer, each of which develops in specific ways. There are many ways of treatment, depending on the specific condition of the patient, the type and location of the tumor, they may use a treatment method or a combination of two or three methods for better recovery and effectiveness[1-10]. Today, due to the advances made in the field of radiotherapy and radiation generating systems, the contribution of radiotherapy in cancer treatment has

increased more than other methods. Radiotherapy is a common cancer treatment method that uses targeted delivery of ionizing radiation such as gamma, beta, or heavier particles (hadrons) to eradicate cancer cells or improve cancer symptoms.

The goal in radiotherapy is to deliver the lowest dose to healthy tissue and the highest dose to the tumor. In external radiotherapy, in the pre-treatment stage, by using imaging systems such as CT scan, MRI, they find information about the location of the tumor and enter the treatment planning stage with this information, and determine the tumor and the area that should be irradiated. In a general classification, tumors are divided into two categories: static and dynamic. The main problem arises when the tumor is of a movement type, which causes them to move for various reasons, including breathing, which is the most important. In this situation, it will be difficult to target the tumor because it is not easy to lock the therapeutic beam on the tumor. In order to solve the problems in the treatment of moving tumors, several solutions have been provided in the past [11-22], including: patient's breath hold [20-22] , following the tumor's movement during radiation, which is divided into two groups: gated radiotherapy [23-25] and radiotherapy based on real time tumor tracking[17-19]. The breath holding method depends on the patient's performance, and patients who are old , children or who have breathing disorders will not be able to cooperate, which makes it difficult to use this method[20-22]. In gated radiation therapy, the beam is irradiated only in a certain part of the breathing interval, which is called the gate, and since the beam is irradiated from different directions, it makes it possible for healthy tissues to receive a lower dose of the beam and, as a result, suffer less damage[23-25]. Both gated radiation therapy methods and radiotherapy based on tumor tracking in real time need to have accurate information about the location of the tumor, which is challenging to obtain this accurate information due to the presence of various respiratory ranges in the respiratory cycle of patients. Among the methods of obtaining this information, continuous imaging of the tumor or the use of external markers can be mentioned. In the process of obtaining the mentioned information, the principle of ALARA should be taken into consideration, which means giving the maximum dose to the tumor while giving the minimum dose to the healthy tissues around the tumor. Therefore, among the two proposed methods, the use of external markers can be a more suitable solution.

In radiotherapy based on external markers, a system is used for real-time tumor

tracking to provide the doctor with the exact location of the tumor at any moment and to give a lower dose to the patient; This system is called Cyberknife, which uses infrared cameras to track the tumor, which follows the external markers installed on the vest that the patient wears, and compares the information obtained from these markers and the information obtained by the x-ray imaging system from the location of the tumor is matched and correlated and creates an adaptive model to be able to predict the location of the tumor at any moment. Of course, the correctness of the model performance during the treatment is checked by using the information obtained from the optical tracking system that provides the coordinates of the external markers, as well as the information provided by the X-ray imaging system of the tumor location, and the model is updated in order to prevent tracking errors. The conducted studies indicate that the accuracy of the model's performance is more due to the uncertainties related to the matching of external and internal markers with each other, while the prediction error is more influenced by the time delay in the performance of the system.

To solve the challenges, studies have been done and models have been designed and implemented. In this study, the investigation of these models and the comparison of the accuracy of their performance on the topic of tumor tracking have been discussed. So far, no comparative study has been conducted in the field of checking the tracking accuracy of the desired models.

The models studied in this research were designed based on Fuzzy Logic, Adaptive Neuro- Fuzzy Inference system and LSTM.

The comparison made between the coordinates obtained from the tracking performance of the proposed models and the model used in the Cyberknife system is related to 10 patients treated with this system.

Methods

The data set analyzed in this research included the movement information of 86 patients treated at Georgetown University Hospital in America, among which 10 patients were randomly selected as samples**.** And based on the available patterns of their respiratory cycle, the patients are divided into two groups: the control and the worst group. The correlation model that is responsible for tracking the tumor in the Cyberknife system

at the beginning of each treatment session and by creating a match and synchronization between the information obtained from the external infrared markers on the vest that the patient wears for treatment And also, the internal marker implanted by a special tool inside or near the tumor volume, which must be made of a non-toxic type of metal, is made so that the robotic arm of this system can be guided in such a way that it can move the body with the least error and As a result, he tracked the movement of the tumor and irradiated the tumor, and during the treatment, the accuracy of the performance of model is evaluated and the model is updated by means of images taken every few minutes from the tumor location.

In order to build the proposed models from a part of the available data, which includes information obtained from external markers that represent the movement of the patient's chest and respiratory cycle, as well as part of the information obtained from the implanted internal

marker that indicates the location of the tumor at any moment. It has been used in such a way that the model is trained at the beginning and in the pre-treatment stage using the presented data, and then during the treatment, only the information obtained from the external indicators is given as input to the model, and the model in The output predicts the location of the tumor.

In order to finally check the performance accuracy of the proposed models, it is necessary to compare the outputs obtained from the proposed models with the outputs obtained from the model used in the Cyberknife system for which the related data sets are available. Therefore, in order to train the model, the number of data equal to the number of data used in Cyberfire should be used. According to the available information from the patients, in this research, on average, 15% of the data were used for model training and 85% of them were used for model testing.

Fuzzy Logic

In this part, a correlation model based on a fuzzy logic inference system is used. In this process, the final result, which is the prediction of tumor location, is a non-linear map of the movement of external markers. Clustering is a method of grouping similar data into a group. In building this logic, clustering is very important. The most famous data clustering techniques in this model can be called subtractive clustering and fuzzy C-

means clustering. To build this algorithm, a matrix with 9 columns containing the data of all three external markers is considered as input. And a matrix of external markers that are the same as the inputs in terms of time is also considered as the output, and its implementation is also done with the fuzzy logic toolbox in MATLAB (The MathWorks Inc., Natick, MA) [27-31].

Adaptive Neuro-Fuzzy Inference System

This system, which is very efficient for describing nonlinear systems, is composed of a combination of adaptive neural network and fuzzy inference system, which can take advantage of the advantages of both methods, namely the power of training neural networks and the linguistic advantage of fuzzy systems to solve complex problems. In this part, Adaptive Neuro- Fuzzy Inference System is used to relate the movements of external markers as input to tumor movement as output. This inference system is based on the Sugeno type, and membership functions are generated by the data clustering algorithm (FCM). The membership functions are generated by the fuzzy c-means (FCM) clustering algorithm. The FCM algorithm examines the data in terms of similarity and collects similar data in a cluster and finally provides a number of clusters that contain similar data. Here, two accumulation and non-accumulation methods are used to perform the model updating process during the treatment. In the accumulation method, the new information obtained from the internal and external indicators by said methods is added to the initial information set that was given to the model. But in the non-accumulation method, for every new data entry, the oldest data is deleted by the model. Overall, it should be said that both methods of updating the model had acceptable performance accuracy, but the time to predict the location of the tumor by the non-accumulation method has been less [32- 35].

Long Short-Term Memory

In this study, in order to achieve successful tracking, the LSTM network has been used to design a correlation model in the form of a time series. At first, using the available data set, the coordinates provided by the external markers were given as input to the network in the form of a matrix and also, a separate file of the coordinates provided by the internal marker implanted in the tumor was prepared, and a part of it was given as output to the network. Here, the Python programming language is used to build the

model. To predict the location of the tumor, a model is needed that predicts the location of the tumor in the output after passing the training stage only by receiving the information and coordinates of the external markers. To build and train the model, first the model should check and train the correct answer by comparing the coordinates of the external markers and the actual location of the tumor (internal marker). The data is defined in such a way that the model can guess the data of the next column every time by checking the previous 11 columns of the given information and proceeding in the same way. Various libraries such as TensorFlow, Numpy and Pandas have been used to build the network and thus build the model. It should be noted that the data are normalized before being used as input and output by the network [36-40]. Before using the data as input and output of the network, it is normalized until all the data are placed on the same scale. Also since in topics related to machine learning, the more data used to train the network, the more accurate the model is built, so in this study, interpolation and increase of data have been done with a factor of 1000. By doing these two things, the LSTM model has been better trained and has succeeded in tracking the tumor with higher accuracy.

Results and discussion

The outputs obtained after using the three proposed models have been collected and the Root Mean Square Error (RMSE) factor has been used to check their performance error. The results of the analysis of the obtained errors have shown a reduction in the tracking error compared to the model used in the Cyberknife device. Among the considered models, the model based on Fuzzy Logic for patients in the control group and the LSTM model for patients in the worst group had the best performance. Figures 1 and 2 show the 3D-RMSE related to the proposed models for two groups of control and worst patients.In general, according to the results obtained from examining both groups of patients, the LSTM model has shown better performance and the final results show that the three-dimensional error is reduced by 1.4 mm and 2.2 mm, respectively, of the LSTM model compared to the Fuzzy Logic and the model based on the Adaptive Fuzzy-Neural inference System. (Table 1)

Table 1. The Three-Dimensional Root Mean Square Error of the studied patients

3D RMSE (mm)	FCM-FIS	ANFIS	LSTM
3D-RMSE for Control patient group	3.202	3.68	3.454
3D-RMSE for Worst patient group	10.19	11.3	7.09
3D-RMSE for all patients	6.7	7.49	5.27

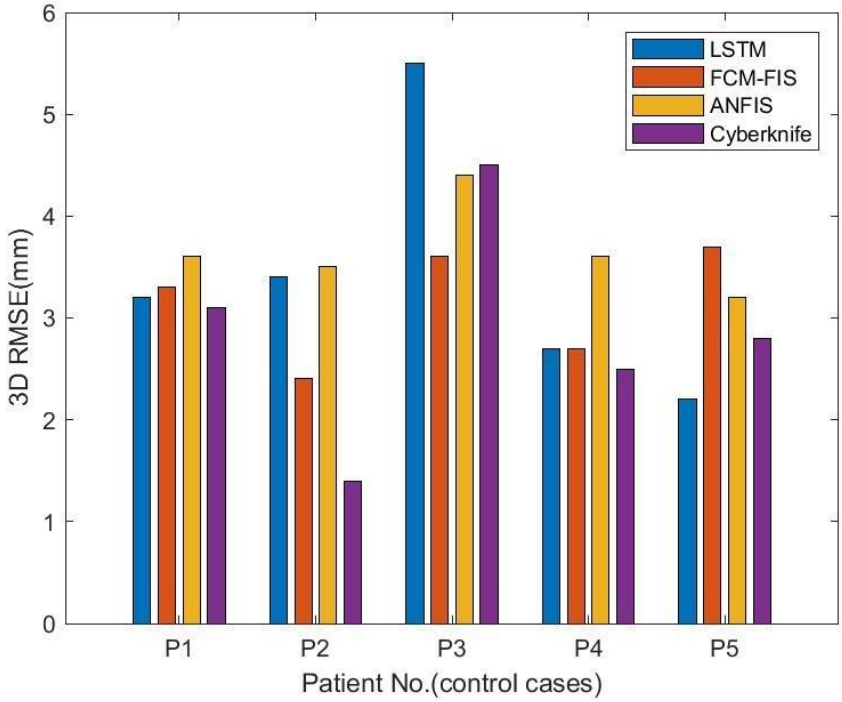

Fig.1. RMSE vs. patient numbers (control group)

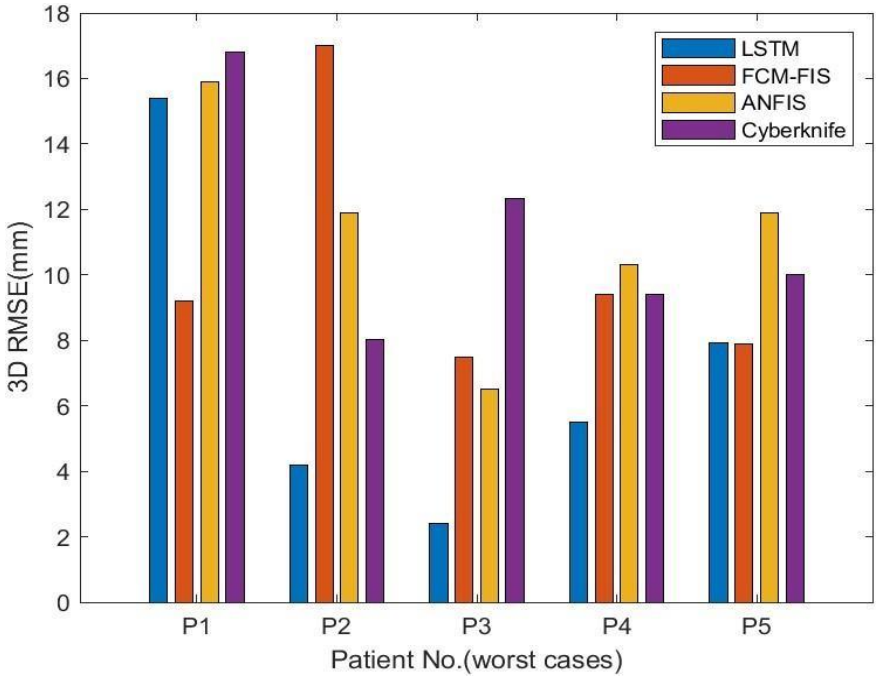

Fig.2. RMSE vs. patient numbers (worst group)

Conclusions

In the radiotherapy of moving tumors, in order to achieve successful tracking, complete information about the patient's respiratory cycle and the location of the tumor must be obtained so that an accurate prediction model can be made to predict the location of the tumor during the treatment**.** Several models have been introduced in the past, and among them, in this study, three models based on Fuzzy Logic, Adaptive Neuro-Fuzzy Inference System, and LSTM have been investigated, and their performance has been compared with each other. The results obtained from this comparison show the better performance of the Fuzzy Logic model for the patients in the control group and the better performance of the LSTM model for the patients in the worst group, and in general, for both groups of patients, it can be concluted that the LSTM model performs more accurately versus other commonly available models.

Acknowledgments

The authors acknowledge Sonja Dieterich for providing access to the clinical database.

References

[1] Lombardo E, et al.(2023) Evaluation of real-time tumor contour prediction using LSTM networks for MR-guided radiotherapy. Radiother Oncol,182.

[2] Hausman, Daniel M.(2019) What is cancer?. Perspect Biol Med,62(4):778-784.

[3] Upadhyay A.(2021) Cancer: An unknown territory; rethinking before going ahead. GENES DIS,8(5):655-661.

[4] Ranjan A, et al. .(2019) Role of phytochemicals in cancer prevention. Int J Mol Sci 2019;20:4981.

[5] Haehl E, et al.(2020) Radiotherapy for geriatric head-and-neck cancer patients: what is the value of standard treatment in the elderly?. Radiat Oncol J,15:1-12.

[6] Ravasco P .(2019) Nutrition in Cancer Patients. *J Clin Med* ,8:1211..

[7] Hanahan D.(2022) Hallmarks of Cancer: New Dimensions. Cancer Discov;12: 31-46.

[8] Brücher B LDM, and Ijaz S J.(2014) Epistemology of the origin of cancer: a new paradigm. *BMC cancer* ,14(1): 1-15.

[9] https://www.cancer.gov/about-cancer/understanding/what-is-cancer

[10] Grizzi F, and Maurizio CI.(2006) Cancer: looking for simplicity and finding complexity. Cancer Cell Int,6(1):1-7.

[11] Guckenberger M, et al.(2020) Definition and quality requirements for stereotactic radiotherapy: consensus statement from the DEGRO/DGMP Working Group Stereotactic Radiotherapy and Radiosurgery. Strahlenther Onkol,196: 417-420.

[12] Lei G, et al.(2021) Ferroptosis, radiotherapy, and combination therapeutic strategies. Protein Cell ,12(11):836-857.

[13] Wang M, Mingqing Q, et al.(2020) A review on application of deep learning algorithms in external beam radiotherapy automated treatment planning. Front Oncol,10: 580919.

[14] Benveniste MF, et al.(2019) Recognizing radiation therapy–related complications in the chest. *Radiographics* ,39(2): 344-366.

[15] Do Huh H, and Seonghoon K.(2020) History of radiation therapy technology. Prog Med Phys,31(3):124-134.

[16] Chandra RA, et al.(2021) Contemporary radiotherapy: present and future. Lancet ,398(10295):171-184.

[17] Hiroshima Y, et al.(2022) Stereotactic Body Radiotherapy for Stage I Lung Cancer With a New Real-time Tumor Tracking System. *Anticancer Res* ,42:2989-2995.

[18] Uchinami Y, et al.(2021) Treatment outcomes of stereotactic body radiation therapy using a real-time tumor-tracking radiotherapy system for hepatocellular carcinomas. Hepatol Res ,51(8):870-879.

[19] Bertholet J, et al.(2019) Real-time intrafraction motion monitoring in external beam radiotherapy. Phys Med Biol,64(15):15TR01.

[20] Stick LB, et al.(2020) Intrafractional fiducial marker position variations in stereotactic liver radiotherapy during voluntarydeep inspiration breath- hold. Br J Radiol Suppl,93(1116):20200859.

[21] Lee S, et al.(2019) Tumor localization accuracy for high-precision

radiotherapy during active breath-hold. Radiother Oncol,137: 145-152.

[22 Dekker J, et al.(2023) Dose coverage and breath-hold analysis of breast cancer patients treated with surface-guided radiotherapy. *Radiat Oncol* ,18(1):72.

[23] Farzaneh MJK,Momennezhad M, and Naseri S.(2021)Gated radiotherapy development and its expansion. J Biomed Phys Eng,11(2):239.

[24] Oh SA, et al.(2019) Optimal gating window for respiratory-gated radiotherapy with real-time position management and respiration guiding system for liver cancer treatment. Sci Rep,9(1):4384.

[25] Chen L, et al.(2020) Accuracy of real-time respiratory motion tracking and time delay of gating radiotherapy based on optical surface imaging technique. Radiat Oncol,15:1-9.

[26] https://www.researchgate.net/figure/Flowchart-of-correlation-model- performance_fig2_221929240

[27] Torshabi, AE, et al.(2013) An adaptive fuzzy prediction model for real time tumor tracking in radiotherapy via external surrogates. J Appl Clin Med Phys ,14(1):102-114..

[28] Torshabi, AE.(2022) "Investigation the efficacy of fuzzy logic implementation at image-guided radiotherapy." *Journal of Medical Signals and Sensors*, 12.2: 163.

[29] Giżyńska, Marta K., et al. (2023) "A novel external/internal tumor tracking approach to compensate for respiratory motion baseline drifts." *Physics in Medicine & Biology*, 68.5: 055017.

[30] Li, Guo-quan, et al. (2020) "Optimized CyberKnife lung treatment: Effect of fractionated tracking volume change on tracking results." *Disease Markers*, 2020.

[31] Wang, Jiateng, et al. (2021) "An improved correlation model for respiration tracking in robotic radiosurgery using essential skin surface motion." *IEEE Robotics and Automation Letters*, 6.4: 7885-7892.

[32] Jöhl, A, et al. (2020) "Performance comparison of prediction filters for respiratory motion tracking in radiotherapy." *Medical physics*, 47.2: 643-650.

[33] Miyandoab, PS, et al. (2015) "The robustness of various intelligent models in patient positioning at external beam radiotherapy." *Frontiers in Biomedical*

Technologies, 2.1: 45- 54.

[34] Nankali, Saber, et al. "Investigation on performance accuracy of different surrogates in real time tumor tracking at external beam radiotherapy." *Frontiers in Biomedical Technologies* 2.2 (2015): 73-79.

[35] Zhou, D, et al. (2022) "Development of AI-driven prediction models to realize real- time tumor tracking during radiotherapy." *Radiation Oncology*, 17.1: 42.

[36] Chang YS, et al.(2020) An LSTM-based aggregated model for air pollution forecasting. Atmos Pollut Res,11:1451-1463.

[37] Yu Y, et al.(2019) A review of recurrent neural networks: LSTM cells and network architectures. Neural Comput,31:1235-1270.

[38] Staudemeyer, RC, and Morris ER. Understanding LSTM--a tutorial into long short- term memory recurrent neural networks. *arXiv preprint arXiv:1909.09586* 2019.

[39] Sun W, et al.(2023) Comparison of initial learning algorithms for long short-term memory method on real-time respiratory signal prediction. Front Oncol,13:1101225.

[40] Ma Y, et al.(2021) Target localization during respiration motion based on LSTM: A pilot study on robotic puncture system. Int. J. Med. Robot, 17: e2247

ICNST 2024
International Conference on Nuclear Science and Technology
6- 8 MAY 2024 | Isfahan, Iran

Investigating The Performance of The Filtering Method in Reducing X-Ray Image Noise (Paper ID : 1169)

A. Zahed[1], H. Jafari[1], H. Kargaran[2], E. Taghavi[1]

[1] *Department of Radiation Application, Shahid Beheshti University, Tehran, Iran*
[2] *Faculty of Engineering, Shahed University, Tehran, Iran*

Abstract

X-ray images are usually subject to various types of noise, either from the surrounding environment, the imaging equipment, or the imaging process itself. The denoising process helps reveal important details, textures, and structures in images, facilitates detailed interpretations and analyses, and improves visual interpretation. In this article, we intend to examine the performance and efficacy of filtering methods for two types of prevalent noise, uniform (Salt-and-Pepper) and non-uniform (Speckle) on regular and X-ray images. To achieve this, four different and widely used filters such as Gaussian, Median, Bilateral, and Non-Local Means (NLM) have been employed. The performance of these filters is evaluated using metrics such as peak signal-to-noise ratio (PSNR) and root mean square error (RMSE). The results show that the median filter, with a kernel size of 3, has a good performance in mitigating salt-and-pepper noise. In addition, the NLM filter, using parameters (20, 3, 7), performs very well in dealing with speckle noise. These findings provide valuable insights into the selection and optimization of denoising methods to enhance X-ray image quality. The study emphasizes the importance of matching filters for specific noise types and provides a pathway for more accurate clinical diagnoses and improved treatment outcomes in medical and objective imaging applications.

Keywords: Denoising, X-ray image Filtering, Image noise

1. Introduction

Image noise is a common issue in digital imaging. The presence of noise can significantly degrade the visual quality of images. Therefore, noise refers to unwanted variations in brightness or color that distort the original image content in the context of image processing[1]. It can originate from various sources during the image processing stages such as sensor noise, and environmental factors like poor lighting conditions, and high temperatures. However, the compression algorithms and various image processing operations can introduce additional

noise or amplify existing noise including salt and pepper, Gaussian, speckle, and poison noises[2].

Specifically, X-ray images commonly encounter various types of noise, stemming from the surrounding environment, imaging equipment, or the imaging process itself. The two primary types of noise in X-ray images are systemic noise and impulse noise (shot noise). This type of noise results from the random nature of the photons creating the image. When a photon interacts with the image sensor, the noise arises due to the stochastic scattering of photons. In addition, systemic noise originates from irregularities in the imaging system, signal transmission, or the image processing pipeline [3].

Since the noise can lead to image degradation, the denoising process helps reveal important details, textures, and structures within images, facilitating accurate interpretations and analysis and improved visual interpretation. The important denoising algorithms aim to eliminate noise while preserving essential image features, such as edges and textures, ensuring minimal loss of valuable information and preservation of information. Image denoising techniques find applications across diverse domains and industries. This is particularly important in fields such as medical imaging, photography and art restoration, computer vision and machine learning, surveillance, and security images[4]. Over the years, numerous studies and advancements have been made in the field, offering a diverse range of methods and algorithms for reducing image noise.

Traditional image denoising techniques, such as linear and frequency domain filters, aimed to mitigate noise by addressing basic spatial or frequency characteristics. The classical Median and Gaussian filters, known for their computational efficiency, apply convolution operations to smooth images [5-9]. While Gaussian filtering is suitable for real-time applications, it tends to blur edges in scenarios with complex noise patterns [5]. This blurring effect can compromise the sharpness of important image features and details, impacting the overall visual quality and interpretability of the denoised image. Despite its effectiveness in removing impulse noise, such as salt and pepper noise, the median filter may introduce artifacts, particularly in regions with high noise density. Additionally, it may not be as efficient in reducing Gaussian noise compared to other methods, limiting its applicability in scenarios where multiple types of noise coexist or when noise levels vary across the image [7]. In the 1990s, wavelet-based methods gained traction, with Donoho and Johnstone pioneering wavelet thresholding for efficient noise

removal while preserving image details. they can be computationally intensive, especially for large-scale or real-time applications.

Additionally, selecting an appropriate threshold for wavelet thresholding poses a challenge, as it requires careful consideration of noise characteristics and image content to achieve optimal denoising performance. The Non-Local Means (NLM) filter, introduced in 2005 by Buades et al., significantly advanced denoising by averaging pixel values based on local patch similarities [8]. which may limit its practicality for real-time or large-scale image processing tasks. The patch-wise comparison process used in NLM involves extensive computations, making it less suitable for applications where processing speed is crucial. Additionally, parameter tuning for NLM, such as the window size and similarity threshold, can be challenging and may require manual adjustment based on image content and noise characteristics. The bilateral filter, proposed by Tomasi and Man Duchi in 1998, preserves edges and details but may struggle with complex noise patterns and entails higher computational costs. Sparse representation and dictionary learning methods like K-SVD and BM3D gained popularity, leveraging sparse representations for noise reduction. Recent advancements focus on real-time denoising tailored for applications like video streaming, surveillance, and medical imaging.

In this article, we intend to examine the performance and efficacy of filtering methods for two types of prevalent noise, uniform (Salt & Pepper) and non-uniform (Speckle) on regular and X-ray images. To achieve this, four different and widely used filters have been employed. The performance of each of these filters is evaluated using metrics such as peak signal-to-noise ratio (PSNR) and root mean square error (RMSE). Understanding the parameters and characteristics of these filters allows for optimal customization and denoising results and, we can choose the most suitable approach to tackle various types of noise and achieve high-quality denoised images.

2. Materials and Methods

2.1.Background

Four filters (Gaussian, Bilateral, Median, and NLM) have been used to investigate the performance of filtering in image denoising. The Gaussian filter is a linear filter that effectively smooths out high-frequency noise components by convolving the image with a Gaussian kernel. It applies a weighted average of neighboring pixel values, where the weights are determined by the Gaussian distribution. While Gaussian filtering is efficient for reducing

Gaussian noise, it may blur edges and fine details in the image. Unlike linear filters, the bilateral filter is non-linear and considers both spatial and intensity information during filtering. It effectively reduces noise while preserving important image structures by applying a weighted average of pixel values based on their spatial proximity and intensity similarity [10]. The bilateral filter is suitable for denoising images affected by various types of noise, including salt and pepper, Gaussian, speckle, and Poisson noises. The median filter is particularly effective in removing impulse noise, such as salt and pepper noise, while preserving edges and fine details [11]. It works by replacing each pixel's value with the median value of the neighboring pixels [12]. Unlike Gaussian filtering, which computes a weighted average, the median filter selects the middle value from the sorted intensity values within a neighborhood. This robust approach ensures noise reduction without blurring edges. The Non-Local Means (NLM) filter operates by averaging pixel values based on the similarity of local image patches. It effectively reduces noise while preserving textures and fine details by considering non-local similarities across the entire image. Each denoising filter has specific parameters that can be adjusted to achieve optimal denoising results[13]. The optimal parameter values depend on the characteristics of the noise and aspects of applicants.

2.2. Proposed method

Therefore, a high-quality standard image with dimensions of 255×255 pixels has been used for this purpose. Initially, we introduce salt-and-pepper noise with a noise density of 0.05 and speckle noise with a variance of 0.02 to the test image. Impulse noise, often referred to as salt-and-pepper noise, is a type of noise that affects image pixels randomly, causing them to take extreme values. This type of noise is characterized by sporadic occurrences of very bright or very dark pixels, resembling grains of salt and pepper. speckle noise typically appears as a common increase or decrease in the vicinity of pixel values, in other words, the distribution of speckle noise is usually described as non-uniform.

Subsequently, the mentioned filters with specified parameters have been utilized. This process was repeated for another test image obtained from a noisy X-ray image with dimensions of 123×123 pixels. In addition, the standard criteria including root mean square error (RMSE),

mean square error (MSE) and peak signal-to-noise ratio (PSNR) have been used to evaluate the performance of the denoise filter, which is formulated as follows:

$$RMSE = \sqrt{\frac{1}{n}\sum_{i=1}^{n}\sum_{j=1}^{n}(I(i.j) - K(i.j))^2}$$

$$MSE = \frac{1}{n}\sum_{i=1}^{n}\sum_{j=1}^{n}(I(i.j) - K(i.j))^2$$

$$PSNR = 10\ log_{10}(\frac{max^2}{MSE})$$

Where the '*max*' denotes the maximum fluctuation in the input image data type. The peak value is 255 if the input image has an eight-bit unsigned integer data type. Moreover, the peak value is one if the input image has a double precision floating point data type. '*n*' is the number of pixels or sampling values, $I(i.j)$is the pixel value in the original image, and $K(i.j)$ is the pixel value in the filtered image.

These formulas are used to calculate the error and draw conclusions about the differences between the original image free of noise and the filtered image. Focusing on achieving the best denoising results while preserving the image structure for images with salt and pepper noise and speckle noise with specific variances, we select the optimal filter and parameters based on the lowest RMSE and highest PSNR values.

A general guide to our image denoising method, which is explained in how the proposed method works, is shown in the diagram in Figure 1.

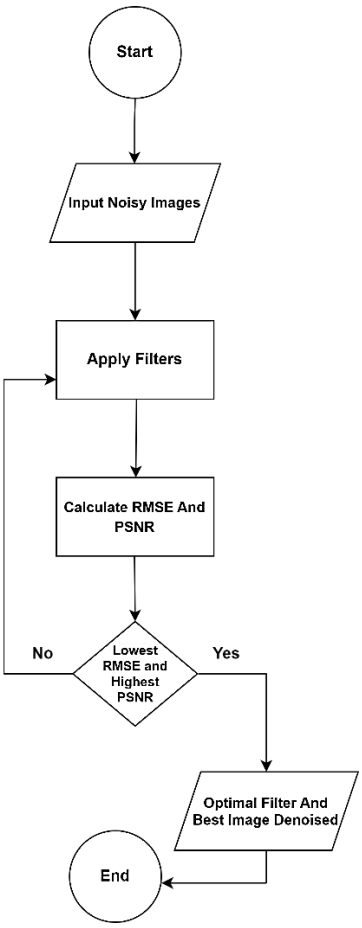

Fig. 1. Process diagram for proposed method

3. Results and discussion

Table 1 illustrates the results obtained for the parametric performance analysis of noise filtering. In the table, first, the type of image and the amount of noise in the image and the type of applied filters are specified. Then, for both types of images with specific types of noise and percentages of noise, the value of each of the parameters PSNR, RMSE, MSE is calculated and each of the obtained values is listed in the table. Then as explained, it can be seen that the Median and Bilateral filters have performed better than other filters for salt and pepper noise (0.05 ND). as shown and highlighted in table, the Median filter (kernel size 3) achieves the highest PSNR of 35.17 dB and the lowest RMSE of 0.0541, making it the optimal filter with the best parameters. For speckle noise (variance of 0.02), the NLM filter yielded the best results with the highest PSNR of 32.85 dB and the lowest RMSE of 0.052. The optimal parameters of this filter are 20, 3, and 7 which correspond to the 'h' parameter, as the smoothing parameter,

controls the amount of smoothing applied during the denoising process, template window size, and search window size respectively. This filter exhibited superior performance in noise reduction compared to other filters.

The same pattern has been seen in the X-ray test image so that for salt and pepper noise, the lowest RMSE of 0.010 and the highest PSNR of 43.92 dB are related to the Median filter (kernel size 3). Also, for speckle noise, the lowest RMSE of 0.015 and the highest PSNR of 39.150 dB are related to the NLM filter with parameters of 30, 7, and 15.

The visual comparison of noisy and denoised images for two typical standard images and an X-ray image is shown in Figure 2. The filters used for denoising in this figure are the optimal filters selected according to the image quality parameters in Table 1.

Image	Filters	Noise type	PSNR	RMSE	MSE
Typical standard	Gaussian	Salt & pepper (0.05 ND)	31.2965	0.0996	48.2416
		Speckle (0.02 var)	32.0978	0.0766	40.1135
	Median	Salt & pepper (0.05 ND)	**35.1791**	**0.0541**	19.7319
		Speckle (0.02 var)	32.0040	0.0877	40.9897
	Bilateral	Salt & pepper (0.05 ND)	32.3056	0.1048	38.2395
		Speckle (0.02 var)	31.9105	0.0721	41.8814
	NLM	Salt & pepper (0.05 ND)	33.8001	0.1557	27.1061
		Speckle (0.02 var)	**32.8598**	**0.0528**	33.6585
X-ray	Gaussian	Salt & pepper (0.05 ND)	33.2173	0.0534	30.9990
		Speckle (0.02 var)	34.2908	0.0358	24.2101
	Median	Salt & pepper (0.05 ND)	**43.9265**	**0.0103**	2.6328
		Speckle (0.02 var)	31.5401	0.0430	45.6101
	Bilateral	Salt & pepper (0.05 ND)	36.8878	0.0593	13.3134
		Speckle (0.02 var)	35.5527	0.0241	18.1054
	NLM	Salt & pepper (0.05 ND)	39.8849	0.0766	6.6770
		Speckle (0.02 var)	**39.1503**	**0.0156**	7.9075

Table 1. Parametric performance analysis for denoising images

In this figure, we first see the main used images without noise. In the first part, the figure on the left is a typical standard image, in the next step, salt and pepper noise (0.05 ND) and speckle noise (0.02 var) have been added to the image. As can be seen in the figure, on the left side, the images are damaged by noise. Then we apply the filter obtained from table 1 on the noisy images and in the output, we see the images that are the best denoised image resulting from the optimal filter. In the second part, the same steps are performed for the main X-ray image

without noise as a test image, on the right side of the figure and all the steps is displayed visually in Figure 2.

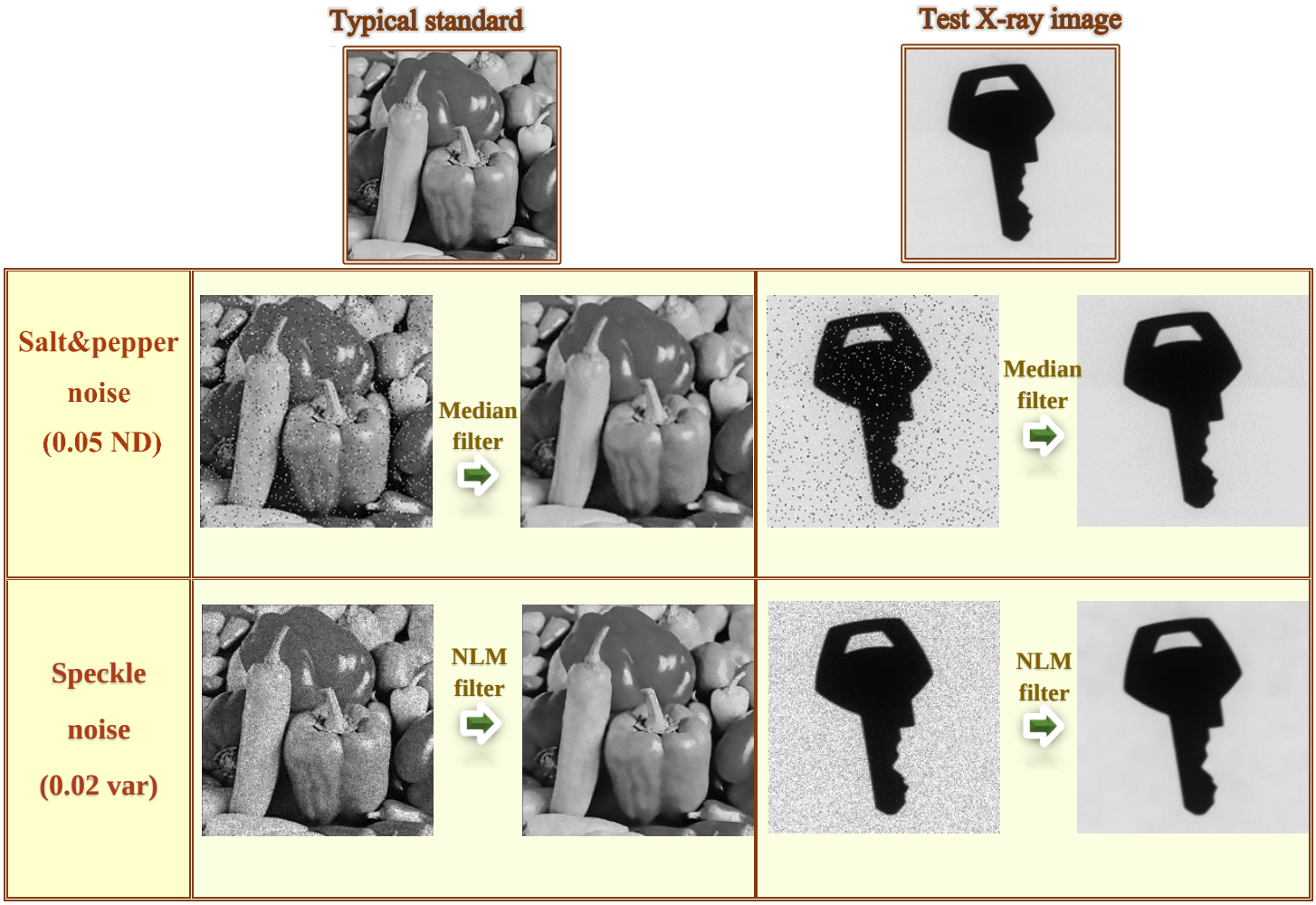

Fig. 2. Visual comparison of noisy and denoised images for a) typical standard image and b) X-ray image

4. Conclusion

In this study, the effectiveness of the filtering method and finding a suitable filter with optimal parameters to reduce noise of different types (uniform and non-uniform) was investigated. For this purpose, a quality standard image and an X-ray test image have been used. The optimal parameters for each filter were determined based on their denoising efficacy. The results were analyzed using PSNR, and RMSE metrics. The comprehensive evaluation revealed the

superiority of specific filters particularly on X-ray images affected by salt-and-pepper and speckle noises. The Median filter, with a kernel size of 3, exhibited optimal performance in mitigating salt-and-pepper noise. In addition, the NLM filter, utilizing parameters (20, 3, 7), excelled in addressing speckle noise.

These findings provide valuable insights into the selection and optimization of denoising methods to enhance X-ray image quality. The study emphasizes the importance of tailoring filters to specific noise types, offering a pathway for more accurate clinical diagnoses and improved treatment outcomes. Continuous refinement of denoising techniques is recommended for further progress in medical and objective imaging applications.

References:

[1] S. S. Mohanty and S. Tripathy, "Application of different filtering techniques in digital image processing," *J. Phys. Conf. Ser.*, vol. 2062, no. 1, 2021, doi: 10.1088/1742-6596/2062/1/012007.

[2] G. Ilango and R. Marudhachalam, "New hybrid filtering techniques for removal of gaussian noise from medical images," *ARPN J. Eng. Appl. Sci.*, vol. 6, no. 2, pp. 8–12, 2011.

[3] M. Mandar, D. Sontakke, M. Meghana, and S. Kulkarni, "Different Types of Noises in Images and Noise Removing Technique," *Int. J. Adv. Technol. Eng. Sci.*, vol. 03, no. 01, pp. 102–115, 2015.

[4] L. Fan, F. Zhang, H. Fan, and C. Zhang, "S42492-019-0016-7.Pdf," vol. 7, 2019.

[5] B. K. Shreyamsha Kumar, "Image denoising based on gaussian/bilateral filter and its method noise thresholding," *Signal, Image Video Process.*, vol. 7, no. 6, pp. 1159–1172, 2013, doi: 10.1007/s11760-012-0372-7.

[6] Y. Zhang, X. Tian, and P. Ren, "An adaptive bilateral filter based framework for image denoising," *Neurocomputing*, vol. 140, pp. 299–316, 2014, doi: 10.1016/j.neucom.2014.03.008.

[7] A. Prakash, T. Pradhan, N. Kumar, and A. Kumar, "e-Prime - Advances in Electrical Engineering , Electronics and Energy Comparison of algorithms for the removal of impulsive noise from an image," *e-Prime - Adv. Electr. Eng. Electron. Energy*, vol. 3, no. January, p. 100110, 2023, doi: 10.1016/j.prime.2023.100110.

[8] J. Wang, Y. Guo, Y. Ying, Y. Liu, and Q. Peng, "Fast non-local algorithm for image

denoising," *Proc. - Int. Conf. Image Process. ICIP*, no. 0, pp. 1429–1432, 2006, doi: 10.1109/ICIP.2006.312698.

[9] T. Indriyani, M. I. Utoyo, and R. Rulaningtyas, "Comparison of Image Smoothing Methods on Potholes Road Images," *J. Phys. Conf. Ser.*, vol. 1477, no. 5, 2020, doi: 10.1088/1742-6596/1477/5/052056.

[10] C. Graphics, P. Kornprobst, J. Tumblin, and F. Durand, "Bilateral Filtering : Theory and Applications By Sylvain Paris , Pierre Kornprobst , Jack Tumblin and Fr ´ edo Durand," vol. 4, no. 1, pp. 1–73, 2009, doi: 10.1561/0600000020.

[11] M. Malik, F. Ahsan, and S. Mohsin, "Adaptive image denoising using cuckoo algorithm," 2014, doi: 10.1007/s00500-014-1552-x.

[12] R. C. Gonzalez, *www.EBooksWorld.ir*.

[13] S. A. Akar, "Determination of optimal parameters for bilateral filter in brain MR image denoising," *Appl. Soft Comput. J.*, vol. 43, pp. 87–96, 2016, doi: 10.1016/j.asoc.2016.02.043.

[14] H. Wang and C. Chen, "A Two-Step Algorithm for Denoising Peach Tree Leaf Images," *2023 8th Int. Conf. Image, Vis. Comput. ICIVC 2023*, pp. 277–285, 2023, doi: 10.1109/ICIVC58118.2023.10270603.

ICNST 2024
International Conference on Nuclear Science and Technology
6- 8 MAY 2024 | Isfahan, Iran

PET/CT attenuation correction based on Pix2Pix deep learning method to reduce CT dependency (Paper ID : 1171)

Sadremomtaz A.[1], Ghanbari Mishamandani S.[2*]

[1] *Department of Physics, Faculty of Science University of Guilan, Rasht, Iran*

[2] *Department of Physics, Faculty of Science University of Guilan, Rasht, Iran*

Abstract

PET/CT combines CT's anatomical detail with PET's metabolic data, offering early disease detection. However, photon attenuation can reduce PET's accuracy. Traditional correction methods require energy scaling from CT to PET. This study introduces a Pix2Pix model to correct photon attenuation in brain PET images directly, thereby eliminating the need for CT images or the approximation of attenuation coefficients and energy scaling from CT to PET. The data were collected from a Siemens Biograph mCT64 scanner and were used for training and evaluation of the Pix2Pix model. The quality of the images was evaluated through a suite of quantitative metrics, including mean absolute error, root mean squared error, peak signal-to-noise ratio, and multi-scale structural similarity index. Additionally, statistical tools such as the Pearson correlation coefficient and joint histogram analysis were employed to establish the linear relation and efficacy of the Pix2Pix model. The paired t-test, specifically, helped to statistically ascertain the equivalence in performance between the two methods. The PSNR of the Pix2Pix images, when compared with CTAC images, was 37.113, and the MS-SSIM value was 0.983. The Pix2Pix and CTAC images were visually and statistically in good agreement. Reducing CT dependency in attenuation correction for brain PET imaging is feasible with high accuracy using the proposed method. Nevertheless, additional assessment in clinical cohorts is crucial to evaluate the clinical efficacy of this approach.

Keywords: PET/CT, brain [18F]FDG PET, CT-free attenuation correction, deep learning-based attenuation correction, Pix2Pix

Introduction

Positron Emission Tomography (PET) uses radioactive tracers to visualize and measure metabolic processes in the body. PET has limitations in anatomical detail, leading to challenges in distinguishing pathological changes. To improve this issue, PET is often combined with CT

for better anatomical precision. The integration into PET/CT not only augments anatomical localization but also facilitates attenuation correction (AC) with CT-derived coefficients at 511 KeV photon energy. This hybrid modality yields more definitive lesion assessment, surpassing the diagnostic capabilities of either modality alone. [1-5]

Utilizing CT images to correct PET emission data for photon attenuation is challenging due to different energy levels and mechanisms. CT values must be scaled to match PET energy using bilinear scaling method. The method converts CT values to attenuation correction factors (ACFs) based on a linear relationship. Calibration curve is needed, obtained by scanning a phantom with known compositions and coefficients. The curve is piece-wise linear with different slopes for tissue types. By using the calibration curve, CT values can be converted to ACFs for more accurate PET images. [6-9]

This scaling is not unique when a complex mixture of materials, such as CT contrast agents or metallic objects, is present. These materials have different attenuation mechanisms and coefficients for low-energy x-rays and high-energy gamma rays. CT images may contain artifacts from respiratory motion, truncation, beam-hardening, or scattered radiation. These artifacts may affect the accuracy of PET images by causing errors in quantification and localization. PET/CT users should be aware of these issues and take steps to avoid or minimize them. [10,11]

One approach to enhance PET/CT image quality is using artificial intelligence (AI), a field creating machines capable of tasks requiring human intelligence. Deep learning (DL), a subfield of AI, uses neural networks to learn patterns from data. A DL model includes a training stage to learn relation between input and output from data, and a prediction stage to apply this relationship to new inputs. DL methods are more adaptable and robust compared to conventional methods, as they automatically optimize performance based on data quality, quantity, network architecture, and hyperparameters. [12-14]

DL methods can be used as alternatives to conventional AC methods, which use anatomical images from CT or MRI to correct the PET emission data. DL approaches can either directly correct the PET emission data without using any anatomical images, or use them as additional inputs to enhance the correction. However, DL methods face challenges like requiring large

datasets, complexity and interpretability of the models, and high computational needs. Overcoming these challenges is crucial for ensuring the reliability and validity of DL methods in PET/CT imaging, which can surmount some limitations of CT-based attenuation correction (CTAC), such as artifacts and radiation dose, thereby allowing for accurate PET quantification in stand-alone PET scanners. [15-17]

Xue Dong and Yang Lei proposed a DL-AC method to produce AC-PET from non-attenuation corrected PET (NAC-PET) images for whole-body PET imaging, without needing anatomical information. They use 3D patch-based CycleGAN to create a NAC-PET to AC-PET mapping and a reverse mapping from AC-PET to NAC-PET, which makes the NAC-PET to AC-PET mapping more like a one-to-one mapping. They train and cross-validate their network on a retrospective sample of 25 whole-body PET patients. They tested their model on different lesions brain, lung, heart, kidney, liver. The brain ME was 1.23 and the NMSE is 0.70. The DL-AC PET and NAC-PET have a high NCC of 0.97 and a PSNR of 29.2, indicating a great similarity in intensity between the AC-PET and DL-AC PET. [18]

Shiri and Ghafarian proposed and tested a new DL-based AC method for brain PET using only emission data: Deep-DAC. They compared it with the measured AC (MAC) method, which uses CT scans. They reported PSNR and SSIM values of 39.2 ± 3.65 and 0.989 ± 0.006 for the external validation set, respectively. They also reported RE of -0.10 ± 2.14% for SUV mean and -3.87 ± 2.84% for SUV max for all brain regions. The results suggested that Deep-DAC is a feasible AC method for brain PET using only emission data. [19]

The aim of this study is to develop and validate a method for attenuation correction in PET imaging, utilizing the Pix2Pix model. This model excels at learning the transformation between NAC-PET images and CTAC-PET images. By training on paired NAC and CTAC PET images from a PET/CT scanner, the Pix2Pix model is designed to generate AC-PET images directly from NAC-PET inputs, thereby circumventing the need for CT images and the associated energy scaling process. This approach promises to streamline the attenuation correction process, potentially enhancing the efficiency and accessibility of PET imaging diagnostics.

Material and methods

The dataset known as CERMEP-IDB-MRXFD offered 37 cases of normal adult human brains, which included [18F]FDG PET, T1 and FLAIR MRI, and CT scans. To obtain the PET and CT data, a Siemens Biograph mCT64 was employed. PET data acquisition started 50 min after the injection of 122.30±21.29MBq of [18F]FDG and lasted for 10 minutes. As for the CT images employed for attenuation correction, they were acquired using a tube voltage of 100kV. The training phase utilized a total of 27 cases, consisting of 2942 2D images. Additionally, the validation phase included 7 cases, comprising 800 2D images. Finally, the testing phase involved 3 cases, comprising 290 2D images. [20]

Pix2Pix is a model has been designed to facilitate Image-to-Image translation. This model consists of two neural networks: the PatchGAN discriminator and the generator. The primary objective of the generator is to produce AC-PET images that closely resemble CTAC-PET images. Conversely, the discriminator's role is to differentiate between the CTAC-PET and the generated AC-PET. Both the generator and the discriminator engage in a competitive training process, wherein they continually strive to outperform each other and enhance their respective abilities.

The generator's architecture is a Unet-inspired encoder-decoder model. The encoder comprises five convolutional blocks, each with a convolutional layer with random normal weight initializer, batch normalization, and parametric ReLU activation, halving the input's spatial dimension. The decoder, whereas, contains five blocks, each consisting of a transposed convolutional layer, followed by a batch normalization layer and a parametric ReLU activation function. It uses the same parameters as the convolutional layer in the encoder, but it increases the spatial dimension of the input by a factor of 2. Skip connections are employed between corresponding encoder and decoder blocks, preserving spatial information and enhancing output quality. The final output is produced by a transposed convolutional layer with a tanh activation function, generating the final image.

The PatchGAN discriminator performs image classification by utilizing a source image (CTAC) and a target image (generated AC-PET) as its input. It subsequently evaluates the likelihood of the target image being a real or generated transformation of the source image. This discriminator consists of five convolution blocks, each comprising a convolution layer followed by batch normalization and leaky ReLU activation. The final block includes a

convolution layer with a one filter and a 1×1 kernel employing a sigmoid activation function. The resultant prediction matrix denotes the probability of the corresponding patch being actual or generated produced.

The loss function of pix2pix consists of two components: the generator loss and the discriminator loss. The generator loss is composed of two terms: the adversarial loss and the L1 loss. The adversarial loss is calculated by comparing the output of the discriminator on the generated AC-PET and the target CTAC-PET, using a binary cross-entropy function. The L1 loss is calculated by taking the mean absolute error between the generated AC-PET and the target CTAC-PET. The discriminator loss, calculated by binary cross-entropy, evaluates how well the discriminator distinguishes real CTAC-PET images from generated AC-PET. The generator and the discriminator are trained using the Adam optimizer with an exponential decay learning rate schedule.

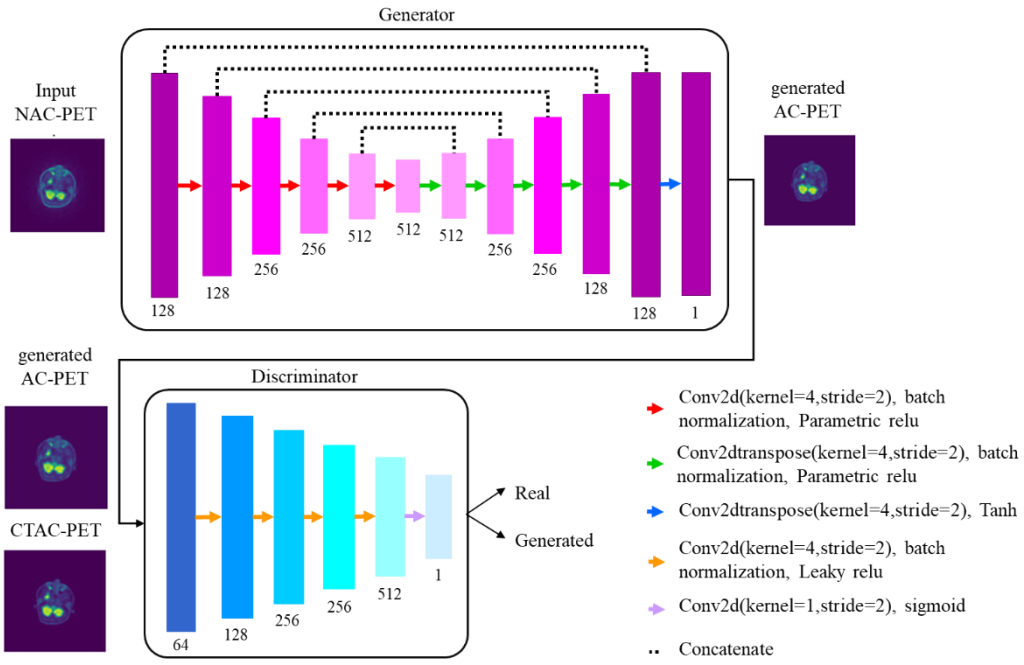

Fig. 7. Architecture of Pix2Pix network: First, the generator creates simulated AC images from NAC images. The discriminator's task is to differentiate CTAC images from generated images.

The performance of the Pix2Pix model was evaluated using 290 images from the test dataset and various image quality metrics. These metrics included root mean square error (RMSE), mean absolute error (MAE), peak signal-to-noise ratio (PSNR), and multi-scale structural similarity index (MS-SSIM).

$$RMSE = \sqrt{\frac{1}{N}\sum_{i=1}^{N}(ds(i))^2} \quad (1)$$

$$MAE = \frac{1}{N}\sum_{i=1}^{N}|ds(i)| \quad (2)$$

$$PSNR = 10\log\left(\frac{max^2}{MSE}\right) \quad (3)$$

$$MS-SSIM = [L_m(x,y)]^{\propto_M} \cdot \prod_{j=1}^{M}[C_j(x,y)]^{\beta_j} \cdot [S_j(x,y)]^{\gamma_j} \quad (4)$$

The absolute error dS(i) measures how much the pixel values of the generated AC-PET images differ from the pixel values of the CTAC images, which are the ground truth. The reference value SR(i) is the pixel value of the CTAC image at the i-th pixel. The MS-SSIM index consists of three components: L_m (x,y) for luminance, C_j (x,y) for contrast, and S_j (x,y) for structure. These components are weighted by α, β and γ, respectively. A joint histogram was used in statistical analysis to show pixel-level correlation distribution between CTAC-PET and AC-PET images. Paired-sample t-tests were conducted for statistical comparisons between the two types of images with a significance threshold of $p < 0.05$.

Results

The study's results, as presented in Table 1, highlight the Pix2Pix method's precision in PET image attenuation correction, as reflected by a notably low MAE of 0.004. The method's robustness is further affirmed by metrics, including a PSNR of 37.113 and an MS-SSIM of 0.983. The minimum and maximum values for these metrics, determined using the Interquartile Range, demonstrate that 99% of the data falls within this range. This finding demonstrates the Pix2Pix method's robust performance across the test set.

Table 4. Statistical analysis of image quality metrics

	RMSE	MAE	PSNR	MS-SSIM
Mean±SD	0.015±0.007	0.004±0.002	37.113±3.898	0.983±0.042
Minimum	0.004	0.000	30.445	0.974
Maximum	0.032	0.009	44.762	0.999

The need for attenuation correction is highlighted by the significant noise evident in Figure 1a. The efficacy of the Pix2Pix approach is demonstrated in Figure 1c. Figure 1d illustrates the discrepancies between the predicted images generated by the Pix2Pix model and the CTAC ground truth. The primary objective of employing the Pix2Pix model is to minimize these discrepancies, thereby aligning the predicted outputs closely with the CTAC.

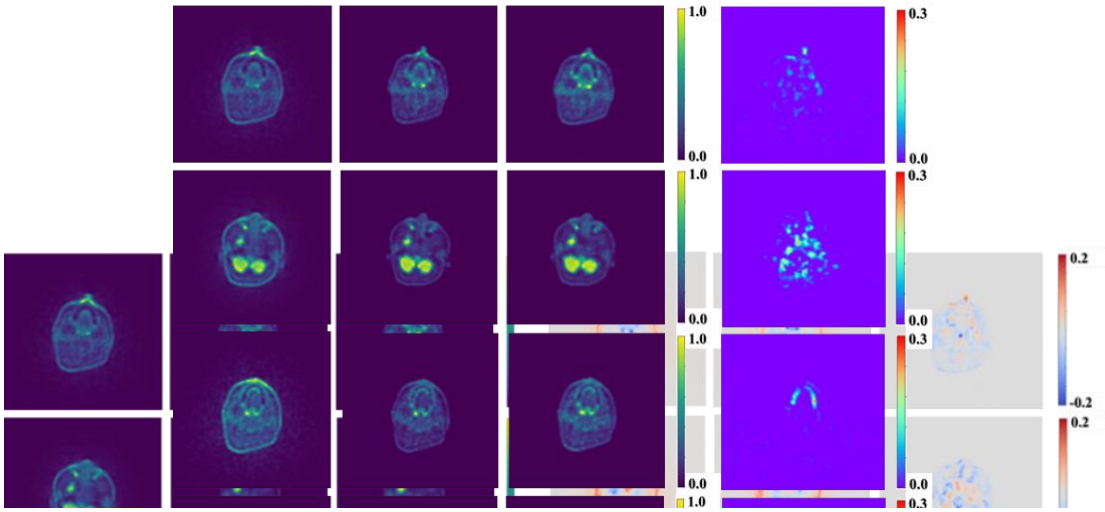

Fig. 2. a) NAC-PET images: Exhibiting high noise levels. b) CTAC images: PET attenuation correction by CT, serving as the reference for comparison. c) Pix2Pix images. d) Absolute pixel differences between the CTAC and Pix2Pix images.

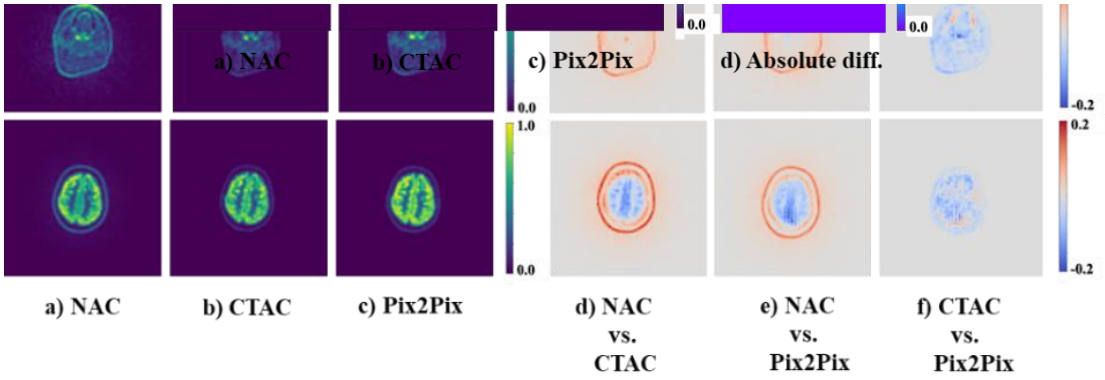

Fig. 3. a) NAC-PET, b) CTAC, c) Pix2Pix. A comparison of the paired t-test results assessing the differences between: (d) NAC-PET vs. CTAC-PET, (e) NAC-PET vs. Pix2Pix AC-PET, (f) CTAC-PET vs. Pix2Pix AC-PET.

The comparative analysis of Pix2Pix and CTAC images was conducted through a paired t-test. The resulting p-value of 0.23 indicates that there is no statistically significant difference in the performance of the two methods. This finding supports the Pix2Pix technique as a feasible

substitute for the conventional CTAC method in the attenuation correction of PET images. The outcomes of the t-test are depicted in Figure 3.

Joint histograms in Figure 3a illustrate a pronounced correlation between Pix2Pix and CTAC images, as evidenced by an R^2 score of 0.99. This signifies a high degree of similarity in pixel values and their distribution. A slope value of 0.87 suggests that Pix2Pix images have slightly lower pixel values than CTAC images. In Figure 3b, the Pearson correlation coefficient, with a value of 0.99, reflects a near-perfect correlation between the two modalities. This high degree of correlation suggests that the Pix2Pix AC method can reliably replicate the attenuation correction traditionally achieved through CTAC, thereby substantially reducing the reliance on CT imaging.

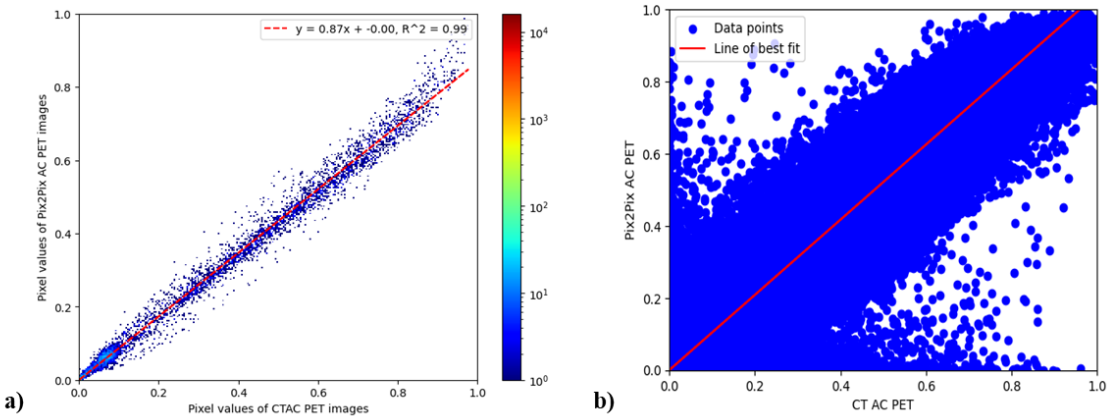

Fig. 4. a) Joint histograms displaying the comparison between Pix2Pix AC PET and CTAC PET techniques. b) A depiction of the Pearson correlation analysis for attenuation correction methods. The linear regression is denoted by the red line.

Conclusions

In cocclution the objective of this study was to evaluate the Pix2Pix model's capacity for direct correction in PET imaging, bypassing the need for attenuation map. By training with CTAC-PET images and subsequently using only NAC-PET inputs, the model generates AC-PET, demonstrating a self-sufficient correction method. The Pix2Pix model's fidelity in PET image correction is confirmed by low RMSE and MAE, and high PSNR and MS-SSIM, indicating precise image reconstruction. A Pearson correlation coefficient near unity and a non-significant p-value reveal no notable difference from the CTAC method. The Pix2Pix model emerges as an efficient CTAC alternative, simplifying the attenuation correction process by foregoing CT images and energy scaling.

This study demonstrated certain limitations that require attention. The Pix2Pix method should be tested on larger datasets to be applicable to a diverse patient population. The training set included only 27 PET brain images, which may not capture all patient variations. Deep learning methods typically require larger datasets to encompass patient diversity. The network performed well on a test set, but its performance on a real clinical dataset remains unknown. Additionally, the Pix2Pix models were trained solely on 18F-FDG PET images, meaning they are only applicable to brain images using the same radiotracer. For other PET applications with different radiotracers, the network would need to be retrained on a new dataset of PET images with those specific radiotracers. Furthermore, the networks focus on 2D attenuation correction and do not utilize 3D image information in the trans-axial (z-axis) direction.

References

[1] Al-Sharify, Z. T., Al-Sharify, T. A., & Al-Sharify, N. T. (2020). A critical review on medical imaging techniques (CT and PET scans) in the medical field. In IOP Conference Series: Materials Science and Engineering (Vol. 870, No. 1, p. 012043). IOP Publishing

[2] Piwowarska-Bilska, H., Aleksandra Supińska, Iwanowski, J., Tyczyńska, A., & Birkenfeld, B. (2019). PET – advanced nuclear imaging technology for medicine. Pomeranian Journal of Life Sciences, 65(3), 45–53

[3] Parghane, R. V., & Basu, S. (2018). PET/Computed Tomography and PET/MR Imaging. PET Clinics, 13(4), 459–476

[4] Sikandar Shaikh. (2021). Pet-Ct In Infection And Inflammation. Springer Verlag, Singapor.

[5] Cal-Gonzalez, J., Rausch, I., Shiyam Sundar, L. K., Lassen, M. L., Muzik, O., Moser, E., Papp, L., & Beyer, T. (2018). Hybrid Imaging: Instrumentation and Data Processing. Frontiers in Physics, 6.

[6] Zaidi, H., & Hasegawa, B. H. (2003). Determination of the attenuation map in emission tomography. PubMed, 44(2), 291–315

[7] Beyer, T., Kinahan, P. E., Townsend, D. W., & Sashin, D. (1994, October). The use of X-ray CT for attenuation correction of PET data. In Proceedings of 1994 IEEE Nuclear Science Symposium-NSS'94 (Vol. 4, pp. 1573-1577)

[8] Abella, M., Alessio, A. M., Mankoff, D. A., MacDonald, L. R., Vaquero, J. J., Desco, M., & Kinahan, P. E. (2012). Accuracy of CT-based attenuation correction in PET/CT bone imaging. Physics in Medicine and Biology, 57(9), 2477–2490

[9] Zaidi, H., Montandon, M.-L., & Alavi, A. (2007). Advances in Attenuation Correction Techniques in PET. PET Clinics, 2(2), 191–217

[10] Kinahan, P. E., Hasegawa, B. H., & Beyer, T. (2003). X-ray-based attenuation correction for positron emission tomography/computed tomography scanners. Seminars in Nuclear Medicine, 33(3), 166–179

[11] Beyer, T., Antoch, G., Müller, S., Egelhof, T., Freudenberg, L. S., Debatin, J., & Bockisch, A. (2004). Acquisition protocol considerations for combined PET/CT imaging. Journal of Nuclear Medicine, 45(1 suppl), 25S-35S.

[12] Alzubaidi, L., Zhang, J., Humaidi, A. J., Al-Dujaili, A., Duan, Y., Al-Shamma, O., Santamaría, J., Fadhel, M. A., Al-Amidie, M., & Farhan, L. (2021). Review of deep learning: concepts, CNN architectures, challenges, applications, future directions. Journal of Big Data, 8(1)

[13] Suganyadevi, S., Seethalakshmi, V., & Balasamy, K. (2021). A review on deep learning in medical image analysis. International Journal of Multimedia Information Retrieval, 11(1), 19–38

[14] Arabi, H., AkhavanAllaf, A., Sanaat, A., Shiri, I., & Zaidi, H. (2021). The promise of artificial intelligence and deep learning in PET and SPECT imaging. Physica Medica, 83, 122–137

[15] Chen, X., & Liu, C. (2022). Deep-learning-based methods of attenuation correction for SPECT and PET. Journal of Nuclear Cardiology

[16] Wang, T., Lei, Y., Fu, Y., Curran, W. J., Liu, T., Nye, J. A., & Yang, X. (2020). Machine learning in quantitative PET: A review of attenuation correction and low-count image reconstruction methods. 76, 294–306

[17] Lee, J. S. (2021). A Review of Deep-Learning-Based Approaches for Attenuation Correction in Positron Emission Tomography. IEEE Transactions on Radiation and Plasma Medical Sciences, 5(2), 160–184

[18] Dong X, Lei Y, Wang T, Higgins K, Liu T, Curran WJ, Mao H, Nye JA, Yang X. (2020) Deep learning-based attenuation correction in the absence of structural

information for whole-body positron emission tomography imaging. Physics in Medicine & Biology. 65(5):055011.

[19] Shiri, I., Ghafarian, P., Geramifar, P., Leung, K. H.-Y., Ghelichoghli, M., Oveisi, M., Rahmim, A., & Ay, M. R. (2019). Direct attenuation correction of brain PET images using only emission data via a deep convolutional encoder-decoder (Deep-DAC). European Radiology, 29(12), 6867–6879

[20] Inès Mérida, Jung, J., Sandrine Bouvard, Didier Le Bars, Lancelot, S., F. Lavenne, Bouillot, C., Jérôme Redouté, Hammers, A., & Costes, N. (2020). CERMEP-IDB-MRXFDG: A database of 37 normal adult human brain [18F]FDG PET, T1 and FLAIR MRI, and CT images available for research. Europe PMC (PubMed Central)

ICNST 2024
International Conference on Nuclear Science and Technology
6- 8 MAY 2024 | Isfahan, Iran

A review article related to the dose received by the fetus during radiotherapy (Paper ID : 1173)

M. Asadi[1, 3*], A. Mosayebi[2]

[1]*Department of Energy Engineering, Sharif University of Technology, Tehran, IRAN*

[2]*Radiation Processing and Dosimetry Research Group, Radiation Application Research Institute, Nuclear Science and Technology Research Institute, Tehran, IRAN*

[3]*Nuclear Science and Technology Research Institute, Tehran, IRAN*

Abstract

This systematic review focuses on specific uncertainties regarding the management of pregnant trauma patients. First, the prognostic value of certain laboratory studies in the pregnant trauma patient remains unclear. The purpose of presenting this article is to examine fetal dose in radiotherapy and expand and update previous research that includes proton therapy. Regardless of the treatment methods used during radiation therapy, out-of-field doses, which are doses received by areas outside the treatment area, are unavoidable. For pregnant patients, fetal dose is a major concern. Despite the low incidence of cancer during pregnancy, the radiotherapy team must be knowledgeable to deal with fetal dose. This is very important because it must be ensured that the fetus is adequately protected while the patient's treatment is effective. In this research, various models of fetal dose will be discussed from different aspects. Also, apart from the fetal dose from conventional photon therapy, it extends the discussion to modern treatment methods and techniques, namely proton therapy and image-guided radiotherapy, all of which have seen a significant increase in use in current radiotherapy. It is expected that this review will provide the readers with a comprehensive understanding of the fetal dose in radiotherapy and full knowledge of the measures that should be taken in providing radiotherapy to pregnant patients.

Keywords: Fetal dose - Proton therapy - Radiotherapy - Dosimetry

INTRODUCTION

The effects of ionizing radiation exposure in offspring and next generations may arise great interest not only among radiation researchers and professionals, but also among the general population[1].

This systematic review focuses on specific uncertainties regarding the management of pregnant trauma patients. First, the prognostic value of certain laboratory studies in the pregnant trauma patient remains unclear [2, 3].

The incidence of cancer during pregnancy is relatively low and its probability is about 0.1% [1-٤]. Some of the most common types of cancer among pregnant women include lymphoma, melanoma, leukemia, breast, cervical, and thyroid cancers, most of which require radiotherapy as part of treatment [٥, 6]. During target irradiation, the dose is inevitably received by the off-target region and the edge of the primary field, resulting in out-of-field (OOF) dose [7]. The three main sources of OOF dose from photon beams are treatment head leakage, scattered radiation from collimators or beam modifiers, such as wedges and blocks, and scattered radiation from patients. For higher-energy beams with energy >10 MV, photoneutron interactions create an additional OOF dose component through neutron production [8-10].

Despite being low, OOF dose to the fetus, it can have severe effects such as lethality, anatomical abnormalities, mental retardation and growth retardation [8]. Therefore, careful planning and discussion should take place before radiotherapy, which is often a multidisciplinary effort involving obstetricians and gynecologists, radiation oncologists, medical oncologists, medical physicists, and other related specialists [8]. The final goal is to achieve a balance between risk and benefit, and the patient needs to be fully informed of the risk if they choose to continue with the gestation.

In order to manage the patient, it is recommended to estimate the fetal dose by calculating or performing measurements in a phantom [8-11]. Special shielding must be designed and constructed to ensure that the fetal dose falls within the acceptable threshold limit. During the course of radiotherapy and with the expected growth of the fetus, *in vivo* measurements should also be done carefully to control the actual dose of the fetus.

There are a several articles or comprehensive reports that address various aspects of fetal dose concerns. Some examples include ICRP Publication 84 [12], the American Association of Physicists in Medicine (AAPM) Task Group 36 report, and the French guidelines by Michelet *et al*. [13], all of which consider the biological effects of fetal dose based on absorbed dose level and gestational age and recommendations on treatment pregnant patients describe. While

the AAPM TG36 report focused mainly on photon radiotherapy, ICRP Publication 84 addressed broader topics that included diagnostic imaging and nuclear medicine in addition to radiotherapy.

Current published reviews [5, 7, 10, 11, 13] are either less physics-oriented or do not include proton therapy and image-guided radiotherapy (IGRT), both of which are increasingly used in modern radiotherapy. Particle therapy, especially proton therapy, is in clinical use due to its conformal dose contribution without exit dose. Image-guided radiotherapy appears to be essential in treatment with a highly conformal dose distribution and hypofractionation regimen. The imaging dose from image-guided radiotherapy, which can lead to fetal dose, has rarely been examined in the current literature. Therefore, the aim of this review is to harmonize and expand our knowledge about fetal dose with the most modern and common radiotherapy method in terms of technology to date.

In this review article, fetal dose will first be discussed from the biological and clinical aspects. The main focus of the article will be on the fetal dose received by photon therapy, proton therapy or in general other types of particle therapy and imaging for the purpose of IGRT. In particular, factors affecting fetal dose levels, dose estimation methods, and dose reduction techniques including shielding will be covered.

1- Investigating the effect of radiation on the fetus based on epidemiological evidence

The main effects of ionizing radiation on mammalian embryos include fetal death, malformations, developmental disorders, mental retardation, induction of malignancies, and hereditary defects. The absorbed dose, the type of radiation and the stage of pregnancy in which radiation exposure occurs are some of the factors affecting the severity of these effects. Here, the effects of radiation at various stages after human conception are generally discussed. The effects of radiation can be classified into two categories: deterministic or random. A deterministic effect has a cause-and-effect relationship where the effect will not occur until a certain threshold is crossed. After crossing the threshold, the significance of the effect increases linearly with the dose. The random effect occurs randomly and no threshold dose is observed. In this section, the definitive and accidental effects of ionizing radiation on the embryo and

fetus are summarized [8, 12, 14]. Table 1 provides an overview of the risk of effects according to postconception (PC) stage as well as dose levels.

2- Fetal dose in clinical cases of radiation therapy during pregnancy

Cancer during pregnancy generally has a rare incidence of about 0.1% [6]. The most common cancers during pregnancy are breast cancer, cervical cancer, Hodgkin's lymphoma, leukemia and melanoma [6]. Radiotherapy plays an essential role in the management of the first three cancers. The effect of radiotherapy on the fetus depends on the dose prescribed at the treatment site, the treatment method, the distance to the fetus and the age of the fetus. Childhood developmental risks as a function of fetal age are described in the previous section, while the remaining three factors are closely related to cancer types. In general, from the point of view of fetal doses, types of cancer can be divided into supra-diaphragmatic or sub-diaphragmatic.

3- Factors affecting fetal dose in radiotherapy

3.1. Megavoltage X-rays

OOF doses can result from photon leakage through the device's treatment head, scattered radiation from collimators and beam modifiers, and intra-patient scattered radiation from treatment beams, as shown in Fig. 1 [8]. In areas close to the treatment area, the dominant source of OOF scattering originates from patient scattering. For distances greater than 20 cm, treatment head leakage becomes the main source of OOF dose [9].

3.2. Proton therapy

The use of proton therapy for treatment can potentially achieve better results than conventional therapy due to the presence of the Bragg peak, which allows the preservation of vital organs and tissues [14]. However, the use of proton therapy produces neutrons, secondary protons, light charged ions, recoiled heavy ions, and photons during treatment, resulting in a secondary equivalent dose [9]. According to AAPM TG-158 [9], the main contribution to the total OOF dose in proton therapy is neutrons, which

Fig. 1. Out-of-field dose sources during photon therapy.

originate from nuclear interactions in components along the beam line and within the patients

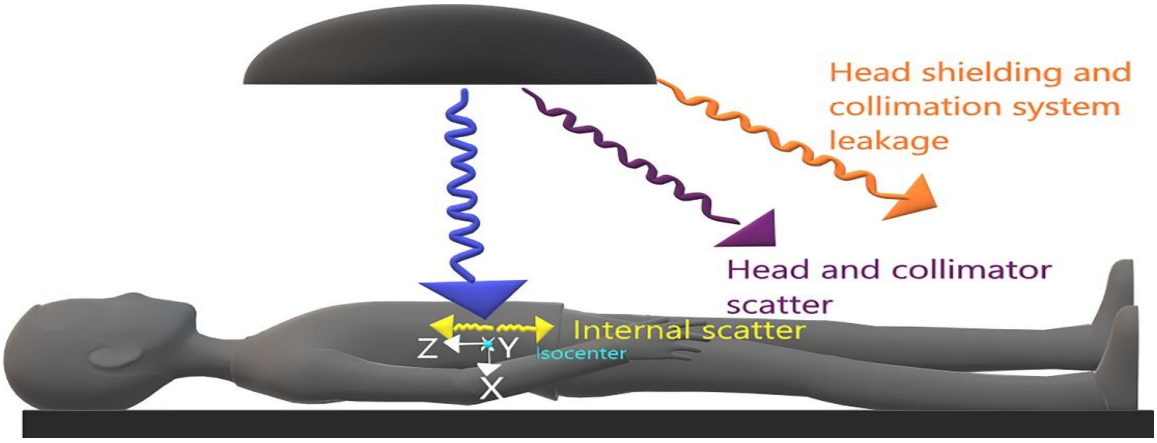

themselves. The contribution of secondary photons is limited to 10% of the contribution associated with neutrons. Two common methods of proton beam delivery are passive scattering and spot scanning. Passive scattering techniques use scatterers, beam planar devices, collimators/apertures, and compensators at the beam delivery nozzle to obtain a homogeneous and flat dose at the target. On the other hand, the spot scanning technique uses a pencil-like beam to scan across the target volume with magnetic dipoles, without the need for other beam components in the beam delivery nozzle [15-18]. As a result, the spot scan method is expected to produce a lower amount of neutrons in patients.

3.3. Imaging dose of image-guided radiotherapy

The use of IGRT in modern radiotherapy has become almost essential due to the increasing use of highly coherent treatment techniques (such as volumetric arc therapy or VMAT) because it provides the ability to precisely deliver dose to the target to improve local control and allow dose reduction to healthy tissues [19]. Using kilovoltage cone beam computed tomography (CBCT) systems on Linac, daily image recording can be done for better patient alignment. However, the imaging dose of CBCT cannot be ignored, as Perks *et al*. [20] showed that intra-regional doses can range from 1.5cGy to 0.3cGy, while Ding *et al.* [21], have reported a tissue dose of up to 8cGy in a pelvic scan. Peripheral dose of IGRT also by Perks *et al.* [20] was measured, where thermoluminescence dosimeters (TLDs) were placed at different distances along the superior-posterior axis on the surface and central plane inside the phantom. The dose of 0.5cGy and 0.2cGy was obtained for a distance of 7 cm and 12 cm from the edge of the

imaging field, respectively. In addition, Kahn *et al.* [22] found that daily CBCT can deliver a significant amount of dose to vital organs. For example, an abdominal scan can result in receiving an additional dose (1.4Gy to 2.2Gy) in the 35 segments of the small intestine and the rectum. The same study also claimed that, based on their findings, the use of low-dose mode for CBCT (where the effective dose of low-dose CBCT is approximately one-fifth of CBCT doses in standard mode) is beneficial for the patient.

Therefore, it is important to weigh the pros and cons of using IGRT in pregnant patients. CBCT may be considered when the edge of the imaging field is at a distance from the fetus. For treatments that require CBCT around the fetus, low-dose CBCT should be recommended despite the reduced image quality.

4- Fetus dose estimation

Fetal dose estimation plays a very important role in radiotherapy planning for pregnant patients. This is because the occurrence and severity of adverse effects on the fetus strongly depend on the dose received by the fetus. If the dose to the fetus exceeds the 0.1Gy threshold, countermeasures such as shielding and modification of treatment techniques should be performed. In this section, different methods of dose estimation will be covered, according to time development.

4.1. X-ray and proton therapy

Measurement by using physical phantom

Anthropomorphic phantoms have been widely used for fetal dose estimation along with TLDs or ionizing chambers for decades. For example, the Rando phantom (Alderson Research Laboratories, Stanford, CA) was used to estimate fetal dose during breast cancer [23], brain cancer radiotherapy [24], and even helical tomotherapy [25]. As described by Mazzonakis *et al.* [24], the phantom consists of numbered slices, each 2.5 cm thick. Different slices were replaced with Lucite slices to simulate the position of the fetus at different gestational ages. To measure the dose absorbed by different parts of the fetus, TLDs are inserted into pre-made holes at different depths of the cut, corresponding to different desired points. The types of TLDs used are lithium fluoride (LiF) and calcium fluoride (CaF2) TLDs. For measurements with ionizing chambers, the slices can be replaced with PMMA sheets [23] or plastic water

blocks [25] to accommodate large-volume ionizing chambers. Recently, optically stimulated luminescence detectors (OSLDs) were also used to measure the fetal dose resulting from an innovative technique called virtual tangential field arc therapy (ViTAT) [26]. Film dosimetry with human phantoms was also used to assess fetal dose due to therapeutic exposures [27].

4.2. Calculations

Computing pantom

Since measurements using physical phantoms can be cumbersome and provide less flexibility in terms of optimizing irradiation conditions and various patient characteristics [28], computational phantoms came into play. Human computational phantoms are models that mathematically represent body organs or tissues or the whole body [29], they can be divided into three categories: 1) stylized 2) voxelized 3) representation border (BREP) [30].

4.3. Algorithms

The commercial treatment planning system (TPS) is the most common dose calculation platform in clinical use today. However, the vendor recognizes and acknowledges that TPS is only accurate in the field of treatment itself and is limited in accurately calculating OOF doses [7, 9, 13, 16]. In a study by Ogertisi *et al.* [31], two different algorithms (Anisotropic Analysis Algorithm and Acuros XB Algorithm) of Eclipse version 13.0.33 were investigated, TPS algorithms failed to accurately calculate OOF doses for a region farther than 13 cm from the edges of the field of refraction. As a result, the fetal dose was given as 0mGy, while the phantom measurement estimated a mean dose of 84.8mGy. This finding calls into question the utility of TPS for fetal dose estimation.

5- The method of protecting the dose received by the fetus and reducing the dose

In radiation therapy for pregnant patients, it is impossible to remove all the radiation that enters the fetus. Therefore, there is a need to understand all sources of secondary radiation that lead to the dose received by the fetus to provide adequate protection to the fetus. The main sources of OOF dose include photon leakage through the Linac gantry head, external radiation scattering from collimators, beam modifiers, and internal radiation scattering in the patient body. Therefore, careful planning during radiation therapy for pregnant patients using

appropriate techniques or other dose reduction techniques (*e.g.* IMRT and VMAT) is necessary.

Table 1. The risk of side effects at different stages after pregnancy and dose levels below or above the 0.1Gy threshold [1].

Postconception (PC) days	weeks	Dose (Gy)	Lethality	Malformation	Mental retardation	Growth retardation	Malignant disease
0 to 8 days PC (Preimplantation stage)	١	< 0/1	NCRPR-174: No increased risk of pregnancy loss at any stage of gestation	-	-	-	ICRP-84: 99.1 % probability that child will develop cancer
		> 0/1	TG-36: Based on animal studies, 1 % - 2 % chance of early death after doses on the order of 0.1 Gy corresponding to a median lethal dose of about 1 Gy	-	-	-	-
8 to 56 days PC (Organogenesis stage)	2 to 8	< 0/1	-	ICRP-84: 97 % probability that child have no malformation	-	-	-
		> 0/1	TG-36: Little risk of damage	NCRPR-174: At all stages of organogenesis the risk of radiation-induced anatomical malformations with a dose of < 0.5 Gy is very low	-	TG-36: High risk of damage	TG-36: Low risk of damage
56 to 105 days PC (Early fetal)	9 to 15	< 0/1	-	ICRP-84: 97 % probability that child have no malformation	-	-	-
		> 0/1	-	-	-	TG-36: Significant risk of damage	TG-36: Low risk of damage
		1	-	-	NCRPR-174: 40 % of fetuses were mentally retarded	-	-
105 to 175 days PC (Mid fetal)	16 to 25	> 0/1	-	-	-	TG-36: Low risk of damage	TG-36: Low risk of damage
		1	-	-	NCRPR-174: 15 % of fetuses were mentally retarded	-	-
> 175 days PC (Late fetal)	٢٥ <	> 0/1	-	-	-	TG-36: Low risk of damage	TG-36: Low risk of damage

Conclusions

Fetal dose management is an effort that requires extensive knowledge of the biological effects of radiation on the fetus, shielding design, measurement and physical arrangement, which must be designed and implemented separately for each clinical case. Meanwhile, the fetus will continue to grow during the radiotherapy treatment and continuous monitoring is important. This review article addresses this issue from different perspectives to provide a comprehensive understanding of the issues and possible solutions that may be helpful when deciding whether to treat or administer radiotherapy to pregnant patients. The continuous progress of radiation therapy will definitely require periodic review of our current knowledge and approaches. However, if radiotherapy is diagnosed for pregnant patients and is unavoidable, our top priority

remains the same "Maximizing treatment for pregnant patients and providing the best fetal protection solutions".

References

[1] Degenhardt, Ä. Dumit, S. and Giussani, A. (2024). Effects of ionising radiation exposure in offspring and next generations: dosimetric aspects and uncertainties. International Journal of Radiation Biology, 1-7.

[2] Liggett, M. R. Amro, A. Son, M. and Schwulst, S. (2023). Management of the pregnant trauma patient: a systematic literature review. Journal of surgical research, 285, 187-196.

[3] Burton, C. S. Frey, K. Fahey, F. Kaminski, M. S. Brown, R. K. Pohlen, J. M. and Shulkin, B. L. (2023). Fetal dose from PET and CT in pregnant patients. Journal of Nuclear Medicine, 64(2), 312-319.

[4] Wong. Y, Wei. K, Lew. S, Chua. C, Nei. W, Tan. H, Lee. J, Mazonakis. M and Damilakis. J. (2023). A review on fetal dose in Radiotherapy: A historical to contemporary perspective. Physica Medica.

[5] Mazonakis M, Damilakis J. (2017). Estimation and reduction of the radiation dose to the fetus from external-beam radiotherapy. Phys Med, 43:148–52.

[6] Pavlidis NA. (2002). Coexistence of pregnancy and malignancy. Oncologist, 7(6):573. https://doi.org/10.1634/theoncologist.7-6-573.

[7] Applegate KE, Findlay Ú, Fraser L, Kinsella Y, Ainsbury L, Bouffler S. (2021). Radiation exposures in pregnancy, health effects and risks to the embryo/ foetus—information to inform the medical management of the pregnant patient. J Radiol Prot, 41(4):S522–39.

[8] Stovall M, Blackwell CR, Cundiff J, Novack DH, Palta JR, Wagner LK, *et al.* (1995). Fetal dose from radiotherapy with photon beams: report of AAPM Radiation Therapy Committee Task Group No. 36. Med Phys, 22(1):63–82.

[9] Kry SF, Bednarz B, Howell RM, Dauer L, Followill D, Klein E, *et al.* (2017). AAPM TG 158: measurement and calculation of doses outside the treated volume from external-beam radiation therapy. Med Phys, 44:e391–429.

[10] Mayr NA, Wen B-C and Saw CB. (1998). RADIATION THERAPY DURING PREGNANCY. Obstet Gynecol Clin N Am, 25(2):301–21.

[11] Martin DD. (2011). Review of radiation therapy in the pregnant cancer patient. Clin Obstet Gynecol, 54:591–601.

[12] Pregnancy and Medical Radiation. (2000). ICRP Publication 84. Annals of the ICRP 30, 1–43.

[13] Michalet M, Dejean C, Schick U, Durdux C, Fourquet A, Kirova Y. (2022). Radiotherapy and pregnancy. Cancer/Radiotherapie, 26(1-2):417–23.

[14] National Council on Radiation Protection and Measurements & National Council on Radiation Protection and Measurements. (2013). Scientific Committee 4-4 on the Risks of Ionizing Radiation to the Developing Embryo, F. Preconception and prenatal radiation exposure: health effects and protective guidance.

[15] Bou´e J, Bou´e A, Lazar P. (1976) RETROSPECTIVE AND PROSPECTIVE EPIDEMIOLOGICAL STUDIES OF 1500 KARYOTYPED SPONTANEOUS HUMAN ABORTIONS. Obstet Gynecol Surv, 31(8):617–9.

[16] Wallch E, Simpson JL. (1980). Genes, chromosomes, and reproductive failure. Fertil Steril, 33(2):107–16.

[17] Brent RL. (1955). the effect of x-irradiation on rat embryos at the twelfth day of gestation. University of Rochester.

[18] Konermann G. (1987). Postimplantation Defects in Development following Ionizing Irradiation. In 91–167. doi:10.1016/B978-0-12-035413-9.50007-8.

[19] Perks JR, Lehmann J, Chen AM, Yang CC, Stern RL, Purdy JA. (2008). Comparison of peripheral dose from image-guided radiation therapy (IGRT) using kV cone beam CT to intensity-modulated radiation therapy (IMRT). Radiother Oncol, 89 (3):304–10.

[20] Ding GX, Duggan DM, Coffey CW. (2008). Accurate patient dosimetry of kilovoltage cone beam CT in radiation therapy. Med Phys, 35(3):1135–44.

[21] Kan MWK, Leung LHT, Wong W, Lam N. (2008). Radiation dose from cone beam computed tomography for image-guided radiation therapy. Int J Radiat Oncol Biol Phys, 70(1):272–9.

[22] Peet SC, Kairn T, Lancaster CM, Trapp JV, Sylvander SR, Crowe SB. (2021). Measuring fetal dose from tomotherapy treatments. Med Dosim, 46(4):342–6.

[23] Fenig E, Mishaeli M, Kalish Y, Lishner M. (2001). Pregnancy and radiation. Cancer Treat Rev, 27(1):1–7. https://doi.org/10.1053/ctrv.2000.0193.

[24] Podgorsak MB, Meiler RJ, Kowal H, Kishel SP, Orner JB. (1999). Technical management of a pregnant patient undergoing radiation therapy to the head and neck. Med Dosim, 24(2):121–8.

[25] Dusi F, Guida F, Garcia ENV, Rossato MA, Germani A, Sapignoli S, *et al.* (2022). Fetal dose estimation for Virtual Tangential-fields Arc Therapy whole breast irradiation by optically stimulated luminescence dosimeters. Physica Medica: Eur J Med Phys, 101:44–9

[26] Bradley B, Fleck A, Osei EK. (2006). Normalized data for the estimation of fetal radiation dose from radiotherapy of the breast. BJR, 79(946):818–27.

[27] Stovall M, Weathers R, Kasper C, Smith SA, Travis L, Ron E, *et al.* (2006). Dose reconstruction for therapeutic and diagnostic radiation exposures: use in epidemiological studies. Radiat Res, 166(1):141–57.

[28] Stratakis J, Papadakis A. (2019). Radiation Dose Management of Pregnant Patients, Pregnant Staff and Pediatric Patients. (IOP).

[29] Xu XG. (2014). an exponential growth of computational phantom research in radiation protection, imaging, and radiotherapy: a review of the fifty-year history. Phys Med Biol, 59(18):R233–302.

[30] Zaidi H, Tsui BMW. (2009). Review of computational anthropomorphic anatomical and physiological models. Proc IEEE, 97(12):1938–53.

[31] Sharma SC, Williamson JF, Khan FM, Lee CKK. (1981). Measurement and calculation of ovary and fetus dose in extended field radiotherapy for 10 MV X rays. Int J Radiat Oncol Biol Phys, 7(6):843–6.

ICNST 2024
International Conference on Nuclear Science and Technology
6- 8 MAY 2024 | Isfahan, Iran

Investigation of the tissue equivalence of Fricke gels used for radiotion dosimetry (Paper ID : 1189)

Edalatkhah E. *, Nasiri F.

Radiation Applications Research School, Nuclear Science and Technology Research Institute, Tehran, Iran

Abstract

Gel dosimeters have been utilized for gamma radiation dosimetry. Fricke gel dosimeters rely on the oxidation of ferrous ions induced by radiation. Radiological properties of the gel dosimeters are often compared against each other as well as against water or tissue. In this work, tissue and water equivalency of Fricke gels with various compositions were analyzed by considering parameters including mass attenuation coefficients, density and effective atomic numbers. Mass attenuation coefficients for photons of the Fricke gels were obtained with win XCOM program, as well as of soft tissue and water. Stopping power for electrons in the gels, water and tissue was also calculated using ESTAR program. Density and effective atomic number of the gels have been compared. The gel equivalence was confirmed by the nearly similarity between the mass attenuation coefficients and the mass stopping powers for the gels and each of the materials. The ratios are almost equal to 1. As a result, the gel can be used as a dosimeter in clinical applications for accurate dose assessments.

Keywords: Equivalent materials, Mass attenuation coefficients, Stopping power for electrons, Fricke gel dosimeters.

Introduction

Development of tissue equivalent dosimeters with three-dimensional dose mapping capabilities would be helpful for radiation dosimetry applications [1]. Addressing this scope, Fricke gel dosimeters are suitable choices. Fricke gel dosimeter formulations based on a variety of gelling agents have been introduced, ranging from the most recent, polyvinyl alcohol, to the conventional ones such as gelatin and agarose [2]. The disadvantage with gelatin formulations is the gradual degradation [3]. Although agarose requires to be heated to high temperatures to dissolve effectively, it is more radiation sensitive than gelatin [4]. Gel formulations based on polyvinyl alcohol have great sensitivity, stability and ease of manufacture [5]. One of the

numerous factors to be taken into account when choosing a gel formulation is how closely the radiological parameters of the gel match those of tissue. Comparing variables like density, mass attenuation, stopping power and effective atomic number is typical in this context [6]. In 1993, electron densities and effective atomic numbers were calculated for agarose gel used for NMR dosimetry [7]. The radiological equivalence of three gels was studied by investigating photon and electron cross section parameters in 1999 [8]. A soft tissue substitute was synthesized for neutron dosimetry in 2003 [9]. Computer programs, MUA_T and MUEN_T, were developed for the computation of mass attenuation coefficient for body tissues and substitutes of arbitrary percentage by weight elemental composition and photon energy ranging between 1 keV and 400 keV in 2007 [10]. A comprehensive set of formulas were proposed for calculating the effective atomic number and electron density for all types of materials and for all photon energies greater than 1 keV in 2008 [11]. Also in this year, mass attenuation coefficient estimations of gelatin Fricke gel dosimeter have been performed by means of PENELOPE simulations [12]. Radiological parameters of polymer gel dosimeters have also been investigated in several researches [13-15]. In 2019, a user friendly online software has been developed for calculation of parameters relevant to photon shielding and dosimetry [16]. In 2022, the effective atomic number and electron density of Four Fricke gel dosimeters were calculated for energy range from 10 keV to 1000 MeV using Auto-Zeff, direct and power law methods. Mass attenuation coefficients for the Fricke gel dosimeters have also been calculated using Win XCOM program in this work [17]. Various photon attenuation software tools have been used by researchers to evaluate the radiological parameters of the elements/compounds/composites. Phy-X, FFAST, XCOM, and XMuDat can be referred as the widely used photon attenuation databases. A comparative study of these photon attenuation tools was carried out in 2023 [18].

The aim of the present study is to quantify parameters which determine tissue equivalence of the dosimetry gels. Three gel formulations based on gelatin, agarose and polyvinyl alcohol were considered in this work. The radiological properties for the gels such as mass attenuation for photons, stopping power for electrons, density and effective atomic number were surveyed.

Data is presented relative to tissue and water to allow direct comparison over a range of energies.

Experimental

A Fricke gel dosimeter is comprised ferrous ammonium sulphate, xylenol orange, sulphuric acid and a gelling agent. More details on the preparation and characterization of the dosimeters have been reported elsewhere [19].

Table 1. Elemental composition of the materials investigated in the study.

	Materials				
Elements	Soft tissue (ICRU 44)	Water	FG1	FG2	FG3
H	10..5	11.1	10.98	11.14	10.97
C	22.6	-	2.54	0.47	5.12
N	2.3	-	0.874	0.00	0.00
O	63.7	88.9	85.42	88.31	83.81

To investigate the tissue equivalence of Fricke gel dosimeters, mass attenuation for photons, stopping power for electrons, density and effective atomic number were analyzed. The three gels surveyed for the radiological properties are different formulations of Fricke gel, referred to as FGl (based on gelatin), FG2 (based on agarose) and FG3 (based on polyvinyl alcohol). Evaluation of the radiological parameters necessitates knowledge of the elemental composition of the materials. Table 1 indicates the compositional details of water, soft tissue and Fricke gel dosimeters investigated in this study. Furthermore, the chemical compositions of the Fricke gels are given in Table 2. FGl, FG2 and FG3 are commonly prepared based on 3 percentage by weight gelatin, 5 percentage by weight agarose and 10 percentage by weight polyvinyl alcohol

respectively. Hence, percentages by weight of the gelling agents were considered as 3, 5 and 10 for FGl, FG2 and FG3 respectively in this study.

Mass attenuation coefficient, μ/ρ, for a mixture is obtained using equation 1[20].

$$\frac{\mu}{\rho} = \sum w_i \left(\frac{\mu}{\rho}\right)_i \quad (1)$$

Where $(\mu/\rho)_i$ is the mass attenuation coefficient for the ith element in the material and w_i is the fraction by weight of the ith element. The values of mass attenuation coefficients for photons were assessed using win XCOM program. The values were actually calculated using the elemental composition of the materials, reported in Table 1, together with the National Institute of Standards and Technology (NIST) reference data [21].

Stopping ower for electrons of a mixture is calculated using equation 2 [20].

$$\frac{dE}{\rho dx} = \sum w_i \left(\frac{dE}{\rho dx}\right)_i \quad (2)$$

Where $(dE/\rho dx)_i$ is the stopping power for the ith element in the material and w_i is the fraction by weight of the ith element. The values of stopping power for electrons in different materials were extracted using ESTAR program. The values were obtained using data on table 1, the elemental composition of the materials together with the NIST reference data. At last, density and effective atomic number of the gels were analyzed.

Table 2. Chemical composition of the Fricke gels investigated in the study.

Material	Gelling agent	Ferrous ammonium sulphate (mM)	Xynelol Orange (mM)	Sulphuric acid (mM)
FG1	Gelatin	0.5	0.165	25
FG2	Agarose	0.5	0.165	25

FG3	Polyvinyl alcohol	0.5	0.165	25

Results and discussion

1. Mas attenuation coefficient

Mass attenuation coefficient of the materials, reported in table 1, were evaluated using equation 1 in the energy interval of 10 keV to 10 MeV. The ratio of the estimated mass attenuation coefficient of the gels to tissue is shown in Fig. 1. In addition, Fig. 2. demostrates this ratio for water. As it can be seen in the figures, the values of the mass attenuation coefficient of the gels are approximate to the mass attenuation coefficient of tissue and water. When the gels are compared with each other, the mass attenuation coefficient of FG3 is closer to that of water.

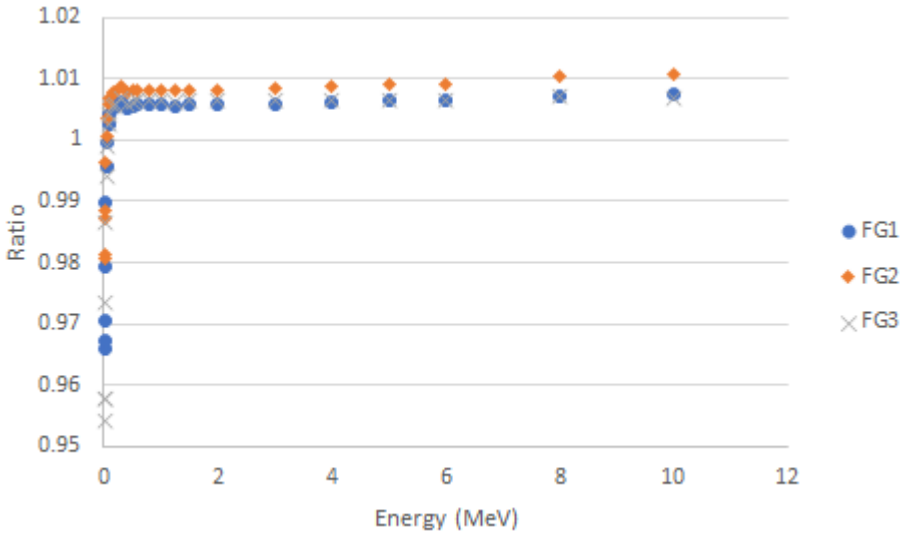

Fig. 1. Ratio of mass attenuation coefficient of different gels to soft tissue.

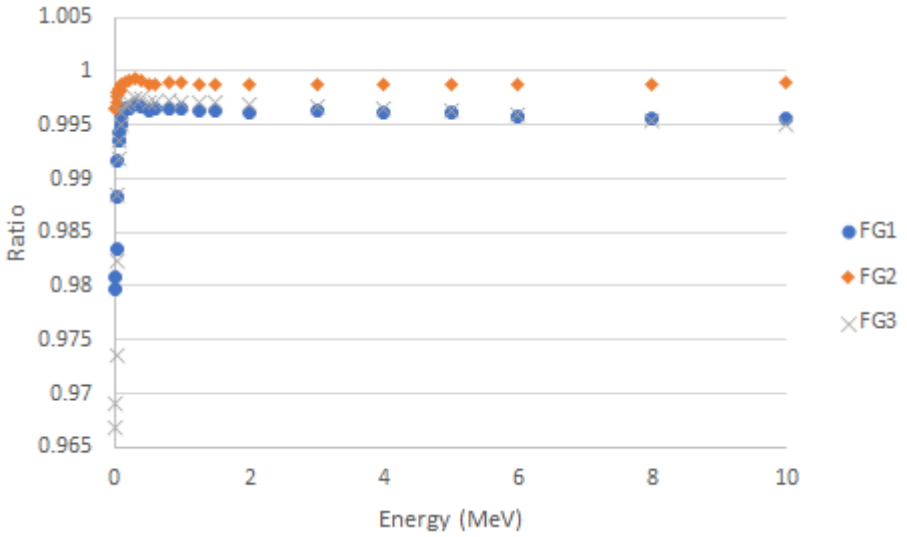

Fig. 2. Ratio of mass attenuation coefficient of different gels to water.

2.Stopping power for electrons

Using equation 2, the mass stopping power for electrons was estimated in the investigated materials in the energy interval of 10 keV to 10 MeV. The ratio of mass stopping power of the materials to tissue is illustrated in Fig. 3. This ratio for water is also depicted in Fig. 4.

In general, as shown in Figures 3 and 4, stopping power behavior for the studied gels are similar. Fig. 3 shows that the values of the stopping powers ratio are in the interval of 0.981 and 0.997.The relative difference between the mass stopping power of the gels is less than 1%.

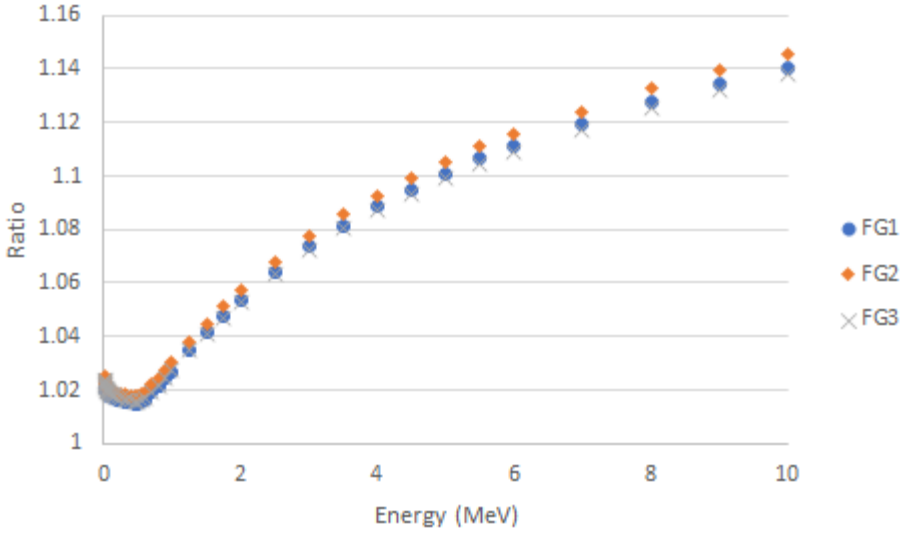

Fig. 3. Ratio of mass collision stopping power of different gels to soft tissue.

3. Density and effective atomic number

Physical density of Fricke gel dosimeters has been measured by the researchers. The reported values are given in Table 3 [17]. For comparison, the effective atomic numbers of the gels calculated by power method are also reported in Table 3 [17]. As reported in the table, the values of the effective atomic number of the gels are between 7.38 and 7.45. The relative difference of the effective atomic number of the gels with water is 0.2%, 0.1% and 0.8% respectively.

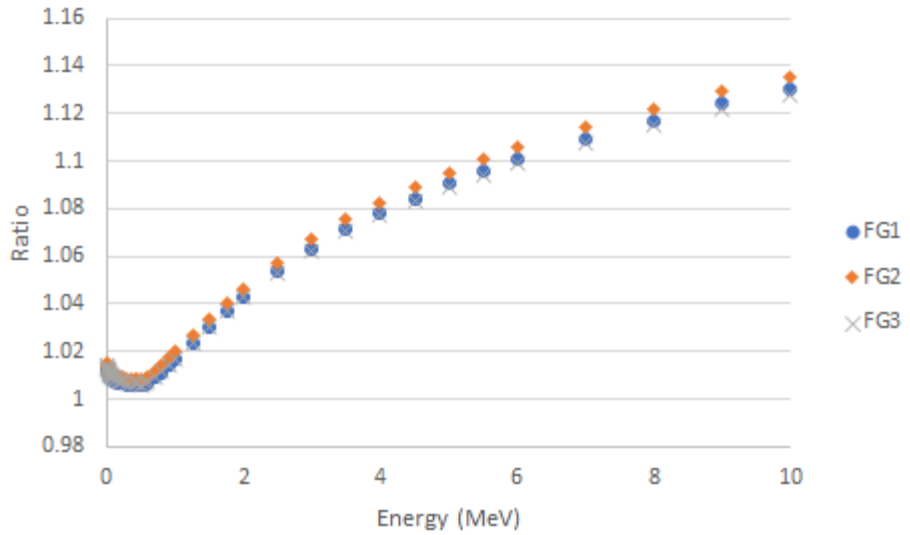

Fig. 4. Ratio of mass collision stopping power of different gels to water.

Table 3. Density and effective atomic number of the gels investigated in the study [17].

Material	Density (g/cm^3)	Effective atomic number
FG1	1.03	7.42

FG2	1.05	7.45
FG3	1.02	7.38

Conclusions

The radiological properties for Fricke gels with various compositions were surveyed using XCOM and ESTAR programs. The ratios between the mass attenuation coefficients and the electrons stopping power for the gels and each of the materials were almost equal to one. The gels match tissue in terms of mass coefficient better than water, although the differences may be considered negligible. For comprehensive comparison of the radiological properties of the dosimeters, total and partial interaction processes.should be considered over the full range of energies.

References

[1] Gallo, S., et al., (2019). Characterization of radiochromic poly (vinyl-alcohol)–glutaraldehyde Fricke gels for dosimetry in external x-ray radiation therapy. J. Phys. D: Appl. Phys. https://doi.org/10.1088/1361-6463/ab08d0.

[2] Galante, A.M.S., et al., (2008). MRI study of radiation effect on Fricke gel solutions. Radiat. Meas. 34, 550–553.

[3] Farajzadeh, E. Sina, S. (2021). Developing a radiochromic dosimeter for dosimetry in blood irradiation chambers. Radiat. Phys. Chem., 188, 109637.

[4] Gambarini, G., et al., (2017). Study of optical absorbance and MR relaxation of Fricke xylenol orange gel dosimeters. Radiat. Meas. 106, 622–627.

[5] Gallo, S., et al., (2021). Effect of ionizing radiation on the colorimetric properties of PVA-GTA Xylenol Orange Fricke gel dosimeters. Dyes and Pigments, 187:109141. https://doi.org/10.1016/j.dyepig.2021.109141.

[6] Taylor, M.L., et al., (2008). The effective atomic number of dosimetric gels, Australasian Physical & Engineering Sciences in Medicine, 31(2), 131-138.

[7] kron, T., (1993). Investigation of the tissue equivalence of gels used for NMR dosimetry. Physics in Medicine and Biology. 38, 139-150.

[8] Keall, P. and Baldock, C., (1999). A theoretical study of the radiological properties and water equivalence of Fricke and polymer gels used for radiation dosimetry, Australasian Physical & Engineering Sciences in Medicine, 22(3), 85-91.

[9] TSUDA, S., et al., (2003). Synthesis and Characterization of a Soft-tissue Substitute for Neutron Dosimetry, Journal of Nuclear Science and Technology, 40(12):1027–1031.

[10] Okunade, A.A., (2007). Parameters and computer software for the evaluation of mass attenuation and mass energy-absorption coeffi cients for body tissues and substitutes, Journal of Medical Physics, 32(3), 124-131.

[11] Manohara, S.R., et al., (2008). On the effective atomic number and electron density: A comprehensive set of formulas for all types of materials and energies above 1 keV, Nuclear Instruments and Methods in Physics Research B, 266, 3906–3912.

[12] Valante, M., et al., (2008). Fricke gel dosimeter tissue equivalence: a Monte Carlo study. Astroparticle, Particle, Space Physics, Radiation Interaction, Detectors and Medical Physics Applications, 4, Proceedings of the 10th Conference, https://doi.org/10.1142/6906.

[13] Pantelis, E., et al., (2004). Polymer gel water equivalence and relative energy response with emphasis on low photon energy dosimetry in brachytherapy, Physics in Medicine and Biology, 49, 3495-3514.

[14] Sellakumar, P., et al., (2007). Water equivalence of polymer gel dosimeters, Radiat Phys Chem, 76, 1108- 1115.

[15] Venning, A., et al., (2005). Radiological properties of normoxic polymer gel dosimeters, Med Phys, 32, 1047-1053.

[16] Sakar, E., et al., (2019). Phy-X / PSD: Development of a user friendly online software for calculation of parameters relevant to radiation shielding and dosimetry, Radiat. Phys and Chem. https://doi.org/10.1016/j.radphyschem.2019.108496.

[17] Moussous, O., (2022). Effective Atomic Number and Electron Density Determination for Fricke Gel Dosimeters Using Different Methods, Journal of Medical Physics, 47, 105-8.

[18] Kumar, S.A., (2023). Photon attenuation computational software tools - A comparative study, Phys. Open, 17, 100175.

[19] Eyadeh, M.M., et al., (2018). Evaluation of ferrous Methylthymol blue gelatin gel dosimeters using nuclear magnetic resonance and optical techniques. Radiat. Meas. 108, 26–33.

[20] Attix, F. H. (2008). Introduction to Radiological Physics and Radiation Dosimetry John Wiley & Sons.

[21] Hubbell H and Seltzer S M Tables of x-ray mass attenuation coefficients and mass energy-absorption coefficients 1 keV to 20 MeV for elements Z= 1 to 92 and 48 additional substances of dosimetric interest, (1995) Tech. rep., National Inst. of Standards and Technology-PL, Gaithersburg, MD (United States). Ionizing Radiation Div. https://physics.nist.gov/PhysRefData/XrayMassCoef/tab2.html (last access at 30 November 2018).

ICNST 2024
International Conference on Nuclear Science and Technology
6- 8 MAY 2024 | Isfahan, Iran

Evaluating the efficacy of the Compton Suppression System for detection of the low energy peaks of 152Eu and 155Eu isotopes in the presence of the high energy isotopes by simulation (Paper ID : 1198)

Hassanzadeh Tabrizi E.[1], Ghasemi B.[1*], Riazi Z.[2], Jokar A.[2]

[1]*Radiation Application Department, Faculty of Nuclear Engineering, Shahid Beheshti University, Tehran, Iran*

[2]*Physics and Accelerators Research School, Nuclear Science and Technology Research Institute (NSTRI), Tehran, Iran*

Abstract

Scattered gamma rays not only complicate the detector's response function but also increase the level of the Compton continuum. Compton suppression reduces the contribution of scattered gamma rays in the detector, resulting in the detection of low-energy or low-intensity peaks in the spectrum. As a result, such a system is particularly useful in proton therapy for evaluating the Bragg peak, as well as in NAA, XRF, and PIGE methods for element identification. This study looked at the performance of a system that used an HPGe detector as the primary spectrometer. BGO was chosen as the guard spectrometer over other detectors because of its high density and atomic number. This system's application has been investigated for elemental analysis of materials. We obtained suppressed and unsuppressed spectra for a wide range of energies using ^{137}Cs, ^{54}Mn, ^{152}Eu, ^{154}Eu, and ^{155}Eu sources. This simulated Compton suppression system allowed us to detect the low energy peaks of ^{152}Eu and ^{155}Eu isotopes in the high continuum caused by ^{137}Cs, ^{54}Mn, and ^{154}Eu isotopes. For this purpose, the minimum relative intensity was 0.001 for ^{152}Eu and 0.002 for ^{155}Eu. The CSF values for the lowest energies such as 105 keV and 344 keV were equal to 1.169 and 1.184. The simulation was performed using the GEANT4 Monte-Carlo toolkit.

Keywords: Compton Suppression System, Elemental Analysis, GEANT4

INTRODUCTION

Photoelectric absorption, Compton scattering, and pair production are three significant interactions of gamma rays with materials. When Compton scattering occurs, depending on the dimensions of the crystal, the energy of the incident photon, and the location of the interaction, the scattered gamma rays may escape from the detector. In other words, a portion of the incident photon energy exits the detector crystal. This occurrence not only complicates the

response function of the detector but also increases the Compton continuum level. Generally, this continuum originates from (i) environmental background gamma-rays, (ii) radioactivity within the diode assembly, (iii) radioactive impurities within any shield surrounding the spectrometer, and (iv) cosmic rays [1].

The main challenge is to choose a suitable configuration for detecting a wide spectrum of gamma rays. Scattered gamma rays produce a continuous background in the spectrum, obscuring the smaller photo-peaks [2]. Reducing the impact of scattered gamma rays improves detection sensitivity, facilitating a more accurate analysis of low-intensity peaks, particularly in techniques like X-ray fluorescence (XRF), prompt gamma-ray neutron activation analysis (PGNAA), and particle-induced gamma-ray emission (PIGE) for elemental identification [3, 4]. The implementation of a Compton suppression system becomes essential in all these applications.

The Compton suppression technique is a method used to reduce the influence of Compton scattering in gamma-ray spectroscopy. By employing a system of multiple detectors in an anti-coincidence mode, scattered gamma rays are suppressed, leading to a clearer spectrum with enhanced peak resolution. Typically, a detector with high energy resolution serves as the primary spectrometer, enclosed by an array of guard detectors. If a pulse is detected simultaneously in both the primary and guard detectors within a defined time frame, it is recognized as a scattering event and is not considered a signal. Thus, by reducing the Compton continuum, previously hidden peaks within the spectrum can be uncovered [5].

An exemplary system, like the setup introduced at the University of Liverpool, includes an HPGe detector measuring 5.23 cm × 5.58 cm with a relative efficiency of 24.5% as the primary detector [6]. Furthermore, eight-segment BGO detectors serve as guard detectors, each optically isolated. The photons detected in each segment are independently amplified by distinct photomultiplier tubes (PMTs). Using different isotopes for a wide range of energies, the minimum relative intensity required to identify ^{152}Eu and ^{155}Eu gamma-ray peaks was determined.

RESEARCH THEORIES

Compton scattering, as mentioned before, is a phenomenon in which a gamma-ray scatters off an electron, resulting in a loss of energy and a change in its direction. This scattering can generate a background signal that interferes with the detection of the desired gamma-ray events. Sum coincidence, pair spectroscopy, and Anti-coincidence are the three main methods of Compton suppression [7]. The sum coincidence method aids in diminishing this background by necessitating two detectors to simultaneously record signals, with their energies summing up to the energy of the original gamma ray. This means that both detectors must detect gamma rays at the same time, with their combined energies matching that of a single gamma ray event.

Pair spectroscopy" is another method used to reduce Compton background in nuclear physics experiments. This method aims to mitigate the background by taking advantage of a specific property of gamma rays: their ability to create electron-positron pairs when interacting with a material. When a gamma ray interacts with the atom's nucleus, it has the potential to create an electron-positron pair. The energy of the original gamma ray is distributed between the electron and positron, and the sum of their energies equals the energy of the initial gamma ray. In pair spectroscopy, detectors are positioned to detect both the electron and the positron concurrently. By mandating the simultaneous detection of both particles, with their energies combined to match the original gamma ray's energy, this approach effectively reduces the Compton background [8]. In the anticoincidence method, when gamma rays undergoing Compton scattering manage to escape from the primary detector, they have the potential to be absorbed and subsequently detected in the Compton suppression guard. As a result, these signals coincide with each other. The occurrence of coincidence signals in both the primary detector and the Compton suppression guard effectively prevents the detection of such signals, categorizing them as Compton interaction events. This approach is known as Compton suppression spectroscopy (CSS). The precise setup of the system and the use of a detector with high energy resolution are crucial [9].

For several decades, various types of guard detectors have been employed as anti-Compton guards in Compton suppression systems, including thallium-doped Sodium Iodide (NaI(Tl)) detectors, plastic scintillators, and more recently, bismuth germanate (BGO) detectors, resulting in a wide range of applications [10]. The high-purity germanium semiconductor

crystal (HPGe) is commonly chosen as the primary spectrometer in the Compton suppression system due to its characteristics such as a small band gap, Fano Factor smaller than 1, and high atomic number [11]. Hence, the choice of detector with high energy resolution is crucial depending on the methodology employed [12]. The combination of energy resolution, large-scale volume, and high impulse throughput contributes to achieving low minimum detectable activities (MDA) [13]. Nal (Tl) and BGO detectors are typically the most commonly utilized active guards in HPGe-based CSS [8, 14]. Each Compton suppression arrangement is evaluated based on its Compton suppression factor (CSF), which is defined by the following relationship [15]:

$$CSF = \frac{P/C_{suppressed}}{P/C_{unsuppressed}} \quad (1)$$

The Peak-to-Compton ratio (PCR), as described by Ge manufacturers, represents the ratio between the height of the peak and the average height of the Compton plateau for the desired peak. This parameter is crucial as it indicates the detector's ability to distinguish low-energy peaks even when higher-energy peaks are present in the spectrum [16].

Simulation Setup

The Monte Carlo technique is a statistical method used to simulate particle transport within various geometries. For this study, we employed the GEANT4 toolkit (version 10.07.p03), well-known for its precise modeling of particle interactions with matter [17]. Each simulation of a particle's trajectory, along with its secondary particles, is considered an "event" and is processed through the G4Event object. During the simulation of a single particle, numerous "steps" occur, indicating changes in particle properties like energy, charge, and weight as they transition between different states. These transitions are logged using the G4Step object [18]. When a gamma ray deposits energy simultaneously in both primary and guard detectors, the energy deposited in the primary detector remains undetected within that particular "event." In our simulation, we meticulously replicated the components of an HPGe detector, which serves as the primary spectrometer, including the entrance window, dead layer, vacuum, cavity, and semiconductor crystal, within the GEANT4 environment [19]. Additionally, the BGO detectors, configured as Compton suppression guards, were segmented in a ring formation surrounding the primary spectrometer. Notably, the wider coverage provided by the guard

detectors results in the detection of a higher number of scattered gamma rays, consequently enhancing the performance of the CSS.

When considering different gamma-ray energies, increasing the thickness of the BGO detector up to 60-70 mm results in further reduction of the Compton continuum. However, beyond this range, additional increases in thickness do not notably impact, keeping them relatively constant. Therefore, the optimal thickness of the BGO detector is typically within the 50-60 mm range [20]. To model the system accurately, a combination of passive and active shielding was employed. The radiation background was minimized by shielding both the primary and surrounding guard detectors with varying thicknesses of passive shielding material. For example, the introduction of a 10-cm Pb shield reduced the radiation background by a factor of 50 in the Nal (Tl) guard detector [14]. It is worth noting that lead shields are often coated with a few millimeters of copper to attenuate 75-80 keV X-rays emitted from lead [21]. Alternatively, a layer of tin with a specific thickness can serve the same purpose [22]. In the simulated CSS system, a three-layer shield consisting of lead, copper, and polyethylene was utilized. The detailed configuration components of this system are outlined in reference [23]. This paper explores the implementation of CSS in the separation of various radionuclides (emphasizing the significance of CSS in isotope separation.).

In this simulation, we generated spectra for both the suppressed and unsuppressed states using sources of ^{137}Cs, ^{54}Mn, ^{152}Eu, ^{154}Eu, and ^{155}Eu. The continuum arising from the peaks of ^{137}Cs, ^{54}Mn, and ^{154}Eu sources masks the detection of the lower energy peaks originating from ^{152}Eu and ^{155}Eu sources. We aim to determine the minimum threshold required to distinguish the peaks associated with ^{152}Eu and ^{155}Eu sources. A diagram illustrating this simulated system is presented in Fig. 1. We assume that if gamma rays scatter from the HPGe detector and undergo Compton scattering or photoelectric interaction within one of the guard detectors, this event is considered a coincidence. Essentially, under these circumstances, these pulses are not recorded as signals and are therefore excluded from the resulting spectrum.

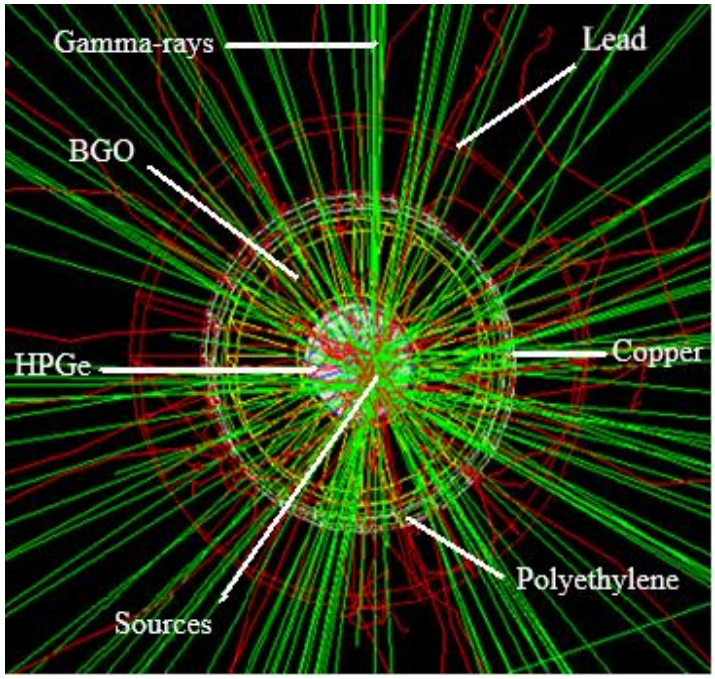

Fig. 1. Simulated CSS using GEANT4

Results and discussion

In this research, a mixture of gamma-ray spectra with varying energy levels from ^{137}Cs, ^{54}Mn, ^{152}Eu, ^{154}Eu, and ^{155}Eu isotopes was analyzed. The objective of this study was to evaluate the efficiency of Compton suppression in determining the lower detection threshold of the system for low-energy isotopes in the presence of high-energy isotopes. By maintaining the intensities of ^{137}Cs, ^{54}Mn, and ^{154}Eu isotopes constant and gradually adjusting the intensities of ^{152}Eu and ^{155}Eu isotopes, we determined the minimum intensity of these isotopes that the system could detect. To standardize this analysis, the intensity of ^{137}Cs was set as the reference (I_{ref}), with relative intensities (compared to the reference isotope) of ^{54}Mn and ^{154}Eu considered as 5% and 14%, respectively. Initially, the relative intensity of ^{152}Eu was set at 0.0005 and ^{155}Eu at 0.001. It was observed that under these conditions, the 105 keV peak corresponding to the ^{155}Eu isotope and the 678 keV and 964 keV peaks corresponding to the ^{152}Eu isotope were barely distinguishable in the suppressed spectrum. Additionally, the 344 keV, 779 keV, and 1086 keV peaks in this spectrum were entirely indistinct. Subsequently, by increasing the intensities to 0.0007 for ^{152}Eu and 0.002 for ^{155}Eu, the 105 keV peak of the ^{155}Eu isotope became visible in the low-energy region. Hence, the lower detection threshold for this isotope was determined at a relative intensity of 0.002. Despite the appearance of the 779 keV and 1086 keV peaks, the

344 keV peak was absent within the Compton continuum. Finally, with a further rise in the relative intensity of ^{152}Eu to 0.001, all its peaks manifested in the suppressed spectrum, thereby establishing the lower detection threshold for this isotope as well. The unsuppressed spectrum for these radioisotopes is depicted in Fig. 2, while the suppressed spectrum for the final state, illustrating all peaks of ^{152}Eu and ^{155}Eu, is presented in Fig. 3.

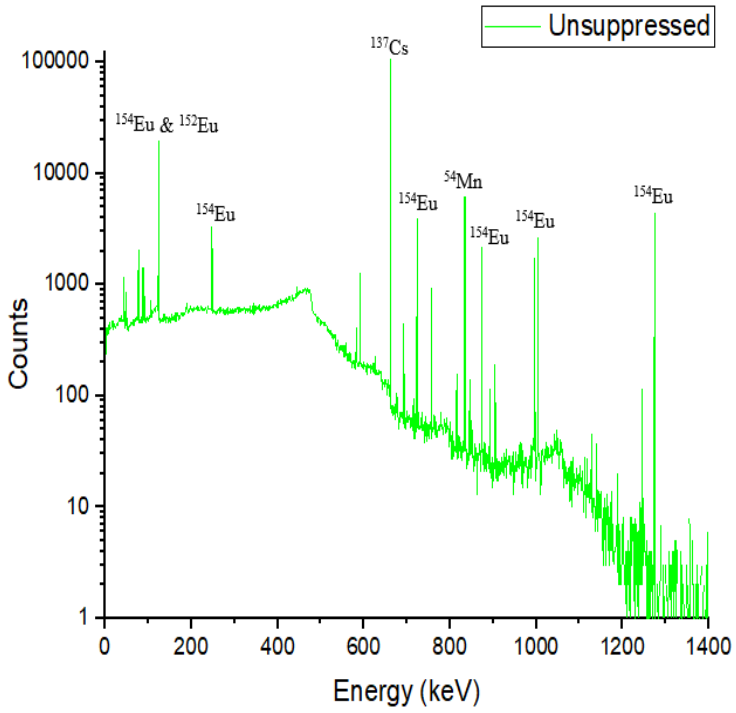

Fig. 2. Unsuppressed spectrum in the simulated CSS

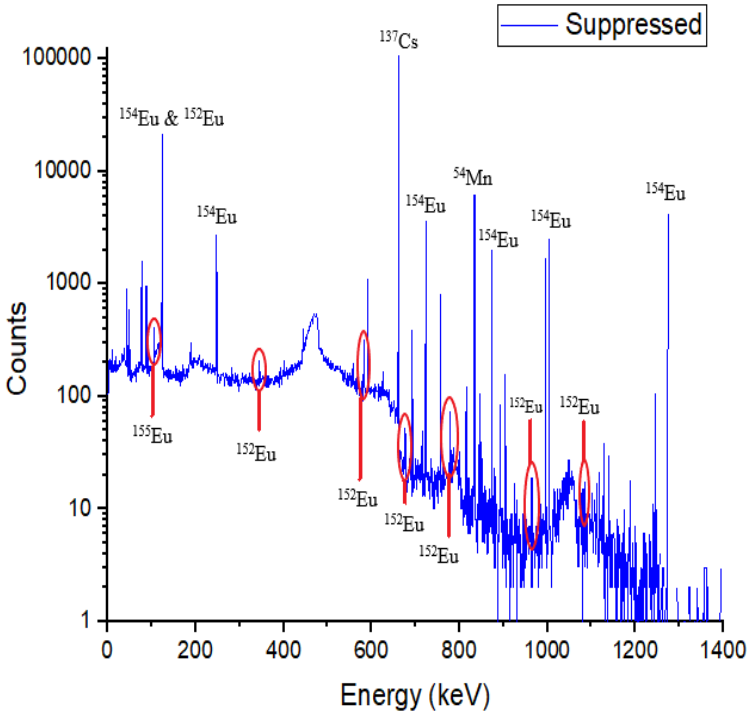

Fig. 3. Suppressed spectrum in the simulated CSS

Table 1 shows the CSF values for various states as well as for the ^{137}Cs, ^{54}Mn, and ^{154}Eu isotopes with constant intensity.

Table 1. CSF values for isotopes with variable and constant intensity.

Isotope	Energy (keV)	I/I_{ref}(%)	CSF	I/I_{ref}(%)	CSF	I/I_{ref}(%)	CSF
^{152}Eu	344	0.05	-	0.07	-	0.1	1.184
	678		1.671		1.683		1.691
	779		-		1.055		1.173
	964		1.064		1.142		1.26
	1086		-		2.04		2.157
^{155}Eu	105	0.1	1.071	0.15	1.118	0.2	1.169
^{137}Cs	662	100	4.628				
^{54}Mn	834.5	5	1.548				
^{154}Eu	1274.4	14	4.44				

Conclusions

In this research, gamma-ray spectra with varying energy levels from isotopes 137Cs, 54Mn, 152Eu, 154Eu, and 155Eu were analyzed. This investigation aimed to evaluate the efficacy of Compton suppression in detecting low-energy isotopes in the presence of high-energy isotopes. By keeping the intensities of 137Cs, 54Mn, and 154Eu isotopes constant and adjusting the intensities of 152Eu and 155Eu isotopes we determined the minimum intensity

at which these isotopes could be detected by the system. The results showed that Compton suppression could establish the necessary minimum intensity for detecting low-energy isotopes in proximity to high-energy isotopes. Initially, detecting the 105 keV peak of the 155Eu isotope and the 678 keV and 964 keV peaks of the 152Eu isotope under Compton suppression posed challenges. However, by increasing the intensities of the 152Eu and 155Eu isotopes, we were able to determine the minimum detectable intensity for them. Overall, the results indicate that Compton suppression can effectively detect low-energy isotopes in environments with high-energy isotopes. By varying the intensities of the low-energy isotopes, we determined the requisite minimum intensity for detection.

References

[1] G. F. Knoll, Radiation detection and measurement. John Wiley & Sons, 2010.

[2] A. Baxter et al., "Compton-suppression tests on Ge and BGO prototype detectors for GAMMASPHERE," Nuclear Instruments and Methods in Physics Research Section A: Accelerators, Spectrometers, Detectors and Associated Equipment, vol. 317, no. 1-2, pp. 101-110, 1992.

[3] R. Acharya and P. Pujari, "Potential of conventional and internal monostandard NAA and PGNAA and PIGE in forensic sciences: an overview," Forensic Chemistry, vol. 12, pp. 107-116, 2019.

[4] S. K. Lee, H. Seo, B. H. Won, H. S. Lee, S.-H. Park, and H.-D. Kima, "Feasibility study of a Compton Suppression system for the X-ray Fluorescence (XRF) using Monte Carlo simulation," 2014.

[5] S. Landsberger and S. Peshev, "Compton suppression neutron activation analysis: past, present and future," Journal of Radioanalytical and Nuclear Chemistry, vol. 202, pp. 201-224, 1996.

[6] P. Nolan, D. Gifford, and P. Twin, "The performance of a bismuth germanate escape suppressed spectrometer," Nuclear Instruments and Methods in Physics Research Section A: Accelerators, Spectrometers, Detectors and Associated Equipment, vol. 236, no. 1, pp. 95-99, 1985.

[7] R. Britton, "Compton suppression systems for environmental radiological analysis," Journal of Radioanalytical and Nuclear Chemistry, vol. 292, no. 1, pp. 33-39, 2012.

[8] R. Britton, J. Burnett, A. Davies, and P. Regan, "Monte-Carlo optimisation of a Compton suppression system for use with a broad-energy HPGe detector," Nuclear Instruments and Methods in Physics Research Section A: Accelerators, Spectrometers, Detectors and Associated Equipment, vol. 762, pp. 42-53, 2014.

[9] N. O. CETINER, "Specifications and performance of the Compton Suppression Spectrometer at the Pennsylvania State University," 2008.

[10] M. Nocente et al., "Energy resolution of gamma-ray spectroscopy of JET plasmas with a LaBr3 scintillator detector and digital data acquisition," Review of scientific instruments, vol. 81, no. 10, 2010.

[11] R. Cooper, M. Amman, and K. Vetter, "High resolution gamma-ray spectroscopy at high count rates with a prototype high purity germanium detector," Nuclear Instruments and Methods in Physics Research Section A: Accelerators, Spectrometers, Detectors and Associated Equipment, vol. 886, pp. 1-6, 2018.

[12] G. Gilmore, Practical gamma-ray spectroscopy. John Wiley & Sons, 2008.

[13] S. Garti et al., "Characterizing low-activity waste containers: A case study for Compton Suppression Systems under challenging signal-to-noise ratio," Nuclear Instruments and Methods in Physics Research Section A: Accelerators, Spectrometers, Detectors and Associated Equipment, vol. 949, p. 162806, 2020.

[14] D. Masse, A. Adam, and J. Laurec, "A Ge□ NaI (Tl) spectrometer with Compton suppression and gamma coincidence counting. Application to 189Ir and 101Rh activity measurements," Nuclear Instruments and Methods in Physics Research Section A: Accelerators, Spectrometers, Detectors and Associated Equipment, vol. 309, no. 1-2, pp. 227-235, 1991.

[15] S. E. Bender, K. Ünlü, C. R. Orton, and J. M. Schwantes, "Geant4 model validation of Compton suppressed system for process monitoring of spent fuel," Journal of Radioanalytical and Nuclear Chemistry, vol. 296, pp. 647-654, 2013.

[16] N. Tsoulfanidis and S. Landsberger, Measurement and detection of radiation. CRC press, 2021.

[17] G. Collaboration, "GEANT4 Physics Reference Manual, 2012 (accessed January 6, 2016), http://geant4. web. cern. ch/geant4/UserDocumentation/UsersGuides/PhysicsReferenceManual/BackupVersions/V9. 6/fo," PhysicsReferenceManual. pdf.

[18] S. Agostinelli et al., "GEANT4—a simulation toolkit," Nuclear instruments and methods in physics research section A: Accelerators, Spectrometers, Detectors and Associated Equipment, vol. 506, no. 3, pp. 250-303, 2003.

[19] F. Saheli, Z. Riazi, A. Jokar, H. Shahabinejad, N. Vosoughi, and S. Ghasemi, "Evaluation the nonlinear response function of a HPGe detector for 59 keV to 10.7 MeV gamma-rays using a Monte Carlo simulation and comparison with experimental data," Journal of Instrumentation, vol. 16, no. 07, p. P07003, 2021.

[20] Q. Zou, J. Zhu, Z. An, and Y. Zhang, "Monte Carlo optimization of a Compton suppression system for gamma-ray diagnosis of combustion plasma," Nuclear Instruments and Methods in Physics Research Section A: Accelerators, Spectrometers, Detectors and Associated Equipment, vol. 879, pp. 57-63, 2018.

[21] C. Chung, L.-J. Yuan, and K.-B. Chen, "Performance of a HPGe-NaI (Tl) Compton suppression spectrometer in high-level radioenvironmental studies," Nuclear Instruments and Methods in Physics Research Section A: Accelerators, Spectrometers, Detectors and Associated Equipment, vol. 243, no. 1, pp. 102-110, 1986.

[22] K. Iniewski, Semiconductor radiation detection systems. CRC press, 2018.

[23] E. Hassanzadeh Tabrizi, B. Ghasemi, Z. Riazi, and A. Jokar, "Feasibility of the Compton Suppressed Gamma-Ray Spectrometry for Proton Therapy Applications," Available at SSRN 4763793.

ICNST 2024
International Conference on Nuclear Science and Technology
6- 8 MAY 2024 | Isfahan, Iran

Investigating the response of Bacillus pumilus spores to kiloelectron volt X-rays for medical sterilization (Paper ID : 1201)

Payman Rafiepour[1*], Sedigheh Sina[1,2], Zahra Alizadeh Amoli[3], Seyed Shahram Shekarforoush[3], Ebrahim Farajzadeh[2], Seyed Mohammad Javad Mortazavi[4], Nadia AsariShik[5]

[1] *Department of Nuclear Engineering, School of Mechanical Engineering, Shiraz University, Shiraz, Iran*
[2] *Radiation research center, School of Mechanical Engineering, Shiraz University, Shiraz, Iran*
[3] *Department of Food Hygiene and Public Health, School of Veterinary Medicine, Shiraz University, Shiraz, Iran*
[4] *Department of Medical Physics and Engineering, School of Medicine, Shiraz University of Medical Sciences, Shiraz, Iran*
[5] *Faculty of Physics, Yazd University, Yazd, Iran*

Abstract

Recently, sterilization of disposable medical instruments with low-energy ionizing radiation has gained worldwide interest. Utilizing the Geant4 Monte Carlo simulation toolkit and MEDRAS (Mechanistic DNA Repair and Survival) model of cell repair, the response of *Bacillus pumilus* spores (as a reference standard in medical sterilization) to low-energy X-rays was investigated. A bacterial cell was simulated based on a random replication of B-DNA segments. The survival curves of *B. pumilus* spores were plotted based on the output of MEDRAS modeling. Experimental work was also performed to validate the simulation. Different D_{10}-values in the range of 1.20 to 1.56 kGy were obtained for *B. pumilus* spores irradiated by X-rays with a cut-off energy of 50, 100, 150, and 200 keV. Survival calculations from misrepairs and apoptosis alone were more consistent with experimental results. D_{10}-value calculations demonstrated that X-rays with lower beam qualities are more effective for the inactivation of *B. pumilus* spores. The results of this study highlighted the power of mechanistic simulation in radiobiological studies of bacteria.

Keywords: Monte Carlo simulation, Bacillus pumilus spores, medical sterilization, low-energy radiation, DNA damage, Geant4-DNA

INTRODUCTION

Various methods have been proposed for sterilizing disposable medical devices among which ionizing radiation has received particular attention. If applied according to standards, irradiation with ionizing radiation can effectively reduce bacterial and viral contamination while causing minimal damage to the product. The current radiation sources are gamma rays

(Co-60), high-energy electron beams (10 MeV), and bremsstrahlung X-rays (5-7.5 MeV) [1]. Using low-energy X-rays (LEEX) and electron beams (LEEB) for the surface irradiation of food products and disposable medical instruments has been of great interest [2]. The main advantages of LEEX and LEEB include not requiring heavy radiation shielding and the ability to perform in-house sterilization. Although several studies have investigated the response of different microorganisms of food products to LEEX or LEEB, limited studies have been conducted on the irradiation of *Bacillus pumilus* spores, as a reference microorganism in industrial sterilization, by LEEX or LEEB. Different D_{10}-values in the range of 1.2-2.6 kGy have been reported in the literature for *B. pumilus* spores irradiated by ionizing radiation [3, 4]. In the case of simulation, many studies have been conducted on the mathematical modeling to estimate cell death in mammalian cells [5, 6]. Moreira et al. [7] estimated the D_{10}-value of *Listeria monocytogenes* and *Escherichia coli* by Monte Carlo simulation. Lampe et al. [8] also simulated an *E. coli* bacterial cell using Geant4-DNA [9] and compared direct and indirect DNA damages induced by electrons and protons of different energies. As far as we know, no MC simulation studies have been performed to examine the response of a bacterium to LEEX and to estimate the D_{10}-value. This study investigated the response of *B. pumilus* spores to LEEX of 50, 100, 150, and 200 keV cut-off energy using the Geant4-DNA toolkit (version 4.11.0), and by implementing a mathematical model of cell repair called MEDRAS (Mechanistic DNA Repair and Survival) [5]. The D_{10}-value obtained from the simulation in standard conditions is compared with the D_{10}-value obtained experimentally.

RESEARCH THEORIES

Modelling and Simulation

The Geant4-DNA can simulate different stages as follows: 1- The physical stage, which consists of simulating the interactions of particles with water, results in the ionization and excitation of water molecules. 2- The pre-chemical stage, that includes the generation of free radicals following water radiolysis. 3- The chemical stage, which consists of the diffusion of free radicals and mutual chemical interactions. 4- The biological stage, which includes the calculation of early direct and indirect DNA damages [9, 10]. The "G4EmDNAPhysics_option2" physics constructor was used for implementing the physical cross-section data. The pre-defined interactions for secondary electrons are ionization, elastic scattering, vibrational excitation, molecular attachment, and electronic excitation. These are

G4DNABornIonisationModel (11-10^6 eV), G4DNAChampionElasticModel (7.4-10^6 eV), G4DNASancheExcitationModel (2-100 eV), G4DNAMeltonAttachmentModel (4-13 eV), and G4DNABornExcitationModel (9-10^6 eV), respectively [9, 10].The "G4EmDNAChemistry_option3" chemistry constructor was used for simulating the chemical stage. The default chemical reactions and the corresponding reaction rates implemented in Geant4-DNA are adapted from the literature [11]. Following [8], the total simulation time of the chemical stage was set to 1 ns. A cylindrical volume of water with a height of 4 μm and a diameter of 1 μm was simulated as a simplified model of *B. pumilus* cell. A virtual elliptical volume with 1.8×0.9×0.9 μm^3 dimensions was defined as the nucleoid that contains the genetic material. The *B. pumilus* genome length was set to 3.6 million base pairs (Mbps) [12]. To construct the genome of *B. pumilus*, 16667 curved B-DNA segments, with 216 bps length [13], were randomly distributed in the nucleoid. A simple cylinder was defined with a height of 0.34 nm and a radius of 0.5 nm as a DNA bp. To model the DNA backbone, i.e., sugar-phosphate parts, a quarter cylinder was simulated with an inner and outer radius of 0.5 and 1.185 nm, respectively. Each quarter cylinder is rotated 36 degrees with respect to the bp axis to make the spiral shape of the DNA strands [13]. The geometrical model and a magnified view of DNA segments are shown in Figure 1-a. The definition of a radiation source was based on our previous work [14]. An X-ray tube with a tungsten anode of 5 mm thickness, a beryllium window of 0.8 mm thickness, and an aluminium filter of 0.5 mm thickness was simulated. The kinetic energy spectrum of generated X-rays under the window was stored in a text file as a phase space. This phase space was defined as a new radiation source on the surface of the nucleoid. An illustration of the primary X-rays emitted from the nucleoid surface with a cosine angular distribution is shown in Figure 1-b.

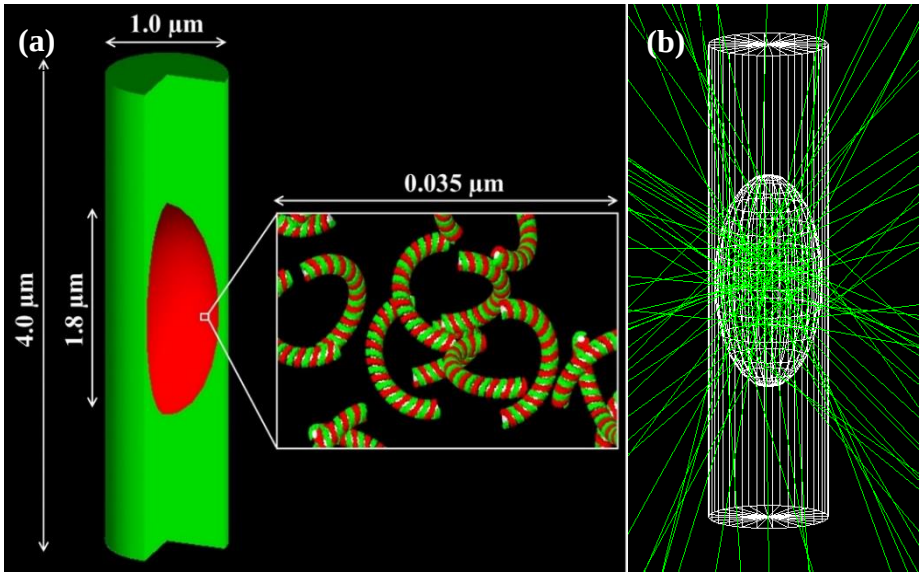

Fig. 1. (a) The bacterial model as a cylindrical volume of water. The nucleoid is defined as an ellipsoid with dimensions of 1.8×0.9×0.9 μm^3. (b) A representation of X-rays emitted from the nucleoid surface with a cosine angular distribution.

The starting point of any mathematical modeling of cellular repair is based on the number and spatial distribution of DSBs since it is assumed that DNA single-strand breaks (SSBs) are easily repaired [5]. The number and position of the SSBs caused by the physical and chemical stages were recorded. We considered DNA sugar-phosphate parts as target volumes; thus, the DNA bp damages were not taken into account. Following [15], a DBSCAN (density-based spatial clustering of applications with noise) algorithm was used to calculate DNA damage. An energy threshold based on a linear function is defined to calculate direct DNA damage. A deposited energy of less than 5 eV will not result in an SSB, while a deposited energy greater than 37.5 eV will result in an SSB. As the deposited energy increases from 5 to 37.5 eV, the probability of an SSB will increase according to a linear relationship. If the distance between two SSBs is less than 10 bp and each is located on the opposite DNA strand, a DSB will replace them. To calculate the indirect DNA damages, just $OH^{\bullet}$ radicals were considered [10]. The spatial distribution of $OH^{\bullet}$ radicals produced in the nucleoid was scored. Since not all $OH^{\bullet}$ radicals induce an indirect SSB, a 42% probability was set for the interaction of an $OH^{\bullet}$ radical with the DNA, according to [8]. A DNA damage yield (DY) is calculated by equation 1 [13]:

(1) $$DY\ (Gy^{-1}Mbp^{-1}) = N_{damage}/(D \times GL)$$

N_{damage} is the number of DNA damage of any kind, D is the deposited dose in the cell (Gy), and GL (Mbps) is the genome length. MEDRAS modelling has been shown to predict well the response of mammalian cells to ionizing radiation. The MC implementation of MEDRAS is freely available: https://github.com/sjmcmahon/Medras-MC [5]. The MEDRAS attributes cell death to three mechanisms: genetic damage (i.e., misrepair yields and chromosome aberrations), apoptosis, and mitotic catastrophe. All these factors follow an exponential relationship to describe their role in cell death. Since most bacteria have only a single chromosome, we ignored chromosome aberrations such as dicentrics, rings, and large deletions (> 3Mbps) in the modelling of bacterial cell death. It has been shown that in the case of bacteria, mitotic catastrophe does not occur in the same way as in the case of mammalian cells [16]; Therefore, only misrepair yields and apoptosis are important for estimating the survival curve of bacteria. According to [5], the mean probability of cell survival from apoptosis is given by equation 2:

$$SF_{apop} = \exp(-\psi N_{G1}) \quad (2)$$

in which N_{G1} is the number of DSBs that occurred in the G1 phase, and ψ is the apoptosis rate that is 0.012 DSB^{-1} for normal cells. It should be noted that since the bacterial cell cycle usually consists of three phases [16], we added a probability of 0.333 for DSB calculation in the Geant4 code to obtain N_{G1}. To consider the effect of misrepairs, the misrepair rates (MRs) obtained by the MEDRAS was plotted in terms of dose, and then a binomial equation was fitted to the data:

$$MR = \alpha D + \beta D^2 \quad (3)$$

After calculating α and β, the mean probability of cell survival from misrepairs is given by equation 4:

$$SF_{mr} = \exp(-MR) \quad (4)$$

Finally, the total cell survival probability was obtained from equation 5:

$$SF_{total} = SF_{apop} \times SF_{mr} \quad (5)$$

The MEDRAS requires a text file in a standard DNA damage data format [17] as input. It must include two general sections: the header and the data. The minimum data required in the data section are: Determining whether the particle is primary or secondary, and the event id, the spatial x, y, and z coordinates of all DSBs (direct and indirect) in μm, and the damage types (base damage, SSB, or DSB).

Experiment

Spray-dried spores of *B. pumilus* (ATCC No. 27142) powder (2×10^{11} spores/gr) were donated by the Pardis Roshd Mehregan Company, Iran. To confirm the spore concentration, a 10% suspension was provided in sterile normal saline (2×10^{10} spores/ml) and heated at 80 °C for 15 min to remove the vegetative cells. After tenfold serial dilution, it was pour plated on the plate count agar (PCA, Merck, Germany). Eighteen metal coupons made of 304 stainless-steel (8 g/cm^3) with dimensions of 5 cm×1 cm were provided. After being sterilized by autoclave, they were glued individually into a sterile disposable Petri dish, 80 mm×15 mm. Then, they were uniformly inoculated with 20 μL of *B. pumilus* spore suspension in normal saline (2×10^{10} spores/ml) and spread and allowed to dry (4×10^{8} spores/coupon). Three coupons that were inoculated with sterile normal saline were considered sterility controls. For irradiation of the samples, Petri dishes containing metal coupons were positioned at a distance of 9.5 cm from the output window of the X-ray source on a fixed table. The radiation field was adjusted to the size of the Petri dish by internal collimators. Irradiation was performed at standard ambient conditions (27°C). The peak tube voltage (kVp) and current (mA) were kept constant at 150 kVp and 20.5 mA, and different doses of 0.0, 0.5, 1.0, 1.5, and 2.0 kGy were delivered to the samples by increasing the irradiation time. The X-ray tube dose rate was 41.25 Gy/min. The dose was measured using a solid-state probe (RTI SoliDose 400). To count the remaining spores after irradiation, the coupons were transferred to tubes of 5 mL of sterile normal saline and vortexed for 10 minutes. Then, they were serially diluted, and the favourable dilutions were cultured in PCA medium by the pour-plate method. The Petri dishes were incubated at 37 °C for two days. Finally, D_{10}-values were calculated using the mean surviving population and the mean initial population for each delivered dose.

Results and discussion

A comparison of the mean direct and indirect DNA DYs, obtained from equation 1, for LEEX of 50, 100, 150, and 200 keV cut-off energies is shown in Figure 3. Figure 3-a shows the survival curve of *B. pumilus* spores resulting from the irradiation by LEEX with a cut-off energy of 50, 100, 150, and 200 keV, considering only the apoptosis (see equation 2). Figure 3-b shows the survival curve of *B. pumilus* spores irradiated by LEEX with a cut-off energy of 50, 100, 150, and 200 keV, considering both apoptosis and misrepairs (see equation 5). Error bars are 10% of the data.

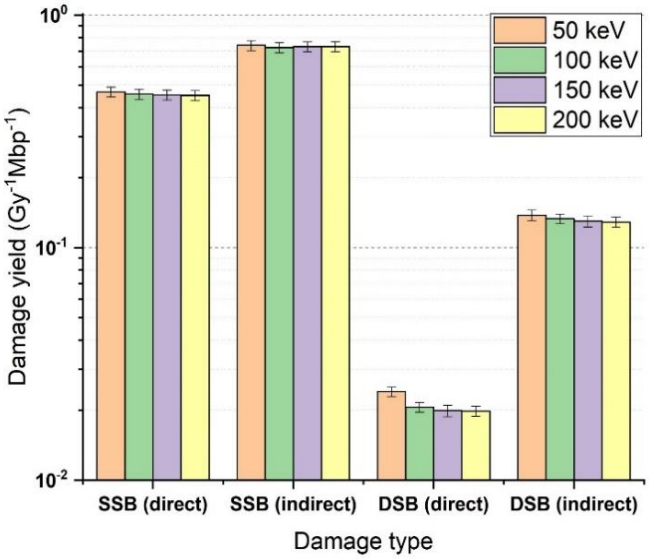

Fig. 2. The single- and double-strand DNA breaks (SSB and DSB) for LEEX of 50 to 200 kV voltages.

According to Figure 2, the normalized DNA DYs are quantitatively close to each other, and their slight differences are within the statistical uncertainty. The slight increase in DNA DYs for lower X-ray voltages may be attributed to their linear energy transfer (LET). Considering that the maximum energy of X-rays with a tube voltage of 50 kV is lower than that of 100, 150, and 200 kV, it will produce more low-energy secondary electrons with a slightly higher LET. This will result in higher dose deposition and thus, more DNA damage.

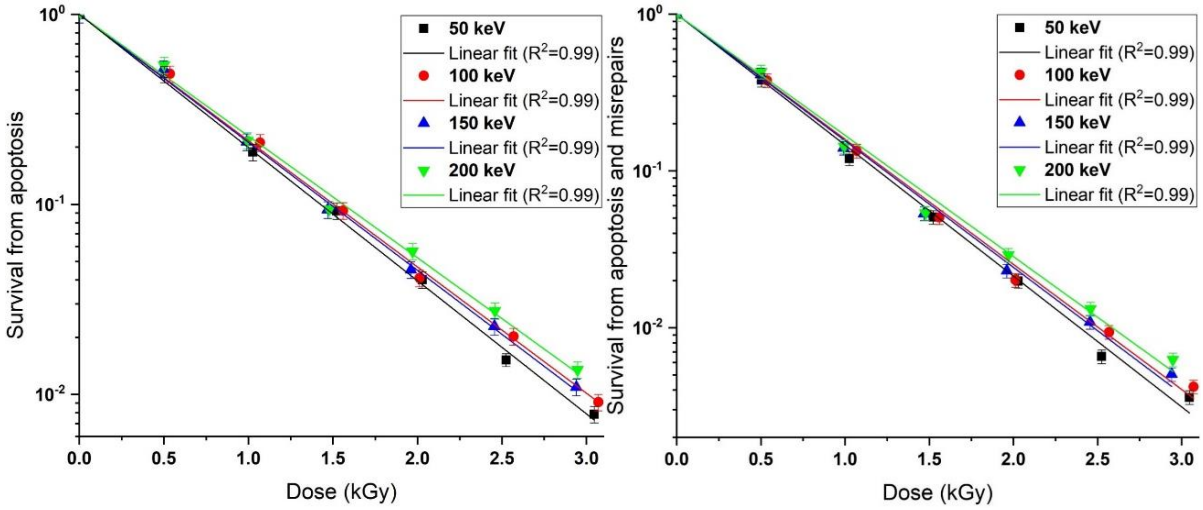

Fig. 3. The survival curve of *B. pumilus* spores irradiated by LEEX with a cut-off energy of 50, 100, 150, and 200 keV, (a) considering only the apoptosis and (b) considering both apoptosis and misrepairs.

As shown in Figure 3, the slope of the survival curves for 50 keV X-rays drops faster than that of 100, 150, and 200 keV X-rays, which is consistent with [18]. This indicates the slightly higher effectiveness of lower tube voltages in the inactivation process of B. pumilus spores. According to Figure 3-b, by considering misrepairs, the slope has increased more, which means a relative decrease in the D_{10}-values. The experimental data were obtained only for 150 kVp tube voltage and up to a 2 kGy dose deposit. Figure 4 compares the survival curves of B. pumilus spores irradiated by LEEX with a tube voltage of 150 kV, both experimentally and by simulation. The inverse of the slope of the survival curves gives the D_{10}-value. The mean D_{10}-values are listed in Table 1.

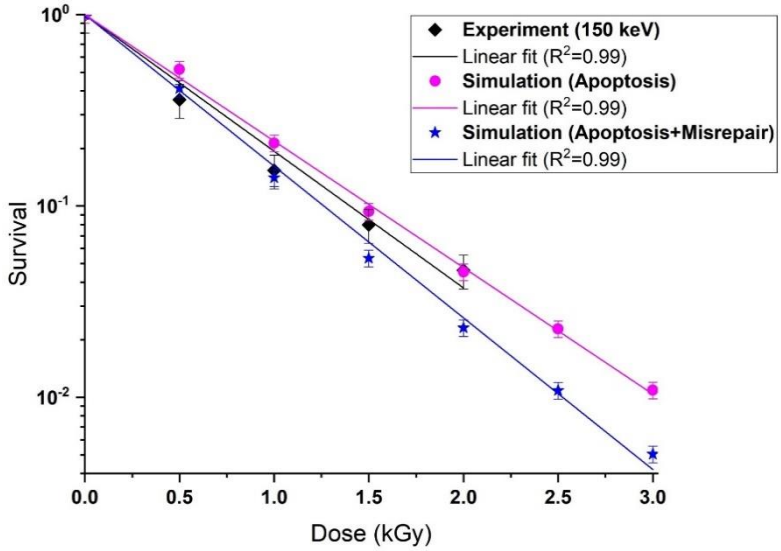

Fig. 4. The survival curve for *B. pumilus* spores irradiated by LEEX with a cut-off energy of 150 keV that was obtained experimentally and by simulation.

Table 1. The mean D_{10}-values (kGy) of *B. pumilus* spores irradiated by LEEX generated with a tube voltage of 50, 100, 150, and 200 kV.

Tube voltage (kV)	Experiment	Simulation (Apoptosis)	Simulation (Apoptosis+Misrepair)
50	N/A	1.20 ± 0.02	1.42 ± 0.02
100	N/A	1.25 ± 0.02	1.49 ± 0.03
150	1.40 ± 0.10	1.24 ± 0.02	1.48 ± 0.02
200	N/A	1.29 ± 0.02	1.56 ± 0.03

As shown in Figure 4 and Table 1, a good agreement is achieved between the experimental and simulation data. Considering misrepairs in survival calculations results in a reduction of D_{10}-value by up to 15% and 20% for LEEX of 50 keV and 200 keV cut-off energy, respectively. Considering just apoptosis in survival calculations gives a more appropriate D_{10}-value consistent with the experimental results. This could be because apoptosis is the most common

death observed in bacterial cells [19]. However, Figure 3 shows that both apoptosis alone and apoptosis with misrepairs agree well with the experimental result, with a relative difference of less than 20%. This highlights the importance of considering all factors involved in cell death modeling for bacterial cells.

Conclusions

Although the normalized DNA DYs (per Gy per Mbps) induced by LEEX with a cut-off energy of 50, 100, 150, and 200 keV were nearly identical, D_{10}-value calculations demonstrated that LEEX with lower energies may be more effective for the inactivation of *B. pumilus* spores. By considering misrepairs in survival calculations, the relative difference of the D_{10}-value with experimental data increases but does not exceed 20%, which is acceptable. Our study highlights the importance of further use of mechanistic simulations to unravel the behind-the-scenes mechanisms in bacterial spore inactivation.

References

[1] Indiarto, R., Pratama, A. W., et al. (2020). Food irradiation technology: A review of the uses and their capabilities. *International Journal of Engineering Trends and Technology*, *68*(12), 91-98.

[2] Zhang, H., & Zhou, W. (2022). Low-energy X-ray irradiation: A novel non-thermal microbial inactivation technology. *Advances in food and nutrition research*, *100*, 287–328.

[3] Y., Moeller, R., Tran, S., Dubovcova, B., Akepsimaidis, G., Meneses, N., Drissner, D. and Mathys A (2018) *Geobacillus* and *Bacillus* Spore Inactivation by Low Energy Electron Beam Technology: Resistance and Influencing Factors. *Front. Microbiol.* 9:2720.

[4] McEvoy, B., Maksimovic, A., Howell, and et al. (2023). Studies on the comparative effectiveness of X-rays, gamma rays and electron beams to inactivate microorganisms at different dose rates in industrial sterilization of medical devices. *Radiation Physics and Chemistry*, *208*, 110915.

[5] McMahon, S.J., and Prise, K.M. (2021). A Mechanistic DNA Repair and Survival Model (Medras): Applications to Intrinsic Radiosensitivity, Relative Biological Effectiveness and Dose-Rate. *Frontiers in oncology*, *11*, 689112.

[6] Chatzipapas, KP, Tran, NH, Dordevic, M, et al. Simulation of DNA damage using Geant4-DNA: an overview of the "molecularDNA" example application. *Prec Radiat Oncol*. 2023; 7: 4– 14.

[7] Moreira, R. G., Ekpanyaskun, N., & Braby, L. A. (2010). Theoretical Approach for the calculation of radiation D10-value. *Journal of Food Process Engineering*, *33*, 314-340.

[8] Lampe, N., Karamitros, M., & et al. (2018b). Mechanistic DNA damage simulations in Geant4-DNA Part 2: Electron and proton damage in a bacterial cell. *Physica medica*, *48*, 146–155.

[9] Incerti S, Baldacchino G, Bernal M, Capra R, Champion C, et al. THE GEANT4-DNA PROJECT. International Journal of Modeling, Simulation, and Scientific Computing. 2010;01(02):157-78.

[10] Kyriakou, I., Sakata, D., Tran, H. N., Perrot, Y., Shin, W. G., and et al. (2021). Review of the Geant4-DNA simulation toolkit for radiobiological applications at the cellular and DNA level. *Cancers*, *14*(1), 35.

[11] Karamitros M, Luan S, Bernal MA, Allison J, Baldacchino G, Davidkova M, et al. Diffusion-controlled reactions modeling in Geant4-DNA. Journal of Computational Physics. 2014; 274:841-82.

[12] Pudova, D.S., Toymentseva, A.A., Gogoleva, N.E., and et al. (2022). Comparative Genome Analysis of Two *Bacillus pumilus* Strains Producing High Level of Extracellular Hydrolases. *Genes. 13*, 409.

[13] Nikjoo H, O'Neill P, Wilson WE, Goodhead DT. Computational approach for determining the spectrum of DNA damage induced by ionizing radiation. *Radiat Res*. 2001;156(5 Pt 2):577-583.

[14] Rafiepour, P., Sina, S., Mortazavi, S.M.J. (2023). A multiscale Monte Carlo simulation of irradiating a typical-size apple by low-energy X-rays and electron beams. *Radiation Physics and Chemistry*, 111016.

[15] Francis, Z., Villagrasa, C., & Clairand, I. (2011). Simulation of DNA damage clustering after proton irradiation using an adapted DBSCAN algorithm. *Comp. Meth. Prog. in Biomedicine*, *101*(3), 265-270.

[16] Wang, J.D., & Levin, P.A. (2009). Metabolism, cell growth and the bacterial cell cycle. *Nature Reviews Microbiology*, *7*(11), 822-827.

[17] Schuemann, J., McNamara, A. L., Warmenhoven, J. W., and et al. (2019). A New Standard DNA Damage (SDD) Data Format. *Radiation research*, *191*(1), 76–92.

[18] Ha, T. M. H., Yong, D., Lee, E. M. Y., Kumar, P., Lee, Y. K., & Zhou, W. (2017). Activation and inactivation of Bacillus pumilus spores by kiloelectron volt X-ray irradiation. *PloS one*, *12*(5), e0177571.

[19] Smith, R. P., Barraza, I., Quinn, R. J., & Fortoul, M. C. (2020). The mechanisms and cell signaling pathways of programmed cell death in the bacterial world. *International review of cell and molecular biology*, *352*, 1–53.

ICNST 2024
International Conference on Nuclear Science and Technology
6 - 8 MAY 2024 | Isfahan, Iran

A Monte Carlo Simulation on the irradiation of Eggs and Potatoes by Low-energy X-rays and Electron Beams (Paper ID : 1204)

Rafiepour P.[1*], Tavakolialahabadi Z[1], Sina S[1,2], AsariShik N[3]

[1] *Department of Nuclear Engineering, School of Mechanical Engineering, Shiraz University, Shiraz, Iran*
[2] *Radiation research center, School of Mechanical Engineering, Shiraz University, Shiraz, Iran*
[3] *Department of Physics, Yazd University, Yazd, Iran*

Abstract

About 20 to 30 percent of agricultural products are lost annually due to pests and spoilage. Using ionizing radiation to inactivate pathogenic microorganisms has received special attention of researchers. Recently, researchers have become interested in using low-energy electron beams and X-rays to inactivate microorganisms on food surfaces. In this study, a simulation study has been performed on eggs and potatoes with the aim of helping the food irradiation industry. Using the Geant4 Monte Carlo toolkit, the structure of eggs and potatoes and their surface bacteria has been simulated. The dose distribution in eggs and potatoes as well as the damage to the DNA of their surface bacteria has been calculated. Two types of low-energy radiation sources were compared: X-rays with a tube voltage of 50 kV, 100 kV, and 200 kV, as well as mono-energetic electron beam with an energy of 50 keV, 150 keV, and 300 keV. The results showed that low-energy X-rays are a good option for decontaminating the surface of eggs and potatoes up to a depth of 0.3 mm. In this case, sample rotation is not important, although it will lead to an improvement in the dose uniformity. Using a two-side electron beam for the surface of eggs and potatoes will not be suitable in any way. Nevertheless, in the sample rotation mode, they can be suitable up to a depth of 0.1 mm. At the microscopic scale, both types of radiation cause approximately the same amount of damage to the DNA of bacteria, and therefore, no particular advantage is observed for each of the radiation sources respect to the surface bacteria inactivation.

Keywords: Food irradiation, Microorganism inactivation, DNA damage, Geant4-DNA, Monte Carlo

Introduction

Food purification from pathogenic microorganisms is an important point in the food processing industry. Using ionizing radiation such as gamma rays of Co-60, electrons with an energy of up to 10 MeV, and X-rays with an energy of up to 5 MeV is has been used to destroy pathogenic microorganisms and enhance food safety [1]. Nowadays, there has been a high interest in low-energy X-rays (LEEX) and low-energy electron beams (LEEB) for the surface treatment of food [2]. Recently, the International Atomic Energy Agency (IAEA) proposed a coordinated research project to examine innovative techniques using low-energy beams for food irradiation [3]. Low-energy radiation is better than high-energy one for surface treatment because of the shielding and economic advantages. Many studies investigate the possibility of microorganism inactivation in food by gamma rays, LEEX and LEEB [4-8]. Monte Carlo simulation has provided an accurate and flexible environment for researchers to simulate difficult conditions that may not be performed experimentally. Brescia et al. studied the surface dose distribution of an apple irradiated with electrons of 1.0, 1.5, and 2.0 MeV using MCNP code. Different positions were investigated by rotating the apple [9]. Kim et al. developed a methodology for dose calculation of complex-shaped foods such as an apple, a chicken carcass and a broccoli, a cantaloupe, and a mango by merging 3D geometries from Computed tomography scans with MCNP5 code [10-12]. Peivaste et al. carried out a Monte Carlo simulation and experimental study to compare the dose distributions of potatoes and onions exposed to high-energy X-rays and electrons [13]. Chernyaev et al. performed a Monte Carlo simulation and experimental study to examine the effectiveness of irradiating trout with electrons and X-rays of 1 MeV energy [14]. Kataoka et al. investigated the surface dose distribution of table eggs irradiated by LEEB [15]. In our previous study, we simulated the irradiation of a typical-size apple with LEEX and LEEB, and obtained the dose distribution on a macroscopic scale [16]. In addition, we calculated the DNA damage of a surface bacterium. The current study is a continuation of that study, which this time was conducted on eggs and potatoes.

Materials and methods

The simulation was carried out in two steps: 1- Calculation of the surface dose distribution in eggs and potatoes irradiated by LEEX and LEEB. 2- Calculation of DNA damage of a surface bacterium. In the first stage, the Geant4 Monte Carlo toolkit [17] with default electromagnetic physics constructor (i.e., G4EmStandardPhysics class) was used. In the second stage, the Geant4-DNA extension [18] with default DNA physics constructor (i.e., G4EmDNAPhysics

class) was used. First, a raw egg is simulated as a double-layered oval; The outer layer, which represents the egg shell, is made of calcium carbonate ($CaCO_3$) with a density of 2.2 g/cm^3. It has a thickness of 0.25 mm. The inner volume, which represents egg white, is defined as an oval of water (1 g/cm^3) with 17.75×40.25×47.75 mm length axes. Then, a raw potato was defined as an oval made of starch ($C_6H_{10}O_5$) with a density of 1.5 g/cm^3, which has 50.6×40.15×60.1 mm length axes. Because the potato skin is very thin and lighter than its flesh, we merged them together. The source of radiation was defined exactly the same as in our previous study [16], so that it was a bremsstrahlung spectrum for LEEX (with a cut-off energy of 50, 100, and 200 keV) and mono-energetic electrons with an energy of 50, 150, and 300 keV for LEEB. These energies were adapted from the literature [5-7]. Two-side and four-side (i.e., representing the sample rotation) irradiation was simulated for each sample. Fig. 1 illustrates a potato with a two-side and four-side LEEX irradiation. The number of histories was 2×10^6 and 2×10^9 for electrons and X-rays, respectively.

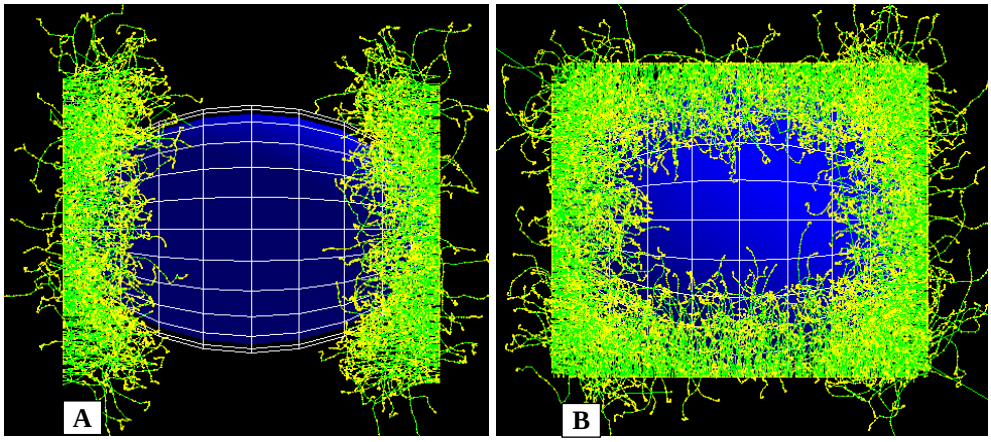

Fig. 1. Irradiating a potato with a two-side (A) and a four-side (B) X-rays.

The dose uniformity ratio (DUR) is the ratio of the maximum dose reached to the product (up to a certain depth) to its minimum dose. Ideally, this ratio should be equal to 1, but up to about 3 has been reported as acceptable for many products [19]. Since only the surface is important in this study, the depth of the sample up to 300 µm is considered. The following equation is used to calculate the DUR:

$$DUR = Dmax/Dmin \quad (1)$$

In the second stage, a simplified model of E. coli bacterium, with a genome length of 4.6 mega base pairs (Mbps) [20], was simulated as an ellipsoid of water with 0.7 µm×0.7 µm×1.5 µm half-length axes. To construct a 4.6 Mbps genome length, 21300 linear segments of DNA with

a length of 216 bp (equal to 73.4 nm), were randomly distributed in the ellipsoid. Every DNA bp is defined as a simple cylinder with a radius of 0.5 nm and a length of 0.34 nm. For simulating sugar-phosphate part of DNA, a quarter cylinder was defined with inner and outer radius of 0.5 nm and 1.185 nm, respectively. To construct the spiral shape of DNA strands, two sugar-phosphate parts on opposite sides were defined and rotated by 36 degrees respect to the bp axis. Fig. 2 shows the simulated model of E. coli. Initial particles were emitted from the bacterium surface with a cosine angular distribution.

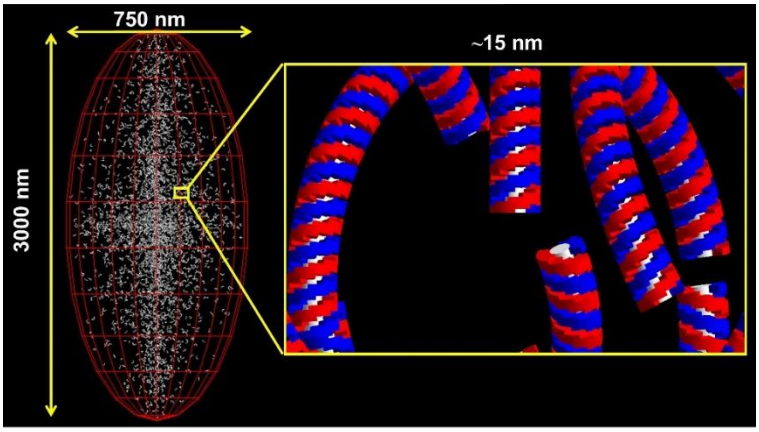

Fig. 2. E. coli bacterium modelling in Geant4 simulation toolkit.

If the energy deposited in a sugar-phosphate part was more than 17.5 eV, one single strand break (SSB) would occur. If the distance of two subsequent SSBs in opposite strands was less than 3.4 nm, one double strand break (DSB) would occur. Any damage yield is obtained by equation 1:

(2) $$\text{Damage yield } (Gy^{-1}Mbp^{-1}) = N_{break}/(D\times N_{bp}),$$

in which N_{break} is the number of breaks, D is the total absorbed dose (Gy) to the bacterium, and N_{bp} (Mbp) is the total number of bps.

Results and discussion

To validate the simulation, the range (μm) of mono-energetic electrons in water was calculated by Monte Carlo simulation and compared with reference [21]. The results are shown in Table 1.

Table 1. The range (μm) of mono-energetic electrons in water.

Energy (keV)	NIST data [21]	Geant4	Relative difference (%)
30	17.7	17.9	1.13
50	44.8	43.9	2.00

100	143.9	145.1	0.83
150	283.3	285.1	0.63
200	451.3	453.7	0.53
300	846.6	850.1	0.41
400	1294	1298	0.31

DURs up to a depth of 100 µm for eggs irradiated with LEEB of 50, 150, and 300 keV energies are given in Table 2. Please note that both 2-side and 4-side irradiation is provided. The same values for the irradiation of LEEX of 50, 100, and 200 kV tube voltages are given in Table 3. DURs for potatoes irradiated with LEEB of 50, 150, and 300 keV energies are listed in Table 4. The corresponding values in the case of LEEX irradiation are listed in Table 5.

Table 2. Dose uniformity ratios at several depths for eggs irradiated by electrons of 50, 150, and 300 keV energies with 2-side and 4-side configurations.

Depth (µm)	Energy (keV) for 2-side irradiation			Energy (keV) for 4-side irradiation		
	50	150	300	50	150	300
100	5.86	3.58	3.42	2.96	2.95	1.98
200	13.9	5.89	5.53	3.96	3.42	2.81

Table 3. Dose uniformity ratios at several depths for eggs irradiated by X-rays of 50, 100, and 200 kV tube voltages with 2-side and 4-side configurations.

Depth (µm)	Tube voltage (kV) for 2-side irradiation			Tube voltage (kV) for 4-side irradiation		
	50	100	200	50	100	200
100	1.96	2.00	2.14	1.18	1.37	1.48
200	3.46	3.48	3.65	2.60	2.20	2.39
300	3.46	3.48	3.65	3.31	3.48	3.56

Table 4. Dose uniformity ratios at several depths for potatoes irradiated by electrons of 50, 150, and 300 keV energies with 2-side and 4-side configurations.

Depth (µm)	Energy (keV) for 2-side irradiation			Energy (keV) for 4-side irradiation		
	50	150	300	50	150	300
100	N/A	13.2	8.84	6.22	2.72	1.30
200	N/A	18.4	14.6	6.22	3.24	3.12

Table 5. Dose uniformity ratios at several depths for potatoes irradiated by X-rays of 50, 100, and 200 kV tube voltages with 2-side and 4-side configurations.

Depth (µm)	Tube voltage (kV) for 2-side irradiation			Tube voltage (kV) for 4-side irradiation		
	50	100	200	50	100	200
100	1.87	1.75	1.88	1.29	1.11	1.04
200	2.46	2.32	2.35	1.77	1.93	1.33
300	2.86	2.60	2.54	2.35	2.32	1.96

The induced SSB and DSB yields in a surface bacterium irradiated by LEEX of 50, 100, and 200 keV cut-off energies are shown in Figure 3-a. The same DNA damage yields irradiated by electron beams of 50, 150, and 300 keV energies are shown in Figure 3-b.

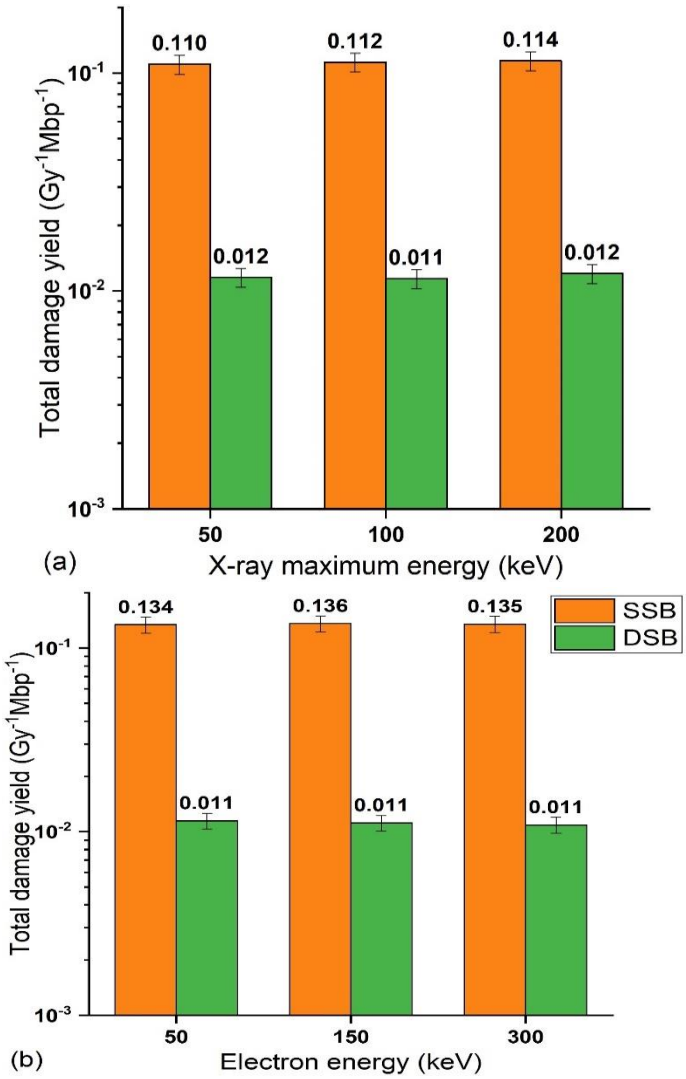

Fig. 3. The normalized DNA damage yields (single- and double-strand breaks) obtained by equation 2 caused by (a) X-rays of 50, 100, and 200 cut-off energies, as well as (b) electrons of 50, 150, and 300 keV.

According to Table 2, for foods such as eggs that have a thicker surface, a two-side LEEB irradiation with sample rotation will be a good choice to clean the surface up to a depth of 100 µm. It should be noted that electrons of 50 keV is not suitable for LEEB which is consistent with the results of [16]. However, in the case of LEEX, it can be seen in Table 3 that they can clean up to a depth of approximately 200 µm. In general, the DUR is well improve with sample rotation. Also, the DUR for LEEB is larger than that of for LEEX irradiation. According to Table 4, which shows the DUR for potatoes irradiated with LEEB, it can be well stated that

DUR is favorable only for LEEB with a four-side irradiation and also with energies greater than 50 keV. But according to DURs in Table 5, which are obtained by LEEX irradiation, they are acceptable up to a depth of 300 µm. Therefore, the final choice of the radiation source depends primarily on the desired depth, which also depends on the type of material. Generally, LEEB with energy greater than 200 keV along with a two-side irradiation with 90-degree rotation of the sample can be used for the surface treatment up to 100 µm depth. In addition, for LEEB, it should also be considered that the dimensions of foods are very important.

Figure 1-a, which represents the results of the microscopic stage, indicates that for the inactivation of surface bacteria, LEEX with tube voltages of 50, 100, and 200 kV will be suitable, since the DNA damage yield does not change significantly for each tube voltages. Therefore, assuming that each of these radiation sources delivers the required dose to the target product, it will result in a similar inactivation in the bacterial population. The destruction of bacteria by LEEB also happens well. Bacteria will be destroyed well by LEEB, according to Figure 1-b. It should be noted that for bacteria that penetrate deeper into the substance and grow and reproduce there, electron beams with higher energies should be used; Therefore, the use of LEEX has more special advantages.

Conclusions

As a conclusion, both two-side and four-side LEEX irradiation with tube voltage of 50, 100 and 200 kV have the ability to clean the surfaces of potatoes and eggs. This means that there is no need to rotate the sample during LEEX irradiation. According to the obtained DURs, electrons are suitable up to a depth of about 100 µm. For sterilization of bacteria, both LEEX and LEEB can be used, and they do not have a special advantage in this regard.

References

[1] Munir MT, Federighi M. Control of Foodborne Biological Hazards by Ionizing Radiations. Foods. 2020;9(7):878.

[2] Hertwig, C., Meneses, N., Mathys, A. Cold atmospheric pressure plasma and low energy electron beam as alternative nonthermal decontamination technologies for dry food surfaces: A review. Trends Food Sci. Technol. 2018,77, 131–142.

[3] Coordinated research activities. International Atomic Energy Agency website. https://www.iaea.org/services/coordinated-research-activities. "Innovating Radiation

Processing of Food with Low Energy Beams from Machine Sources". https://www.iaea.org/projects/crp/d61025.

[4] Kawasaki S, Saito M, Mochida M, and et al. Inactivation of Escherichia coli O157 and Salmonella Enteritidis in raw beef liver by gamma irradiation. Food Microbiol. 2019; 78:110-113.

[5] Jeong S, Marks BP, Ryser ET, and et al. Inactivation of Escherichia coli O157:H7 on lettuce, using low-energy X-ray irradiation. J Food Prot. 2010;73(3):547-551.

[6] Mahmoud BS. Effect of X-ray treatments on inoculated Escherichia coli O157: H7, Salmonella enterica, Shigella flexneri and Vibrio parahaemolyticus in ready-to-eat shrimp. Food Microbiol. 2009;26(8):860-864.

[7] Chalise PR, Hotta E, Matak KE, Jaczynski J. Inactivation kinetics of Escherichia coli by pulsed electron beam. J Food Sci. 2007;72(7):M280-M285.

[8] Gryczka, U., Madureira J., Verde S.C., Migdał, W., and Bułka, S. (2021). Determination of pepper microbial contamination for low energy e-beam irradiation. Food Microbiology, 98, 103782

[9] Brescia, G., Moreira, R., Braby, L., & Castell-Perez, E. (2003). Monte Carlo simulation and dose distribution of low energy electron irradiation of an apple. Journal of Food Engineering, 60, 31–39.

[10] Kim J, Moreira RG, Huang Y, Castell-Perez ME. (2007). 3-D dose distributions for optimum
radiation treatment planning of complex foods. Journal of Food Engineering 79: 312–21.

[11] Kim, J., Moreira, R.G., Castell-Perez, M.E., 2008. Validation of irradiation of Broccoli with a 10 MeV electron beam accelerator. Journal of Food Engineering 4, 595– 603.

[12] Kim, J., Moreira, R.G., and Braby, L. (2011). Simulation of Gamma-Ray Irradiation of Lettuce Leaves in a 137Cs Irradiator Using MCNP. Prog. in Nucl. Sci. and Technology. 2. 442-446.

[13] Peivaste, I., Alahyarizadeh, G. Comparative Study on Absorbed Dose Distribution of Potato and Onion in X-ray and Electron Beam System by MCNPX2.6 Code. MAPAN 34**,** 19–29 (2019).

[14] Chernyaev, A.P., Avdyukhina, V.M., Bliznyuk, U.A. et al. Study of the Effectiveness of Treating Trout with Electron Beam and X-Ray Radiation. Bull. Russ. Acad. Sci. Phys. 84**,** 385–390 (2020).

[15] Kataoka, N., Kawahara, D., & Sekiguchi, M. (2023). Uniform irradiation of table eggs in the shell with low-energy electron beams. Radiation Physics and Chemistry, 202, 110553.

[16] Rafiepour, P., Sina, S., & Mortazavi, S. M. J. (2023). A multiscale Monte Carlo simulation of irradiating a typical-size apple by low-energy X-rays and electron beams. Radiation Physics and Chemistry, 111016.

[17] Agostinelli, S., Allison, J., Amako, K., Apostolakis, J., Araujo, H., and et al. (2003). Geant4—a simulation toolkit. Nucl. Instruments Methods Phys. Res. Sect. A Accel. Spectrometers, Detect. Assoc. Equip. 506, 250–303.

[18] Incerti S, Baldacchino G, Bernal M, and et al. THE GEANT4-DNA PROJECT. International Journal of Modeling, Simulation, and Scientific Computing. 2010;01(02):157-78

[19] International Atomic Energy Agency (IAEA), 2002. Dosimetry for Food Irradiation. Technical Reports Series 409. International Atomic Energy Agency, Vienna, Austria.

[20] Blattner FR, Plunkett G, Bloch CA, and et al. The complete genome sequence of Escherichia coli K-12. Science. 1997;277(5331):1453-1462.

[21] Berger, M.J., Coursey, J.S., Zucker, M.A. and Chang, J., 2005. NIST Standard Reference Database 124: Stopping-Power & Range Tables for Electrons, Protons, and Helium Ions.

ICNST 2024 International Conference on Nuclear Science and Technology
6 - 8 MAY 2024 | Isfahan, Iran

Calculations and analysis of effective parameters to produce a diamond sample as a maximum temperature crystal sensor (Paper ID : 1208)

Hasanzadeh M[1] and Rahimian A[1*]

1. Nuclear Science and Technology Research Institute (NSTRI), Tehran, Iran

Abstract

The use of maximum temperature crystal sensors (MTCS) is one technique that has drawn a lot of attention in the design and optimization of engines and turbines with high efficiency. Because of their tiny size, these sensors can be positioned anywhere inside the turbine to detect the highest temperature. It should be mentioned that the production of these sensors requires a high fluence with fast neutrons flux. The phenomenon of high temperature to repair the modifications produced to the crystal lattice by neutron radiation is the basis of the MTCS measurement technique. In this article, first, through the simulation of the core of the Tehran research reactor (TRR), calculations of the maximum flux of fast neutrons for the diamond sample were carried out with MCNP6 code. Also, activity calculations were done using ORIGEN2 code. The maximum flux of fast neutrons is calculated and the sample's activity dropped dramatically after 40 days, and the dose rate approached 1.4 μSv/h at a meter's distance. In this article, the lattice number and unit cell volume for the diamond sample were determined using the XRD method. The obtained results indicate that the diamond sample can be recommended for the fabrication of crystal sensors in the TRR from the perspectives of neutronics, dosimetry, and changes in crystal lattice structure.

Keywords: Crystal sensor, MCNP6 code, ORIGEN2, XRD method, Tehran research reactor

1. Introduction

The construction and design of engines and turbines with high efficiency, in such a way that they can withstand more heat, is one of the important challenges of automobile, turbine and space industries. The efficiency of engines increases with the increase of their working temperature, but this increase is limited by the characteristics of the materials used. In other words, in order to have more efficiency, the working temperature of the engine must be increased, but this increase is possible to such an extent that the properties of the used materials do not change. An increase in temperature causes a decrease in strength, so it is necessary to

find an effective method for cooling the system that is monitored by temperature sensors. Nowadays, with the complexity of devices and systems, the conditions and requirements of sensors to measure suitable temperature must also become more difficult and complicated. For example, the ability to work at high temperature, high temperature resolution, and small dimensions with negligible effect on system operation are the requirements of a suitable temperature sensor [1].

Temperature measurement methods are divided into contact and non-contact categories based on the reading mechanism. The use of each of these methods has its own advantages and disadvantages depending on the type of application. Contact methods refer to methods in which the sensor is connected to the reader with an electrical connection. One of the advantages of this method is the continuous recording of temperature, and its disadvantages are its complexity and cost. Among these types of sensors, we can refer to types of thermocouples, resistance sensors and thin layer resistance sensors. Non-contact devices include molten metal thermometers, thermal paints and maximum temperature crystal sensor (MTCS) [2].

Non-contact methods allow measuring the maximum temperature after the test and removing the sensor from the installed place and performing the analysis. Therefore, one of the most advanced methods of temperature measurement is the use of maximum temperature crystal sensors. These sensors are mainly used to measure the maximum temperature in constant conditions. These sensors can be used to measure the maximum temperature in a transient state if we know the temperature changes with time [2-4].

The process of these sensors is that the crystalline network of the crystal expands due to neutron irradiation, and when it is heated, this expansion decreases in proportion to the maximum temperature and the time it was at that temperature. By measuring the parameters of the crystal lattice before and after receiving heat, it is possible to accurately detect a temperature of about a few degrees up to more than 1400 degrees Celsius. To produce these sensors, a very high fluence of fast neutrons is required. Therefore, the maximum temperature crystal sensor method is based on the high temperature phenomenon to restore the changes made in the crystal lattice caused by neutron radiation. There are many materials that experience a crystal lattice change due to neutron radiation, including: diamond, 3C-SiC, graphite, beryllium oxide, alumina oxide, boron nitride, boron carbide and some others [5].

Diamond is made of carbon and is basically one of the allotropes of carbon. According to most sources, the diamond crystal lattice is cubic. In diamond, each carbon atom is connected to four other carbon atoms by four single bonds. In this case, the carbon atom has a tetrahedral structure with a bond angle of 109.5 degrees, and all four carbon atoms attached to it are placed in the four corners of a tetrahedron. The main crystallographic planes of diamond are cubic, dodecahedron and octahedron. It should be mentioned that the diamond shape is an allotropic form of carbon [6].

According to the concentration of impurity compounds present in the diamond sample through experimental measurement with the XRF method according to Table 5, the impurities in the sample have been measured. Therefore, according to this table, its purity is around 99.14%. By studying and checking the sources, it is clear that this amount of impurity in the chemical composition of diamond is not more than normal. Usually, around 0.05 to 0.10 percent impurity is mentioned for diamonds.

Table 5. XRF analysis of natural diamond samples

	Composition	Concentration(ppm)	intensity
1	SiO_2	0.49	37.7
2	SO_3	0.16	27.9
3	CaO	0.13	136.7
4	Fe_2O_3	350	158.6
5	CuO	250	48.2
6	ZnO	100	26.1
7	ZrO_2	100	129.3

2. Procedure

Due to the necessity of calculating the neutron flux and the total dose rate are required. In this article, the MCNP6 code [10] is used to determine the neutron flux and the total dose rate, and the ORIGEN2 code [11] is used to calculate activity.

To use the diamond sample as a maximum temperature crystal sensor, it is irradiated in the Tehran research reactor, this sample should be irradiated with a neutron flux of $2x10^{20}$ n/cm^2 in one of the irradiation channels of the Tehran research reactor core with a fast neutron flux [1, 3]. Also, the amount of fast neutron flux should be calculated to determine the irradiation

time, temperature changes inside the irradiation channel, and the activity level of the diamond sample after irradiation. As mentioned, this material measures the temperature in the range from 100 to 900 ˚C, which increases the volume of the crystal network from 2.5 to 3%. The error of crystal lattice volume increase is 0.01-0.02% [3].

In Figure 8, the core number 18 includes a plate fuel arrangement made of U_3O_8Al with a richness of less than 20%, water as cooling and moderator, graphite as a reflector, special channels for irradiation.

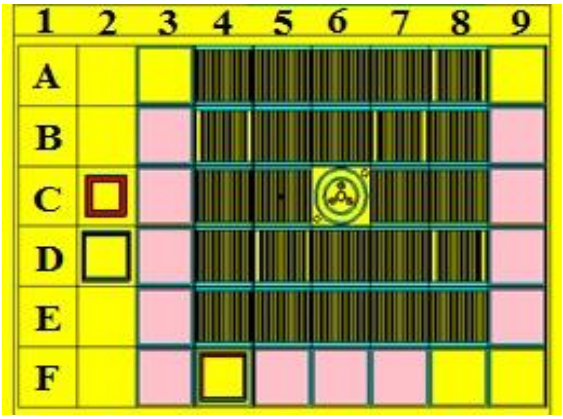

Figure 8: Core No. 18 of Tehran Research Reactor

3. Results

3.1. Calculation of fast neutron flux

According to the results presented in literature [1], finding the maximum flux of fast neutrons at high energy E> 0.18 MeV is necessary for the feasibility of making a maximum temperature crystal sensor. Therefore, first, the flux values of fast neutrons for different irradiation channels were calculated using the F4 command in the MCNP6 code, the results of which are shown in Figure 9. The calculation results show that channel F8 has the highest fast neutron flux (7.74×10^{12} n/cm^2.s), which can be suitable for a crystal sensor.

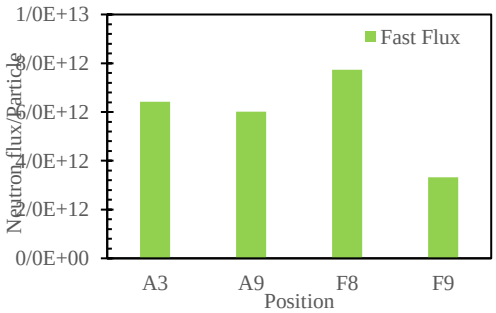

Figure 9: Fast neutron flux values for different radiation channels in Tehran research reactor.

The values of fast neutron flux in the axial direction have been calculated for core number 18 and for channel F8 in Tehran research reactor, which is shown in Figure 10. The active height of the fuel plate is approximately 61.5 cm. The dimensions of the irradiation box are 61.5 × 8 × 1.7 cubic centimeters. According to the calculations, the maximum fast neutron flux is located at the height in front of the core, that is, at a height of 10 cm, at a distance of -5 to -15 cm near the core (this is the optimal height compared to the center of the height of the fuel plate in the core). Its maximum value is approximately 4.0 $\times 10^{13}$ n/cm^2.s. Of course, it should be mentioned that the neutron flux values depend on the position of the control rods and the distance to the center of the core. The smaller the distance from the core center, the higher the values will be. In these calculations, the error value of the fast neutron flux resulting from the code is less than 1% and the ENDF/VII library available in the code is used.

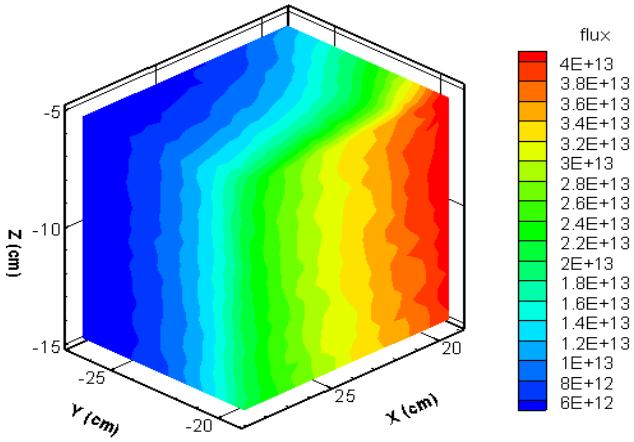

Figure 10: Fast neutron flux values in the axial direction for core number 18 and for box F8 in Tehran research reactor

As stated before, the amount of neutron fluence required to produce this sensor is 2×10^{20} n/cm^2. Therefore, according to the maximum fast neutron flux of about 1×13 n/cm^2.s calculated for channel F8 of Tehran reactor, the minimum time required for continuous irradiation of diamond samples inside the core of Tehran reactor is 232 days.

3.2. Total dose rate Calculation

The amount of diamond sample dose at different cooling times was investigated. Since in the MTCS technique, the diamond sample is subjected to neutron irradiation, activation of the

sample (due to the presence of impurities) is inevitable. The challenge at this stage is the amount of sample dose after discharge from the reactor.

For this purpose, first, the sample photon spectrum (continuous spectrum) of 18 photon groups in the time period of 0 and 40 days from the cooling time was extracted using the ORIGEN2 code, and then it was given to the MCNP6 code as an input for dosimetry calculations. The simulation continued in electron and photon modes until all statistical parameters were passed. Photon dosimetry calculations were performed for 1.6 grams of natural diamond sample at different distances from the sample. Figure 11 shows the dose drop graph at different distances from the sample and at cooling times between 0 and 40 days. The simulation data show that the dose rate of the sample after 0 and 40 days of cooling time will drop by 21 µSv/h and 1.4 µSv/h per hour at a distance of one meter from it, respectively.

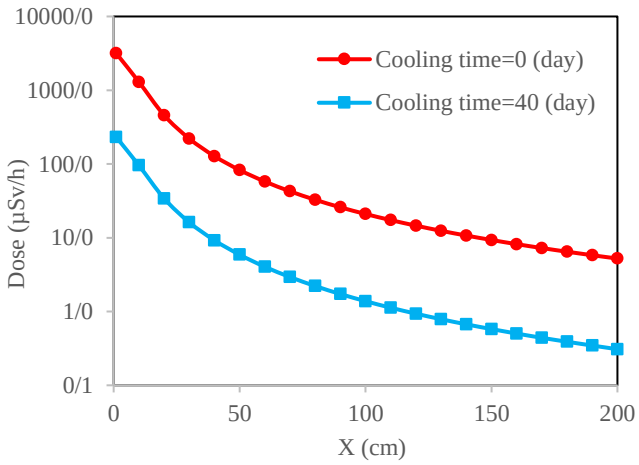

Figure 11: Diamond sample dose rate at different intervals based on cooling time

The experimental value of the dose rate of the diamond sample after two months of continuous irradiation was measured at the place attached to the sample using ALNOR gamma dosimeter, which was about 5 mSv/h. The measurement range of this dosimeter is from 0.05 µSv/h to 10 Sv/h and its measurement accuracy is ±15%. In the results of the simulation, this value was obtained at the same place with the same duration of irradiation of about 2.3 mSv/h, which is much lower compared to the values of the experimental results. The reasons for the error can be many things, including activation of the sample container due to the presence of aluminum, calculation error, difference in the measurement location, error of the dosimeter, error in the amount of reactor power, exact duration of irradiation and another physical condition.

3.3. Lattice parameter calculation

To identify the phases in a material with the help of XRD patterns, at least 2 or 3 peaks are required. The XRD pattern of the sample prepared for the diamond sample is shown in Figure 12. By measuring the diffraction angle of different crystal planes from the XRD diagram, the distance between the crystal planes (d) is obtained from Bragg's relation. The lattice constants can be calculated with d. In order to accurately determine the lattice constants, the peaks located at higher angles should also be included in the XRD pattern. In this way, the measured constants will be closer to the real values.

But recording a peak at high angles is often not possible. For example, in the diffractometry method, usually the counter moves only within the range of angle up to θ2 = 160°. The common method is to draw the constant values of the lattice in terms of θ2 and continue the obtained graph up to an angle of 180° to obtain the constant value of the lattice up to an angle of 180°. But since the obtained graph is not linear, it is not possible to accurately extrapolate the curve in the above way. Therefore, instead of θ2, the constant value of the network can be plotted as a function of θ so that the graph becomes a straight line.

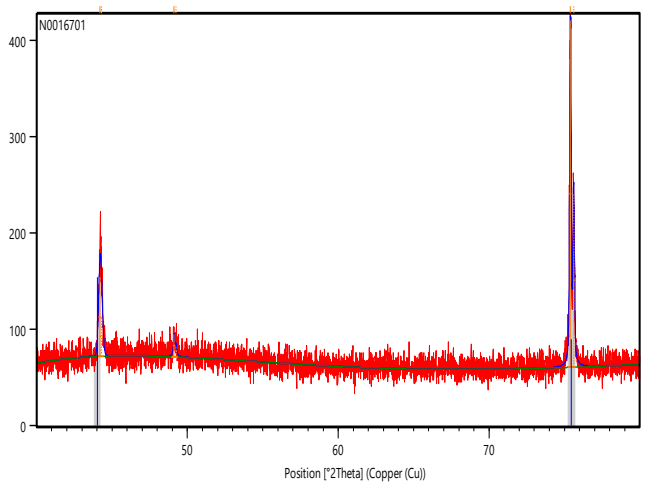

Figure 12: X-ray diffraction pattern of diamond sample

Figure 12 shows the X-ray diffraction pattern of the diamond sample. Two peaks were detected at the angles of θ=244° and θ=275°. Using the Miller indices (relation 2) related to diamond, which is equal to (111) at 2θ=44° and equals (220) at 2θ=75°, a_0 or lattice parameter by the relation (3) which is shown in Table 2, is obtained. In order to obtain the lattice parameters, the sum of squares method is used. As a result, the lattice parameter value is calculated as follows.

Table 6 .The measured values of d, Θ2 and a_0

d	2θ	a_0
1.25962	75.4007	3.562743
2.04628	44.2265	3.544261
2.04789	44.1899	3.54705
1.25991	75.3806	3.563564

For the cubic unit cell, the lattice parameters are: a=b=c and α=β=γ=90°; Therefore, the sum of the cubic unit cell will be $V=a^3$.

$V= (3.5544)^3 = 44.9054$ (Å)

4. Conclusion

In this article, diamond material was selected as the non-contact maximum temperature crystal sensor material. The application of these sensors is that they can be placed in inaccessible places, for example, inside the turbine or engine and measure the maximum temperature created. Therefore, according to the dimensions of these sensors and the very high accuracy of the measurement, a very accurate spatial distribution of the created temperature can be obtained.

Therefore, the simulation of the reactor core and calculations related to the neutron flux were performed in order to find the maximum fast flux and shorten the irradiation time. Also, dose rate calculations were performed to predict the amount of activity after irradiation inside the channel with the desired codes, and the results showed that after about 40 days, the amount of total dose rate and activity of the sample decreases drastically. Also, based on the results of the XRD test, the lattice parameters and unit cell volume were calculated. Finally, it can be shown that in order to reach the neutron fluence value of 2×10^{20} n/cm^2, according to the maximum fast neutron flux of about 1×10^{13} n/cm^2.s in channel F8, the time required for continuous irradiation of the diamond sample inside the Tehran reactor core is at least 232 days.

5. References

1. Volinsky, A.A., et al., Irradiated Single Crystals for High Temperature Measurements in Space Applications. MRS Online Proceedings Library (OPL), 2004. **851**: p. NN1. 4.
2. Rai, V.K., Temperature sensors and optical sensors. Applied Physics B, 2007. **88**: p. 297-303.

3. Kuryachiy, V.G., Irradiated single crystal 3C-SiC as a maximum temperature sensor. 2008.
4. Haile, E. and J. Lepkowski, Oscillator circuits for RTD temperature sensors. Application note AN895, Microchip Technology Inc, 2004: p. 21-22.
5. Nikolaenko, V. and V. Karpukhin, Temperature measurement by means of irradiated materials. 1986.
6. Raafat, A., Radiation damage of diamond and its application to the determination of the temperature in pile. 1977, Ustav Jaderneho Vyzkumu CSKAE.

ICNST 2024
International Conference on Nuclear Science and Technology
6 - 8 MAY 2024 | Isfahan, Iran

Synthesis and quality control of Methylene Diphosphonic acid (MDP) as an active ingredient of bone imaging after labeling with Technetium-99m (Paper ID : 1211)

Maryam Rezaei1*, Mostafa Erfani, Sima Attar Nosrati, Mostafa Goudarzi, Saeed Kakaei, Masood Mola

[1]*Radiation Application Research School, Nuclear Science and Technology Research Institute (NSTRI), Tehran, Iran*

Abstract

This research aimed to synthesis a bisphosphonate derivative Methylene Di phosphonic acid (MDP). Diethyl phosphite [(EtO)2PHO] is converted to sodium diethyl phosphite [(EtO)2PONa] using NaH by heat treatment. In the next step, Tetraethyl methylene diphosphonate is derived from addition of Dichloromethane. Then the resulted phosphonate is hydrolyzed with HCl(conc.). The title compound is achieved in good yield after recrystallization. In quality control tests, high bone uptake followed by rapid blood clearance are two important characteristics for prepared product labeled with technetium-99m as an ideal bone imaging agent.

Keywords: MDP, Bisphosphonate, Bone imaging

INTRODUCTION

The skeleton is one of the most common organs to be affected by metastatic cancer. Carcinomas of Breast, lung, prostate, kidney, and thyroid have a tendency to easily metastasize to bone. Although there has been significant advancement in imaging technologies, such as CT and MR, nuclear medicine bone imaging has been the optimum diagnosis for the detection of bone disorders such as bone metastases, because of its high sensitivity. Namely, bone-seeking radiopharmaceuticals usually localize in skeletal lesions before the appearance of symptomatic and radiographic changes and the resulting easy evaluation of the entire skeleton [1].

Technetium-99m radiopharmaceuticals play an important role in wide range of applications in nuclear medicine. Bone imaging agents are among the first developed ^{99m}Tc-radiopharmaceuticals and the most widely used them in diagnostic nuclear medicine [2]. The first bone-seeking ^{99m}Tc-compound, a complex of reduced technetium-99m and sodium tripolyphosphate, was reported in 1971, followed by a long chain linear polyphosphate and

pyrophosphate. Pyrophosphate is composed of only two phosphate moieties and is the simplest polyphosphate. Unfortunately, pyrophosphate and polyphosphate are susceptible to in vivo degradation by enzymes such as alkaline phosphatases, resulting in the release of free technetium from the complexes [3]. Bisphosphonates (BPs) are synthetic organic compounds characterized by a P-C-P backbone structure. They are chemically stable analogues of the endogenous metabolites, inorganic pyrophosphates. The biological effects of BPs on calcium metabolism were originally ascribed to their physicochemical effects to impede the dissolution of hydroxyapatite crystals. Because of their inhibitory effect on the bone resorption, various types of BPs are used in bone scanning, and provide an effective way of diagnosis of primary bone cancer, metastatic bone disease, Paget's disease, Osteoporosis, bone trauma, etc. [4].

^{99m}Tc-Methylene diphosphonic acid (MDP) was introduced by Subramanian 1n 1973 which showed superior biodistribution compared to other BPs. In the clinical studies an interval of 2 to 6 hours is required between an injection of ^{99m}Tc-labelled bisphosphonates and obtaining bone images. Although the accumulation of bisphosphonate compounds in bone is achieved by binding the phosphonate groups with the Ca^{2+} of hydroxyapatite crystals [5]. The phosphonate group in ^{99m}Tc-MDP serve as both coordinating ligands and Ca^{2+} binding functional group [6] which might decrease the inherent accumulation of it in bone P. Nylen synthesized methylene diphosphonic acid (MDP) for the first time in 1930.Among the methods described for the formation of carbon phosphorus bond Michaelis-Arbuzov [7] and Michaelis-Becker reactions represent the easiest and more used synthetic pathways toward the obtaining of phosphonate. To continue the previous efforts to improve logical design for synthesis of BPs have been proposed.

This manuscript describes the synthesis of methylene diphosphonic acid (MDP) and investigate its radiolabeling abilities with technetium-99m. Subsequently preliminary in vivo studies in rats as a convenient bone-seeking agent is performed.

EXPERIMENTAL

Materials and measurements

All chemical reagents and solvents were supplied by Sigma-Aldrich and Merck Co..NMR spectra Were acquired using VARIAN-INOVA 500 MHz (500 MHz for ^{1}H and 125 MHz for ^{13}C. Chemical shifts δ were expressed in ppm relative to tetramethyl silane (TMS).as an

internal standard.The mass spectra were recorded on a Agilent Technology (HP) mass spectrometer equipped with a combined electron impact/chemical ionization source .(MS Model :5973 Network Mass Selective Detector) The source condition were: temperature 230 ^{o} C, electron energy 70 EV .Melting point(MP) determination was performed using a digital melting point instrument from Stuart model SMP3.

Synthesis of Methylene Di Phosphonic acid (MDP)

Diethyl phosphite was added to the reaction mixture of sodium hydride and tetrahydrofuran , maintaining the temperature below 60 ^{o} C .After the addition was complete , the reaction mixture mas cooled to and charged sequentially with dimethylformamide and dichloromethane .The reaction mixture was stirred overnight. The reaction mixture was quenched with H2O. The resulting solution was extracted with dichloromethane. The organic layers were combined and dried over magnesium sulfate. The dichloromethane was evaporated to produce tetraethyl methylene bisphosphonate. It could be purified by vacuum distillation. BP=128^{o}C

^{1}HNMR(D_2O): 1.35(t,12 H, P-O-C-CH_3), 2.45 (t,2H, P-CH_2-P), 4.15 (d q, 8H, P-O-CH_2)

^{13}CNMR(D_2O):16.4 (P-O-C-CH_3), 25.7(t, P-C-P), 62.55(P-O-CH_2)

^{31}PNMR(D_2O) :19.05

m/z:289,288(M. $^{+}$),261,243,233,215,205,187/177,159,152(100%),141,125,97

It was treated with concentrated HCl , left for 12 h at room temperature and reflux for 4 h. The solution was concentrated. and the residue was dissolved in H_2O and concentrated, treated with AcOH and allow to stand at room temperature. The solid product was separated by filtration and washed with AcOH to produce the corresponding product up to %70 yield. MP=199-201 ^{o} C

^{1}HNMR(D_2O): 2.525 (t,2H, P-CH_2-P)

^{13}CNMR(D2O): 25.9(t, P-C-P)

^{31}PNMR(D_2O) :16.7

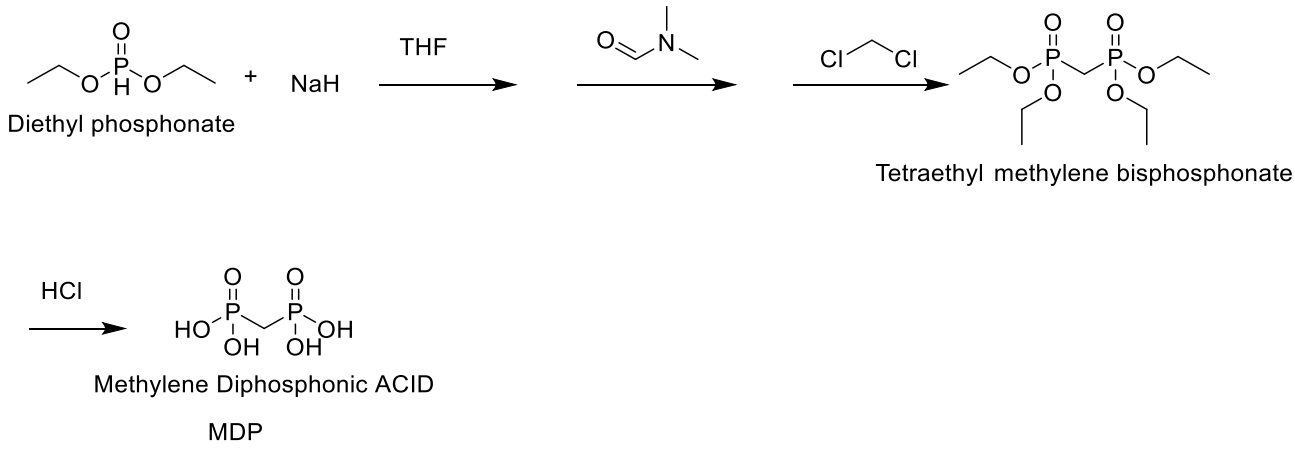

Scheme.1

Results and discussion

Mono- and polymethylenediphosphonic acids can be prepared in nearly quantitative yield by the hydrolysis of the corresponding tetra-alkyl esters with conc.HCl:

$$(RO)_2OP(CH_2)\ n\ PO(OR)_2 + 4HCl \rightarrow (HO)_2OP(CH_2)\ n\ PO(OH)_2 \qquad (1)$$

Recrystallization usually yields the acids in a very pure state. The tetra alkyl esters of mono- and polymethylenediphosphonic acids required for the above hydrolysis reaction can be prepared by either one of two general reactions (X: Halid, M: Alkali metal):

$$X(CH_2)X + 2MOP(OR)_2 \rightarrow (RO)_2OP(CH_2)_n\ PO(OR)_2 \qquad (2)$$

$$X(CH_2)X + 2P(OR)_3 \rightarrow (RO)_2OP(CH_2)_2\ PO(OR)_2 \qquad (3)$$

Equation (2) is a Michaelis-Becker-type reaction and equation (3) is an Arbuzov-Michaelis reaction.

For the preparation of methylene diphosphonates with n=1 or 2 a variation of the Michaelis-Becker is applicable. The method is based on a stepwise of the molecule. Suitable compounds are first made with one P-C bond in the molecule, which are subsequently reacted with dialkyl phosphite salts to give the desired diphosphonates.

The compound tetraethyl methylene bisphosphonate of formula(I)

(CH_3CH_2O) -P(O)-CH_2-P(O)-(OCH_2CH_3)

is a useful intermediate for a variety of purposes. For instance, certain aza bisphosphonic acid compounds are described in PCT application number WO95/10188 as having herbicidal activity. An intermediate in the synthetic generation of these bisphosphonic acids is tetraethyl methylene bisphosphonate.

In addition to the above utility, tetraethyl methylene bisphosphonate may be converted to ethylidene bisphosphonate which is useful as a pharmaceutical intermediate and as a monomer for the preparation of phosphorous containing polymers.

Tetraethyl methylene bisphosphonate was prepared according to the method of G.M.Kosolapof (8). The synthesis from methyl iodide and triethyl phosphite ied to a reasonably pure product in %18 yield.

Tetraethyl methylene bisphosphonate was synthesized as described O.E.O.Homi (9).It was achieved in two weeks with %50 yield.

It would be desirable to reduce the reaction time and increase the yield of tetraethyl methylene bisphosphonate over the above procedures.

This paper describes that employing polar aprotic solvents or mixtures thereof, can decreases the reaction time and the product yield.

The preferred reaction temperature is between 25-60 ^{o} C.

Conclusions

In this research we have prepared methylene diphosphonate which after labeling with technetium-99m can be used for bone Scintigraphy to distinguish skeletal metastasis. The results showed that yields are comparable or generally higher than the similar preparation reactions and methods. According to the results sum up in this article, the cost-effectiveness and easy preparation of raw material for common bone radiopharmaceutical can be shown..Subsequently we are performing its radiolabeling with ^{99m}Tc and investigating in vivo studies in rats.

Acknowledgements

The supports by Nuclear Science and Technology Research Institute, Tehran, Iran, is gratefully acknowledged.

References

[1]Ogawa.K.,Saji.H.,(2011) Advances in Drug Design of Radiometal-Based Imaging Agents for Bone Disorders. International Journal of Molecular Imaging, 2011:1-7.

[2] Trzpizur,D.,Brodzka,A.;Koszelewski,D.Ostaszewski,R.Selective Esterification of Phosphonic Acids,Molecules2021,26,5637.

[3]Subramanian.G and MacAfee.J.G.Bell,B.G.,Blair,R.J.,R.E.O'Mara,and P.H.Ralston.(1972) "99mTc-labeled polyphosphate as a skeletal imaging" Radiology,102,no.3,pp.701-704

[4].K.Libson,Deutsch.E.,and Barnett.B.L.,(1980) Structural characterization of a ^{99}Tc-diphosphonate complex.Implications for the chemistryof ^{99m}Tc skeletal imaging agents,Journal of the American Chemical Society ,102,no.7,pp.2476-2478.

[5]Ilia.G.,Petric.M.Balint.E.Kglevich.G.(2015) Synthesis of the mixed alkyl esters of phenylphosphonic acid by two variations of the Atherton-Todd protocol.Heteroat.Chem.26.29.

[6]Verbelen.B.Dehaen.W.Binnemans.K.(2018) Selective substitution of $POCl_3$ with organometallic reagents:Synthesis of phosphinates and phosphonates.Synthesis.

[7].Kem.K.M.Nguyen.N.V.Cross.D.J.(1981) Phase-transfer-catalyzed Michaelis-Becker reaction.J.Org. Chem.46.5188.

[8].G.M.Kosolapoff.(1952) The chemistry of aliphatic phosphonic acuds,L alkylation of methanediphosphonic acid. J.Am. Chem.Society, vol75,1500-1501.

[9]O.E.O.Homi.(1990) A cheap one-pot approach to tetraethyl methylene diphosphonate. Synthetic communications,20(12),1865-1867.